RC
Range
Commanders
Council

EIGHTEENTH TRANSDUCER WORKSHOP

20 - 22 JUNE 1995

COLORADO SPRINGS, COLORADO

TELEMETRY GROUP
**WHITE SANDS MISSILE RANGE
KWAJALEIN MISSILE RANGE
YUMA PROVING GROUND
DUGWAY PROVING GROUND
COMBAT SYSTEMS TEST ACTIVITY**

**ATLANTIC FLEET WEAPONS TRAINING FACILITY
NAVAL AIR WARFARE CENTER WEAPONS DIVISION
NAVAL AIR WARFARE CENTER AIRCRAFT DIVISION
NAVAL UNDERSEA WARFARE CENTER DIVISION, NEWPORT
PACIFIC MISSILE RANGE FACILITY**

**30TH SPACE WING
45TH SPACE WING
AIR FORCE FLIGHT TEST CENTER
AIR FORCE DEVELOPMENT TEST CENTER
AIR FORCE WEAPONS AND TACTICS CENTER
SPACE AND MISSILE SYSTEMS CENTER,
SPACE TEST AND EXPERIMENTATION PROGRAM OFFICE
ARNOLD ENGINEERING DEVELOPMENT CENTER**

REPORT DOCUMENTATION PAGE

*Form Approved
OMB No. 0704-0188*

1. AGENCY USE ONLY *(Leave blank)*	2. REPORT DATE	3. REPORT TYPE AND DATES COVERED
	June 1995	

4. TITLE AND SUBTITLE

EIGHTEENTH TRANSDUCER WORKSHOP

5. FUNDING NUMBERS

6. AUTHOR(S)

7. PERFORMING ORGANIZATION NAME(S) AND ADDRESS(ES)

Telemetry Group
Range Commanders Council
White Sands Missile Range, NM 88002-5110

8. PERFORMING ORGANIZATION REPORT NUMBER

NA

9. SPONSORING / MONITORING AGENCY NAME(S) AND ADDRESS(ES)

STEWS-RCC
Range Commanders Council
White Sands Missile Range, NM 88002-5110

10. SPONSORING / MONITORING AGENCY REPORT NUMBER

NA

11. SUPPLEMENTARY NOTES

NEW DOCUMENT.

12a. DISTRIBUTION / AVAILABILITY STATEMENT

APPROVED FOR PUBLIC RELEASE:
DISTRIBUTION IS UNLIMITED.

12b. DISTRIBUTION CODE

13. ABSTRACT *(Maximum 200 words)*

This document contains papers presented at the Eighteenth Transducer Workshop. This document has been published for information purposes only. The material contained herein does not necessarily represent the position or conclusions of the Range Commanders Council.

DTIC
SELECTED
JUN 0,6 1995
B

14. SUBJECT TERMS

transducer

15. NUMBER OF PAGES

380

16. PRICE CODE

17. SECURITY CLASSIFICATION OF REPORT	18. SECURITY CLASSIFICATION OF THIS PAGE	19. SECURITY CLASSIFICATION OF ABSTRACT	20. LIMITATION OF ABSTRACT
UNCLAS	UNCLAS	UNCLAS	NONE

The Report Documentation Page (RDP) is used in announcing and cataloging reports. It is important that this information be consistent with the rest of the report, particularly the cover and title page. Instructions for filling in each block of the form follow. It is important to *stay within the lines* to meet *optical scanning requirements.*

Block 1. Agency Use Only *(Leave blank)*.

Block 2. Report Date. Full publication date including day, month, and year, if available (e.g. 1 Jan 88). Must cite at least the year.

Block 3. Type of Report and Dates Covered. State whether report is interim, final, etc. If applicable, enter inclusive report dates (e.g. 10 Jun 87 - 30 Jun 88).

Block 4. Title and Subtitle. A title is taken from the part of the report that provides the most meaningful and complete information. When a report is prepared in more than one volume, repeat the primary title, add volume number, and include subtitle for the specific volume. On classified documents enter the title classification in parentheses.

Block 5. Funding Numbers. To include contract and grant numbers; may include program element number(s), project number(s), task number(s), and work unit number(s). Use the following labels:

C	- Contract	PR	- Project
G	- Grant	TA	- Task
PE	- Program Element	WU	- Work Unit Accession No.

Block 6. Author(s). Name(s) of person(s) responsible for writing the report, performing the research, or credited with the content of the report. If editor or compiler, this should follow the name(s).

Block 7. Performing Organization Name(s) and Address(es). Self-explanatory.

Block 8. Performing Organization Report Number. Enter the unique alphanumeric report number(s) assigned by the organization performing the report.

Block 9. Sponsoring/Monitoring Agency Name(s) and Address(es). Self-explanatory.

Block 10. Sponsoring/Monitoring Agency Report Number. *(If known)*

Block 11. Supplementary Notes. Enter information not included elsewhere such as: Prepared in cooperation with...; Trans. of...; To be published in.... When a report is revised, include a statement whether the new report supersedes or supplements the older report.

Block 12a. Distribution/Availability Statement. Denotes public availability or limitations. Cite any availability to the public. Enter additional limitations or special markings in all capitals (e.g. NOFORN, REL, ITAR).

DOD	-	See DoDD 5230.24, "Distribution Statements on Technical Documents."
DOE	-	See authorities.
NASA	-	See Handbook NHB 2200.2.
NTIS	-	Leave blank.

Block 12b. Distribution Code.

DOD	-	Leave blank.
DOE	-	Enter DOE distribution categories from the Standard Distribution for Unclassified Scientific and Technical Reports.
NASA	-	Leave blank.
NTIS	-	Leave blank.

Block 13. Abstract. Include a brief *(Maximum 200 words)* factual summary of the most significant information contained in the report.

Block 14. Subject Terms. Keywords or phrases identifying major subjects in the report.

Block 15. Number of Pages. Enter the total number of pages.

Block 16. Price Code. Enter appropriate price code *(NTIS only)*.

Blocks 17. - 19. Security Classifications. Self-explanatory. Enter U.S. Security Classification in accordance with U.S. Security Regulations (i.e., UNCLASSIFIED). If form contains classified information, stamp classification on the top and bottom of the page.

Block 20. Limitation of Abstract. This block must be completed to assign a limitation to the abstract. Enter either UL (unlimited) or SAR (same as report). An entry in this block is necessary if the abstract is to be limited. If blank, the abstract is assumed to be unlimited.

EIGHTEENTH TRANSDUCER WORKSHOP

20 - 22 JUNE 1995

COLORADO SPRINGS, COLORADO

VEHICULAR INSTRUMENTATION/TRANSDUCER COMMITTEE

TELEMETRY GROUP
RANGE COMMANDERS COUNCIL

Published and Distributed by

Secretariat
Range Commanders Council
White Sands Missile Range, NM 88002-5110

DISCLAIMER

THIS DOCUMENT HAS BEEN PUBLISHED FOR
INFORMATION PURPOSES ONLY. THE MATERIAL
CONTAINED HEREIN DOES NOT NECESSARILY
REPRESENT THE POSITION OR CONCLUSIONS OF
THE RANGE COMMANDERS COUNCIL (RCC).

TABLE OF CONTENTS

TABLE OF CONTENTS (CONT'D)

TABLE OF CONTENTS (CONT'D)

TELEMETRY GROUP COMMITTEES

Chairman Norm Lantz (SMC (STEPO))
Vice Chairman Ray Faulstich (YPG)

Data Multiplex
RF Systems
Recorder/Reproducer
Vehicular Instrumentation/Transducer

MEMBERSHIP OF THE VEHICULAR
INSTRUMENTATION/TRANSDUCER COMMITTEE

Steve F. Kuehn (Chairman)
Sandia National Laboratories
P.O. Box 5800
Albuquerque, NM 87185-0319

John T. Ach
Wright Laboratory
WL/FIB
2130 Eighth STE 11
Wright Patterson AFB, OH 45433-5723

Daniel S. Skelley
Naval Air Warfare Center
  Aircraft Division
Test & Evaluation Group
Test Article Preparation Dept.
Code 542000A Hanger 101 Mail Stop 1
Patuxent River, MD 20670-5304

Gary D. Bartlett
Naval Air Warfare Center
  Weapons Division
NAWCWPNS Code 411230D
China Lake, CA 93555-6001

Kenneth F. Temple, Jr.
Air Force Flight Test Center
412 TW/TSID
25 N. Wolfe Ave
Edwards AFB, CA 93524-8300

Norm Rector
Lawrence Livermore National
  Laboratory
P.O. Box 808
Livermore, CA 94550

John Rupp
U.S. Army Dugway Proving Ground
West Desert Test Center
STEDP-WD-TS
Dugway, UT 84022-5000

Mark A. Long
Naval Air Warfare Center
  Aircraft Division
Test & Evaluation Group
Test Article Preparation Dept.
Code 542110A Hanger 101 Mail Stop 1
Patuxent River, MD 20670-5304

Raymond J. Faulstich
U.S. Army Yuma Proving Ground
STEYP-RS-EL
Yuma, AZ 85365-9110

TRANSDUCER COMMITTEE OBJECTIVES

This committee apprises the Telemetry Group (TG) of significant progress in the field of transducers used in telemetry systems; maintains any necessary liaison between the TG and the National Institute of Standards and Technology and their transducers' program or other related telemetry transducer efforts; coordinates TG activities with other professional technical groups; collects and passes on information on techniques of measurement, evaluation, reliability, calibration, reporting and manufacturing; recommends uniform practices for calibration, testing and evaluation of vehicular instrumentation components; and contributes to standards in the area of vehicular instrumentation.

Transducer Workshop Summary

Workshop Number	Date	Host	General Chairman	Number Attendees	RCC TG Transducer Chairman
1	March 1960	Albuquerque, NM			
2	25-26 July 1961	Holloman AFB Alamogordo, NM	W. H. Sanders Holloman AFB, NM	46	Paul Polishuk Wright-Patterson Dayton, OH
3	21-23 June 1962	NBS Washington, DC	Arnold Wexler NBS Washington, DC	106	Paul Polishuk Wright-Patterson Dayton, OH
4	18-19 June 1964	Wright-Patterson Dayton, OH	Jack Lynch NATC Patuxent River, MD	53	Jack Lynch NATC Patuxent River, MD
5	3-4 October 1967	NBS Gaithersburg, MD	Loyt L. Lathrop Sandia Labs Albuquerque, NM	106	Loyt L. Lathrop Sandia Labs Albuquerque, NM
6	22-24 October 1969	Langley Research Crt NASA Hampton, VA	Paul Lederer NBS Albuquerque, NM	49	Loyt L. Lathrop Sandia Labs Albuquerque, NM
7	4-6 April 1972	Sandia Labs Albuquerque, NM	W. G. James AFFDL Wright-Patterson Dayton, OH	111	Pat Walter Sandia Labs First Mfg's Panel Boo-Boos
8	22-24 April	Wright-Patterson Dayton, OH	Pierre F. Fuselier Lawrence Livermore Labs Livermore, CA	74	Pat Walter Sandia Labs Albuquerque, NM
9	26-28 April 1977	Eglin AFB Fort Walton Beach, FL	Kenny Cox NWC China Lake, CA	100	William Anderson NATC Albuquerque, NM

Workshop Number	Date	Host	General Chairman	Number Attendees	RCC TG Transducer Chairman
10	12-14 June 1979	North America Air Defense Command Colorado Springs, CO	Richard Hasbrouck Lawrence Livermore Labs Livermore, CA	106	William Anderson NATC Patuxent River, MD
11	2-4 June 1981	Air Force Plant Rep Office, Det 9 Seattle, WA	Leroy Bates NSWSES Port Hueneme, CA	96	William Anderson NATC Patuxent Rive, MD
12	7-9 June 1983	Patrick AFB Melbourne, FL	Kenny Cox NWC China Lake, CA	116	William Anderson NATC Patuxent River, MD
13	4-6 June 1985	Naval Postgraduate School Monterey, CA	Richard Krizan Patrick AFB, FL	112	Leroy Bates NSWSES Port Hueneme, CA
ᴎ 14	16-18 June 1987	Air Force Academy Colorado Springs, CO	Stephen F. Kuehn Sandia National Labs Albuquerque, NM	118	Leroy Bates NSWSES Port Hueneme, CA
15	20-22 June 1989	ESMC, Patrick AFB Cocoa Beach, FL	John T. Ach WRDC/FIBGA Wright-Patterson AFB, OH	90	Leroy Bates NSWSES Port Hueneme, CA
16	18-20 June 1991	Automotive Research Facilities San Antonio, TX	Raymond Faulstich Naval Air Test Center Patuxent River, MD	81	Leroy Bates NSWSES Port Hueneme, CA
17	22-24 June 1993		Stephen F. Kuehn Sandia National Labs Albuquerque, NM		Ray Faulstich U.S. Army Yuma Proving Ground Yuma, AZ
18	20-22 June 1995		Norman F. Lantz The Aerospace Corp. P.O. Box 92957 M/S M5-649 Los Angeles, CA		Steve F. Kuehn Sandia National Labs Albuquerque, NM

EIGHTEENTH TRANSDUCER WORKSHOP

18TH

Colorado Springs, Colorado
June 20 - 22, 1995

Sponsored by
Vehicular Instrumentation/
Transducer Committee of the
Range Commanders Council
Telemetry Group
and
Society for Experimental Mechanics

Definition of the Transducer Workshop

History

The Workshop has been sponsored by the Vehicular Instrumentation /Transducer Committee, Telemetry Group, of the Range Commanders Council. This committee develops and implements standards and procedures for transducer applications. The previous workshops, beginning in 1960, were held at two year intervals at or near various US Government installations around the country. This year, the Society for Experimental Mechanics has joined the RCC in cosponsoring the Transducer Workshop.

Attendees

Attendees are working-level people who must solve real-life hardware problems and are strongly oriented to the practical approach. Their field is making measurements of physical parameters using transducers. Test and project people who attend will benefit from exposure to the true complexity of transducer evaluation, selection, and application.

Subjects

Practical problems involving transducers, signal conditioners, and read-out devices will be considered as separate components and in systems. Engineering tests, laboratory calibrations, transducer developments, and evaluations represent potential applications of the ideas presented. Measurands include force, pressure, flow,
acceleration, velocity, displacement, temperature, and others.

Emphasis

The Workshop

1. Is a practical approach to the solution of measurement problems,

2. Strongly focuses on transducers and related instrumentation used in measurements engineering,

3. Has a high ratio of discussion to presentation of papers, and

4. Allows attendees to share knowledge and experience through open discussion and problem solving.

Goals

The workshop brings together those people who use transducers to identify problems and to suggest some solutions, identifies areas of common interest, and provides a communication channel within the community of transducer users. The primary goals are to:

1. Improve the coordination of information regarding transducer standards, test techniques, evaluations, and application practices among the national test ranges, range users, range contractors, other transducer users, and transducer manufacturers;

2. Encourage the establishment of special sessions so that attendees with measurement problems in specific areas can form subgroups and remain to discuss these problems after the workshop concludes; and

3. Solicit suggestions and comments on past, present, and future Vehicular Instrumentation/Transducer Committee efforts.

General Chairman

John R. Rupp
Department of the Army
Dugway Proving Ground
Attn: STEDP-WD-TO-TD
Dugway, Utah 84022-5000
(801) 831-5602
(801) 831-5733 fax

Program

MONDAY, JUNE 19, 1995

2000   Social hour, at the Colorado Springs Marriott Hotel, courtesy of the Vehicular Instrumentation/Transducer Committee and the Society for Experimental Mechanics. All attendees welcome!

TUESDAY, JUNE 20, 1995

0730   Registration

0800   John Rupp, General Chairman
        Eighteenth Transducer Workshop

        Introductions:
        Steve Kuehn, Chairman
        Vehicular Instrumentation/
        Transducer Committee, RCC/TG

0830   **Session 1: Applications**

        Chairman: Pat Walter,
                       Sandia National Laboratory

        Cochairman: Martha Willis,
                     Rockwell Aerospace/
                     Rocketdyne Division

        •   "Strain Gage Based Sensors for
            Determining Bending Force On The
            Dante 2 Robotic Explorer," **Robert V.
            Magee**, Hitec Corporation

        •   "Miniature Sensor for Measuring Solid
            Grain Rocket Motor Case Bond
            Stresses," **Herbert Chelner**, Micron
            Instruments

        •   "Displacement Gages and Strain
            Extensometers for Special
            Applications," **John Shepic**, John
            Shepic Company

1000   BREAK

        •   "Stress Measurement in Solid Rocket
            Motors," **Jim Buswell**, Defense
            Research Agency, **Herbert Chelner**,
            Micron Instruments

        •   "At Last, Rugged Sensors for Vehicular
            Field Test Applications," **Jim Lally**, PCB
            Piezotronics, Inc.

        •   "Torque Sensor for Robotic
            Applications," **Mohammad Mahinfalah**,
            North Dakota State University

1200   LUNCH

1330   **Session 2: Applications**

        Chairman: Lawrence M. Sires,
                       Naval Air Warfare Center,
                       Weapons Division,
                       China Lake, California

        Cochairman: Ken Galione,
                     SEM Managing Director

        •   "A Design for a Transducer Capable of
            Sensing the Proximity of a Steel
            Plunger," **James Alich**, 412 TW/TSIDE,
            Axel Sehic, 412 TW/TSIDI

        •   "High Shock, High Frequency
            Characteristics of an Mechanical
            Isolator for a Piezoresistive
            Accelerometer," **Vesta I. Bateman**,
            Sandia National Laboratories

        •   "Strain Gage Based Sensors for
            Suspension Pushrods on Indy Race
            Cars," **Robert V. Magee**, Hitec
            Corporation

        •   "Corrosion Monitor Based on Time
            Domain Reflectometer Measurements of
            a Deformed Optical Fiber," **Jack R.
            Kayser**, Lafayette College

1515   BREAK

        •   "Mass Loading in Back-to-Back
            Reference Accelerometers," **Robert D.
            Sill**, Endevco

        •   "New Dynamic Pressure Generator and
            Its Application," **Benjamin Granath**,
            PCB Piezotronics

        •   "A Multi Function Heat Flux Transducer:
            Ballistic Test Data," **R. Daniel
            Ferguson**, Physical Sciences, Inc.

- "On Analog Feedback Control for Magnetostrictive Transducer Linearization," **David L. Hall**, Iowa State University

- "Remote Hydrogen Sensing for the Space Shuttle System," **Billy R Stover**, Lockheed Space Operations Company

---

WEDNESDAY, JUNE 21, 1995

0800   **Session 3: Tutorial**
Signal Conditioning for Resistance-Based Transducers for Steady State and Transient Tests

     Speaker: Peter K. Stein
                 Stein Engineering Services, Inc.
                 Phoenix, AZ

         • Introduction
         • The Interrogating Input
         • The Balancing Circuit

1000   BREAK

1015   • Step Input "Calibration"
                   • Conclusions

1200   LUNCH

1330   **Session 4: Development**

     Chairman: Vesta I. Bateman,
                    Sandia National Laboratories

     Cochairman: Robert D. Sill,
                    Endevco Corporation

- "Low Cost Piezoelectric Smart Transducers," **Steven C. Chen**, PCB Piezotronics, Inc.

- "Development of a Guidance Document for Lightning Safety Systems," **Richard T. Hasbrouck**, Lawrence Livermore National Laboratory

- "Development of Fiber Optic Sensors for Ballistic Measurements," **W. Scott Walton**, US Army Combat Systems Test Activity

- "Development of a Micromachined Silicon Servo Accelerometer," **Michael Young**, ENDEVCO

1515   BREAK

- "Evaluation of an Accelerometer for Improved Low Frequency Vibration Measurements During Rocket Engine Testing," **Martha P. Willis**, Rockwell AeroSpace/Rocketdyne Division

- "Inertial Sensor Alignment Mechanism (ISAM)," **Douglas T. Wong**, NASA Langley Research Center

- "Development of a Modulation System for Voice Transmission in PCM," **Lee Olyniec**, 412 TW/TSID

1830   Banquet at Hotel

THURSDAY, JUNE 22, 1995

0830   **Session 5: Techniques and Calibration**

     Chairman: Richard W. Krizan,
                    45 Space Wing, Patrick AFB

     Cochairman: W. Scott Walton,
                    US Army Combat Systems
                    Test Activity

- "PDCue," **Naill B. Mcnellis**, A. A. I. Corporation

- "Measuring Surface Forces on a Clamping Mechanism with Dual Friction Interfaces," **Alex C. Lee**, Delco Chassis Division, GMC

- "In Situ Verification of Accelerometer Function and Mounting," **Torben R. Leiht**, Bruel & Kjaer, Denmark

- "The NIST Super Shaker Project," **Bev Payne**, NIST

1000   BREAK

- "Continuing Developments in Accelerometer Calibration Techniques," **Michael J. Lally**, The Modal Shop, Inc.

- "Transverse Response of Piezoelectric Accelerometer," **Jing Lin**, PCB Piezotronics, Inc.

- "Utilization of Static Calibration Data to Correct Nonlinear Measured Dynamics Pressure Data," **David Banaszak**, Wright Laboratory

- "Surface Position Calibration System," **Robert L. Grant**, Douglas Aerospace-East

1200   Closing Remarks: General Chairman

1330   Tour of Olympic Facilities

General Information

The Eighteenth Transducer Workshop will be held June 20-22, 1995, at the Colorado Springs Marriott Hotel in Colorado Springs, Colorado.

Registration

The registration consists of a completed registration form, a written "Murphyism," and a fee of $100.00 (payable in advance or at the door) to:

Ray Faulstich, Treasurer
Transducer Workshop
P. O. Box 235
Yuma, AZ. 85366-0235
(520) 328-6382

A "Murphyism" can describe any measurement attempt that went awry with the objective of learning from our errors and keeping our feet on the ground. It should be something generic rather than common human oversight; something from which we can learn. The tone should be anonymous so no person, organization, or company is embarrassed. While a "Murphyism" is not a requirement, submissions are strongly encouraged and the best will be included in the program.

Advance registration is desirable. Please use the enclosed registration form, include a check or money order for $100.00 payable to the Transducer Workshop, and mail to the Workshop Treasurer by May 19, 1995 **(Note: Purchase orders are not acceptable.)**

The registration fee covers the cost of coffee, tea, soft drinks, doughnuts, evening banquet, and a tour. A copy of the workshop proceedings is supplied to all attendees. Late registration will be provided at the workshop registration desk in the hotel.

Hotel Accommodations

A block of rooms has been reserved for the 18th Transducer Workshop at the special rate of $95.00 (Plus 8.3% tax). For Government employees, a limited number of rooms are available at the prevailing government rate. Identification will be required to get the government rate. These special room rates will apply the weekend before and after the conference. All attendees are encouraged to make reservations early. To obtain the discounted group rate, all reservations must be made by May 19, 1995. After the cutoff date, of May 19, 1995, rooms and rates are subject to availability. When making reservations mention the 18th Transducer Workshop. The hotel information is listed below:

Colorado Springs Marriott
5580 Tech Center Drive
Colorado Springs, Colorado 80919
(719) 260-1800

Guests

No formal program will be planned for spouses or guests. However, they will be most welcome at the social hour on Monday and the banquet on Wednesday ($20.00 additional per guest for the dinner).

Tour—Thursday Afternoon

A tour of the US Olympic Center is planned for Thursday, June 22, 1995. The tour will consist of a video of the history of the Olympics, a tour of the grounds and a behind the scenes look at some of the instrumentation designed to further the Olympic athlete's performance.

Format and Background

Workshops are just what the name implies; everyone should come prepared to contribute something from their knowledge and experience. In a workshop, the attendees become the program in the sense that the extent and enthusiasm of their participation determine the success of the workshop.

Participants will have the opportunity to hear what their colleagues have been doing and how it went; to explore areas of common interest and common problems; and to offer ideas and suggestions about what is needed in transducers, techniques, and applications.

Additional Information

May be obtained from the General Chairman, or

VI/T Committee Chairman
Steve F. Kuehn
Sandia National Laboratories
PO Box 5800 (Dept. 2645) m/s 0319
Albuquerque, NM 87185-5800
(505) 844-8383
(505) 844-3593 fax

Facilities Chairman
Daniel S. Skelley
NAWCAD MS1
47723 Ranch Rd.
Patuxent River, MD 20670-5304
(301) 826-1570
(301) 826-7630 fax

Papers Chairman
Norman L. Rector
Lawrence Livermore National Laboratory
P. O. Box 808, L-154
Livermore, CA 94551
(510) 422-3994
(510) 423-3144 fax

SESSION 1

APPLICATIONS

STRAIN GAGE BASED SENSORS
FOR DETERMINING BENDING FORCE
ON THE LEGS OF THE DANTE 2 ROBOTIC EXPLORER

Robert V. Magee

Sensor Applications Engineer   -

HITEC Corporation

65 Power Road

Westford, MA 01886

(508) 692-4793

ABSTRACT:

The purpose of this paper is to show how strain gaging the legs of the Dante 2 Robot Explorer was done to supply the operator with a warning signal when the kick out load on the leg exceeded a maximum recommended force. The installed strain gaged based sensor would provide load information from a transducerized leg to the amplifier on board the robot. The legs would exceed recommended loads when it caught up in the rocky terrain. If it exceeded for a prolonged period of time, the legs would fail. It was necessary to be able to measure these forces.

This robot was designed by Carnegie Mellon University Field Robotics Center (CMU) to descend into a volcano in the Arctic and explore the crater of that volcano and provide scientific information to NASA. This simulated NASA's exploration of the moon and Mars. This paper will conclude that transducerizing the legs of the DANTE 2 was a more reliable and a better solution than modifying components to adapt to an in line transducer.

NOMENCLATURE:

P = Load   L = Length

M = Bending Moment   E = Modulus of Elasticity

OD = Outer Diameter   ID = Inner Diameter

I = Moment of Intertia   c = OD/2

σ = Stress   ue = Micro Strain

mV/V = Milli Volt / Volt

1. INTRODUCTION:

Dante 2 made its decent down Alaska's Mt. Surr in July of 94. This time with more technology than the first Dante robot. Dante 2 has a strain gage based sensor installed at each of the eight legs sending load data to the operators of the robot.

The operators were CMU and the project is funded by NASA [1]. The original Dante was found to be too vulnerable to the side way forces experienced as it moved along the crater wall, now with the new leg motion design and sensors including the strain gaged sensors on each of the eight legs engineers can monitor loads as it crawls along the crater wall. In slightly sloping snow fields the Dante 2 robot could be on autopilot, which allowed it to monitor and interpret strain sensor loads and go forward to its next destination unaided by human commands [2][3][4][5][6].

2. THE DESIGN THEORY:

Calculations were made to determine the best location for the strain gages in order to obtain the maximum bending beam strain on the leg. This provides the highest output for CMU's signal conditioner. Based on the determination of the greatest bending of the robot leg, when modeled, the estimated output would be approximately 2.5 mv/v, which was suitable for use with CMU's signal conditioner. The legs were made from 6061-T6 Aluminum Alloy. The leg motion also had a vertical 4440 newton (1000 pound) load which was required to be negated in the output of the bending bridge. Another factor which needed to be of concern was the operating climate. The Dante 2 would travel in Arctic snow, volcano crater walls, and therefore see extremes of temperature and moisture. To use an existing transducer, it would have had to be made hermetically sealed and the leg assembly would have had to been modified in some fashion. Installing strain gages on the leg itself was the most efficient way.

The signal strength estimate was based on the assumption of a bending beam fixed at the locations shown in Figure 1. Using the following formulas the output in milli Volt / Volt was determined.

$$(1) \quad M := W \cdot 1 \quad \text{in-lbs} \qquad\qquad C := \frac{OD}{2}$$

$$(2) \quad I := \left[\frac{\pi}{64} \cdot \left[OD^4 - ID^4\right]\right] \quad \text{in}^4$$

$$(3) \quad \sigma := M \cdot \frac{C}{I} \qquad\qquad \text{PSI}$$

$$(4) \quad \varepsilon := \sigma \cdot \frac{10^6}{E} \qquad\qquad \mu\text{in/in}$$

$$(5) \quad \varepsilon \cdot \left[\frac{4}{2000}\right] = \qquad\qquad \begin{array}{l} \text{mv/v} \\ \text{F.S.} \end{array}$$

Using the modulus of elasticity for Aluminum and with an OD of 82.5 mm (3.25 in) and an ID of 63.5 mm (2.50 in) an output of 2.5 mV/V was to be expected at a load of 3108 newtons (700 Lbs.) and a length of about 1.1 meter (42.5 in.). The actual calculation used is shown in Figure 2.

3. THE SENSOR:

The sensor used on the robot leg is a resistive encapsulated strain gage circuit consisting of four strain gages arranged in the basic Wheatstone circuit (Figure 3) [7]. Two gages measuring bending in tension at the surface strain on one side and on the opposite side two strain gages are in compression measuring bending on the other surface. Using constantan wire for bridge balancing, 0.05 mV/V bridge balance is achieved. The final full bridge output, converted into mV/V allows the user to monitor force equivalent to strain. The gages are protected for a temperature environment of -40 degree C to 300 degrees C. First an electrical moisture protection coating was applied to the strain gage bridge circuit. Then a RTV coating was applied to additionally protect gages from the moisture environment. Teflon and steel braided shielding minimized noise in the output signal from the sensor and protected it from the harsh environment of extreme temperatures and moisture.

4. THE AMPLIFIER

CMU had chosen the T Hydronic 3 mV / 5 volt Inline Amplifier (Figure 4.). It provides a bridge excitation of 5 volts giving a signal output of 0-10 mV output. The amplifier then produces an output of 0-5 volts to be sent to the Dante 2's data acquisition system.

5. DISCUSSION:

Having a transducerized robot leg allowed for a simple way to determine critical load information. When an obstruction was sensed by the transducerized leg (Figure 5) a voltage signal is sent to the amplifier signal conditioner. The output from the amplifier went to the Dante 2 data acquisition system where load information was then transmitted remotely up to 80 miles away. Engineers could then give Dante 2 new movement information or stop it from forcing the legs beyond its design strength. Calibration of each leg transducer was done by taking a reference bending load and calibrating output versus a known load.

6. CONCLUSION:

Although mainly the user must monitor and manually implement changes when the sensor warns about an obstruction, Dante 2 also has the ability to initiate its own corrective movement by backing off the obstruction when put into an auto pilot mode. Using sensors in this fashion will improve Dante's ability to move in the environment it was designed for without the risk of yielding or breaking the its robotic legs during an excessive resistance load from an obstruction. The operators will have to depend on the information Dante 2 receives from the strain gage sensors when it is miles away in space on its Mars exploration mission. In this case incorporating an off the shelf transducer was not going to be a suitable choice, because of the lack of room available and the major modifications to the robot that would have been necessary. Directly installing a strain gage bending bridge on each of the legs illustrates how using existing components is a better choice than modifying to accommodate a standard transducer (See Figure 6.).

7. ACKNOWLEDGEMENTS:

8. REFERENCES:

[1] Reichhardt, Tony, "Robotic To Hell and Back", Popular Science, July, 1994.

[2] N/A, "Events In Motion", Motion Control, pp. 5-6, Winter 1994.

[3] Gunther, Judith Anne, "Dante's Inferno", Popular Science, pp. 66-68, November, 1994.

[4] Henkel, Stephanie, "Robotic Explorer Dante II Challenges a Volcano", Sensors, pp. 12-15, September, 1994.

[5] Puttre, Michael, "Undated Dante Readies for Inferno," Mechanical Engineering, pp. 58-59, December 1993.

[6] Hammonds, Keith H., "The Robot Workers Are Coming", Business Week, p. 46, May 16, 1994.

[7] Dove, R. C. and Adams, Paul H., "Experimental Stress Analysis and Motion Measurement", Charles Merrill Books, 1964.
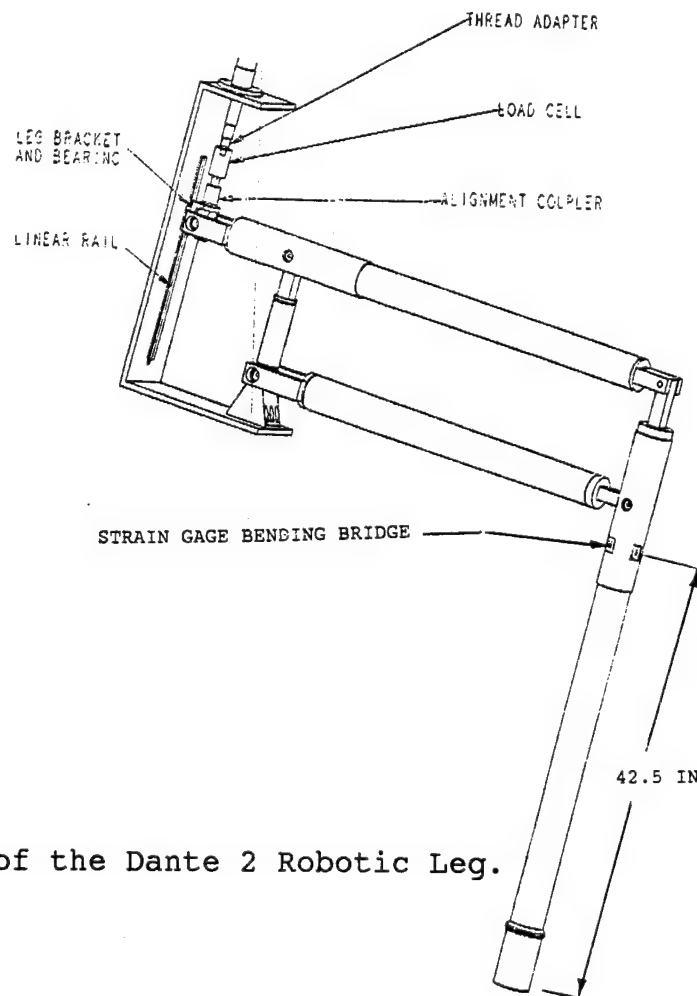
Figure 1. Sketch of the Dante 2 Robotic Leg.

$P := 700$ lbs $\qquad\qquad\qquad\qquad l := 42.5$ in

$M_1 := P \cdot l$ in-lbs $\qquad M_1 = 29750$ in-lbs

$E := 10.6 \cdot 10^6$ $\qquad OD := 3.25$ in $\qquad ID := 2.50$ in

Al alloy 6061

$c := \dfrac{OD}{2}$ $\qquad\qquad I := \left[\dfrac{\pi}{64} \cdot \left[OD^4 - ID^4 \right] \right]$ in^4 $\qquad I = 3.559$ in^4

Defection: inches $\qquad \delta := \dfrac{P \cdot l^3}{3 \cdot E \cdot I}$ $\qquad \delta = 0.475$

Stress: p.s.i. $\qquad\qquad \sigma_1 := M_1 \cdot \dfrac{c}{I}$ $\qquad \sigma_1 = 13583.417$ PSI

Strain: μ $\qquad\qquad\qquad \varepsilon_1 := \sigma_1 \cdot \dfrac{10^6}{E}$ $\qquad \varepsilon_1 \cdot \left[\dfrac{4}{2000} \right] = 2.563$ mv/v   F.S.

$\varepsilon_1 = 1281.454$ μin/in

Figure 2. Sample Calculation Determining mV/V Output on the Sensor.

8

Figure 3. Strain Gage Circuit for The Dante II Strain Gage Sensor
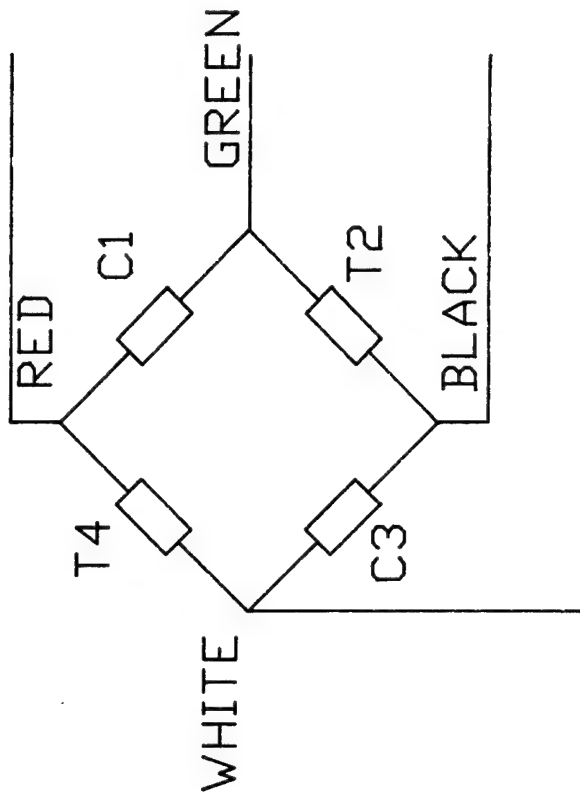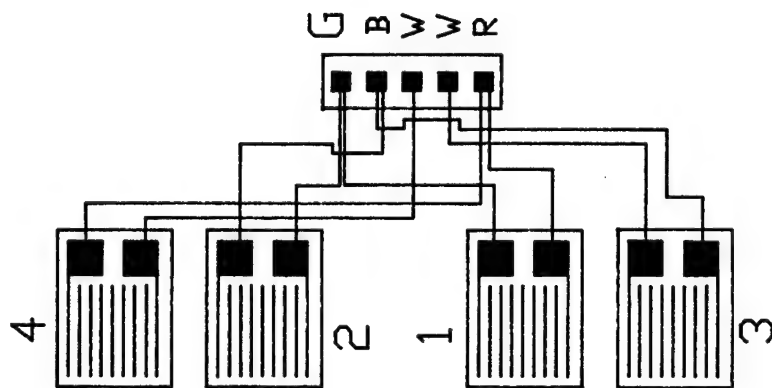
HITEC CORPORATION
WESTFORD MASSACHUSETTS

BENDING BRIDGE

SCALE: NTS
DATE:
APPROVED BY
DRAWN BY   RVM

FILE: BENDI

DRAWING NUMBER
2100-0022

CONN WIRING

A + (5 VOLT) SIGNAL
B – SIGNAL
C – EXCITATION
D + EXCITATION (28 V.D.C.)
E ⌐ NO CONN.
F

BENDIX PT1H-10-6P OR EQUAL
BOTH ENDS MATES WITH
BENDIX PT06-10-6S [SR] OR
EQUAL

ZERO

SPAN

$1\frac{1}{2}$ DIA

.43

TYPE_____ SER.NO.
RANGE_____
EXCITATION_____
HYDRONICS

3.0
MAX

WIRING
HDR – TRANSDUCER

A + (3MV/V) SIGNAL
B – SIGNAL
C – EXCITATION
D + EXCITATION (15V)

DRILL PT.

A

D

C

B

Figure 4. T Hydronics Amplifier.

10
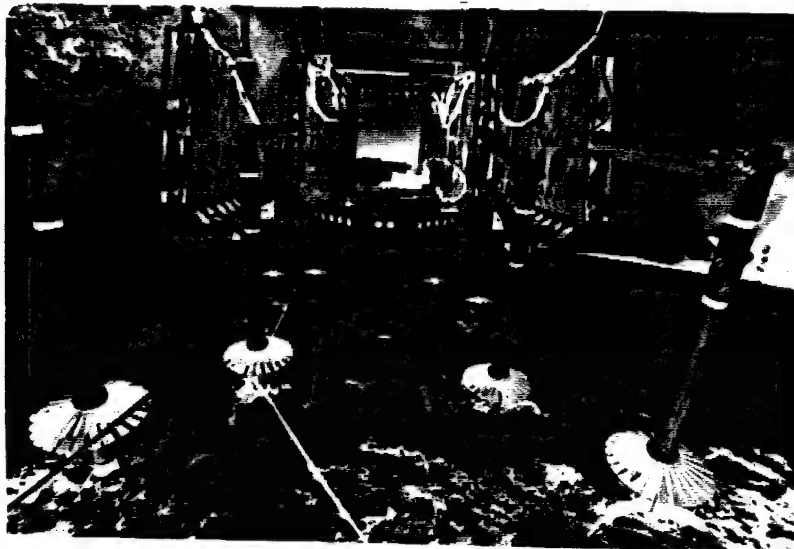
Figure 5. Dante II's Leg Sensors. (Bill Ingalls/NASA)
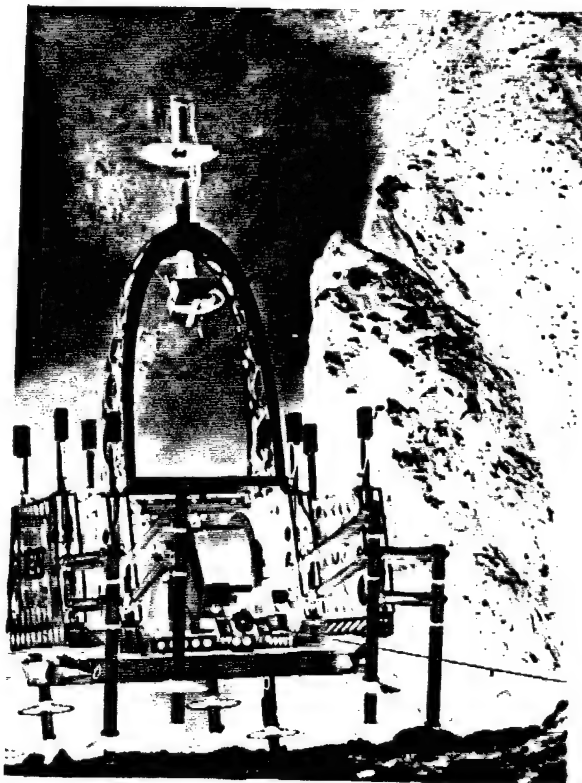
Figure 6. Dante II Robotic Explorer. (Bill Ingalls/NASA)

MINIATURE SENSOR FOR MEASURING SOLID GRAIN ROCKET MOTOR CASE BOND STRESS

by

HERB CHELNER*

JIM BUSWELL**

*MICRON INSTRUMENTS, SIMI VALLEY, CA 93063.

**DRA, FORT HALSTEAD, KENT,TN14 7BP, ENGLAND.

ABSTRACT

MINIATURE SENSOR FOR MEASURING SOLID GRAIN
ROCKET MOTOR CASE BOND STRESSES

Presented in this paper is a miniature high-stability semiconductor strain gage normal stress sensor capable of measuring the bond stress of solid grain rocket motors during hot pouring at 150°F to cold soak at -50°F. This sensor is also capable of accurately measuring the long term ageing bond stresses and thermal cycling stresses. It can also measure the chamber pressure up to 3000 psi at ignition until destroyed by temperature. Perhaps its most desirable use is as a health monitoring device to predict potential failure before ignition.

TABLE OF CONTENTS

TABLE OF CONTENTS
GRAPHS/DRAWINGS

1.0 Executive Summary

Solid propellant normal bond stress profiles are calculated and used in the predication of motor service and storage life. Bond stresses are calculated instead of measured due to the belief that making the measurement is difficult and available sensors too inaccurate.

This program, to improve the sensor accuracy and provide a design that is more easily installed with minimal effect on the grain stress distribution was successful. The design goal for thermal hysteresis, when thermally cycling between -50 to +150°F was ±1 psi. Sensors with less than ±0.5 psi were produced. The long term stability design goal of 1.0 psi per year was exceeded. The average drift of all sensors tested was less than 0.7 psi per year with many sensors drifting less than 0.25 psi per year.

For ease of installation the low flat miniature profile of 7.6 mm diameter by 2.0 mm thick will easily fit into the motor lining or may be bonded to the case wall. Only a 1.0 mm hole is required for the 5 conductor cable which can be disconnected from the remote bridge completion package for installation and routing.

This sensor can sense changes in the normal stress due to case bond separation or grain cracking making it also useful as an *instant health* monitoring device.

1.1 Work Statement

Micron Instruments will design, develop, fabricate and test a miniature low profile sensor specifically oriented to measure solid rocket propellant bond stress.

The first year testing will be on two materials; 17-4 PH CRES to H-900 and Titanium 6AL4V. Three semiconductor P-Doped strain gage types will be tested (.060 long, .037 long and .026 long) on each of the two metals.

A second year study is presently in progress using the best gage material combination for both 17-4 and 6AL4V. This study is evaluating process procedures which improve measurement accuracy. Design features providing ease of installation and external bridge connections will be implemented.

1.1.1 1993-1994 Performance Design Objective

Accurate measurement of the normal bond stress is the goal of this program. The objective of this first year is to determine which gaged sensor combination had the best performance. Measurement accuracy consists not only of the sensor standard performance considerations such as static error band, balance temperature coefficient and sensitivity coefficient, but also is affected by the sensor grain interface which can affect the normal bond stress distribution.

To minimize the bond stress potential errors, a small flat sensor capable of being flush with the container surface and having a very low compliance (high spring constant) is

16

having a very low compliance (high spring constant) is desirable. Although the sensor is very small some perturbation of the bond stress will occur at the outside diameter corner. Making the walls thick allows room for the stress to normalize before it gets to the active portion of the top surface containing the diaphragm. Cleaning the sensor surface is essential to permitting a good propellant bond.

Since voltage offsets, if repeatable, can be corrected, the most important performance features are stability and repeatability. For this reason the parameters of most interest are pressure hysteresis, non-repeatability, thermal hysteresis and long term stability.

1.1.2 1994 - 1995 Performance Design Objective

The second year performance objective was to improve the measurement accuracy using the best steel and titanium gage combinations determined by analyzing the first year data. Specific goals are as indicated below.

Static Error Band	$< \pm 0.25$ psi
Thermal Hysteresis	$< \pm 1.0$ psi
Thermal Repeatability Balance	$< \pm 0.25$ psi
Long Term Stability	< 1.0 psi/year

One of the design objectives is to provide an external water resistant bridge completion package with detachable cable for ease of routing thru the motor. A special five conductor over molded cable was developed of less than 0.040 inches in diameter. A diameter this small has insignificant perturbation to the grain stress . A very small diameter exit hole is required which will not compromise case integrity and is easy to seal.

2.0 Sensor Uses

Some uses of a normal bond stress are presented herein.

2.1 Chamber Pressures

Design of this sensor is very conservative. It has 30 X over pressure capability and can be used to measure chamber pressure. A number of sensors mounted around the case can be used to establish a pressure profile of the motor during operation until the flame front reaches the sensor. The natural frequency of the sensor is approximately 150,000 Hz and the sensor is operational to 3000 psi and to 300°F.

2.2 Health of the Sensor

I have been informed there are two general ways that motors fail[1]. As the motors age the propellant may soften and turn to mush or the propellant may harden and crack and/or separate from the case wall.

---

[1]Private communications Gene Francis (formerly of UTC Chemical Division)

Each motor design is different and the designer knows where the maximum normal stress regions should occur and what constitutes a change that would be considered dangerous. Certainly a rocket under the wing of a high speed jet is more of a problem if it misfires than one on a mobile ground launcher. The jet could fly into its own missile. If it explodes in front of the jet there is shrapnel to fly through. The rocket could explode in its launcher.

It has already been proven that the sensor can sense cracks projecting through a grain which shows as a drop in bond stress[2]. With long term stability, the sensor is capable of measuring debonding due to ageing whether from hardening or softening of the grain.

2.3   Verification of Normal Bond Stress Calculations

Assuming that the sensor can be installed without affecting the normal bond stress, the data would prove the designer's theoretical calculations. Even more important, if the actual stress does not agree with the theoretical stress, it signifies a problem with the assumptions or the design.

3.0   Reluctance to Instrument Motors

Designers of solid propellant rocket motors are sensitive to payload which translates to minimum inert mass. Motor container cases comprise the most inert portion of the motor. These containers are as thin as possible to be consistent with good design parameters but with little margin for over stress. Anything requiring holes thru the case weakens it and is resisted by the designers. Where wires and electrical connections are absolutely required, the designer thickens the case and provides sealable ports.

Anything protruding significantly into the motor grain will affect its cure stresses. A potential result is debonding or cracking of the grain which would affect the thrust profile and therefore would be objectionable.

Electrical voltages operating in close proximity to the motor grain can cause an accidental ignition should a spark type failure occur.

Although there are good reasons to avoid unnecessary instruments, with care, measurements can be obtained safely and benefits can exceed the risks.

4.0   Environmental and Operational Sensor Design Considerations

A program to develop a sensor for the measurement of normal bond stress in solid grain rocket motors requires that the transducer be capable of performing in demanding environments. Since such rockets are generally made by hot pouring the motor propellant mix into a shell or housing, the sensor must be capable of accurately measuring the stress as the pour cools from as much as 160°F[2].

---

[2]J. Buswell et al Stress Measurement in Solid Motors (March 1995)

18

It is conceivable that a motor could be installed on an aircraft in weather ranging from a -50 to +160°F and then be subjected to relatively sudden thermal changes as the aircraft flies its course.

Motors can be stored for long durations before being used. Since many of the storage facilities are not air-conditioned and some are not insulated, the sensor must operate over a wide temperature range and over long periods of time with good accuracy.

Motors are often cycled between -50 and +150°F to determine their ability to withstand sudden thermal changes and as an expedited life test. So that accurate measurements can be made during such testing, the sensor should be thermal transient temperature compensated and have low thermal hysteresis.

To measure the bond stress accurately it is necessary for the sensor to have low compliance. Accuracy of the bond stress measurement is more largely determined by how the sensor is installed in the motor which is the subject of another paper. Best accuracy is obtained when the sensor is flush with the inside surface containing the propellant. Thusly, one of the design goals is to make the sensor small. The height of the sensor should be less than 0.100 of an inch. A low mass stiff sensor with low compliance is desirable.

Most designers of rocket motors use minimum case thickness since every inert pound of mass subtracts from the motor performance. Designers therefore resist putting holes into their cases which potentially increase the chance of failure. Strain gage full bridge sensors with external bridge completion require five wires. An electrical cable containing these wires must be routed through the motor case. Therefore, an important design consideration is to miniaturize the electrical cable requiring a corresponding small hole through the case and therefore minimize or eliminate the need for additional weighty reinforcement. There are two limiting factors to the extent that the cable can be miniaturized. The first is cable strength. Since working the cable under insulation and through the exit hole will require reasonable force, the cable should not fall below five pounds of pull. A second consideration is line resistance. To eliminate line resistance changes which will affect sensitivity, constant current excitation is used which will also compensate for most poor electrical connections.

It would be desirable if the sensor has good over range capability so that it could be used to measure the chamber pressure during ignition.

Safety is always an issue when working with solid grain rocket propellants. Any small spark is potentially dangerous. Installing electrical wires of any significant power inside rocket motors is resisted. To minimize the potential of sparking, the sensor was designed to activate with only 4 mA constant current into a maximum bridge impedance at 160°F of 320 ohms requiring 1.25 volts of excitation. The sensor impedance drops with decreasing temperature. The constant current source is limited to 6 mA maximum. If a gage fails, no current will flow through the bridge. The sensor housing is completely enclosed and the four strain gages are purely resistive with no other components. It is very unlikely that a spark can be generated at 6 mA and less than 2 volts, the maximum of the signal conditioner. However, the gages are completely enclosed by the sensor housing and lid which is the most probable place for a potential open or shunt.

5.0 Sensor Design Considerations

Earlier stress sensors used fixed edge circular diaphragms for the stress measurement member. Since most of the finite element analysis and actual testing was performed using[3] this transduction approach, the design therein uses the same principles and diaphragm diameter to thickness ratios.

5.1 Mechanical Design Details

Sensor Detail Drawing 440306, Page 9, shows the titanium transducer dimensions. These dimensions are the same as the 17-4 PH CRES Steel versions.

Pages 10 thru 12 show the orientation of the three types of different length semiconductor strain gages as they were bonded onto the diaphragm with epoxy. A five-conductor cable enters the sensor though the side wall hole and is soldered to the open bridge formed at the solder tabs. The other end of the cable is attached to a bridge completion and temperature compensation board. After the sensors have been computer tested over temperature in a temperature chamber, which defines the values and locations of the bridge completion balance Tc and sensitivity Tc resistors, the resistors are installed on the circuit board. These resistors bias the strain gages to force dynamic self thermal transient compensation.

The cable is round and is 0.040 inches in diameter. Routing the cable though the rocket motor casing would require holes no bigger than 0.42 diameter. Small size holes minimize the damage and weakening of the rocket motor case. Sealing a small hole is much easier.

A lid is bonded to the rear of the sensor after all electrical connections are made and the cable is bonded at the exit hole.

5.2 Theory of Operations (Normal Stress)

As pressure is applied to the diaphragm, it deflects. The resulting surface strain is sensed by the gages. The two gages in the center go into tension showing an increase in resistance and the two gages at the edges go into compression decreasing in resistance. These gages are connected to form a fully active bridge. When properly activated and thermally compensated, an output signal is obtained which is linear and proportional to pressure (normal stress) when operated within its design limits.

The polarity is such that positive pressure (compression) to the diaphragm develops a positive signal and negative pressure (tension) has a negative signal.

6.0 Performance Testing Details

Following is a description of the testing performed on the sensors and the results. Since it is difficult to simulate bond stress, gaseous nitrogen

---

[3]The Development of Improved Normal Stress Transducers for Propellant Grains, E.C. Francis, R.E. Thompson and W.C. Briggs (31 Jan 79)

pressure was used. The full scale range of the sensors is 100 psig. Errors or deviations are expressed in percent of full scale or psi.

Details on each set up are not given. Our quality control system requires all measurements to have recent calibration traceability and our pressure standards are referenced to the Bureau of Standards. The accuracy of our pressure standard is better than 0.05% of reading.

6.1 Static Error Band (S.E.B.)

The static error band is comprised of the non-linearity, hysteresis and non-repeatability at ambient temperature. Design considerations of the sensor were initiated to meet the design goal of ±0.25 psi best fit straight line. Testing of 46 sensors produced an average S.E.B. of 0.11 psi. Page 13 and 14 show two data sheets containing S.E.B. data.

Zero stress offset and full scale offset are not considered errors. They are corrected for during data reduction.

6.2 Balance Temperature Coefficient (BTC)

Balance (0 psi) electrical offset over temperature is compensated for by shunting a gage on the side of the bridge changing fastest with a resistor. Since the resistor does not need to see the temperature change, it can be located remotely in the bridge completion external box. Although the four gages are computer matched for intercept at 78°F and between -50 and 278°F for Tc, variations in diaphragm surface finish, epoxy bond thickness, etc. can cause offsets due to different bond stresses. Passive balance temperature compensation forces the bridge to be self-compensated. A high degree of thermal transient compensation is achieved.

It is more important that the thermal balance Tc be repeatable, than very low. The thermal hysteresis data is used for data correction.

Average balance Tc's for titanium sensors is 2.0% FS/100°F and steel 2.2% FS/100°F. The lowest BTC for titanium is 0.23% FS/100°F, S/N 12236 Page 15 and for steel is 0.43% FS/100°F, S/N 12253 Page 16.

6.3 Sensitivity Tc

The algebraic difference between the 0 psi electrical output and the 100 psi electrical output is herein defined as the sensor sensitivity.

Sensitivity Tc is the change in sensitivity over temperature. This change can be a straight line or a slightly curved line continuous function. Sensitivity Tc is obtained by using a resistor shunt across the constant current power supply. The power supply is set for 4.0 mA constant current. It is not required that the resistor be located in the sensor. This forces the sensor to be self-compensated and can be mounted in the external bridge completion box.

Titanium average sensitivity Tc was 1.15% FS/100°F with one unit S/N 12222 showing a sensitivity Tc of 0.05% FS/100°F Page 17.

21

The average steel sensitivity Tc is 1.62% FS/100°F with the lowest Tc S/N 12246 of 0.16% FS/100°F Page 18.

6.4   Thermal Hysteresis

At zero pressure with the sensor properly excited, an output is obtained over the limits of its temperature compensated range. The curve thus obtained is called the balance temperature coefficient and is often expressed as percent of full scale per 100°F. This curve can be established by measuring the sensor output as it is thermally changed from hot to cold which for the testing herein is +150 to -50°F. If the balance Tc curve obtained from +150 to -50°F is different from the curve obtained from -50 to 150°F, that difference is herein defined as thermal hysteresis.

What causes thermal hysteresis is not obvious and will not be discussed herein. To minimize the thermal hysteresis the sensors are treated to processes which are known to optimize general performance such as heat treatment of metals after machining, thermal cycling to stabilize components, specialized curing of epoxy, etc.

It is a design goal to obtain a thermal hysteresis of less than 1.0 psi over the thermal range shown.

For the curves shown on Pages 19 thru 24, the temperature of the chamber containing the sensors was held constant for 120 minutes at each temperature shown. The complete thermal cycles were run over 110 hours and generated 55 data points.   Except for a few problem sensors, all sensor curves had similar signatures with the following characteristics.

1.   For each sensor the -50 and +150°F end points repeated.

2.   Increasing temperature data points between the limits were always more positive than the decreasing temperature points.

3.   The increasing temperature data points were repeatable.

4.   The decreasing temperature data points were repeatable.

Most rockets are relatively massive and the heat exchange rate with air is poor.   Motor temperature changes will be slow.   The sensor thermal hysteresis testing was slow to simulate the use conduction.

Following are some charts showing the thermal hysteresis curves generated from the test proven.   Page 19 is S/N 7607 for a titanium sensor with 0.026 gages, Page 20 S/N 7610 with 0.039 gages and Page 21 S/N 7619 with 0.060 gages.   The steel sensors with the same gages are S/N D Page 22, S/N 7630 Page 23 and S/N 7638 Page 24.

6.5   Long Term Stability

The sensors were put into a box to eliminate wind currents and slow ambient temperature changes.   All sensors were tested for balance approximately twice per week.   Each sensors electrical output was measured by plugging its electrical connector into a mating

connector, wired to a constant current supply and digital readout. No attempt was made to compensate for temperature.

Although the constant current power supply was always reset prior to taking data and the current was recorded with each data point, no attempt to correct the data was made. It was assumed these small fluctuations of current would average out during the long test period.

Some sensors such as S/N 7638 Page 25 seem to have a stabilization lead time of approximately 30 days. Page 26 shows a sensor requiring no stabilization lead time. Pages 27 thru 31 show other sensors with different size gages on both titanium and steel bodies. Most of the long term cycle changes shown in the data is due to long term building temperature changes. These long term cycles are greater on sensors having larger balance Tc's.

Page 31 is a resistor bridge reference test balance Tc chart. This shows how stable the recording meter was.
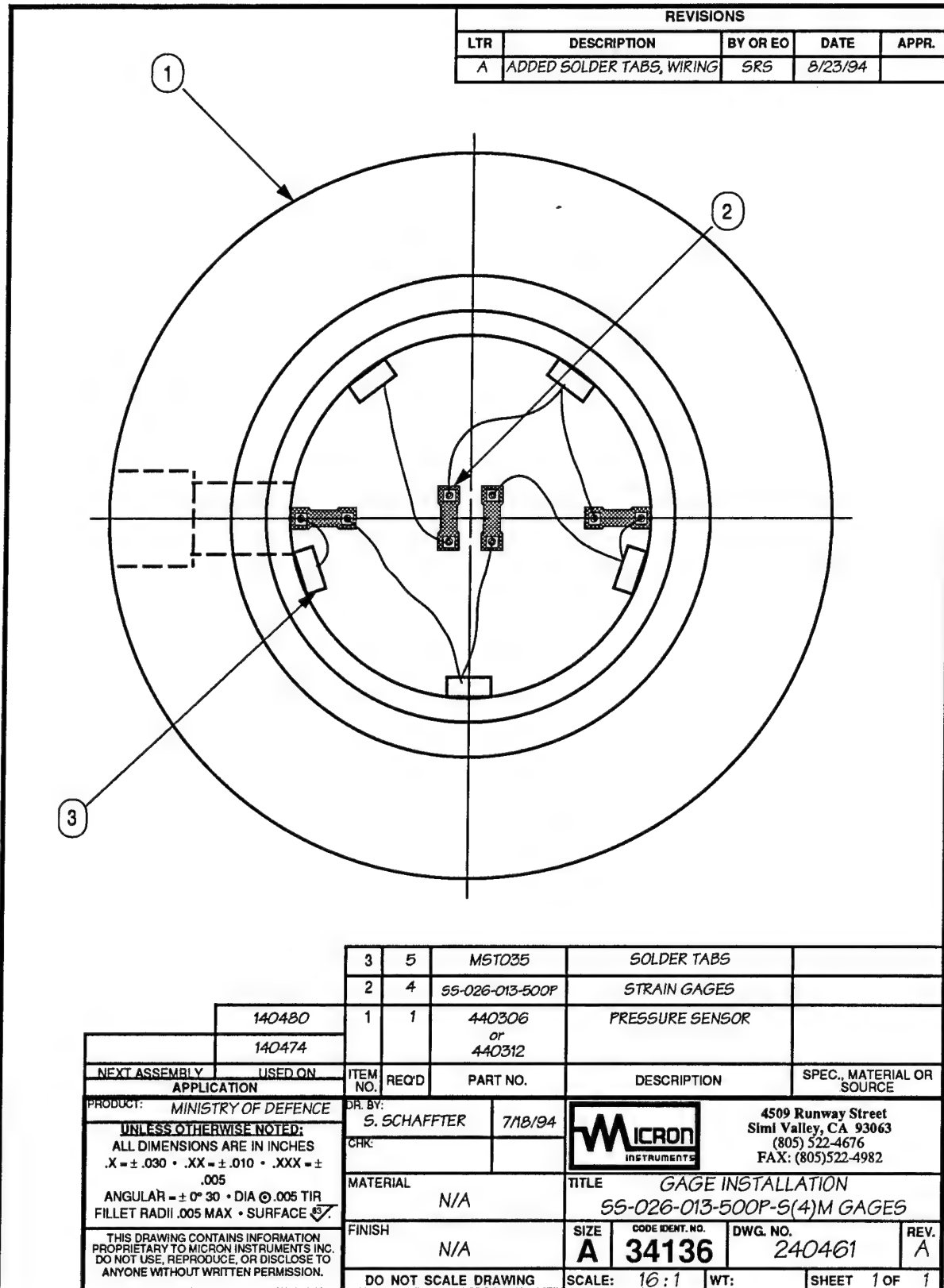
REVISIONS				
LTR	DESCRIPTION	BY OR EO	DATE	APPR.
A	ADDED SOLDER TABS, WIRING	SRS	8/23/94	

		3	5	MST035	SOLDER TABS	
		2	4	SS-026-013-500P	STRAIN GAGES	
140480		1	1	440306 or 440312	PRESSURE SENSOR	
140474						
NEXT ASSEMBLY	USED ON	ITEM NO.	REQ'D	PART NO.	DESCRIPTION	SPEC., MATERIAL OR SOURCE
APPLICATION						

PRODUCT: MINISTRY OF DEFENCE

UNLESS OTHERWISE NOTED:
ALL DIMENSIONS ARE IN INCHES
.X = ± .030 • .XX = ± .010 • .XXX = ± .005
ANGULAR = ± 0° 30 • DIA ⊙ .005 TIR
FILLET RADII .005 MAX • SURFACE 63/

THIS DRAWING CONTAINS INFORMATION PROPRIETARY TO MICRON INSTRUMENTS INC. DO NOT USE, REPRODUCE, OR DISCLOSE TO ANYONE WITHOUT WRITTEN PERMISSION.

DR. BY: S. SCHAFFTER   7/18/94
CHK:

MATERIAL   N/A

FINISH   N/A

Micron INSTRUMENTS

4509 Runway Street
Simi Valley, CA 93063
(805) 522-4676
FAX: (805)522-4982

TITLE   GAGE INSTALLATION
SS-026-013-500P-S(4)M GAGES

SIZE A	CODE IDENT. NO. 34136	DWG. NO. 240461	REV. A

DO NOT SCALE DRAWING   SCALE: 16:1   WT: SHEET 1 OF 1

24

LTR	DESCRIPTION	BY OR EO	DATE	APPR.
A	ADDED SOLDER TABS, WIRING	SRS	8/23/94	

3	5	MST035	SOLDER TABS		
2	4	SS-037-026-500P	STRAIN GAGES		
1	1	440306 or 440312	PRESSURE SENSOR		

NEXT ASSEMBLY	USED ON	ITEM NO.	REQ'D	PART NO.	DESCRIPTION	SPEC., MATERIAL OR SOURCE
140480						
140474						
APPLICATION						

PRODUCT: MINISTRY OF DEFENCE	DR. BY: S. SCHAFFTER 7/18/94		4509 Runway Street Simi Valley, CA 93063 (805) 522-4676 FAX: (805)522-4982

UNLESS OTHERWISE NOTED:
ALL DIMENSIONS ARE IN INCHES
.X = ± .030 • .XX = ± .010 • .XXX = ± .005
ANGULAR = ± 0° 30 • DIA ⊙ .005 TIR
FILLET RADII .005 MAX • SURFACE

MICRON INSTRUMENTS

CHK:

MATERIAL N/A

TITLE *GAGE INSTALLATION*
SS-037-026-500P-S(4)M GAGES

FINISH N/A

SIZE A	CODE IDENT. NO. 34136	DWG. NO. 240462	REV. A

DO NOT SCALE DRAWING | SCALE: 16:1 | WT: | SHEET 1 OF 1

		3	5	MST035	SOLDER TABS	
		2	4	SS-060-033-500P	STRAIN GAGES	
140480		1	1	440306 or 440312	PRESSURE SENSOR	
140474						
NEXT ASSEMBLY	USED ON	ITEM NO.	REQ'D	PART NO.	DESCRIPTION	SPEC., MATERIAL OR SOURCE
APPLICATION						

PRODUCT: MINISTRY OF DEFENCE	DR. BY: S. SCHAFFTER 7/18/94	**Micron** INSTRUMENTS	4509 Runway Street Simi Valley, CA 93063 (805) 522-4676 FAX: (805)522-4982
UNLESS OTHERWISE NOTED: ALL DIMENSIONS ARE IN INCHES .X = ±.030 • .XX = ±.010 • .XXX = ± .005 ANGULAR = ±0° 30 • DIA ⊙.005 TIR FILLET RADII .005 MAX • SURFACE	CHK:		

THIS DRAWING CONTAINS INFORMATION PROPRIETARY TO MICRON INSTRUMENTS INC. DO NOT USE, REPRODUCE, OR DISCLOSE TO ANYONE WITHOUT WRITTEN PERMISSION.	MATERIAL N/A		TITLE GAGE INSTALLATION SS-060-033-500P-S(4)M GAGES				
	FINISH N/A		SIZE **A**	CODE IDENT. NO. **34136**	DWG. NO. 240463		REV. A
	DO NOT SCALE DRAWING		SCALE: 16:1	WT:		SHEET 1 OF 1	

26

DASH	"T" DIMENSION
- 1	.0077 / .0073
- 2	
- 3	
- 4	

.080

.300±.001

.150±.001

-B-

⊚ B .001

"T"
DIM.

-A- ⟋ A .0003

⟋ .0003   ⟋ .0003

	140474						
NEXT ASSEMBLY	USED ON	ITEM NO.	REQ'D	PART NO.	DESCRIPTION		SPEC., MATERIAL OR SOURCE
APPLICATION							

PRODUCT: MINISTRY OF DEFENCE

UNLESS OTHERWISE NOTED:
ALL DIMENSIONS ARE IN INCHES
.X = ± .030 • .XX = ± .010 • .XXX = ± .005
ANGULAR = ± 0° 30 • DIA ⊕ .005 TIR
FILLET RADII .005 MAX • SURFACE

DR. BY: D. ROSMAN   6/18/93

CHK: S. SCHAFFTER   7/18/94

MICRON
INSTRUMENTS

4509 Runway Street
Simi Valley, CA 93063
(805) 522-4676
FAX: (805)522-4982

MATERIAL   N/A

TITLE   STRESS TRANSDUCER

FINISH   N/A

SIZE	CODE IDENT. NO.	DWG. NO.	REV.
A	34136	440306–	

DO NOT SCALE DRAWING

SCALE: 8 : 1   WT: SHEET 1 OF 1

27

Pressure Transducer Calibration Data

Date 4 Apr 1995

MICRON INSTRUMENTS

Model Number 140474   Serial Number 12217   Diaphragm Materials

Excitation   4.0 mA   Type ⦿ Constant Current ◯ Constant Voltage   Titanium

Pressure Range   100 PSI ◯ Absolute ⦿ Gage ◯ Reference

AMBIENT PRESSURE CALIBRATION DATA

Date Calibration Run   27 Mar 95

Pressure	Increase (1)	Decrease	Increase(2)	Ideal	Linearity (%FS)	Hysteresis (%FS)	Repeatability (%FS)
0PSIG	-.04 mV	-0.05 mV	-.05 mV	-0.04 mV			0.0254%
20PSIG	7.81 mV	7.80 mV	7.80 mV	7.83 mV	0.0508%	0.0254%	0.0254%
40PSIG	15.69 mV	15.68 mV	15.68 mV	15.70 mV	0.0254%	0.0254%	0.0254%
60PSIG	23.57 mV	23.56 mV	23.56 mV	23.57 mV	0.0000%	0.0254%	0.0254%
80PSIG	31.45 mV	31.45 mV	31.46 mV	31.44 mV	0.0254%	0.0000%	0.0254%
100PSIG	39.31 mV		39.31 mV				0.0000%
SENSITIVITY	39.35 mV						

STATIC ERROR BAND ± 0.0254% FS

THERMAL CALIBRATION DATA

Date Temperature Data Run   22 Mar 95

	Ambient	Low Temp.	High Temp
Temperature	70 °F	-50 °F	150 °F
0 PSI	-0.40 mV	-0.93 mV	-0.43 mV
Full Scale	38.68 mV	38.31 mV	38.80 mV
Sensitivity	39.08 mV	39.24 mV	39.23 mV

Average Thermal Balance Shift ± 0.0061% FS/°F

Average Thermal Sensitivity Shift ± 0.0041% FS/°F

Pressure Transducer Calibration Data

MICRON INSTRUMENTS

Date 5 Apr 1995

Model Number 140480

Serial Number 12244

Diaphragm Materials   Steel

Excitation   4.0 mA   Type ◉ Constant Current ◯ Constant Voltage

Pressure Range   100 PSI ◯ Absolute ◉ Gage ◯ Reference

AMBIENT PRESSURE CALIBRATION DATA

Date Calibration Run 28 Mar 95

Pressure	Increase (1)	Decrease	Increase(2)	Ideal	Linearity (%FS)	Hysteresis (%FS)	Repeatability (%FS)
0PSIG	-0.57 mV	-0.57 mV	-0.57 mV	-0.57 mV		0.0000%	0.0000%
20PSIG	3.73 mV	3.73 mV	3.72 mV	3.72 mV	0.0373%	0.0000%	0.0466%
40PSIG	8.02 mV	7.99 mV	8.01 mV	8.01 mV	0.0280%	0.1398%	0.0466%
60PSIG	12.30 mV	12.28 mV	12.29 mV	12.31 mV	0.0280%	0.0932%	0.0466%
80PSIG	16.60 mV	16.57 mV	16.59 mV	16.60 mV	0.0093%	0.1398%	0.0466%
100PSIG	20.89 mV	20.88 mV	20.88 mV				
SENSITIVITY	21.46 mV						0.0466%

STATIC ERROR BAND ± 0.0186% FS

THERMAL CALIBRATION DATA

	Ambient	Low Temp.	High Temp
Temperature	70 °F	-50 °F	150 °F
0 PSI	-0.13 mV	-0.56 mV	-0.61 mV
Full Scale	21.02 mV	20.58 mV	20.38 mV
Sensitivity	21.15 mV	21.14 mV	20.99 mV

Date Temperature Data Run 21 Mar 95

Average Thermal Balance Shift   ± 0.0223% FS/°F

Average Thermal Sensitivity Shift   ± 0.0049% FS/°F

Pressure Transducer Calibration Data

Date 5 Apr 1995

MICRON INSTRUMENTS

Model Number 140474 Serial Number 12236 Type ◉ Constant Current ○ Constant Voltage

Excitation 4.0 mA

Pressure Range 100 PSI ○ Absolute ◉ Gage ○ Reference

Diaphragm Materials Titanium

AMBIENT PRESSURE CALIBRATION DATA

Date Calibration Run 27 Mar 95

Pressure	Increase (1)	Decrease	Increase(2)	Ideal	Linearity (%FS)	Hysteresis (%FS)	Repeatability (%FS)
0 PSIG	-1.70 mV	-1.70 mV	-1.70 mV	-1.70 mV		0.0000%	0.0000%
20 PSIG	6.33 mV	6.28 mV	6.33 mV	6.40 mV	0.1679%	0.1235%	0.0000%
40 PSIG	14.39 mV	14.35 mV	14.40 mV	14.50 mV	0.2618%	0.0988%	0.0247%
60 PSIG	22.51 mV	22.46 mV	22.50 mV	22.59 mV	0.2075%	0.1235%	0.0247%
80 PSIG	30.64 mV	30.59 mV	30.63 mV	30.69 mV	0.1284%	0.1235%	0.0247%
100 PSIG	38.79 mV	38.79 mV	38.79 mV				0.0000%
SENSITIVITY	40.49 mV						

STATIC ERROR BAND ± 0.1309% FS

THERMAL CALIBRATION DATA

Date Temperature Data Run 20 Mar 94

	Ambient	Low Temp.	High Temp
Temperature	70 °F	-50 °F	150 °F
0 PSI	-0.36 mV	-0.29 mV	-0.26 mV
Full Scale	39.92 mV	40.31 mV	40.86 mV
Sensitivity	40.28 mV	40.60 mV	41.12 mV

Average Thermal Balance Shift ± 0.0023% FS/°F

Average Thermal Sensitivity Shift ± 0.0163% FS/°F

30

Pressure Transducer Calibration Data

Date 5 Apr 1995

MICRON INSTRUMENTS

Model Number 140480 Serial Number 12253 Diaphragm Materials
Excitation 4.0 mA Type ● Constant Current ○ Constant Voltage Steel
Pressure Range 100 PSI ○ Absolute ● Gage ○ Reference

AMBIENT PRESSURE CALIBRATION DATA

Date Calibration Run 28 Mar 95

Pressure	Increase (1)	Decrease	Increase(2)	Ideal	Linearity (%FS)	Hysteresis (%FS)	Repeatability (%FS)
0 PSIG	0.00 mV	0.00 mV	0.00 mV	0.00 mV		0.0000%	0.0000%
20 PSIG	4.56 mV	4.54 mV	4.56 mV	4.58 mV	0.0699%	0.0874%	0.0000%
40 PSIG	9.12 mV	9.11 mV	9.11 mV	9.15 mV	0.1399%	0.0437%	0.0437%
60 PSIG	13.70 mV	13.69 mV	13.70 mV	13.73 mV	0.1224%	0.0437%	0.0000%
80 PSIG	18.31 mV	18.29 mV	18.30 mV	18.30 mV	0.0262%	0.0874%	0.0437%
100 PSIG	22.88 mV	22.89 mV					0.0437%
SENSITIVITY	22.88 mV						

STATIC ERROR BAND ± 0.0699% FS

THERMAL CALIBRATION DATA

Date Temperature Data Run 21 Mar 95

	Ambient	Low Temp.	High Temp
Temperature	70 °F	-50 °F	150 °F
0 PSI	-0.05 mV	-0.21 mV	-0.10 mV
Full Scale	22.70 mV	22.63 mV	22.68 mV
Sensitivity	22.75 mV	22.84 mV	22.78 mV

Average Thermal Balance Shift ± 0.0043% FS/°F

Average Thermal Sensitivity Shift ± 0.0025% FS/°F

Pressure Transducer Calibration Data

Date 4 Apr 1995

ICRON INSTRUMENTS

Model Number 140474

Serial Number 12222

Diaphragm Materials Titanium

Excitation 4.0 mA   **Type** ◉ Constant Current ○ Constant Voltage

Pressure Range 100 PSI ○ Absolute ◉ Gage ○ Reference

AMBIENT PRESSURE CALIBRATION DATA

Date Calibration Run 27 Mar 95

Pressure	Increase (1)	Decrease	Increase(2)	Ideal	Linearity (%FS)	Hysteresis (%FS)	Repeatability (%FS)
0 PSIG	-1.21 mV	-1.22 mV	-1.22 mV	-1.21 mV		0.0226%	0.0226%
20 PSIG	7.60 mV	7.55 mV	7.61 mV	7.63 mV	0.0679%	0.1131%	0.0226%
40 PSIG	16.46 mV	16.40 mV	16.46 mV	16.47 mV	0.0226%	0.1357%	0.0000%
60 PSIG	25.31 mV	25.25 mV	25.30 mV	25.31 mV	0.0000%	0.1357%	0.0226%
80 PSIG	34.17 mV	34.10 mV	34.16 mV	34.15 mV	0.0452%	0.1584%	0.0226%
100 PSIG	42.99 mV		42.98 mV				0.0226%
SENSITIVITY	44.2 mV						

STATIC ERROR BAND ± 0.0679% FS

THERMAL CALIBRATION DATA

Date Temperature Data Run 20 Mar 95

	Ambient	Low Temp.	High Temp
Temperature	70 °F	-50 °F	150 °F
0 PSI	-0.04 mV	-1.84 mV	-0.82 mV
Full Scale	44.15 mV	42.34 mV	43.40 mV
Sensitivity	44.19 mV	44.18 mV	44.22 mV

Average Thermal Balance Shift ± 0.0280% FS/°F

Average Thermal Sensitivity Shift ± 0.0005% FS/°F

Pressure Transducer Calibration Data

Date 5 Apr 1995

MICRON INSTRUMENTS

Model Number 140480
Serial Number 12246
Diaphragm Materials Steel
Excitation 4.0 mA Type ◉ Constant Current ○ Constant Voltage
Pressure Range 100 PSI ○ Absolute ◉ Gage ○ Reference

AMBIENT PRESSURE CALIBRATION DATA

Date Calibration Run 28 Mar 95

Pressure	Increase (1)	Decrease	Increase(2)	Ideal	Linearity (%FS)	Hysteresis (%FS)	Repeatability (%FS)
0 PSIG	-0.68 mV	-0.69 mV	-0.69 mV	-0.68 mV		0.0456%	0.0456%
20 PSIG	3.72 mV	3.69 mV	3.71 mV	3.71 mV	0.0547%	0.1367%	0.0456%
40 PSIG	8.10 mV	8.07 mV	8.09 mV	8.10 mV	0.0182%	0.1367%	0.0456%
60 PSIG	12.48 mV	12.45 mV	12.47 mV	12.48 mV	0.0182%	0.1367%	0.0456%
80 PSIG	16.87 mV	16.85 mV	16.86 mV	16.87 mV	0.0091%	0.0912%	0.0456%
100 PSIG	21.26 mV		21.25 mV				
SENSITIVITY	21.94 mV						

STATIC ERROR BAND ± 0.0684% FS

THERMAL CALIBRATION DATA

Date Temperature Data Run 21 Mar 95

	Ambient	Low Temp.	High Temp
Temperature	70 °F	-50 °F	150 °F
0 PSI	0.22 mV	-0.03 mV	0.33 mV
Full Scale	22.15 mV	21.97 mV	22.27 mV
Sensitivity	21.93 mV	22.00 mV	21.94 mV

Average Thermal Balance Shift ± 0.0079% FS/°F
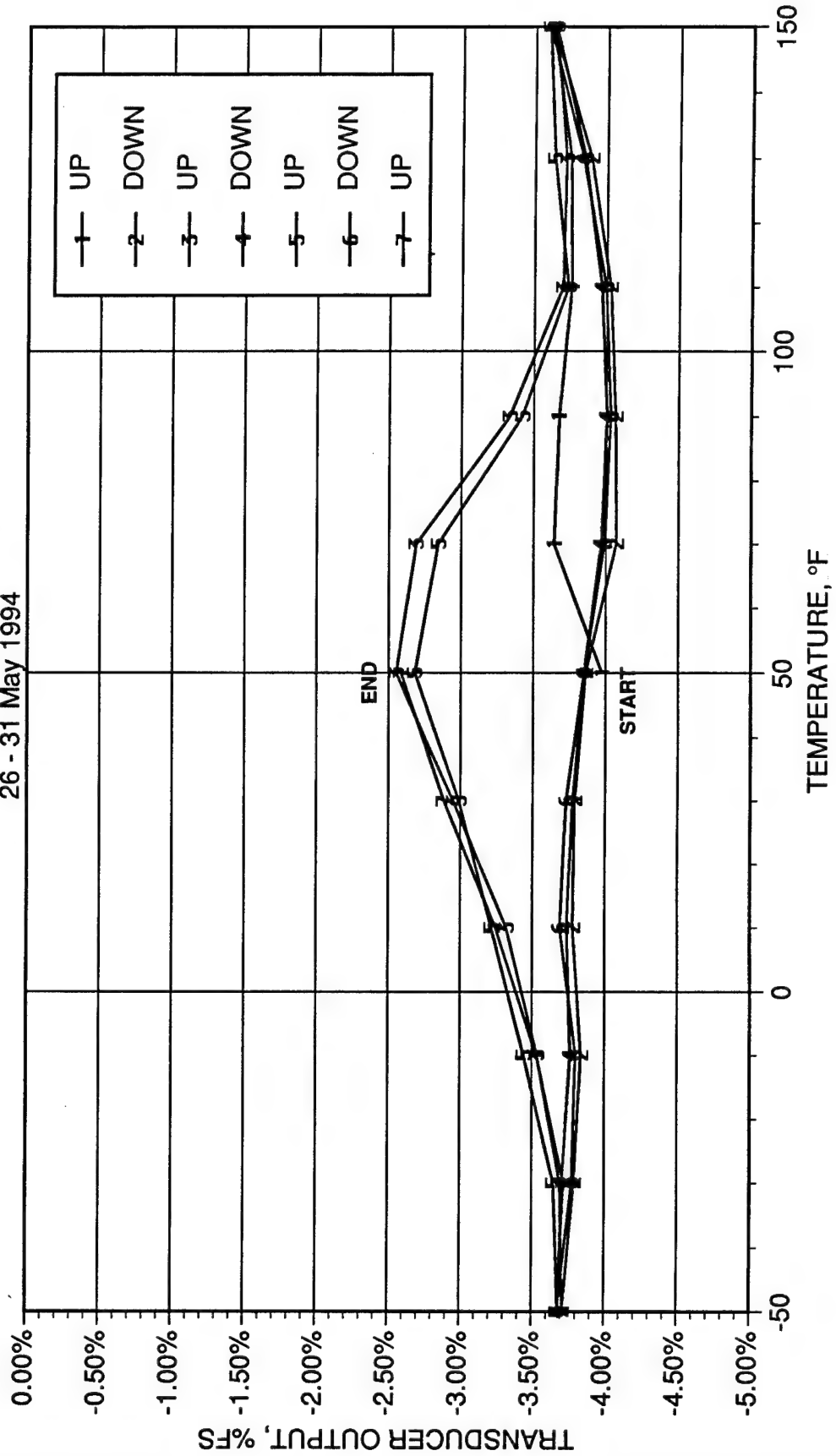Average Thermal Sensitivity Shift ± 0.0016% FS/°F

33

THERMAL HYSTERESIS DATA
Micron Instruments P/N 140358
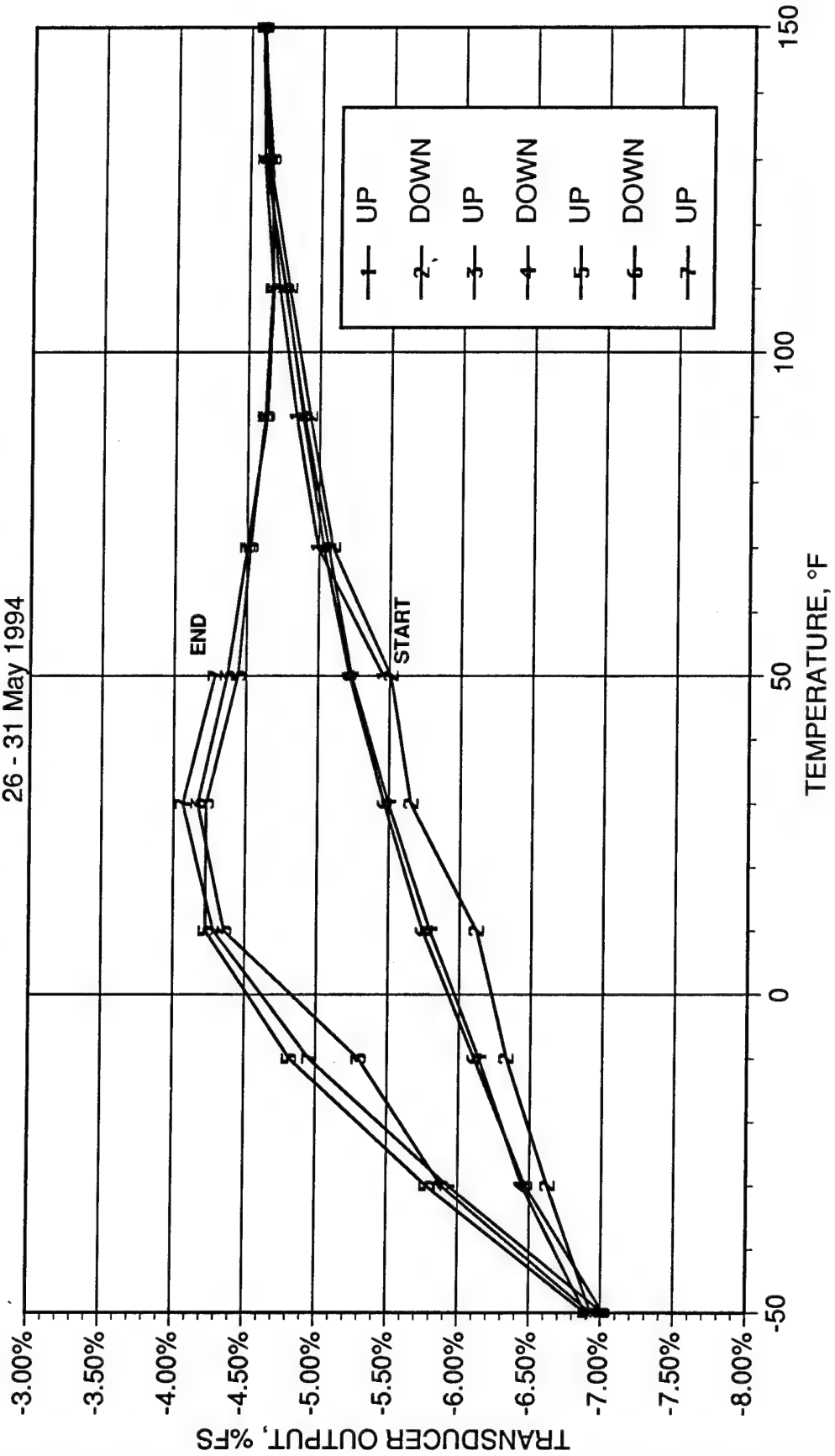S/N 7607 – TITANIUM .026

26 - 31 May 1994
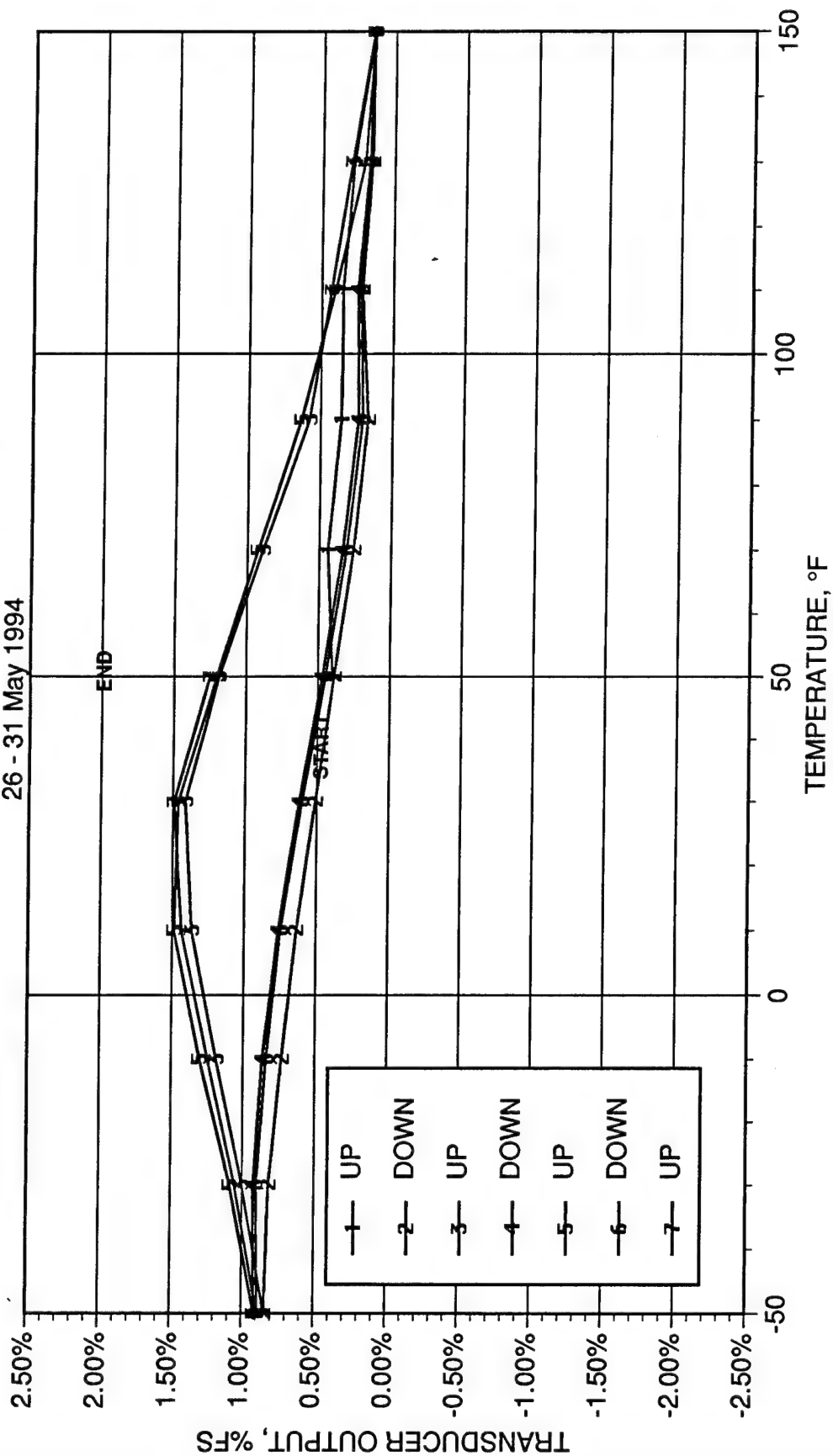
THERMAL HYSTERESIS DATA
Micron Instruments P/N 140358
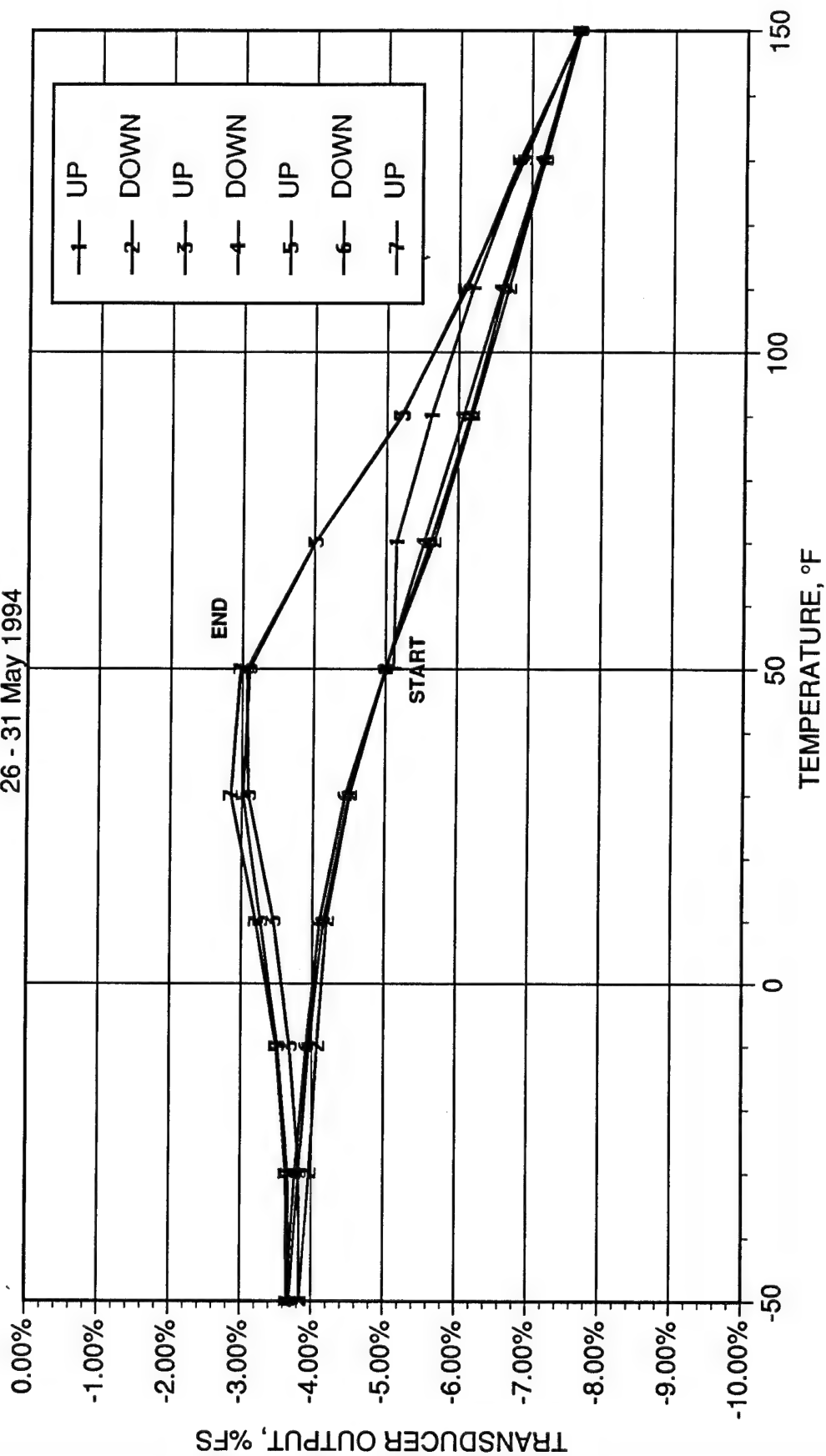S/N 7610 – TITANIUM .037

26 - 31 May 1994

THERMAL HYSTERESIS DATA
Micron Instruments P/N 140358
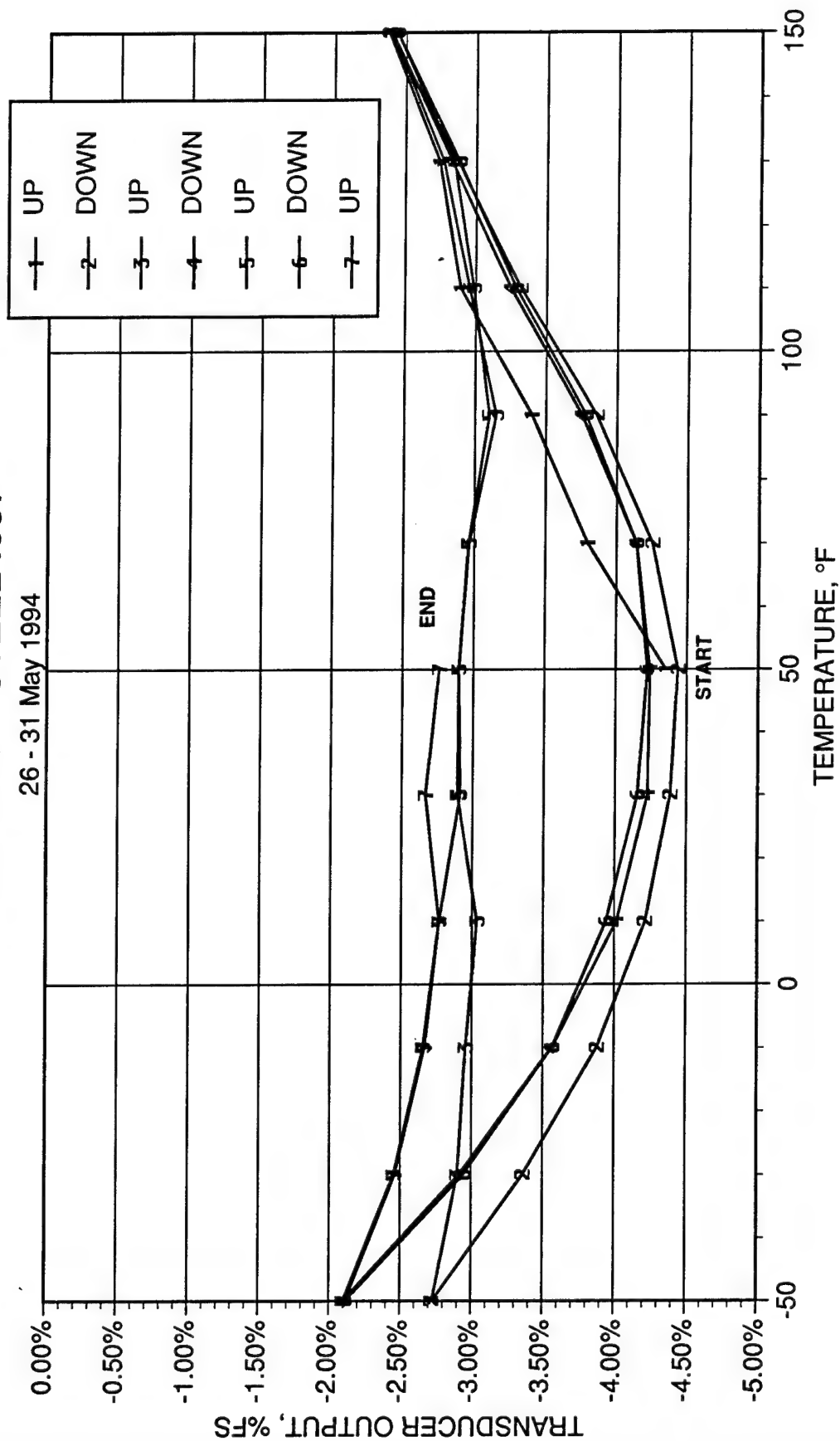S/N 7619 – TITANIUM .060

26 - 31 May 1994

THERMAL HYSTERESIS DATA
Micron Instruments P/N 140358
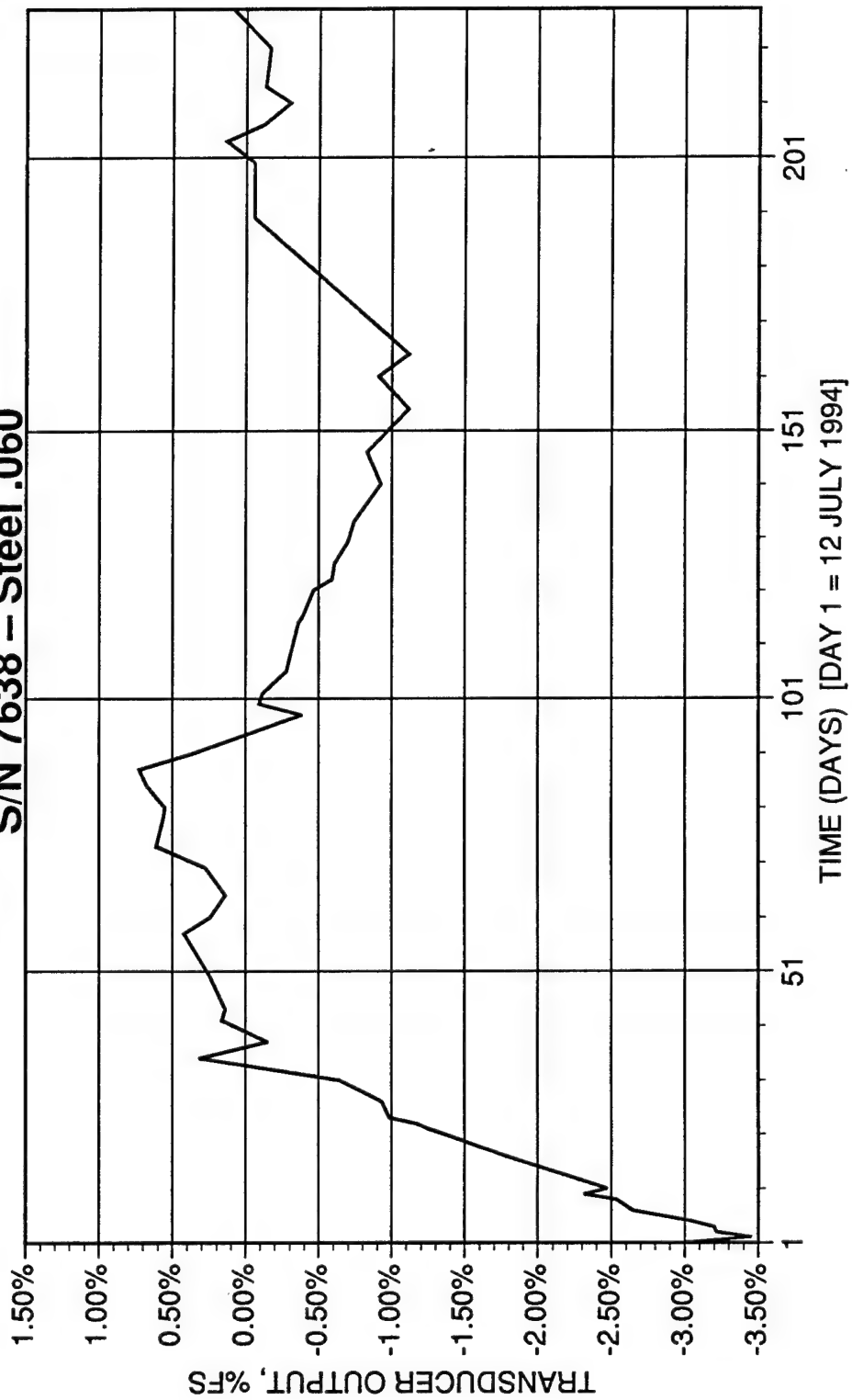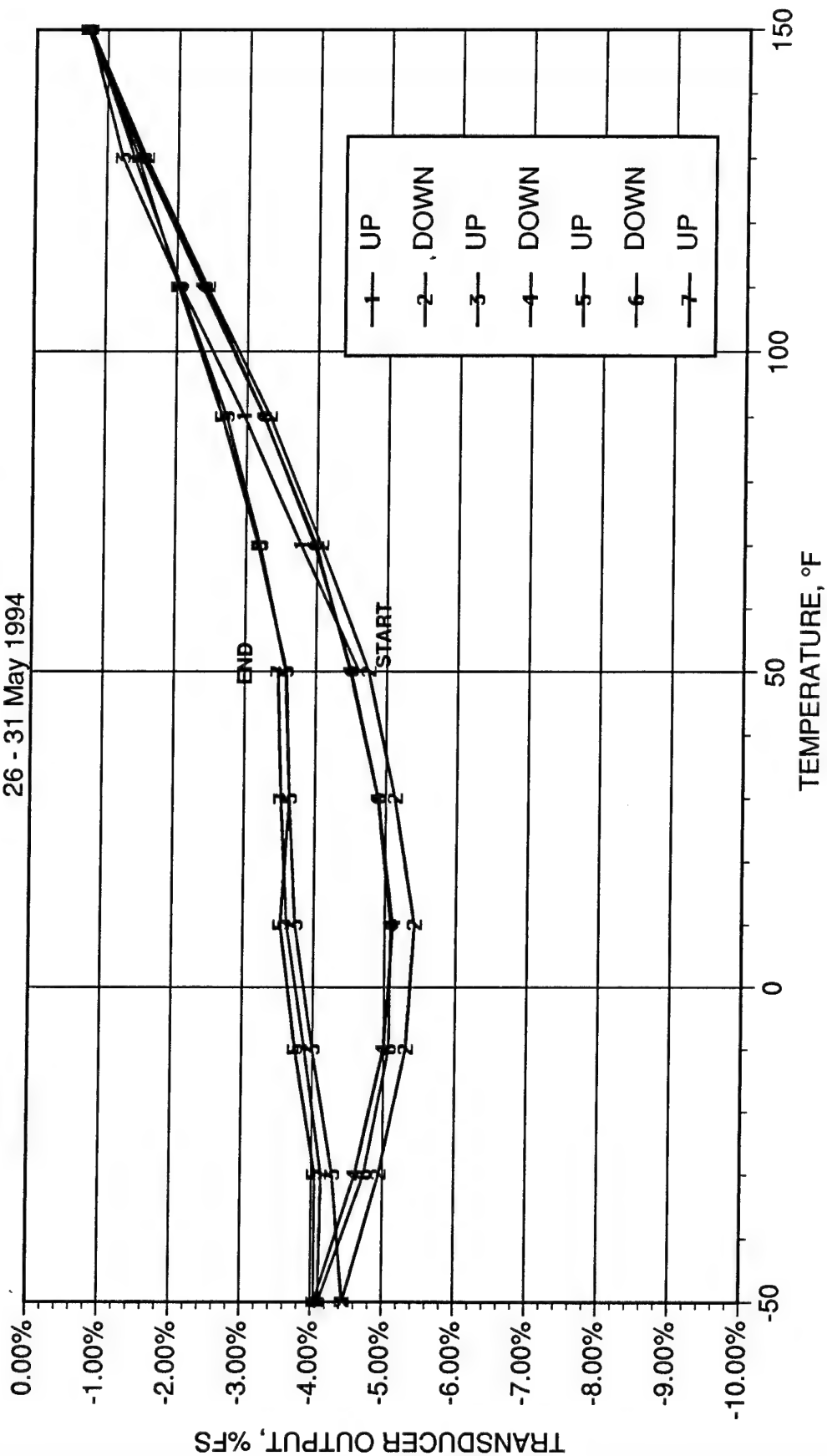S/N "D" – STEEL .026
26 - 31 May 1994

37

THERMAL HYSTERESIS DATA
Micron Instruments P/N 140358
S/N 7630 – STEEL .037
26 - 31 May 1994

LONG-TERM STABILITY DATA
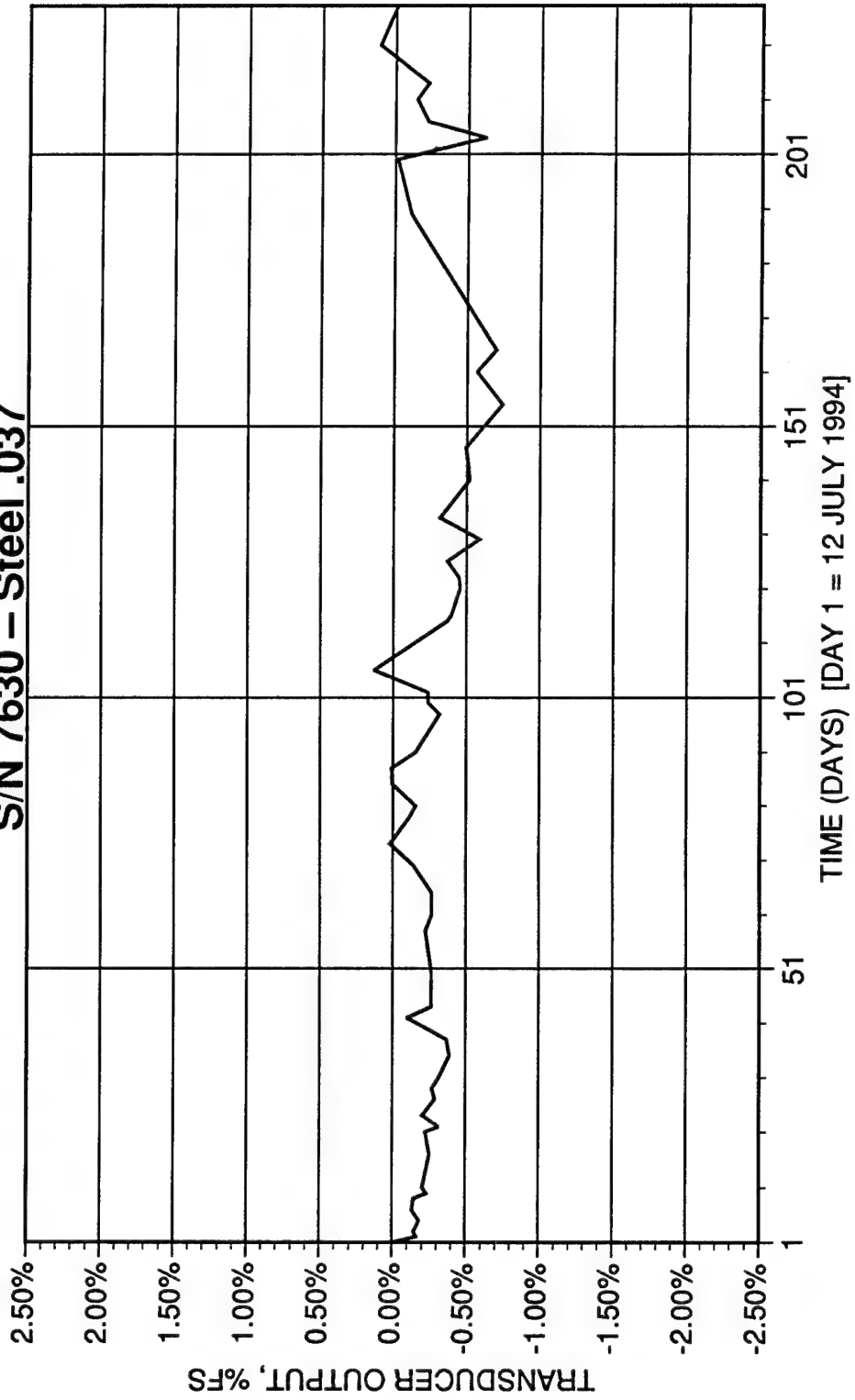Micron Instruments P/N 140358
S/N 7638 – Steel .060

TIME (DAYS) [DAY 1 = 12 JULY 1994]

TRANSDUCER OUTPUT, %FS

39

THERMAL HYSTERESIS DATA
Micron Instruments P/N 140358
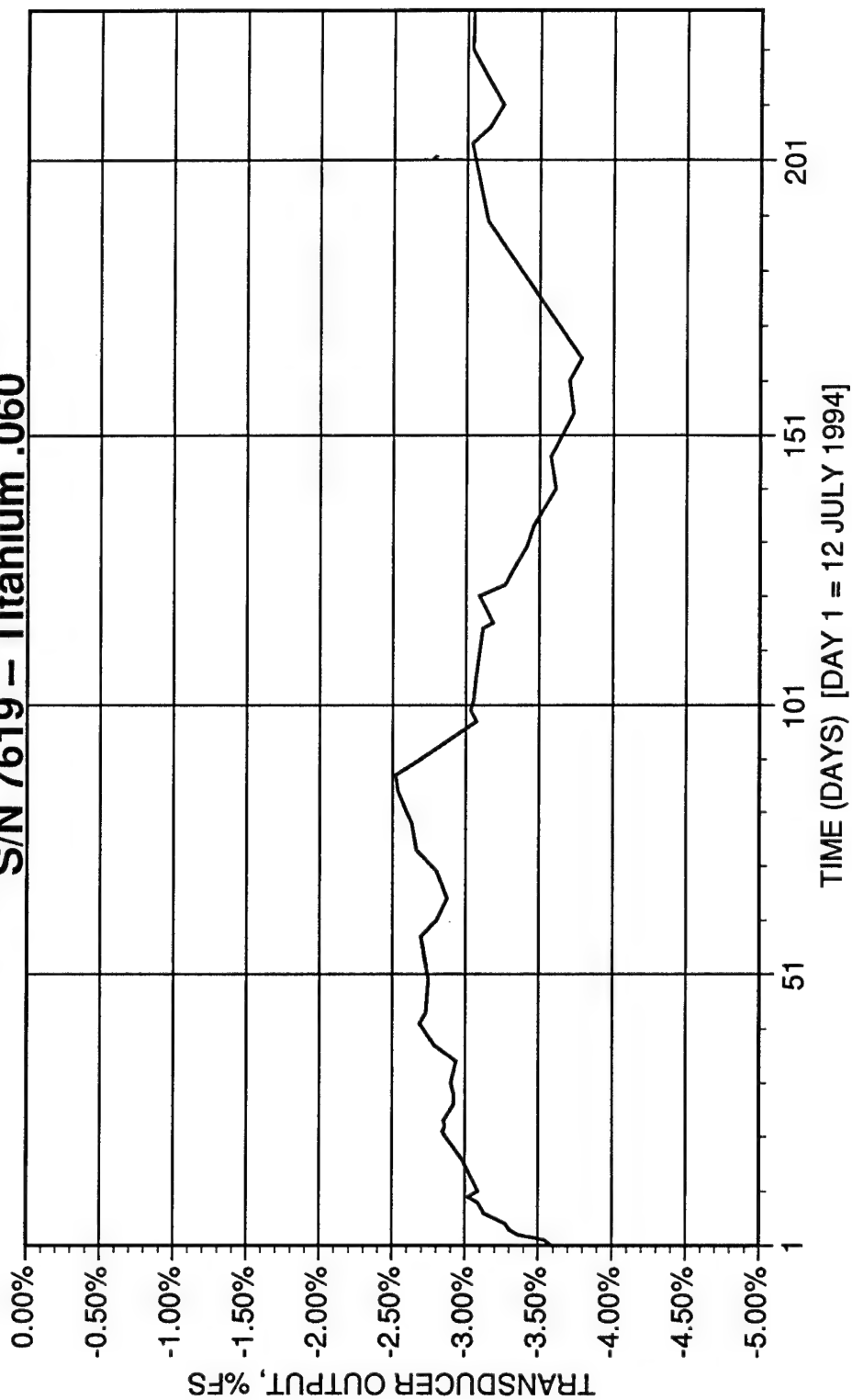S/N 7638 – STEEL .060

26 - 31 May 1994

40

LONG-TERM STABILITY DATA
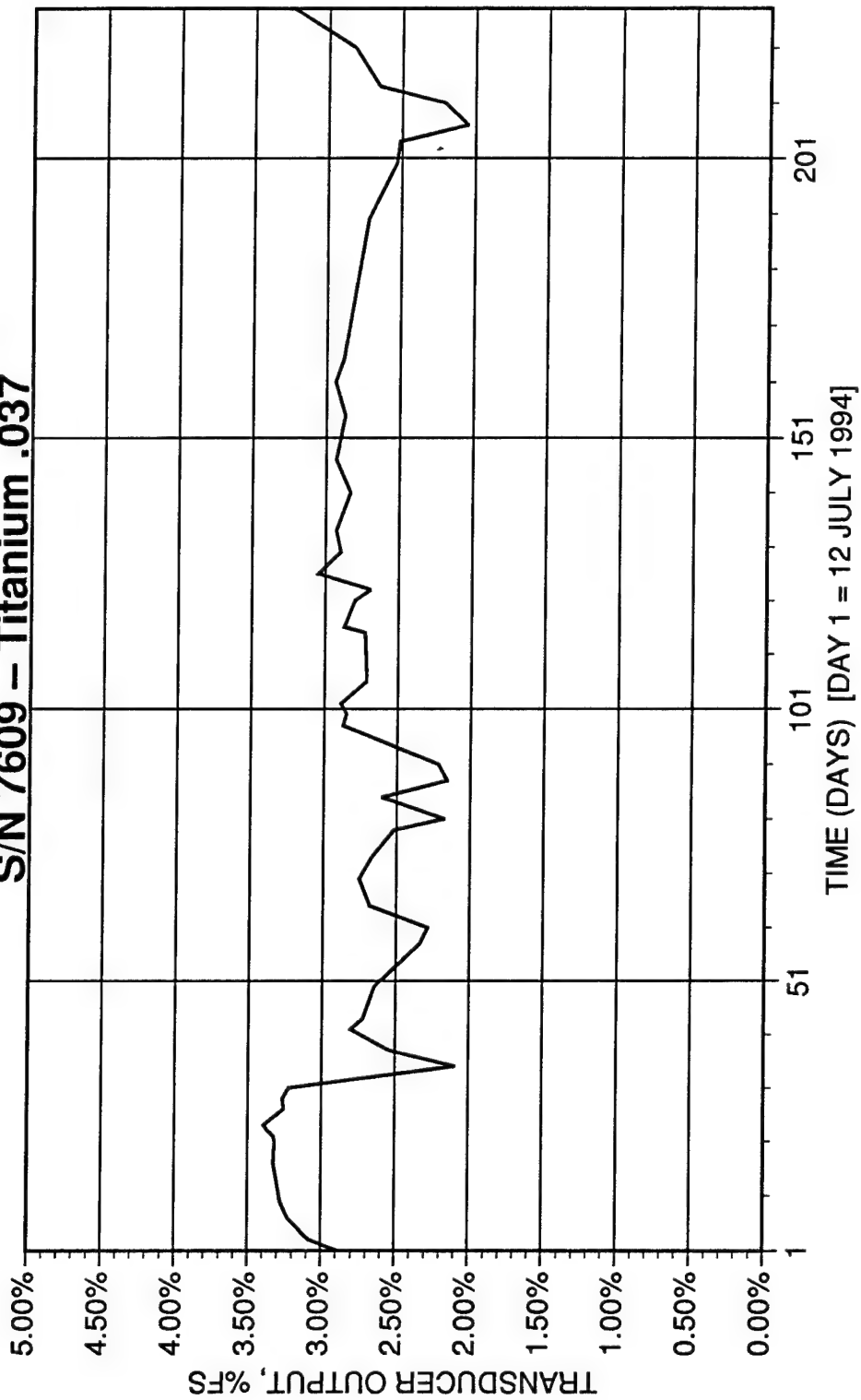Micron Instruments P/N 140358
S/N 7630 – Steel .037

LONG-TERM STABILITY DATA
Micron Instruments P/N 140358
S/N "D" – Steel .026

TRANSDUCER OUTPUT, %FS

2.50%
2.00%
1.50%
1.00%
0.50%
0.00%
-0.50%
-1.00%
-1.50%
-2.00%
-2.50%

1   51   101   151   201
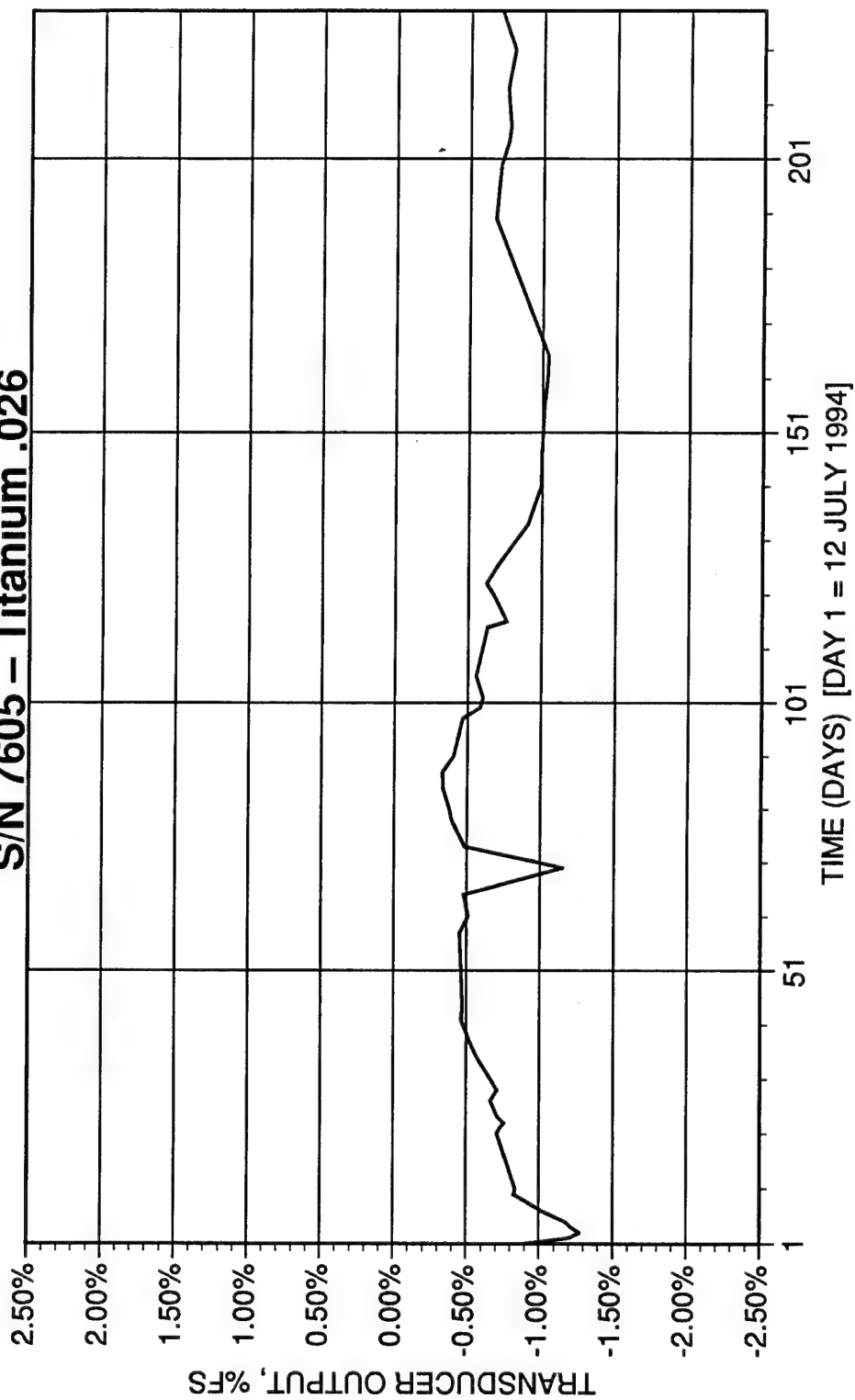
TIME (DAYS) [DAY 1 = 12 JULY 1994]
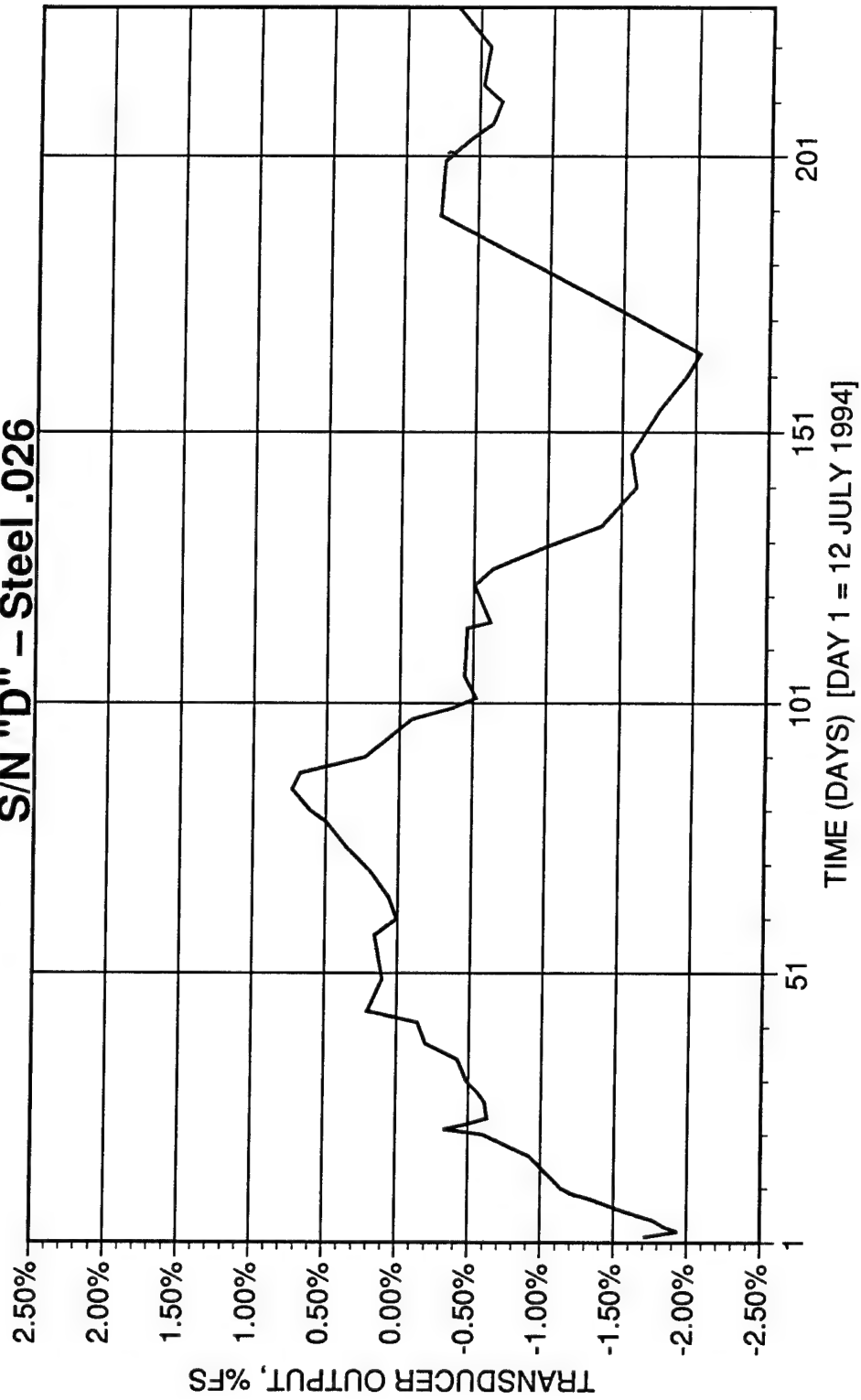
LONG-TERM STABILITY DATA
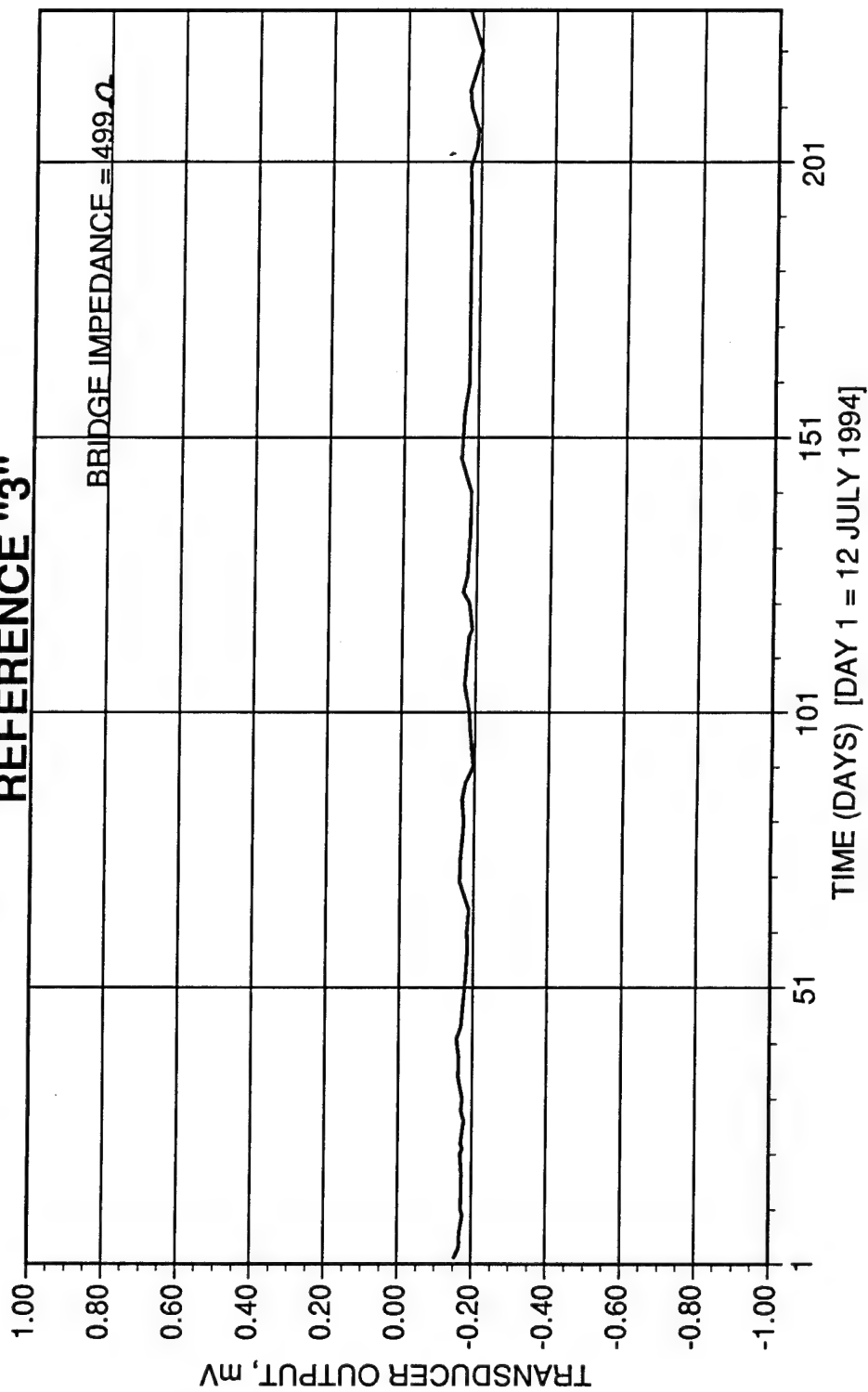Micron Instruments P/N 140358
S/N 7619 – Titanium .060

LONG-TERM STABILITY DATA
Micron Instruments P/N 140358
S/N 7609 – Titanium .037

44

LONG-TERM STABILITY DATA
Micron Instruments P/N 140358
S/N 7605 – Titanium .026

TIME (DAYS) [DAY 1 = 12 JULY 1994]

TRANSDUCER OUTPUT, %FS

LONG-TERM STABILITY DATA
REFERENCE RESISTOR NETWORK OUTPUT
REFERENCE "3"

BRIDGE IMPEDANCE = 499 Ω

TRANSDUCER OUTPUT, mV

TIME (DAYS) [DAY 1 = 12 JULY 1994]

46

DISPLACEMENT GAGES AND STRAIN EXTENSOMETERS FOR SPECIAL APPLICATIONS

by

John Shepic
John Shepic Co.
14031 West Exposition Drive
Lakewood, Colorado 80228

I am a manufacturer of custom strain gage instruments addressing unique mechanical testing situations. Instruments will be shown that have been developed for deep cryogenic (-452F) strain and displacement measurements of tensile specimens and compact tension fracture specimens. A displacement gage that attaches to EDM machined surface defects or a .05" diameter hole (depending on specimen type), will also be shown. Also to be shown and discussed are a diametral extensometer for low cycle fatigue testing and a force transducer used as a training aid by Olympic kayakers.

Examples of several actual instruments will be shown to workshop attendees.

Shown in Figure 1 is a displacement gage which meets ASTM E 399[1] criteria for use on fracture toughness specimens. The design has an advantage or two over the more common double cantilever beam style of displacement gage:
  a) Higher displacement range for a given transducer length.
  b) The contact beams can be modified or replaced without consequence to the transducer because they are not instrumented with strain gages.
For deep cryogenic applications (liquid hydrogen or liquid helium temperature) this design works reliably. Several different double cantilever beam configurations were tried which would not work at all in liquid helium even though they worked well in liquid nitrogen.

Shown in Figure 2 is a transfer arm that is used on compact tension fracture specimens in conjunction with a displacement gage. Made of G-10 fiberglas laminate, it allows displacement monitoring of the specimen in corrosive or electrically conductive solutions without having to immerse the displacement gage in the solution. The G-10 is non-conductive and does not create a galvanic cell with the test specimen. The pivot consists of a minature ball bearing sealed off from contact with the solution by two o-rings. The lever ratio of this unit is 1 to 1; other ratios are certainly possible.

A tensile strain extensometer designed for use in cryogenic liquids is shown in Figure 3. In use, the extensometer is compressed and placed between two clamps that are mounted on the tensile specimen at a preset gage length. The separable design permits easy use of this extensometer in cryostats and environmental chambers where manual detachment of the extensometer prior to specimen failure is not feasible. Various gage length versions (0.5", 1", and 2") have

been built and used successfully. Strain ranges up to about 70% are possible. On strain ranges above 20%, the clamp screws are spring loaded to maintain clamping pressure as specimen diameter decreases during elongation. The extensometer simply self-detaches upon specimen failure.

A surface flaw displacement gage is shown in Figure 4. This device was developed for displacement measurements on surface crack tension (SCT) specimens which have small slit-like defects introduced by EDM machining or a thin slitting saw. The defects are typically fatigue-cracked by cyclical loading. Fatigue crack growth rate studies (da/dn) can then be performed, or the specimen can be fractured by monotonic loading to failure. In either case, monotoring of the crack mouth displacement during the test is desirable. The gage shown can attach directly to a narrow slit only .020" wide. The body design is similar to the displacement gage shown previously, only much narrower (0.24" vs. 0.4" for the DG-25 displacement gage). The small prongs which attach to the flaw or narrow slit are dovetail mounted into the displacement gage body. A clamping screw locks the assembly together. There is adjustment to allow for openings larger than .020". In the past, adaptors were usually made up to allow use of a standard displacement gage or extensometer on a surface defect. This practice is outlined in ASTM E 740. Results were usually less than acceptable because there were specimen to specimen variations in how well the adaptors were located and attached. Often times the adaptors would fall off before the test was completed. Standard displacement gages generate excessive pressure to be used successfully in this manner. The surface flaw displacement gage can also be used on center cracked specimens as outlined in ASTM E 561.

Pictured in Figure 5 is a diametral extensometer developed for fully reversed, strain-controlled low cycle fatigue of small (0.25" dia.) specimens at cryogenic temperatures. Low cycle fatigue specimens are typically hourglass shaped to avoid buckling during compressive loading. Diametral strain measurement (and control) is the method of choice for this specimen configuration since specimen cross-section is variable along its length. Unlike commercially available units, this extensometer design is self supporting because of its light weight and the symmetry of its design. An external mounting arm and support spring or bracket are not required. Figure 6[2] is an example of a hysteresis curve generated using this extensometer. Note the work hardening with each successive load cycle and the good control at each strain reversal.
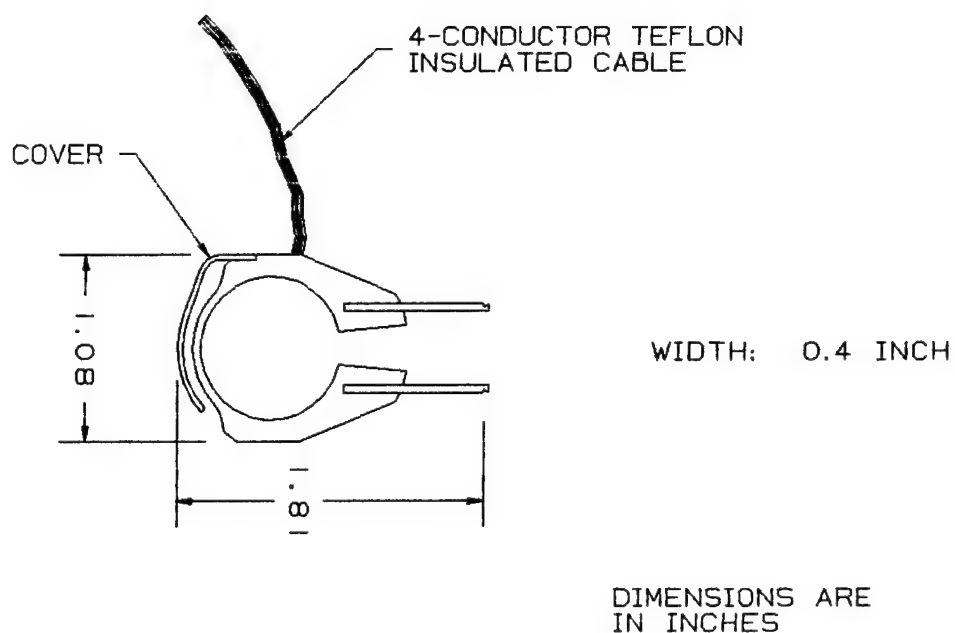
This next item is an interesting application involving a kayak paddle. Shown in Figure 7 is a transducer designed to pick up deflection that occurs as the result of a bending moment generated in the paddle as it is used by an athlete. Each athlete has his own paddle which satisfies his personal preference as to size, weight, stiffness, etc. I was asked by the U. S. Olympic Committee to design a transducer that would work reasonably well on all the various paddle designs so that they could measure the force applied

and its duration and thus evaluate an athlete's performance. The transducer consists of a split yoke type of clamp designed to work over a limited range of paddle handle diameters, and two instrumented deflection beams that are preloaded against the paddle when the clamp is tightened. Two beams are necessary since the ends of the paddle are not co-planer. After the transducer is mounted to a paddle, a calibration is performed by dead weighting each end of the paddle. The athlete is then sent out on a trial. Data is sent via telemetry from the kayak to a nearby portable data aquisition system.

1."Plane Strain Fracture Toughness of Metallic Materials", Annual Book of ASTM Standards, American Society for Testing and Materials, 1916 Race Street, Philadelphia, Pa. 19103

2.F. R. Schwartzberg and J. A. Shepic, "Fatigue Testing of Stainless Steels", Materials Studies for Magnetic Fusion Energy Applications at Low Temperatures, Volume 1, April 1978, National Institute for Science & Technology, Boulder, Co.
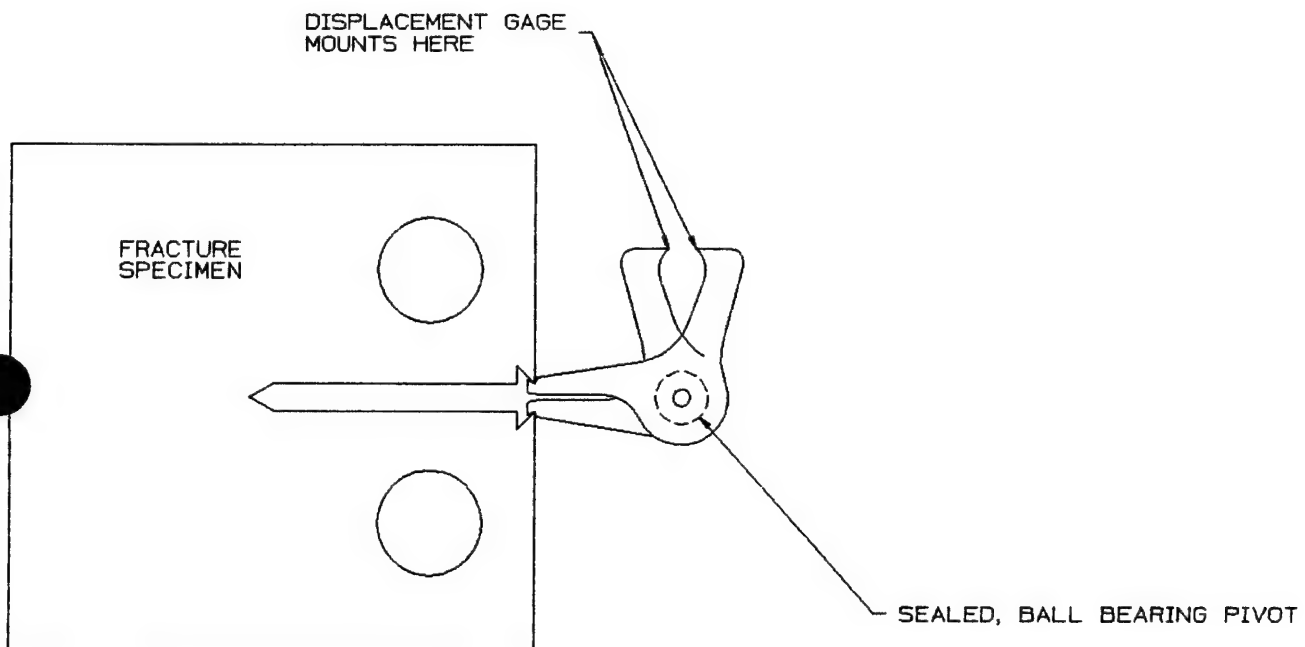
FIGURE I

4-CONDUCTOR TEFLON
INSULATED CABLE

COVER

1.08

1.8

WIDTH: 0.4 INCH

DIMENSIONS ARE
IN INCHES

DG-25 DISPLACEMENT GAGE
.1" TO .35" OPERATING RANGE

-454F TO +200F TEMP. RANGE

350 OHM STRAIN GAGE BRIDGE

AVAILABLE IN NONMAGNETIC CONSTRUCTION

50

FIGURE 2

DISPLACEMENT GAGE
MOUNTS HERE

FRACTURE
SPECIMEN

SEALED, BALL BEARING PIVOT

TRANSFER ARM
RATIO: I TO I
MAT'L: G-IO FIBERGLAS

DESIGNED FOR COD MEASUREMENTS
IN CORROSIVE OR CONDUCTIVE
SOLUTIONS (BRINGS CLIP GAGE
UP OUT OF THE SOLUTION)

J. SHEPIC
3/12/93

51

FIGURE 3

TENSILE STRAIN EXTENSOMETER, MODEL SE-1

GAGE LENGTH: 1 INCH

STRAIN RANGE: 15%

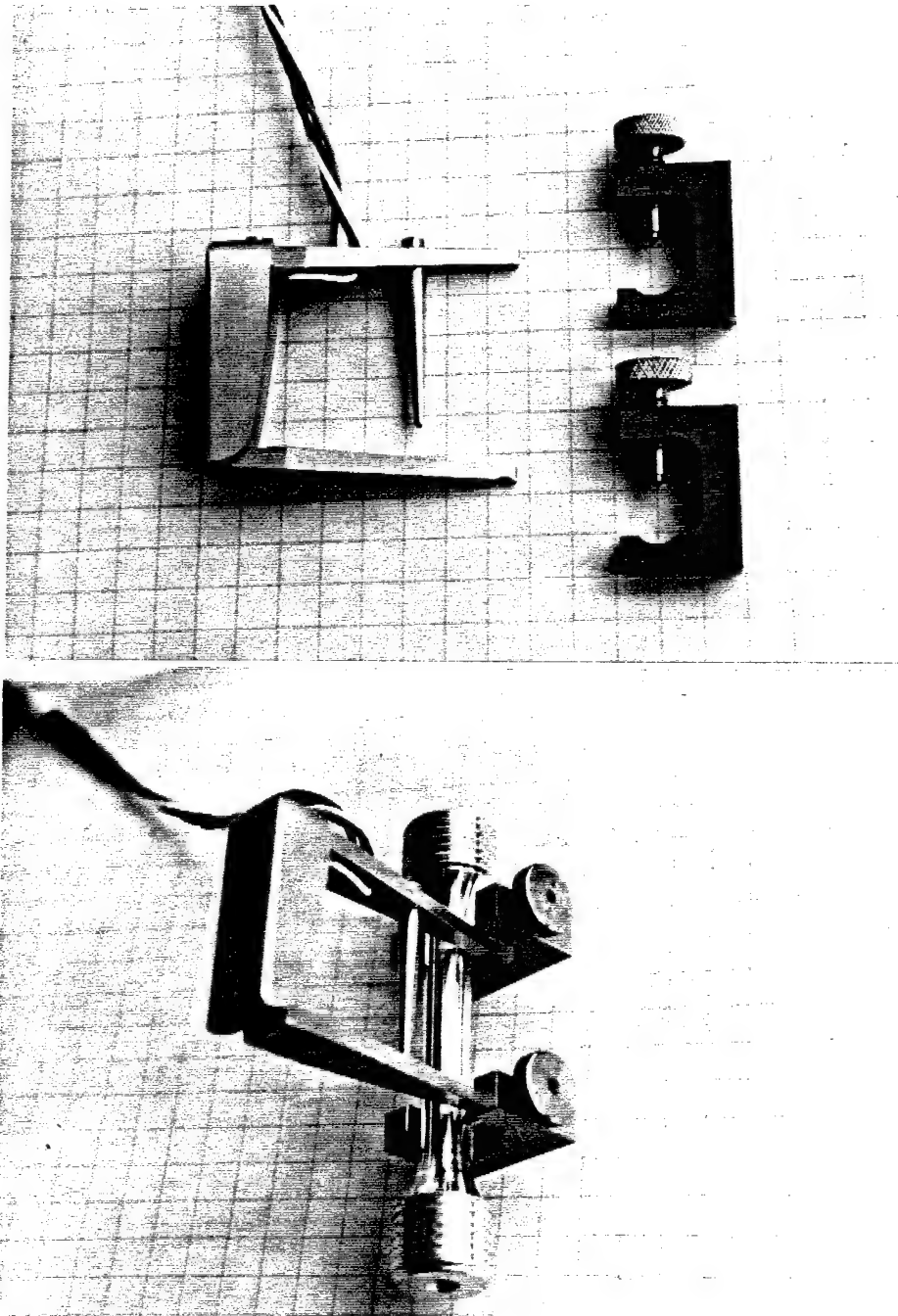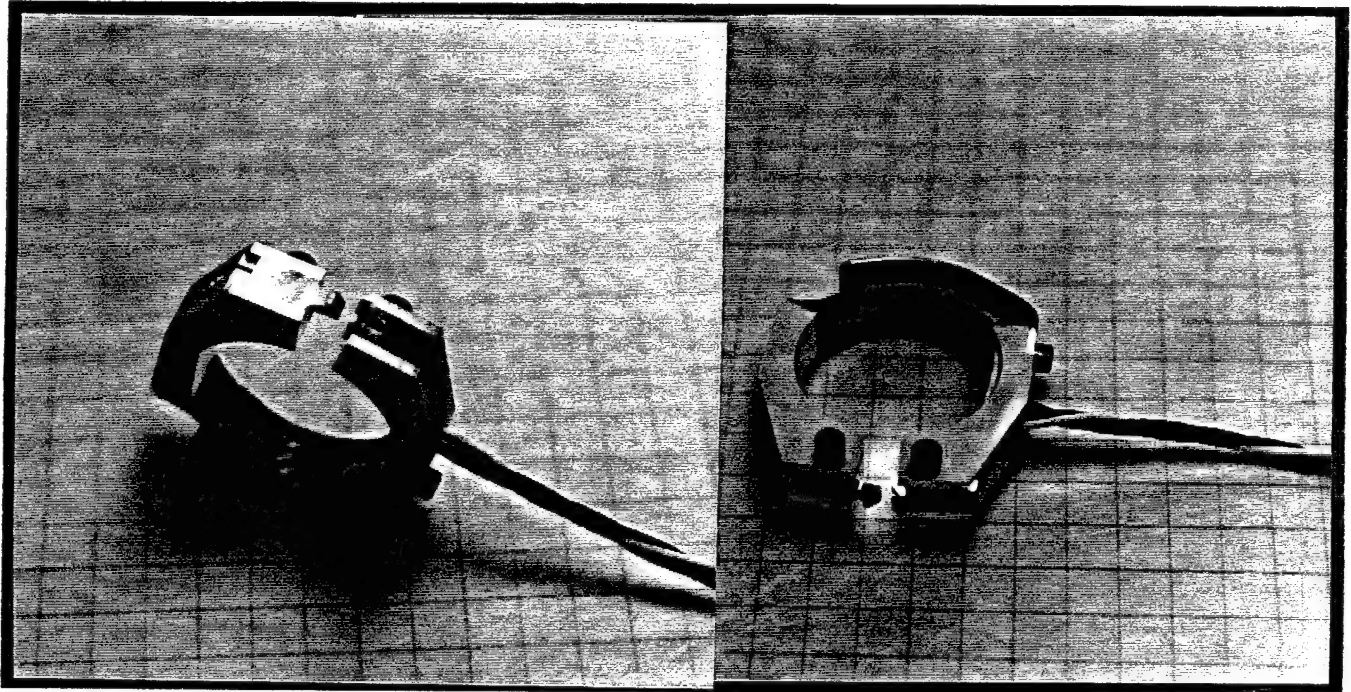BRIDGE RESISTANCE: 350 OHMS

TEMPERATURE RANGE: -452F to +200F

FIGURE 4

SURFACE FLAW DISPLACEMENT GAGE

DISPLACEMENT RANGE: 0.070 INCHES

SMALLEST FLAW SIZE (SURFACE DIMENSIONS): 0.100" WIDE (2C), BY .020"

TEMPERATURE RANGE: -454F TO +250F

BRIDGE RESISTANCE: 350 OHMS

THIS DISPLACEMENT GAGE ATTACHES TO THE INSIDE SURFACES OF THE STARTER NOTCH. LOCATION IS MAINTAINED BY CONTACT FRICTION. KNIFE EDGES OR SPECIAL ATTACHMENT DEVICES PLACED NEAR THE FLAW ARE NOT REQUIRED. THE COD GAGE SELF DETACHES UPON SPECIMEN FAILURE. A FULLY ACTIVE STRAIN GAGE BRIDGE PROVIDES OUTSTANDING SENSITIVITY AND LINEARITY. THE ATTACHMENT PRONGS ARE DOVETAILED INTO THE GAGE BODY AND ARE ADJUSTABLE OVER A RANGE OF APPROXIMATELY 0.2 INCHES. THIS FEATURE ALLOWS CONTACT PRESSURE TO BE ADJUSTED AS WELL AS MAKING THE GAGE ADAPTABLE TO VARIOUS STARTER FLAW DIMENSIONS. OTHER TYPES OF ATTACHMENTS CAN ALSO BE DEVISED TO FIT THE GAGE BODY, ALLOWING USE OF THE INSTRUMENT ON OTHER KINDS OF SPECIMENS OR MEASUREMENTS. TWO SETS OF ATTACHMENT PRONGS ARE PROVIDED WITH EACH GAGE.
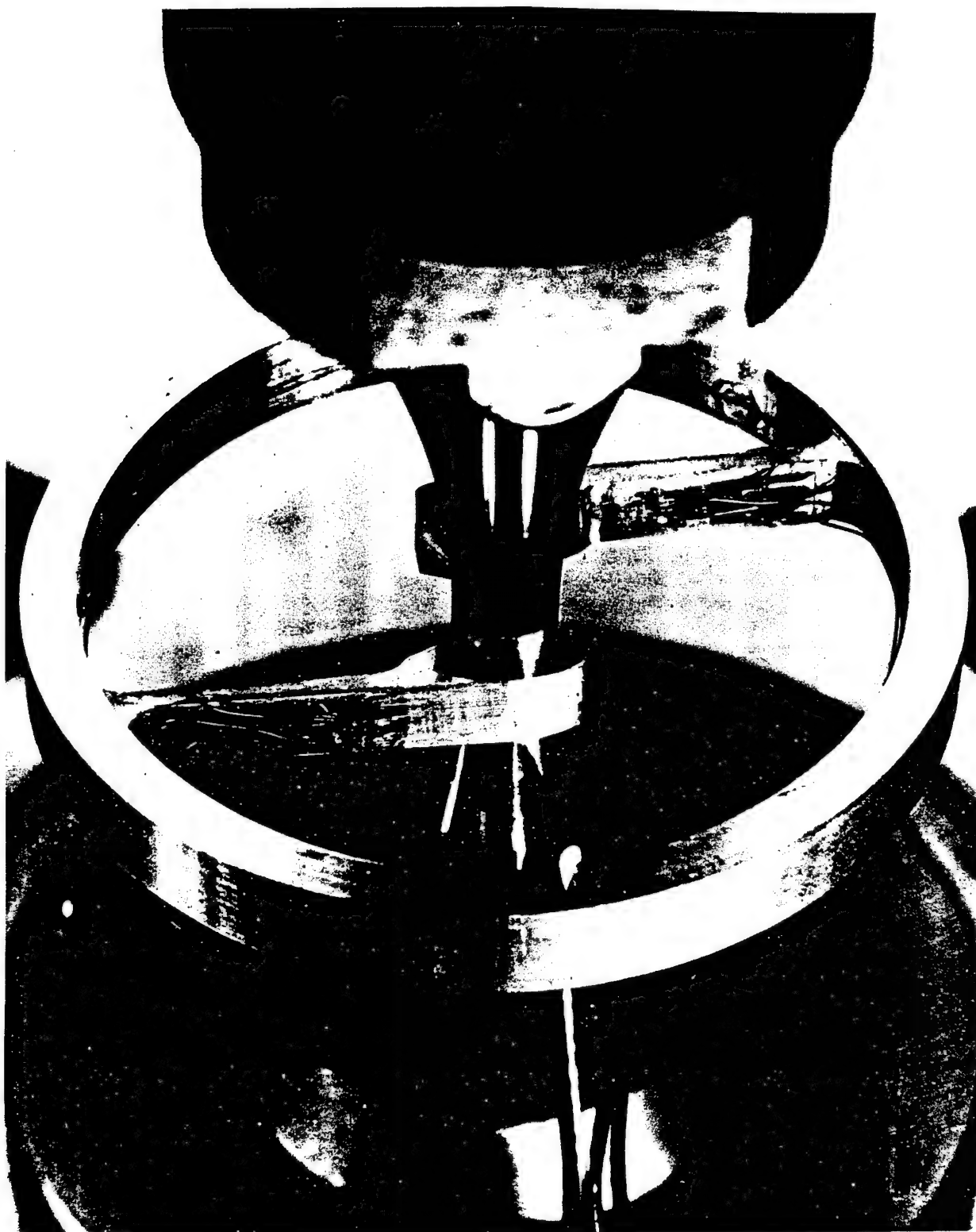
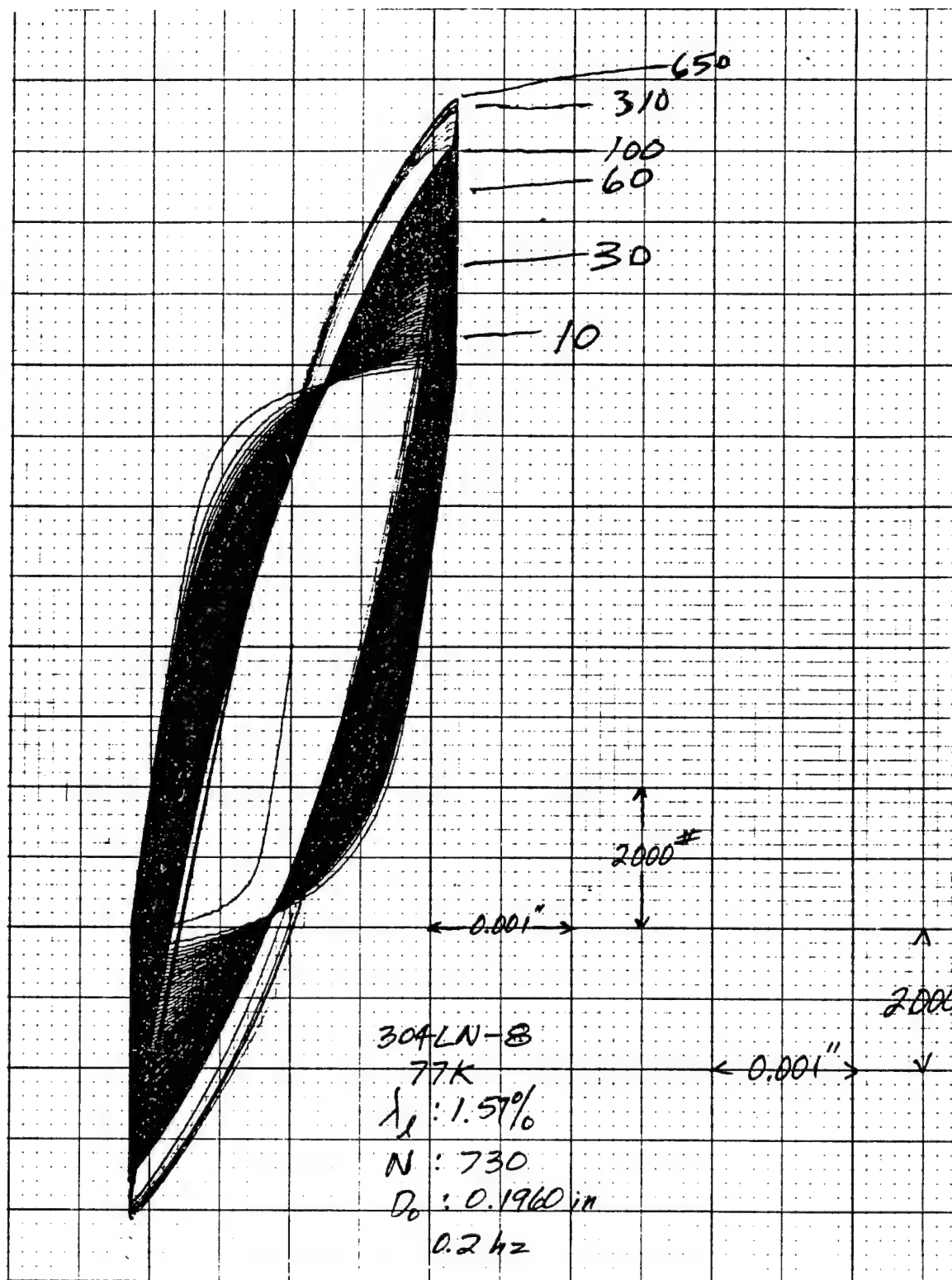Figure 5. Diametral Strain Extensometer.

650
310
100
60

30

10

2000#

←0.001"→

304LN-8
77K
λ_i : 1.57%
N : 730
D_0 : 0.1960 in
0.2 hz

←0.001"→

Figure 6.   Load-Deflection Curve for Specimen 304LN-8.

55
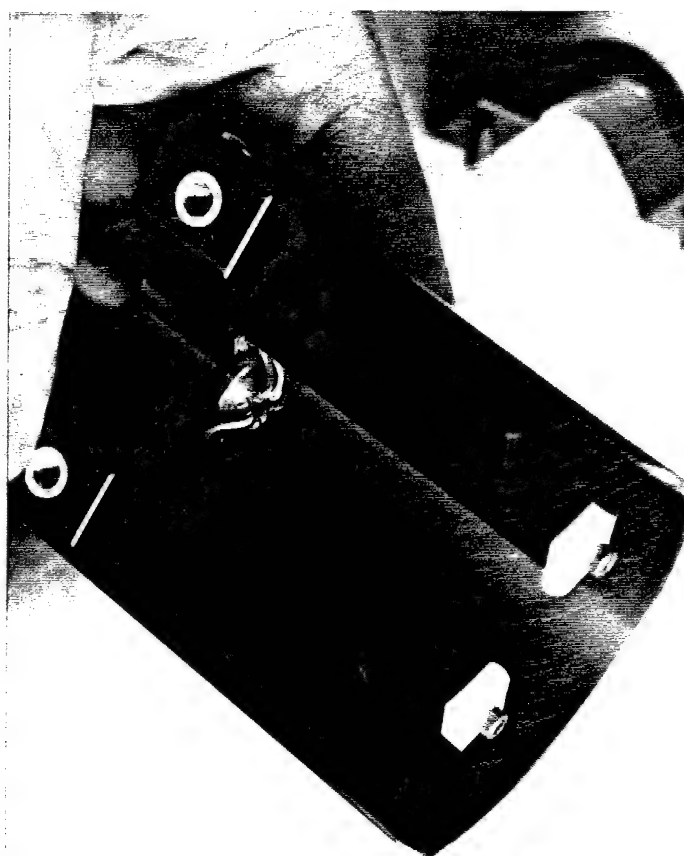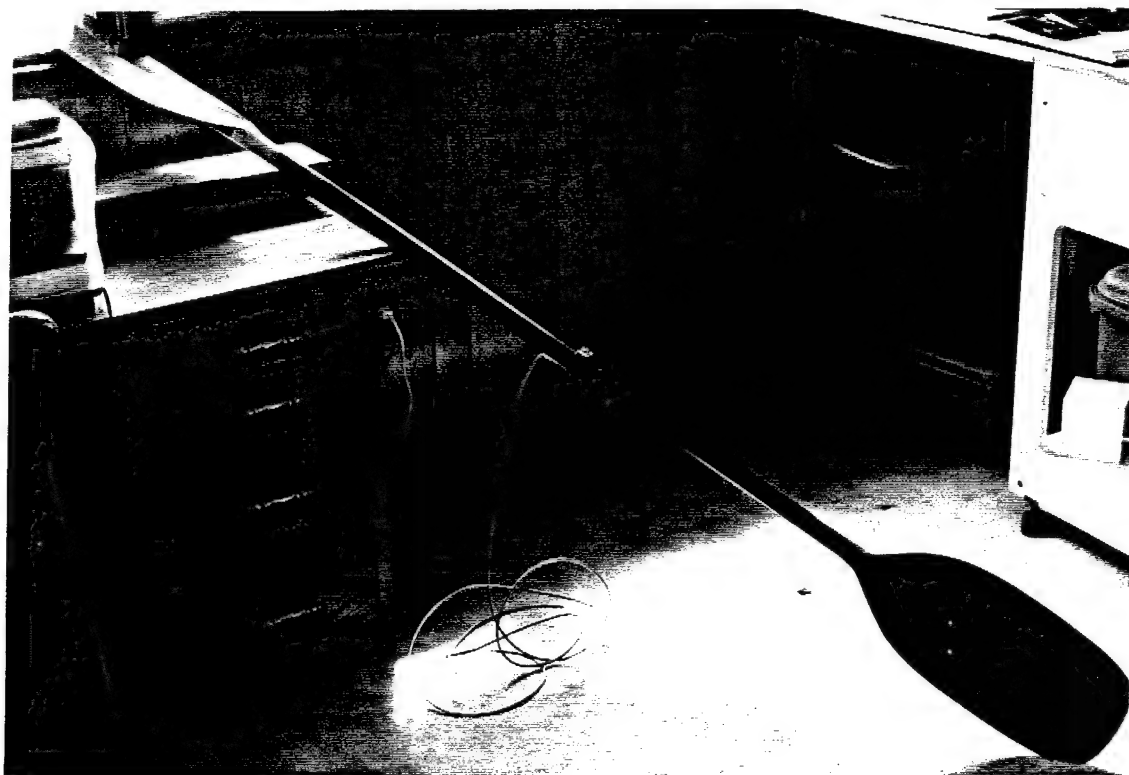
Figure 7. KAYAK Paddle Force Transducer.

56

STRESS MEASUREMENT IN SOLID ROCKET MOTORS

by

JIM BUSWELL*

HERB CHELNER**

STEVE FAULKNER***

DICK MORRELL*

*   DRA, FORT HALSTEAD, KENT,TN14 7BP, ENGLAND.
**   MICRON INSTRUMENTS, SIMI VALLEY, CA 93063.
***   RO(RMD) SUMMERFIELD, WORC, DY11 7RZ, ENGLAND.

Abstract

The design of solid rocket motors and the prediction of their service life depends on the accurate measurement of the induced stress in the propellant charge and at the bond-line. This measurement permits the prediction of maximum safe service life. Some results from a major international collaborative program to compare measured stress with prediction is presented herein. The accurate measurement of stress and the long term stability of the sensor is essential to the evaluation of the problem. It is shown that the current sensors are suitable for this purpose and have the potential for long term health monitoring.

CONTENTS

1   Introduction

Major causes of failure in rocket motors are cracking of the propellant charge
and debonding of the charge from the insulating lining. These generally occur
either at low temperature when high stress levels are set up due to differential
thermal contraction, which may be compounded by ageing processes within the
propellant itself, or on ignition, when high shock type stresses are experienced.
The design of solid rocket motors and the prediction of their service life depend
largely on the accurate prediction of these stresses and strains. In the past,
classical elastic, steady-state methods have been used for stress analysis. More
recently, linear viscoelastic finite element codes which assume the material to
behave in a thermorheologically simple manner have become available[1]. Non-linear
correction functions are available but their formulation is a time-consuming
task[2].   However, even with the use of actual laboratory measured mechanical
properties, discrepancies remain between theory and observed propellant behaviour
particularly on temperature cycling. Bond stress transducer technology provides
a means of obtaining stress data which can be compared directly with material
characterization data. This eliminates the uncertainty associated with stress
analysis results which still lack conclusive experimental verification.

A major collaborative programme has been conducted to acquire results from cast-
in strain gauges and stress transducers[3]. This data-base will be used to compare
predicted and measured stress and strain at various critical points in the
propellant charge and relating this to observed failure. A full understanding
not only reduces the risk of catastrophic failure on firing but will also prevent
motors from being withdrawn prematurely from service. The programme successfully
demonstrated the use of the " through-the-case" stress transducers for measuring
bondline stresses in solid rocket motors. These transducers were mounted on the
outside of the motor case and secured in place by a fixing collar and four studs.

The terminology of "through-the-case" refers to the fact that a small cylindrical
hole is made in the case, through which the transducer face is inserted so as to
be in contact with the propellant. Although capable of monitoring the stress
levels in the instrumented charges, this type of transducer is not fully
practicable because the rocket motor case can no longer function as a pressure
vessel because of the aforementioned hole. This type of transducer has been used
for research purposes only on analogue charges and is not suitable for project
missiles.

Recent advances in transducer technology have lead to the introduction of a
smaller version of the bondline stress transducer which can be mounted on the
inside of the rocket case wall. The introduction of this miniature stress
transducer into motors offer the potential of in-service health monitoring of
rocket motors that could also be fired.

2   Motor details and transducer preparation

The United Kingdom test motor for this work was referred to as the "Structural
test motor" or STM for short. The charge configuration is a slotted-radial
design, with four slots at the aft end of the charge and is shown in Figure 1.
The STM is typical of a lightweight tactical motor containing 9.5kg (20 lbs) of
reduced smoke, i.e. non-aluminised, composite propellant with a butyl stress
relieving boot at the head end. Several of the charges were instrumented with
thermocouples and stress transducer which monitored the stress levels at the
bondline between motor case and the outer diameter of the propellant charge.
These instrumented motors are called " STIMs" and the transducer layout is shown
in Figure 2. A total of twenty motors were cast in batches of four at a time and
the details are given in Table 1.

The stress transducer and thermocouple output were captured on a specially built data-logging system. The constant current supply is 5mA and the output is typically in the range of 0 to 40 mV DC. The transducer long term stability is the most important criterion for successful stress monitoring. So, before the instrumented motors are filled and the transducers isolated from further calibration, it is required to prove that the transducers are repeatable, stable and have acceptable hysteresis.

Senso-Metric's (stainlees steel) 601511 stress transducers are carefully manufactured to give minimum thermal hysteresis. Screening tests are performed and transducers that show variation of greater than 75 microvolts after temperature cycling are eliminated[4]. A minimum repeatable output with temperature is therefore ensured and the variations for six corrected transducers are shown in Figure 3.

The transducers are dead-weight calibrated to establish their pressure response and the typical output is linear with pressure loads up to 1 Mpa (150psi). Data correction programs were written to read in the raw output from the data-logger and correct it for zero-offsets and with pressure calibration measured for each transducer. To check if the presence of the transducer had any measurable effect on the stress magnitude, an elastic finite element analysis was conducted. The results indicted that the bondline stress transducer had negligible effect on the measured stress levels and amounts to less than a 1% error. In the data correction algorithms the effect has therefore been ignored. The reason for minimal interaction is that the transducer diaphragm is mounted flush with the liner/propellant interface, and that the case is relatively stiff and of large radius compared with the transducer.

As a final check of transducer performance before filling the response from the tranducer when assembled into the empty case is monitored when temperature cycled over the required temperature range -40°C to 60°C (140°F). The result from such a test on STIM 4 is given in Table 2 and the error of less than +/- 5 kPa (1psi) is considered acceptable.

3   Motor trials

The motors were assembled with calibrated transducers, thermocouples and a central mandrel to form the bore. The motors were then filled with the propellant slurry and cured at 60°C for a period of three days. During this period the hydrostatic pressure, indicated in Figure 4 as a negative stress, changed to a positive stress with the propellant trying to pull away from the case due to curing shrinkage. At the end of the cure period with the cross-link network complete the stress level can be seen as low with a magnitude of 10 +/- 5 kPa. The motor with the mandrel still in place is removed from the cure ovens and allowed to cool to ambient temperature. This is to allow the mandrel to be withdrawn with minimal propellant damage, however as can been seen, from Figure 5, the propellant sticks to the mandrel and high stress levels are induced as the motor cools. The indicated order of stress level is the opposite to that expected from geometry because of the extra constraint caused by the mandrel vanes. This phenomenon was repeated for all the motors, with the average induced stress of 127 kPa as shown in Table 3.

Extraction of the mandrel is conducted remotely by hydraulic ram with no recorded stress peaks which could damage the propellant. The stress level decreased rapidly as soon as the mandrel released from the propellant as can be seen in Figure 6. After mandrel removal the stress level was similar for all the motors with an average value of 49 kPa (7psi), giving a stress change of nearly 100kPa. STIM6 only had one operating transducer so the indicted change in Table 3 is considered to be low for this motor. Even after an overnight soak the order of stress levels were opposite to that expected indicating a memory of the previous

state. However, heating the STIM4 motor to 45⁰C for the first temperature trial removed this memory and the stress levels reverted to the correct order.

4   Temperature cycling tests

As an indication of the use of stress transducers to measure the health of a rocket motor two series of tests will be considered:

(a) Arctic cycle.

This test sequence is shown in Figure 7 and consists of a long term soak at 40⁰C, then two cooling cycles down to -45 C at which temperature the motor is again soaked for a prolonged period of 20 days, before two heating cycles back to ambient temperature. The rest at -20⁰C in both direction was designed to measure the relaxation modulus in an attempt to assess any cumulative damage. The cycle was started with an uncontrolled heating back to 40⁰C before the sequence was repeated. This temperature history is considered to accelerate service life by at least a factor of two.

(b)   Thermal shock cycle.

This test is considered to be the most severe test and can lead to motor failure. The motor soaked at a high temperature of 60⁰C is placed straight into a low temperature chamber running at -54⁰C and the sequence is repeated every 24 hours. After five cycles the motor is left at ambient conditions for 48 hours during which time it is visually inspected for damage. The sequence of cycles can be repeated until failure.

In this reported work neither trial actually lead to a charge failure but gave interesting results which provides information on which service life calculations can be made.

5   Arctic cycle trials and results

The time-temperature profile for the first cycle of the trial is shown in Figure 9, together with the induced stress as shown in Figure 10. As can be seen from the temperature plot a problem occurred with obtaining the low temperature and a mid-time correction was required. It should also be noted that the order of stress level is as expected with the higher magnitude at the head-end gauge (No 9F393). The recorded peak values of 330 kPa or 365 kPa is at least 25% higher than the stress measured at thermal equilibrium. These values are given in Figure 11 together with the corresponding values at the other temperatures in the cycle. The allowable stress level for the temperature of -45⁰C has been measured as 650 kPa. This implies that bondline separation is unlikely as a failure mode providing reasonable precautions have been taken during motor manufacture to ensure a good bond.

Even though bond failure is not predicted it can be seen that the results do indicate some mechanical damage. The excursion to -45⁰C has caused a change in the apparent modulus since the equilibrium stress level at both -20⁰C and 20⁰C during the heating part of the cycle are lower than measured during the initial cooldown. The values are listed in Figure 11 for comparison. As can be seen the stress level on returning to 20⁰C after the excursion has decreased on average by 35%. However, the stress levels at -20⁰C would appear to have decreased by an average of 47%. This implies that the amount of damage is dependent on the induced strain level, being 10% and 20% respectively. This behaviour has been observed previously and subjected to extensive study[2].

After a recovery period at 45⁰C the second cycle induced very similar stress levels. The recorded thermal equilibrium stresses at -45⁰C are given in Table

4.   Again the induced damage was not recovered during the low temperature storage.   Between cycle 2 and subsequent cycles, a delay of several months was incurred due to malfunction of the data-logging equipment.   The data-logger was returned to the manufacturer for repair with the loss of internal calibration settings.   Hence results for cycles 3, 4 and 5 are presented in comparative form with the stress values corrected so 2 and 3 correspond.

As can be seen the same pattern is repeated for all the cycles with the average values of the five cycles being the same as the actual values for the first cycle.   At the end of the trials the motor, STIM4, was visually inspected and found to be in good condition with no visible damage and no cracks apparent.

The ability to measure the actual stress level at any time in the history of the trial and that the stress magnitude did not exceed the allowable values gave confidence that the sister motor, which followed the same trial, was also serviceable.   The motor was subsequently successfully fired at -53^0C, the required low temperature operating limit.

6   Thermal shock trials and results

Thermal shock trials were carried out on STIM7 following the temperature profile given in Figure 8. The first cycle from 60^0C to -54^0C induced a peak head-end stress level of over 600kPa with a equilibrium value of 420kPa. The allowable stress level under these conditions is 1.14 MPa so there is little danger of bond failure.   However, the induced strain level is 27%, close to the allowable value of 30%, and it is by this mechanism that the motor usually fails.   The stresses on subsequent cycles decreases rapidly indicating large amounts of damage which is not recovered. The values are given in Figure 12 in the form of percentage decreases against cycle.   Over the first five cycles the stress decreased the order of 25% of the original value, and in this case that equated to a drop of around 112kPa.   Stress decreases of this order could be due to gross damage in the bore or due to the present of a crack.

7   Modelling of crack propagation

The use of miniature stress transducers (Micron Instruments' Titanium 140474) as a possible in-service technique depends on the ability to detect propellant bulk damage or bore cracking under thermal loading[5].   A typical crack starts on the surface of the bore, at a point of maximum concentration, and grows normal to the surface. The actual initiation mechanism was not part of this study.

Finite element analyses were carried out to determine the effect that the growth of a crack from the inner bore surface would have on the stress levels in the charge.   In particular, attention was paid to the orientation of the crack relative to the transducer.   In all cases a linear elastic material model was assumed on the grounds that crack propagation under thermal storage conditions would proceed at a slow rate and therefore material properties in the equilibrium elastic portion of the stress relaxation curve would apply.   The actual elastic modulus used for this work was 5.25 MPa.

Figure 14 shows some typical results.   Located near to the case wall was a miniature stress transducer.   Boundary conditions have been applied to the model to take symmetry into account.   The crack path being modelled was for propagation at a site 90 degrees to the transducer.   The stress predictions are also shown in Figure 14 with a constant decrease in the stress levels as the crack grows. The stress level fall from 575 kPa to less than 100 kPa and hence would be easily detectable.   The results also showed the growth of a crack in a direction normal to the transducer face would be detected by a suitably located transducer. However, the use of one transducer would not be sufficient to detect the extent and location of a growing crack in a complex geometry, and it is therefore

recommended that several transducers are located at 90 degrees to each other and spaced along the motor so that it is possible to detect the crack and to assess its location.

8   Conclusions and future work

The measured stress reduction obtained from the thermal shock trials , as discussed in Section 6, could be the result of a bore crack. STIM7 was carefully examined at ambient temperature after the trial and although some surface damage was visible no actual crack was detected. However, this motor was considered to be damaged beyond that which could be fired without risk. So the use of stress transducers as a health monitor has been demonstrated. This work will continue to compare the actual measured stress values in instrumented rocket motors and the best available prediction techniques.

It has been shown that stress changes in composite propellant rocket motors are complex. The ability to measure these stress magnitudes are an essential precursor to accurate structural integrity calculations. From this information an informed decision can be made about the current state of the in-service instrumented rocket motor. Significant cost avoidance can be obtained from this possible extension of service life. However, no matter how sophisticated the measuring system the fact remains that the stresses in the motor situation are extremely complex. It still requires careful analysis of the data obtained to ensure validity of any of the readings.

References

(1) G S Faulkner
     An introduction to the use of the ABAQUS code for the analysis of solid propellant rocket motor charges,
     RO RMD, TN 92/158 (August 1992).

(2) E C Francis & H J Buswell
     Service life prediction and testing of composite propellant rocket motors,
     ICT Conference, Karlsruhe, Germany (June 1989)

(3) Final Report on KTA-14, Service life prediction methodologies,
     TTCP-WTP4-KTA-14 (November 1994)

(4) E C Francis & R E Thompson
     Stress transducer screening and calibration tests,
     United Technologies CSD, CSD 2992TR (June 1992)

(5) H. Chelner et al.
     Miniature Sensor for Measuring Solid Grain Rocket Motor Case Bond Stresses.
     18th Transducer Workshop, Range Commanders Council, (June 1995)

Serial Number	Motor type	Propellant batch No.	Trial
101574	STM	49M	Old build standard
101575	STM		Old build standard
STIM1	STIM1		Initial datalogging trials
STIM2	STIM2		Initial datalogging trials
98365	STM	56M	LTF
97917	STM		LTF
97918	STM		Fired to assess instability
101581	STM		Fired to assess instability
FTM10	STIM3	57M	Instrumented motor
101583	STM		LTF
FTM11	STIM4		Arctic cycle
101584	STIM		Arctic cycle + Fire (-54 °C)
2757C	STIM5	58M	Accelereated ageing
2749C	STM		Accelerated ageing + Fire
2755C	STIM6		Gauge failure
2752C	STM		LTF
FTM9	STIM7	59M	Thermal shock
FTM12	STM		No allocation
2742C	STM		LTF
2751C	STM		LTF

Table 1: UK STM Motors
Batches 56M onwards contain 2% TiO2
LTF = Low Temperature Firing.

TABLE 1

Sensometrics gauges : Thermal hysteresis temperature cycling of gauges and case only.

STIM 4

gauge 9F393 connected to channel 3 (cable 5)
gauge 9F394 connected to channel 8 (cable 8)
gauge 9F397 connected to channel 6 (cable 7)

All stress gauge readings below are in kPa.

				Temperature ($^{\circ}$C)			
Gauge		60	40	24	-10	-20	-42
9F393	i			2			
	ii	11	9		-9	-12	-19
	iii	8	7		-12	-15	-20
	iv	10	9		-9	-14	-20

				Temperature ($^{\circ}$C)			
Gauge		60	40	24	-10	-20	-42
9F394	i			6			
	ii	6	9		38	38	34
	iii	5	6		33	30	34
	iv	-1	2		33	38	39

				Temperature ($^{\circ}$C)			
Gauge		60	40	24	-10	-20	-42
9F397	i			-5			
	ii	-18	-12		-10	-15	-33
	iii	-15	-13		-8	-9	-20
	iv	-18	-17		-8	-13	-23

TABLE 2

MANDREL REMOVAL AT AMBIENT

MOTOR	Average Stress Before /kPa /(psi)	Average Stress After /kPa /(psi)	Change /kPa /(psi)
STIM 4	154 (22.3)	62 (9.0)	92 (13.3)
STIM 5	133 (19.3)	32 (4.6)	101 (14.6)
STIM 6	104 (15.1)	67 (9.7)	37 (5.4)
STIM 7	116 (16.8)	34 (4.9)	82 (11.9)
AVERAGE	127 (18.4)	49 (7.1)	78 (11.3)

TABLE 3

ARCTIC CYCLE RESULTS

Corrected   stress induced at -45 °C   /kPa
/psi

GAUGE # CYCLE	397	394	393	Average
1	163 (23.6)	238 (34.5)	288 (41.8)	230 (33.3)
2	146 (21.2)	226 (32.8)	296 (42.9)	223 (32.3)
3	(145) (21.0)	N/R	(300) (43.5)	223 (21.5)
4	(176) (25.5)	(267) (38.7)	(307) (44.5)	250 (36.3)
5	(215) (25.6)	(231) (36.7)	(248) (44.5)	231 (36.3)
AVERAGE	169 (24.5)	241 (34.9)	288 (41.7)	232 (33.7)

(Numbers in parenthesis represent a span change)

TABLE 4

STM CHARGE DESIGN
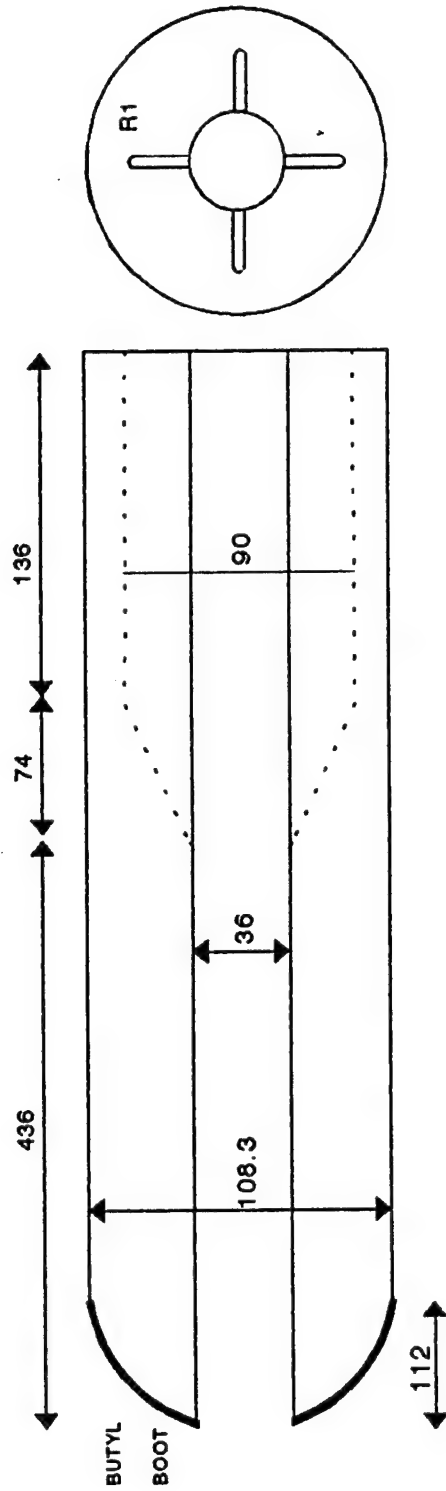
CASE THICKNESS = 1mm

SLOT WIDTH = 2.83 mm

FIGURE 1

69

STIM4 GAUGE AND
THERMOCOUPLE
LAYOUT.

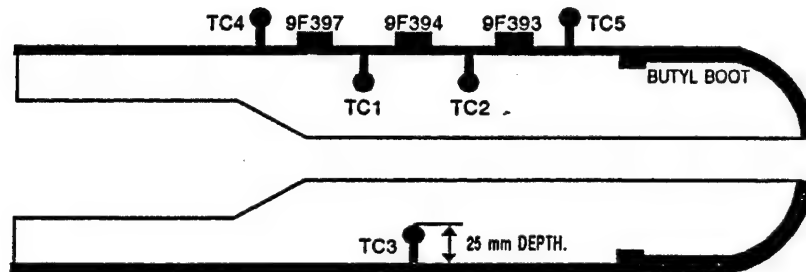

FIGURE 2

FIGURE 3
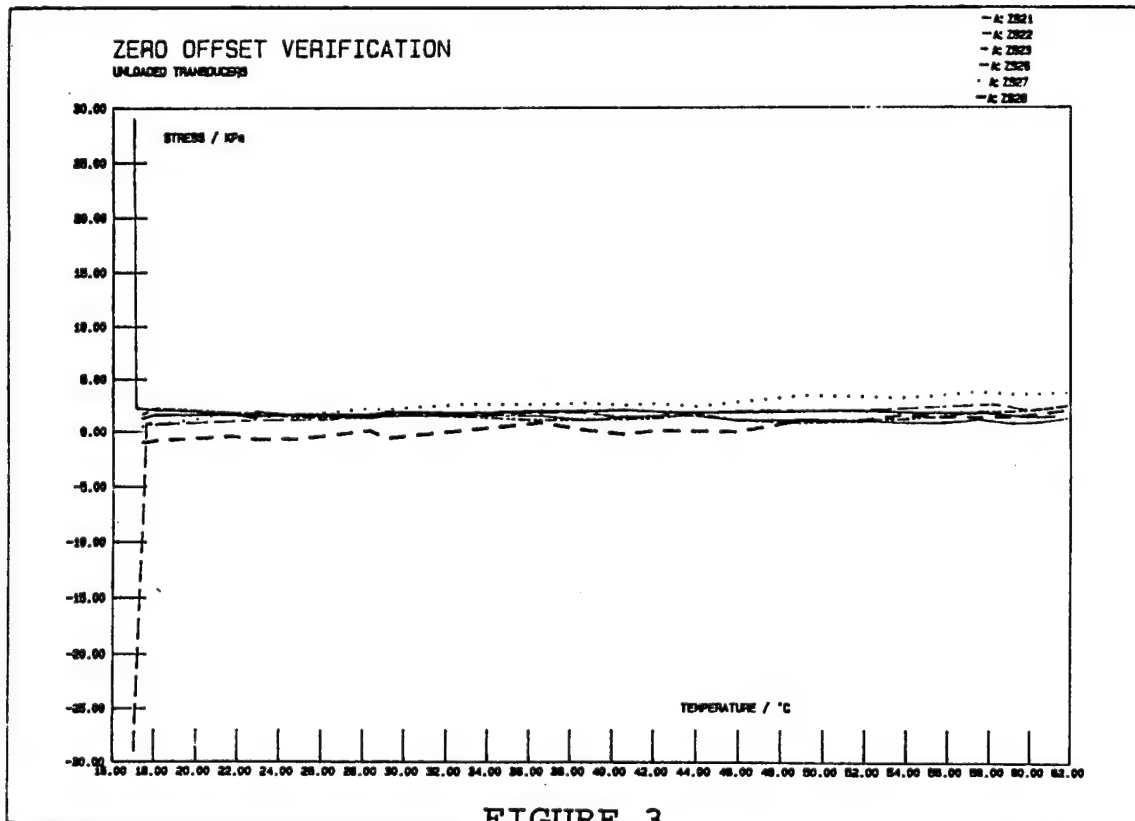
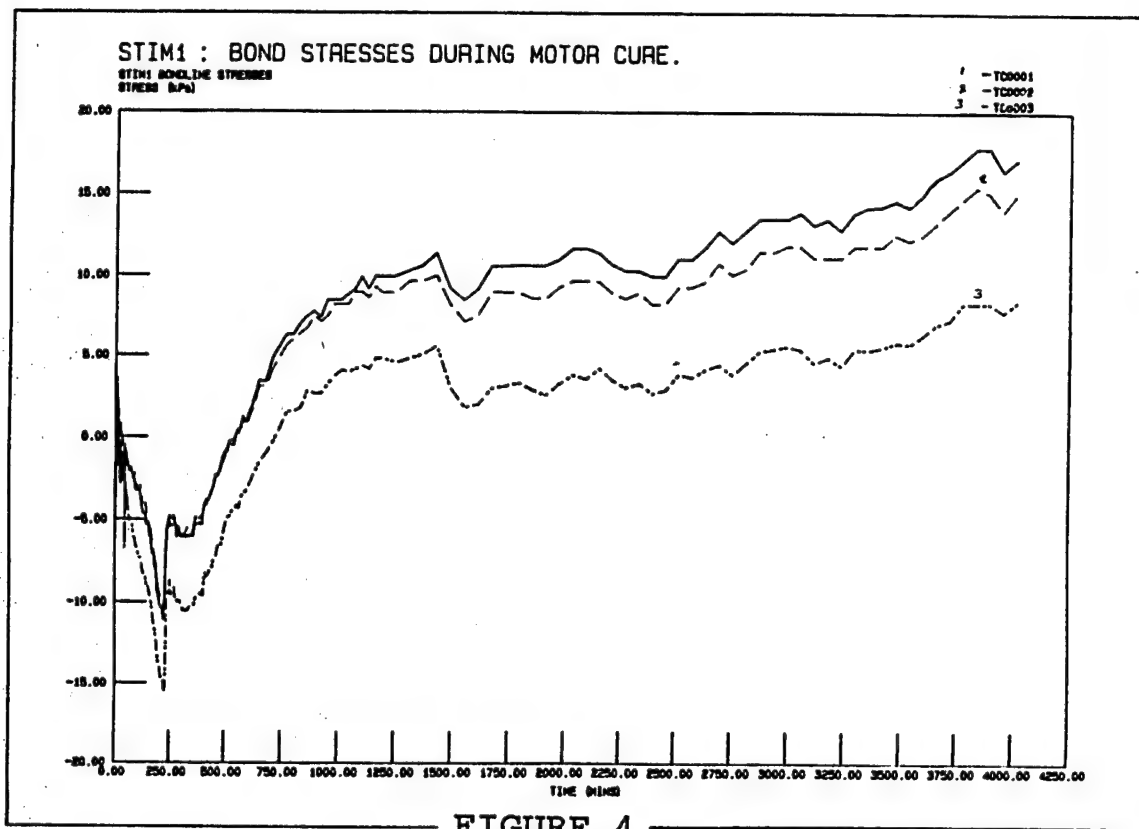STIM1 : BOND STRESSES DURING MOTOR CURE.

FIGURE 4

STIM4 COOLING FROM CURE TO AMBIENT

MANDREL STILL IN PLACE

FIGURE 5
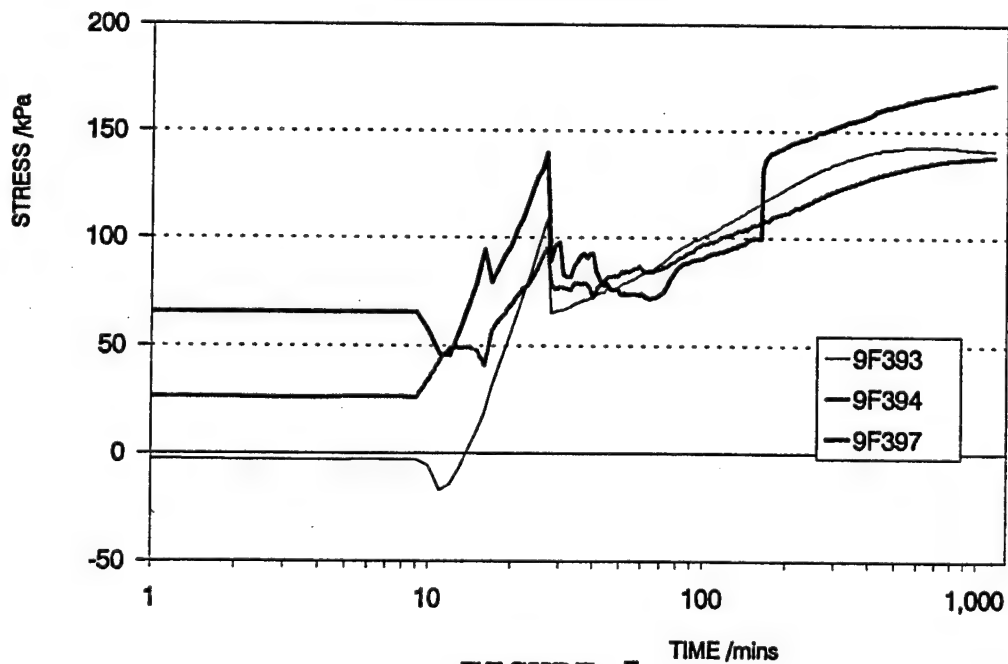
71

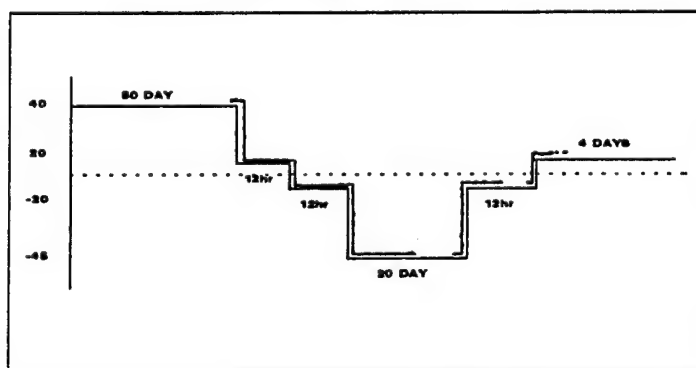## STIM4 MANDREL REMOVAL AT AMBIENT
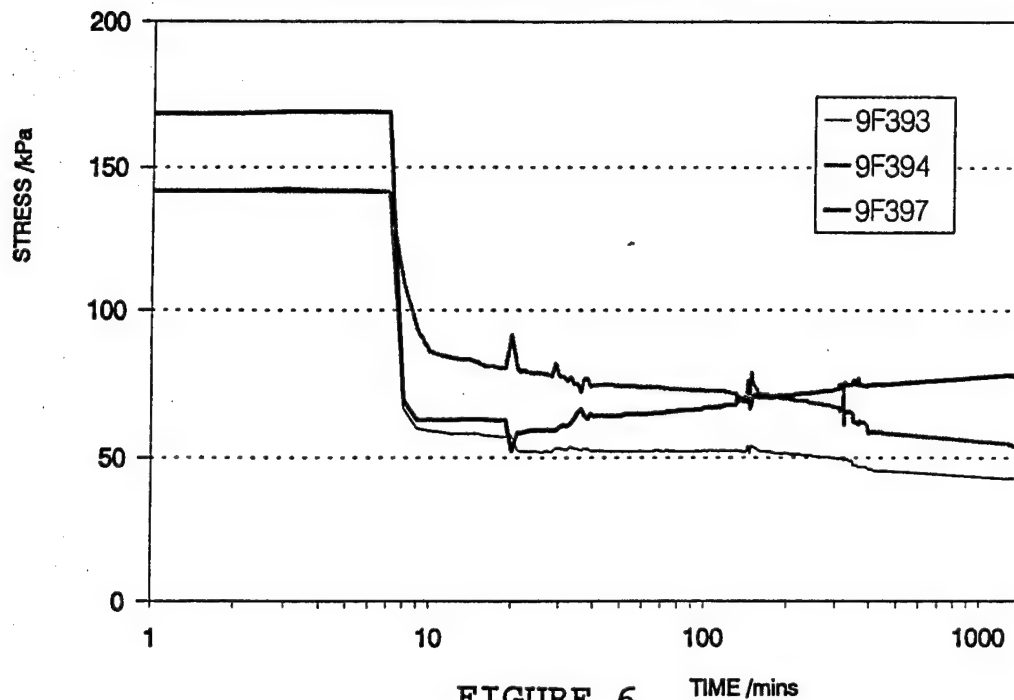
FIGURE 6

ARCTIC CYCLE ENVIRONMENT

ONE CYCLE

———————— DATALOGGING PERIOD.

FIGURE 7

72

THERMAL SHOCK ENVIRONMENT
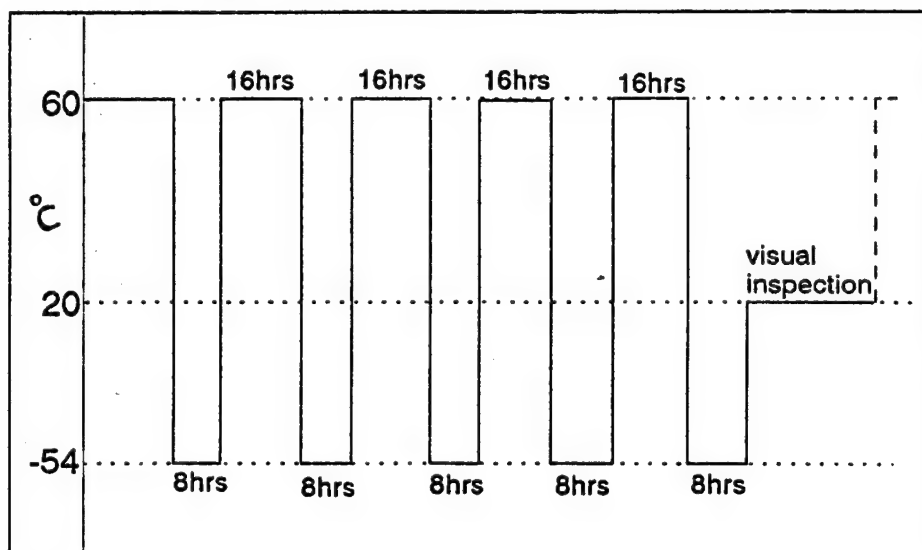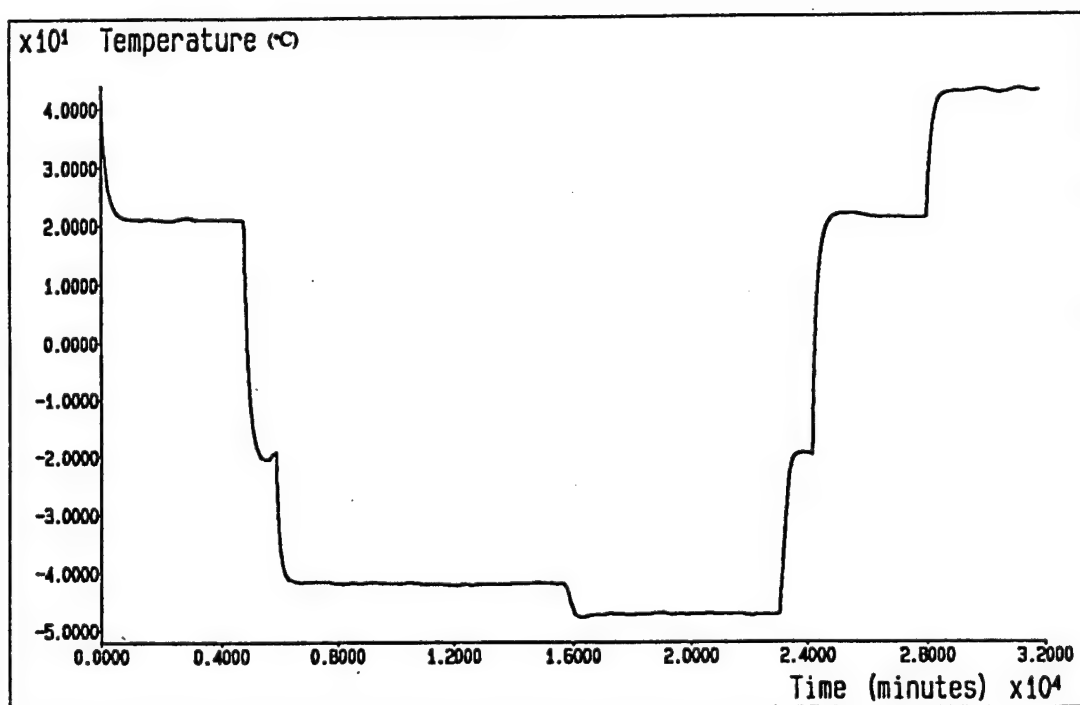

FIGURE 8

FIGURE 9

73
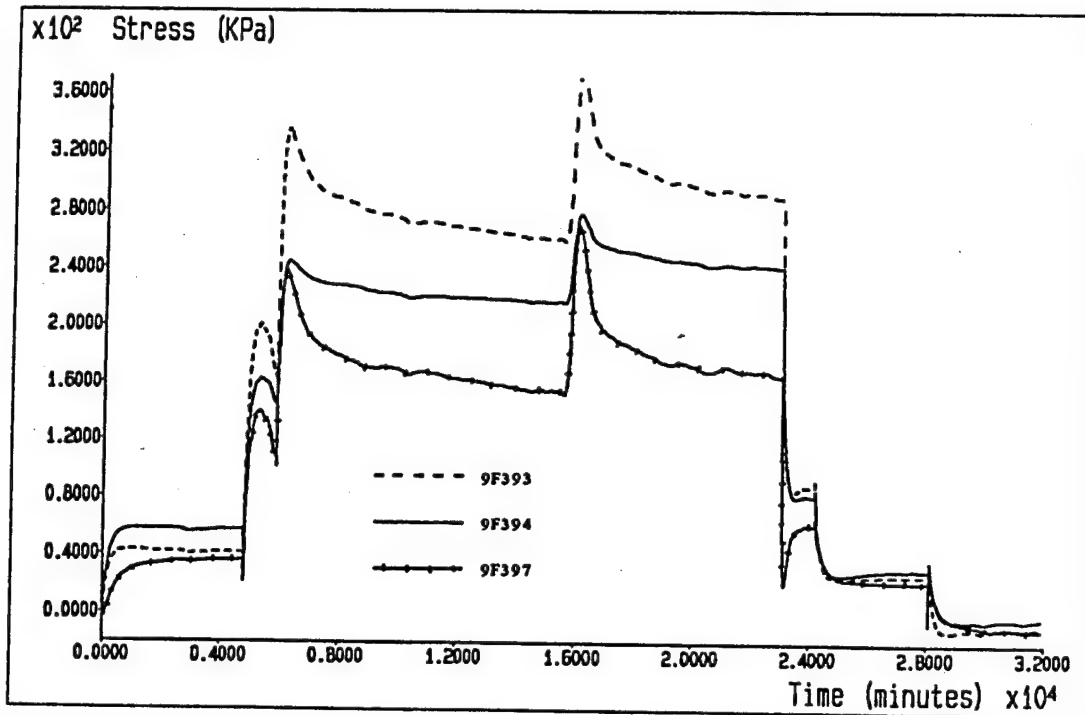
FIGURE 10

ARCTIC CYCLE : BOND STRESSES - FIRST CYCLE
(DATA FOR COOLING AND HEATING)

		60	45	20	-20	-45	-20	20
9F393	1		5	40	173	288	92	26
9F394	2		12.5	57	155	238	80	39
9F397	3		5	36.2	110	163	61	22

TEMPERATURE (°C)

FIGURE 11

74

CYCLE 1

% DECREASE IN STRESS AT -54°C

UK	■	100	88.6	81.3	80.1	72.8
CANADA	+	100	88.1	81.8	77.3	76.1
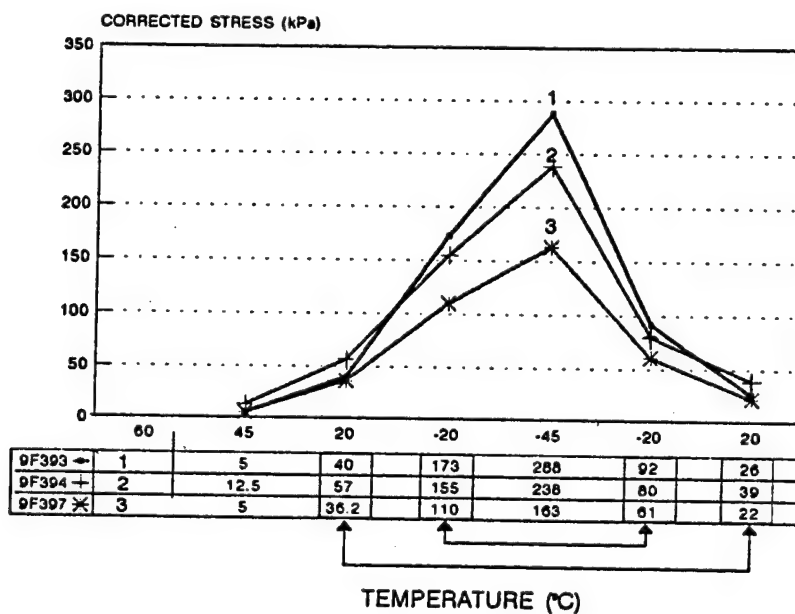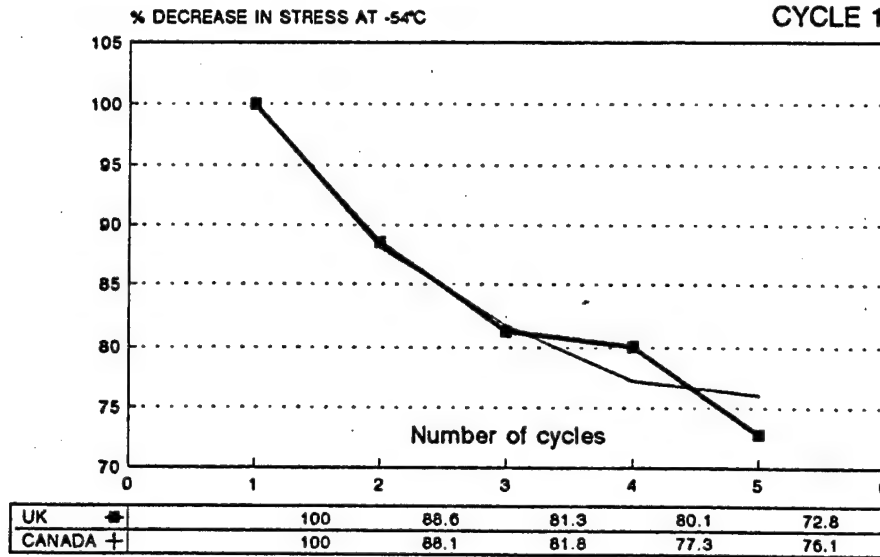
INDUCED STRESS 420 kPa

FIGURE 12

RADIAL STRESS AT THE GAUGE FACE AS A FUNCTION
OF CRACK LENGTH

FIGURE 13

STRESS (KPa)

Conduit surface to gauge face
distance=36.95mm

CRACK LENGTH (MM)

75
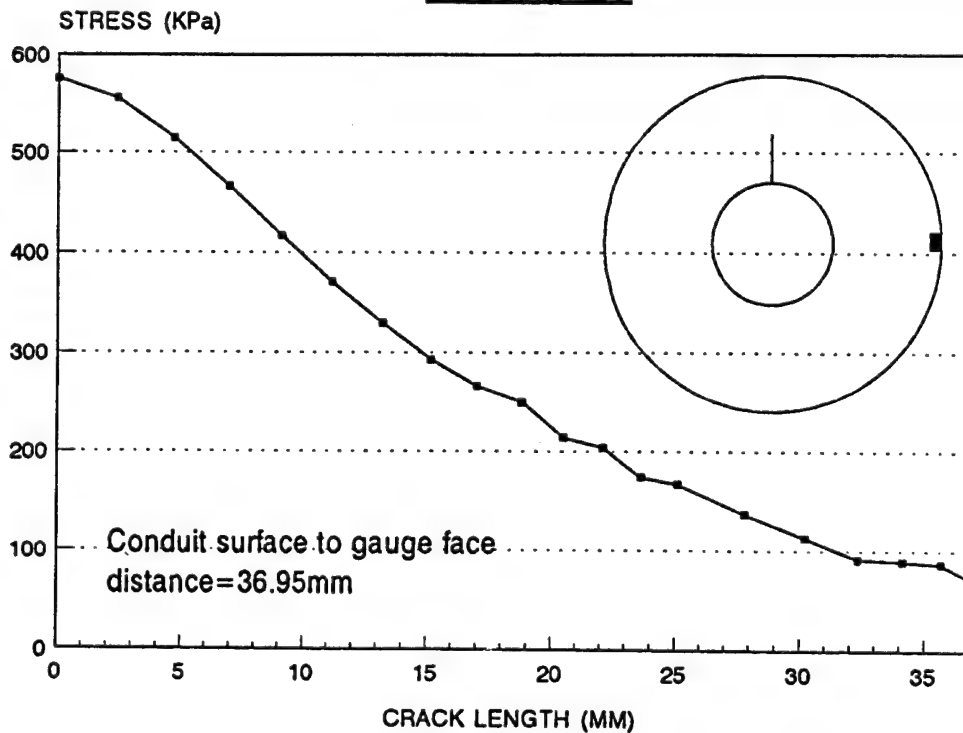
FINALLY, DURABLE INDUSTRIAL ACCELEROMETERS FOR VEHICULAR SHOCK & VIBRATION TESTING

Author: Jim Lally
               PCB Piezotronics, Inc.
               3425 Walden Ave.
               Depew, N.Y. 14043

Presented at: 18th TRANSDUCER WORKSHOP
               Colorado Springs
               June 20-22, 1995

ABSTRACT:

Environmental conditions associated with vehicular laboratory and field test measurements present a severe challenge to most sensors.

In the past, engineers faced with field test measurements had no other choice than to adapt small laboratory type sensors, with delicate miniature connectors, to harsh environments involving dust, sand, water, wind and salt spray.

As a result of technological advancements in compact, portable FFT analyzers combined with the development of durable low output impedance accelerometers designed for rough handling and operation in harsh factory environments, a new technology known as "Machine Vibration Health Monitoring" has emerged.

Today, rugged, durable, hermetically sealed, case ground isolated accelerometers continuously monitor shock and vibration on machinery and structures in hostile environments in paper mills, rolling mills, power plants, factories, on shipboard and seismic exploration vehicles.

Characteristics of these rugged industrial sensors include laser hermetic sealing, MIL Spec connectors, integral vulcanized waterproof connections, case ground isolation and shock protection.

Incorporating stable shear structured sensing elements and integral microelectronic signal conditioners, these rugged industrial sensors offer a low cost commercial solution meeting the technical and field requirements for vehicular shock and vibration measurements.

Environmental and operating conditions associated with vehicular shock and vibration measurements in laboratory and field test applications have always been tough! Environmental conditions vary widely and operating conditions are usually rough. Meeting these needs with durable accelerometers, cables and connections presents a real challenge.

Out of necessity, engineers have had to use instrumentation that was not designed for operation under adverse conditions associated with environmental testing. An example of this would be high impedance charge type accelerometers which use somewhat delicate miniature connectors and cable which are highly susceptible to moisture,dirt and other contamination. However,"resourceful" engineers made the best of the situation by using extra care in routing cables and sealing connections. Protective covers,or shields,have been used to protect the accelerometers, cables and charge amplifiers from mechanical damage.

Today, the measurement task is much easier. As a result of technological advancements in machinery health monitoring in factories and power plants, durable industrial grade [1]ICP® accelerometers with rugged connectors and cables have been developed for operation in some of the worst possible environments.

Aside from larger housings necessary to accommodate more rugged connectors, ICP Industrial Accelerometers incorporate many of the same features found in the smaller aerospace accelerometers you may be more familiar with.Such features include shear structured quartz or ceramic sensing elements, laser welded hermetically sealed connectors and housings, electrical case ground isolation,rugged "MIL Spec." connectors, electrical & mechanical shock protection and built-in microelectronics to provide a low impedance voltage signal suitable for operation in contaminated environments.

Shear Mode
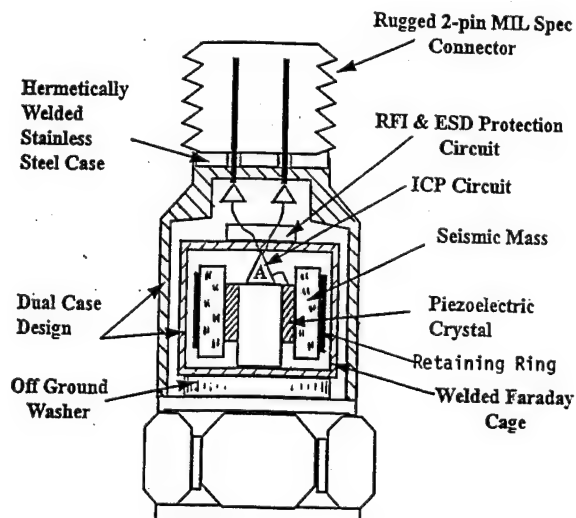
Typical Quartz Shear Structured Industrial ICP Accelerometer

ICP Industrial accelerometers operating in wet, humid or
underwater environments, incorporate protective boots or
integral vulcanized waterproof cable connections. Most of
you are aware of integral cable problems associated with
smaller accelerometers. Often the integral connection is
not rugged enough and if cable accidentally gets pulled,the
connection tends to become "non-integral". In order to
avoid this rather expensive type "accident" with ICP
Industrial Accelerometers, the integral cable connection has
been designed and tested to pass a 200 pound pull test.

Industrial Accelerometers with
Waterproof Connections

The paper machine is a good example of an industrial
accelerometer application involving a wide range of
mechanical apparatus and environmental conditions.Up to 300
sensors may be permanently installed on a single paper
machine which is about a block long. The paper machine,
which starts with slurry and finishes with completed paper,
consists of motors, rollers, bearings, gears, filters,
heaters, presses and slicers. Environmentally, sensors
operate in a paper slurry, underwater, in oil, grease, high
humidity, dryer section heat and they must survive punishing
fire hose like water pressures when the machines are
cleaned.
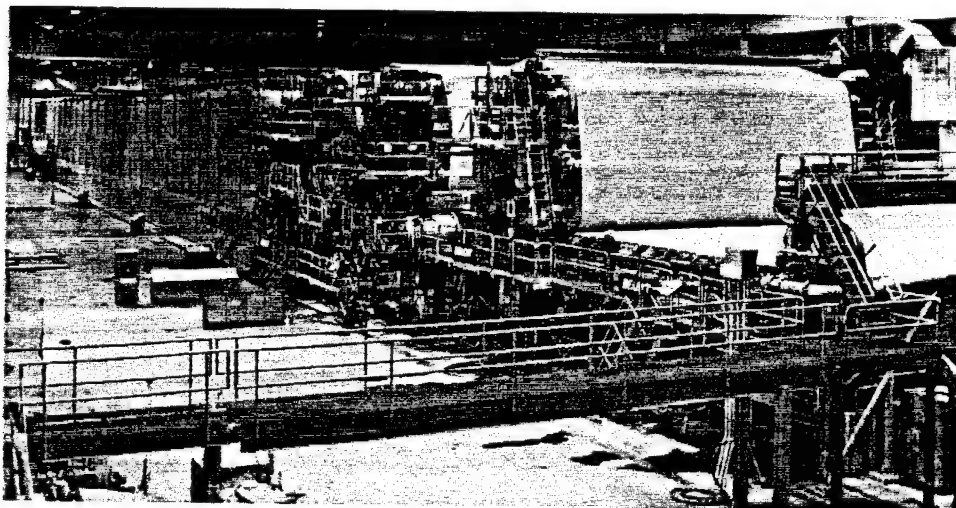
Paper
Machine
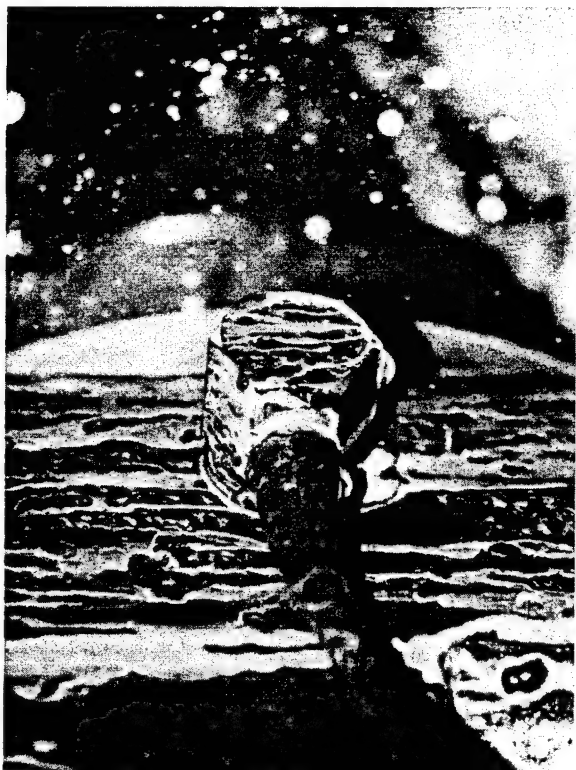
Industrial Accelerometers provide reliable operation in oil, cutting fluid and other chemical environments.
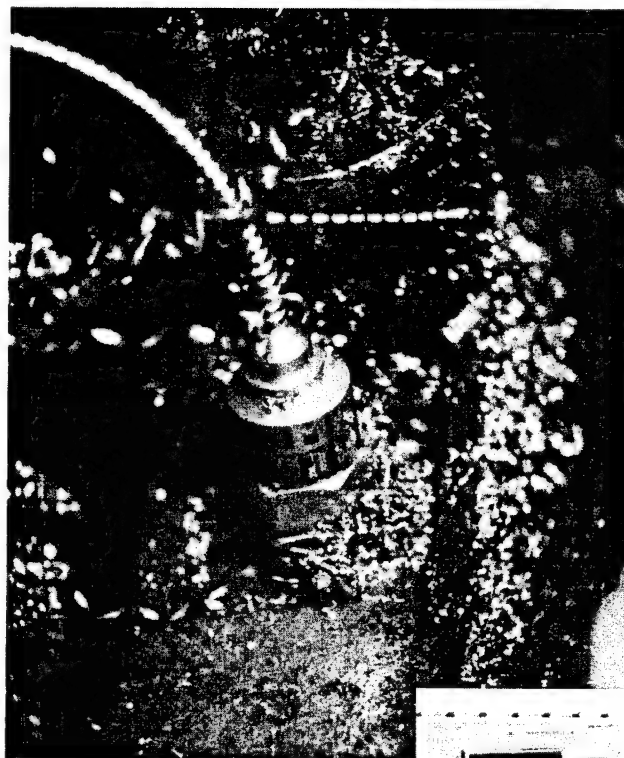
Rugged, steel-jacketed, integral cable protects against metal shavings.

Industrial Accelerometers installed on this Seismic Exploration Vehicle measure impact shock.

ICP Industrial Accelerometers suitable for vehicular
measurements are available in a wide variety of mechanical
configurations with top or side connectors, thru-hole
mounting, in single and triaxial configurations. Most models
have good response down to 0.5 hz making them well suited
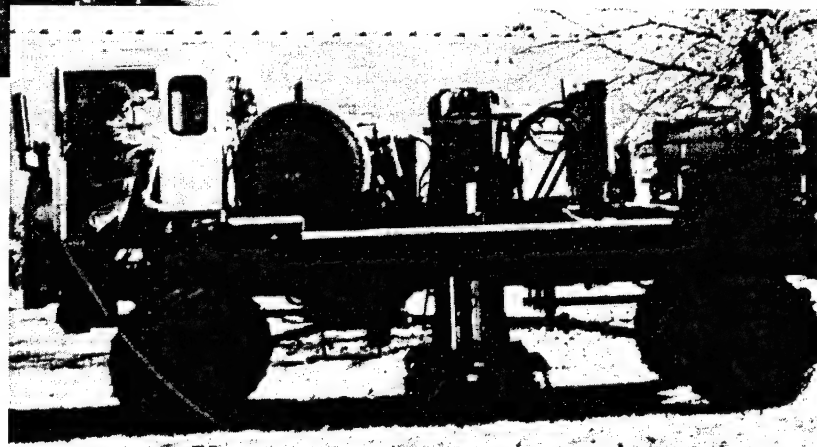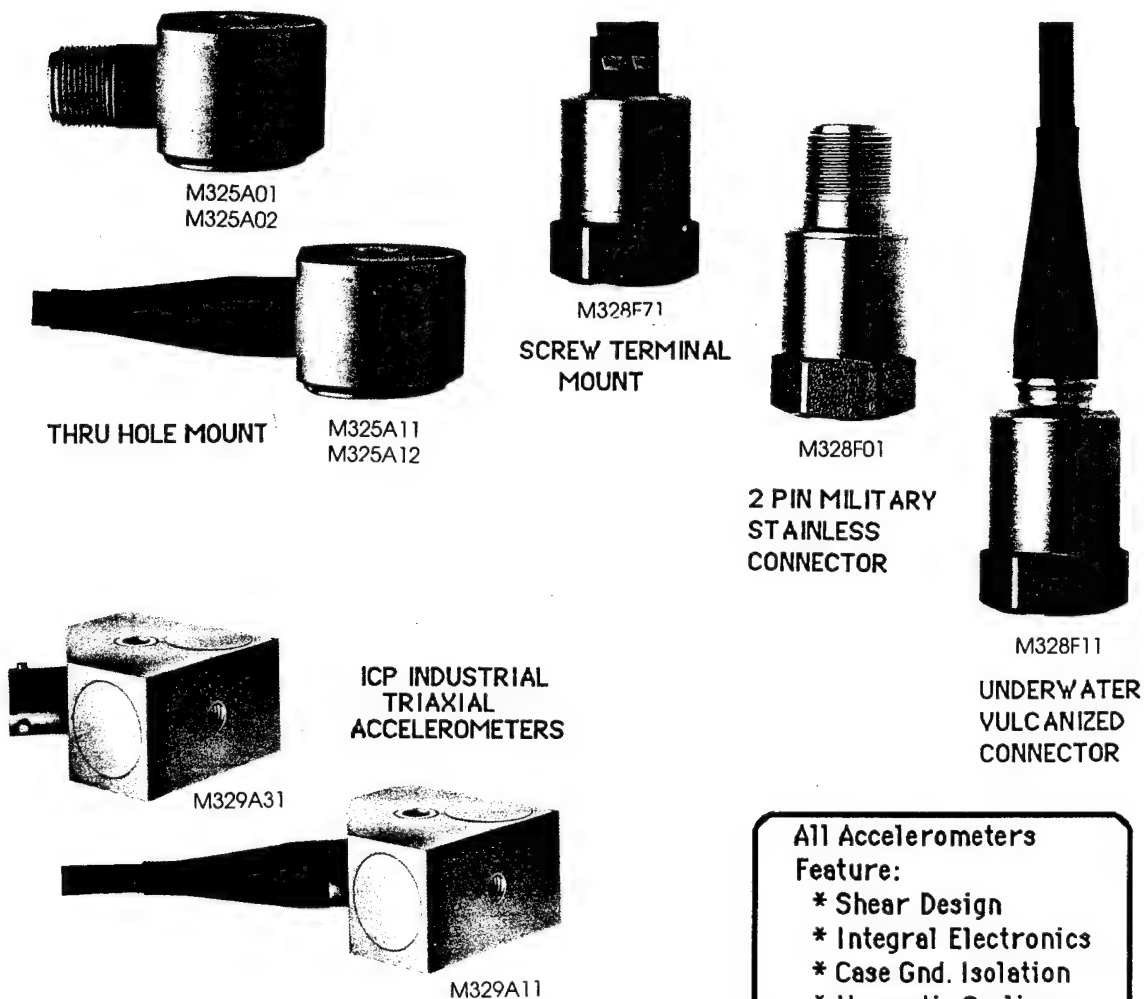for low frequency vehicular motion measurements. There are
high frequency models with response to 8000 hz, high
temperature ICP models to 350°F, models with velocity output
and models that provide simultaneous temperature and
acceleration output. ICP accelerometers are designed for
continuous duty applications.

TYPICAL ICP INDUSTRIAL ACCELEROMETERS:

M325A01
M325A02

THRU HOLE MOUNT   M325A11
                   M325A12

M328F71

SCREW TERMINAL
MOUNT

M328F01

2 PIN MILITARY
STAINLESS
CONNECTOR

M328F11

UNDERWATER
VULCANIZED
CONNECTOR

ICP INDUSTRIAL
TRIAXIAL
ACCELEROMETERS

M329A31

M329A11

All Accelerometers
Feature:
* Shear Design
* Integral Electronics
* Case Gnd. Isolation
* Hermetic Sealing

ICP industrial accelerometers are volume manufactured at the
PCB facility in Depew N.Y. to the same high quality standards
as all PCB sensors, electronics and calibration products.
You are invited to visit our plant anytime you are in
Western NY.

1. ICP® is a registered trademark of Piezotronics Inc.

References:
      Catalog QSG-200, IMI Div. of PCB Piezotronics Inc.

SESSION 2

APPLICATIONS

SUU-20 BOMB EJECTOR END-OF-STROKE TRANSDUCER

Authors

James Alich
Axel Sehic

Air Force Flight Test Center
412 TW/TSID
25 N Wolfe Ave.
Edwards AFB CA 93524-8300

Author: James A. Alich
AF Flight Test Center
412 TW/TSIDE
25 N Wolfe Ave.
Edwards AFB, CA 93524-8300

Abstract

This paper presents a design for a transducer capable of sensing the proximity of a steel plunger located inside an enclosed steel housing. The purpose of the transducer development was to measure average plunger velocity and time to end-of-stroke for a SUU-20 bomb ejector rack during bomb delivery tests. A harsh environment and physical constraints prevent the use of conventional instrumentation on the steel bomb ejector housing.

A major advantage of the transducer is simplicity of installation. Installation does not require machining of the plunger or housing because the transducer clamps to the outside of the housing and uses a magnetic flux circuit and a Hall Effect sensor to detect the presence of the plunger. Determination of average plunger velocity and time to end-of-stroke are possible from the transducer output. Six transducers and a signal conditioning box provide complete bomb release instrumentation for a SUU-20 bomb ejector rack.

To date, an F15E aircraft complete with two fully instrumented SUU-20 bomb racks has successfully flown a qualification flight in preparation for data collection on future bombing runs. Test data will be entered into a statistical data base to track the mean and distribution of time to end-of-stroke.

This paper will show how a transducer of this type overcomes many design constraints, will discuss the problems solved during the design phase of the transducer, and will present actual flight test results. Finally, this paper will explore a number of other possible uses for this unique sensing technology.

Introduction

The design of the SUU-20 end-of-stroke transducer answers a customer requirement to instrument a bomb ejector for stroke time of a bomb ejector plunger. The instrumentation that was already in place consisted of a micro-switch pressed up against the store (bomb) that toggled when the bomb began ejecting. The new requirement stated a need to determine the end-of-stroke of the plunger, used in calculating the initial bomb velocity. Since the bomb drop process initiates by a pyrotechnic charge, data analysts wanted a way to be sure they had a "good burn" before spending analysis resources on a particular bombing run. The computation of initial velocity also allowed analysts to cross check the central computers predicted time line for a weapon drop.

Instrumentation engineers investigated several different designs to determine the end-of-stroke of the bomb ejector plunger. Most of the designs probably would have rendered usable data, but with the consideration of operating environment and maintenance procedures on the bomb rack, would not have been robust enough to endure over time. The chosen design sought to minimize:

> Changes to the bomb rack maintenance cycle
> Modification to the bomb ejector housing
> External components in the airstream
> Installation complexity and time

The transducer described in this paper meets these stipulations with a relatively simple and inexpensive design.

Bomb Ejector Description

Figure 1 below illustrates the bomb ejector assembly. Six similar devices mount on a bomb rack (SUU-20) which hangs from a wing pylon on an aircraft. This particular ejector design drops MK-106 or BDU-33 inert practice bombs. Large jaws hold the bomb and lock in place around the outside of the bomb case. The ejector plunger has a pin fitted into a small detent in the bomb case and fully retracts with the bomb in place. A chamber on the housing holds an explosive charge that detonates by an electrical fire command to release the weapon. The ejection sequence begins with the opening of the large jaws, followed by a forceful ejection of the bomb by the plunger. The plunger fully extends when the bomb is away allowing excess exhaust gasses to expel through vent holes near the base of where the plunger exits the housing. **Figure 2** demonstrates this bomb ejection sequence.
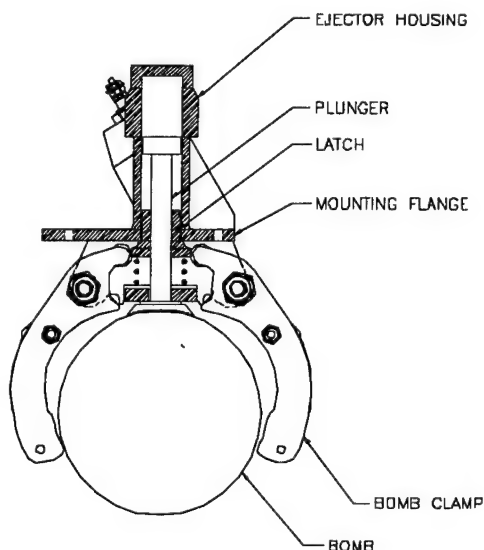
Figure 1 Bomb Ejector Housing Assembly

The bomb ejector housing mounts to the SUU-20 bomb rack by the mounting flange. The portions of the structure above this mounting flange are inside the enclosed bomb rack. Portions below the mounting flange are exposed to the open air stream around the pylon.
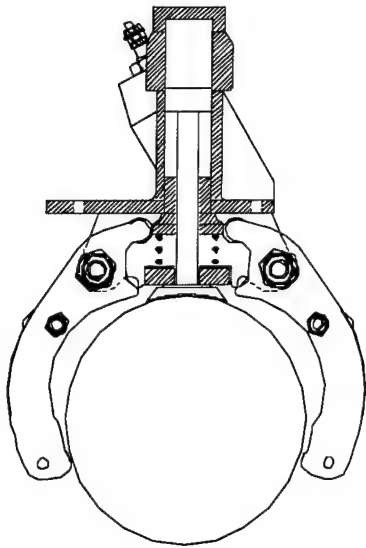
Figure 2A Locked Bomb Ejector and Store

This figure shows the bomb ejector locked around the bomb. Note how the bomb latch locks the large jaws around the store holding it securely. A strong spring, located below the latch, keeps the latch in position.
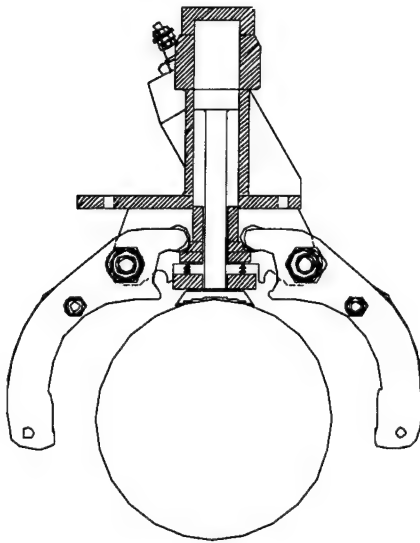
Figure 2B Latch Release

The bomb release command electrically ignites the pyrotechnic charge. The charge produces gasses that work behind the latch. These gasses push the latch and release the jaws.
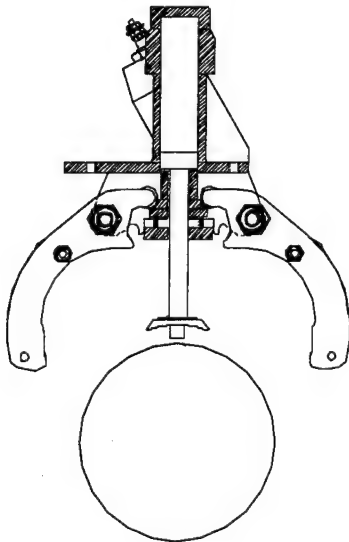
Figure 2C Bomb Ejection

Latch release frees both the bomb and plunger. The hot gasses continue working against the plunger. The plunger pushes the bomb until full extension when the bomb begins free fall. This important sequence gives the bomb an initial velocity.

Design Constraints

The first factor considered was the bomb rack construction. The bomb ejector housing and the front part of the plunger mount externally, so engineers sought a design that mounted internally to the SUU-20 bomb rack. The rack itself encloses the electrical controls and wiring. Because the rack also acts as the mounting point for the six ejector housings, it allows access to the bomb ejector housings from the rear.

The second factor considered was maintenance, which occurs after each flight, and requires removal of the bomb rack. The pyrotechnic charge used to eject the weapon leaves behind burn residues that clog and jam the plunger upon cooling. Maintenance personnel remove the plunger, soak it in solvents and flush the ejector housing with solvents to remove any residues. Finally, they lubricate the plunger and re-install it into the housing. Maintenance conducts this operation on all six of the ejectors at once and usually work on two SUU-20 racks at a time. Any instrumentation installed could not contact the plunger externally and, if mounted on the housing externally, would have to withstand the solvent flush operation.

The third consideration was the nature of the pyrotechnic charge. During weapons release, this powerful charge produces the gasses that work to eject the store as described previously. This event produces a shock to the SUU-20 rack, and to the particular bomb ejector being fired. Any instrumentation would have to survive this shock.

A final consideration in the instrumentation design was the construction of the housing and plunger. The bomb ejector housing is a drop forged, single piece unit. A detailed stress analysis would have to accompany any instrumentation that involved machining or changing this part. During the design phase, no data was available on stress or shock loads experienced during a mission. Also, stress analysis tools were not available to the designers, and due to the one-piece design of the ejector, would have been costly and time consuming to perform. The plunger is a machined steel part. Modifications to this part may change the mass and affect the initial velocity figure.

Transducer Principle

The chosen design approach takes advantage of the access and space on the rear side of the ejector mount. The design uses a magnetic flux circuit that routes flux through the side of the ejection plunger cross-section and detects the presence of the plunger as it moves forward. **Figure 3** illustrates the cross section of the rear side of the plunger and shows how this cross section changes with plunger motion.
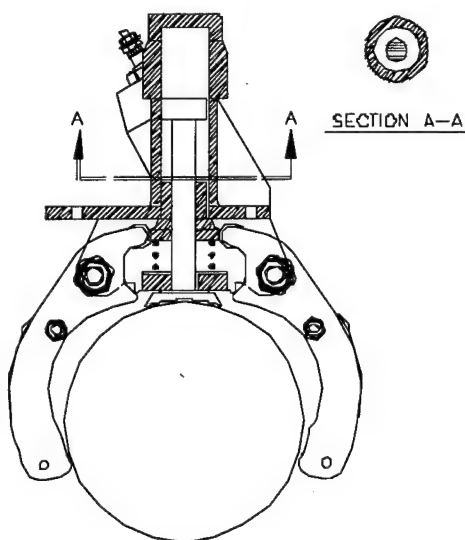

SECTION A—A

Figure 3A Retracted Plunger Cross Section

This figure shows the ejection housing and plunger along with the respective cross section. Section A-A shows a cutaway view of this section. Note the gap between the plunger shaft and the housing sidewall.
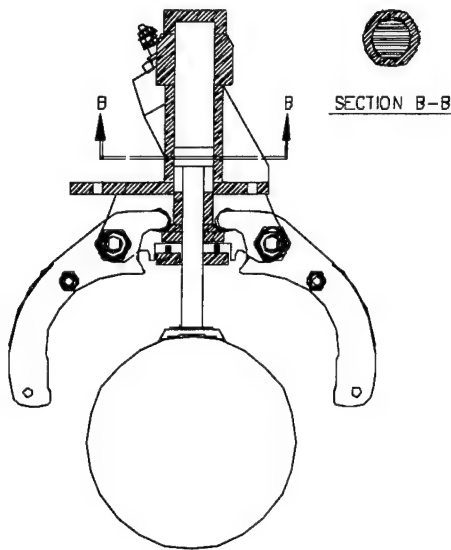
SECTION B-B

Figure 3B Forward Plunger Cross Section

This figure shows the plunger approaching full extension. Section B-B shows the aft portion of the plunger in the cross section. Note the absence of gaps in the cross section.

Figure 4 shows how magnetic flux could be routed through this cross section and how the presence and absence of the aft portion of the plunger affects the amount of flow. Section A-A, with the presence of an air gap, forces the flux to flow in a longer path through the section. Section B-B, with no air gap, provides the shortest path and thus a greater flux density. The difference in flux flow through the cross section provides an easy way to determine the position of the plunger.

Section A-A   *Section B-B*
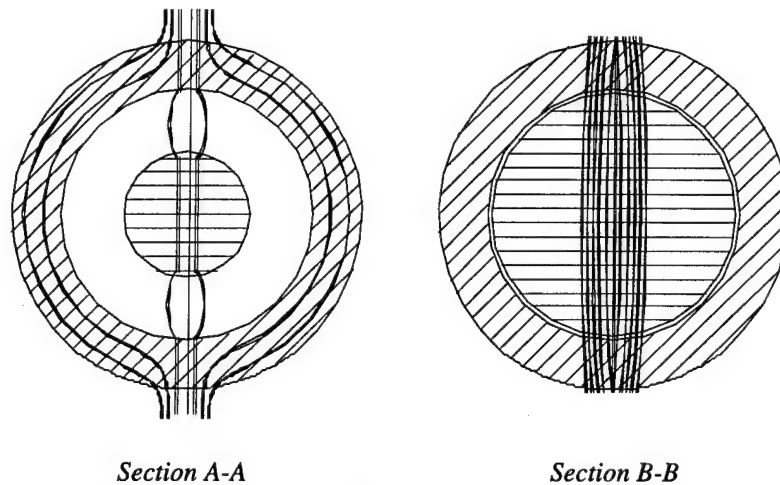
Figure 4

The major benefit of this method to detect the plunger position is that the transducer mounts on the back-side of the ejector, away from the external environment. Also, this design requires no machining of the bomb ejector housing or attachments to the plunger.

Transducer Design, Mechanical

Mechanically, the transducer consists of three components: steel legs, a clamp assembly and a permanent magnet to provide flux. The transducer clamps onto the ejector housing, around the cross section discussed earlier. **Figure 5** shows the prototype transducer and all the major components.
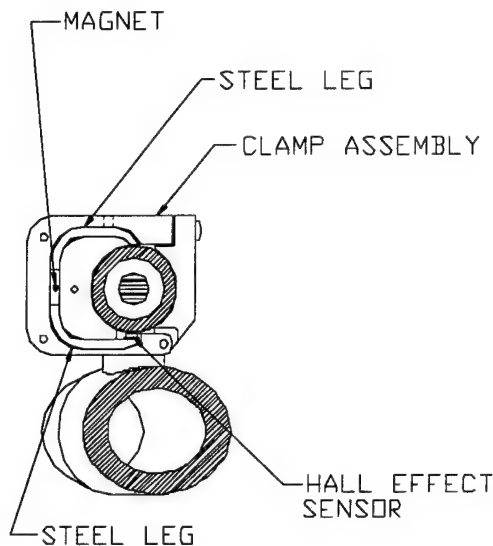
Figure 5 Transducer Illustration

The transducer shown at left mounts at the location of the cross sections discussed earlier. The top portion of the bomb ejector has been clipped for clarity.

Steel Legs

The steel legs comprise the parts of the magnetic circuit external from the ejector. They act as a path for flux to and from the flux source (the permanent magnet). There is an air gap designed into this pathway, allowing the insertion of a flux detecting Hall Effect Sensor. This gap, located at the side of the housing, provides a flat surface for mounting of the sensor directly on the steel leg.

Clamp Assembly

The clamp assembly holds the steel components in place. The requirements of this part were that it be non-ferrous and have a material compatibility with the steel. The chosen material was 1/2 hard brass formed into two parts, one part to hold the magnet, steel legs and transducer and the other part to act as a clamp around the housing. An access cover enclosed the magnet and steel pieces.

Permanent Magnet

The simplicity, variety of composition materials and greater possible flux densities made the permanent magnet the choice over an electromagnet for the flux source. The initial prototype transducer contained a magnet made from Alnico that matched the size of the steel legs in cross-section and was 1/2 an inch long.

Transducer Design, Electrical

The design for the initial prototype used a MicroSwitch SS94A1F Hall Effect sensor. This sensor, built upon a ceramic body, has a Hall Effect sensor and signal conditioning electronics built-in. The device meets MIL-STD-883 test condition A for shock and vibration, and operates over a temperature range of -40° to 125°C. These characteristics along with the geometry were important factors in part selection. **Figure 6A** shows the dimensions of the sensor.

The sensor takes a supply voltage of 8VDC and outputs a DC voltage proportional to the magnetic flux density through the sensor. The SS94A1F has a sensitivity of 25mV per gauss and is sensitive to flux flow in both directions. At null flux, the sensor outputs an offset voltage of 1/2 the supply voltage (4VDC) and moves up or down depending on the flux density and sign. **Figure 6B** shows the sensor electrical characteristics.
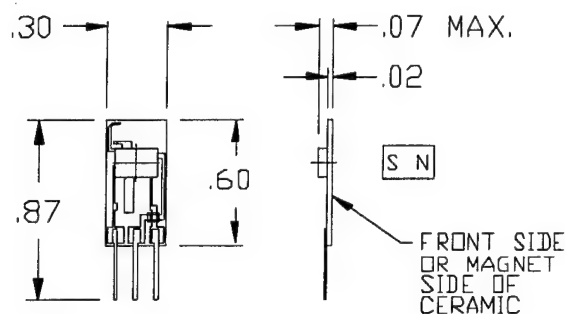
Figure 6A Mounting Dimensions

The diagram shown at left covers all sensors in the SS94 series of Analog Position Sensors. Refer to product data sheets for complete details.
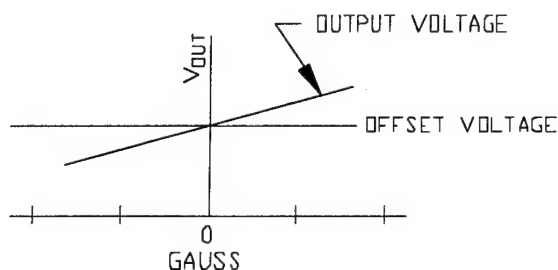

Figure 6B Transfer Characteristics

This diagram shows the output of the sensor along with the initial offset.

An early concern about using the part was the affect of temperature on the offset voltage. A test fixture was developed and the sensor was run through the range -20° to 125°C with a set flux density of 107 gauss. The sensor appeared to drift within the manufacturers maximum of +/- 0.1 %/°C. The procedure asked that the technician note any anomalies of the sensor output during the test, for example, noise picked up by the oven heating elements or fans, etc.

The technician noted an interesting susceptibility of the sensor during this test- that of photosensitivity. Cycling of the oven inspection lamp and verification with a flashlight showed that the offset of the sensor changed with ambient light. The sensor, however, mounts inside the bomb ejector rack, where ambient light cannot strike the sensors and affect the readings. A complete procedure of the test, diagram of the fixture and the results appears in Appendix A.

Prototype/Ground Test

Engineers and technicians conducted a ground test to verify that the transducer would work under the operating conditions of flight. The test placed transducers on four of the SUU-20s six stations, three stations with permanent magnets installed, and one station with a piece of unmagnetized Alnico. This station acted as a control station for possible EMI or EMC effects.

The test involved attaching the SUU-20 to an aircraft wing pylon, rolling the aircraft to a safe location and dropping inert practice bombs into a crate lined with mattresses. The powered up aircraft collected data while dropping four practice bombs one at a time. The following points outline the results of this test and the lessons learned during its preparation.

Flux stealing

The first problem noted was during the installation of the transducer to the bomb ejector. The transducer's position was near where the plunger stops upon full extension. This puts the transducer near the internal latch that releases the ejector jaws. When locked, the internal latch rests close enough to the transducer flux path to act as a flux path itself. This results in a greater total flux flow around the flux circuit. When the latch releases, it moves away from the sensor thus lowering the total flux just before the plunger starts

to move. This action causes a drop in the reading from the Hall Effect sensor. **Figure 7** illustrates the flux flow through the area of the latch.
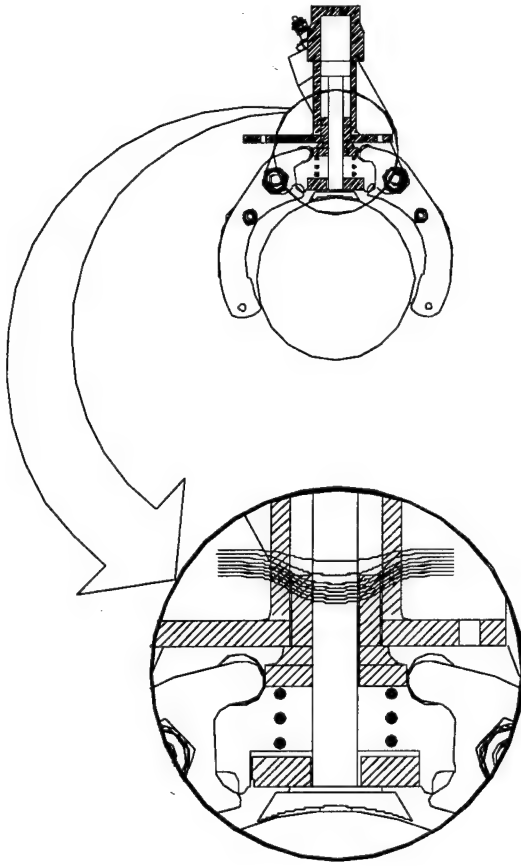
Figure 7 Flux Stealing Bomb Latch

The figure at left shows a detail of the flux path through the release latch. This flux path occurs into the paper on the cross section illustrations shown in Figure 4. Upon release, the latch moves down, thus lowering the flux flow.

Residual Magnetism

Magnetized parts of the bomb ejector housing and plunger caused inconsistent readings between stations during lab tests of the SUU-20. A large ring degausser alleviated much of the problems.

Air Gaps

Also noticed before the test, but not corrected until later, were readings that varied in amplitude. During testing, station 3 showed a higher maximum reading than the other two stations. Ring degaussing did little to solve the problem. Careful measurements showed the cause. The bomb ejector's cast steel housing had slightly different dimensions between stations. These variations caused non-design air-gaps to appear. This gap occurred between the non Hall Sensor steel leg and the housing and appeared in stations 1 and 2 and acted to reduce the maximum readings at these stations. The transducer fitted tightly on station 3 and gave higher readings.

Design Changes

The designers studied the problems described previously and implemented several design changes making the final instrumentation system as consistent as possible for all stations.

Changing the transducer location minimized the flux stealing effect of the bomb latch. Moving the transducer to a location close to the midpoint of plunger motion kept it well away from the flux stealing component. This position provides good start-of-stroke data as well. The ejector housing structure limited the final placement of the transducer however, and prevented it from mounting exactly on center.

Decreasing the sensitivity of the Hall Sensor by 1/5 prevented stray magnetic effects from altering the reading. A stronger permanent magnet allowed for plunger detection with the new sensor. The new magnet, constructed from a rare earth alloy called Neodymium, fits in the same location as the old Alnico magnet. These changes did not decrease the overall sensitivity of the transducer, but rather made the transducer less prone to outside influence.

Finally, a set screw installed on the side of the brass housing opposite the Hall Sensor forces the steel leg into contact with the side of the bomb ejector housing. This screw securely holds the steel in place so no air gaps appear.
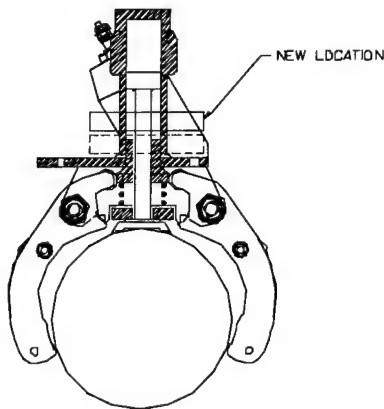
Figure 8 Design Changes

The two figures at left illustrate the changes made to the transducer and the installation as a result of the ground test.
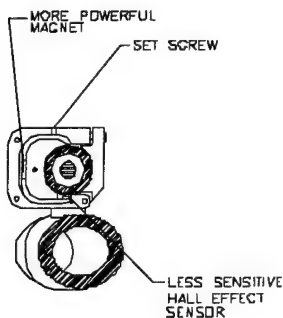
Waveform Data

Figure 9 shows two waveforms from different SUU-20 stations. The figures describe what the different inflection points represent.
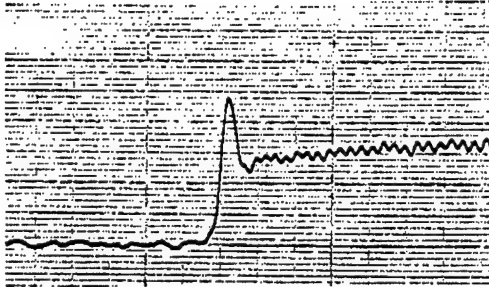
Figure 9A Waveform

The diagram at left was copied from a high speed oscillograph from taped data of an actual bomb drop. The three inflection points represent different portions of the ejector release- start of stroke, crossover and end-of-stroke. Crossover occurs when the aft portion of the plunger passes by the transducer.
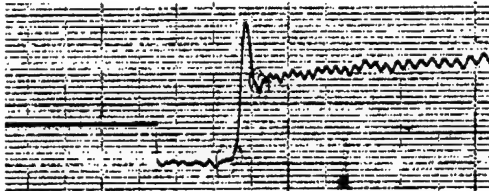
Figure 9B Waveform

This figure shows another typical waveform from a SUU-20 bomb release event.

Conclusion

The SUU-20 bomb rack in general and the bomb ejector housing in particular had many design challenges for the determination of end-of-stroke. Through careful planning and consideration, designers derived a simple, elegant and effective solution. This transducer represents an excellent detection scheme for the SUU-20 end-of-stroke, but does have some disadvantages.

For the flux circuit detection strategy to work, the parts involved must be ferromagnetic. This does not necessarily require a ferrous housing, but the moving part of interest must certainly conduct flux for non-intrusive detection. This disadvantage rules out applications that have aluminum alloy, or other non-ferrous alloys as the material for the plunger.

Another consideration is space. The SUU-20 bomb ejector and rack had space to spare in the areas of importance in the installation. Other bomb ejector racks studied for possible installation of a similar transducer did not have adequate space external to the plungers to apply a magnetic circuit.

References

David K. Cheng, *Field and Wave Electromagnetics*, Chapter 6, Menlo Park, California: Addison-Wesley, 1983.

Rollin J. Parker, "Analytical Methods for Permanent-Magnet Design-1", *Electrical Manufacturing*, pp. 102-110, September 1960.

Rollin J. Parker, "Analytical Methods for Permanent-Magnet Design-2", *Electro-Technology*, pp. 154-162, October 1960.

R.K. Tenzer, "Estimating Leakage Factors for Permanent Magnets from Geometry of Magnetic Circuit", *Electrical Manufacturing*, pp. 94-97, February 1957.

S. Middelhoek and S. A. Audet, *Silicon Sensors*, pp. 242-245, San Diego, California: Academic Press, 1989.

I. J. Garshelis and W. S. Fiegel, "A Magnetic Position Sensor", *Journal of Applied Physics*, pp. 5699-5701, Vol. 64, No. 10, November, 1988.

Jeffrey A. Lienau, *Magnetic Sensing of Projectile Position*, PAT-APPL-288595, AD-D008 909, July 1981.

Appendix A

SS94A1F   HALL EFFECT SENSOR   TEMPERATURE TEST

PURPOSE:

The purpose of this test is to characterize temperature vs offset voltage for the Microswitch SS94A1F Hall Effect Sensor.

DESCRIPTION:

The SS94A1F Sensor is sensitive to magnetic flux and outputs a voltage linearly proportional to magnetic flux flow across the sensor. This sensor will be used to measure plunger position unintrusively on the SUU-20 bomb drop rack. The sensor has an offset close to 4V at 0 Gauss. The data of interest is a small variation in the output (40-45mV). The design of the high gain amplifiers to see this variation depend on a good understanding of any changes in offset. Temperature will fluctuate in the area of measurement. This test will show how these temperature fluctuations can be expected to affect the sensor.

EQUIPMENT:

1.   A DC power supply. (9VDC required)

2.   Digital Voltmeter.

3.   Oscilloscope.

4.   Temperature oven.

TEST SETUP:

Set up the test as shown below:
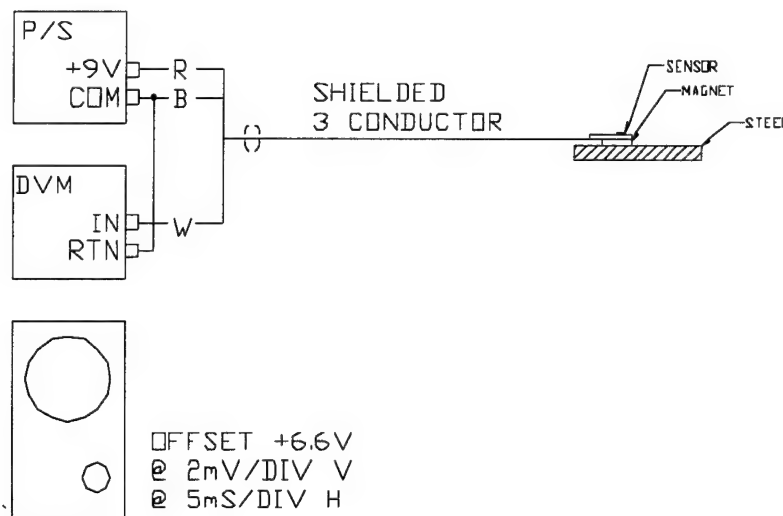
PROCEDURE:

1.   Set up the fixture inside the oven and make sure it is secure.

IMPORTANT The fixture must remain fixed for the entire duration of the test!

2.   Dial up 9VDC on the supply and check with the voltmeter.

3.   Apply power to the sensor and connect the oscilloscope.

4.   Cycle the fan, heating elements and cooler and note any 60 Hz noise or glitches in DC offset levels during switching.

5.   Record DC offset at the following temperatures: -20C, -10C, 0C, 10C, 20C, 30C, 40C, 50C, 60C, 70C, 80C, 90C, 100C, 125C.

6.   At each temperature make sure enough time passes for fixture to reach the appropriate temperature.

NOTES:

handwritten notes:

4 — oven light "on" trace deflects down 2mv & stays rising

Heater "on"/"off" no change

cooler "on"/off" no change 3 @ 2mv /div DC w/ni
                              + 6.67xx offset to bring
                              trace on center of screen

Jim This turns out to be sensitivity to
     light rays falling you coil. shift
     is about -2mv @ nom 20°C & about
     -12mv @ 125°C.

HALL SENSOR | TEMP CYCLE

TEST #	TEMP °C	VOLTAGE
1)	-85°C NOMINAL	+ 6.677 VDC
2)	-20°C	+ 6.671
3)	-10°C	+ 6.675
4)	0°C	+ 6.677
5)	+10°C	+ 6.675
6)	+20°C	+ 6.672
7)	+30°C	+ 6.666
8)	+40°C	+ 6.665
9)	+50°C	+ 6.663 VDC

OVERNITE COOL –

1)	19.9°C NOM AFT 20MIN WARMED	+ 6.689 } + 6.676 } WARMED
2)	+40°C	+ 6.667 VDC
3)	+50°C	+ 6.664
4)	+60°C	+ 6.657
5)	+70°C	+ 6.621
6)	+80°C	+ 6.613
7)	+90°C	+ 6.404
8)	+100°C	+ 6.572
9)	+125°C	+ 6.559 VDC

– OVERNITE COOL –

1)	19.5°C AFTER 20MIN	+ 6.685 VDC + 6.673 VDC

STRAIN GAGE BASED SENSORS
FOR SUSPENSION PUSHRODS
ON INDY RACE CARS

Robert V. Magee

Sensor Applications Engineer

HITEC Corporation

65 Power Road

Westford, MA 01886

(508) 692-4793

ABSTRACT:

The purpose of this paper is to illustrate the use of strain gage based sensors to monitor the static and dynamic forces on INDY suspension pushrods. The purpose of strain gaging suspension pushrods on INDY race cars is to provide the driver and his crew additional information on the bounce and rebound forces of the car during cornering on various oval tracks and road courses. By monitoring these forces, engineers can adjust shocks, suspension rocker arms, stabilizers, and other components to give the driver a more competitive edge. Strain gaging the suspension pushrod allows for transducer performance and quality using actual components rather than modifying the component to accept a transducer. Recent design improvements include tighter balancing of the strain gage bridge specification, gage placement to eliminate output due to bending, cross sectional area reduction for increased strain gage sensor sensitivity and protection, and, with shielded cable, reduction of electrical signal noise due to rotating components. These improvements have increased the accuracy of the data and has eliminated the need for expensive custom transducers. This report will demonstrate how making existing components into or part of a transducer has also been applied to NASCAR Racing to obtain suspension loads, by monitoring all four load cells to measure spring loading, and to the first US built bobsled to gather data from its ski runners during course testing, by measuring dynamic bending loads.

NOMENCLATURE

P = Load   A = Cross Sectional Area

E = Modulus of Elasticity σ = Stress

e = Strain   ue = Strain X 106

mV/V = Milli Volt / Volt

1. INTRODUCTION:

INDY Racing teams have made significant improvements in the
measurement of forces with the addition of strain gage based
sensors applied to suspension pushrods to measure dynamic
loading (Figure 1. and Figure 2.)[1]. In the beginning,
bridge balance had to be within plus or minus 0.025 mv/v,
bridge resistance of 350 ohms was required, and reduction of
signal noise due to rotating machinery (because of the high
gain needed to amplify the signal) was needed to work with
the early models of the Pi Research amplifier (Figure 3.).
Additional modifications have now been added to improve
sensor performance by designing the cross section for
improved sensitivity, better installation protection, and
orientating the strain gages to eliminate cross talk due to
bending and to improve linearity of output. Both the
improvement to the strain gage sensor on the pushrod and the
stable, accurate amplification provided by the Pi system has
created a full system for force measurement. This is the
information that the teams are actively using for increased
vehicle performance.

2. THE SENSOR AND AND ITS USE:

The sensor used on the pushrod is a resistive strain gage
circuit consisting of four strain gages arranged in a basic
Wheatstone bridge circuit (Figure 4.)[2][3]. Two strain
gages measure the axial strain compressive force, while the
remaining two gages measure the tensile force perpendicular
to the axial load. The two strain gages measuring strain in
the Poissons' Ratio direction only see a third of the total
strain along the pushrod. As the resistance of the gages
change, due to the compressive strain force (ie. 35,520
Newtons (8000 pounds) equals 2mV/V in a typical pushrod) the
voltage potential changes, increasing proportionally to the
strain applied.

Calibration of the suspension pushrods is performed using mainly one of two methods. One method is using a press with an inline load cell. The second method used to calibrate the pushrods is to place the car on scales at the four corners while the car is at the track garage at the track. For the second method to be performed, team members gather on each corner of the car while the instrumentation engineer calibrates output voltage on each amplifier. The first method is used when calibration is performed by the manufacturer or the team decides to calibrate before going to the race site. A sample calibration sheet is shown in Figure 5.

Once the calibration is complete the vehicle is run around the track, while samples of dynamic loading are logged into the on board data-logger (Figure 6.) [4]. Data can then be retrieved by telemetry or by down-loading off the computer port on the INDY car. The software has various data reduction and linearization curve programs, which improves the usefullness of the data retrieved from the vehicle. A sample output is shown on Figure 7.

3. THE STRAIN GAGE AMPLIFIER

The model number 01B-050049 Pi strain gage amplifier was designed specifically for use with INDY and Formula 1 strain gage transducers and bridge circuits which have a 350 ohm resistance. The amplifier has two channels each and gain can adjust from 200-1000. Weighing 65 grams and about 2 x 3 x 6 cm, output from the bridge, once amplified, sends 0-5 volt out to the data logger, for later downloading. The 0.5 V or 2.5 V available offset (depending on whether measurement is desired for one force direction or both, respectively) is the reason for the need for 0.05 mV/ V balance specification.

4. THEORY AND APPLICATION:

There have been four significant variations to the INDY car suspension pushrod. First, there was installations on the tubular section of the rod. The cross sectional area of the rod was very thick at the time and required the gain settings of the early amplifiers to be redesigned for higher settings. Because the sensor and application were just being introduced to the teams, additional design modifications for sensor based pushrod were constantly updated. While trying to reduce the bulky appearance of the sensor on the rod, pocketed areas were machined into the pushrod. Not only were the sensors being better protected, but the cross sectional area was greatly reduced. Finally, sensors were installed on rod ends of calculated cross section to properly amplify the signal, so that at 2mV/V load is 26,640 newtons (6000 pounds) for front pushrods and 35,520 newtons (8000 pounds) for rear suspension pushrods.

Employing a full four gage Wheatstone bridge circuit the strain calculation for proper output is as follows:

$$(1) \qquad A := \pi \cdot \frac{D_1^2 - D_2^2}{4} \qquad IN^2$$

$$(2) \qquad \sigma := \frac{P}{A} \qquad PSI$$

$$(3) \qquad \varepsilon := \frac{\sigma}{E} \cdot 2.6$$

To convert to mV/V output:

$$(4) \qquad \frac{\varepsilon}{2000} = \qquad MV/V$$

A sample calculation is at 2 mV/V, the Pi amplifier applies 5 V excitation across the sensor giving an output of 10 mV out at capacity. An amplification of 400 gain increases output to the on board data logger to 4 V.

5. UPDATES IN SENSOR DESIGN:

The balanced Wheatstone bridge requirement came about with the need to interchange amplifiers and pushrods in the pit and garage area at the track. The compact amplifier could not be easily adjusted and balance pots required a trained technician to adjust for each pushrod. A constantan wire is used to balance the strain gage bridge circuit within plus or minus 0.025 mV/V. This enables the teams to easily adjust the proper offset of the amplifier to obtain a zero on their instrumentation. The latest Pi amplifiers now provide variable gain and zero adjustments, specifically modified to improve the signal output of the strain gage bridge. This development was due to several types of pushrods had different sensitivities from various cross sectional areas on the components.

Most pushrods have reduced pocketed areas machined into them, specifically for strain gages. This allows for similar amplifier requirements for each pushrod and provides excellent mechanical protection of the sensor. Rod ends are still gaged for a few INDY teams. To get proper sensitivity, the fronts have a 9.5 mm (0.375 in.) diameter while the rears are 12.5 mm (0.50 in.) in diameter. Benefits to using rod ends is it can be reused in accidents involving the pushrod only and it's comparatively more linear than the pushrods during calibration. But the Pi software can compensate for the nonlinearity of the pushrods, so both successfully work in the application.

Gage orientation is also important to eliminate output due to bending which is also present during dynamic loading of suspension pushrods. A two element "T" Rosette gage is positioned on center in the machined pocket with the Poisson gage directly behind the axial element to compensate for bending. Another is placed in the opposite side machined pocket. The adhesive used for gage installation is AE/15. The protective coatings, which are used after the installation is complete, are M-coat D and then Gage-Kote 5. These adhesives and coatings were selected because of the temperature restrictions to the bushings on the pushrods and rod ends. The AE/15 is an excellent performance low cure temperature epoxy and using first an acrylic coating, then a poly-sulfide epoxy coating prevents any oil, moisture, even gasoline type contaminants from reaching the sensor. Encapsulated gages also add sensor protection. Proper installations with these adhesives and coatings has made the pushrod sensor endure the entire race season with trouble-free data collection.

The signal is protected from outside electrical noise by using braided shielded cable. The cable is also teflon coated, because of the temperature environment the sensor sometimes sees. Although the pushrod sensor itself never experiences temperatures over 80 degrees C, leadwires often come up near exhaust manifolds and other hot components of the vehicle where vinyl leads would not endure the heat.

6. CONCLUSION:

This paper has shown an example of how using actual components for strain gage "transducerizing" can benefit INDY car racing teams by instrumenting their suspension pushrods rather than modifying components to accommodate an off-the-shelf transducer. In this case making a transducer out of the suspension pushrod has evolved in the last year to accommodate the amplifiers used by most of the INDY teams. The amplifier has also evolved to accommodate the limits of strain gage transducers by increasing the balance range pot and adding adjustable gain pot on the amplifiers to allow individual team instrumentation engineers to experiment with other components such as the wishbone suspension parts or shift linkages. Transducerizing and testing of the wishbone components added information on how the tires of the INDY cars performed, while the typical suspension pushrod mainly provided dynamic compression loads. Shift linkages gave engineers information on when the driver is shifting. Additionally NASCAR has needed to monitor dynamic load on the four corners of a stock car suspension. A transducer, which is customized to the size of the spring retainer plate, is used again with the same amplifier system to record loads during course testing. The load cells are proving to be suitable for this type of load measurement gathering, but is currently in its early use.

A similar application involved instrumenting US Bobsled runners. By installing sensors on the bobsled's shoes, dynamic load data could be recorded during bobsled race trials in order for teams to modify sleds for the following season or later races.

Transducerizing suspension pushrods for INDY car (Figures 8 & 9) racing has proven to be a better solution than adapting the component for an off-the-shelf load cell. It is a more reliable and efficient solution for obtaining important load information which could not be obtained by standard transducer adaptation methods.

7. ACKNOWLEDGMENTS

8. REFERENCES

[1] Carlton, Rick, "Full Speed Ahead", On Track, pp.40-42, October 21, 1994.

[2] Technical Staff, Strain Gage Based Transducers, Measurements Group, Raleigh, p.54, NC, 1988.

[3] Dove, R.C. and Adams, Paul H., Experimental Stress Analysis and Motion Measurement: Charles Merrill Books, Inc., 1964.

[4] Fey, Buddy, Data Power Using RaceCar Data Acquisition, Towering Publishing, Inc., p. 3-4, 1993.
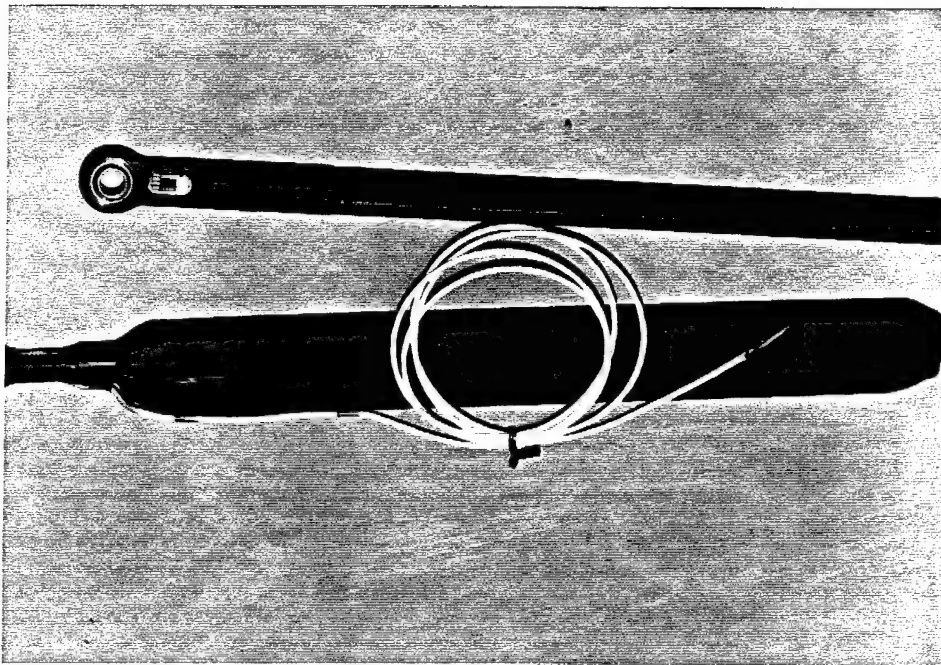
Figure 1.   Suspension Pushrod.

WISHBONE SUSPENSION PUSHRODS

REAR SUSPENSION PUSHRODS

FRONT SUSPENSION PUSHRODS

TELEMETRY SYSTEM SUCH AS PI SYSTEM IV
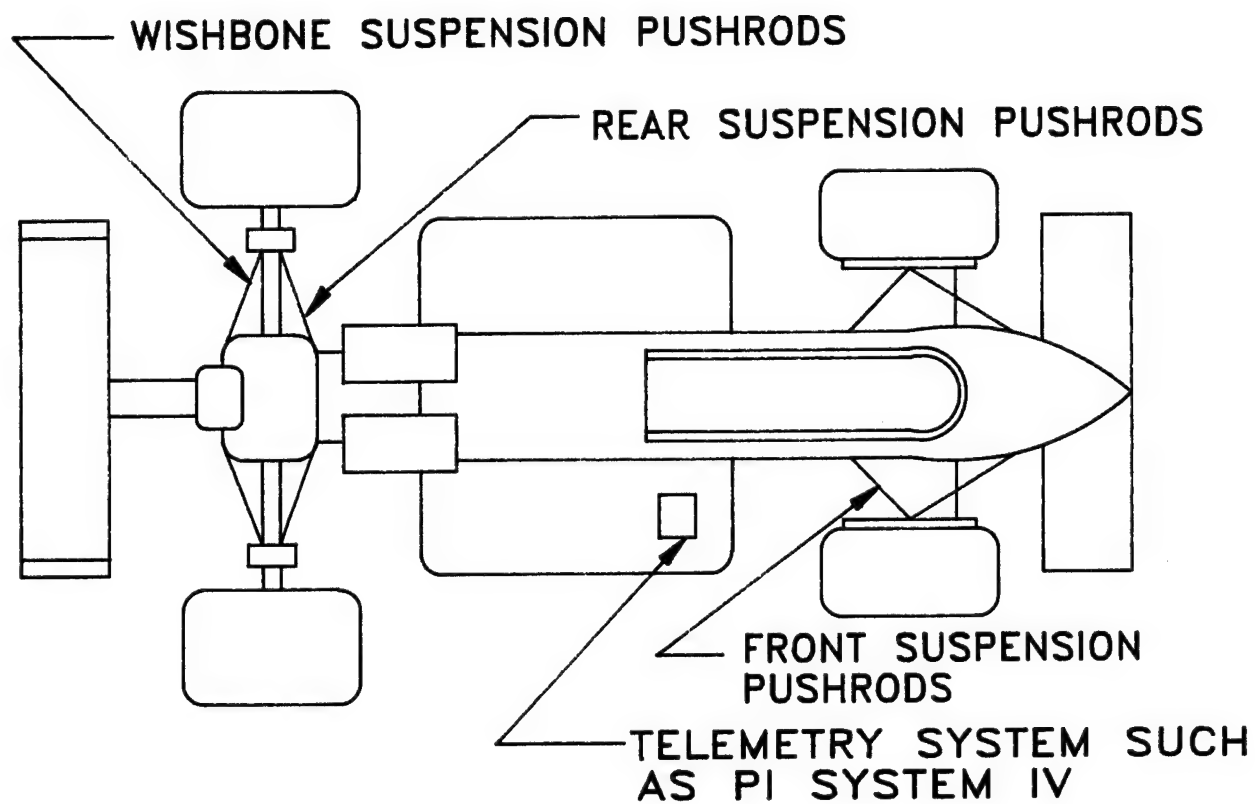
Figure 2.   Suspension Pushrod Locations.
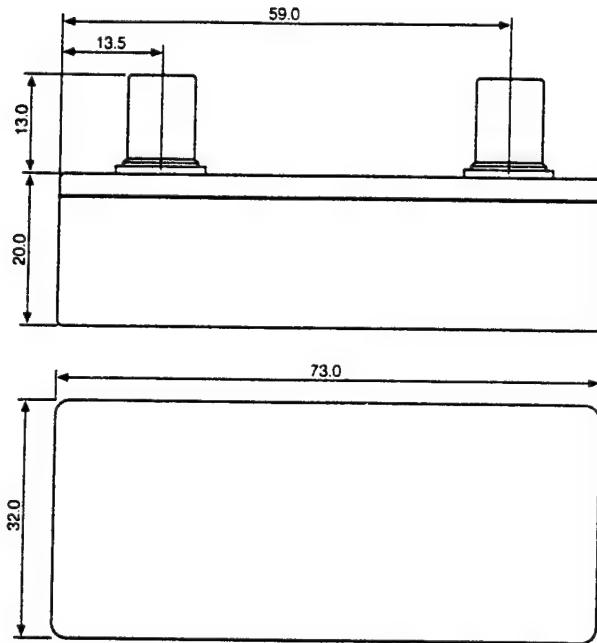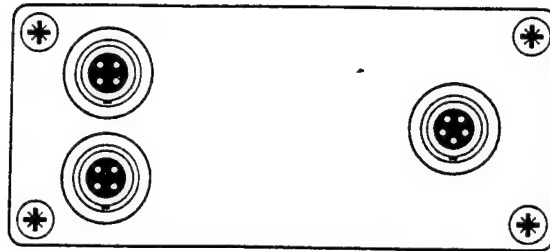
Functional Specification

Construction Material	Anaodised Aluminium
Dimensions (h w l)	33mm x 32mm x 73mm
Operating Temperature Range	+10°C to +60°C
Weight	60 grammes
Connectors	Sealed Lemo connectors
Environmental	Fully waterproof

Figure 3. Pi Amplifier.

106

Figure 4. Strain Gage Circuit.

107

HITEC CORPORATION/HALL RACING
PUSHROD INSTALLATION SUMMARY/CALIBRATION DATA SHEET

HITEC CORPORATION JOB NUMBER: 20-10750
PURCHASE ORDER NUMBER:
MODEL:
SERIAL NUMBER: 01
PART NUMBER: 951F1032
STRAIN GAGE BRIDGE LOCATION: COMPRESSION BRIDGE IN POCKETED AREA
CABLE EXIT: END OF PUSHROD
STRAIN GAGE TYPE: EA-06-062UT-350

STRAIN GAGE ADHESIVE: PE-15
CABLE TYPE: 4 CONDUCTOR
CABLE LENGTH: SIX FEET
PROTECTIVE COATING: GAGEKOTE 5
CONNECTOR: NONE
INSTRUMENTATION PRINT:

CALIBRATION REQUIREMENTS: INSTRUMENT GAGE FACTOR; 2.0
                          FULL SCALE; 5000 POUNDS
                          INCREMENTS; 1000 POUNDS
                   TESTING MACHINE; TINIUS OLSON
              REFERENCE TRANSDUCER; 5K NIST CERTIFIED

NEGITIVE/POSITIVE BENDING CALIBRATION DATA		
LOAD (IN-LBS)	OUTPUT (Ue/IN)	OUTPUT mV/V
0	000	000
1000	550	0.28
2000	1173	0.59
3000	1805	0.90
4000	2442	1.22
5000	3052	1.53
0	-3	0

SHUNT CAL: 5037 Ue = 34.650K OHMS

CALIBRATED BY: RVM   DATE: 01/17/95
==
HITEC CORPORATION, 65 POWER ROAD, WESTFORD, MA 01886 (508) 692-4793

Figure 5. Sample Calibration Data Sheet.

Post Mld-Ohio Test

9400-4039-72
RR PR

9400-4039-71
LR PR
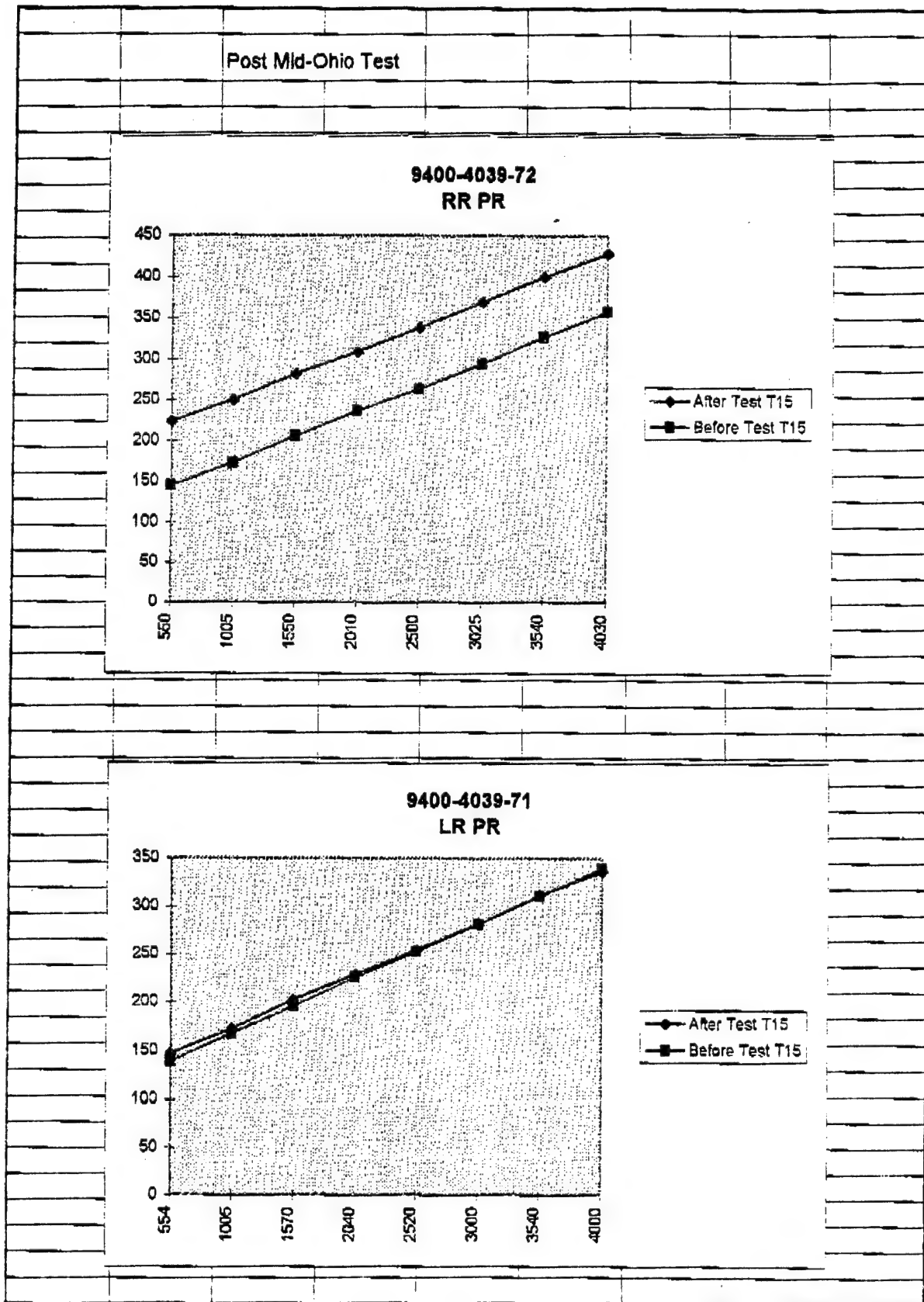
Figure 6.   Pi System Pushrod Calibration Data.
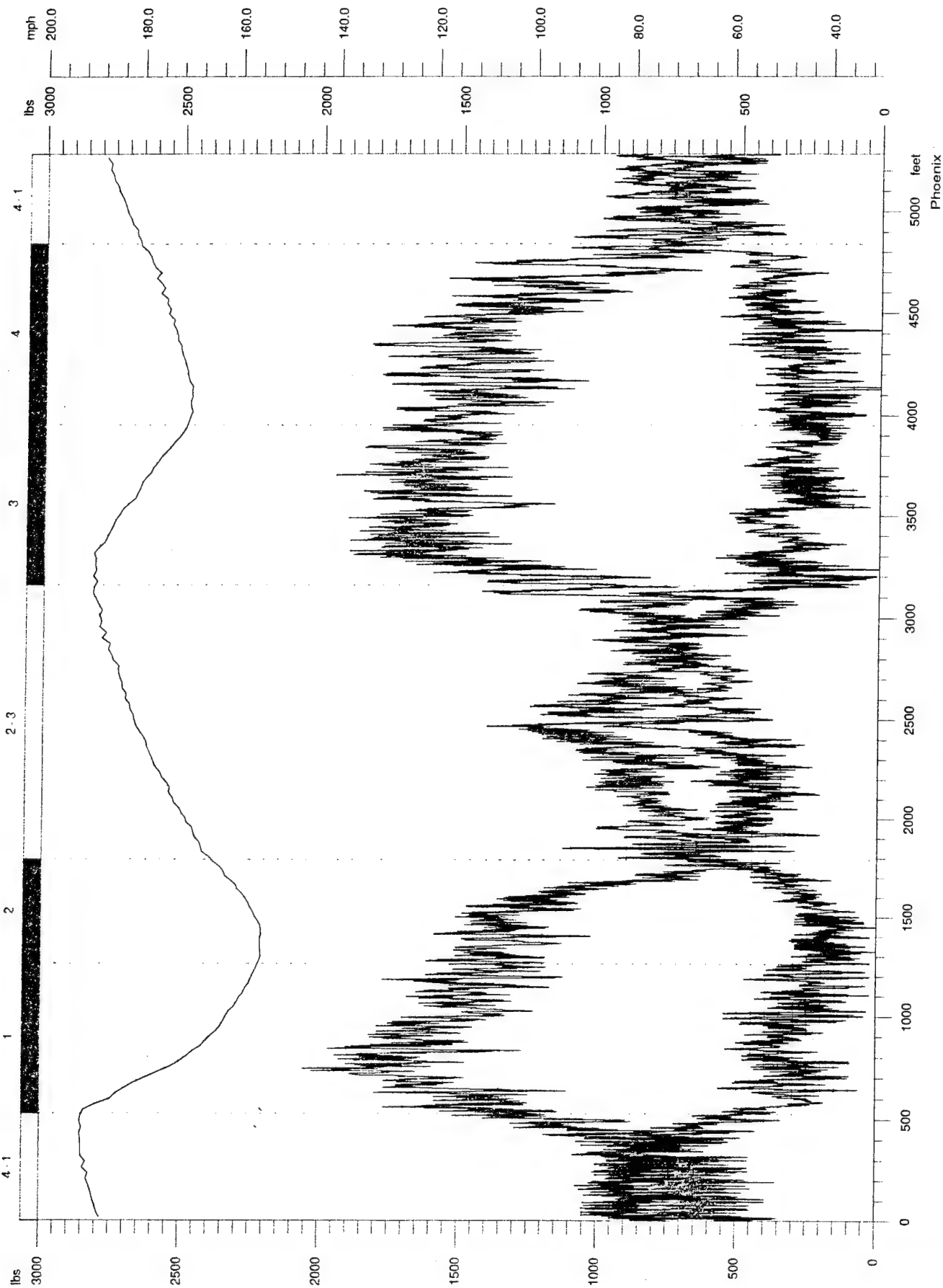
FIGURE 7 - SAMPLE P1 OUTPUT

Channel	Filter	Driver	Lap Time	Data Set	Car	Date & Time
RF Pushrod		Doe, J	0:20.528	<119:015:078>	Reynard	Fri Feb 17 17:25:50 1995
LF Pushrod		Doe, J	0:20.528	<119:015:078>	Reynard	Fri Feb 17 17:25:50 1995
Speed		Doe, J	0:20.528	<119:015:078>	Reynard	Fri Feb 17 17:25:50 1995

110
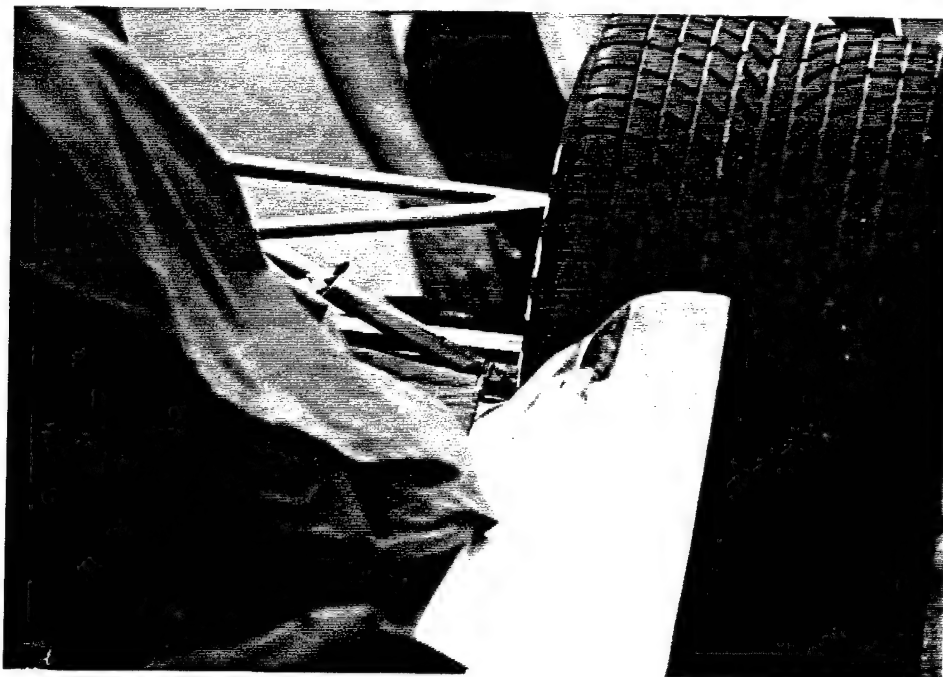
Figure 8.   INDY Car with Instrumented Pushrods.
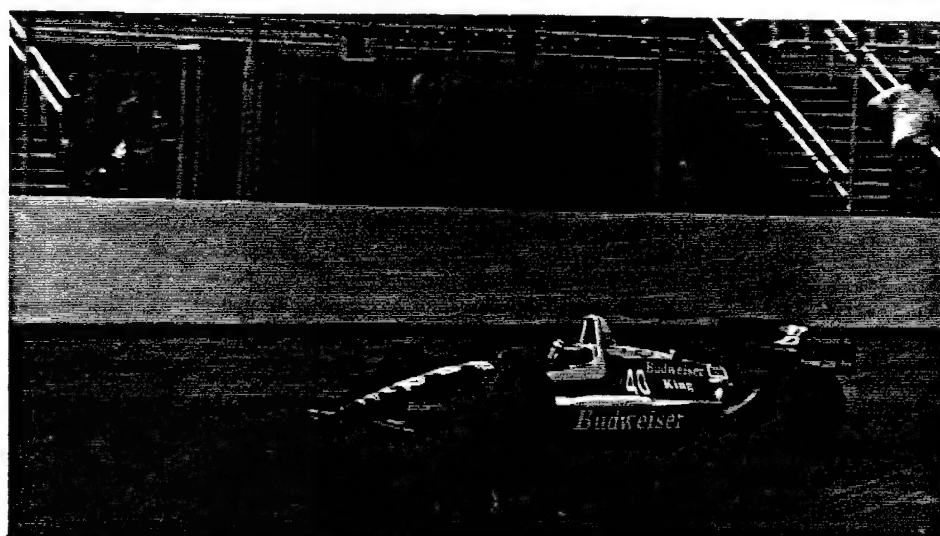
Figure 9.   INDY Car.

CORROSION MONITOR BASED ON TIME DOMAIN REFLECTOMETER MEASUREMENTS OF A DEFORMED OPTICAL FIBER

Jack R. Kayser and Todd M. Meade*
Kim D. Bennett and Leslie R. McLaughlin**

*Department of Civil and Environmental Engineering
**Department of Electrical Engineering

Lafayette College
Easton, PA 18042

ABSTRACT

A corrosion fuse has been developed which attaches to an optical fiber. When the fuse is intact, the fiber is distorted into a tight bend. Once the fuse corrodes, the fiber straightens out. The distortions in the fiber are detected as light loss using an Optical Time Domain Reflectometer (OTDR). Changes in the OTDR output represent the occurrence of corrosion failure in the fuse. An advantage to using an OTDR is that several corrosion fuses can be monitored using a single fiber. An experiment was conducted using three carbon steel fuses placed in a simulated marine environment. The fuse failures were successfully detected using the OTDR and the time of failure was used to calculate an average rate of uniform corrosion.

INTRODUCTION

It is estimated that in the United States, the correction of functional bridge deficiencies will require an investment of 8.2 billion dollars per year [1]. These functional deficiencies arise from two sources; geometric inadequacy and structural weakness. Structural weakness can result from obsolescence or from deterioration. Corrosion is a major form of deterioration in steel bridges, directly affecting structural performance by decreasing carrying capacity and overall safety [2].

Management of corrosion damage in steel bridges can be categorized into three areas: monitoring and load control; prevention and maintenance; and repair and replacement. This paper focuses on a new monitoring technique which can be used to estimate corrosion damage. Knowledge of this damage can then be used to evaluate ultimate capacity, allowable load, and probable rate of failure [3].

Currently there are several methods for monitoring corrosion. The basic and simplest method is visual inspection. The next method is physical examination using devices such as calipers or ultrasonics to measure thickness [4]. The efforts required to visually or physically inspect for corrosion can be expensive in terms of facility shutdown and risky to personnel attempting to access structural members.

Corrosion can also be monitored by using small sacrificial specimens that are placed in the vicinity of a structure [5]. These specimens are periodically checked for section loss. This section loss is then correlated to the rate of uniform corrosion occurring on the exposed structure. Electrochemical methods are also used to estimate rate of corrosion [6]. These electrochemical methods depend on either measuring current or electrical resistance, and correlating these electrical measurements to the rate of corrosion.

This paper presents an alternative method of corrosion monitoring which uses a metallic fuse connected to an optical fiber [7]. When the fuse corrodes, a switch is set which indicates the presence of a corrosive environment. The switching mechanism relies on the deformation of an optical fiber, which is monitored by an Optical Time Domain Reflectometer (OTDR). Since an OTDR is capable of monitoring several hundred meters of fiber, multiple fuses can be installed on a single fiber at several locations. The fuse/fiber combination is practical because it allows the monitoring of a location on a structure without requiring periodic access to that location. The system is also immune to electrical interference.

PROCEDURE

An experiment was conducted to test the performance of the fuse/fiber monitor. This experiment involved the assembly of an environmental chamber (humidity tank) which contained heated salt water, three monitors attached to one fiber, and an OTDR to measure light transmission in the fiber. The tank was covered by a thin film of plastic in order to maintain humidity. The humidity tank was loosely based on a chamber design used in testing water resistance [8]. Figure 1 illustrates the test configuration.
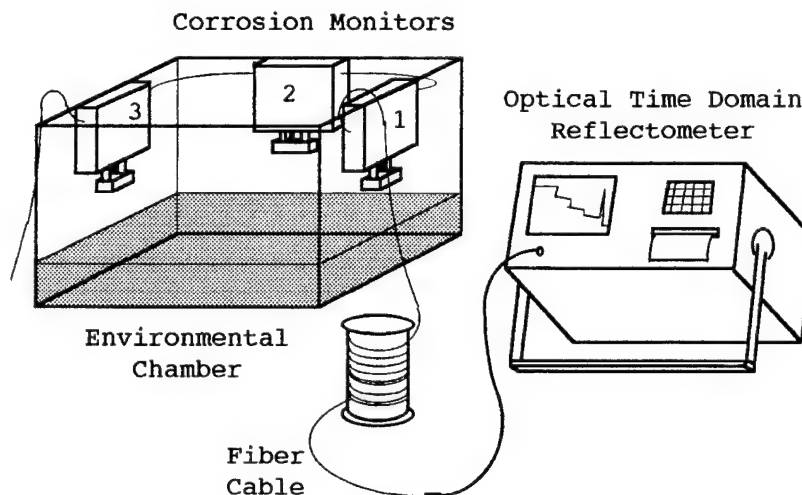
Figure 1: Configuration of environmental chamber, corrosion monitors, and the Optical Time Domain Reflectometer.

A corrosion monitor was comprised of a 3 mil (76 μm) carbon steel fuse attached to a spring loaded pin, as illustrated in Figure 2. The pin held a distorted segment of optical fiber in between two support blocks. The spring support mechanism was contained within an aluminum frame, covered by a plexiglass plate on each side. The corrosion fuse was supported outside of the frame and exposed to the corrosive environment. When the fuse decayed, the springs were released and the optical fiber was forced to straighten out.

113
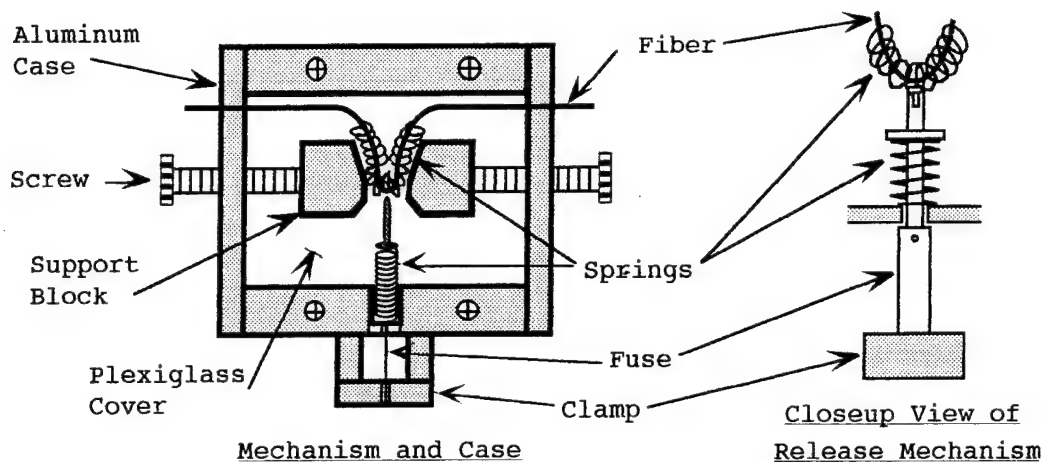
Figure 2: Design of the corrosion fuse mechanism.

One end of the fiber was connected to a Photodyne 5400XQ High Resolution OTDR which monitored the transmission of light through the fiber as well as the magnitude and location of light loss. Previous experiments were conducted to calibrate the OTDR and size the corrosion fuse mechanism [7]. The effect of the bend in the optical fiber can be understood by applying Snell's Law at the core/cladding interface. As shown in Figure 3, light traveling at an angle less than the critical angle, θc, is totally reflected within the core [9]. This is the case for propagating rays in a straight fiber. However, when the fiber is bent into a tight curve, some rays may strike the boundary at an angle greater than θc, and be lost due to refraction. Before the onset of corrosion in the experiment, the metal fuse held the fiber in a bend, which was detected as a light intensity loss by the OTDR. When corrosion broke the fuse, the fiber straightened and the OTDR detected a net increase in the propagating light.
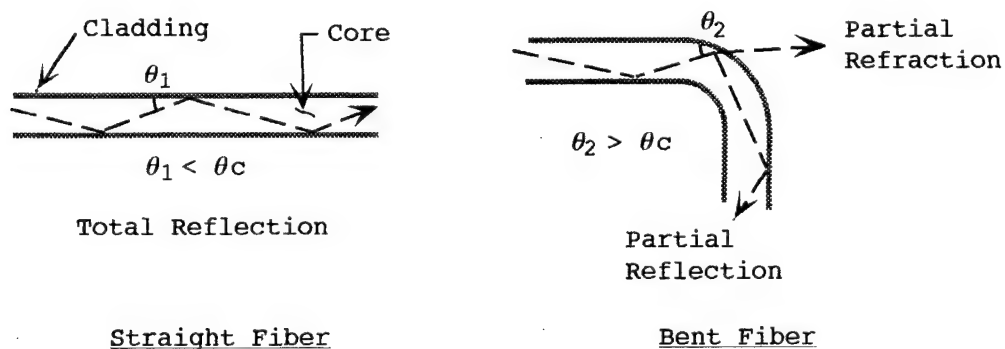
Snell's Law: $\theta c = \cos^{-1}(n_2/n_1)$

n_1 index of refraction of core

n_2 index of refraction of cladding

Figure 3: Principle of Snell's Law applied to the transmission of light in a deformed optical fiber.

114

The environmental chamber was operated at 30°C, with the monitors and OTDR being checked on a daily basis. After 36 days no apparent corrosion had occurred. In order to ensure timely results, the temperature was increased to 44°C and a mild solution of phosphoric acid was sprayed on the fuses each subsequent day.

RESULTS

On day 66 one of the fuses corroded to failure and created approximately a 0.1 dB increase in power transmission at the location of the fuse. The remaining two fuses failed at 73 and 76 days with subsequent increases in power transmission of approximately 0.25 dB and 0.5 dB, respectively. Figure 4 illustrates the OTDR output at each stage of the experiment.

The average failure age of the fuses was 72 days. Assuming that the spring loaded mechanism released the optical fiber when the flat metal specimens corroded 1.5 mils through each side, an estimated 7.6 mils per year (193 μm/yr.) uniform corrosion rate had occurred.
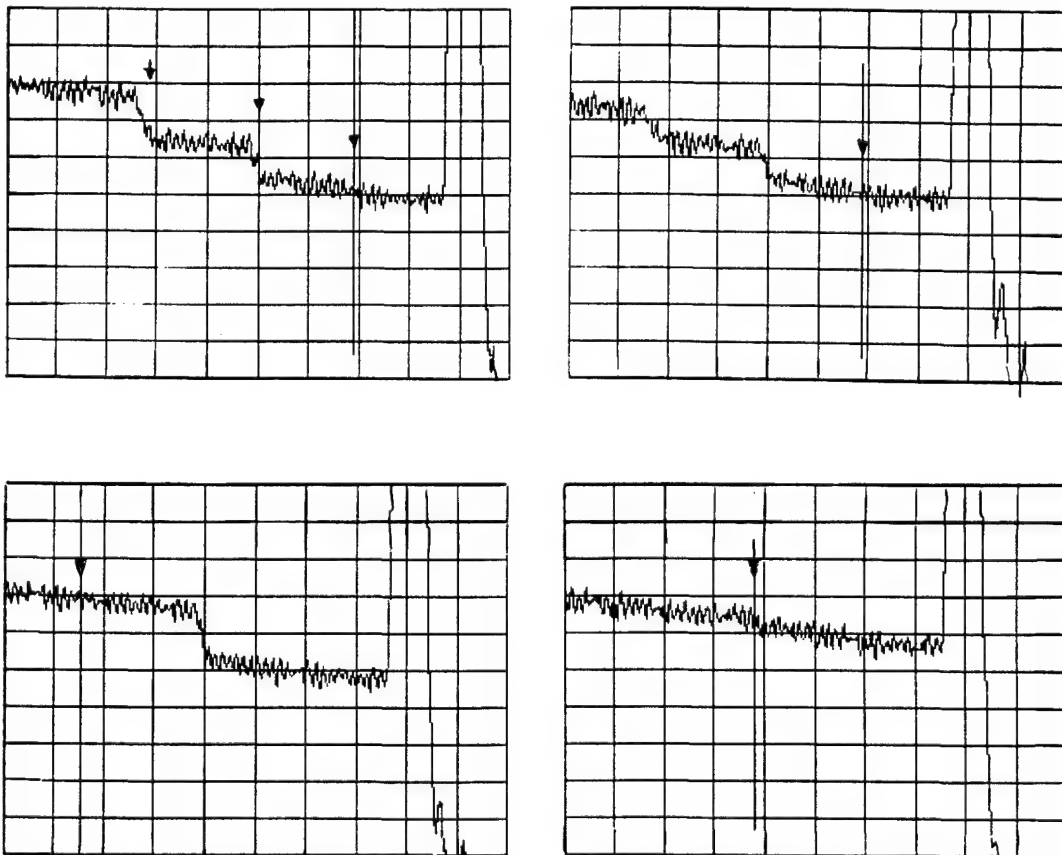
Figure 4: a) (top left) OTDR output from the corrosion monitors at day 1, the location of each monitor along the cable is indicated by an arrow. b) (top right) Break of fuse No.3 at 66 days. c) (bottom left) Break of fuse No.1 at 73 days. d) (bottom right) Break of fuse No.2 at 76 days.

115

The 7.6 mils/year rate is similar to a corrosion rate which would be expected for a moderate to severe marine environment [10]. This correlation of corrosion within the environmental chamber to corrosion in a marine environment can only loosely be made, however, due to the introduction of mild acid to the environmental chamber midway through the experiment. The acid lowered the ambient pH of the fuse surface, thereby accelerating the rate of corrosion.

CONCLUSION

The fuse/fiber monitor accurately detected the occurrence of corrosion in the environmental chamber. The average rate of 7.6 mils/year corrosion was determined by assuming a uniform loss from each side of the fuse. This average rate of corrosion provides a measure of the relative corrosivity within the environmental chamber. Additional testing will take place in order to correlate the fuse corrosion rate with specific environments, such as tropical marine or acid rain.

Further refinements will be made to the fuse/fiber/OTDR system. Monitor improvements will primarily occur in the operation of the fuse/fiber release mechanism and in the substitution of plastic for metal parts. Additional research will also focus on improving the fiber/OTDR response and determining the operational limits, such as the maximum number of fuses that can be attached to a fiber. The overall objective in making these changes is to improve detection performance, reduce manufacturing cost, and create a corrosion monitor that has practical application in the field.

ACKNOWLEDGMENTS

REFERENCES

1. "Status of the Nations Highways, Bridges and Transits", Report of the Secretary of Transportation to the United States Congress (103-2), March 1993, pg. 181.

2. Kayser, J. and Nowak, A. "Capacity Loss Due to Corrosion in Steel Girder Bridges", American Society of Civil Engineers Journal of Structural Engineering, Vol. 115, No. 6, 1989, pp. 1525-1537.

3. Schneider, J. "Concepts and Procedures in Assessing Existing Structures", Proceedings of the Symposium on Risk Analysis, University of Michigan, August 1995, pp. 203-212.

4. "Guideline for Structural Condition Assessment of Existing Buildings", ASCE 11-90, American Society of Civil Engineers, 1991, pp. 18-28.

5. "Standard Practice for Conducting Atmospheric Corrosion Tests on Metals", ASTM Standard G50-76, American Society for Testing and Materials.

6. Uhlig, H.H. and Revie, R.W. "Corrosion and Corrosion Control", Third Ed., J. Wiley, 1985, pp. 35-45.

7. Bennet,K.D. and McLaughlin, L.R. "Monitoring of Corrosion in Steel Structures Using Optical Fiber Sensors", <u>Proceedings</u> of the SPIE 1995 North American Conference on Smart Structures and Materials, February 1995.

8. "<u>Standard Practice for Testing Water Resistance of Coatings in 100% Relative Humidity</u>", ASTM Standard D2247-87, American Society for Testing and Materials.

9. Snyder, A.W. and Love, J.D., "<u>Optical Waveguide Theory</u>", Chapman and Hall, New York, 1983, pp. 8-9.

10. "<u>Metal Handbook Volume 13 Corrosion</u>", Ninth Ed., American Society of Metals, 1987, pg. 532.

MASS LOADING IN BACK-TO-BACK REFERENCE ACCELEROMETERS

Robert D. Sill
ENDEVCO Corporation
San Juan Capistrano, California

Abstract

Mass loading on Back-to-Back Reference accelerometers can be a significant source of uncertainty in comparison calibrations. Modeling the effect of the mass of the unit-under-test on case resonance of the Reference accelerometer allows correction of these "relative motion" errors and reduction of uncertainty. Theory is given of mass loading on Reference accelerometers in general, and data is presented for the particular case of an integral transducer in a beryllium high frequency shaker.

Introduction

This paper will discuss mass loading and other frequency-dependent characteristics of Back-to-Back Reference Accelerometers. If ignored, they can cause significant errors and uncertainties in comparison calibrations. Errors and uncertainties can be minimized with proper understanding and correction. An example of correction of these effects is the use of the published mass loading correction curves of ENDEVCO® comparison standards. These curves assist in correcting for Reference accelerometer frequency response, as well as the less-well-understood mass loading effect. In this paper, data and theory are given behind the curves, and a description of how the data was obtained. Formulae for the correction curves are given, as they are applied in ENDEVCO's Automated Accelerometer Calibration System.

Background

Comparison calibrations require that the motion applied to a Unit Under Test (UUT) be measured faithfully by a Reference accelerometer. Using the Reference output to determine input acceleration, the calculation of the UUT sensitivity is simply the UUT output divided by that acceleration level. In the simplest calculation, the Reference is assumed to have a fixed value of sensitivity, and both transducers are assumed to be experiencing the same acceleration.

At least two effects invalidate these assumptions, and are the topics of this paper. The first is the frequency response of the Reference itself. Of course, the Reference sensitivity is not a single value but is a function of frequency, typically increasing as the frequency approaches the resonance of the sensor assembly inside the Reference. The second is that there is flexibility in the structure between the transducers, allowing what is called "relative motion".

To ignore this flexibility implies belief that the structure between the transducers is infinitely stiff: that it does not deflect when transmitting the force required to accelerate the UUT. If this were so, the motions of the two transducers on each end would be identical. In reality any force on any structure will cause a deflection. The structure between the UUT and the Reference sensor responds to the

118

forces by deflecting, therefore the motion at the UUT will not be the same as measured by the Reference. One moves "relative" to the other. There will be a difference in both phase and amplitude of their motions.

Usually the difference in motion is negligible, but particularly at high frequencies and/or with large values of UUT mass, it can be significant. In such conditions the forcing frequency may be near an undamped resonance of the structure. Deflections and calibration errors can become large.*

In the example of the Model 2270 Primary Comparison Standard, the structure is the upper part of the Case of the Reference accelerometer. Similarly, in the Model 2270M7A, built into the beryllium armature of the Model 2901 High Frequency Shaker, the structure is the material which physically connects the two accelerometers. These examples are depicted in simplified form in Figure 1.
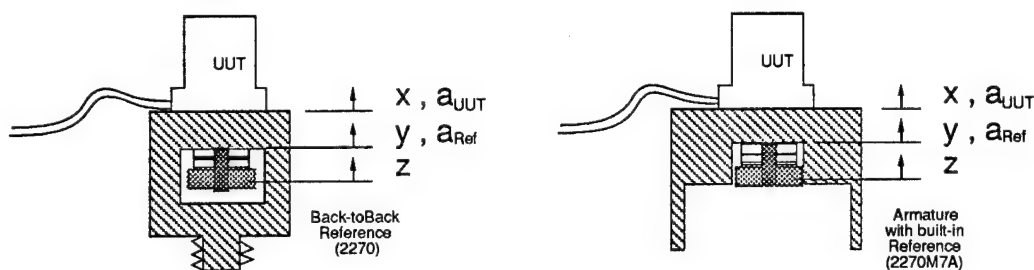
Figure 1. Two types of Back-to-Back Reference accelerometers. The "piggyback" style Endevco 2270 is depicted on the left, and the shaker armature with built-in 2270M7A is on the right.

Resonances in the structure between UUT and Reference will be referred to as the "Case resonance". For this discussion, the structure will be modeled as a one dimensional spring between the accelerometers, with the Case resonance being the natural frequency of the spring. (A lumped parameter diagram is shown in Figure 2.) This resonance is determined by its stiffness and its distributed mass. Note that this is the resonance without the additional mass of the UUT.

---

* No discussion will be made of differences in *direction* of the motion, such as if rotations are involved in the relative motion. Only single-axis motion will be assumed, along the line between the transducers. In addition, the discussion will be limited to UUTs below their resonance frequencies, and mounted directly to a Back-to-Back Reference. Any fixtures mounted between the accelerometers or any large-amplitude resonances of the UUT in the frequency band of interest will invalidate the correction models described in this paper. The theory can be applied generally, however any correction values would need to take into account fixture mass and stiffness and the mechanical impedance of the UUT.

mass of UUT **M**
Effective mass of case between Ref and UUT
Stiffness of case between Ref and UUT — **k**
Armature (Ref mounting surface)
Ref seismic mass

x, a_{UUT}
y, a_{Ref}
z
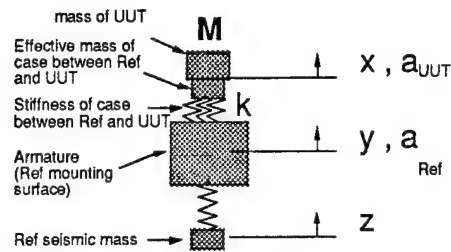
Figure 2. Lumped parameter model of Back-to-Back accelerometers. See text for definitions.

As shown in Figure 2, the motion x is at the UUT mounting surface, and is the motion which defines UUT sensitivity. The motion y is what is measured by the Reference. Z is the motion of the inertial mass of the Reference. The UUT is shown as a lumped mass as if its effect on the system were modeled with only the value of its mass, M. In fact the inertial mass and the stiffness elements in the UUT will cause the force required to drive the UUT to vary with frequency and complicate the mass loading discussion that follows. These effects will be ignored for frequencies below such resonances, since variations will occur only near UUT resonances, at which presumably the accuracy of mass loading corrections are less important.

Theory

Referring to Figure 2, the displacement of the base of the UUT is given by the value x, and the acceleration is given by its second derivative $\ddot{x}$. This is the motion which the UUT senses. Output is the product of that acceleration, the sensitivity, and any gain introduced by signal conditioning, according to

$$UUTOutput = \ddot{x}\ UUTSens(\omega)\ UUTGain(\omega)$$

In this expression the sensitivity and gain can vary with frequency ω.

To determine the UUT sensitivity, once the output is measured accurately and the gain (and frequency response) of the signal conditioning is known, only the acceleration remains to be found. In comparison calibration, of course, that is the purpose of the Reference transducer. Referring again to Figure 2, its output is related to input by

$$RefOutput = \ddot{y}\ RefSens(\omega)\ RefGain(\omega)$$

Note that its sensitivity too can vary with frequency. We will model the response as an undamped single degree of freedom system, given by

$$RefSens(\omega) = \frac{RefSens_o}{\left(1 - \left(\frac{\omega}{\omega_n}\right)^2\right)}$$

At frequencies low compared to the natural frequency of the Reference, ω_n, the sensitivity is very close in value to $RefSens_o$. As frequency

120

approaches the resonance, the value of the denominator becomes smaller and sensitivity increases in the classic amplification curve.**

One of the most important points of this paper is that the acceleration measured by the Reference is $\ddot{y}$, not $\ddot{x}$. Therefore, what is needed is a relationship to determine from y the motion of x , described below.

As mentioned above, the Case will be considered to be a spring with distributed mass. The distributed mass can be modeled as a lumped mass at the end of the spring (which in a simple linear model has an effective mass equal to one third of the total)[1]. The mass of the UUT is added to the effective mass, and its motion relates to the stiffness k of the Case according to the relation

$$(M_{eff} + M)\, \ddot{x} = k\,(y - x)$$

Leaving the details to the engineering textbooks (using the Laplace transform, which effectively substitutes $\ddot{x}$ with $-\omega^2 X$ by assuming the solution to be the complex periodic $x = X\, e^{-j\omega t}$), this expression can be solved and rearranged to get the transmissibility of the Case

$$\frac{x}{y} = \frac{k}{k - (M_{eff} + M)(\omega)^2}$$

The ramifications of this expression will be easier to see after a few more substitutions are made. Consider that the unloaded Case resonance (that is, the resonance frequency of the Case with no UUT) is defined by

$$\frac{k}{M_{eff}} = \omega_o^2$$

determined by the effective mass and stiffness of the Case. A further substitution is made with a mass loading ratio

$$\mu = \frac{M + M_{eff}}{M_{eff}} \qquad\qquad \text{(Eq. 1)}$$

which represents the multiplier by which the Case is loaded with the mass of the UUT. Making these substitutions gives

----

** The fact that a Reference is not ideally flat should not be a detriment to calibration accuracy. If it is stable (that is, if the resonance frequency does not change) this curvature is simply a fixed characteristic that can be part of the overall calculation of the UUT sensitivity. Generally the actual sensitivity variations of the Reference are measured by techniques traceable to absolute standards. For those frequencies above which there are no traceable sensitivity data, we can use the model above. Regarding traceability, unlike the described mass loading corrections, compensating resonance response of Reference transducers generally is useful in frequency ranges which are too high to be traceable. Is the reduction of uncertainty by such methods moot because the measurement is not strictly traceable? An important function of a calibration system is in the characterization of transducer performance, such as the resonance search. To include corrections for well-behaved characteristics, such as a resonance rise of the Reference transducer, simply makes good engineering sense.

$$y = x\left(1 - \mu\left(\frac{\omega}{\omega_o}\right)^2\right)$$

This is the desired relationship between motion at the UUT and the Reference. As with the expression for the behavior of the Reference frequency response, at very low values of frequency, the two motions are very nearly the same, and at frequencies approaching the modified Case resonance (altered by the added mass) the motions differ. The motion at the Reference sensor may be very much smaller than that out on the end of the resonating spring, which is the Case with the UUT attached.

Finally, combining all the formulae gives Equation 2, in which UUT sensitivity is equal to the ratios of the outputs and the gains multiplied by the Reference accelerometer sensitivity and a correction factor. Provided the frequencies are low enough, each of the frequency dependent terms in the correction factor will have a value less than one. In the numerator (on top) is the correction due to the Case resonance and mass loading; in the denominator is the effect of the natural frequency of the Reference[***] .

$$UUTSens = \frac{UUTOutput}{RefOutput}\ \frac{RefGain}{UUTGain}\ RefSens_o\ \frac{\left(1 - \mu\left(\frac{\omega}{\omega_o}\right)^2\right)}{\left(1 - \left(\frac{\omega}{\omega_n}\right)^2\right)} \qquad \textbf{(Eq. 2)}$$

Having a value less than one, the upper term corrects the value of calculated sensitivity downward. This counteracts the effect of the relative motion, which is to inflate the UUT output by creating motion larger than is measured by the Reference. The larger motion is the result of the resonant amplification due to the Case resonance. Larger UUT mass increases the need for correction, since larger UUT mass (larger μ) lowers the Case resonance. At a particular frequency, the motion of the heavier UUT would be farther up the amplification curve, requiring smaller absolute value of the correction term.

The Reference correction term also has a value less than one, but this time effects an increase in sensitivity because it is in the denominator. Since the actual Reference output becomes larger due to its crystal resonance ω_n, (that is, motion at z is larger than at y) if uncorrected it would result in a calculated sensitivity that is too small. The term corrects for this inflated Reference output.

The contributions of these two competing terms are depicted in Figure 3. A qualitative summary of the effects is listed in Table I.

[***] As mentioned in the previous footnote, this term would be replaced by the actual Reference frequency response measurements at those frequencies traceable to absolute standards.
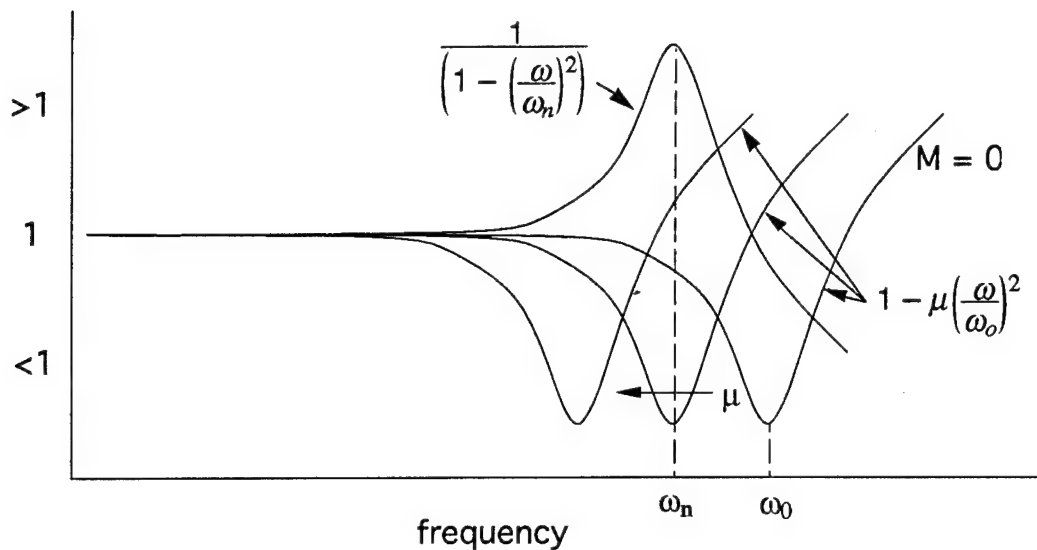
Figure 3. Frequency response contributions of the terms of the correction equation. The upper curve shows the effect of the Reference transducer resonance, peaking at ω_n. The three curves below show the effect of increasing UUT mass. The unloaded curve is on the right (M=0), and the curves with increased UUT mass to the left. The combined effect is the product of the top curve with the appropriate lower curve.

Note in the curves that there are conditions in which the competing effects of sensor resonances and mass loading might cancel, suggesting that Back-to-Back Reference accelerometers could be designed to have a Case resonance with a typical UUT which is matched to counteract the crystal resonance. However, as will be seen in the data below, the required Case mass would be substantial, reducing the drive capability of the shaker by a significant factor. Also, this would only work for a narrow range of UUT mass. It is thought to be better for the sake of overall uncertainty to keep the size of the correction to a minimum, considering the uncertainty of the correction itself is not insignificant.

Table I.
Effects of Resonance and Transmissibility on Correction Factor

Condition	Reference Resonance Effect Ref output will be:	Trans-missibility Effect UUT output will be:	Apparent (Uncorrected) UUT Sens UUTOut/ RefOut	Correction Factor multiply by Apparent Sens
low freq, low mass	negligibly increased	negligibly increased´	correct as is	=1 (no correction)
low freq, high mass	negligibly increased	moderately increased	slightly high	less than 1
med freq, low mass	slightly increased	negligible	slightly low	greater than 1
med freq, high mass	slightly increased	slight amplification	slightly high	effects tend to cancel
high freq, low mass	significantly increased	negligibly increased	significantly decreased	can be much greater than 1
high freq, high mass	significantly increased	significantly increased	will have large uncertainties	use for trend only

Data

Three sets of tests were performed, on one Endevco 2901 High Frequency Standard-Shaker and two 2270M15 accelerometers. The 'M15 is a back-to-back transducer with a 1.8 inch (46 mm) diameter solid beryllium case, structurally similar to the 2901 armature, with a sensor assembly identical to the 2270M7A inside the shaker. Each test used a miniature 2250AM1 transducer adhesively mounted to a beryllium stud in the UUT position. Prior to the test, it was characterized with transient techniques to have a resonance frequency of approximately 80 kHz, with no detectable minor resonances.

To simulate mass loading effects, rings were mounted around the UUT using #8 screws in a triangular hole pattern, as depicted in Figure 4. All rings had an inner diameter of 0.45" (11.4 mm) to accommodate the miniature UUT. Outer diameters of the rings ranged from 1.25" to 2" (32 to 50 mm), with thicknesses from 0.25" to 0.375" (6 to 9.5 mm), and all were made of a tungsten material (except the lightest one, made of aluminum). The intent of the rings was to allow the mounting of different masses to the shaker without having to dismount the UUT. Since the 2250AM1 was mounted only once per set of tests, base strain, transmissibility of the adhesive, and other characteristics pertaining to mounting were eliminated as sources of uncertainty.
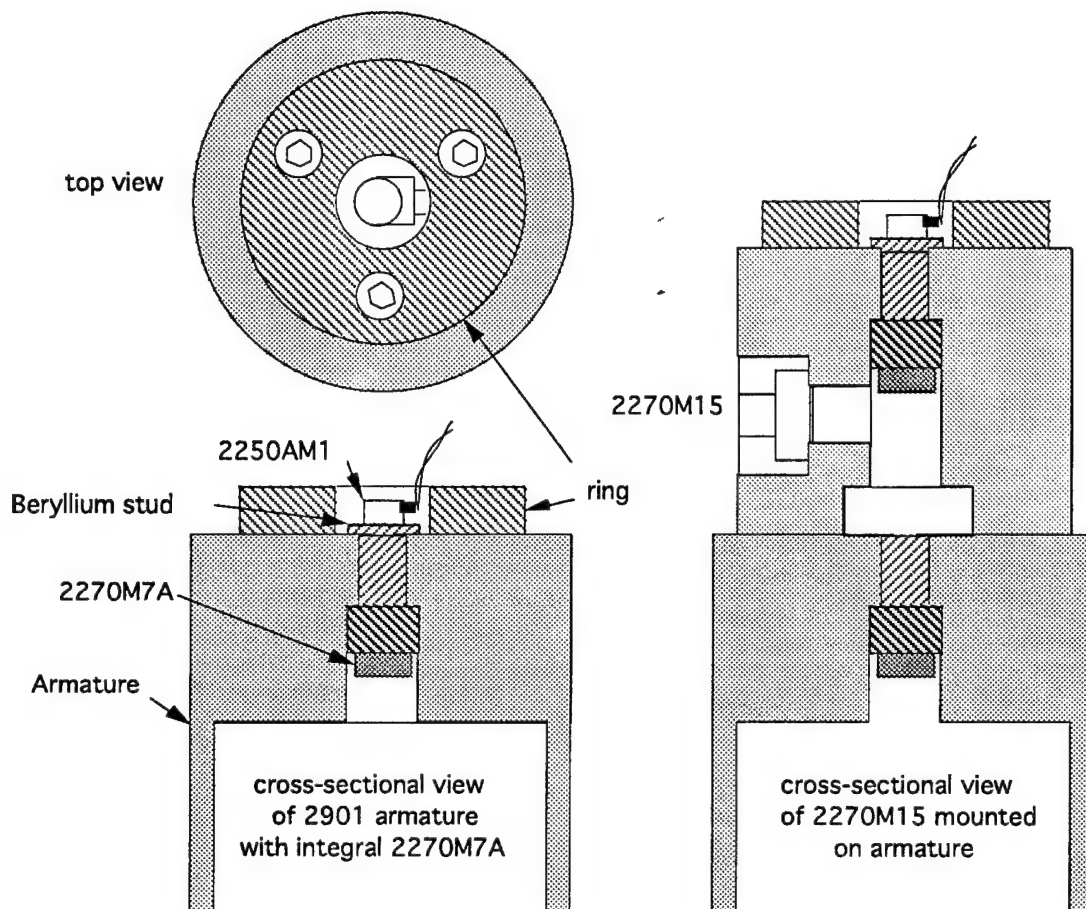
Figure 4. Configuration of the tests. The 2250AM1 was adhesively mounted to a beryllium stud and remained untouched throughout each set of tests. Rings of different mass were bolted to the armature or the 2270M15 to simulate different masses of UUT. When testing the 2270M15, the transducer in the shaker was not used.

Using the output of the 2250AM1 as the Reference, and correcting for its resonance rise using the classic single-degree-of-freedom equation, frequency response plots were generated for each attached mass. The data on one of the tests is given in Figure 5. As seen in the data, deviations of the curves below approximately 20 kHz is generally well below 1%. At 20 kHz and above, particularly if simulated UUT mass was greater than 100 grams, deviations appear to be on the order of 1/2 of the correction values. At least some of the variability, also apparent in the other two sets of data, may be due to minor connector resonances in the 2270 series transducers.

It should be noted that the data indicates strain sensitivity of the transducers was not a factor. The deviations at low frequency were essentially zero for all applied masses. A discussion of strain sensitivity is given in Reference [2].

125
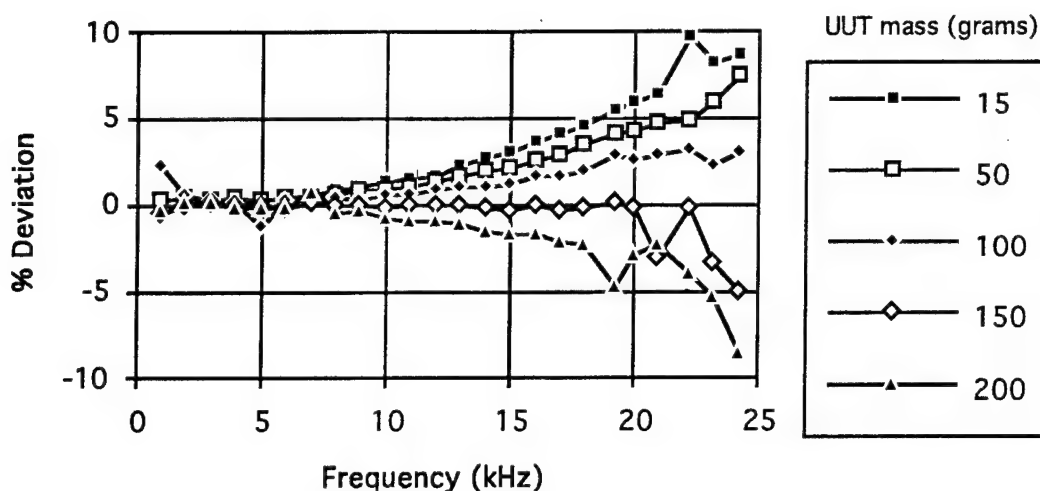
Figure 5. Sensitivity deviations of the 2270M7A Accelerometer. Data plotted in this figure are the sensitivity deviations of the Back-to-Back standard for different simulated masses, compared to an Endevco 2250AM1 transducer in the UUT position as the Reference. The adhesively-mounted miniature transducer was not removed between tests as masses were changed.

Figure 6 below includes the curves generated to fit the data of Figure 5, by choosing values of Crystal resonance, Case resonance, and effective mass of the Case.
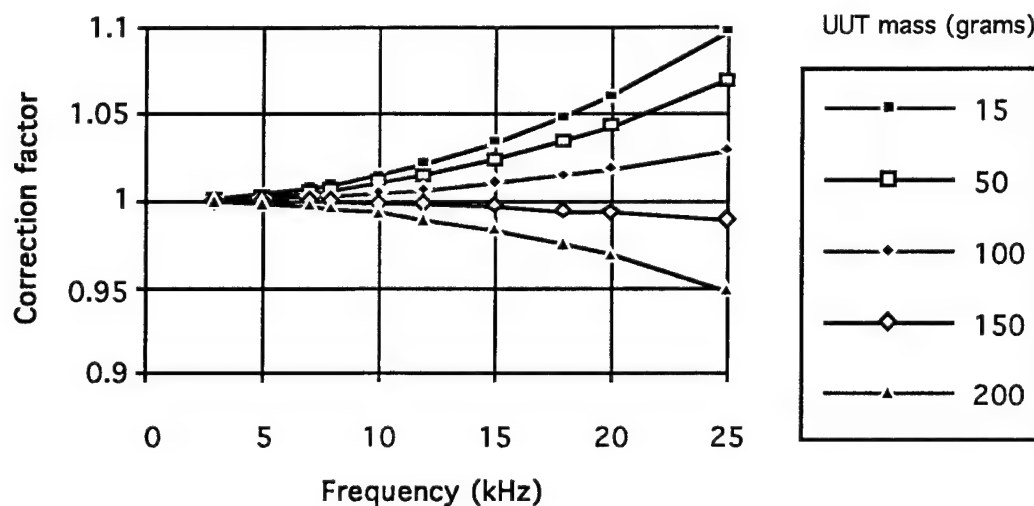
Figure 6. Calculated correction curves for the 2270M7A and 2270M15 accelerometers. Values of Effective Mass, Case Resonance, and Crystal resonance which provided the best fit using **Eq.** 1 and **Eq.** 2 are found in Table II.

For comparison, a copy of the published correction curves from the 2270M15 Performance Specification is shown in Figure 7.
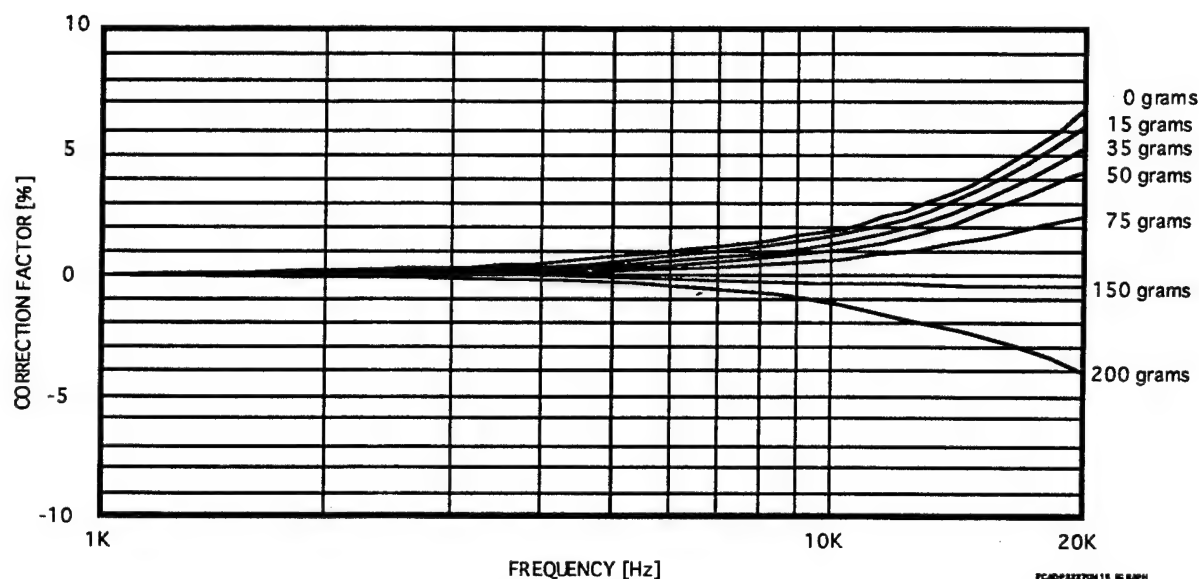
Figure 7. Published correction curves for the 2270M7A and 2270M15 accelerometers. These curves are found in the Performance Specificatons for these Back-to-Back Reference accelerometers. The user of these accelerometers would multiply the frequency response results of a UUT by the appropriate curve to get a response corrected for the UUT mass.

Justification or rationalization comes from the physically reasonable values used in the calculated curve, based on characteristics and dimensions of the structures. However, recent data have not been taken to confirm the published 2270 correction factors. (The data for the 2270 curves simulated with these coefficients predate the author.)

Table II.
Parameters for calculatation of correction factors.

Reference Transducer	Effective Mass (grams)	Case Resonance (kHz)	Crystal Resonance (kHz)
2270	6	130	50
2270M7A (or 2270M15)	6	380	78

Note that because the effective mass of the Case of the Reference is low, even lightweight UUTs can significantly change the loaded Case resonance. Only when the unloaded Case resonance is much higher than the UUT usable frequency range is this effect small. Note also the significant difference between the 130 kHz Case resonance of the steel case of the 2270 and the 380 kHz for the beryllium Case of the 2270M7A and 2270M15. This extraordinary value is reasonable, considering the fact that the speed of sound in beryllium (equal to the square root of the ratio of Young's modulus to density) is nearly 2.5 times as large as that of steel. (Beryllium is 40% stiffer but more than 4 x lighter than steel.) At nearly 500,000 in/sec (12,500 m/sec), a wave could travel between the Reference sensor and the UUT (across a distance of approximately 0.6 inch or 1.5 cm) approximately 500,000 / (2 x 0.6) or 417,000 times per second. This remarkable stiffness and velocity explains why such an exotic material is used.

Conclusions

Mass loading effects on Back-to-Back Reference accelerometers can follow predictable and physically reasonable patterns. They can be modeled, and therefore corrected, knowing the total mass of the UUT and the values of the Case resonance and the effective mass of the Reference. This technique can be used to reduce calibration uncertainty when using Back-to-Back Reference accelerometers. Whereas uncertainty estimates in the past were made unnecessarily large to swallow the relative motion effect of a range of UUT masses and frequencies, (or the estimates were subject to limits to UUT mass and frequency), use of the equations and modeling parameters described in this paper can reduce the size of the contribution of mass loading effects on overall uncertainty.

Future work is planned, using laser interferometric techniques to monitor motion at the UUT mounting surface with an absolute method, again using simulated UUT masses. The intent is to reduce the uncertainty of the correction, and provide more direct traceability.

References

1.   Thomson, W. T., "Theory of Vibration with Applications", Prentice-Hall, Inc., New Jersey, 1972, p20.

2.   "Instruction Manual No. 101 for Piezoelectric Accelerometers", ENDEVCO.

Acknowledgments

NEW DYNAMIC PRESSURE GENERATOR AND ITS APPLICATION
        Benjamin Granath, PCB Piezotronics

                    ABSTRACT

A brief description of a simple hydraulic pressure
calibrator is given. Pressure to 10000 atmospheres can be
generated at frequencies useful for the calibration of
ballistic sensors. Application of the device is for precise
calibration of sensors and representative wave forms from
the device will be presented.

From BRL Memorandum Report #1843
Dynamic Calibration of Pressure Transducers at the Shock
Tube Facility, May 1967.
From communications from Sandia Laboratories in that year
we built at BRL a drop test calibrator that would generate
pressures up to 50000*psi.(photo)
Low viscosity silicone oil was the liquid that was
compressed.The oil changed viscosity with pressure and
almost became a solid. For those not familiar with the
drop tester.

A mass is constrained to move only up and down vertically.
It is dropped from a selected height and strikes a small
diameter piston coupled to a small chamber containing a
liquid. The liquid is slightly compressible at the high
pressures of concern. Pressure transducers are placed in
side ports to measure the pressure developed in the liquid
by impact of the mass and piston.

The mass strikes the piston which moves against the liquid
and compresses it generating a decelerating force.
When the downward velocity of the rod becomes zero the
pressure in the chamber is at a maximum, and the liquid is
at the peak of compression.

Many liquids experience phase changes in the range of
pressures that we wish to measure, water for example
freezes to ice at 20 deg C when compressed isothermally to
about 9 kb.

From the American Institute of Physics Handbook, tables
compiled By P Bridgeman can be found that give the
compression data of various liquids. Glycerin,an alcohol,
seems to be first choice for a high pressure medium. Sandia
Laboratories and AVL Inc. Transducer workshop Proceedings
May 1991.

Up to 1986, the pressures in the pressure-cells
were compared to transfer standards that could be traced
back to NIST dead weight testing devices. The AVL device
was the first that considered and indeed did calculate the
pressure from measured impact velocity. The last page of a
paper given by AV1 at the 1991 Workshop
was of most interest to me because it showed an
accelerometer on the mass. Mass*acceleration/area of piston
seemed to be the most direct way to determine pressure.
Volume of fluid,friction of piston,any other losses could
be corrected by a measure of the deceleration of the mass.

It also helps to have a simple mass and a ICP® Quartz Shear Impact Accelerometer.

The dynamic high pressure generator that we have developed at PCB, is portable, requires shop air to operate and has built in safety features. Eight quick disconnect air lines provide all the power needed. Pressures up to 10000 bars can be generated. A different range of pressures can be selected by simply changing the mass.

The accelerometer used on the mass is one of a control group that has been calibrated at frequent intervals against reference standards. All PCB ballistic sensors are calibrated using this device and a Harwood strain sensor. We are in the process of collecting data for a more detailed paper to be presented next year, but here are some of the preliminary data and waveforms.

References:

1. Stein, Peter K. Pyro- Shock,Impact and Other High Speed Transients: Some Thoughts On "TQM"-Total Quality Measurements,Lf/MSE Newsletter No 39,January 1993

2.Coulter George A. Dynamic Calibrations of Pressure Transducers at the BRL Shock Tube Facility, Memorandum Report 1843,May 1967

3.Riegebauer Joseph, Dynamic Pressure Calibrator AVL, Graz, Austria,Proceedings Workshop on the Measurement of Transient Pressure and Temperature April 1991

4. Youden W.J.,Experimentation and Measurement Nist Special Publication 672

5. C.O.Bennet and B.Vodar,Calibration of a Controlled Clearance Pressure Balance up to 8000 Bars,National Center of Scientific Research,Bellevue, France,1963

6. ICP is a registered trademark of PCB Piezotronics, Inc. Depew,N.Y.

BRL
PRESSURE
CALIBRATOR
1967

mass

frame

base

DYNAMIC PRESSURE GENERATOR

guide

mass

pressure cell

base

pneumatic lift & release
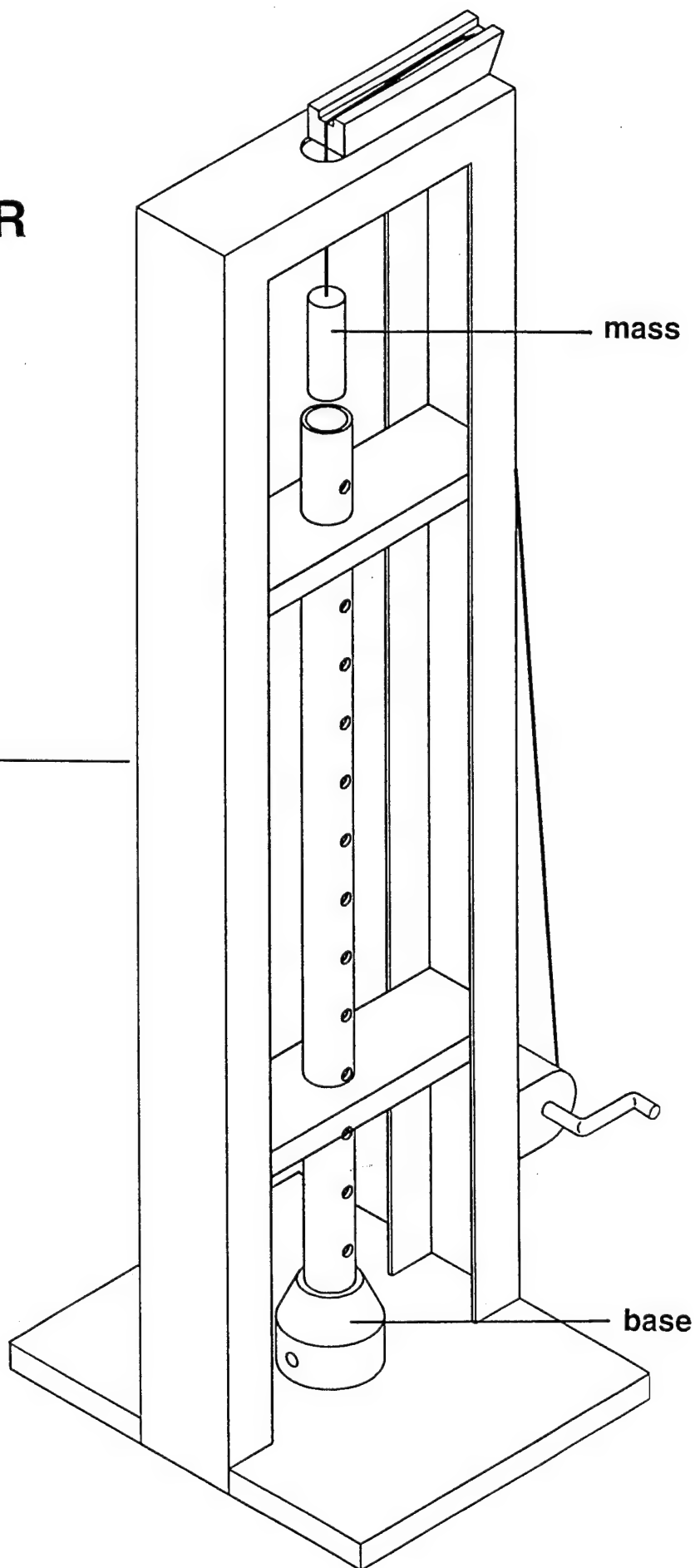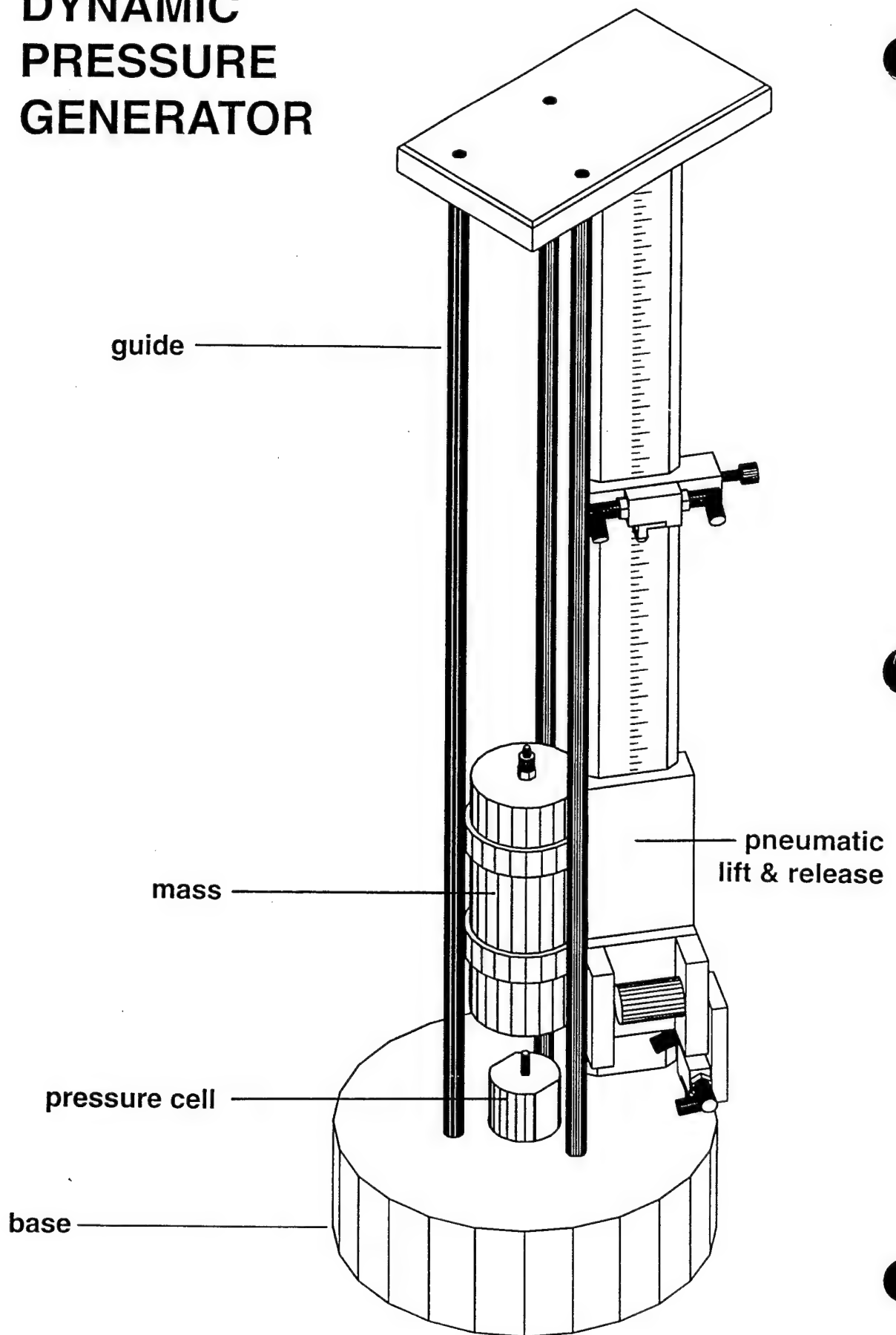
Cursor= Set2: Set 2, 1B   H2

Pnt#4487   6.526 @ 3.02mS

130,000 psi
(896E6 Pa)

133
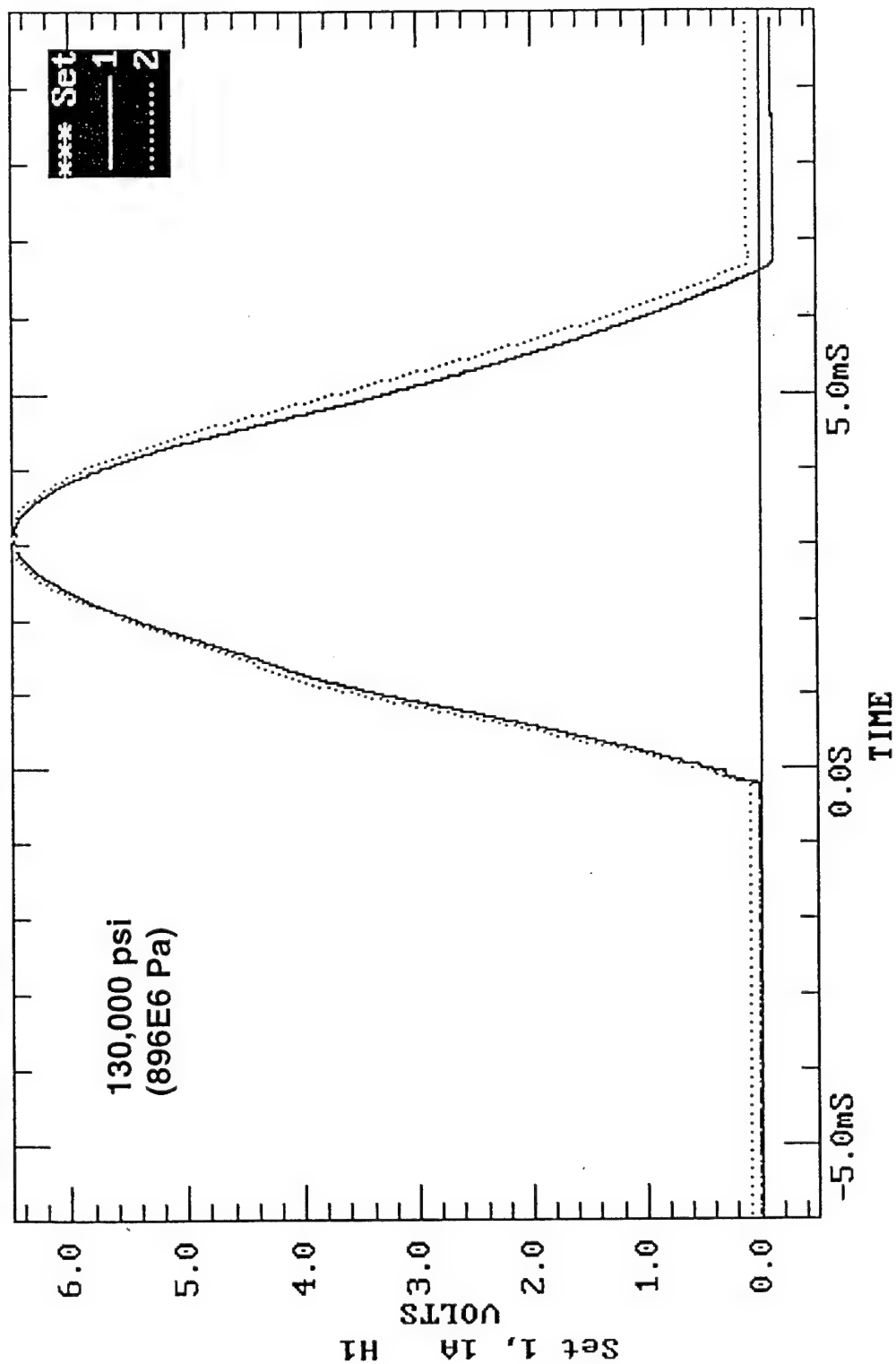
Cursor= Set1: Pressure from Droptester (psi)
Pnt#3463   1.1752E+4 @ 3.928mS
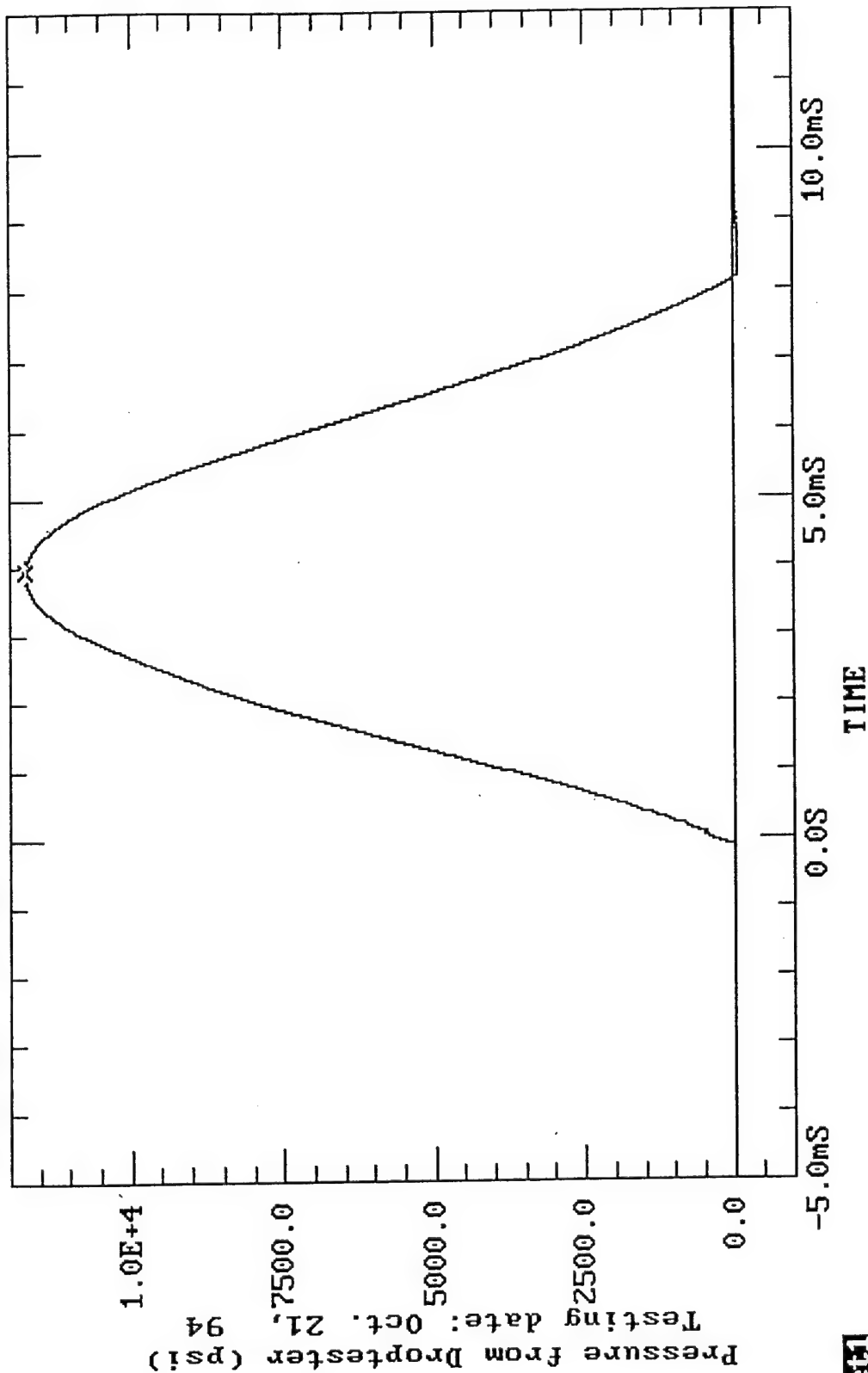
Pressure from Droptester (psi)
Testing date: Oct. 21, 94

Set1

134

Cursor= Set2: Set 2, 1B   H2
Pnt#3500   9.66 @ 2.615mS

96,600 psi
(666E6 Pa)

*** Set
1
2

TIME

Set 1, 1A   H1
VOLTS

10.0
7.5
5.0
2.5
0.0

-2.5mS   0.0S   2.5mS   5.0mS   7.5mS

Set2

135
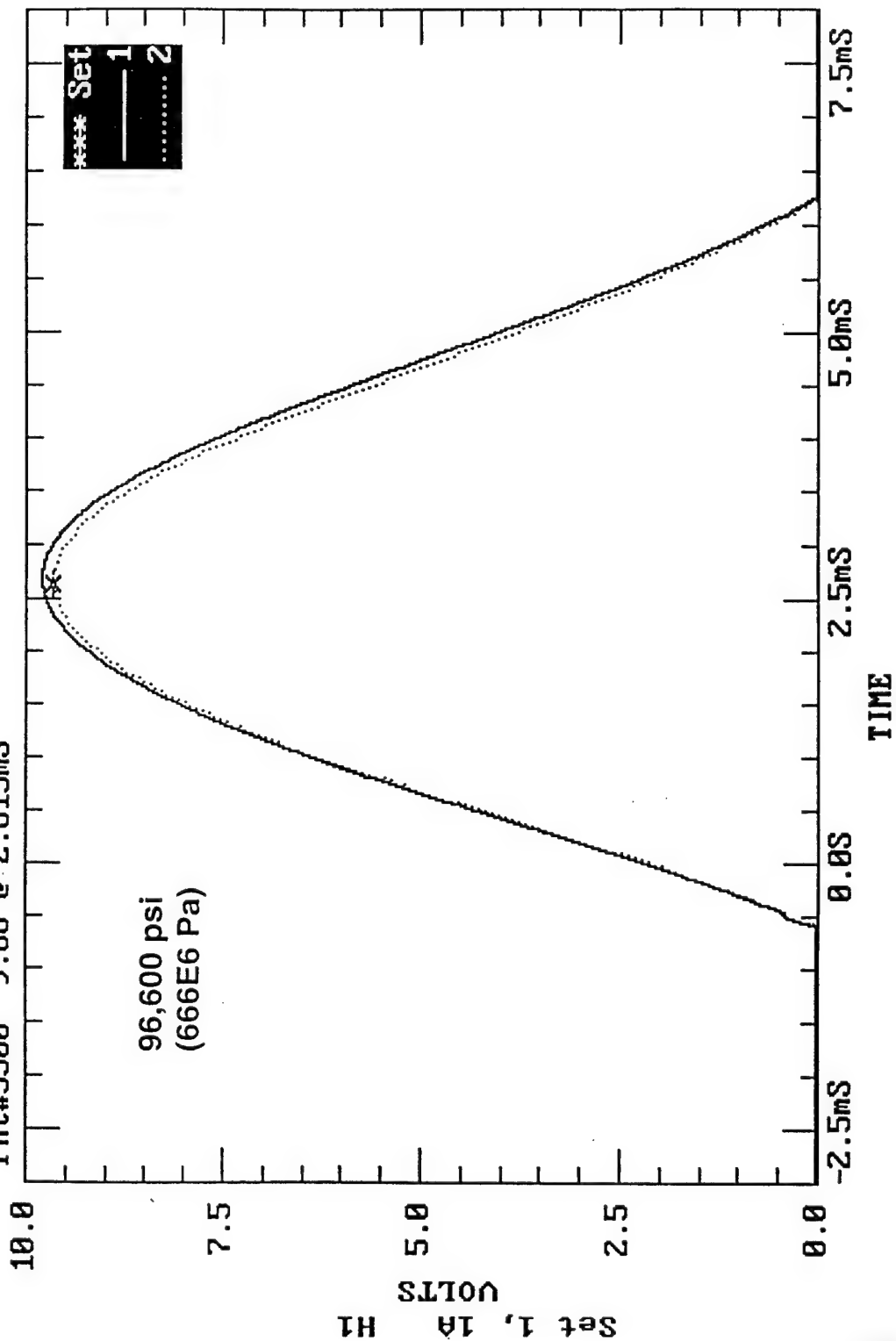
Cursor= Set2: Set 2, 1B   H2
Pnt#3450   5.85 @ 2.365mS

58,500 psi
(403E6 Pa)

Multiple Calibrations

-238.0 mS	79.36 mS	396.8 mS	714.2 mS	1.031 S
-238.0 mS	79.36 mS	396.8 mS	714.2 mS	1.031 S

7.092 V — 7.055 V

6.092 V — 6.055 V

5.092 V — 5.055 V

4.092 V — 4.055 V

3.092 V — 3.055 V

2.092 V — 2.055 V

1.092 V — 1.055 V

92.25 mV — 55.00 mV

-907.7 mV — -845.0 mV

137

Cursor= Set2: Set 2, 1B   H2
Pnt#3292 6.85595 @ 2.64mS

60,559 psi
(417E6 Pa)

*** Set
2
1

0.0S   5.0mS   10.0mS
TIME

6.0 5.0 4.0 3.0 2.0 1.0 0.0
VOLTS
Set 2, 1B   H2

Set2

138
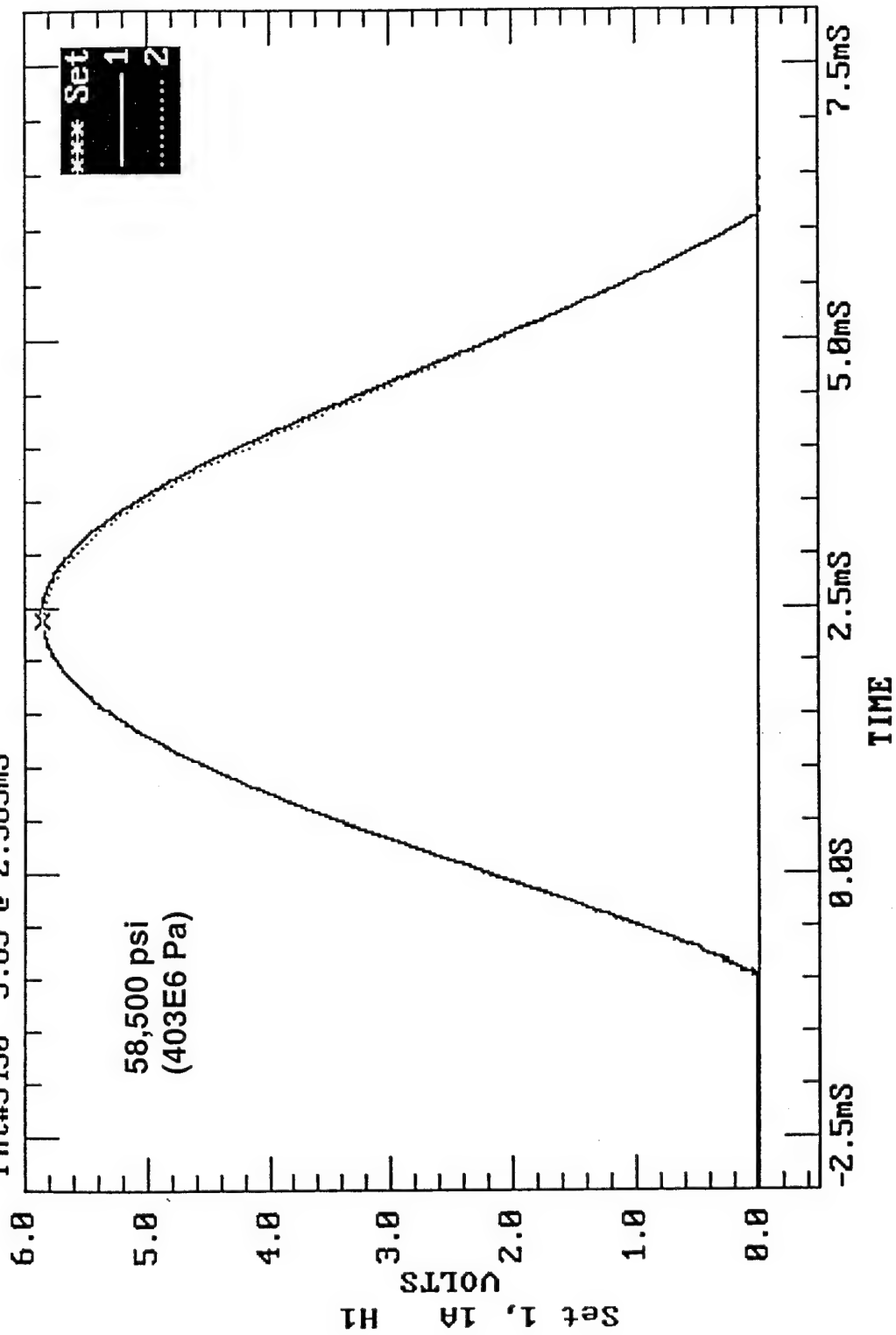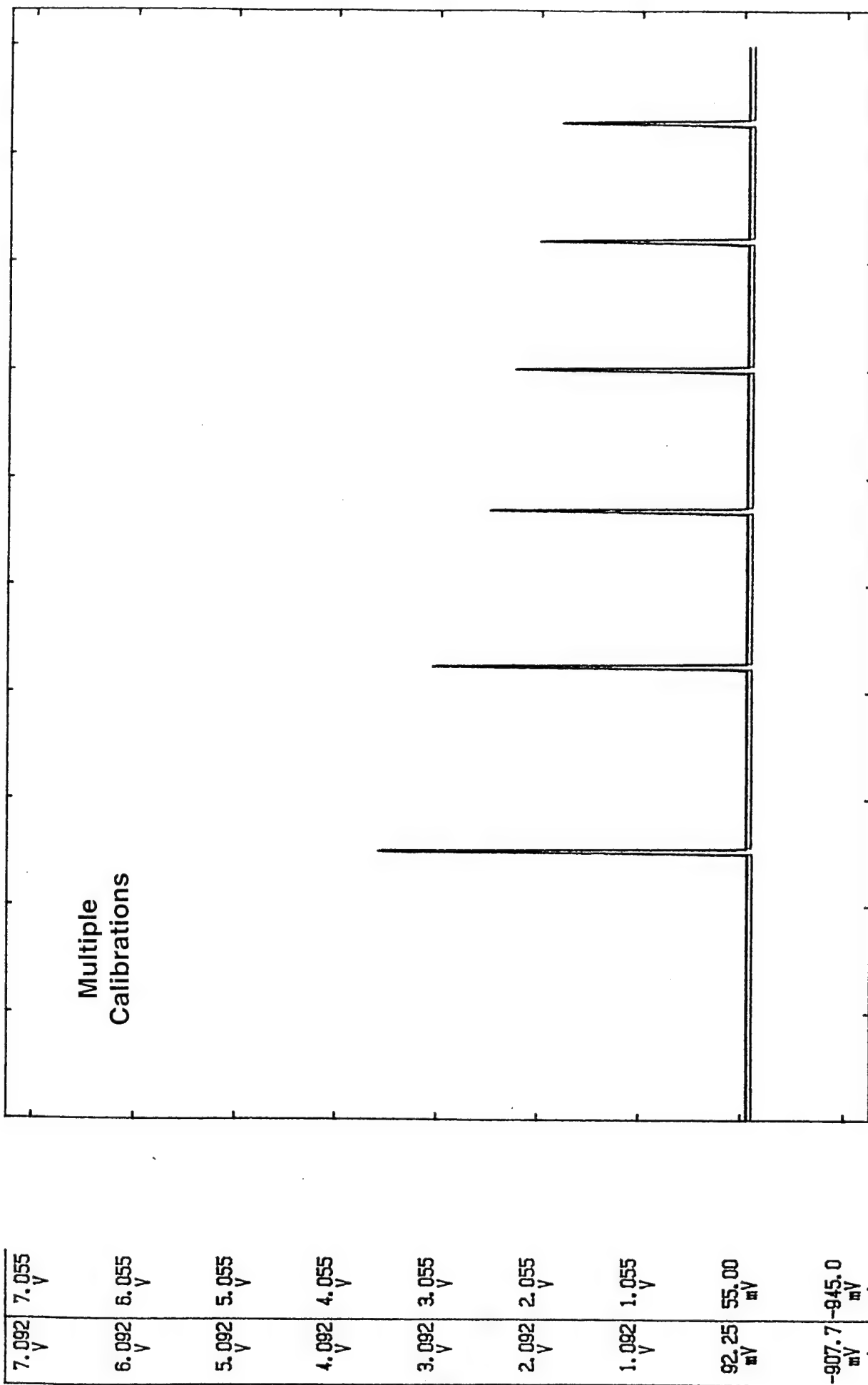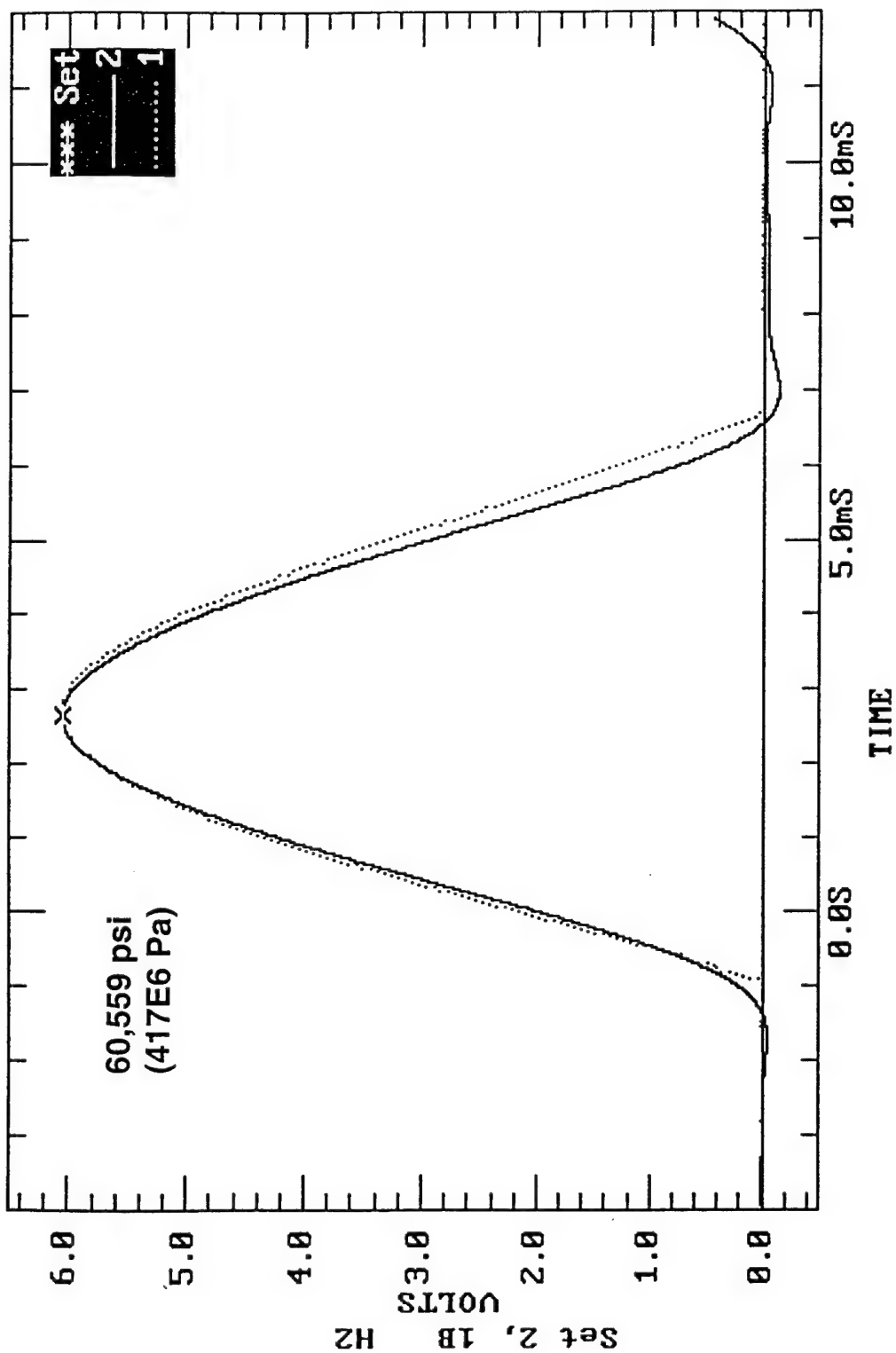
Cursor= Set1: Set 1, 1A   ALL
Pnt#7585   0.5525 @ 4.541mS

55.25 *g

FFT
of accelerometer
data
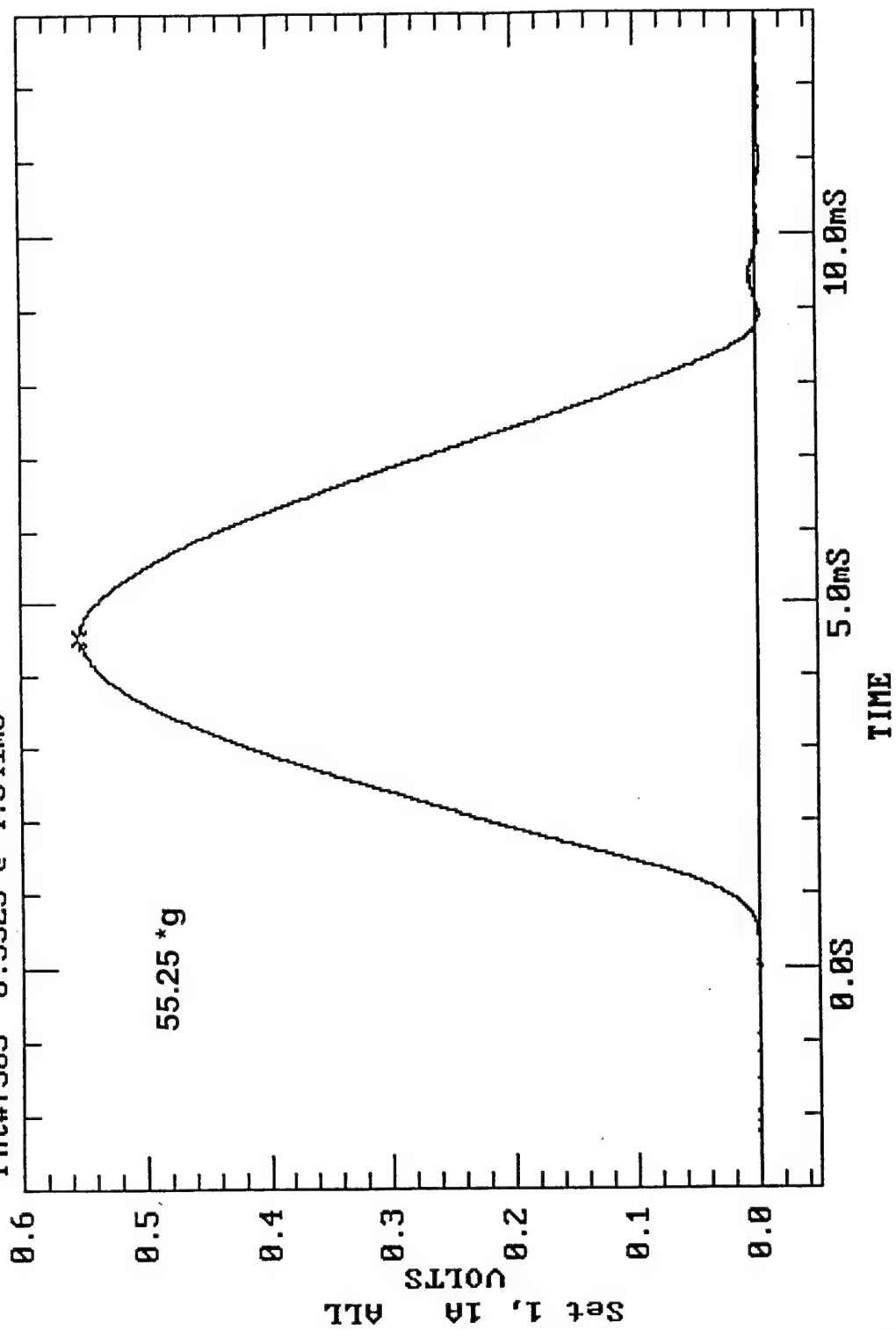
18Apr95 @ 15:18:53

Cursor= Set1: FFT of Set 2: VOLTS
Pnt#165 1.18352E-4 @ 10.00977kHZ

140
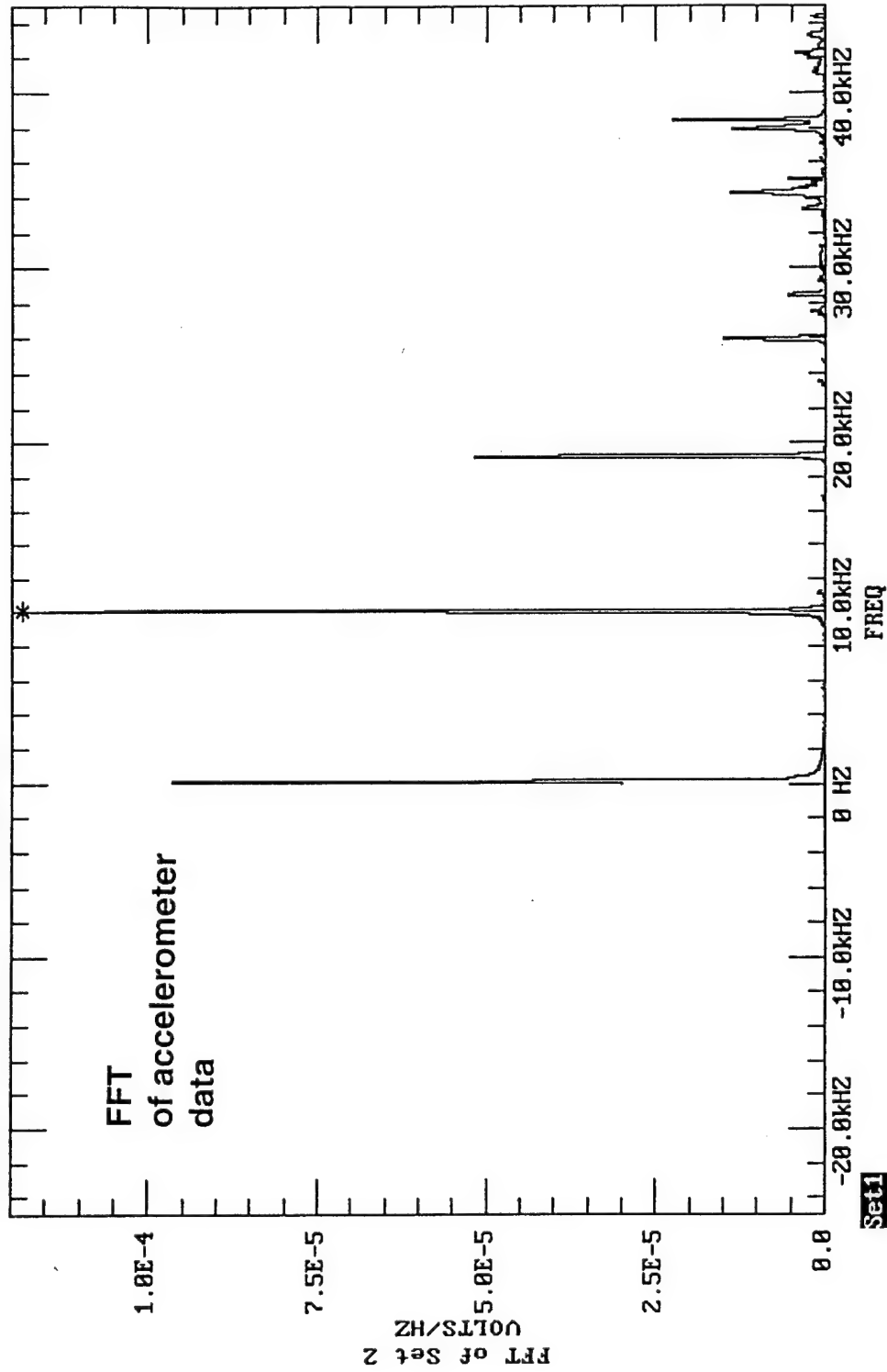
PRELIMINARY DATA

Trace # mdy (a-z)	Volt Out P Transducer	mv peak accel	peak g's	m x a area	pressure transducer	± % diff
3/8/95a	0.7915	62.54	58.94	66,046	66,513	(-).7
3/8/95b	0.7822	62.485	58.89	65,987	65,731	(+).4
3/8/95c	0.76698	60.9	57.39	64,313	64,454	(-).2
3/8/95d	0.75649	60.51	57.026	63,901	63,571	(+).5
3/8/95e	0.75623	60.52	57.035	63,911	63,546	(+).6
3/8/95f	0.742	59.45	56.027	62,781	62,353	(+).7
3/8/95g	0.72748	57.98	54.7	61,292	61,134	(+).3
3/10/95c	0.884	165.6	65.2	72,471	72,459	
3/10/95d	.89.65	168.7	69.21	73,827	73,483	(+).5
3/22/95a	10.0321	228.54	92.17	100,298	100,321	
3/24/95a	0.635	67.217	27.22	29,499	29,589	(-).3
3/24/95b	0.6385	67.897	27.499	29,797	29,753	(+).1

A MULTIFUNCTION HEAT FLUX TRANSDUCER: BALLISTIC TEST DATA

R.D. Ferguson, C.L. Goldey, E.Y. Lo,
and P.E. Nebolsine.
Physical Sciences Inc. Andover, MA   01810

J.G. Faller and W.S. Walton
U.S. Army Combat Systems Test Activity
Aberdeen Proving Ground, MD   21005-5059

ABSTRACT

We describe a heat flux transducer which detects and discriminates radiative and convective heat flux as well as pressure and temperature transients at its surface. This multifunction device has been developed primarily for the application of thermal hazard evaluation. The transducer sensing elements utilize piezoelectric films which are sensitive to both pressure and temperature changes. The electrical signals are processed to obtain incident heat flux with a thermal response time of order 10 ms, and a total accumulated heat flux capacity of over 100 J/cm^2. Ballistic range test results for prototype transducers are reported.

1.   INTRODUCTION

Heat flux gauges are used in many testing environments to characterize fires and to assess potential thermal hazards for humans.[1],[2] Typical gauges are thermocouple-based calorimeters. These conventional devices are generally limited to measurement of total incident thermal energy, are often difficult to calibrate, and are subject to some ambiguity in data interpretation. To address these issues, a new class of heat flux transducers has been developed under the sponsorship of the U.S. Army SBIR program which meet specified requirements. Transducer theory of operation, design, fabrication and data analysis method have been previously described[3] and will be only briefly summarized below.

The transducer is comprised of two layered piezo/ pyroelectric polarized polyvinylidine fluoride (PVDF) films on a copper heat sink which are embedded in, and protected by, polymer matrix. The difference in the thermal signatures of the films is a direct measure of the thermal gradient, and thus the heat flux. Because the films are below the protective surface, causing a delayed thermal response, these signals must be processed to yield the instantaneous flux at the transducer surface. Pressure signals are common to both films, so that they cancel when the film signals are subtracted to obtain thermal gradients. Once the thermal signal is known, however, the pressure signal can be extracted.

The generic prototype design is illustrated in vertical cross section in Figure 1. Films 1 and 2 are embedded in a plastic and are separated by a known thickness, d. Most electromagnetic noise is eliminated by shielding with the
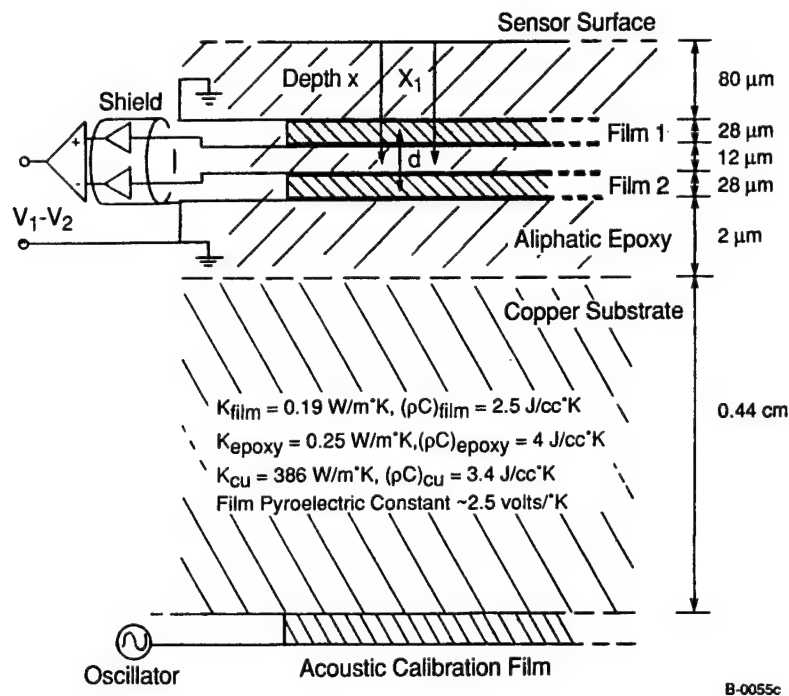
Figure 1. Simple schematic of the prototype transducer shown in vertical cross section. The voltage difference of the plane parallel film pair, measured with a differential amplifier, is proportional to the temperature difference between the films.

exterior ground plane configuration. The thermal response function, and therefore the response time, depends upon the depth of film pair. The depth x_1 at which the film pair is embedded is selected to provide the most rapid response time while assuring that the film temperature does not exceed its damage threshold at any time after the onset of heating. Survivability is determined by the film depth and the thermal diffusivity of the embedding material, the proximity and thermal conductivity of the substrate, and the maximum temperature that the PVDF films can withstand.

An important virtue of this design is the purely one-dimensional nature of the thermal problem, which lends itself to complete and computationally efficient analysis. The required multilayer thermal analysis consists of straightforward matrix manipulations to determine the (Fourier or Laplace) transformed flux and temperature histories at successive layer interfaces. This multilayer thermal analysis was programmed on a computer and used to compute response curves, verified by direct calibration, and for processing ballistic range data.

To fully characterize a thermal event, it is desirable to discriminate the surface-average radiative and convective components of the flux incident on the transducer surface. This is accomplished by dividing each sensor film into two interdigitated sensor patterns, one with an optically absorbing surface coating and the other with an optically broadband infrared/visible reflecting coating. These provide measurements of total incident flux and the purely convective component of heat flux, respectively. Therefore by subtracting these surface average values, the radiative component of heat flux is obtained. The film patterns are etched at PSI using standard photolithography techniques.

Miniaturized pre-amplifier circuits have been incorporated into the transducer package. The inexpensive sensing elements have been designed for easy replacement if damaged. An additional feature of this transducer is a self-contained acoustic calibration/monitoring of proper operation capability. Since the PVDF films are both piezo and pyro active, detection of an acoustic signal can be used

144

at any point prior to, or during, a test to ensure the proper operation.

The transducer specifications and features are listed below.

1. Precise measurements of time-integrated heat flux or fluence to at least 100 J/cm^2, and instantaneous heat flux (J/cm^2-s) within a bandwidth of 0.001 to 100 Hz with excellent noise rejection.

2. Sensor active area of several cm^2 for surface-average flux measurement or any desired area down to a few millimeters square, with no loss of response time.

3. Surface preparation and film designs which permit radiant and convective portions of the thermal signatures to be independently characterized.

4. Individual film signals proportional to local temperature changes versus time and containing the acoustic signature of the event.

5. Laboratory calibration of transducer response curves using pulsed CO_2 lasers.

6. Acoustic methods for remote field verification of operation and calibration.

7. A capability to survive fires subjecting the transducer to temperature and heat flux levels much greater than those associated with third-degree burns.

An exploded view of the prototype device is provided in Figure 2. Data analysis methods and some initial ballistic test data are described in the following sections.
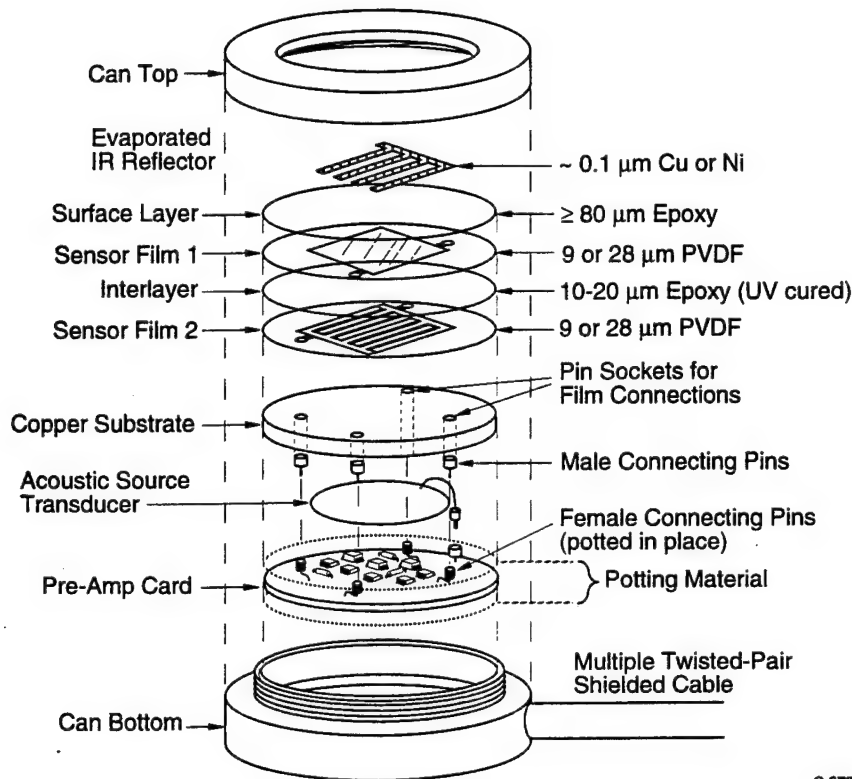
Figure 2. Exploded view of PSI heat flux transducer.

2. CALIBRATION

In preparation for ballistic range tests, calibrations were performed with a short pulse CO_2 laser. Comparisons were made between the calculated and measured temperature difference across the PVDF film pairs in the heat flux sensor at 1 J/cm^2 fluence for calibration. The 1 µs pulses are reasonable representations of a delta-function and are therefore expected to generate the theoretical response curve predicted by the multilayer analysis. This calibration was performed to check predicted against measured response. A typical response curve and its integral is shown in Figure 3a. After processing (digital filtering or deconvolution) with the multi-layer code, the expected bandwidth-limited representation of the delta-function laser pulse is obtained as shown in Figure 3b. This is purposely rolled off at a finite frequency to suppress noise, though the integral is invariant in any case. These curves have been scaled by the appropriate calibration constants to produce the known fluence of 1 J/cm^2 determined by conventional laser pulse calorimetry.
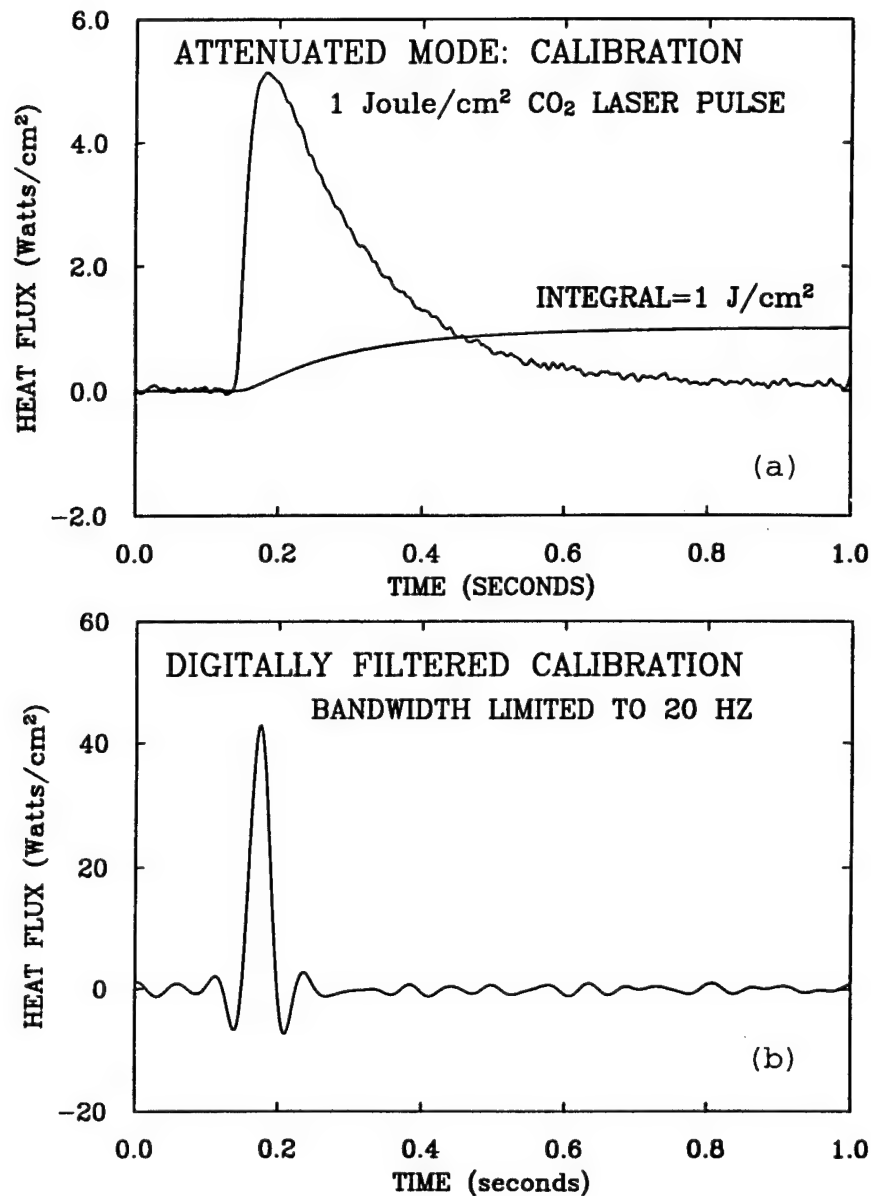
Figure 3.   Laser Calibration(a) film signal difference for
             CO_2 laser pulse and it integral with a known
             fluence of 1 Joule/cm^2,(b) bandwidth-limited
             representation of the incident surface flux
             after data processing. Note that the long
             thermal tail of (a) has been eliminated.

    Calibration with the laser pulse must be performed
after spin-coating a thin, IR-absorbing layer of carbon-
black laden epoxy but prior to application of the IR-
reflecting layer (by Cr/Al evaporation).

3. BALLISTIC RANGE TEST DATA

The following tests were conducted at Aberdeen Proving Ground in Fall 94. PSI provided heat flux transducers with 100 ft of cable and a powered buffer/line driver patch box for driving the remaining several hundred feet of coaxial cable for each signal line to the instrumentation trailer. Data for only a few trial cases is available, and these cases were plagued by intermittent electrical connections. The robustness and redundancy of the transducer is encouraging, however, since a great deal of useful data can still be extracted.

3.1 Shot #1

Heat flux transducer data for a ballistic range test characterized by penetration of and combustion within a closed compartment is shown in Figure 4. This is designated shot #1. A gain-switch at early time is evident. These two channels are the for the total flux measurement (IR-absorbing film pair). Unfortunately, in this shot, and subsequent shots, only two channels of the possible four were acquired. In this case two data acquisition channels failed during testing so no radiative flux measurement was possible
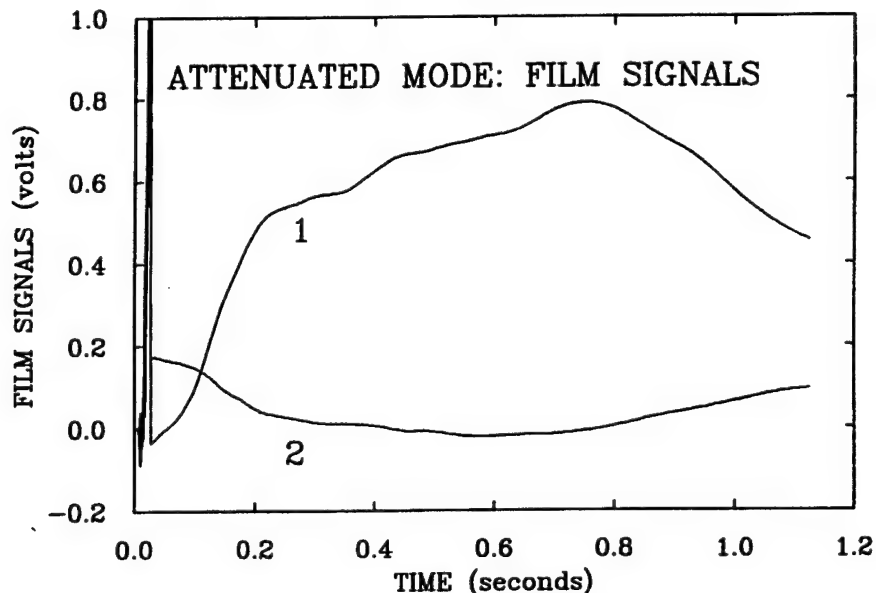
Figure 4. Shot #1. Shallow(1) and deep(2) film signals (IR-absorbing side). Gain-switch near 30 ms is evident.

Pressure transients are typically of most interest at very early times while thermal events tend to be cumulative over seconds. But for 28 μm PVDF film, the thermal response in volts/degree C (~6 V/C) is more than ten times the voltage developed per bar of pressure (~0.3 V/atm). Thus the typical temperature signature is orders of magnitude greater than typical blast overpressures or acoustic transients. For these reasons, an automatic gain-switching capability was incorporated into the integral pre-amplifier in order to maximize information content at early time. The film voltages are buffered at unity gain. When the positive going (shallow/IR-absorbing) film voltage exceeds a preset threshold, a capacitive voltage divider (0.66 μF) is switched in parallel with each sensor film (1000 pF). This is referred to as the attenuated mode, since otherwise film potentials would reach hundreds of volts. The signals are attenuated by a factor 660, the RC time constant is increased by the same factor (to > 600 s). The shallow and deep film are actually arranged with opposite polarity.

For the high (unity) gain mode at early time, the thermal and pressure signals can be separated by forming appropriate sums and differences. It is essential to properly account for any small gain differences between films and for the capacitive coupling between the paired deep and shallow films. For this sensor the inter-electrode capacitance is actually twice the film capacitance. The unscaled results are shown in Figures 5a, b and c.

Because the thermal signal is known prior to the gain switch, it can be matched afterward, so there is no difficulty patching across the gain switch. This is illustrated in Figure 6a. Using the multi-layer code and the calibration data the heat flux incident at the sensor surface is derived. The flux and its time-integral are shown in Figure 6b. Based upon the calibration, we obtained more than 11 Joules/cm^2 thermal dose in the recorded interval. The slow response of the large thermal mass of the transducer is compensated by the bandwidth-boosting capability of the thermal code, up to a limit determined by the signal-to-noise ratio of the raw data. This signal-to-noise ratio easily accommodates 100 Hz bandwidth, but this adds nothing when only thermal dosimetry is required. The
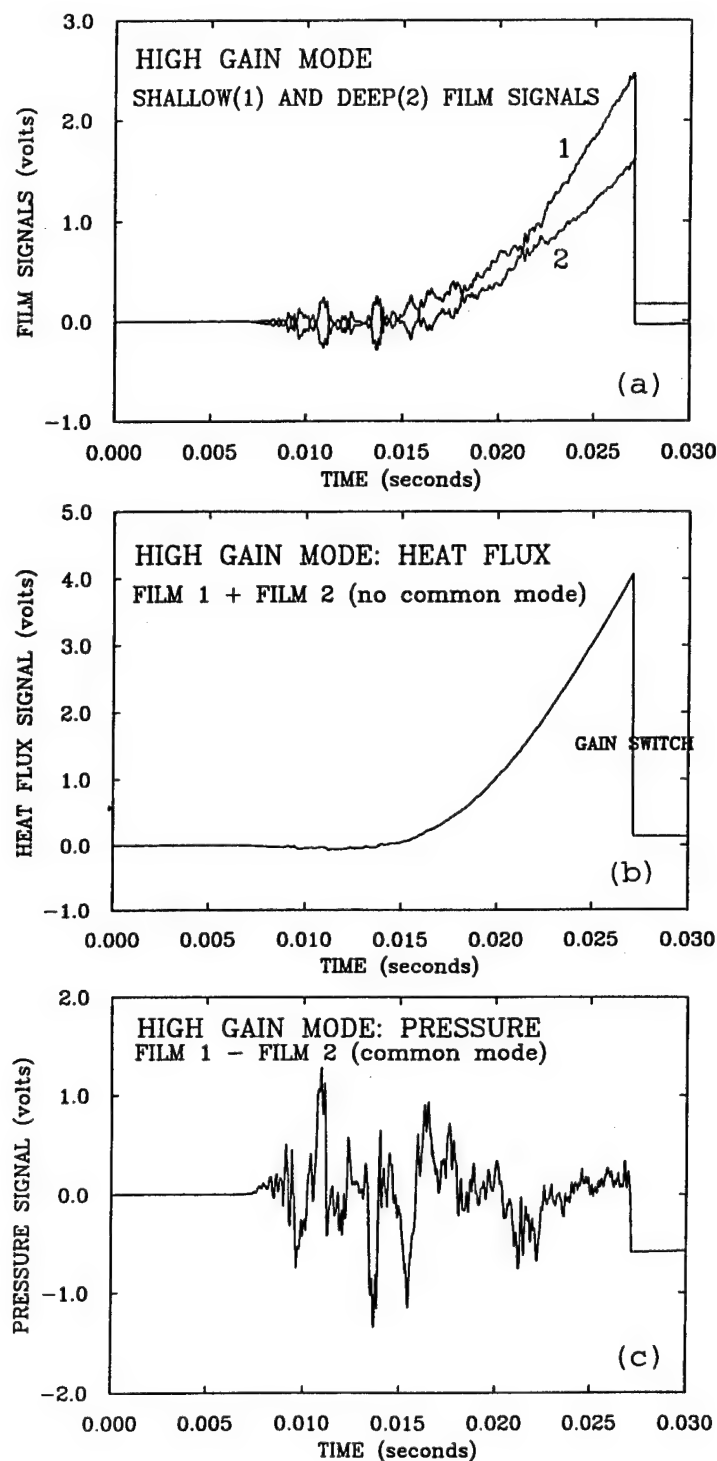
Figure 5. Shot #1. High gain mode (prior to gain-switch);
(a) raw film signals (b) sum signal cancels common
mode pressure signal leaving temperature
difference (gradient) of the films. (c) difference
leaves pressure signal and mean film temperature
(which can be computed and subtracted).

150
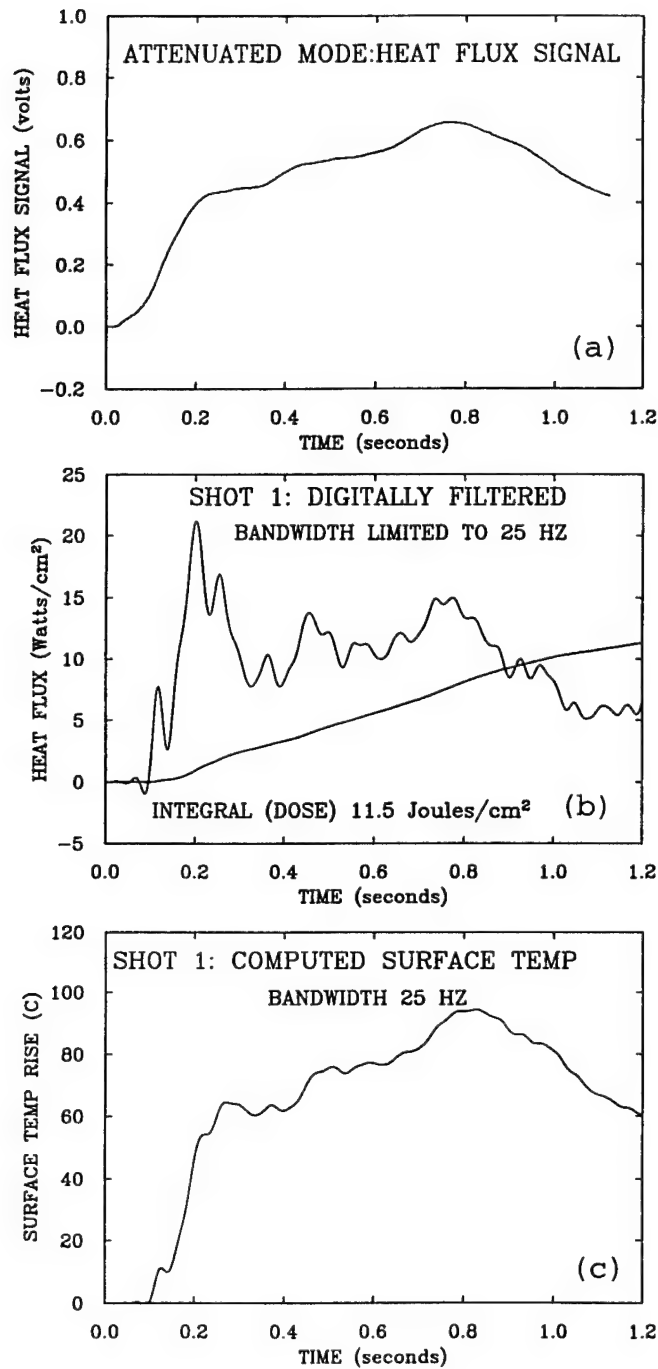
Figure 6. Shot #1. Attenuated Mode.(a) sum signal (temperature difference), (b)Processed surface flux history with bandwidth set to 25 Hz and its integral, (c) processed surface temperature history.

151

code can switch between flux and temperature at any surface, so for example, the surface temperature history can also be computed directly as shown in Figure 6c.

3.2 Shot #2

Using the same transducer as in shot 1, problems in acquiring a full set of data channels persisted in shot 2. Though the transducer behaved well in mild laboratory shakedown tests, these shots were the first remote operation and potentially harsh conditions encountered. Again, the absorbing pair were obtained in shot 2. Raw thermal signal and the reduced flux data are presented in Figures 7a and b. The sensor was purposely put in the attenuated mode (low gain) before the shot. The fire suppression response was delayed till rather late in the record and the dose was more than 20 Joules/cm^2. The deep film signal appear to be unphysical due to its rise above the baseline (implying rapid cooling of the substrate). One of the few plausible explanations of this effect--leakage between the films--has no effect on the flux measurement. Indeed, a dead short between the inner electrodes would result in a common signal proportional the temperature difference of the films. We have proceeded on this assumption, even though this has not been proven. This could be an effect of fragments from the first shot, or thermal cycling and/or contamination during sensor lamination. The latter are amenable to simple assembly process improvements. A full, post-test assessment of this transducer has not yet been completed.

3.3 Shot #3

For shot 3 a replacement sensor was provided, but could not be properly evaluated in situ prior to the shot. In this case only the absorbing-side deep film, and the reflecting-side shallow films produced data. Shot 3 included penetration and fire, but the fire suppression system was active rapidly.

Note that signals from overlaying film pairs were not obtained. The processed signals in this case use yet another feature of the multi-layer thermal analysis code. Surface flux can be extracted from single film data via its
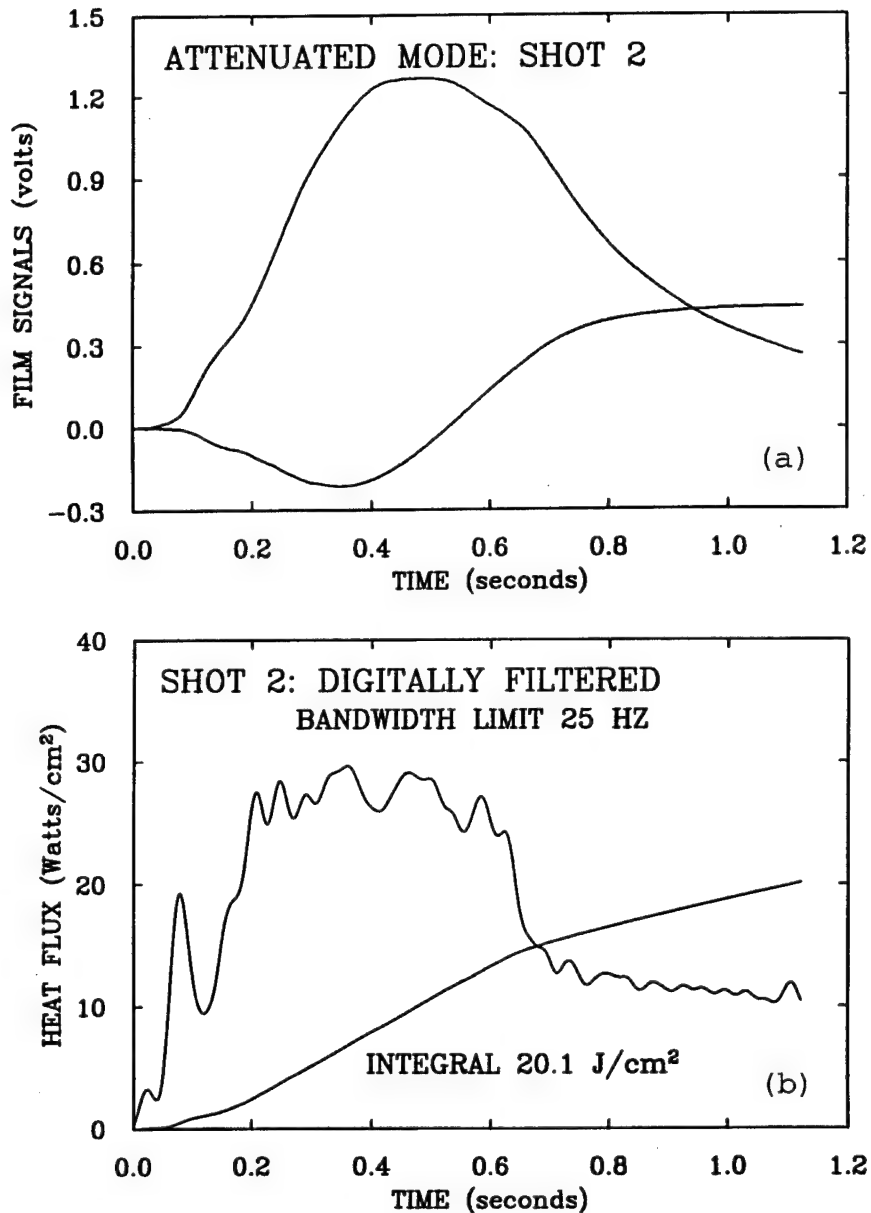
Figure 7. Shot #2 (a) Raw film signals (b) Processed surface
         flux history and its integral.

time derivative. Of course, there is no common-mode
rejection with the single film, and subsequent differen-
tiation leads to significant noise increase. The need for
more significant filtering leads to phase distortions. This
can be addressed partly by digital filtering prior to
differentiation.

    Both the deep/absorbing and shallow/reflecting signals
were processed in this way, and the resulting surface fluxes

are shown in Figure 8. Both initially rise rapidly and the flux quickly drops off as fire suppression commences. In fact, the instantaneous flux goes negative briefly as if the sensor surface has been hit by something cold. The integrals, also seen in the figure, indicate that the peak energy on the absorbing side (radiative and convective) is about 2 Joules/cm^2, whereas the reflective side (convective only) was about 1.5 J/cm^2. These are not sufficient to cause a burn. The difference of 0.5 J/cm^2 is a measure of the radiative component of the flux. However, without a more detailed calibration, the accuracy of this value is uncertain. Note that the transducer is apparently cooling (convectively) as the integral curves show by sloping gently down at the same rate. The proper operation of all channels obviates the need for the kind of analysis performed above. Direct, accurate representation of the time-dependent radiative flux could be obtained by simple subtraction of the processed pairs. Additional testing is needed.
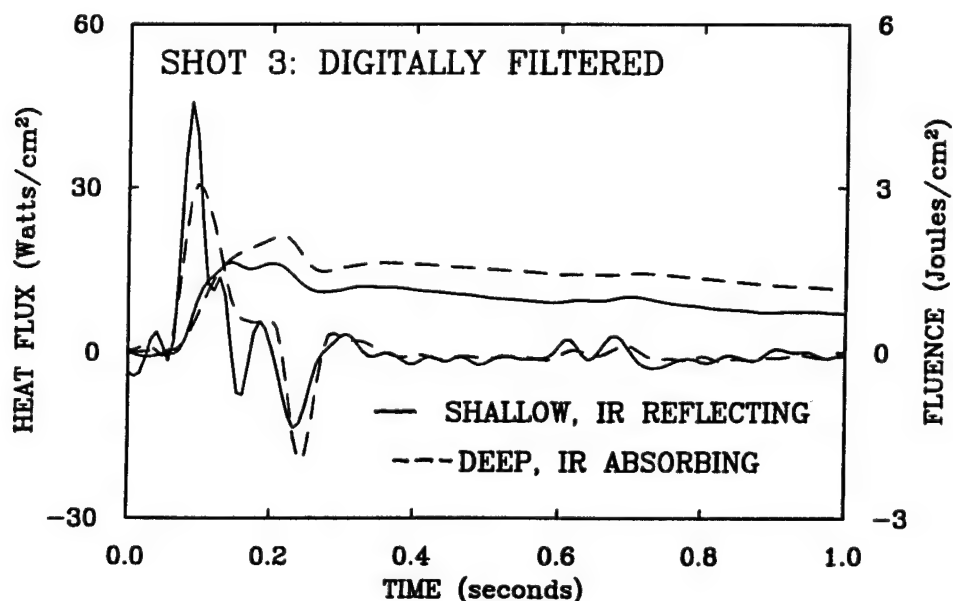
Figure 8. Surface flux is computed independently from the deep/absorbing and shallow/reflecting films. The difference in the integral curves is the radiative flux dose.

4. CONCLUSION

This multi-function transducer and associated software has been demonstrated in most of its available operating and

analysis modes. Because of the design and fabrication
methods, this transducer is readily scalable in active area,
overall size, flux and pressure dynamic range, and speed of
response. Integral pre-amps can be configured for several
operating modes. Plug-in sensing elements make repair a
cost-effective option in harsh environments. After further
shakedown tests and elimination of some remaining minor
instrumentation issues, this device will be suitable for a
wide variety of testing environments.

5. ACKNOWLEDGMENTS

6. REFERENCES

1. Faller, J.G., Herud, C., Lukens, L.K. and Walton, W.S.,
    "Methodology Investigation (Final Report) of Evaluation
    of Crew Vulnerability in Live Fire Testing of Armored
    Combat Vehicles (Thermal, Toxic Fume, Blast
    Overpressure, and Acceleration Effects), U.S. Army
    Combat Systems Test Activity, October 1991.

2. Takata, A.N., Zaneveld, L., and Richter, W., "Laser-
    Induced Thermal Damage in Skin", USAF School of
    Aerospace Medicine, Brooks AFB, TX, Report SAM-TR-77-
    38, 1977

3. Ferguson, R.D., Lo, E.Y., Nebolsine, P.E., and Faller,
    J.G.,"Multi-function Transducer for Measure of Heat
    Flux and Pressure Transients in Live Fire Tests,"
    Proceedings of the 17th Transducer Workshop, San Diego,
    June,1993.

ON ANALOG FEEDBACK CONTROL FOR MAGNETOSTRICTIVE TRANSDUCER LINEARIZATION

David L. Hall and Alison B. Flatau
Department of Aerospace Engineering and Engineering Mechanics
Iowa State University
2019 Black Engineering Building
Ames, Iowa 50011

ABSTRACT

Terfenol-D is a "giant" magnetostrictive material offering mechanical strains on the order of 1000 $\times 10^{-6}$ m/m (1000 μ strain). Dynamic actuators constructed using Terfenol-D as the motion source offer displacements based on approximately ± 500 μ strain. These actuators are known to be nonlinear; however, in some applications they can be treated as linear systems and their behavior approximated by the classic pair of linear transduction equations. The transducer in this study is assumed to be a linear system (to facilitate analysis) and simple, analog, PD (proportional plus derivative) acceleration feedback control is used to improve its linearity.

Expressions are derived and discussed for output displacement and acceleration from an input reference voltage signal. The expressions are functions of frequency and controller, load, and transducer parameters. Experimental measurements are presented to validate the expressions. Limits on the accuracy of the analysis arise through use of the classical assumptions that constant coefficients can be used to provide a "good" model of the transducer parameters. It is shown that prediction accuracy improves when the parameters are calculated using a technique which includes the deleterious effects of eddy currents occurring in various transducer components. However, reasonable estimates are available by using even the simplest transducer estimating techniques ("reasonable" by the standards for simulations of Terfenol-D transducers).

A nonlinearity of particular importance when using Terfenol-D transducers is wave form distortion. The distortion is a result of nonlinear strain vs magnetization relationships and the magnetic hysteresis occurring within the Terfenol-D. The net result is varying amplitude integer harmonics present in the transducer voltage, current, and output velocity. The amplitudes typically increase with increasing excitation level. Assuming the harmonics to be disturbances, expressions are developed for predicting the change in harmonic amplitudes of displacement and acceleration as functions of frequency and parameters for the controller, load, and transducer. Experimental measurements comparing controlled and uncontrolled output accelerations (at the same drive-current level) are presented to validate the approach. Changes in the harmonic acceleration amplitudes of from +2 to -30 dB (depending upon the frequency of the disturbance input) are predicted and demonstrated. A significant extension of the linear range of transducer behavior, due to feedback control, is also demonstrated.

INTRODUCTION

It is assumed that the reader has a passing familiarity with linear controls. The same is not assumed about their knowledge of magnetostrictive transducers.

Magnetostrictive materials are the magnetic analogs of the more familiar piezoelectric materials. Magnetostrictives transduce strain and magnetic

156

energies. Terfenol-D is a magnetostrictive material which was discovered at the Naval Ordinance Laboratory and it is produced by alloying the rare-earths terbium and dysprosium with iron. Thus, Terfenol-D stands for Ter(bium) + fe (iron) + nol (Naval Ordinance Laboratory) + D(ysprosium). It has been commercially available since the late 1980s. An authoritative discussion of the physics of the material is available in reference 4. Terfenol-D was the magnetostrictive material used in this study because of its relatively large strains (compared with, for example, nickel) and because it was readily available.

Terfenol-D is typically produced in a cylindrical geometry. The manufacturer grows the crystals so that when solidified, most of the magnetic domains in the material are oriented perpendicular to the axis of the rod. A magnetic field directed along the axis of the rod will cause the domains to rotate (in an effort to align with the applied field), resulting in the rod increasing in length (and decreasing in diameter). To a first approximation, one can control the length of the rod by controlling the magnetic field within the magnetostrictive rod. A popular implementation of Terfenol-D as a motion source is to place a rod of the material down the bore of a wound wire electric solenoid, thereby controlling the length of the rod by controlling the electric current in the solenoid. One end of the rod is usually "fixed" while the other end provides the motion/force output.

Engineering realities that should be observed when using Terfenol-D as a motion source follow.
1) Terfenol-D filings are flammable.
2) Terfenol-D can only be described as a "brittle" metal. One should not design a transducer in which the Terfenol-D rod will be drilled, threaded, or welded. It chips easily, thus mating parts must be closely aligned. Fortunately, a rod which has been dropped can usually be glued back together, especially if the fractures are perpendicular to the axis of the rod, without resulting in a significant loss in the performance of the material.
3) Terfenol-D yields larger net strains if it is compressively prestressed. The prestress translates to a prestrain which tends to improve the statistical distribution of the magnetic domain orientations, i.e., it rotates more domains closer to being perpendicular to the rod's axis.
4) Terfenol-D's compressive strength is much greater than its tensile strength. For most practical purposes, the rod must be kept in an overall state of compressive stress-another reason to prestress the rod.
5) Bidirectional motion from a Terfenol-D rod can be obtained if the quiescent state is defined as that of the rod when it is magnetically biased, typically to approximately half of its maximum low frequency strain. The magnetic bias can be provided by permanent magnets placed somewhere in the magnetic circuit or by running a 0 Hz electric current through a surrounding wound wire coil. The first method is usually employed because of reduced power requirements and reduced heating.
6) Eddy currents can be a problem. Terfenol-D is a conductor, thus, varying in time the axial magnetic field in the material induces large scale eddy currents within the material (and other transducer components!) resulting in magnetic shielding of, and heating within the material.

A schematic representation of the magnetostrictive transducer used in this study is shown in Fig. 1. The view is that one would see if the transducer had been cut lengthwise along its axis. As discussed above, the Terfenol-D rod is positioned in the bore of a cylindrical wound wire solenoid. The rod is kept in an overall state of compressive stress via the prestress adjusting bolt and the prestress spring washer. Note that the rod butts against the motion output and the prestress adjusting bolt (no threads or welds!). As a result, if a tensile force were applied to the motion output and it exceeded the product of the prestress and the area of the Terfenol-D rod, the motion

157
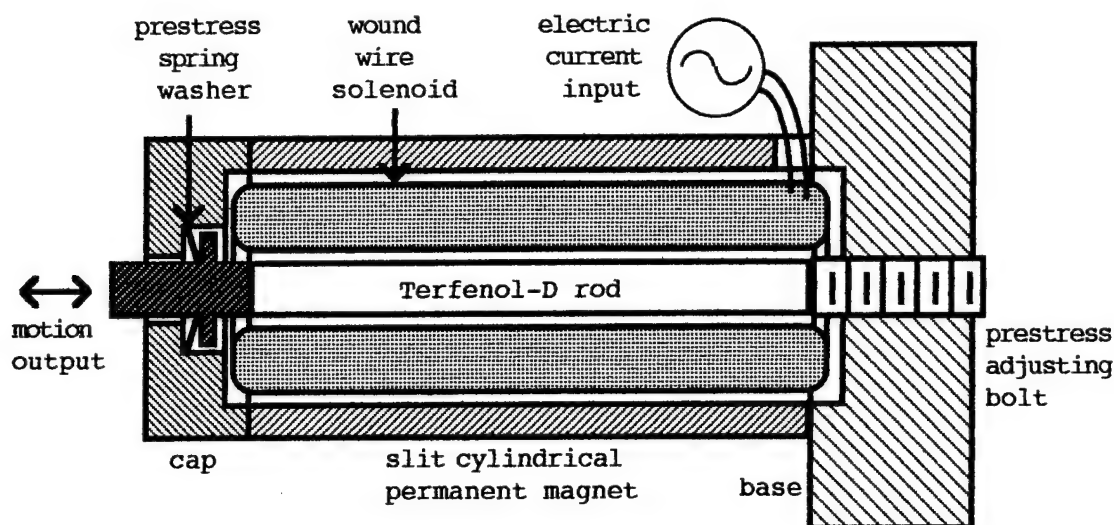
Figure 1. Schematic section view of the Terfenol-D magnetostrictive transducer used in this study.

output would pull away from the rod. Note, then, that the prestress and area of the rod define the largest bidirectional force amplitude possible for the transducer. Magnetic biasing is accomplished via the slit cylindrical permanent magnet. The magnet was slit lengthwise (viewed from either end it is "C" shaped) to physically disrupt a conducting path which otherwise would have been a major source of performance robbing eddy currents.[2] The base is a seismic mass. The input for the transducer is the oscillating electric current. For the tests in this study, the base mass was adjusted so that the base motion amplitudes were less than 5% of the amplitude of the motion output. It was thus assumed that the transducer was a reasonable approximation of a 1-DOF system.

Magnetostrictive transducers are traditionally considered as being reasonable approximations of linear systems at low drive amplitudes[1,2,4] and as becoming very nonlinear at high drive amplitudes.[3,4,5] These are all relative terms. A more concrete example is shown in Fig. 2 which displays plots of percent harmonic distortion (%HD) and displacement from current ($||u/I||$ as a percentage of the value measured when driven at 800 mA) versus drive current amplitude (displayed as a percentage of 800 mA). The datums in Fig. 2 were calculated from the information given in Table 5.1 of reference 2. For the tests, the transducer was driven by 200 Hz sinusoidal drive currents of various amplitudes using an amplifier with a current-control module. Acceleration autospectral density functions (0 - 2 kHz) were calculated for each of the 200 Hz drive-current amplitudes. %HD was calculated as the ratio of the summation of the harmonic amplitudes to that of all of the amplitudes (the harmonics occurred at integer multiples of the fundamental, i.e., at 400, 600, 800, ..., and 2000 Hz). Displacement from current values were those corresponding to the 200 Hz component only, and all are shown as percentages of the 800 mA value (11.2 μm/A). For the transducer in question, a "high" drive current amplitude was 800 mA zero to peak.

As shown in Fig. 2, the measure of wave form harmonic distortion is a minimum at the lower drive current amplitudes. If 20% harmonic distortion were arbitrarily defined as the upper limit of the transducer's "low signal linear range," one would be limited to drive currents below 100 mA for this transducer (as loaded and operated at 200 Hz). Note, however, that this
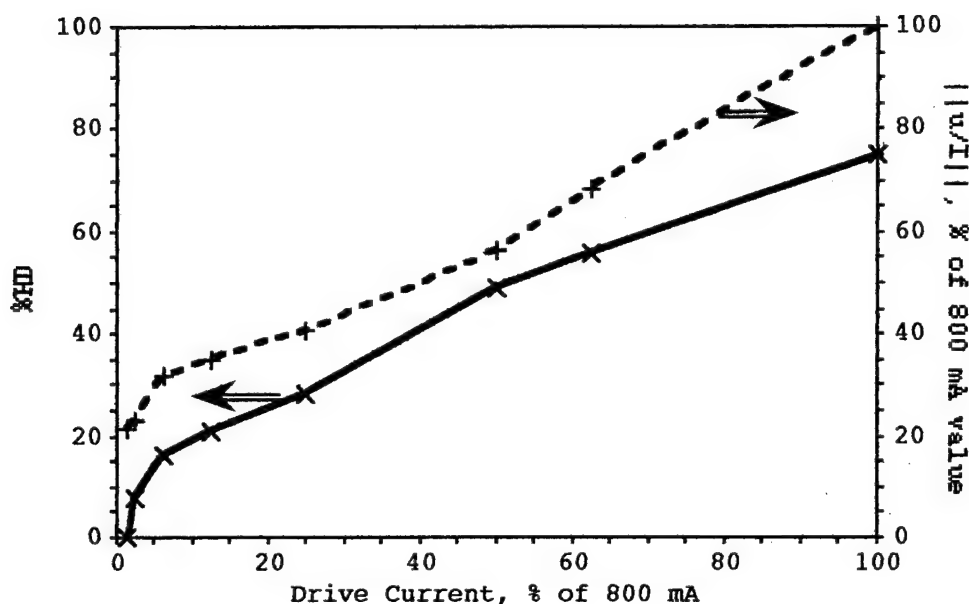
Figure 2. Percent harmonic distortion (%HD) and percent of displacement from drive-current amplitude ($||u/I||$) versus sinusoidal 200 Hz drive-current amplitude. Current and u/I are expressed as percentages of their "high" drive-current amplitude (800 mA) values.

places a severe limitation on the possible output displacements in the "linear" range. From the figure, for 13% drive current (100 mA), displacement per ampere is about thirty-four percent of the 800 mA value. Thus, the displacement at 100 mA is about one-third of one-eighth of that at 800 mA, i.e., u(100 mA) ≈ u(800 mA)/24. One would thus like to decrease the output harmonics in order to increase the linear range of transducer operation. That was the impetus for the investigation reported here.

Figure 2 shows two types on nonlinearities common to Terfenol-D magnetostrictive transducers. Harmonic, or wave form distortion exists and increases with drive-current amplitude. Another, more subtle nonlinearity is the change in displacement from current with increasing current amplitude. At very low frequencies, u/I is proportional to the fabled magnetostrictive linear coupling coefficient, aka, the "d constant." As shown in the figure, it increases by a factor of five over this drive-current range and exhibits its steepest slope (highest sensitivity to current amplitude changes) in the low signal linear range (below 10% drive current, i.e., 80 mA).

MODELING APPROACH

The magnetostrictive transducer will be modeled as a linear system satisfying a pair of linear simultaneous equations. The harmonic frequencies present in the state variables will be thought of as disturbances.

The canonical form of the transduction equations, as applied to a magnetostrictive transducer, is:[1]

$$V = Z_e I + T_{em} v \qquad (1a)$$

$$0 = T_{me} I + z_x v \qquad (1b)$$

159

where: V = voltage over the transducer leads, volts;

Z_e = blocked electrical impedance of the transducer (blocked physically, i.e., the electrical impedance one would measure if the output velocity were held at zero) = $sL_e + R_e$, where s is the Laplace operator, L_e is the blocked electrical inductance, henries, and R_e is the dc resistance of the wound wire solenoid, Ω;

I = electric current passing through the wound wire solenoid, amperes;

T_{em} = the transduction coefficient, electrical due to mechanical, V/(m/s);

v = the mechanical output velocity of the transducer, m/s;

T_{me} = the transduction coefficient, mechanical due to electrical, Newton/A; and

z_x = the mechanical impedance, based on velocity, of the transducer and the load, which, in its simplest applicable form is given as: $z_x = sm_x + b_x + k_x/s$, where m_x is the sum of the internal dynamic mass of the transducer plus the load mass, in kg, b_x is the sum of the damping within the transducer and that due to the load, N/(m/s), and k_x is the combined stiffness of the transducer and the load, N/m.

It is shown in the literature[1,2,6] that for magnetostrictive transducers, ignoring eddy current effects, $T_{em} = -T_{me}$ = a drive amplitude dependent pseudo-constant. In this communication, T will be defined as: $T = T_{em} = -T_{me}$. Using this substitution in Eqns. (1), one can solve for some useful fundamental input-output relationships of the transducer when operating in its linear range. In particular:

$$\frac{v}{I} = \frac{T}{z_x} \tag{2}$$

$$\frac{V}{I} = \frac{Z_e z_x + T^2}{z_x} \tag{3}$$

$$\frac{v}{V} = \frac{v}{I} + \frac{V}{I} = \frac{T}{Z_e z_x + T^2} \tag{4}$$

$$\frac{u}{V} = \frac{1}{s}\frac{v}{V} = \frac{T}{s\left(Z_e z_x + T^2\right)} \tag{5}$$

$$\frac{a}{V} = \frac{sv}{V} = \frac{sT}{Z_e z_x + T^2} \tag{6}$$

where: u = transducer output displacement, meters, and
a = transducer output acceleration, m/s^2.

All of these equations will be useful when modeling the transducer as part of the overall controlled system.

Feedback Models Using a Current-Control Amplifier

Figure 3 shows a block diagram for the system consisting of a PID (proportional, integral, and derivative) controller; a current-controlled amplifier, of gain K_a, A/V; the transducer (expressed as displacement per

Figure 3. Block diagram of feedback system assuming a PID controller, a current-controlled amplifier of gain K_a, a displacement sensor of sensitivity S_u, and disturbance displacements, u_d.

ampere = Eqn. (2) divided by s); disturbance displacements, u_d; and a displacement transducer of sensitivity, S_u, V/m. The reference signal is shown as V_r; it is the input for the controlled system. Using the definitions for the impedances (Z_e and z_x) detailed below Eqns. (1), the system transfer function u/V_r is calculated as:

$$\frac{u}{V_r} = \frac{\left(sk_d + k_p + k_i / s\right) K_a \dfrac{T}{sz_x}}{1 + \left(sk_d + k_p + k_i / s\right) K_a \dfrac{T}{sz_x} S_u}$$

which reduces to:

$$\frac{u}{V_r} = \frac{\left(s^2 k_d + sk_p + k_i\right) K_a T}{s^3 m_x + s^2\left(b_x + k_d K_a TS_u\right) + s\left(k_x + k_p K_a TS_u\right) + k_i K_a TS_u} \tag{7}$$

This function has two, possibly complex zeros in the LHP (left half-plane) given as:

$$s_{1,2} = [-k_p \pm (k_p^2 - 4k_d k_i)^{1/2}]/2k_d$$

and the Routh-Hurwitz criteria[10] guarantees that it will have its three poles in the LHP if:

$$k_x b_x + k_d(k_x + k_p K_a TS_u)K_a TS_u + k_p k_x K_a TS_u > m_x k_i K_a TS_u$$

This derivation assumes that the system parameters are constants, independent of drive magnitude and frequency. These are tenuous assumptions when dealing with Terfenol-D transducers, as will be described later. (T, R_e, L_e, K_a, and k_x are all of particular concern with these actuators.)

Other relations could be developed assuming one had a current-controlled amplifier that was robust enough to be a reasonable approximation of the constant K_a. That was not the case in this investigation. (These transducers are very active loads and they gave the Techron current control module fits.) Therefore, the balance of this communication will deal with a voltage-controlled amplifier. In addition, emphasis will be placed on oscillatory drive conditions using an accelerometer as the feedback transducer. This was done for two reasons: 1) The equipment was available. 2) Small amplitude

disturbance displacements are anticipated and using an accelerometer as the feedback transducer exploits the ω^2 signal amplification inherent to acceleration measurements. For example, if $u(500\text{ Hz}) = 1$ μm and the first harmonic is $u(1000\text{ Hz}) = 0.01$ μm, then $u(1000\text{ Hz})$ is "40 dB down." Compare that with the acceleration case: $a(500\text{ Hz}) = -(2\pi500)^2u(500\text{ Hz})$, $a(1000\text{ Hz}) = -(2\pi1000)^2u(1000\text{ Hz})$, and $20\log[(2\pi1000)^2u(1000\text{ Hz})/(2\pi500)^2u(500\text{ Hz})] = 20\log[4u(1000\text{ Hz})/u(500\text{ Hz})] = -40 + 20\log[4] = -28$ dB. Similarly, the second harmonic (1500 Hz) would be $20\log[9]$ dB larger than the corresponding displacement measurement.

Feedback Models Using a Voltage Control Amplifier

Figure 4 is a block diagram of the feedback system assuming a voltage-controlled amplifier. (Voltage is much easier to control than is current when driving a Terfenol-D transducer.) The transducer's transfer function for acceleration per volt is given in Eqn. (6). Using the PID controller defined in Fig. 4, the relations for the impedances detailed below Eqns. (1), and Eqn. (6), the transfer function for the closed loop system, as a/V_r, is given as:

$$\frac{a}{V_r} = \frac{\left(k_d s + k_p + k_i/s\right)K_V\dfrac{sT}{Z_e Z_x + T^2}}{1 + \left(k_d s + k_p + k_i/s\right)K_V S_a\dfrac{sT}{Z_e Z_x + T^2}}$$

which "reduces" to:

$$\frac{a}{V_r} = \frac{s\left(k_d s^2 + k_p s + k_i\right)K_V T}{\left(L_e m_x + k_d K_V S_a T\right)s^3 + \left(L_e b_x + R_e m_x + k_p K_V S_a T\right)s^2 + \left(L_e k_x + R_e b_x + T^2 + k_i K_V S_a T\right)s + R_e k_x}$$

(8)

The transfer function for output acceleration from a given input disturbance acceleration is given as:

$$\frac{a}{a_d} = \frac{1}{1 + \left(k_d s + k_p + k_i/s\right)K_V S_a\dfrac{sT}{Z_e Z_x + T^2}}$$
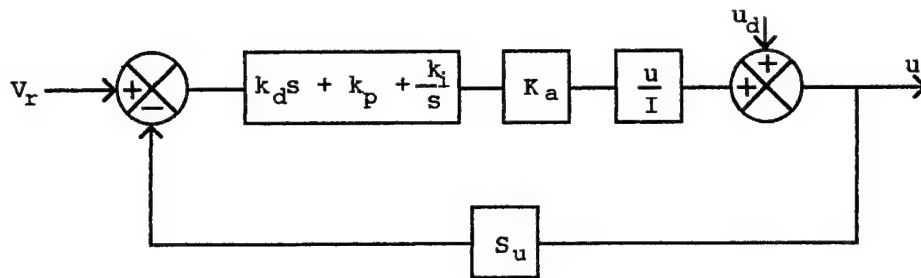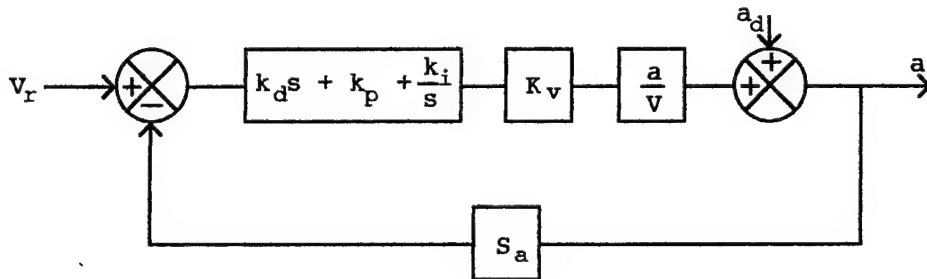

Figure 4. Block diagram of feedback system assuming a PID controller, a voltage-controlled amplifier of gain K_V, an acceleration sensor of sensitivity S_a, and disturbance accelerations, a_d.

162

which reduces to:

$$\frac{a}{a_d} = \frac{L_e m_x s^3 + \left(L_e b_x + R_e m_x\right) s^2 + \left(L_e k_x + R_e b_x + T^2\right) s + R_e k_x}{\left(L_e m_x + k_d K_V S_a T\right) s^3 + \left(L_e b_x + R_e m_x + k_p K_V S_a T\right) s^2 + \left(L_e k_x + R_e b_x + T^2 + k_i K_V S_a T\right) s + R_e k_x}$$

(9)

Note that Eqns. (8) and (9) have the same characteristic equations (same denominators) and that the control parameters appear as coefficients of the higher powers of s (which contains the frequency). Thus, it can be expected that derivative feedback will be most helpful at reducing harmonics at the high frequencies. Similarly, k_p will be most useful at medium to high frequencies and k_i will help in the low to medium frequency range.

Classical stability analysis might be applied to these characteristic equations. However, it was not done in this study owing to the variability of coefficients with excitation frequency, excitation amplitude, magnetic bias point, material prestress, and even actuator load (T changes with different loads in the presence of eddy currents[2]). Reasonable estimates of stability criteria might be obtained by using empirical and/or analytical relationships for L_e, R_e, b_x, k_x, and T, as functions of all of the parameters mentioned previously, if they all existed. Awaiting further research into those relationships, stability issues were resolved empirically in this study.

Models have been developed for prediction of magnetostrictive transducer behavior using a PID controller in the forward loop. It has been assumed that the transducer was a linear system which satisfied the pair of simultaneous equations, Eqns. (1), with the harmonic frequencies (that are known to exist) modeled as disturbance inputs. The primary goal of this endeavor is to reduce the harmonic signal content of the magnetostrictive transducer; thus extending its linear range to larger displacements, velocities, and accelerations. To test the modeling technique, a PD controller was fabricated and experimental measurements were performed.

RESULTS

In this section of the communication, experimental evidence is offered to show that the control system generally improves the linearity of the transducer, realities of the circuits and components employed will be discussed (including procedures for obtaining transducer parameters), and model predictions will be compared with experimental measurements of magnetostrictive transducer behavior. Emphasis will be placed on the voltage-controlled version, i.e., the drive amplifier was a voltage-to-voltage converter, as opposed to a voltage-to-current transducer.

An example of the effects of simple proportional feedback on the output acceleration of the transducer is shown in Fig. 5. In the figure are two different experimental measurements of transducer output acceleration as functions of time. For both tests, the transducer was driven by a 1000 Hz, 1/4 amp drive-current. As shown in the figure, the proportional feedback made a significant difference in the output wave form. Note that the second harmonic frequency component (3000 Hz) was reduced dramatically by simple proportional feedback.

Figure 6 shows experimental acceleration amplitudes for two cases each of three different drive-current amplitudes. The two cases are controlled (simple proportional acceleration feedback) and uncontrolled. In all cases the drive-current was oscillating at 1000 Hz. The other frequencies were harmonics. Each set of data was normalized by its acceleration amplitude at

163
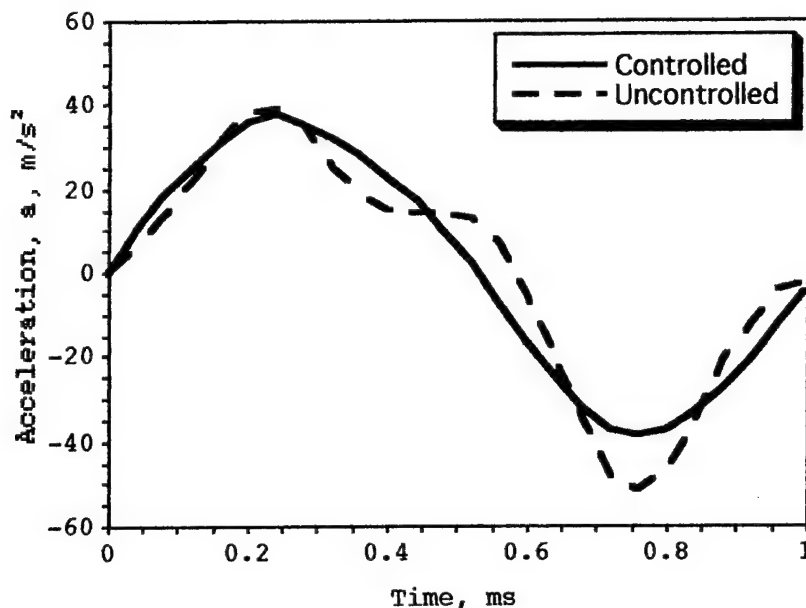
Figure 5. Experimental time traces of transducer output acceleration versus time for the case of proportional acceleration feedback control and the case of no feedback control. Drive conditions for both tests were 1000 Hz, 1/4 ampere (0 - peak).

1000 Hz (thus all show 0 dB at 1000 Hz). As shown in the figure, proportional acceleration feedback control generally decreased the harmonic amplitudes, over this frequency range, when compared with the corresponding uncontrolled drive-current test. Note that at 4 kHz for the 250 mA drives, the controlled case is approximately 30 dB below the uncontrolled case. Note also that for this range of drive-currents the largest harmonic for any of the controlled cases is about 25 dB down; for the uncontrolled cases the largest is approximately -12 dB. The data in Fig. 6 confirms the harmonic distortion trend displayed in Fig. 2: harmonics grow disproportionately with increasing drive-current amplitude.

The datums in Table 1 were calculated from experimental measurements like those shown in Fig. 6 (the 250 mA high gain data is that shown in the figure). For these tests, two different proportional gains (the "low" gain was approximately half of the "high" gain) were used at three different amplitude 1000 Hz drive-currents. In all cases increasing the proportional feedback reduces the harmonic distortion and the distortions increase with increasing drive-current amplitudes. The second trend is in agreement with that shown in Fig. 2 and implied by Fig. 6. During the course of this study, the first trend was repeatedly observed experimentally (until the onset of instabilities). Note that the 250 mA high feedback case had lower distortion than that of the 80 mA uncontrolled case. It is interesting to note that this corresponds to increasing the "linear range" displacements by a factor of almost 15 (assuming linear range implies less than 13% harmonic distortion).

The input-output relationship for the Techron 7520 amplifier was measured. (The amplifier was fitted with a 75A08 control module, set for voltage control.) The system behaved somewhat like a first order system with a -3 dB point at about 57 kHz. Unless specified otherwise, it was modeled as a constant gain with a linear phase lag over the appropriate frequency range (usually 0 to 6 or 10 kHz).

164

Table 1. Percent harmonic distortion of output acceleration as a function of proportional feedback status for a single transducer driven by three different 1000 Hz drive-currents. Percent harmonic distortion was calculated as 100 x (Σ all amplitudes - 1000 Hz amplitude) / Σ all amplitudes.

Drive-Current, I, mA	Proportional Feedback	% Harmonic Distortion
80	none	13
	low	5
	high	3
150	none	19
	low	7
	high	5
250	none	32
	low	12
	high	9

Figure 6. Experimental acceleration amplitudes resulting from 1000 Hz drive-currents at three different amplitudes. "C" represents the case of proportional acceleration feedback control; "U" stands for uncontrolled. Datums were taken from acceleration autospectral density functions.

The control circuit was built in-house. Input-output relationships for each stage of the circuit were measured and compared with the theoretical relationships. Theory and experiment were found to be in excellent agreement. However, difficulties were encountered. There was this pesky 47 kHz oscillation (it turned out to be the mounted resonant frequency of the accelerometer). It was thought that the large number of output frequencies produced by the transducer almost always contained a component near 47 kHz, which, in turn, excited the accelerometer. It was necessary to place a band-pass filter between the accelerometer and the summing amplifier in order to avoid feeding back and oscillating (it was also needed to block the low frequency drift of the accelerometer signal conditioner). The transfer function for this filter was:
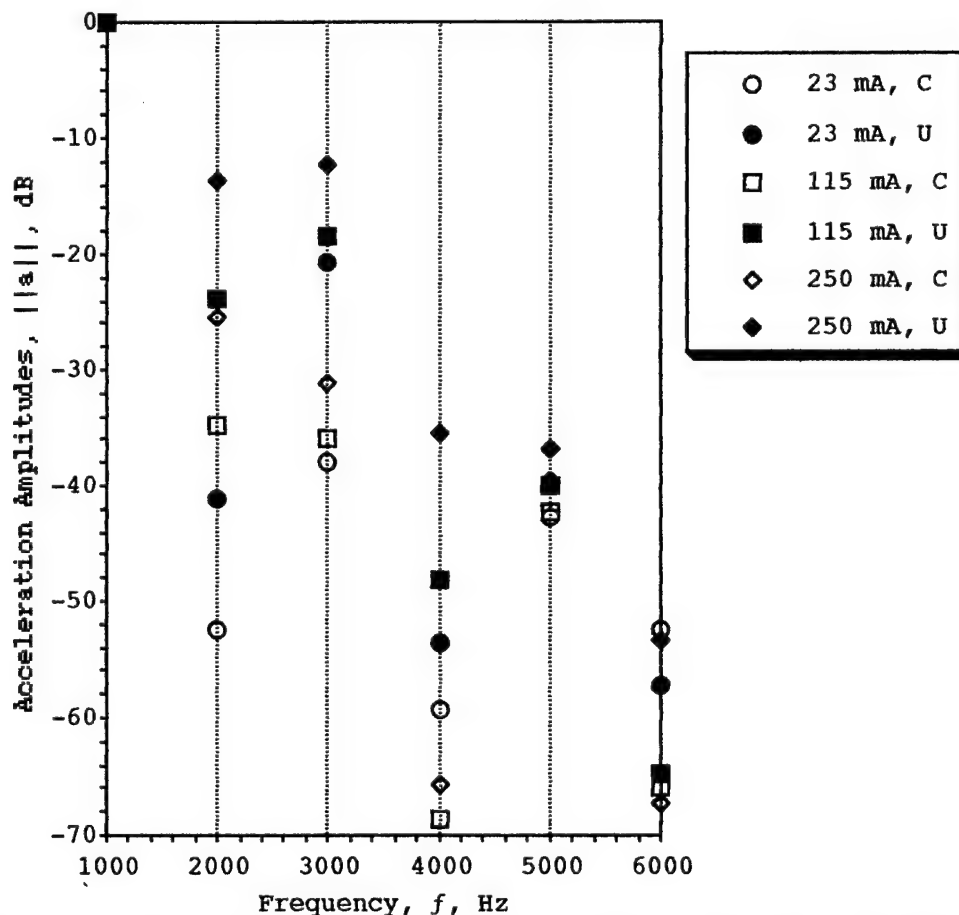
$$\frac{V_{out}}{V_{in}} = \frac{sR_2C_2}{sC_2\{R_1(sR_2C_1 + C_1/C_2 + 1) + R_2\} + 1} \tag{10}$$

where: $R_1 = 30$ kΩ, $R_2 = 100$ kΩ, $C_1 = 1000$ pF, and $C_2 = 0.1$ μF. Its lower -3 dB frequency was 10 Hz; its upper was 7000 Hz. (This filter had a strong influence on the behavior of the control system. As is shown later, it modified magnitudes and phases when compared with simulations from which it was omitted. It is suggested that a better accelerometer/filter system be located.) Since this filter was placed in the feedback loop, it can be thought of as modifying the sensitivity of the accelerometer. Therefore, everywhere S_a appears in Eqns. (8) and (9), one should use the quantity: S_a x Eqn. (10).

The differentiator built for this investigation was simply an active first order band-pass filter with an adjustable gain. (See, for example, reference 7.) Its transfer function, assuming the op amps to be ideal, was:

$$\frac{V_{out}}{V_{in}} = \frac{sR_2C_1}{(sR_2C_2 + 1)(sR_1C_1 + 1)} \text{ x Adjustable Gain} \tag{11}$$

where: $R_1 = 2.2$ kΩ, $R_2 = 10$ kΩ, $C_1 = 0.01$ μF, and $C_2 = 470$ pF. The phase on the output was $+90°$ at low frequencies, reducing to $+45°$ at 5075 Hz, i.e., its first -3 dB frequency was 5075 Hz. The proportional plus derivative summing amplifier also included an adjustable gain. Its effects on k_p and k_d were included in the reported values. Since the differentiator was not a pure derivative, sk_d values in Eqns (8) and (9) were replaced with:

$$sk_d/\{(sR_2C_2 + 1)(sR_1C_1 + 1)\}.$$

The reported values of k_d were calculated as the product of R_2C_1 x Adjustable Gain x Summing Gain.

At this point, circuit parameters are known. For all tests reported in this communication, the transducer was mass loaded such that the first mechanical resonant frequency occurred between 2500 and 4000 Hz. It was mentioned earlier that the transducer in this study had a slit cylindrical permanent magnet positioned around the wound wire solenoid (recall Fig. 1). This magnet was used to position the cap and base relative to each other; bolts (not shown in the figure) pulled the cap toward the base, compressing the magnet in the axial direction. Unfortunately, slitting the magnet resulted in a radial mode of vibration which affected transducer behavior around 7 kHz. As a result, model values reported in this communication (which are based on a 1-DOF mechanical model) will be limited to frequencies less than 6 kHz.

Quantities applicable to the magnetostrictive transducer must be estimated in order to model the transducer, thus the system behavior. One needs estimates of T, the transduction coefficient, Z_e, the blocked electrical impedance of the transducer, and z_x, the sum of the mechanical impedances of

the transducer and the load. One might consult the literature for "nominal" material properties, or build a transducer and measure them. Typical results from both methods are shown in Fig. 7 for the case of simple proportional feedback control. Also shown in the plots are the experimental measurements (X). The figure shows the product of S_a and Eqn. (6) = $S_a a/V_r$ = V_{acc}/V_r = accelerometer over reference voltage, magnitude and phase, versus frequency.
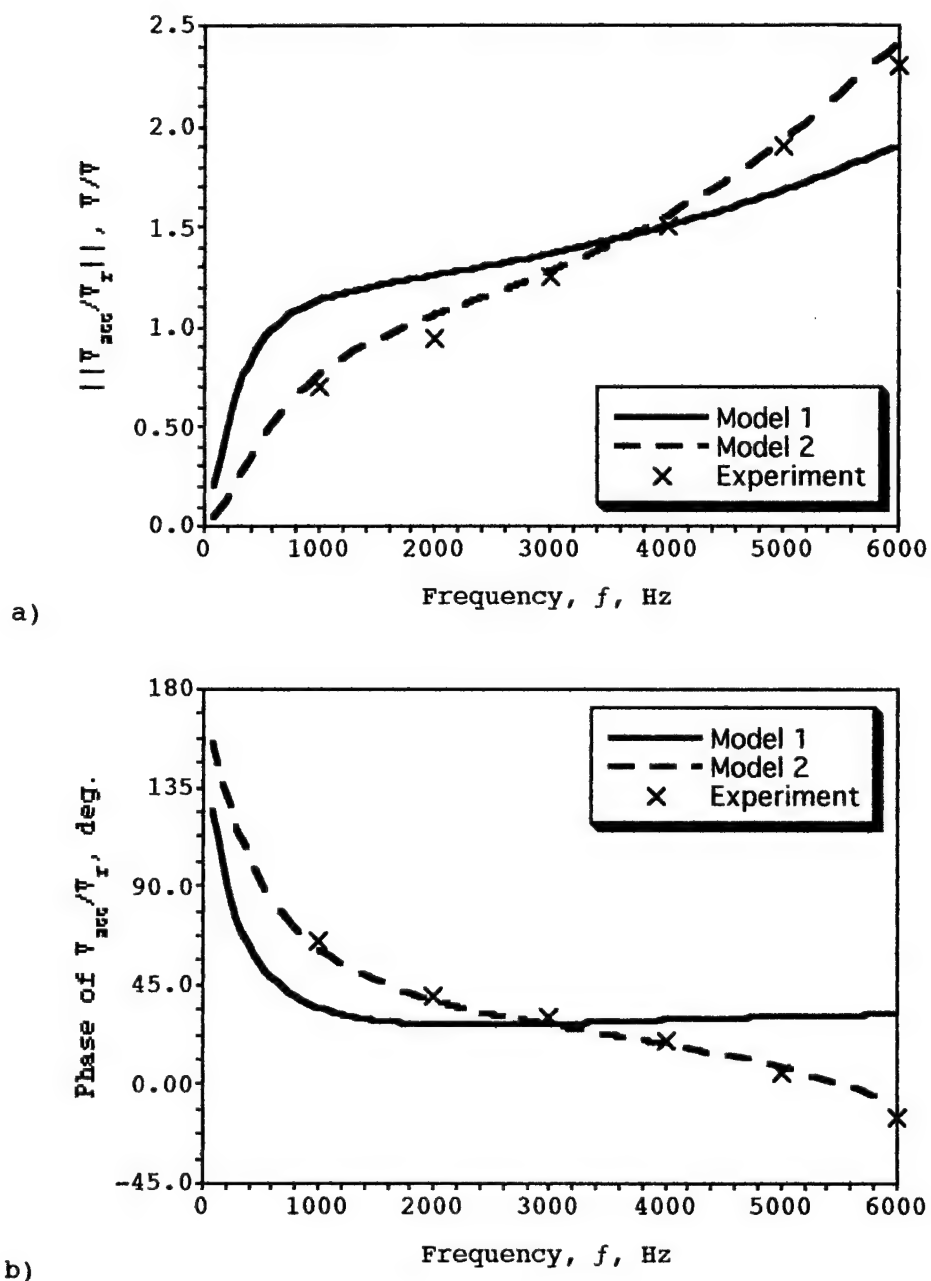

a)

b)

Figure 7. Magnitude (a) and phase (b) of accelerometer voltage from reference voltage for simple proportional feedback control of a magnetostrictive (Terfenol-D) transducer. Model 1 was calculated using "nominal" material properties. Model 2 used properties/functions measured and modeled (see text).

167

In the figure, Model 1 was calculated using published "nominal" Terfenol-D parameters,[8] relations from the literature,[6] and the details of the control circuit discussed above. The transduction coefficient was calculated as $T = N d E_y^H \pi r^2 / l_r$ where: N = turns of the wound wire solenoid (N = 1300 turns); d = the linear coupling coefficient of the Terfenol-D rod ($d \approx 1.5 \times 10^{-8}$ m/A); E_y^H = Terfenol-D's Young's modulus as measured at constant field strength ($E_y^H \approx 3.0 \times 10^{10}$ Pa); r = the radius of the magnetostrictive rod (r = 0.125 x 0.0254 m); and l_r = the rod length (l = 2 x 0.0254 m). Thus, $T \approx 365$ N/A. The blocked electrical impedance of the transducer, Z_e, was estimated as the dc resistance ($R_e \approx 6 \ \Omega$) plus $j\omega L_e$, where $j = \sqrt{(-1)}$, $\omega = 2\pi f$ = frequency of oscillation in radians per second, and $L_e \approx \mu^\varepsilon n^2 \pi r_s^2 l_s = 2.5 \ \mu_o \ 23264^2 \ \pi \ 0.00385^2 \ 0.0559 = 4.43$ mH (μ^ε is the blocked magnetic permeability of Terfenol-D $\approx 2.5 \ \mu_o$, $\mu_o = 4\pi \times 10^{-7}$ Tesla meter per amp-turn, r_s is the inner radius of the solenoid, and l_s is the length of the solenoid). The mechanical impedance of the transducer, as loaded, was calculated using simple second order mechanical relations[9], i.e., $k_x = E A / l_r = E_y^H \pi r^2 / l_r = 18.7$ MN/m, m_x was measured = mass of the load plus some attaching components plus 1/3 the mass of the Terfenol-D rod (m_x = 0.086 kg), $\omega_n = (k_x/m_x)^{1/2}$, and b_x was estimated based on a four-percent damping coefficient, i.e., $b_x \approx 2 \times 0.04 \ \omega_n m_x$.

Model 1 ignores the presence and effects of eddy currents within the magnetostrictive rod, and it uses simple formulas from physics and published values for material parameters. Considering those gross simplifications and misplaced trusts, the Model 1 simulation shown in Fig. 7 was thought to be surprisingly good. Model 2, however, did a better job of matching the experimental measurements.

Model 2 in Fig. 7 was calculated using the electrical impedance modeling technique developed in reference 2. A brief outline of the technique follows. Transducer and material parameters are measured/inferred by electrical impedance and admittance analysis performed on experimental measurements of the transducer's electrical impedance and displacement from electric current functions. These functions are measured using a current-control driver since material parameters are very sensitive to magnetic field strength drive levels. Thus, V/I and a variation on v/V are measured. From these measurements and knowledge of the mechanical aspects of the transducer under test (i.e., m_x, solenoid specifications, the stiffness of the prestress mechanism, electrical conductivities, and dimensions), one can calculate E_y^H, magnetomechanical coupling (aka, k^2), the "d constant," the mechanical damping coefficient (aka, ζ), and the magnetic permeability at constant stress and/or constant strain. All of these parameters are used to calculate analytical solutions (a plethora of modified Bessel functions) for Maxwell's Equations using a complex valued, frequency and load dependent "dynamic magnetic permeability" for the magnetostrictive material within the transducer. In this way, the effects of eddy currents in the magnetostrictive rod (and housing, if applicable) are included. An analytical solution for the electrical impedance is then calculated, i.e., one performs a simulation to calculate V/I including motional and eddy current effects. This is the same V/I as Eqn. (3) and it should be a reasonable approximation ($\pm 10\%$ in both magnitude and phase) of the experimental measurement performed earlier.

Recall that Eqn. (3) was derived by substituting Eqn. (1b) into (1a). Therefore, the pair of simultaneous equations have now been solved. What remains to be done is to calculate the yet unknown coefficients, Z_e and T, which are presently needed for the controls modeling. One can calculate Z_e, the blocked electrical impedance of the transducer, *including* the effects of

168

eddy currents, by calculating V/I again. However, this time through, use the measured/calculated value of the blocked magnetic permeability of the magnetostrictive material instead of the "dynamic magnetic permeability" which was used the first time through. The transduction coefficient, T, can now be calculated—including the deleterious effects of the load and frequency dependent eddy currents—by solving Eqn. (3) for T, i.e., $[(V/I - Z_e)z_x]^{1/2} = T$.

The procedure outlined above was carried through one time with the transducer operated at a representative drive-current amplitude and with a representative load. The process would likely need to be repeated if the magnetic bias point or the prestress of the transducer were changed. However, they remained constant for the experiments which are compared with model calculations in this communication.

It should be mentioned that a third method of estimating Z_e and T was tried, and it resulted in fairly reasonable approximations of the feedback control system behavior. One can measure V/I for the transducer, as run, perform a *linear* curve fit to the real and imaginary parts separately, and use the resulting empirical relations for $Z_e(f)$. These relations will include an approximation of the eddy current effects, i.e., the real part will be a function of frequency. One can then estimate T by solving Eqn. (3) as above, only this time using the experimental measurement of V/I. It is a small point, but when using either of the latter two methods of transducer parameter estimation, one would likely use the "unreduced" forms of Eqns. (8) and (9) for their model calculations.

Attention will now be paid to the effects of the feedback control system on the amplitudes of the harmonic accelerations. (Recall Eqn. (9) for a/a_d.) For the experimental "measurements" of this function, one test was run at a given current amplitude at a single frequency (e.g., 0.15 A @ 1000 Hz) without feedback control, followed by an otherwise identical test with feedback control. In each case, acceleration autospectral density functions were calculated over an extended frequency range (e.g., 0 - 10000 Hz) in order to measure the harmonics. The experimental "measurement" of a/a_d was calculated as the difference, in dB, between the uncontrolled and the controlled experimental measurements.

Figure 8 displays experimental measurements (X) and model predictions (line) for simple proportional feedback control of the transducer. The model used was that of Eqn. (9) for the reduction in disturbance (harmonic) acceleration amplitudes. Transducer parameters used in the simulation were obtained by the method of reference 2. For both experimental measurements (controlled and uncontrolled), the transducer was driven with a 0.25 amp, 500 Hz sinusoidal current, thus, the first disturbance/harmonic would be at 1000 Hz, the second at 1500 Hz, the third at 2000 Hz, etc. The largest discrepancies between model and experiment occurred at 4000, 5000, and 6000 Hz. The experimental measurements at these frequencies were in excess of 60 dB below the fundamental's amplitude; thus, while still above the noise floor, they are suspect due to the instrumentation's dynamic range. For this test the mechanical resonant frequency was approximately 3200 Hz. Note the 15 dB attenuation near resonance and the increase in amplitude of the disturbance accelerations for 5000 Hz and above, and for frequencies below 1000 Hz.

The effects of including a derivative controller are seen by comparing Figs. (9) and (8). Note that the differentiator improved the high frequency disturbance attenuation of the system. This trend was anticipated in the discussion below Eqn. (9). As in Fig. (8) the 4, 5, and 6 kHz experimental measurements in Fig. 9 were more than 60 dB down, thus they are suspect. Note, however, the substantial agreement between experiment and the model simulation.

Figure 10 shows the difference in system behavior ($||a/a_d||$) at two different values of differential feedback. For the figure, models were
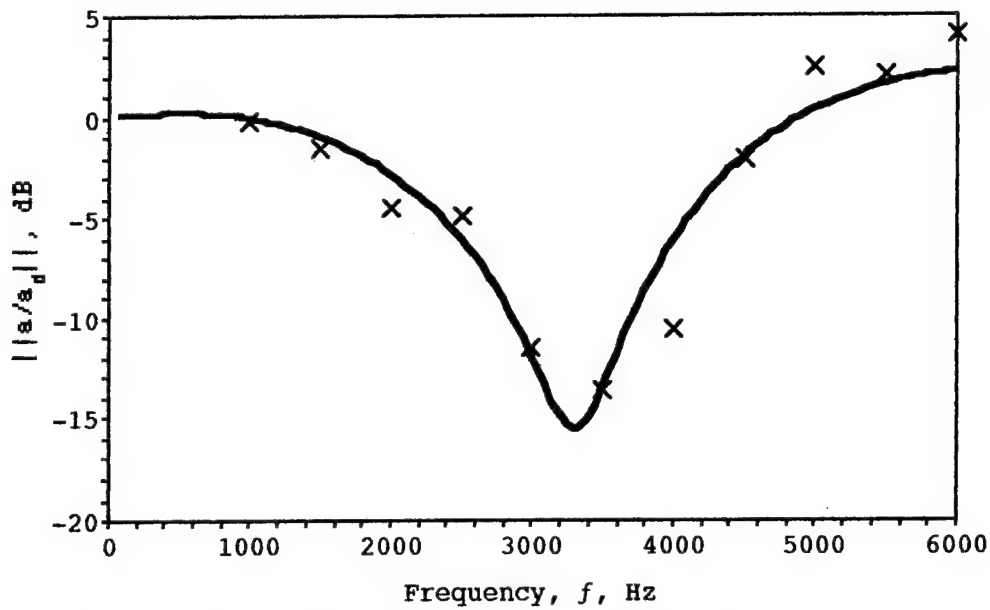
Figure 8. Output acceleration due to input disturbance accelerations for the case of simple proportional feedback control of the magnetostrictive transducer, k_p = 2.73 V/V. Model predictions are shown by the line, experimental measurements are indicated by Xs.
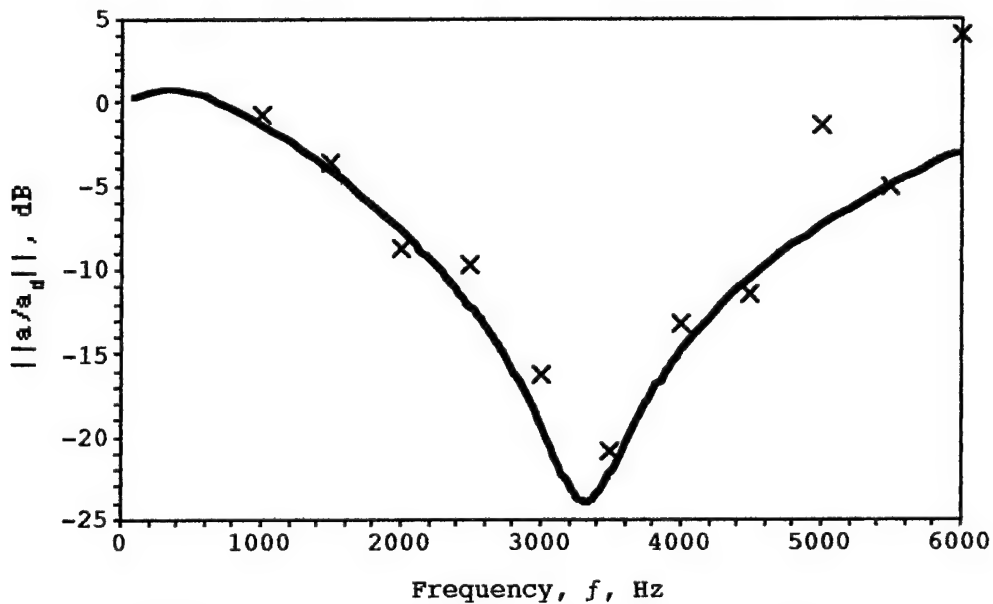
Figure 9. PD feedback control of magnetostrictive transducer, k_p = 6.2 V/V, $k_d \approx 90 \times 10^{-6}$ Vs/V.
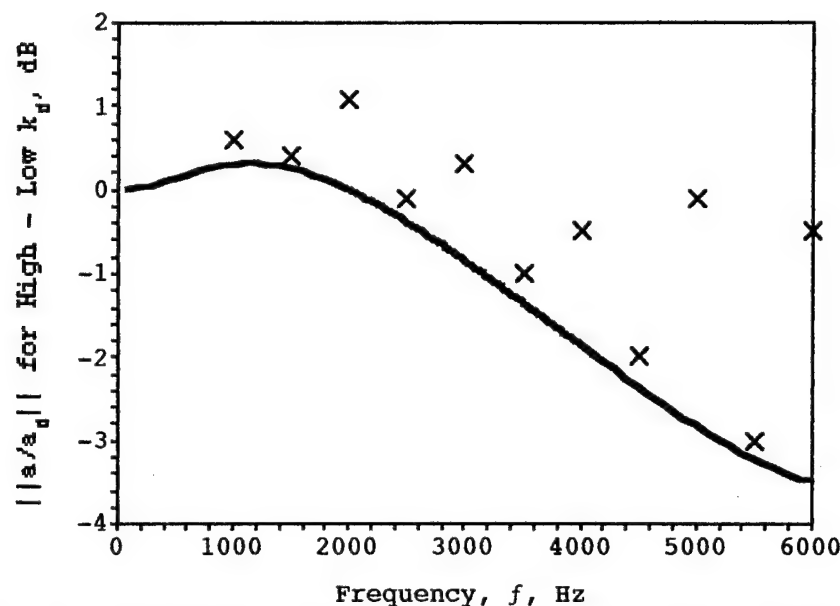
Figure 10. Model predictions (line) and experimental measurements (X) of the change in acceleration amplitude attenuation of harmonic frequencies due to a change in differentiator gain, k_d. Datums displayed were calculated from $k_d \approx 90 \times 10^{-6}$ simulations and measurements minus the values from $k_d \approx 8 \times 10^{-6}$ Vs/V simulations and experiments. For all cases, $k_p = 6.2$ V/V.

calculated for two different differentiator gains ($k_p = 6.2$ V/V for both tests), then the model for the low gain was subtracted from that for the high gain (the high gain version is shown in Fig. (9)). The experimental values were calculated in a similar fashion. For this plot, suspect experimental measurements (low original acceleration amplitudes) were, again, at 4, 5, and 6 kHz. As shown by the figure, there is substantial agreement between actual system behavior and the predictions of the modeling procedure developed in this communication. It is also apparent from the data that increasing the differential feedback increases the harmonic distortion at the lower frequencies and decreases the distortion as frequencies increase.

DISCUSSION

Now that some confidence exists that the models developed in this study yield predictions which resemble actual system behavior, some trends predicted by the models will be examined. It was mentioned previously that the filter on the accelerometer effected the system response appreciably. Its effects will be investigated. There was not an integrator in any of the implemented control systems of this study. The effects of adding an integrator will also be investigated. Figures 11 and 12 display the results.

The curves labeled "starting point" are for the PD system shown in Fig. 9. The "no filter" curves correspond to system behavior if the band-pass filter of Eqn. (10) had been removed (as if a low drift, low noise accelerometer and conditioner were used). The curves labeled "with integrator" show the effects of adding a modest amount of integration to the "no filter" control algorithm. (Integrators are usually high gain, first order low pass active filters. The integrator modeled here had the transfer function: 1/(s x 2.2 kΩ x 0.1 μF + 2.2 kΩ / 22 kΩ) x Summing Gain. The -3 dB point for this circuit was

171

approximately 90 Hz, i.e., it resembled an integrator (1/s) for frequencies greater than 90 Hz. As presented, $k_i \approx 16,500$ V/(sV).)

As shown in the figures, removing the filter would help immensely. It has the net effect of restoring the high frequency feedback signal. Incorporating an integrator into the controller would improve the system behavior at the lower frequencies. As shown in Fig. 12, the addition of the integrator and removal of the filter ensures that harmonic frequencies will be reduced over the whole frequency range of the study (it removed the characteristic hump below 1 kHz of the previous implementations).
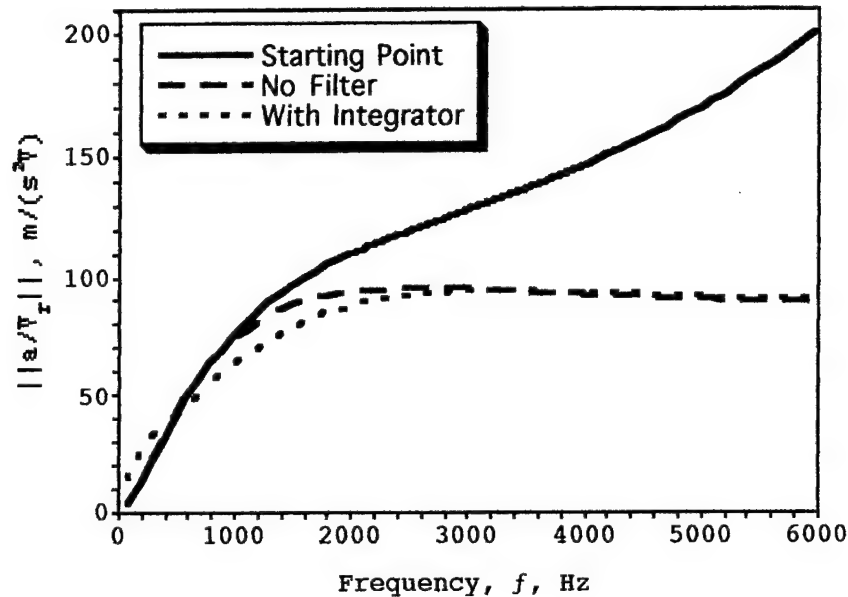
a)
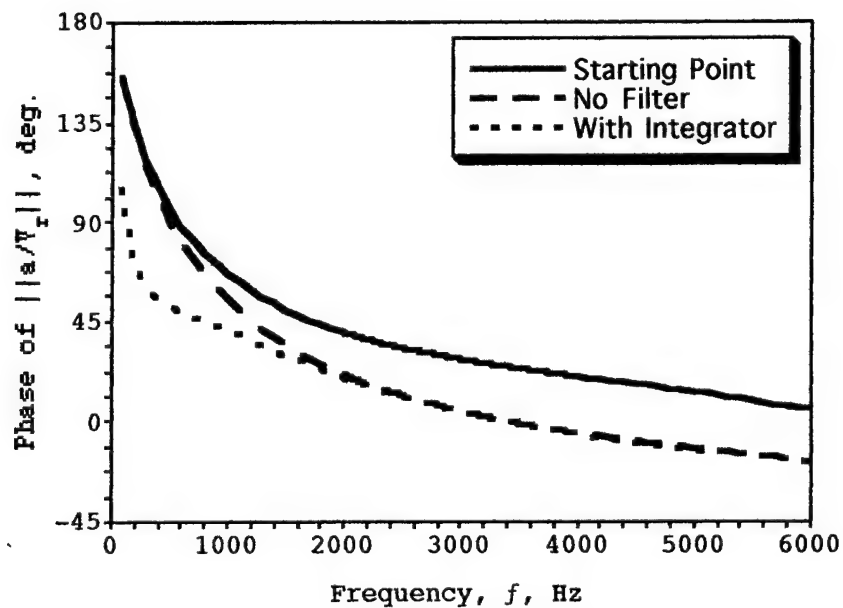
b)

Figure 11. Magnitude (a) and phase (b) for models of a/V_r showing the effects of a cleaner accelerometer/conditioner and then adding an integrator to the control algorithm.

172
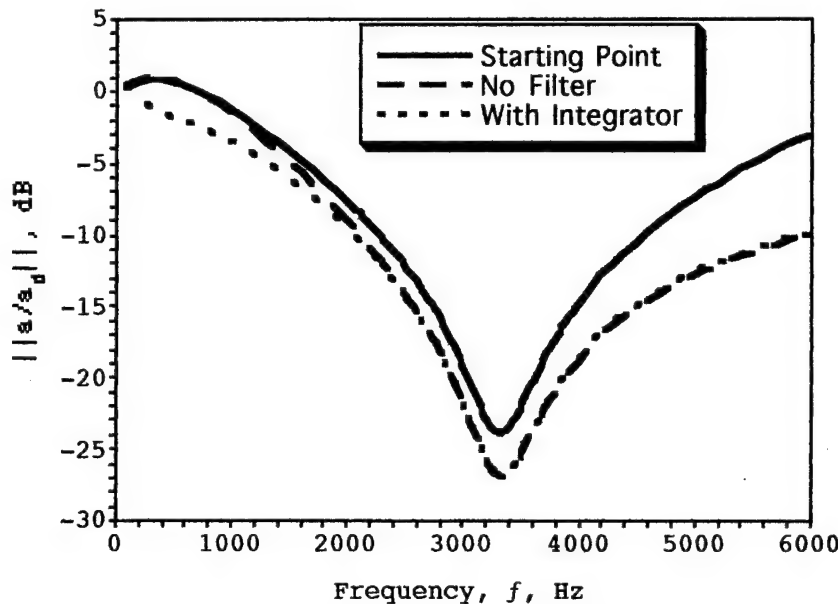
Figure 12. Model predictions of the output acceleration magnitude due to input disturbance accelerations. 0 dB = 1 m/s^2.

CONCLUSIONS & RECOMMENDATIONS

The addition of an acceleration feedback control system improves the linearity (reduces harmonic distortion) of the output of a magnetostrictive transducer. In one case, 32% harmonic distortion was decreased to 9% via simple proportional feedback control. This improvement translates to increasing the magnitude of the low distortion, linear range displacements by a factor of approximately 15 (when compared to the uncontrolled transducer). Thus, simple feedback control has been demonstrated to increase the "linear range" of transducer outputs. Harmonics occurring at frequencies near the mechanical resonant frequency of the loaded transducer show the greatest attenuations (approaching 30 dB in this study). Differential feedback tended to increase harmonics at the lower frequencies and decrease those occurring at the higher frequencies. Modeling implies that adding an integrator to the control algorithm would tend to reduce the low frequency harmonics.

A method for modeling analog feedback control using magnetostrictive transducers was presented. The method assumed the transducer to be a 1-DOF linear system described by the classic pair of linear simultaneous transduction equations. These equations were used to derive input-output relationships for the transducer. These relationships were then used in elementary linear systems control theory to formulate models for the closed-loop system. The harmonic frequencies present in the transducer's output were assumed to be disturbance inputs. Emphasis was placed on the case of driving the transducer with a voltage-control amplifier (as opposed to a current-control amplifier). Relations were developed for modeling output acceleration per input reference volt and output acceleration due to input disturbance accelerations. The first was shown to offer reasonable approximations of real system behavior. The latter was useful for predicting how the harmonic output accelerations behaved in response to control system effects. In both cases, the models were shown to agree with experimental measurements to within ± 3

173

dB. Larger variations occurred between models and experiments when the experimental measurement became suspect, i.e., when the measurements approached the limits of the dynamic range of the instrumentation.

In this study, parameters pertaining to the control circuitry were well defined. The same cannot be said for transducer parameters. As with most modeling endeavors, the better the input, the better the output. The best model results were obtained using parameters derived from a magnetostrictive transducer modeling technique that included the deleterious effects of eddy currents in its estimates of the blocked electrical impedance and the transduction coefficient. However, reasonable closed-loop system performance estimates ("reasonable" for simulations involving Terfenol-D) were obtained even when transducer parameters were estimated by the simplest of methods. Thus, closing the loop has improved the quality of the predictions of system behavior—especially when compared with attempts at predicting behavior of an open-loop transducer. It is recommended that any application involving Terfenol-D as the motion source include a feedback system. It improves the behavior of the system and it improves the engineering predictions of system behavior, when compared with the predictions of open-loop transducer systems.

The techniques developed in this study are applicable to general vibration control applications that employ magnetostrictive transducers. For example, if one were trying to isolate a platform from vibrations, the reference voltage in this control system would be set at zero (no accelerations are desired) and the actuator system would attenuate accelerations as shown in Figs. 8, 9, and 12.

Other feedback systems can be designed using the approach detailed in this communication. It has been demonstrated here that one can use Eqns. (2) - (6) to model the transducer's behavior in the closed-loop system.

REFERENCES

1.   Hunt, F. V., "Electroacoustics: The Analysis of Transduction, and Its Historical Background," Acoustical Society of America, Woodbury, NY, 1982.
2.   Hall, D. L., "Dynamics and vibrations of magnetostrictive transducers," a PhD Dissertation, Iowa State University, Ames, IA, 1994.
3.   Clark, A. E., Teter, J. P., Wun-Fogle, M., Moffett, M. B., Lindberg, J., "Magnetomechanical Coupling in Bridgman-Grown $Tb_{0.3}Dy_{0.7}Fe_{1.9}$ at High Drive Levels," J. Appl. Phys., Vol. 67, pp. 5007-9, 1990.
4.   Clark, A. E., "Magnetostrictive rare earth-Fe_2 compounds," Ch. 7 of *Ferromagnetic Materials*, Vol. 1, E. P. Wohlfarth Editor, North-Holland Publishing Co., Amsterdam, pp. 531-589, 1980.
5.   "Measurements of ultrasonic magnetostrictive transducers," International Electrotechnical Commission IEC Report, Publication 782, 1984.
6.   Hall, D. L., Flatau, A. B., "One-Dimensional Analytical Constant Parameter Linear Electromagnetic-Magnetomechanical Models of a Cylindrical Magnetostrictive (Terfenol-D) Transducer," J. of Intelligent Materials Systems and Structure, Technomic Publ. Co., Inc., Lancaster, in press.

174

7.   Horowitz, P., Hill, W., *The Art of Electronics*, 2nd Ed., Cambridge University Press, Cambridge, pp. 224-5, 1989.
8.   "Typical Material Properties," Edge Technologies, Inc., Ames, 1988.
9.   James, M. L., Smith, G. M., Wolford, J. C., Whaley, P. W., *Vibration of Mechanical and Structural Systems: With Microcomputer Applications*, Harper & Row Publishing, Inc., New York, 1989.
10.   Franklin, G. F., Powel, J. D., Emami-Naeini, A., *Feedback Control of Dynamic Systems*, Addison-Wesley Publishing Co., Reading, 1986, pp. 113-8.

REMOTE HYDROGEN
SENSING SYSTEM
FOR THE
SPACE SHUTTLE SYSTEM

BY

Billy R. Stover, Lead Engineer
Lockheed Space Operations Company
Hazardous Warning Systems

and

Greg Hall, Design Engineer
National Aeronautics and Space Administration
Transducer Development
Kennedy Space Center, Florida

Abstract:

The most hazardous operation performed at Kennedy Space Center is the loading of liquid Hydrogen onto the Space Shuttle and External Tank. One of the most valuable systems used to monitor this hazardous operation is the Remote Hydrogen Leak Detection System. The current system is an enhanced second generation design. This design is the result of the past fourteen years of lab testing and field experience. The design incorporates both technology changes and improvements and increased system requirements for real time troubleshooting.

The Remote Hydrogen Leak Detection System design allows for the detection of Hydrogen from purged umbilical cavities connected to the Space Shuttle. These umbilical cavities because of their design and location make it impossible to physically mount detection hardware into the areas of concern. This system's leak detection technology requires the presence of Oxygen for the Leak Detectors to operate. The umbilical cavities use Helium and Nitrogen as the purge media. This situation created the need for the Remote Hydrogen Sensing System. The system uses sample lines from the various purged umbilicals to transport a sample to a fixed location where the sensing instrumentation performs the analysis. The result of the analysis is transmitted to the Engineering control room for real time monitoring during actual Cryogenic loading operations.

The original design primarily was based on Lab results from tests performed to determine ranges and mixing ratios for optimum leak detector operation. Two ranges for Hydrogen detection were selected. These detection ranges were based on safety factors used to control the hazard level of Cryogenic loading and the Lower Flammability Limit(LFL) of Hydrogen. One range selected for operation was zero to four percent. This range is used by detectors that are sampling for Hydrogen in Air or Nitrogen environments. The second range selected for operation was zero to six percent. This range is used by detectors that are sampling for Hydrogen in a Helium environment. The same Leak Detector is used for both ranges (4% and 6%) where the signal output is mathematically treated to allow for the range differences. Mixing ratios became the hardest technical hurdle to overcome. The mixing ratio is the volumetric ratio of sample gas mixed with ambient air. It was discovered that certain mixing ratios could produce incorrect responses. From Lab testing and field uses it was determined that the composition of the sample and sampling pressures had significant impacts on the performance of the detector.

The current design incorporates the original lab testing results and the practical field experiences and knowledge gathered during the past fourteen years. Most of this practical knowledge helped determine how much and what kind of control and health measurements were required to aid System Engineering in real time situations. Controls were implemented that allow for Calibration and Test Gasses to be remotely selected to verify instrumentation accuracy. Health measurements were implemented that allows System Engineers to evaluate the sampling quality in real time for determination of data accuracy. Lastly the design incorporated remote control for real time manipulation and troubleshooting of the system during Hazardous Operations(Cryogenic Loading Operations); this prevents exposing personnel to a hazardous situation(Red Crew operation).

The Remote Hydrogen Leak Detection System in use at Kennedy Space Center is a significant tool to aid in monitoring the most hazardous operation performed in launching the Space Shuttle. The current system is the result of extensive Lab testing and fourteen years of field experience. New data and knowledge are still being learned as this system continues to fulfill its mission.

177

System Overview:

The Remote Hydrogen Leak Detection System is comprised of four individual cabinets. Two of these cabinets are located on the Launch Pad, one each on the Fixed Service Structure(FSS) and Rotating Service Structure(RSS). The remaining two cabinets are located inside a Mobile Launch Platform(MLP). The 6145 cabinet on the FSS samples the External Tank Ground Umbilical Carrier Plate(ET GUCP). The 6292 cabinet on the RSS samples the Orbiter Midbody Umbilical Unit(OMBUU). The two cabinets inside the MLP sample various areas within the LH2 Tail Service Mast(TSM), the LH2 17 inch External Tank Orbiter Disconnect, and the LH2 T-O Umbilical Carrier Plate. The 6407 cabinet samples two distinct areas within the LH2 T-O Umbilical Carrier Plate. The 6660 cabinet samples two distinct areas within the TSM and two specific positions on the LH2 17 inch ET/Orb Disconnect. Three cabinets are specifically used to support ET Cryogenic Loading operations(Reference the above Figure). The three cabinets are the 6145, 6407, and 6660. A fourth cabinet(6292)not shown is used only to support Fuel Cell Cryogenic Loading operations. The 6145 cabinet and 6407 cabinet leak detectors are zero to six percent detectors that sample Hydrogen from a Helium purged cavity. The 6660 cabinet leak detectors are zero to four percent detectors that sample Hydrogen from both Air and Nitrogen environments. These three cabinets are activated prior to beginning the ET Cryogenic loading of Hydrogen.

Each cabinet operates independently, but together completes the entire detection system. Cabinet activation involves turning on the sampling system, verifying leak detectors have power, and verifying the system indicates nominal responses. Activating the sampling system includes powering the Mass Flow Controllers and allowing a minimum five minute warm-up followed by activating the sample pumps. Each leak detector has two associated Mass Flow Controllers that control the mixing ratio of the sample and air. The reliability and data accuracy of the operation depends on the mixing ratio. The sample is drawn from the umbilical or cavity to the cabinet and then mixed with air prior to entering the leak detector's mixing chamber. The leak detector responds to the mixture within the mixing chamber. Each leak detector provides continuous data at a frequency of one sample per second. From continuous sampling a standard leak signature is recorded and data analysis provides correlation to an event.

REMOTE LEAK DETECTOR / HUMS LINE SCHEMATIC
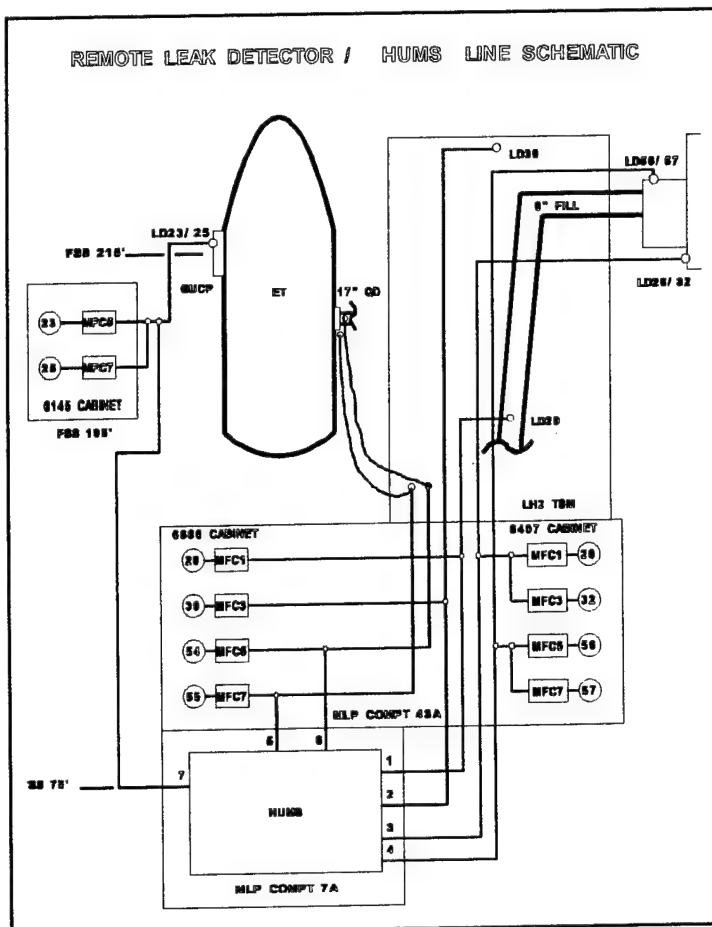
Cabinet Operation:

The cabinets all operate by drawing a known amount of sample through one quarter inch stainless steel tubing (0.25in OD by 0.187in ID). The sample is drawn from a purged cavity at a volumetric flowrate of 4.0 slpm per sensor. The purged cavities are all at 0 to 5 inches of water positive pressure. The sample is drawn by a vacuum pump from the sample point within the purged cavities to the cabinet at distances ranging from 50 feet to 150 feet. The sample enters the cabinet and is controlled by the sample mass flow controller which is then allowed to mix with the equivalent volume of air. This combination is mixed in the mixing chamber at the sensor. The sensor reacts to the mixture and generates a response. The mixture is continuously renewed by the influx of new sample and air. The old mixture is evacuated and dumped external of the cabinet through the exhaust system. All of the leak detectors used to monitor the purged cavities are sensor redundant. This means the same sample source is analyzed in parallel by two sensors at the same time. The sample is split at the cabinet input bulkhead. The total volumetric flow through these one quarter inch sample lines is 8.0 slpm. Two of the four cabinets have redundant sensors. The 6145 cabinet that monitors the ET GUCP and the 6407 cabinet that monitors the LH2 T-0 Umbilical Carrier Plate are the two cabinets. The remaining two cabinets 6292 and 6660 have four separate sample inputs for four separate sensors.
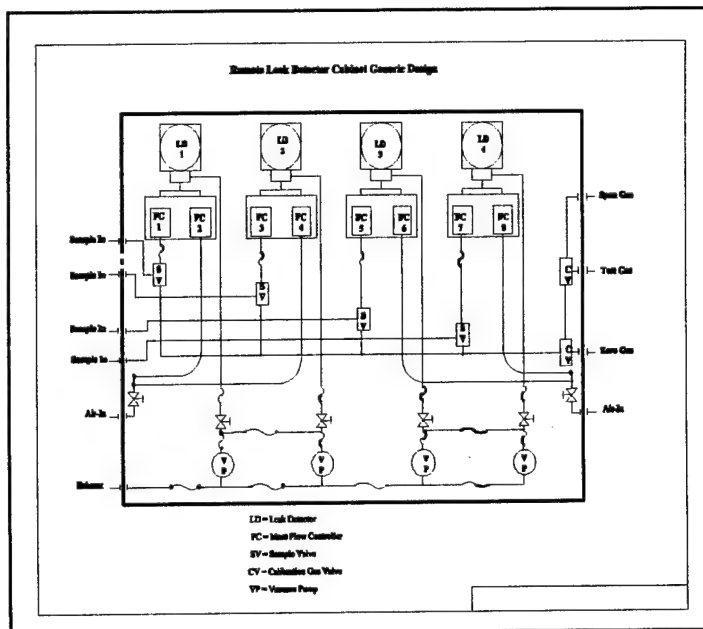
The mixing chamber is a KSC design to minimize dead volume and maximize response time. The sample pumps are Gast Model PN:DOA-P101-FB with a pumping capacity of 1.8 Standard Cubic Feet per Minute. This combination of mixing chamber design, Sample Pump, and sample tubing enhances the mass flow controllers operation thus increasing the data accuracy and reliability of the sensor. The sampling system design is low cost and low maintenance with high reliability.

Leak Detector:

The leak detector is a Detronics Model 400N Combustible Gas Detection Transmitter with a Detronics Combustible Gas Sensor. The leak detector technology is a catalytic reaction on an electronic RTD element within a Wheatstone Bridge configuration. The Detronics Combustible Gas Sensor Element contains two legs of the Wheatstone Bridge. The sensor contains an active electronic element and a matched reference element. The active element contains Platinum that creates the catalytic reaction in the presence of Hydrogen. This catalytic reaction causes the resistance of the electronic element to increase. This increase creates an imbalance in the Wheatstone Bridge thus creating a current signal. The remaining two legs of the Wheatstone Bridge are contained in the Model 400N Combustible Gas Detection Transmitter. The transmitter contains all the signal processing and transmitting functions. The model 400N is designed specifically for NASA. The "N" designation identifies additional signal processing and voltage isolation that is required in a launch environment. The additional signal processing simply converts

179

the standard 4 to 20 mA signal generated by the sensor to 0 to 5 volts DC. The voltage isolation is in place to prevent sensor and system crosstalk. The leak detector supports two different operating ranges with the same sensor and the same output signal. The two different ranges are created by a mathematical interpretation of the signal output The 0 to 4 percent sensor uses the conversion factor : 1 VDC is equal to 10,000 ppm(1 percent). The 0 to 6 percent sensor uses the conversion factor : 1 VDC is equal to 15,000 ppm(1.5 percent). All sensors use a 1 volt offset where 0 ppm is equal to 1.00 VDC. The full operating range of the 0 to 4 percent sensor is -10,000 ppm to 40,000 ppm with a data resolution of 200 ppm. This data resolution is limited by the data interpretation capabilities of the Launch Processing System(LPS). LPS allows the user 250 bits per data measurement which for the 4 percent sensor converts to 200 ppm per bit. The 6 percent sensors have data resolution of 300 ppm per bit with an operating range of -15,000 ppm to 60,000 ppm.

The basic operation uses the transmitter legs of the Wheatstone Bridge to set the calibration points of the sensor in reference to the sensing element and reference element. Once this is set the unit is operational and data is considered real. The vendor recommends that each leak detector be calibrated every 60 to 90 days depending on the oper-ating environment. Standard operating procedure at KSC requires that each leak detector be calibrated within 4 to 6 weeks of their support operation. This is required due to the operating environment at KSC. If either component is changed, calibration must be performed to balance the new Wheatstone Bridge. Lastly, it is critical to calibrate the leak detector in the media from which the sample is composed i.e. Helium, Nitrogen, or Air. The difference between Air and Nitrogen is negligible but, the difference in sensor response between Air and Helium is enor-mous. The sensor elements are computer matched by the vendor to provide optimum performance with maximum stability and minimum drift in the desired sample media. The leak detector has to be calibrated in the desired sample media for any sampling affects to be eliminated.

Mass Flow Controllers:
The Mass Flow Controllers are Sierra Model 840 Low Flow Body 0 to 10 Standard Liter per Minute units. The Flow Controllers perform three primary functions for the Remote Hydrogen Sensing System. The first function is the control of the sample to air mixture ratio. The second function is to minimize input sample pressure affects on the sensor. The third function is to provide real time monitoring of the actual flow during operations. The first function of the flow controllers is the most critical to the operation of this system. There are several oper-ating factors that have to be accounted for the Mass Flow Controllers to operate properly. The input pressure or the differential pressure across the flow controller must be known. If the input pressure or differential pressure is not sufficient the solenoid valve within the mass flow controller will not regulate the sample or air flow properly. The solenoid controls the flow accurately when its control voltage is between -5 to-10 volts DC. The full control voltage is 0 to -15 volts DC where 0 volts is full close and -15 volts is full open. With the controllers powered on without flow, the control voltage will be -15 volts DC. Once flow is established the control voltage should drop to the -5 to -10 volt DC range. If the control voltage is not within range, then one of two conditions exist. First, the input pressure to the Mass Flow Controller may be insufficient. Second, there may be insufficient flow to the flow controller for it to control at the desired set point. For example, the flow controller is set to regulate flow at 5.0 slpm and the total flow being provided is equal to or less than 5.0 slpm the flow controller will drive the solenoid full open(-15 volts DC) trying to control at the desired flow rate. With the con-troller full open the Hydrogen sensor is responding more to variations in the sample pressure than actual changes in Hydrogen concentrations. With the controller trying to control flow right at the set point, its response will show up as an oscillation of the Mass Flow Controller's

signal out and possibly as a shift of the Hydrogen sensor's baseline. This information and knowledge is critical in multiple flow situations where sample or air is common to more than one flow controller.

Mixing Ratio:

The system's detection limits, accuracy, reliability, and stability are largely dependent on the Mixing Ratio. The mixing ratio is the volumetric ratio of sample to air. Extensive testing of various ratios and varying sample concentrations at a constant mixing ratio generated empirical graphs that were evaluated to determine the best operating mixture for NASA's application. The data generated from this testing paralleled testing later performed by the vendor on different gasses. Referencing Graph 1 there is a distinct point where the mixing ratio will negatively affect the sensor's output thus its data accuracy and reliability.

Sample to Air Ratio
2, 4, 6% Hydrogen in Helium
Ratios in Volume (Actual corrected Sample/air)

Note: These Mixture ratios are in volume. The voltage data from the sample flow controller output was placed into the equation. -0.017*V^3+.193*V^2+2.802*V-0.012 where V is the sample flow controller voltage output.

The equation was derived by taking a third order curve fit of the average data from ten flow controllers. This data was the actual He flow through controllers calibrated in N2 and setpoints set from 0 to 5 Volt

D-7 1

Graph 1

As shown on Graph 1, the optimum mixing ratio is between 2 to 3.5 parts sample to 1 part air. This is one hundred percent operating efficiency of the sensor with the sensor operating at its lowest gain setting. This would provide the sensor its best signal. The problem with operating the sensor at the optimum mixing ratio is falling on the right side of the curve due to flow measurement error. The effect of sampling on the right side of the curve in Graph 1 could be disastrous. A high Hydrogen leak could occur and the sensor would only reflect a small increase in measured leakage. The right side of the curve shows where the sensor loses its ability to correctly measure the amount of Hydrogen present in the sample. As shown on Graph 1 the further right the data goes the less response the sensor generates for the same sample source. From Graph 1, the mixing ratio determined to be the maximum allowable for use was 3:1 sample to air for the six percent sensors in a Helium background. Further testing was completed to determine how far to the left of the optimum mixing ratio would be of best use for the Space Shuttle's application.

181

Graph 2

LD LINEARITY
SENSOR CAL @ 6% H2/HE=5VDC
SENSOR RECAL'ED AT EACH FLOW RATIO
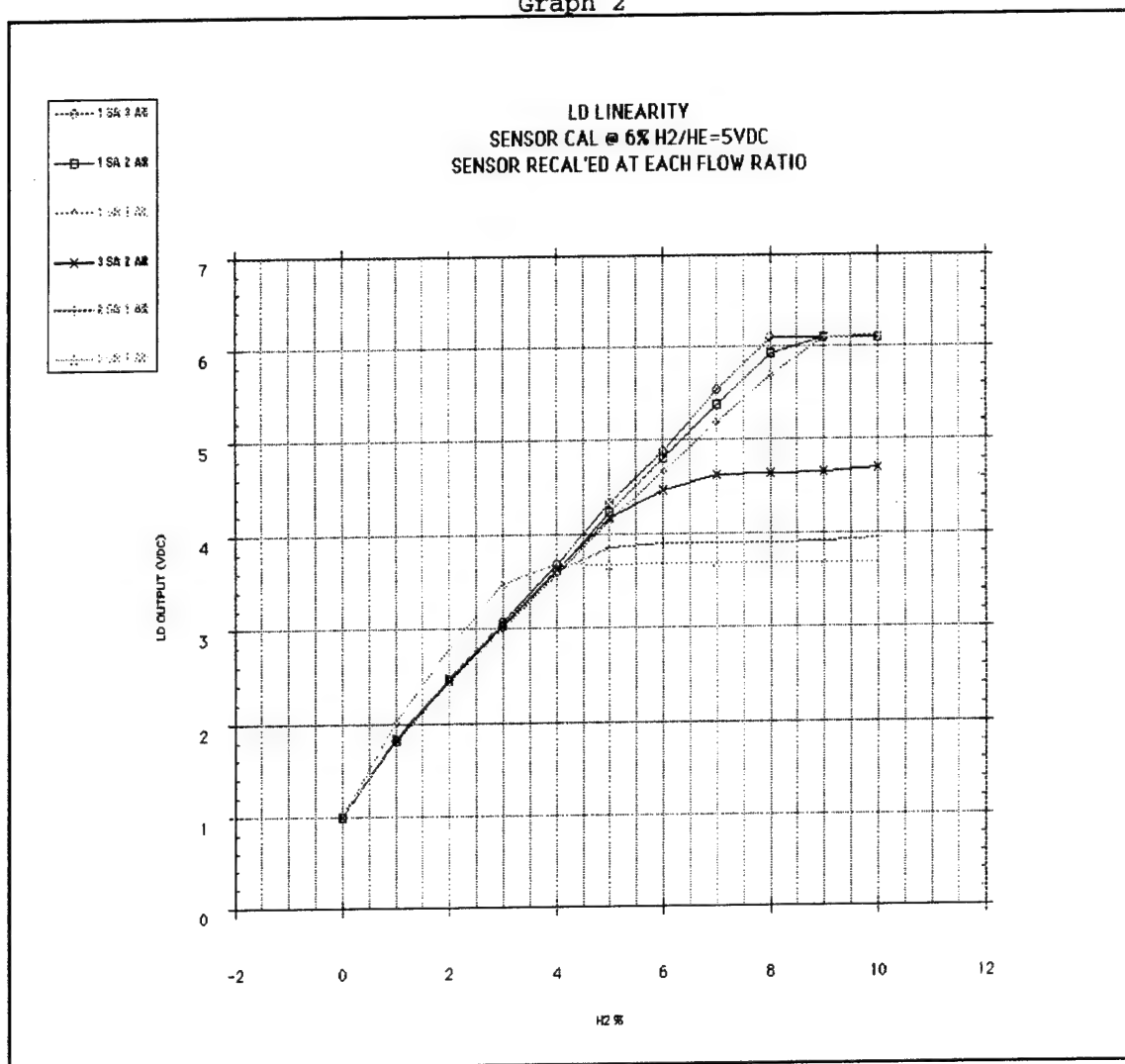
As shown on Graph 2 there is a distinct breakover point in the sensor's response between the 1:1 to the 1.5:1 sample to air ratio. This break-over point is significant because the indicated voltages for the 3SA:2Air, 2SA:1Air, and 3SA:1Air flow ratios are not representative of the actual Hydrogen concentration present at the Hydrogen sensor once the actual concentration exceeds 4 percent. From this graph the 1:1 mixing ratio appears to be the best suited for the application. Lastly from Graph 3 further testing with varying sample concentrations shows that the 1:1 mixing ratio was acceptable for NASA KSC's application. During the testing and later data analysis different mixing ratios could have been chosen. Any of the mixing ratios that were less than 1:1 sample to air, where the sample volume was decreased, would also be acceptable. The reasons for choosing the 1:1 ratio ties back into the sensor, Mass Flow Controllers, and the sampling system operation. The following is a list of advantages to using the 1:1 mixing ratio. This ratio provides the most stable data over the sensor's operating range. The ratio provides a safety margin for flow measurement error that will still keep the sensor operating on the left side of the curve in Graph 1. By using this higher sample ratio it increases the overall input pressure and flow into the Mass Flow Controllers.

Graph 3

SENSOR RESPONSE
CAL @ 6% H2/HE=5 VDC
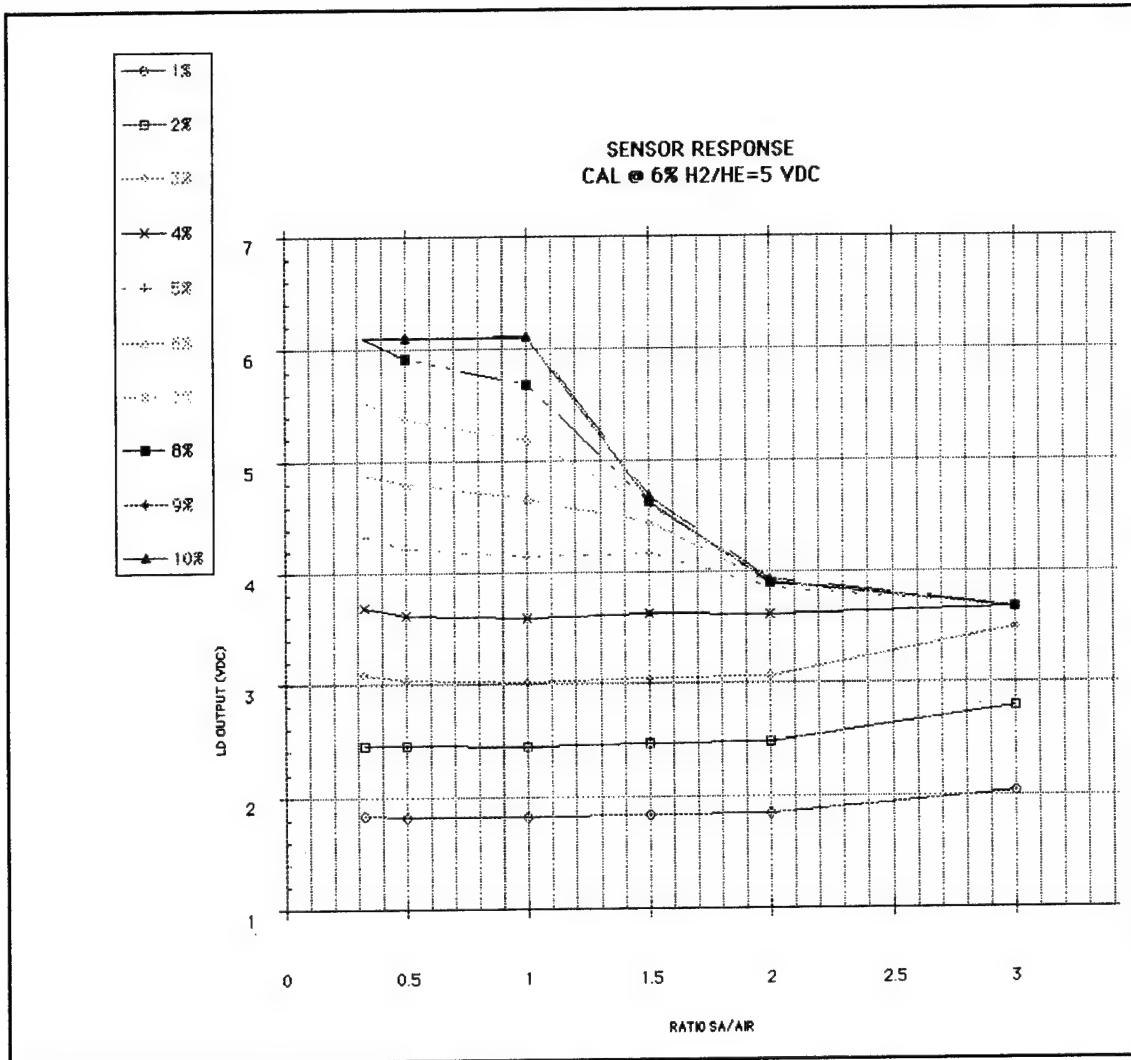
Summary:
The Remote Hydrogen Sensing System in use at the Kennedy Space Center adequately serves to monitor the hazard level of the Cryogenic loading of Hydrogen. The system is the result of many years of lab and field testing and practical experience. The system has optimized the best of each of the individual components. Testing is still ongoing to continue the improvements and innovations possible through this type of system. This type of system can be used for many applications not pertaining to Hydrogen. The knowledge and lessons learned during this system's evolution should make the conversion to other applications fairly easy. The existing system is accurate, reliable, durable, and low cost. This system provides a simple means for continuous monitoring of a hazardous operation.

SESSION 3

TUTORIAL

SIGNAL CONDITIONING FOR RESISTANCE-BASED TRANSDUCERS

by Peter K. Stein, Director, Short Courses
The Engineering and *The Dynamics of Measurement Systems for Test & Evaluation*
5602 East Monte Rosa, Phoenix, AZ 85018

Telephone & Telefax Numbers: (602)-945-4603. (800)-MEASurement SYStems, in the U.S.

0.0 INTRODUCTION

The type of signal conditioning and the manner in which a test is conducted will totally determine the data which are harvested. This brief survey hits the high points of how the test procedure and the choice of signal conditioning will affect the data.

Some conventional definitions and concepts, even though raised to international standards, may be pure nonsense, obscuring rather than clarifying these questions.

Thus the definition of *Thermal Output* is totally inadequate. For the same process being observed with the same transducer the choice of signal conditioning will yield totally different characteristics for *Thermal Output*, which may be apart by orders of magnitude. The *Unified Approach* presented here will clearly identify the reasons for the discrepancies.

Three main features which distinguish signal condition for impedance-based transducers from other types of signal conditioning are:

1.0 THE INTERROGATING INPUT (BRIDGE SUPPLY):

Impedance-based transducers and strain gage-based ones in particular are non-self-generating and require an external, design-controlled input to interrogate the impedance-changes stimulated by the Measurand. This input is often called the *bridge supply* if a bridge circuit is used.

1.1 *Amplitude:*

The amplitude of the supply voltage affects the self-heating of the transducer. For utmost versatility this amplitude should be variable to accommodate strain gages or resistance thermometers on bad heat conductors such as composite materials, plastics, wood, or very thin sections of aluminum, steel, etc., or very small transducers where space limitations prevent good heat transfer. It is preferable if such controls are recessed so that inadvertent changes in bridge supply can be avoided.

Since it is the amplitude at the transducer bridge input terminals which must be kept constant, six-wire arrangements are possible, which include two *Remote Sensing* leads. Their function is to keep the signal conditioning output amplitude at whatever level is necessary to maintain the transducer input amplitude constant. This is one method of suppressing the effects of long lead wires.

A *Zero Amplitude* or *Bridge Power Defeat* position on the control should be available, either manually adjustable or computer programmable. When bridge excitation is zero and the transducer still shows an output, then self-generating voltage noise levels have been documented and must be suppressed before any data are acquired.

Amplitude Polarity Reversal is an alternate method of documenting such voltage noise levels. When both input and output polarities are reversed simultaneously, any changes in output represent such noise levels.

1.1.1 Constant Voltage:
Constant voltage excitation is most commonly used for strain gage based transducers. The voltages typically vary from 0 to 15 volts for transducer resistances from 120 ohms to 5000 ohms.

1.1.2 Constant Current:
Constant current excitation is often used to avoid problems with long lead wires when the *Remote Sensing* option is either not available or not desired.

1.1.3 Internal Impedance:
A variable resistor in series with the bridge supply voltage is sometimes used as a *Gain Control*, which makes the equivalent internal impedance of the bridge power supply variable. For precision transducers temperature compensated for sensitivity with temperature transducers in *series* with the supply voltage – i.e. *Modulus Compensated*, the internal impedance of a voltage supply must be close to zero and not variable, or else the compensation is compromised. The series-resistance gain-control technique must be avoided for such transducers.

For current supplies the internal impedance should be close to infinity. This feature is important for precision transducers temperature compensated for sensitivity with temperature transducers in *parallel* with the current supply. Any gain control mechanism which produces a variable equivalent internal resistance of the current source should be avoided for those types of transducers.

1.2 *Wave Shape.*

The wave shape of the bridge supply voltage or current is critically important to the performance capabilities of the transducer and signal conditioning.

1.2.1 DC: The majority of signal conditioning power supplies are DC. They suffer from one major disadvantage which can be circumvented if the recommendations in 1.1 are followed. The problem is that voltages generated within the transducer due to thermal, electrical, magnetic, triboelectric, or strain-induced causes cannot be separated from the voltages due to the interrogated resistance changes. This problem is particularly severe in vibration tests involving electromagnetic exciters and in all pyroshock, explosion and impact tests. In all of those tests there are noise-voltages stimulated which occupy the same frequency range and time scale as the signals and are correlated with the signal. Unless the *Zero Amplitude* control on supply amplitude is invoked *during* the test, such noise levels can neither be documented nor suppressed.

1.2.2 Sinusoidal: Sine wave excitation is commonly used for capacitively and inductively based transducers, but also often with resistively based ones. The main advantage of sine wave excitation is that all voltage noise levels can be suppressed with appropriate output filtering so that strain-induced voltages, thermally, magnetically, electrically, etc.-induced voltages are automatically suppressed.

Thus in all strain-gage-based transducers the so-called *Thermal Output* will be quite different for sine-wave-fed transducers than for DC-fed transducers since thermoelectric and other voltage effects are suppressed by the sine-wave carrier. This makes the definition of *Thermal Output* as commonly accepted, useless.

The disadvantage of sine wave fed systems is their sensitivity to capacitive unbalance as possibly produced by cables during a test unless rather sophisticated carrier systems are used.

1.2.3 Pulse Train: Pulse-train-fed bridges are far less sensitive to cable capacitance effects than sine wave systems, and also permit the filtering of all voltage noise levels of the types mentioned above. Furthermore their *peak-to-peak* to *rms* ratio is [1/duty cycle of the pulse train] and hence adjustable. For self-heating problems such as in resistance thermometers, very small strain gage based transducers, strain gages on bad heat conductors, etc., pulse-fed signal conditioning is ideal to avoid heat generation while maintaining output levels.

In some commercial signal conditioning the choice between DC-fed, Sine-Wave-fed and Pulse-fed bridges is computer programmable as is the choice between constant current or constant voltage excitation.

1.2.4 Frequency: The frequency of the sine wave or pulse train will be dictated by the frequency response requirements of the measurement system. The usual *Sampling Criteria* also need to be obeyed. In general, the carrier frequency needs to be higher than 3 to 10 times the maximum signal frequency of interest. Some commercial signal conditioning have provision for changing the carrier frequency.

2.0 THE BALANCING CIRCUIT

Signal conditioning units divide into two major groups: those with provision for initial balance and those with no such provision.

2.1 *No Balancing Circuit*

In large, multi-channel data handling systems, the system often stores the initial unbalance of each channel and then subtracts that value from subsequent readings to acquire the data. Such systems suffer from the problem that any changes in excitation voltage or current, producing changes in system gain (sensitivity, transfer ratio, calibration factor) will produce zero shifts. An interactive link between gain controls or amplitude control of the interrogating input and the stored initial zeroes is required to avoid that problem. Some commercial units exhibit this feature.

To avoid excessive self-heating of transducers, the excitation voltage or current must sometimes be changed *during* a test, which is when the above problem is the most severe.

2.2 *Balancing Circuits*

There are two major families of balancing circuits each suffering from its own disease. All balancing circuits should have a disconnect switch. In Autozero systems, which automatically maintain balance, an Autozero-defeat switch is desirable.

2.2.1 Resistance Injection: A resistive balancing network such as the common T-type (slide wire and limiting resistor) for example, will shunt two arms of the transducer bridge and may produce calibration changes (gain changes) during the balancing operation. They may also produce changes in linearity, zero shift vs. temperature compensation, transverse sensitivity, and common mode rejection ratio. This effect varies from 0.1% to 5% in commercial units and should be

evaluated. A switch which disconnects the balancing circuit will prevent such errors in cases where the utmost data validity is desired.

2.2.2 Voltage Injection: Instead of balancing the *Bridge* itself, as the *Resistance Injection* scheme does, the *Voltage Injection* scheme balances the *System* by injecting a voltage in series with the bridge output to produce a net zero output from the *System*. The voltage source for such an injection should be linked with the system gain control or bridge supply amplitude so that any changes in those will not produce zero shifts. See also 2.2, and for the same reason.

2.2.3 Documenting Overloaded Transducers with Disconnected Balancing Circuits

The first sign of an overloaded transducer is a zero shift. Such transducers will have degraded performance such as for zero vs. temperature compensation, stability, creep, linearity etc. The best way to detect overloaded transducers is to check their output for zero input. This can only be done if the balancing circuit is disconnected or is in exactly the same position as when the original transducer zero was determined, a more difficult requirement. It is also necessary to determine the as-delivered initial zero for each serial number transducer since transducer manufacturers usually do not provide serial-number-specific data.

3.0 *Step Input "Calibration"*

System "Calibration" should be possible by means of step inputs. These serve two distinct purposes: Amplitude Calibration and Frequency Response Documentation.

3.1 Amplitude Calibration:
Two major methods of injecting signals which serve to calibrate the measurement system are commercially available.

3.1.1 Resistance Injection: *Shunt Calibration* is almost universally used for resistance-based transducers. A precision resistor of known value is shunted across one arm of a bridge or across the strain gage or resistance thermometer or other known resistance. The known resistance change thus produced serves as a "calibration signal" and produces a step output from the measurement system. From this calibration signal when combined with the *transducer calibration*, which must be available, a *system calibration* can then be determined.

If possible three such resistors should be available. It is then possible to verify system

performance not only for amplitude response (calibration) but also for linearity since three "calibration" points are available. Resistance injection can produce positive and negative outputs. Both should be available to check the system calibration and linearity from the operating point both *down* into the region from which one has just come, and *up* into the region into which one is headed, warning, perhaps, of up-coming non-linearity problems before the are actually encountered during a test.

3.1.2 Voltage Injection: Injection voltage steps or square waves (i.e. repeated steps) are another popular calibration method. It is one step further removed from the transducer calibration than the resistance-injection and hence burdened with higher tolerances. The system frequency response determination is also more difficult since it depends on the location of the voltage step injection.

3.2 Frequency Response Documentation:
The response of the *entire measurement system* except for the input transducer itself, can been documented by the Resistance Injection procedure. For the voltage Injection procedure, the frequency response of the bridge circuit itself and any interconnecting cables from the input transducer up to the point of voltage injection are *not* included in the step response and must be factored in separately.

3.2.1 Upper Frequency Limit: The response of the measurement system forward of the input transducer has been documented. The 10%-90% rise-time of the response of that portion of the measurement system to a step will permit calculation of the upper 3dB point of the system. The rise-time of the transducer itself can then be factored in by established techniques.

3.2.2 Lower Frequency Rolloff: The long-term response of the measurement system forward of the input transducer has been documented. From the number of zero-crossings in that response it is possible to determine the ultimate roll-off of the low end of the frequency response curve for magnitude and to evaluate the system behavior for undershoot due to transient excitations.

4.0 CONCLUSIONS

It is seen that a number of factors in the signal conditioning design will affect different performance characteristics of the overall

measurement systems. Depending on the combinations of the features in commercial hardware, a wide variety of performance characteristics can be achieved.

5.0   REFERENCES

1. Stein, Peter K. *Signal Conditioning*, **Measurements & Control**, April 1994, pp. 114-119.

2. Stein, Peter K., *Pyro-shock, Impact, Explosions and other High-Speed Transients: Some Thoughts on 'TQM' — Total Quality Measurements*, **Proc. Western Regional Strain Gage Committee Meeting, August 11-12, 1992**, Albuquerque, NM. From WRSGC, 44 North Benson Avenue, Upland, CA 91786. **Proceedings, 14th Aerospace Testing Seminar, March 9, 10, 11, 1993**, Manhattan Beach, CA, from Institute of Environmental Sciences, 940 East Northwest Highway, Mount Prospect, IL 60056. Invited Paper – Shortened Version, **Proc. 64th Shock & Vibration Symposium**, Vol. 1, pp. 91-100, 1993 SAVIAC, 2231 Crystal Drive, Arlington, VA 22202

3. Stein, Peter K. **The Unified Approach to the Engineering of Measurement Systems for Test & Evaluation**, Part I – Basic Concepts, April 1992, Stein Engineering Services, Inc., 5602 East Monte Rosa, Phoenix, AZ 85018, ISBN No. 1-881472-00-0

4. Stein, Peter K. *Measurement System Performance Capabilities as Governed by Input Conditioning Design*, **Proc. Western Regional Strain Gage Committee Meeting, Sept. 20-21, 1970**, Las Vegas, NV, see Ref. 2 for source. Also available as **Lf/MSE Reprint #30** from the author, see Ref. 3.

Figure 1:
Typical Signal Conditioning showing bridge supply disconnect switch and three resistance-injection shunt calibration resistors

Figure 2:
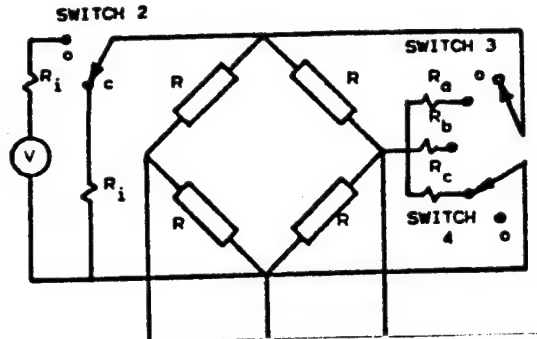Typical Resistance Injection balancing network. The smallest errors are made when $R_{13} \gg R_{11}$. The disconnect switch is a desirable feature.

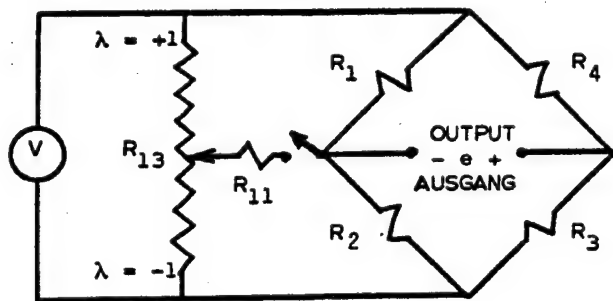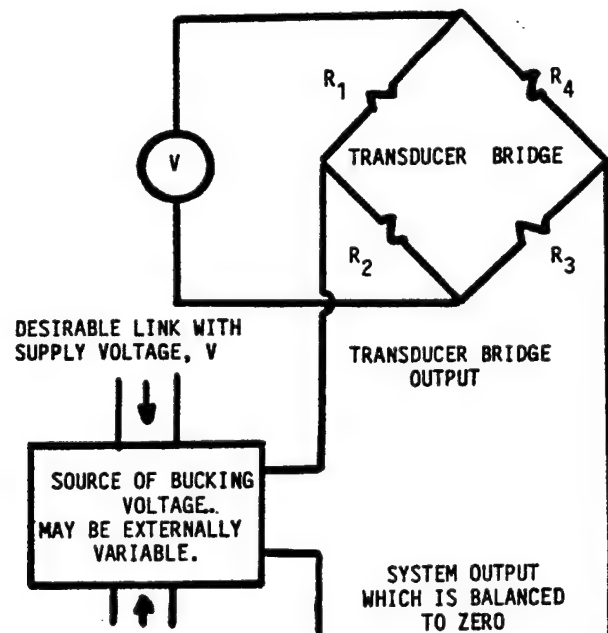**Figure 3**
A typical Voltage Injection Balancing Network

DESIRABLE LINK WITH SUPPLY VOLTAGE, V

SOURCE OF BUCKING VOLTAGE. MAY BE EXTERNALLY VARIABLE.

TRANSDUCER BRIDGE OUTPUT

SYSTEM OUTPUT WHICH IS BALANCED TO ZERO

POSSIBLE EXTERNAL CONTROL

SWEEP SPEED EFFECTS IN RESONANT SYSTEMS: A UNIFIED APPROACH

A Compendium of Information from Richard E. Zimmermann (mostly) [97] and Ronald V. Trull [72, 73]
with editorial comments by Peter K. Stein

Edited by Peter K. Stein, Director of the Short Courses
The Engineering and *The Dynamics of Measurement Systems for Test & Evaluation*
5602 East Monte Rosa, Phoenix, AZ 85018
Telephone & Telefax: (602)-945-4603. In the U.S. 1-(800)-632-7797

INTRODUCTION
by Peter Stein (from [94])

The performance coefficients or parameters of all systems and system components are functions of signal frequency. Plots of magnitude and phase of such coefficients with respect to frequency are known as *Frequency Response Curves*. Special presentations of such data are variously known as *Bode, Nyquist, Pole-Zero, Co-Quad, Nicholls* charts or plots and serve important functions in system design, control, performance and stability studies.

The determination of such frequency-response curves is usually assumed to be under steady-state conditions, i.e., dwelling at each frequency an indefinite length of time until all transient responses have decayed to negligible levels. In practice, such a procedure is either impossible or undesirable and test frequency is varied with time. The rate of change of signal frequency with time is known as the *Sweep Speed, Frequency Velocity* or *Angular Acceleration* and represents a special case of a system under frequency-modulated excitation.

Characteristics determined from such swept excitations will, in general, differ from steady-state characteristics. This effect is known as the *Sweep Speed Effect*, which, like all other effects, may be advantageous or detrimental. The effect occurs in systems of all kinds, processing energy of all types. Thus examples could be drawn from acoustics, electrical engineering (communications, signal analysis), optics (filtering), chemistry (infrared analysis), mechanical vibrations (reciprocating or rotational), etc. The common factors for systems to exhibit such sweep speed effects are:

- Underdamped resonant conditions of any degree of freedom
- Excitations for which the frequency is time-dependent.

The differences between system responses to swept inputs and to steady-state excitations are: (Figure 1)

- The maximum response (dynamic magnifier, transfer ratio, ("Q") is lower for swept-frequency excitation than for steady state. The effect also depends on whether frequency velocity is positive (increasing in frequency through resonance) or negative. The effect is not symmetrical around the resonance.
- The indicated resonance moves in the direction of the sweep and is different from (either higher or lower than) the steady state resonance.
- Under swept conditions there are indications of numerous resonant frequencies other than the ones shown for steady state conditions, These spurious indicated resonances occur after the main resonance on a time scale. They may be at frequencies higher or lower than the main resonance depending on whether frequency velocity is positive or negative through the main resonance. The effect is not symmetrical about the main resonance.

- The apparent bandwidth of the swept resonance increases over the actual bandwidth of the steady-state resonance. In other words, the apparent damping under swept conditions appears higher than the actual damping is under steady state conditions, which may lead to serious data misinterpretation

If system properties are determined at sweep speeds other than those which will excite the system in use, erroneous "properties" or "calibration curves" will result from the frequency response test. Thus "quick" vibration tests may reveal resonances much higher than intended operating frequency, with peaks which appear acceptably low. Steady-state operation can then result in system destruction. Numerous cases of this type have been documented in the engineering literature.

However, sweep speeds of high value can be used to avoid the effects of serious resonances through which one must pass to reach operating conditions. This procedure is common practice in rotating machinery such as turbines, where the effects of several critical speeds can be minimized by accelerating through them fast enough. If your car shimmies at 40 mph you can still drive at 60 mph if you just accelerate through 40 mph fast enough. An interesting application is provided by [87], an instruction manual for a helicopter which emphasizes:

CAUTION: Avoid continuous rotor rpm in a range between 200 and 230 rpm because of stabilizer bar resonance.

The severity of the sweep-speed effect depends on *system undamped natural frequency*, the *system damping ratio* at each such frequency, and *the frequency velocity* of the excitation during passage through a system natural frequency.

Figure 1

Effects of Sweep Speed on the Apparent Frequency Response of Resonant Systems
From Wright [96]. See also Figure 10, p. 16 from Trull [72]

191
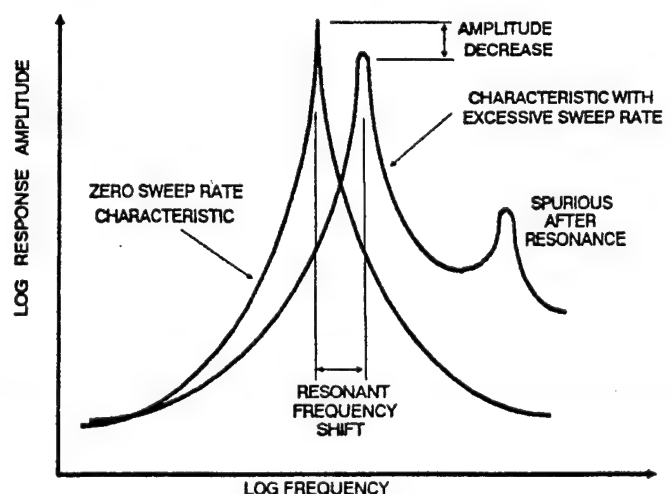
Past theoretical solutions attempting closed form mathematical solutions are listed and discussed in this survey (mostly from Zimmermann [97] but also from Trull [72], [73]. They include Lewis [41], Dimentberg [21] and Cronin [18], [19]. Lewis presents a graphical and nomographical solution to the problem; furthermore, the input data required for use of the solution are not readily available from the normal formulation of any real, physical problem. Dimentberg formed his solution with the use of Fresnel Integrals of which tables for complex arguments are not readily available. Cronin's solution uses Error Functions, and his equations, though complicated, are usable. He requires different equations for increasing and decreasing sweep speed.

The solution proposed by Trull is based on the Auxiliary Function of the Error Function and has many advantages over past solutions. It is simple, it fits the standard vibration solution format, and the functions involved are readily accessible in tabulated form. The solution is in the form of a steady-state FM response for which a computer program was designed, and a transient FM response which, for most mechanical engineering applications has died out by the time the system passes thorough its first resonance. Furthermore, it uses the same equation for increasing and decreasing sweep speeds.

Zimmermann [97] conducted the first thorough study of the literature and tied it all together, as is shown in this survey. He also extended Trull's solution to include the transient response with computer programs. Quoting from Zimmermann, whose unpublished Master's Thesis was completed in April 1973, but whose conclusions are still timely:

"Quantitative methods of analyzing engineering problems associated with sweep frequency excitations are available, but, based on the techniques used in the recent literature, the availability of these methods does not appear to be very widely recognized. Because the problems can be encountered with literally any physical system, papers which have dealt with the topic have been published in the journals of many different technical disciplines, and cross-referencing between these disciplines has been limited. As a result, some techniques have been re-derived several times while others have never been applied in areas where they would be most useful. Also, many of the approaches to the problems have been very specific in nature, with the result that they were of limited usefulness. For example, a solution for the transmissibility of a mechanical system is the solution to a single problem, while the solutions for the responses of the three elements of a second order linear system (which is what Zimmermann did) can be used to solve a multitude of problems.

"While the qualitative effects of sweep frequency excitations on the response of resonant systems are commonly known, effective quantitative means of dealing with the problem have not been readily available due to the fact that the solutions to the differential equations describing the response of systems subjected to sweep frequencies were not expressible in terms of functions commonly used in engineering analysis.

"Apparently this thesis represents the first attempt at organizing the literature related to the resonant response of sweep frequency excited systems into a systematic body of knowledge. Since the classifications appeared quite definitive, and since the methods for dealing with them are quite different, three types of problems were identified.

"There are actually three types of associated problems, as shown in Table 1. All three of these problems are complicated by the presence of a sweep frequency input, and the techniques for dealing with the three problems varies considerably.

"The three types of engineering problems associated with sweep frequency excitation of resonant systems are identified by the *unknown quantity* involved: (1) The Output, (2) The System Transfer Function, (3) The Input. It is seen that the techniques used to solve the three types of problems differ considerably.

Engineering Objective #1: (Table 1)
"The first problem: *Determination of System Output*, is generally encountered in design, and is mathematical in nature: *given a model of a system and a specified input, determine the response of the system.* Means of dealing with the problem mathematically are discussed at length in Chapter IIIa (of the Zimmermann Thesis [97]). If mathematical analysis fails, as it often has in the case for these problems, analogs are usually constructed, and this approach is considered in Chapter IIIb. The problem is of a mathematical nature and can be solved, in general, only by numerical methods. Closed-form solutions for linear sweeps are obtainable for Gaussian systems, compression filters and all second order linear systems. Emphasis is placed on *solutions for the response of all elements of a second order linear system,* and the solutions obtained are shown to be easily evaluated. The response of each portion of a second order linear system is also evaluated for a logarithmic sweep. References are cited for solutions for other systems, including nonlinear systems. Analogs are also discussed.

Engineering Objective #2: (Table 1)
"The second problem: *Determination of System Transfer Function,* is experimental. In that type of problem, *a piece of hardware exists, and its response to a range of input frequencies is desired.* What is really wanted is the envelope of all the responses that would be obtained if each individual frequency were applied separately, at steady state. In practice, a response is usually obtained by sweeping an input across the frequency spectrum. Obviously, if the sweep is too rapid, nothing resembling the desired objective results. Means of dealing with this problems are discussed in Chapter IV. They include techniques for limiting the sweep rate to acceptably low levels and means of inferring by numerical methods, the steady state transfer ratio, or function, from outputs due to rapid sweeps. References using both approaches are discussed.

Table 1

THREE TYPES OF ENGINEERING OBJECTIVE [68]

ENGINEERING OBJECTIVE

SYSTEM PARAMETERS	1	2	3
SYSTEM PARAMETERS	DESIGN	FREQUENCY RESPONSE	SPECTRAL ANALYSIS
SYSTEM INPUT	KNOWN (Specified)	KNOWN (Specified)	UNKNOWN
SYSTEM TRANSFER RATIO	KNOWN (Specified)	UNKNOWN	KNOWN (Specified)
SYSTEM OUTPUT	UNKNOWN	KNOWN (observed)	KNOWN (observed)

Engineering Objective #3: (Table 1)

"The third problem: *Determination of the Input*, also experimental, can be dealt with by using the techniques associated with the second problem, but more effective methods are available. They consist of designing the system to respond to the input in a manner independent of the sweep velocity encountered. Chapter V briefly considers the third type of problem, where *the frequency spectrum of the input is desired*. This generally involves the analysis of some signal other than a sweep frequency, but the analysis of its frequency content necessitates sweeping a filter across the frequency spectrum, or heterodyning the frequency spectrum itself across the bandwidth of the filter. The latter technique is generally used, but, in either case, the problem becomes a sweep frequency problem.

"The 85 references which are reviewed give numerous examples of physical systems associated with the three types of problems.

"The partial collection of literature presented in this thesis demonstrates that a considerable amount of theory and technique related to sweep frequency excitation of resonant systems, exists. Unfortunately it is entirely unorganized and, as a result, there is very limited awareness of its existence. Since sweep frequency excitations are so commonly encountered in various physical systems, the analysis of the associated problems should become commonly recognized and fully developed engineering techniques. The first step in this direction should be a more complete collection and organization of the pertinent literature. The importance of this is well illustrated by the repeated re-discovery of the quasi-steady-state criterion discussed in Chapter IV.

Table 2

ANALYSIS TECHNIQUES

PARAMETER TECHNIQUE OPERATES ON

UNKNOWN SYSTEM PARAMETER	OUTPUT	TRANSFER FUNCTION	INPUT
OUTPUT		Closed form mathematical solutions Numerical methods Analogs	Closed form mathematical solutions Numerical methods Analogs
TRANSFER FUNCTION	Direct Fourier analysis Auto-correlation		Quasi steady state approximation
INPUT	Direct Fourier analysis Auto-correlation	Increase bandwidth	

"Secondly, the theory should be extended where it would be useful; for example, the sweeping of other wave forms might be considered. The history of the development of the solution for the response of a linear second order system to a linear sweep as discussed in Chapter III suggests that the necessary effort to accomplish this may be greatly reduced by initially enlisting the participation of mathematicians.

"Finally, successful theories and analysis techniques should be given the widest possible dissemination. This should include publication in large circulation journals of various engineering disciplines and perhaps a collection of the material in a text for engineering students."

Well, over 20 years ago Zimmermann's thesis was sent to a major organization in the field of shock and vibration and was refused as *an elegant solution to a non-existing problem*. As editor of this small piece, I do not believe things have changed substantially in those 20 years.

SWEEP-SPEED AWARE ENGINEERS FROM OUR CAMPUSES
by Peter Stein

The Sweep-Speed, Frequency-Velocity; Angular-Acceleration effect was considered so vital that since the earliest days of the Laboratory for Measurement Systems Engineering (Lf/MSE) it was incorporated into the first, Junior level course in Measurement Systems Engineering. The discussion and the experiments were purely phenomenological since the mathematics have defied even many a doctoral student. Two case studies were included among the experiments, [92], [94], [93] starting in 1960.

Case Study #1: Mechanical System

A mechanical system in the form of a cantilever beam, Figure 2, [92] was presented. The students had done sufficient experimental work on that beam to predict the first two modes of vibration. Step Inputs (beam deflection) and Impulse Inputs (hammer blows) were used as excitations.

Figure 2

Frequency Response of a Cantilever Beam
(The *Instructor* is a strain-gaged Cantilever Beam design, with supporting stand, on which a large number of static and dynamic student experiments can be performed. There are more strain gages than shown here, for other experiments.)
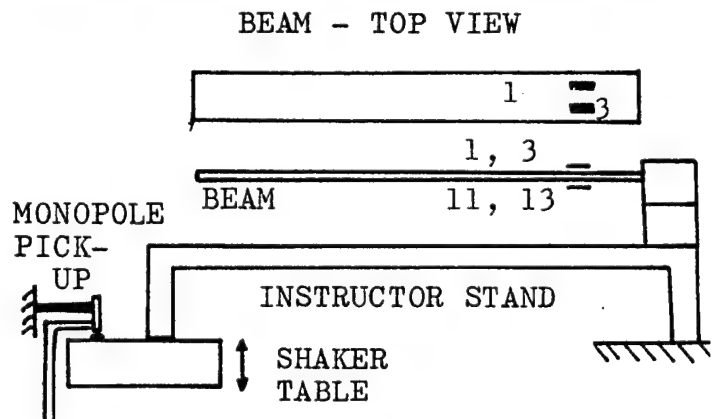
The results of those transient tests permitted prediction of the values of the undamped natural frequencies and the damping ratios for the first two modes of vibration. Those in turn permitted prediction of the Resonant Frequencies, Bandwidths, Maximum Transfer Ratio ("Q", Dynamic Magnifier) and

permissible Sweep Speeds through those resonances so that behavior close to steady state response could be evaluated. The commonly-used Figure of Merit also found by Trull [72], [73] and Zimmermann [97] was employed to determine permissible sweep speeds.

The Maximum Transfer Ratio, plus results from an earlier, static experiment on the beam relating beam deflection and maximum strain at the clamped end, permitted prediction of the maximum input deflection at low frequencies so that the beam, when excited at resonance, would not be destroyed by a fatigue failure. Sinusoidal excitation was then used.

In other words, the experiment included a *complete study of how vibration tests can be completely planned by first obtaining transient response information.*

The beam was placed on a mechanical vibrator with excitation frequency varying linearly with time by means of a cam drive. Frequency could also be varied manually, slowly enough to determine the maximum Steady State Transfer Ratio.

Strain gages on the beam, as shown, were used to measure the *strain* as the beam Response and a Monopole Magnetic Transducer measures vibration *frequency*. The beam vibratory input *displacement* is constant so that the Transfer Ratio is in Strain per Unit Displacement.

The assumption that each of the beam modes acts as its own second order system is common in all modal analyses.

The results from the transient tests were:

First Mode:

Damped natural frequency:	f_d = 8.53 Hz	ω_d = 53.5 rad/s
Time constant of decay:	τ = 6.8 secs	

rom which one can compute the system characteristics:

Damping ratio	$[(\tau.\omega_n.h) = 1]$ h	= 0.0028
Undamped natural frequency	f_n	= 8.53 Hz

Predicting steady state response:

Maximum Transfer Ratio, "Q":	T = 182	$[T = 1/(2h)]$
Resonant frequency:	f_r = 8.53 Hz	
Bandwidth $[\Delta\omega = 2.h.\omega_n]$	Δf = 0.05 Hz	
Maximum sweep speed	df/dt = 550×10^{-6} Hz/sec	

or *a half an hour per Hz through that resonance!* That is not an unusual requirement for high-"Q" systems unless the techniques discussed later in this paper, are used. For turbine blade resonant frequency determination, Glober [89] reports the use of 1 Hz/min sweep speed.

Second Mode:

Only the predictions for Steady State response are given here

Resonant Frequency	f_r	= 52 Hz
Bandwidth	Δf	= 1.3 Hz
Maximum Transfer Ratio, "Q"	T	= 41
Permissible sweep speed	df/dt=	0.4 Hz/sec

or 2.5 sec/Hz, much faster than permitted for the 1st mode.

Figure 3 illustrates typical test results from the mechanical case study with the cam-driven linear frequency sweep from 5 Hz to 60 Hz in about 30 seconds, both increasing and decreasing.

The Maximum Transfer Ratio depression, the spurious after-resonances in the sweep direction and their non-symmetry for up and down sweeps are well illustrated in that experiment. The frequency scale does not permit sufficient resolution to determine the resonant frequency shift involved.

Figure 3

RESPONSE OF A CANTILEVER BEAM TO LINEARLY SWEPT FREQUENCY EXCITATION
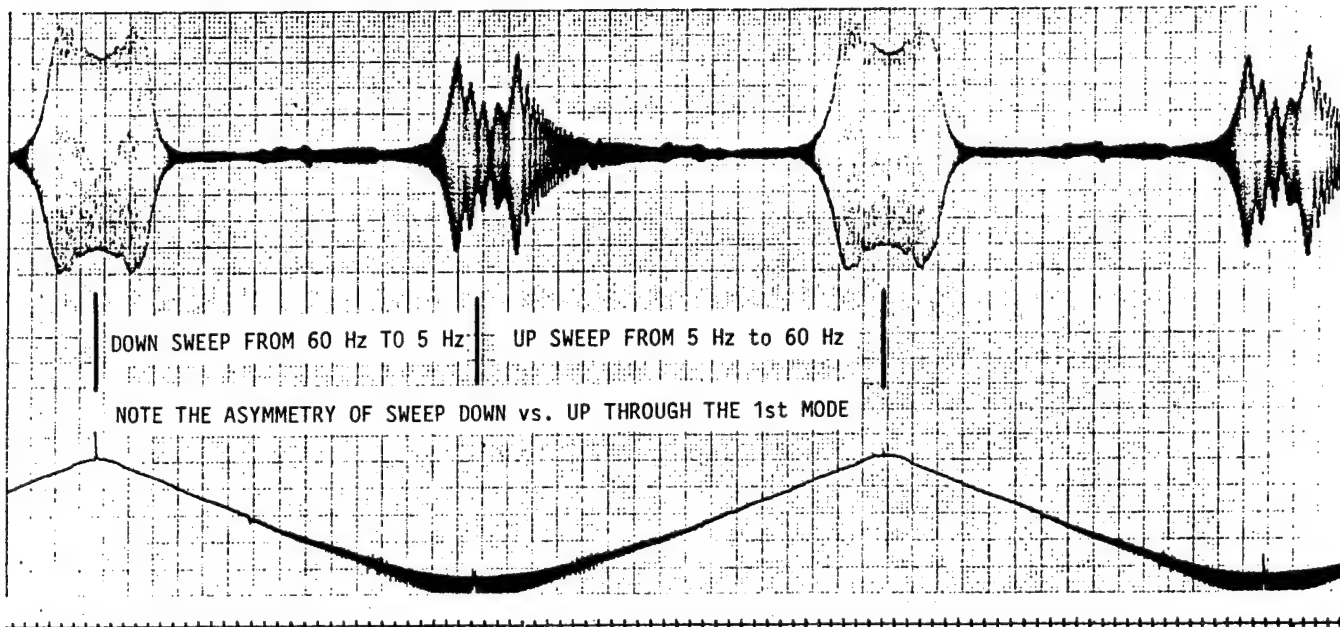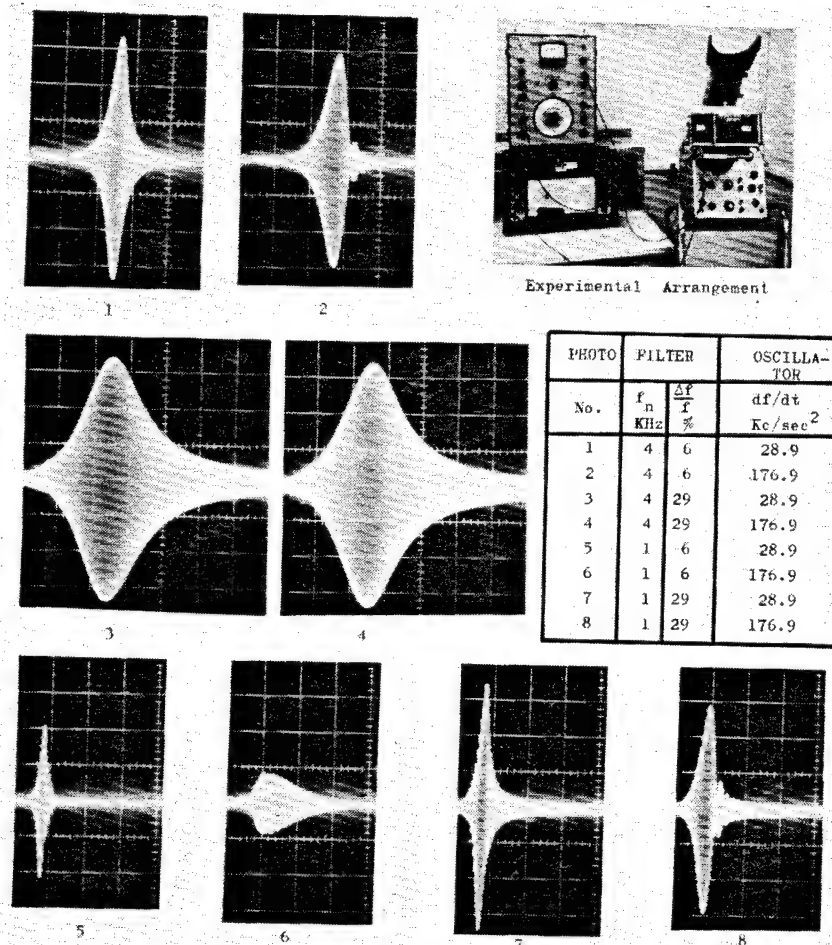TOP : Beam response through the strain gages CENTER: Frequency BOTTOM: Time in 1-second increments

DOWN SWEEP FROM 60 Hz TO 5 Hz   UP SWEEP FROM 5 Hz to 60 Hz

NOTE THE ASYMMETRY OF SWEEP DOWN vs. UP THROUGH THE 1st MODE

Figure 4 (from [68])

THE EFFECT OF SWEEP SPEED ON NARROW-BAND FILTERS
The pairs of figures such as 1 & 2, 3 & 4, etc., illustrate the effect of sweep speed.
In Fig. 5 even the "slow" sweep is already too fast.

Experimental Arrangement

PHOTO	FILTER		OSCILLA-TOR
No.	f_n KHz	$\frac{\Delta f}{f}$ %	df/dt Kc/sec^2
1	4	6	28.9
2	4	6	176.9
3	4	29	28.9
4	4	29	176.9
5	1	6	28.9
6	1	6	176.9
7	1	29	28.9
8	1	29	176.9

Clough-Brengle 282A Audiomatic Generator #2037 swept from 1 KHz – 11KHz (photos 1-4), and from 100 Hz – 10.1 KHz (photos 5-8) through B & K 2107 Filter #73243 with center frequency, f_n, and band-width, $\Delta f/f$. Observed with Tektronix 502 (modified) oscilloscope, on the Y_1 vs. Y_2 display mode.

Tovey & Nettles, Dec. 68

Question: The steady state predictions from the transient tests show only 2 modes of vibration in that frequency range, and the Transfer Ratio for the *first mode* as *over 4 times that for the second mode*. The "slow" test of about 2Hz/sec shows the *second mode Transfer Ratio about 30% higher than that for the first mode*, and numerous apparent resonances. What is wrong: the predictions or the actual swept experiment?

Case Study #2: Electrical System (from [68])
In the experiment on Frequency Selective Filtering [94], [93], an electrical example was presented by sweeping frequency linearly through filters of various percentage-bandwidths at various speeds. Figure 4 illustrates the experimental set-up and the data. Filters of 6% and 29% bandwidth with center frequencies at 1 KHz and 4 KHz were swept through "slowly" and "rapidly" illustrating the sweep-frequency effects.

Students were expected to determine whether the Sweep Speed Figure of Merit permitted the interpretation of any of those responses as Steady State.

DETERMINATION OF A SYSTEM STEADY STATE TRANSFER RATIO FROM SWEPT FREQUENCY TESTS (From Ref [97])(See also Table 1)

The problem considered here is experimental in nature. A physical system exists, and the transfer or output-to-input ratio of the system is desired as a function of frequency. Often the phase of the output with respect to the input is also desired. Clearly the transfer ratio and phase of the system depend not only upon the frequency but also upon the rate at which the frequency is changing.

And, in any real system, they are also a function of amplitude. In order to simplify the problem to the extent where usable results can be obtained, the system is considered to be linear, at least for some range of amplitude, and the input is considered to be discrete constant frequencies. The Transfer Ratio is then a function of frequency only, and is termed the Steady State Transfer Ratio since it is the envelope of all the responses that would occur if the system were excited at each of the individual frequencies.

There are several methods for getting the approximate Steady State Transfer Ratio from Swept-Frequency tests.

1. Quasi Steady State Approximation
(Adapted from [97] with editorial comments)

The determination of the steady state transfer ratio can be troublesome. Ideally, it should be determined by exciting the system at discrete frequencies until the envelope is obtained, and this is actually done at times. However, time requirements and the endurance of the system usually eliminate such a direct approach. Usually the frequency is swept at a rate low enough to allow the response to approximate the steady state response envelope. This quasi-steady-state assumption requires some criteria for determining the maximum allowable rate of sweep, and a number of papers in the literature were devoted to determination of such criteria.

Estimation of the Sweep Speed Effect:

Based on analog studies of the response of second order linear systems to linear and logarithmic sweep frequencies, Cronin [19] determined that the amount of peak attenuation and broadening (higher indicating damping) depended upon

the natural frequency and damping ratio of the system and upon the rate of sweep:

$$n = \frac{df/dt}{(f_n.h)^2} \quad \text{in units of 1/cycles}$$

where: n = a Figure of Merit and a measure of the peak attenuation or reduction of the maximum transfer ratio or rise in apparent damping.

f_n = undamped natural frequency in Hz

h = damping ratio

It is interesting that the bandwidth of the system, for low values of damping ratio, h is:

$$\Delta f = 2f_n h$$

so that the Figure of Merit depends only on the system bandwidth. But see also comments below.

For Cronin's Figure of Merit [18]:

If $n \ll 1$ results are close to steady state.

If $1 < n < 3$ the primary effect of sweeping is peak depression and broadening

If $n > 4$ More and more, the spurious after-resonances also occur

Other investigators cited in [97] obtained Figures of Merit in the same form but differing by factors of 2 or 2π from Cronin's especially if natural frequencies are used (radians/second), but then the criteria for n also change.

A plot of Cronin's result is shown in Figure 5 for peak depression, in Fig. 6 for increase in apparent damping and in Fig. 6A for movement of the apparent first resonant frequency. Within about 2% Fig. 6A is symmetrical for ±q. Several years later, Drain [22] obtained a similar result for the peak depression, also by analog means, and applied it in the determination of the frequency response of jet aircraft engines. Drain referenced the works of Lewis, Hok and Reed and reported agreement with Lewis but not with Reed.

Cronin's Fig. 5 implies symmetry of the peak depression with respect to the *sign* of the sweep (up or down). This is not really the case and Trull [72], [73] and Zimmermann [97] developed solutions in which the same equation can be used for increasing and decreasing frequency sweeps.

Mathematical derivations for the quasi-steady-state criteria were published 20 years before Cronin and Drain studied the problem, but they are found in the electrical engineering literature and have never been referenced in the mechanical engineering literature. The solutions by Van der Pol [76] and Clavier [15], resulted in a series solution for the sweep frequency transfer ratio in terms of the steady state transfer ratio.

Clavier showed that for the energy dissipating, response across the R in an RLC circuit, the Figure of Merit is 1/4 Cronin's, and for the potential energy storing response it is 1/8 Cronin's. Chang [14] developed the criterion for a Gaussian transfer function as 1/8 Cronin's.

It is interesting that the Figure of Merit is independent of the *potential energy storing response* γ, for a second order system:

$$\alpha.\frac{\delta^2 Q}{\delta t^2} + \beta.\frac{\delta Q}{\delta t} + \gamma.Q = f(t)$$

where Q is whatever parameter is being studied,

$$\frac{\beta}{\alpha} = 2.h.\omega_n \quad \text{where} \quad \frac{\gamma}{\alpha} = \omega_n^2$$

so that only α and β enter into the Figure of Merit.

ω = frequency in radians/sec = $2\pi f$

The choice of a suitable sweep rate is more difficult for multidegree of freedom systems since the multiple damping ratios may be unequal and difficult to determine. Granick [29] determined empirical formulas for selecting sweep rates for such systems.

2. Bidirectional Sweeps
(From [97] with editorial comments)

Another technique for analyzing multidegree of freedom systems is to simply sweep in two directions as was done by Lukens [45]. If the resonances due to both sweeps occur at the same frequencies, it can be concluded that the sweep was slow enough for the response envelope to approximate the steady state response envelope.

For reasons not apparent in the published literature, the frequency at which the upward and downward sweep envelopes intersect coincides with the true resonant frequency of the system. But the true response peak cannot be easily derived from the swept data.

For non-linear systems, response data taken for increasing frequencies will also differ from data taken for decreasing frequencies, but there will be clearly marked *jump* phenomena due to the hooked frequency response curves for non-linear systems, so that a confusion between sweep speed effects and non-linear system behavior is unlikely, unless a non-linear system is subjected to swept excitation.

3. Feed-Back-Controlled Sweep Rate
(From [97] with editorial comments)

If the maximum allowable sweep rate cannot be calculated, the system can be designed to select a sufficiently low sweep rate. Lorenzo [43,], [44] reports using test apparatus which applied a variable sweep rate for vibration testing at Lewis Research Center. Feedback control was applied to the sweep generator so that the sweep was slowed in the region of resonant response only, and a 7 to 1 reduction in test time was achieved on a particular test.

It has been the conclusion of several of the researchers referenced in this survey, that it is the sweep rate *through the resonance* which is important, and the feedback concept, slowing the sweep rate according to the slope of the Transfer Ratio vs. Time or Frequency curve accomplished that aim.

4. Direct Fourier Transformation (from [97])

Another means of dealing with the errors due to sweep rate in vibration testing is to record the data from an arbitrary sweep and analyze it as a transient to determine the correct frequency response. This is generally done with Fourier transformations determined by numerical analysis, the transfer function being simply the ratio of the Fourier transform of the output to the Fourier transform of the input.

Reed, Hall and Barker [59] applied this technique to the vibration analysis of aircraft wings. They determined the frequency response by both steady state and transient methods and compared the results, which they found to be very close. White [80], [82] reports applying this method to a system with a cubic nonlinearity.
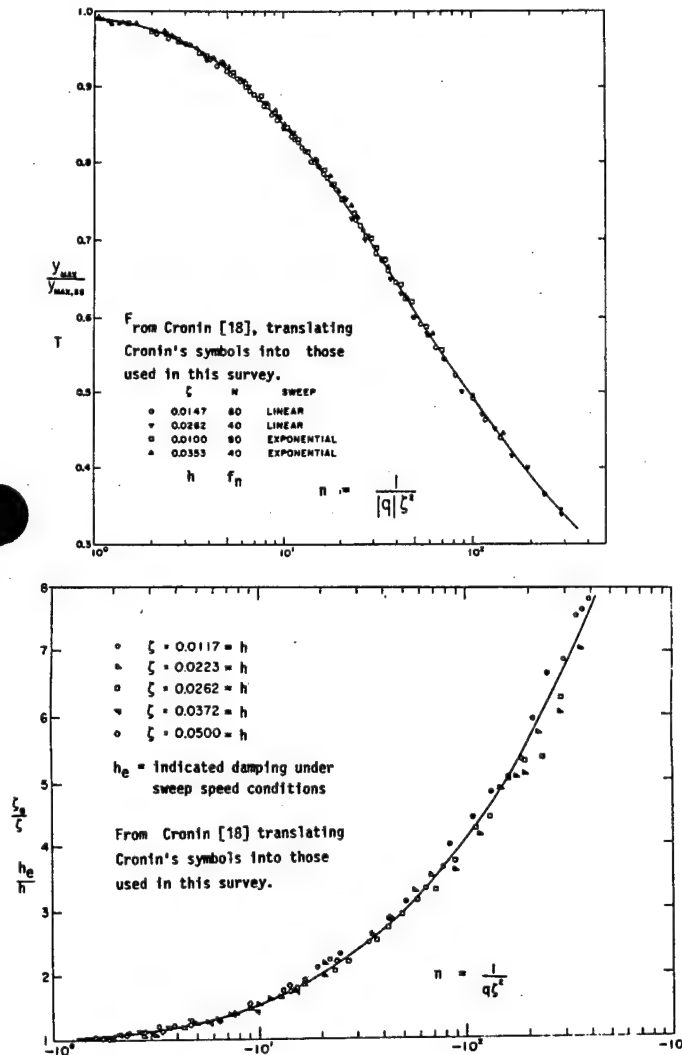
5. Autocorrelation (From [97])

As an alternative to the Fourier transformation technique for the determination of system frequency response, Skingle

Figure 5, Top
THE EFFECT OF SWEEP SPEED ON PEAK OBSERVED RESPONSE, T_{MAX}
From Cronin [18]. The symbols for Figure of Merit, n; Transfer Ratio, T; Resonant Frequency, f_r; Apparent Resonance, f_{r-max} have been added to Cronin's symbols

Figure 6, Center
THE EFFECT OF SWEEP SPEED ON APPARENT DAMPING RATIO, h

Figure 6A, Bottom
THE EFFECT OF SWEEP SPEED ON APPARENT FIRST RESONANT FREQUENCY, f_r

[64] described a correlation technique. The method utilizes the fact that the auto-correlation of the system output is a series summation of exponentially decaying functions, the decay rates and oscillation frequencies of which are defined by the damping and resonant frequencies associated with the various modes of the system. Skingle presents mathematical justification for this assertion, and presents some actual test results. By selective filtering, correlograms for the various modes are obtained from which resonant frequencies and damping can be determined. Appendix C of Skingle's paper contains a derivation of the autocorrelation function of a linear sweep function.

The reason for using a linear sweep is because, as shown by Reed [59], it produced an impulse-like autocorrelogram, a condition which is necessitated by approximations made in the development of the technique. The primary advantage of this method is that it can be used successfully with low signal to noise ratios. But see the section near the end of this survey on *Other System Parameters* for disadvantages.

White [80], [82], applied this technique to the analysis of systems with, nonlinearities and found that it yielded a response curve with less distortion than the direct Fourier analysis method. He also applied the autocorrelation technique in the study of the frequency response of a ship's hull [79]. The autocorrelation of the response was formed via digital computer, and the computer was then also used to form the Fourier transformation of the autocorrelation function, thus producing the frequency response characteristic of the hull. The method was used with rapid linear sweeps of several seconds duration and also with excitation provided by turbulence as the ship moved through the water.

DETERMINATION OF SYSTEM INPUT (From [97])

The problem considered in this chapter is generally associated with measurement or instrumentation systems. The calibration of the system establishes the transfer function which is thus a known quantity, the output is observed, and inferences are made about the input to the system - see also Table 1. Obviously the input is not necessarily a sinusoidal wave form. Since calibration procedures generally establish a *steady state transfer function* for the system, considerable difficulty can result if the input is a *sweep frequency*.

A prime example of a system susceptible to this difficulty is a spectrum analyzer. In principle, a spectral analysis could be performed by three methods:

- A comb of filters over the spectrum of interest
- A single filter with variable center frequency
- A single filter with constant center frequency used in conjunction with a variable frequency oscillator to heterodyne the signal frequencies across the center frequency of the filter.

The first system would be immune to the problem, but is sometimes impractical. As noted by Van der Pol [76] and Hok [35], the second and third methods are mathematically equivalent and would present identical problems. In practice the third method is frequently used.

If the heterodyning procedure results in too rapid a sweep, the filter response will be decreased in amplitude and increased in bandwidth. Thus the amplitude of any particular frequency component will be in error, and the ability to distinguish between distinct, individual frequencies will be diminished. The latter characteristic is known as *resolving power*, and it has long been recognized that the resolving power of such a system is proportional to the square root of

197

the ratio of the bandwidth to the time required to sweep through that bandwidth [83]. Thus an obvious means of insuring accurate results from a spectrum analyzer is to limit the rate of sweep by the same criterion as used to establish the quasi-steady state approximation.

Unfortunately, the expedient method of reducing the sweep rate until an accurate response is obtained from the filter often results in unacceptably long analysis time, just as test time became too long for the Transfer Ratio Determination application.

The methods used to circumvent this difficulty can also be used to advantage here. However, there is an important difference between the problems encountered here and the one previously considered; in this case the system may be arbitrarily specified. The freedom to specify the system can be used to advantage to limit the problem cause by the velocity of the sweep.

1. Variable Filter Bandwidth

One means of taking advantage of the freedom of specifying the system is to use a filter of variable bandwidth. If the bandwidth is increased, the amount of peak attenuation due to sweep speed will be diminished. The absolute resolving power will unfortunately be increased, but it is possible to maintain the same percentage resolving power and still increase the allowable sweep rate.

2. Time Domain Compression

A more powerful method of coping with this problem is to move the center frequency of the filter to a higher frequency and to move the frequencies of the input to a higher frequency range by compressing the signals in the time domain. An understanding of the advantage obtained by this technique is easily deduced from the quasi-steady-state criteria shown earlier:

$$n = \frac{df/dt}{(h.f_n)^2} = \frac{(f_2 - f_1)}{T(f_n.h)^2}$$

where the frequency is swept from f_1 to f_2 in time T.
If all frequencies are multiplied by a factor k, then:

$$n_k = n/k$$

It is now possible to sweep k times as fast for the same Figure of Merit, n. Even in the 1970s commercial frequency analyzers used factors of k = 250,000 for "real time" frequency analysis. Extensive literature on the subject of data compression is available [86].

An extensive analysis of scanning spectrum analyzers was conducted by Kincheloe [37]. The most remarkable result of his efforts is that the degradation in sensitivity and resolving power of a filter due to sweep speed is not inevitable, but can be eliminated, at least theoretically, by properly matching the phase of the filter and sweep generator.

BRIEF HISTORICAL SURVEY [97]

(In the following excerpt from Zimmermann's master's thesis, the mathematical formulations have been omitted. They are contained in full in the original document.)

Mathematical Solutions

The problem of predicting the response of resonant systems to swept frequency excitations has inspired an abundance of literature which has accumulated for over 40 years (written in 1973). One of the earliest, and probably the most well known paper so far as mechanical engineers are concerned, was published by F. M. Lewis in 1932 [41]. He used variation of parameters which yielded a solution in terms of four integrals which could not be reduced to any function which had been evaluated in 1932. The rapid oscillation of the integrand made numerical evaluation impossible so Lewis applied contour integration. He selected a transformation so that the troublesome integrals were more tractable with the path of integration a section of a parabola in the complex plane. He was then able to apply the residue theorem to evaluate these integrals using asymptotic expansion for large values of the variable, a convergent series for small values, and graphical methods for intermediate values.

The evaluation of these integrals was no doubt extremely tedious, but Lewis produced a series of response envelopes in terms of non-dimensional parameters which were useful to designers and are still being referenced in current papers.

The design of a spectrum analyzer for ocean waves led Barber and Ursell [6] to consider a gliding tone excitation in which case the frequency decreases exponentially with time. They then approximated the exponential function by the first three terms of its series expansion, so the form of the excitation was the same as for a linear sweep. Using Duhamel's integral they ended up with an integral form for the solution, which they found advantageous since it had been evaluated by the Admiralty Computing Service.

A graphical technique was developed by Bishop and Johnson [8] which, though perhaps not practical in view of the available analytic solutions, is interesting and provides insight into the physical process. The method consists of assuming the input to be a set of successive sine wave cycles, each with a period shorter than that of the preceding one, rather than a continuously time varying frequency.

Temporarily neglecting damping, they computed the response to a single frequency acting over one cycle by Duhamel's integral. After further mathematical manipulation they arrived at a vector diagram that could be plotted. The method was extended to include damping.

Dimentberg [21] published a text on rotating shafts in 1961. Chapter 3 of that text considers the case of transition through resonance. The variables are defined with respect to the center of mass of the shaft, hence the input function is of constant amplitude. However, a change of variables is introduced to provide a coordinate system which rotates with the shaft, thus facilitating stress analysis within the shaft. Dimentberg formulated the problem in terms of Fresnel's integrals for the case without damping. He also considered the damped case, and worked out an approximate solution for small damping ratios. Several Russian papers considering the transition of a shaft through resonance are referenced in the bibliography.

Parker [54] sought to evaluate the integrals obtained in the variation of parameters for of the solution for the logarithmic weep. Recognizing the futility of any attempt at direct numerical integration he wrote the solution in exponential form and then expressed the exponentials in terms of their series expansion. These series expansions were then manipulated into a form which allowed the excitation frequency to be factored out, leaving the desired envelope of the response.

Unfortunately the series became difficult to evaluate for the region of particular interest: small damping ratios and frequency ratios greater than one. By using an extensive amount of computer time, Parker evaluated the series for damping ratios of 0.167, 0.05, 0.01 and 0.005 for the log sweep and presented graphical results in terms of transmissibility vs. frequency ratio.

In 1964 Hawkes [33] published a method by which the

envelope of the response of a second order system to a general sweep frequency function would be obtained. Those equations can be integrated numerically for any rate of sweep. Hawkes used this method to evaluate the system response to octave sweeps and published the results. Hawke's work is referenced in several subsequent papers, but it is always reported to be the solution for an octave sweep. The generality of the method appears to have gone unnoticed.

Hawkes' equations are integrated in his Appendix V for linear and logarithmic sweeps and for responses of kinetic energy (masses and inductances for example) and potential energy (capacitors and springs for example) storing element responses and the dissipation element response (such as dashpot dampers and resistances, to give examples from mechanical and electrical applications.)

A doctoral thesis by Fearn [25] considered the problem with a linear frequency sweep. The majority of his thesis is directed towards the zero-damping case. He discussed the damped case but did not evaluate the integrals he obtained. He references the paper by Lewis but was apparently unaware of the literature published on the subject between 1932 and 1965.

A second order linear system modeled for an aircraft landing gear with displacement input was considered by Stronge [69]. The excitation function for sinusoidal displacement input to the potential energy storage and energy dissipating elements was computed. Expressing the solution by means of the convolution integral, Stronge observed that the solution was easily put in the form of the Error Function or Fresnel integrals. In either case the argument is complex, and only the zero-damping case was evaluated. Stronge also considered the response for several random waveform excitations.

In the same year the Stronge completed his thesis, NASA published a table of complex Fresnel integrals and Stronge then published a solution in terms of these tabulated values [70]. The exact solution given is quite complex and is the time domain solution. Stronge also gave an expression for an upper bound on the envelope, but, although he reported that it checked with Lewis' solution in the case of zero damping, the assumptions made in obtaining the bound are not given in the paper and there is no means of evaluating the accuracy of the approximation when damping is present.

Cronin [18] devoted considerable effort to the investigation of a response for a general sweep function. Since a closed form solution for the envelope is clearly not possible, he sought expressions for the maximum amplitude and the frequency at which is occurs by obtaining upper bounds on the integrals. He applied perturbation theory techniques to obtain a general system response.

Cronin derived some exact closed form solutions for several sweep functions. For the linear sweep he obtained a solution in terms of the error function, but it is fairly complex and of little interest since simpler formulations are available. He noted that a series solution for the exponential sweep is easily obtained by expanding the sine function in its series. representation, but made no attempt to evaluate the series.

A paper on the acceleration of rotors through their critical speed was published by A. Capello in 1967 [11]. He referenced his equations to the axis of the shaft rather than the center of mass, hence his forcing functions are of variable amplitude. In addition to viscous dissipation, Capello considered the elastic hysteresis of the shaft material due to difference in angular velocities of the shaft and the shaft deflection. The model used to account for the elastic hysteresis causes the equations for the x and y displacement to be coupled. Capello does not present the development of his solution, but references a previous paper published in Italian. Capello referenced an Italian paper by Domig for a

converging series method of evaluating the integrals with which he presented his solution. His paper describes an experimental apparatus for checking the theoretical solution, and reports qualitative agreement. He references the text by Dimentberg, but none of the American references discussed here.

Though numerous investigators had observed that the solution for a second order linear system excited by a linear sweep is expressed in terms of error functions of complex argument, they assumed that such a solution was not usable. Apparently Trull [71] (his Master's thesis), [72] was the first to discover that the error function could easily be evaluated via digital computer using a series expansion originally published in 1948. Trull's derivation of the response envelope in terms of the error function yielded excellent results for absolute values of q greater than 50 and low damping. q is the linear sweep factor: $\omega_n^2/(4\pi\epsilon)$ where ϵ is half the linear sweep speed.

His Appendix B contains a program which computes envelope and phase of the three responses of a second order linear system: potential energy storing response (γQ), kinetic energy storing response $\alpha.d^2Q/(dt)^2$ and energy dissipating response $\beta(dQ/dt)$, for any values of damping, sweep factor, and initial frequency. By superposition of these results, any linear system can be easily evaluated. For example, taking the root of the sum of the squares of the potential and dissipating responses will yield the transmissibility as computed by Parker and Stronge, or, equivalently, the response of an unbalanced rotating shaft as computed by Dimentberg and Capello.

It is interesting to compare this solution with the solution of Lewis who effectively evaluated the error function for complex arguments, a task which was then avoided by all subsequent investigators until Trull discovered that it could be evaluated by digital computer.

The implications to the logarithmic sweep problem are obvious. A closed form solution requires the evaluation of integrals which are easily expressed in a series but not one which can be evaluated. This will probably also be accomplished by a mathematicians, and perhaps has been already. Further efforts by engineers to manipulate the integrals into a form more amenable to evaluation are not likely to be very productive.

Gaussian Systems

It happens that a closed form solution to the problem is readily obtainable for the case of a Gaussian transfer function and is contained in detail in Appendix A of the Polarad Corporation's Handbook [56]. That result was also published by Saul and Luloff [63] in Appendix B.

A more general derivation is presented by Batten [7]. Here the input was considered to be a pulse signal, and the continuous wave case was obtained from the solution as a special case. The form of the solution for the continuous wave case is the same a in the Polarad handbook. Batten had researched the papers by Lewis, Barber, Hok and others, but did not formulate a solution for the simply resonant case, Based on comparison with analog solutions, it was concluded that the Gaussian solution was a good approximation for systems with two or more simply resonant subsystems of the same resonant frequency. Unfortunately, it does not reflect the apparent shift in resonant frequency since the Gaussian transfer function does not account for phase. The same solution was derived independently by Chang [14] in 1954.

Compression Filter

A physical example consisting of an acoustic compression filter is described by Kino [38], and the experimental response verifies the calculation.

General Linear Systems

While any linear system can, in principle, be analyzed by the error function solution for linear sweeps or by Hawkes' solution for logarithmic sweeps, there may be occasions when a direct solution in terms of a generalized transfer function is more desirable. Also much of the literature which considers this problem predates the availability of the digital computer, and, since there was then no effective means of uncoupling the equations of multi-degree of freedom systems, the direct solution in terms of a generalized transfer function was the only practical approach. There is also the possibility of modeling a system with a transfer function which is not describable in terms of second order linear differential equations.

The published papers dealing with general linear transfer functions are usually found in the electrical engineering literature. There appear to be two reasons for this. One is that few electrical circuits can be modeled as a single loop, thus the solution to the single second order linear equation was not as useful in electrical engineering as it is in mechanical engineering. The other reason, which is probably a result of the first, is that electrical engineering literature approached the problem with different mathematical techniques. The mechanical engineering papers usually applied variation of parameters and sometimes Duhamel's integral, while the electrical engineering papers generally used Laplace or Fourier transforms which more readily lend themselves to a general transfer function.

The earliest referenced paper in the electrical engineering literature was published by Salinger [62] in 1929, and thus predates Lewis by several years. An excellent survey of much of the electrical engineering literature as of 1962 is given in an annotated bibliography in Kincheloe's thesis [37].

In 1937 Carson and Fry published a paper on circuit analysis with frequency modulated input [13]. They derived a series expression for the response in terms of steady state admittance. Van der Pol [76], in 1945, published a derivation which is more heuristic but extremely concise. His transfer function was expressed in terms of derivatives of the modulation function and derivatives of the steady state transfer ratio evaluated at the instantaneous frequency. Clavier [15], in 1949, gave a slightly more rigorous derivation by beginning with the convolution integral and evaluated the first four terms. The evaluation is complicated by the fact that the exponential function must be expanded in a series itself before the indicated operations can be performed. It is in effect a series within a series.

Unfortunately, the derivatives of the transfer ratio become very large near the natural frequency of a resonant system. Thus it is not possible to compute the output in the frequency region of greatest interest with this solution. Carson and Fry formulated a second series expression which should have better convergence but the problem was not actually eliminated. The solution is useful for other purposes, but it is of little value for the computation of the envelope of the response.

In 1947, Hok [35] published a solution for a linear sweep which was derived by means of Laplace transforms. The system transfer function emerged as a series summation. Hok suggested the name "Fresnel function" or "fresneloid" for a term within the series, and evaluated it by means of convergent series expression given in the appendix of his paper. Hok was apparently unaware of the work of Carson and Fry, and Van der Pol, and stated in the introduction that Lewis' paper was brought to his attention when he presented his solution to the Physical Society,

A modification to Hok's solution was published in 1952 by Marique [47]. It gave the system response for a sawtooh varying frequency input. Marique had read the literature and referred to the works of Luis, Van der Pol, Clavier, Barber and Ursell, and Hok. He had also discovered the paper by Salinger. Marique's derivation proceeds along the line of Hok's except that he employs a property of the Laplace transform. Thus his solution is a summation of the responses to all preceding sweeps.

Gersch and Kennedy [26] devised a method for numerically convolving the impulsive response of a system with the spectrum of the sweep frequency. The function in his solution is easily evaluated for many systems by looking it up in tables of transformations. Another form of his solution can be evaluated in terms of error functions or Fresnel integrals, and has the advantage that the argument of these functions is not complex. Once it has been evaluated, it can be used with any filter function.

Gersch and Kennedy referenced the papers by Barber and Ursell, Hok, and Batten and noted that their solution had the advantage of requiring the evaluation of the difficult sweep frequency spectrum only once after which it could be used to evaluate any system.

Nonlinear Systems

If the system is nonlinear, there is no apparent way of obtaining an exact solution. However, solutions have been formulated in terms of asymptotic expansions with very satisfactory results. This technique can also be used to advantage for linear systems in the case where the forcing function is of a form which cannot be analyzed by the closed form solution.

Mitropolskii [50], [51], [52] published several texts in the 1960s dealing with the application of the asymptotic expansion techniques to nonlinear, nonstationary systems. Because the procedure becomes algebraically tedious, first and second order approximations are generally used. Fortunately these are of sufficient accuracy to solve many practical problems. The method is completely general. Hence solutions for nonlinear systems are obtained as easily as for linear systems, and any sweep function desired may be introduced.

Examination of the bibliographies of Mitroposkii's texts reveals that Russian scholars have been actively engaged in the application of this method for over 30 years (written in 1973), Chapter 3 of [52] discusses some of the solutions and correlations with experimental results.

Dr. R. M. Evan-Iwanowski of Syracuse University and a former student of his, B. N. Agrawal, have published a number of papers applying to the asymptotic expansion method to the nonstationary vibrations of nonlinear systems [1], [2], [3], [23], [24].They have extended the solution to nonlinear multidegree of freedom systems and have generalized it so that the same form applies to all types of resonances of a multidegree of freedom system. They have shown, among other things, that a change in the rate of frequency variation can cause a shift of the system from one stable mode to another,

Kevorkian [36] published a solution for the response of a one dimensional nonstationary oscillator using an asymptotic expansion technique and extended the solution to multidegree of freedom systems. However, only the case of zero damping was considered. Kevorkian was apparently not aware of the works of Mitropolskii, Evan-Iwanowski, or Agrawal.

Beams and Plates on Elastic Foundations

There is a class of problem not specifically discussed by Zimmermann [97] or Trull [72], [73] where the sweep speed effect appears, and that is when dynamic loads are applied to beams or plates. Thus [90], [91] treat the case of a moving vehicle on an ice sheet supported by water and [95] discusses trains of high speed air cushion vehicles traveling at arbitrary speeds over beams. In those studies the water and the beams are considered elastic foundations. There is a critical velocity at which resonance is excited which will lead to failure if allowed to exist for any length of time if damping is insufficient.

The problem there is to produce a fast enough sweep speed through the resonance so as to *minimize* its effect, exploiting the depression of the peak response, "Q", Dynamic Magnifier or Maximum Transfer Ratio of the system. That problem of *resonance avoidance* is discussed by Zimmermann and by Trull although not for the above type of examples.

Analog Solutions

The difficulties encountered in attempts to mathematically analyze the response of systems to sweep frequency inputs inspired numerous analog solutions. One of the earlier studies was done by Baker [4] who, in 1939, published a mechanical mathematical machine-generated response for an unbalanced rotor subjected to constant angular acceleration. The results are plotted in terms of nondimensional parameters as used by Lewis [41]. Baker was aware of Lewis' work, and had assisted in the construction of the experimental apparatus used to verify Lewis' calculations, but apparently made no effort to extend the analytical technique to the case of rotating unbalance,

In 1949, McCann and Bennett [48] used the then newly constructed electrical analog computer at Cal Tech to determine the response of a two-degree of freedom torsional system to an oscillating torque of constant amplitude and linearly varying frequency. The system was described in terms of nondimensional parameters representing the sweep rate, the damping ratio, and stiffness and inertia ratios. The maximum output of the system for a positive sweep was plotted as a function of sweep rate, shaft stiffness ratio and disc inertia ratios. The damping factor was assumed to be 0.01 in all cases and the output was defined as the ratio of shaft torque due to elastic twisting to the amplitude of the input torque. This solution could have been determined from Lewis' calculations, but the analog technique was unquestionably easier. McCann and Bennett did check a few of their curves against Lewis' results.

Parker [54] determined the response of a second order linear system to linear sweeps in terms of transmissibility by analog methods. Responses are presented for various sweep factors and damping ratios. Morse [53] generated analog solutions for the response of second order linear systems to logarithmic sweep displacement input to the spring and damping elements. The output was presented as the ratio of the acceleration of the spring-mass to the acceleration of the displacement input (transmissibility). Cronin [18] developed analog solutions for both linear and logarithmic sweeps. He expressed the response as the ratio of the displacement output to the maximum displacement output that would be obtained at steady state resonance.

Quazi and McFarlane [58] published an analog solution for the response of a rotating shaft to angular acceleration. The response was considered to be the shaft deflection in this case, as opposed to shaft twist. They had studied the papers of Lewis, Hok, Dimentberg, Johnson and others, and

concluded that analytical solutions became "prohibitively difficult." Since they desired to apply torque according to control laws to limit deflection, this was a quite reasonable conclusion. The paper is actually directed toward the determination of a feedback control system to keep the system response within specified limits rather than the determination of system output for a specified input.

Some attention was directed toward the case of acceleration through resonance of a torsional system in a 1967 paper by Pollard [57]. Lewis' solution was applied and was extended where necessary by an analog simulation on a digital computer. For multiresonant systems, Pollard determined the response at each resonance considered separately. He then multiplied the amplitude of the first resonance by an exponential and added it to the maximum response of the second resonance to obtain the maximum output of the system. The value used in the exponential expression depended on the time required for the excitation frequency to travel between the two resonant frequencies. This technique yielded results which compared with those obtained by McCann and Bennett.

Godwin and Merrill [28] published a paper on the resonant response of a synchronous motor due to oscillatory torques during starting. The results of some special-case computer solutions are presented graphically, but the formulation of this solution is not discussed. The use of Lewis' solution for design purposes is recommended in their paper.

A NASA report by Drain, Bruton and Paulovich [22] briefly presents the results of analog solutions for both linear and logarithmic sweeps. Their objective was not actually the response characteristic but rather the maximum allowable sweep for quasi-steady-state testing. An interesting result of their study was that the peak attenuation for a given system is the same for linear and logarithmic sweeps if the velocity of the sweep at the resonant frequency is the same, a condition which is satisfied if the sweep factors are equal. This had also been observed earlier by Cronin [19], see Figures 5 and 6.

It is interesting that the analog solutions in the literature are all directed toward a specific problem, Although they are in terms of nondimensional parameters, they only apply for the specific input and output simulated in the analog. If the response of the three basic elements of a second order linear system had been obtained for linearly and logarithmically sweeping sine waves only, then the results could have been superimposed to analyze any system composed of these elements.

CONTRIBUTIONS BY THE LABORATORY for MEASUREMENT SYSTEMS ENGINEERING (Lf/MSE)

For most of the 18 years of the existence of the Laboratory for Measurement Systems Engineering (Lf/MSE) at Arizona State University under the editor's direction (1959-1977), over 900 undergraduate and graduate students emerged from the first (Junior level) course being *measurement - aware, measurement - conscious* and *measurement - oriented*. They had been exposed to two lectures and laboratory experiments involving the sweep-speed effect. Thus, later in their careers they could recognize it if they saw it even if they were not able to solve the sweep-speed problem which has defied many a doctoral candidate, as has been seen. Those experiments were briefly described earlier in this survey, and illustrated in Figs. 2, 3, and 4.

Two Master's Theses were completed, by Trull in 1969 [72], [73] and by Zimmermann in 1973 [97]. Both were

201

Figure 7 (from Trull [72]

EXAMPLES OF SYSTEM RESPONSES WITH VARIOUS BANDWIDTHS AND SWEEP SPEEDS

SECOND ORDER SYSTEM WITH LOW DAMPING: h = 0.03 f_n = 10,000 HZ
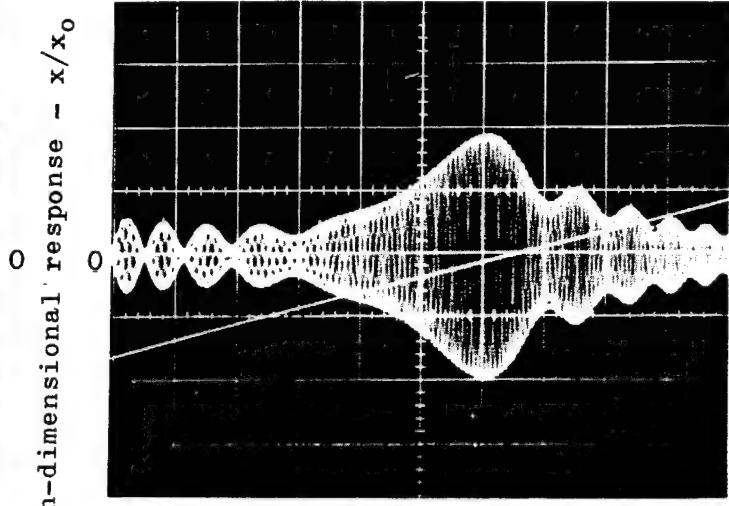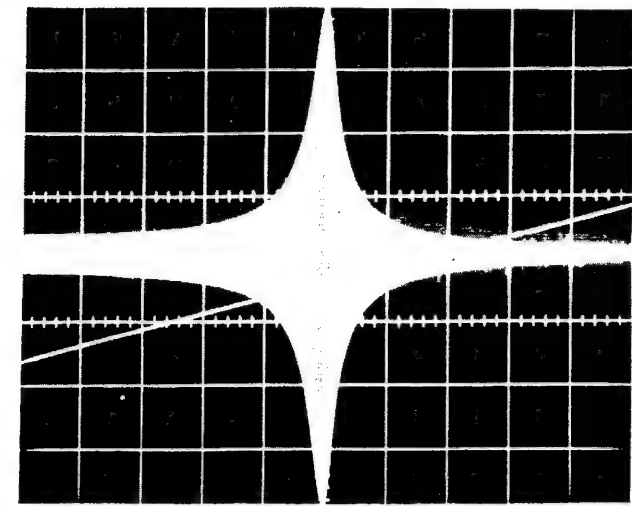
Q = 1000   v = 100,000 Hz/sec

Q = 10   v = 10,000,000 Hz/sec

Note that the photo on the ight represents a combination of sweep speed nd damping ratio for which the transient effects of starting the sweep (between f/f_n zero and 1) have not died out by the time the system enters the main resonance. Such effects occur only at extremey high sweep speeds and are not accounted for in the computer-programmed portion of the theoretical solution

SECOND ORDER SYSTEM WITH HIGH DAMPING: h = 0.1 f_n = 10,000 Hz
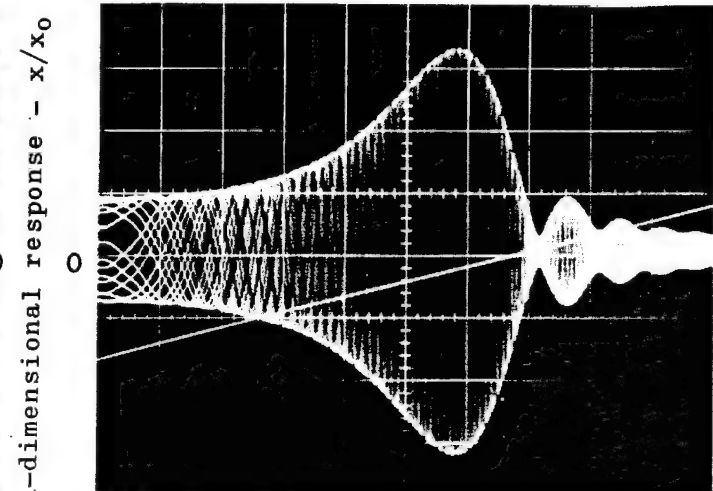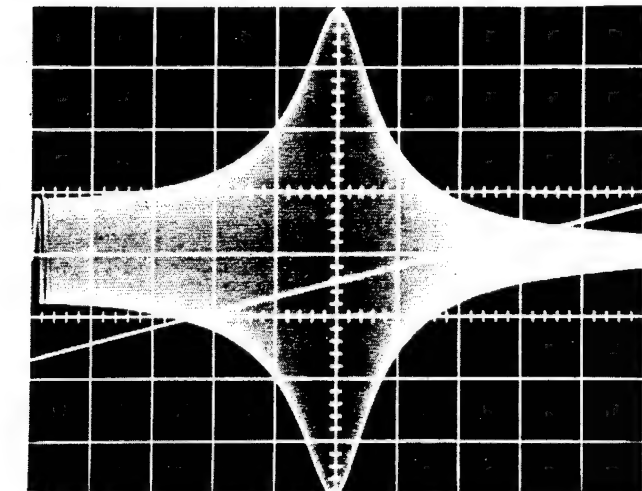
Q = 1000   v = 100,000 Hz/sec

Q=10   v = 10,000,000 Hz/sec

Note the absence of evidence of a starting transient near r = 0
Displays on the left are at essentially steady state conditions. Note the presence of the three major speed speed effects in the displays on the rigfht.

Figure 8 (From Trull [72])

SOLUTION BASED ON THE AUXILIARY FUNCTION OF THE ERROR FUNCTION: THEORY & EXPERIMENT

THEORETICAL APPROACH: The bases of the theoretical solution are described below. The steady-state FM portion of the response was evaluated over a wide range of parameters by means of a computer program which also plotted the response as a function of non-dimensional frequency (X) for steady-state excitation (Y1), linearly increasing sweeps (Y2) and linearly decreasing sweeps (Y3).

THEORETICAL APPROACH

For a system which can be modelled by a linear, second order differential equation:

$$\frac{d^2x}{dt^2} + 2\,h\,w_n\,\frac{dx}{dt} + w_n^2\,x = P.\,Sin\,wt$$

under steady-state sinusoidal excitation.

x = system response
P = amplitude of forcing function
h = damping ratio
w_n = undamped natural frequency in radians/second
t = time in seconds
v = frequency acceleration in rad/sec/sec
w_o = starting frequency of sweep
$w = w_o + vt$, instantaneous frequency
W(z) = auxiliary function of the error function
z = argument of W(z)
Ω = non-dimensional sweep-rate parameter: $\Omega = \dfrac{w_n^2}{(\frac{v}{2})}$
x_o = system response at zero frequency (static, DC).

When the frequency of the forcing function is time-dependent the problem of sweep speed (or frequency modulation) appears.
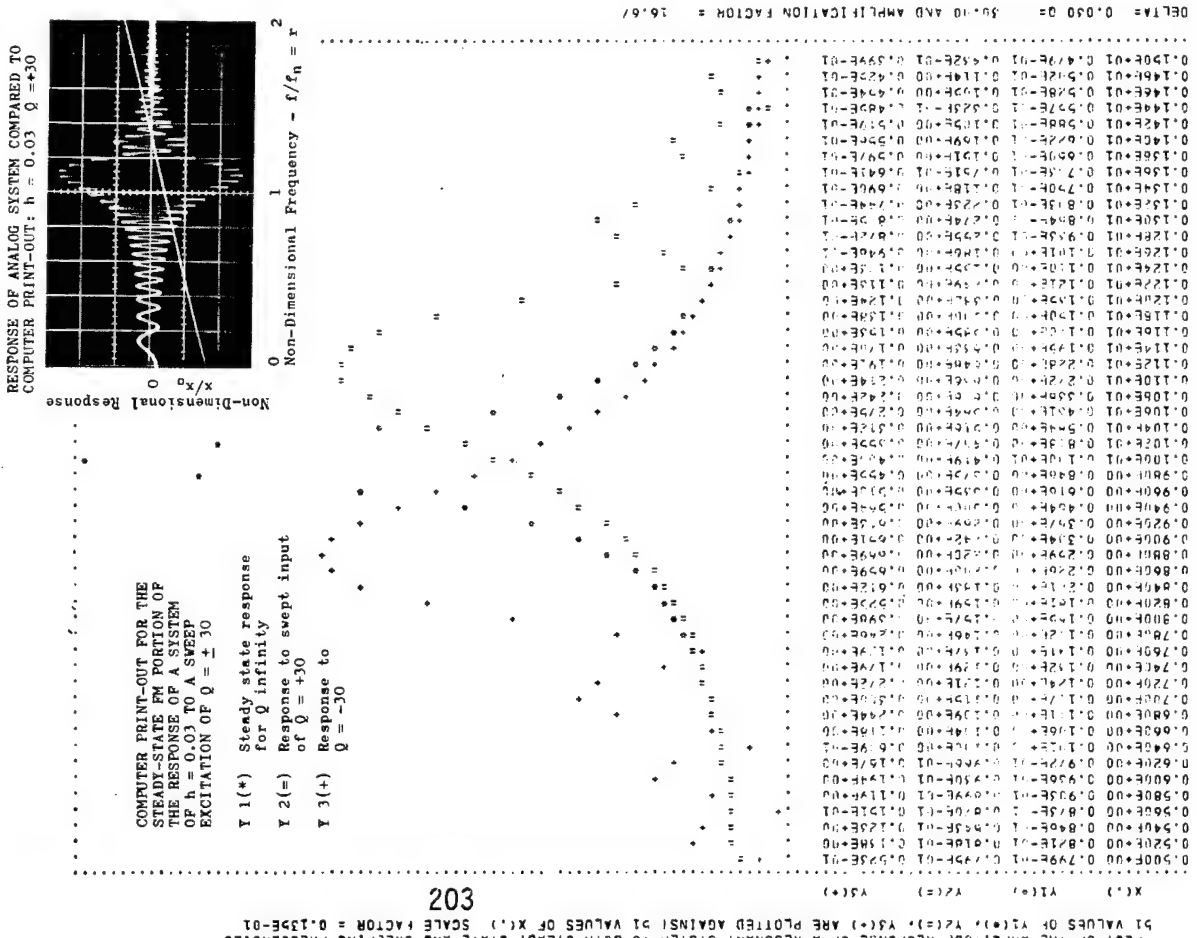
$$P.\,Sin\,wt = P.\,Sin\,(vt^2 + w\,t)$$

The closed form solution to this equation, as developed in this project takes the following form:

$$\boxed{(x/x_o) = T.Sin(vt^2 + w_o t + \phi) + (\text{Transient FM})\ \text{Response}}$$

T is the magnitude of the Steady-state FM Response and ϕ is the phase angle of the response with respect to the forcing function.

$$T = \frac{\sqrt{\pi\Omega}}{4\sqrt{1-h^2}}\ \sqrt{\Big(Re\big[W(z_1)\big] - Re\big[W(z_2)\big]\Big)^2 + \Big(Im\big[W(z_1)\big] + Im\big[W(z_2)\big]\Big)^2}$$

$$\phi = \tfrac14\pi + Arc.tan.\left\{\frac{Re\big[W(z_1)\big] - Re\big[W(z_2)\big]}{Im\big[W(z_1)\big] + Im\big[W(z_2)\big]}\right\}$$

$$W(z) = e^{-z^2}\left[1 + \frac{2i}{\sqrt{\pi}}\int_0^z(e^{t^2})dt\right]\ \text{the auxiliary function of the error function}$$

$$z_1 = \tfrac12 e^{\frac14 i\pi}\sqrt{\Omega}\ (\,r + \sqrt{1-h^2} - ih\,) \qquad z_2 = -\tfrac12 e^{-\frac14 i\pi}\sqrt{\Omega}\ (\,r - \sqrt{1-h^2} + ih\,)$$

(Transient FM) Response $= \dfrac{\sqrt{\pi\Omega}}{4\sqrt{1-h^2}}\ e^{-h w_n t}\left[e^{-\frac{i h \Omega r^2}{\ldots}}\cdot Sin(w_n\sqrt{1-h^2}\,t).Sin\phi_1 + e^{\frac{i h \Omega r^2}{\ldots}}\cdot Cos(w_n\sqrt{1-h^2}\,t).Cos\phi_2\right]$

$$\phi_1 = \left\{\tfrac14\pi - \tfrac12\Omega\left[r_o + \sqrt{1-h^2}\,\right)^2 - h^2\right\}$$

$$\phi_2 = \left\{\tfrac14\pi - \tfrac12\Omega\left[r_o - \sqrt{1-h^2}\,\right)^2 - h^2\right\}$$

$r = f/f_n = w/w_n$
$r_o = f_o/f_n = w_o/w_n$

The above solution holds for linear sweeps of increasing frequency (v and Ω positive). The solution for decreasing-frequency sweeps has the same form as the one above, only the arguments of the functions are different. Dimentberg also presents a solution for both cases, but they are in the form of Fresnel integrals which have apparently not been tabulated for complex numbers, so the solution is difficult to use. Cronin's solutions exhibit different forms for increasing and decreasing sweeps, with solutions for increasing-frequency sweeps much longer than that for decreasing-frequency sweeps. Lewis's graphical and nomo-graphical solutions are presented for both cases.

REFERENCES: Among the numerous past investigators of the sweep-speed problem, the following have been mentioned in this summary:

CRONIN, Donald L., RESPONSE OF LINEAR, VISCOUS DAMPED SYSTEMS TO EXCITATION HAVING TIME-VARYING FREQUENCY, Doctoral dissertation, California Inst. of Technology, 1965. Dynamics Laboratory Report under NASA Contract NAS-8-24-51.

DIMENTBERG, F. M., FLEXURAL VIBRATIONS OF ROTATING SHAFTS, Butterworth, London, 1961, Chapter 3 (translated from an original Russian book).

LEWIS, F. M., VIBRATIONS DURING ACCELERATION THROUGH A CRITICAL SPEED, Trans. ASME, Vol. 54, (1932) pp. 253-261.

RESPONSE OF ANALOG SYSTEM COMPARED TO
COMPUTER PRINT-OUT Q = +30

Non-Dimensional Frequency – f/f_n = r

Non-Dimensional Response x/x_o

COMPUTER PRINT-OUT FOR THE
STEADY-STATE FM PORTION OF
THE RESPONSE OF A SYSTEM
OF h = 0.03 TO A SWEEP
EXCITATION OF Q = ± 30

Y 1(*) Steady state response for Q infinity
Y 2(=) Response to swept input of Q = +30
Y 3(+) Response to Q = -30

advances in the state of the art, presenting closed-form solutions capable of computer programming. Trull's work has been described by Zimmermann in this survey (page 9). His solution divided into a Transient FM portion and a Steady State FM portion. He provided a computer program for the Steady State FM portion which is useful for cases where the sweep speed is slow enough so that the transients have died out before the resonant peak is reached, which is the case for a vast multitude of problems. One example of where this is not the case is shown in Fig. 7. He supplemented his work with two analog studies. The results of his work are summarized in Figures 7 and 8. The solution is a special case for low damping and q >50.

Zimmermann [97] not only produced a masterful summary of the literature for his Master's Thesis, most of it brought in this survey, but also modified and extended Trull's analysis so that the response of any system can be determined, including the transient FM response. The same equations and computer program hold for sweeps of increasing and decreasing frequency, and each of the responses of a second-order system was treated:

$$\alpha \cdot \frac{\delta^2 Q}{\delta t^2} \;+\; \beta \cdot \frac{\delta Q}{\delta t} \;+\; \gamma \cdot Q \;=\; f(t)$$

$\alpha \cdot \dfrac{\delta^2 Q}{\delta t^2}$ = the system kinetic energy storing response

$\gamma \cdot Q$ = the system potential energy stolring response

$\beta \cdot \dfrac{\delta Q}{\delta t}$ = the system energy dissipating response.

The power of presenting these individual responses in non-dimensional form (i.e., per unit of forcing function) is shown in *The Unified Approach to Differential Equations*, Chapter 5 in the editor's now out-of-print book [68], but retained in the Lf/MSE Reprint Series as Reprint #65 and used in the Short Courses on *The Dynamics of Measurement Systems for Test & Evaluation*.

Zimmermann's solution and the program are shown in Table 3 and on p. 17.

Figure 9
(From Zimmermann [97])

Difference in Initial Conditions for the Potential Energy Storing Element
q = 100, ζ = 0.03
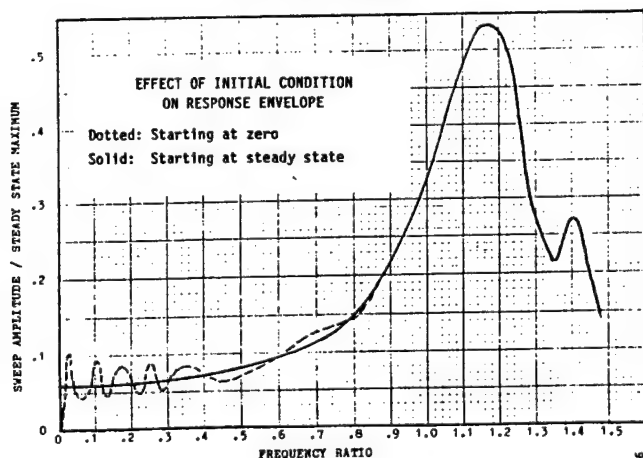
The program in Table 3 evaluates the exact solution; no simplifying assumptions or approximations are made. The input consists of the sweep factor, q, the damping ratio ζ, and the initial frequency ratio, FRi. The sweep factor may be either positive or negative, since no restrictions were placed on the direction of the sweep in the derivation of the solution. Care must be exercised in specifying q, since its definition is not consistent in the literature. It may be defined in terms of either cycles per second (Hz) or radians per second, and the two differ by a factor of 2π. In the program presented here, q is multiplied by 2π internally. With this instruction present, q is based on Hz. If the instruction is removed, q is based on rad/sec.

Satisfactory results will not be obtained for absolute values of q on the order of 1000. This is because large values of the argument of the error function result in very large values for the error function in the |x| < |y| portions of the complex plane, and the magnitude of these values will exceed the capability of the (1973!) computer. This difficulty can be avoided by using the approximation which was discussed in the derivation (not shown in this survey) and which results in an equation of the form evaluated by Trull [72]. This approximation is in terms of a function which does not take on the large values that the erf-function does. For |z| > 3, the exact solution and the approximation will yield the same result.

The printout displays the normalized response of all three elements and the phase of these responses with respect to the input. Since the phase variation exceeds 360° in some cases, and since the program does not distinguish between two different angles in the same quadrant, 360° must be subtracted from the printed value in a few cases to obtain the correct phase. The response of a Gaussian system is also calculated and printed (infinite sweep range approximation), see [97], and it is seen that the Gaussian response is not nece-ssarily a good approximation for a second order linear system.

Inspection of the results reveals that *the maximum response of the potential energy storing portion of the system is less for a positive sweep than it is for a negative sweep.* This effect was noted in the literature but not explained. It is due simply to the inherent asymmetry of the response; the steady state response is greater below the critical frequency than it is above it. Exactly the opposite effect is experienced by the kinetic energy storing response.

The literature has usually displayed the response as the amplitude of the response vs. the frequency ratio, as was first done by Lewis. Other types of plots which include phase information may be more useful in some applications.

Note about Figure Numbers: Figure numbers are now from Zimmermann's Thesis [97] and not continuous with the other figures in this survey.

Figures 17 and 18 show the standard amplitude vs. frequency plot along with the corresponding phase plot. It is seen that for a slow sweep the phase oscillates about the steady state phase, but for a rapid sweep it becomes an entirely different function. From the co-quad plots in Figures 19 and 20 it can be seen that this difference is caused by the real component of the envelope changing sign more than once.

The polar or Nyquist plot in Figure 21 displays the fact that the response vector spirals about the origin after transition through resonance for a rapid sweep, but only oscillates about -180° for a slow sweep. At higher frequency ratios, the response spirals about a point other than the origin, as also observed by Barber and Ursell. They also showed that a transform of coordinates based on the sweep function could be used to display the response envelopes as variations of the Cornu spiral.

204

<div style="text-align:center">

Table 3

THE ERROR FUNCTION SOLUTION FOR LINEAR SYSTEMS AND LINEAR SWEEPS FOR A UNIT OF FORCING FUNCTION

THE ERROR FUNCTION SOLUTION FOR LINEAR SYSTEMS

AND LINEAR SWEEPS

</div>

It was shown in Chapter III that the particular solution to

$$\ddot{Q}_s + 2\varsigma\omega_n \, \dot{Q}_s + \omega_n^2 \, Q_s = \sin(\sigma t + \varepsilon t^2)$$

is

$$\dot{Q}_s = \left| \frac{I_1 - I_2}{\lambda_1 - \lambda_2} \right| \sin(\sigma t + \varepsilon t^2)$$

where

$$I_K = \exp(z_K^2) \left[\tfrac{1}{2} \sqrt{\pi/a} \; \mathrm{erf}(z_K) + C_K \right]$$

$$z_K = \frac{1}{\sqrt{a}} \, (a\tau + b_K)$$

$$a = - i \, \frac{q}{2}$$

$$b_K = - \tfrac{1}{2} \, (i \; FRi - \lambda_K)$$

$$\lambda_K = - \varsigma + (-1)^{K+1} \sqrt{\varsigma^2 - 1}$$

FRi = initial frequency ratio (σ/ω_n)

FR = frequency ratio $(\dot{\phi}/\omega_n)$

Note that $\tau = (FR - FRi) \, q$

The value of C_K depends upon the initial conditions of the equation. If the response is zero at time zero, then

$$C_K = - \tfrac{1}{2} \sqrt{\pi/a} \; \mathrm{erf}(z_{K_0})$$

where $z_{K_0} = z_K$ at $\tau = 0$

Program Inputs: q, ς and FR
Program Outputs: Amplitude and phase of the three system responses for steady state and swept excitation.

ς	=	damping ratio
ω_n	=	undamped natural frequency, rad/s
σ	=	initial frequency at start of sweep, rad/sec
ε	=	(1/2) linear sweep velocity, rad/sec²
t	=	time, seconds
erf	=	error function, see program p. 21.
q	=	linear sweep factor = $\dfrac{\omega_n^2}{4\pi\varepsilon} = \dfrac{f_n^2}{df/dt}$

See p. 20 for physical explanation

i	=	$\sqrt{-1}$
ϕ	=	angle, $d\phi/dt$ = radian frequency
f	=	frequency in Hz

However, if the system is operating at steady state when the sweep begins, then the constant C_K has a second term:

$$C_K = -(1/2) \sqrt{(\pi/a)} \cdot \mathrm{erf}(z_{K_0}) + \exp(-z_{K_0}^2)\lambda_K$$

This difference in initial condition is significant even when the sweep begins at zero frequency, because the envelope of the potential energy response is equal to one for the steady state envelope. This is illustrated in Fig. 9. These curves were obtained from both programs in Zimmermann's Master's Thesis and the results were precisely the same with three places printed out.

The program presented here solves the equation for the steady state envelope initial condition. It can be converted to zero initial condition by setting xx = 0.

The initial phase of the system is not explicitly included in the solution, and is generally unimportant since the solution is for the envelope of the response. However, it should be kept in mind that for a very rapid sweep the response will not fill the envelope and the maximum response will depend on the initial phase. This could be computed by multiplying the envelope by $\exp(i\phi)$ to get the actual response and by adding the initial phase to FRi.

The program also computes the kinetic and dissipating responses by integration by parts. This allows all three responses of a second order linear system to be obtained by expending very little more computer time than is required for the evaluation of the response of a single element.

Comparison of the results from this program with the results for numerical integration of Hawkes' equation are also shown in Zimmermann's Master's Thesis and shows agreement to at least three decimal places. Also since the maximum response for a linear sweep is equivalent to the maximum response for a log sweep if the sweep factors are equal, this program can be used to evaluate the maximum response for a log sweep.

Practical Application of Lf/MSE's Solutions to the Sweep Speed Problem

Charles P. Wright, 1968 Master's in Mechanical Engineering with a Measurement Systems Engineering major from

Lf/MSE, has implemented almost all of the data validation techniques recommended by the *Unified Approach to the Engineering of Measurement Systems* in his state-of-the-art data acquisition, handling and analysis system at TRW Space & Electronics Group, Redondo Beach, CA where he heads the Measurements Engineering Department.

His 1994 book [96]: *Applied Measurements Engineering: The Design of Effective Measurement Systems* (Prentice Hall) describes these validation checks in some detail. One for sweep speed effects will be implemented shortly.

The philosophy of *Validation Checks* is that data are validated for numerous effects before they are analyzed or handled or turned over to the test requester. The emphasis is on TQM – Total Quality *Measurements*.

OTHER SYSTEM PARAMETERS
(From Zimmermann [97])

Although the system input, output or transfer ratio are the items of most general concern, there are other system parameters which may assume foremost importance in engineering problems associated with sweep frequency excitation of resonant systems. One of these is the number of excitation cycles experienced by the system during the transition through resonance. This actually is a property of the system output. However, these considerations require neither the envelope nor the phase of the response, and the calculations involve only the number of cycles of excitation applied to the system.

The number of cycles applied to a system are of particular importance in mechanical vibration testing since the structure may be destroyed by fatigue damage before the test is completed if the sweep speed rate is too low. A number of papers have been devoted to fatigue considerations. Curtis [20], Harris [31], and Gertel [27] considered the number of stress cycles as a function of sweep rate for linear sweeps. Patrick [55] computed the level and duration of a swept sine test to duplicate the damage to be experienced in the service environment, and Spence and Luhrs [66], [67] determined the octave sweep rate required to produce the same damage as a random vibration test. Granick [29] and Parker [54] also considered the fatigue aspects of sweep frequency excitation. Parker pointed out the interesting fact that both linear and log sweeps are poorly suited for distributing fatigue equally among the resonances of a multi-degree of freedom system. Assuming the same damping ratio at two resonant frequencies a factor of b apart, a linear sweep will apply b^2 as many cycles at the lower frequency and a log sweep will provide b times as many. Parker determines a sweep function which would apply an equal number of cycles at each resonance.

In some systems the capability of the readout device becomes a limiting factor. In the design of a magnetic field spectrum analyzer Greenstein [30] found that the persistence of available phosphors for the cathode ray screen required a sweep rate for an acceptable image which resulted in only 70% response at resonance. Waldron [78] found that microwave systems with sawtooth sweeps were subject to additional errors due to the uncertainty of the frequency at the beginning of the sweep, and Bozich [9] determined that sweep frequency analysis requires its own data sampling criterion

A system parameter of interest to all engineers is the cost. Broch [10] proposed a hybrid test method consisting of sweeping a narrow band of random excitation. This is claimed to combine all the advantages of random vibration testing with the simplicity and lesser capital expenditure of swept sinusoidal testing. Hayasaka [34] applied sweep frequency calculations in proposing that acoustical equipment can achieve comparable performance with less stringent design criteria. He determined that human speech consists of frequencies sweeping up to 3700 Hz/sec. Using the theoretical results of Lewis and several Japanese papers, and by performing a number of experiments, he showed that the resonances of a typical acoustic system are appreciably flattened in actual use and concluded that a flat steady state frequency response is an unrealistic requirement.

ADDITIONAL REFERENCES
(Continued from page 24)

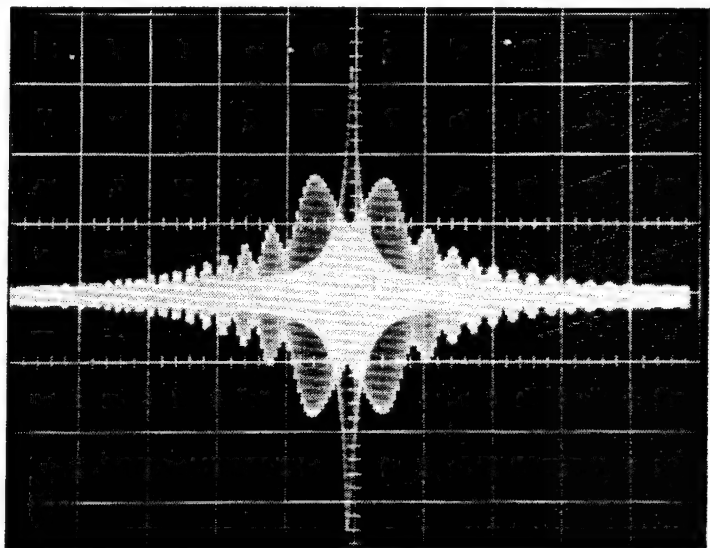87. **Bell Helicopters**. Pilot Instruction Manual TM55-1520-204-10, UH-1, Huey, Chapter 3, Section III, p. 6. Bell Helicopter/Textron, Hurst, TX. 1956.

88. **Haslinger**, Karl Heinz. *Criteria for Proper Selection of Sine Sweep Test Parameters*, Test, April/May 1986.

89. Glober, M. and W. Maly, Wechseldehnungs-messungen an Modell- und Original- Turbinen-schaufeln, **Proc. 6th Intern. Stress Analysis Congress**, Munich, Germany, Sept. 1978, pp. 343-361, V.D.I. Verlag, Düsseldorf, Germany.

90. **Nevel**, Donald E. *Moving Loads on a Floating Ice Sheet*, U.S. Army Cold Regions Research & Engineering Lab Report, May 1968, Hanover, NH.

91. **Nevel,** Donald E. *Vibration of a Floating Ice Sheet*, Research Report 281, U.S. Army Cold Regions Research & Engineering Lab Report, August 1970, Hanover, NH.

92. **Stein**, Peter K. *The Cantilever Beam as a Transducer: Dynamic Characteristics – A Junior Level Student Experiment*. Chapter 13 in Measurement Engineering, Vol. I, Basic Principles, 1st Ed. 1960 through 6th Ed. 1970, Stein Engineering Services, Inc., Phoenix, AZ (OP)

93. **Stein**, Peter K. *Frequency Selective Filtering and Frequency Analysis: A Comprehensive Student Experiment (Junior Level)*, **Lf/MSE Reprint 24**, 1970, Stein Engineering Services, Inc., 5602 E. Monte Rosa, Phoenix, AZ 85018. In Ch. 9 of [68] since 1960.

94. **Stein**, Peter K. *Frequency Analysis* Chapt. 9, Measurement Engineering, Vol. I, Basic Principles, 6th edition, 1970. Stein Engineering Services, Inc., Phoenix, AZ (OP)

95. **Wilson**, James F., Sherrill B. Biggers. *Dynamic Interactions Between Long, High Speed Trains of Air Cushion Vehicles and Their Guideways*. Trans. ASME, March 1971, pp. 16ff.

96. **Wright** Charles P. Applied Measurements Engineering: The Design of Effective Measurement Systems, Prentice Hall, 1994.

97. **Zimmermann**, Richard E. *Sweep Frequency Excitation of Resonant Systems*. Unpublished Master's Thesis, Arizona State University, Laboratory for Measurement Systems Engineering, Tempe, Arizona, 1973. See p. 20 for acquisition details.

Figure 10 (From Trull [72])(See also Fig. 3)

Illustration of Sweep Speed Effects
Triple Exposure for Steady State and
Rapid Sweeps Up and Down in Frequency
Note the difference between up and down sweeps and that the true resonance is at their intersection.

FORTRAN PROGRAM FOR LINEAR SINE WAVE SWEEP (From Zimmermann [97])

103

```fortran
   70 CONTINUE
      U=U-UB
      V=V-VB
      TXY=2.*G*Y
      C=COS(TXY)
      S=SIN(TXY)
      EXY=EXP(-Q*ZETA*(FR+SZ))
      XR(1,N)=(U*C-V*S)*EXY
      XI(1,N)=(U*S+V*C)*EXY
      TAU=(FR-FR1)*Q
      EB=EXP(-TAU*ZETA)
      YB=-(SZ*FR1)*TAU-TAU**2/(2.*G)
      CB=COS(TB)
      SB=SIN(TB)
      ZR=EB*(CB*ZETA-SB*SZ)
      ZI=-EB*(CB*SZ-SB*ZETA)
      XI(1,N)=X(1,N)-(ZR-ZI)*XR/(2.*SZA)*B1
      XR(1,N)=XR(1,N)-(ZI-ZR)*XY/(2.*SZA)*B1
      XR(2,N)=ZETA*XR(1,N)+S2*XI(1,N)
      XI(2,N)=-ZETA*XI(1,N)-S2*XR(1,N)
      XR(3,N)=TS*XR(1,N)-2.*ZETA*SZ*XI(1,N)
      XI(3,N)=TZS*XI(1,N)+2.*ZETA*SZ*XR(1,N)
  200 CONTINUE
      DO 500 K=1,3
      SR=XR(K,1)-XP(K,2)
      SI=XI(K,1)-XI(K,2)
      IF(K.GT.2)SR=SR*XX
      IF(K.GT.2)SI=SI-XX
      T(K)=SQRT(SR**2-SI**2)
      AR=SR-SI
      AI=SR+SI
      F(K)=ATAN(AI/AR)/RAD
      IF(AR.LT.0.)F(K)=F(K)+180.
      IF(K.LT.2)GO TO 250
      IF(AR.GT.0..AND.AI.LT.0.)F(K)=F(K)+360.
      IF(K.GT.2..AND.F(K).LT.0.)F(K)=F(K)+360.
  250 CONTINUE
      L=K+3
      F(L)=FASE/RAD+(K-1)*90
      T(K)=T(K)*C1
  500 CONTINUE
      B=1./SQRT((1.-FR**2)**2+4.*(FR*ZETA)**2)
      T(4)=2.*ZETA*B
      T(5)=FR*T(4)
      T(6)=FR*T(5)
      H=EXP(((FR-1.)/(2.*ZETA))**2*AL2/(-2.))
      THETA=-AL2*((FR-1.)**2)*G/QZZ
      A=SQRT(ABS(Q))*G*(-.25)*EXP(THETA)
      PRINT 10,FR,T(6),F(6),T(5),F(5),T(4),F(4),H,A
     1,T(3),F(3),T(2),F(2),T(1),F(1),A
  400 CONTINUE
      GO TO 50
```

102

```fortran
      DIMENSION XR(3,2),XI(3,2),T(6),F(6)
   10 FORMAT(38X,F5.3,2X,F7.3,F5.0,F7.3,F5.0,F7.3,F5.0,F7.3,
     1,4X,F4.3,F5.0,2X,F4.3,F5.0,2X,F4.3,F5.0,2X,F4.3)
   15 FORMAT(72X,1F4.2,2X,3F6.0,8X,3F6.0)
   20 FORMAT(40X,2HFR,5X,7HKINETIC,5X,9HDISSIPATE,3X,9HPOTENTIAL,
     5X,7HKINETIC,2X,9HDISSIPATE,2X,9HPOTENTIAL.
      13X,5HGAUSS.
      12X,5HGAUSS)
   25 FORMAT(3F10.3)
   30 FORMAT(56X,21HSTEADY STATE RESPONSE.
  120X,24HSWEEP FREQUENCY RESPONSE./)
   35 FORMAT(59X,2H0=,F6.1,3X,5HZETA=,F6.5,3X,12HINITIAL FR =,F5.2,/)
   45 FORMAT(1H1,/////,60X,10HSECOND ORDER LINEAR
     1,21H AND GAUSSIAN SYSTEMS)
      PI=3.1415927
      SQ2=1.414214
      RAD=.017453292
      AL2=ALOG(2.)
   50 CONTINUE
      PRINT 45
      READ 25,Q,ZETA,FR1
      PRINT 35,Q,ZETA,FR1
      PRINT 30
      PRINT 20
      Q=2.*PI*Q
      G=Q*2.*AL2**2/ZETA**4
      GZ=4.*G-ZETA**2
      TZS=2.*G-ZETA**2-1.
      C1=ZETA*SQRT(PI*ABS(Q)/(2.*(1.-ZETA**2)))
      XX=2.*ZETA/(SQ2*C1)
      SB=SQRT(ABS(Q)/4.)
      SZA=SQRT(1.-ZETA**2)
      B1=1./SQRT((1.-FR(P)**2)*2+(4.*(FR*ZETA)**2)
      DO 400 I=11,41
      FR=.05*(I-1)
      SN=FR*ZETA
      SD=1.-FR**2
      FASE=ATAN(SN/SD)
      IF(SD.LT.0.)FASE=FASE+PI
      FASE=-FASE
      DO 200 N=1,2
      SZ=SZA*(-1.)**N
      XB=(FR1-ZETA*SZ)*S8
      YB=(FR1+ZETA*SZ)*S8
      X=(FR+ZETA*SZ)*S8
      Y=(FR-ZETA*SZ)*S8
      IF(Q.GT.0.)GO TO 60
      Y=-Y
      YB=-YB
      CALL ERF(UB,VB,Y9,XB)
      CALL ERF(U,V,Y,X)
      GO TO 70
   60 CALL ERF(UB,VB,XB,YB)
      CALL ERF(U,V,X,Y)
```

FORTRAN PROGRAM FOR LINEAR SINE WAVE SWEEP (From Zimmermann [97])

102

```fortran
      DIMENSION XR(3,2),XI(3,2),T(8),F(8)
   10 FORMAT(36X,F5.3,2X,F7.3,F5.0,F7.3,F5.0,F7.3,F5.0,F7.3
     1,4X,F4.3,F5.0,2X,F4.3,F5.0,2X,F4.3,F5.0,2X,F4.3)
   15 FORMAT(72X,1F4.2,2X,3F6.0,HX,3F6.0)
   20 FORMAT(40X,2HFR,5X,7HKINETIC,5X,9HDISSIPATE,3X,9HPOTENTIAL,
     13X,5HGAUSS)    5X,7HKINETIC,2X,9HDISSIPATE,2X,9HPOTENTIAL,
     12X,5HGAUSS)
   25 FORMAT(3F10.5)
   30 FORMAT(56X,21HSTEADY STATE RESPONSE.
     120X,24HSWEEP FREQUENCY RESPONSE/)
   35 FORMAT(59X,2HQ=,F6.1,3X,5HZETA=,F6.5,3X,12HINITIAL FR =,F5.2,/)
   45 FORMAT(1H1,/////,60X19HSECOND ORDER LINEAR
     1,21H AND GAUSSIAN SYSTEMS)
      PI=3.1415927
      SQ2=1.414214
      RAD=.017453292
      AL2=ALOG(2.)
   50 CONTINUE
      PRINT 45
      READ 25,Q,ZETA,FRI
      PRINT 35,Q,ZETA,FRI
      PRINT 30
      PRINT 20
      Q=2.*PI*Q
      G=0.**2+AL2**2/ZETA**4
      GZ=4.*G*ZETA**2
      TZS=2.*ZETA**2-1.
      C1=ZETA*SQRT(PI*ABS(Q))/(2.*(1.-ZETA**2))
      XX=2.*ZETA/(SQ2*C1)
      S8=SQRT(ABS(Q)/4.)
      SZA=SQRT(1.-ZETA**2)
      BI=1./SQRT(1.-FRI**2)**2+4.*(FRI*ZETA)**2)
      DO 400 I=11,41
      FR=.05*(I-1)
      SN=FR*ZETA
      SD=1.-FR**2
      FASE=ATAN(SN/SD)
      IF(SD.LT.0.)FASE=FASE+PI
      FASE=-FASE
      DO 200 N=1,2
      SZ=SZA*(-1.)**N
      X3=(FRI-ZETA*SZ)*S8
      YB=(FRI+ZETA*SZ)*S8
      X=(FR-ZETA*SZ)*S8
      Y=(FR+ZETA*SZ)*S8
      IF(Q.GT.0.)GO TO 60
      Y=-Y
      YB=-YB
      CALL ERF(UB,VB,Y3,XB)
      CALL ERF(U,V,Y,X)
      GO TO 70
   60 CALL ERF(UB,VB,X3,YB)
      CALL ERF(U,V,X,Y)
   70 CONTINUE
      U=U-UB
      V=V-VB
      TXY=2.*X*Y
      C=COS(TXY)
      S=SIN(TXY)
      EXY=EXP(-Q=ZETA*(FR+SZ))
      XR(1,N)=(U*C-V*S)*EXY
      XI(1,N)=(U*S+V*C)*EXY
      TAU=(FR-FRI)*Q
      EB=EXP(-TAU*ZETA)
      TB=-(SZ*FRI)*TAU-TAU*Q/(2.*0)
      CB=COS(TB)
      SB=SIN(TB)
      ZR= EB*(CB*ZETA-SB*SZ)
      ZI=-EB*(CB*SZ+SB*ZETA)
      XI(1,N)=XI(1,N)-(ZR+ZI)-XX/(2.*SZA)*BI
      XRI(1,N)=XR(1,N)+(ZI-ZR)*XX/(2.*SZA)*BI
      XR(2,N)=-ZETA*XR(1,N)+SZ*XI(1,N)
      XI(2,N)=-ZETA*XI(1,N)-SZ*XR(1,N)
      XR(3,N)=TZS*XR(1,N)-2.*ZETA*SZ*XI(1,N)
      XI(3,N)=TZS*XI(1,N)+2.*ZETA*SZ*XR(1,N)
  200 CONTINUE
      DO 500 K=1,3
      SR=XR(K,1)-XR(K,2)
      SI=XI(K,1)-XI(K,2)
      IF(K.GT.2)SR=SR*XX
      IF(K.GT.2)SI=SI*XX
      T(K)=SQRT(SR**2+SI**2)
      AR=SR+SI
      AI=SR+SI
      F(K)=ATAN(AI/AR)/RAD
      IF(AR.LT.0.)F(K)=F(K)+180.
      IF(K.LT.2)GO TO 250
      IF(AR.GT.0..AND.AI.LT.0.)F(K)=F(K)+360.
      IF(K.GT.2..AND.F(K).LT.90.)F(K)=F(K)+360.
  250 CONTINUE
      F(K)=180.*(K-1)-F(K)
      L=K+3
      F(L)=FASE/RAD+(K-1)*90
      T(K)=T(K)*C1
  500 CONTINUE
      B=1./SQRT((1.-FR**2)**2+4.*(FR*ZETA)**2)
      T(4)=2.*ZETA*B
      T(5)=FR*T(4)
      T(6)=FR*T(5)
      H=EXP(((FR-1.)/(2.*ZETA))**2*AL2/(-2.))
      THETA=-AL2*((FR-1.)*6.)**2*27GZ2
      A=SQRT(ABS(Q))*G*(-.25)*EXP(THETA)
      PRINT 10,FR,T(6),F(6),T(5),F(5),T(4),F(4),H
     1,T(3),F(3),T(2),F(2),T(1),F(1),A
  400 CONTINUE
      GO TO 50
```
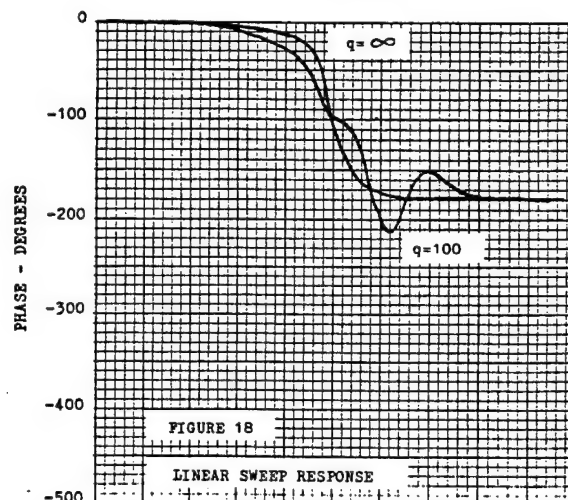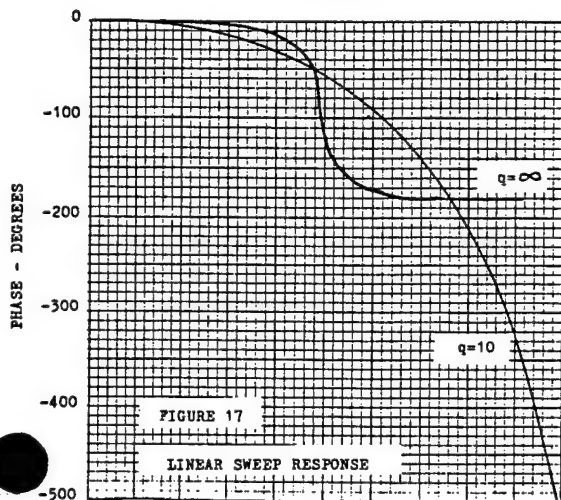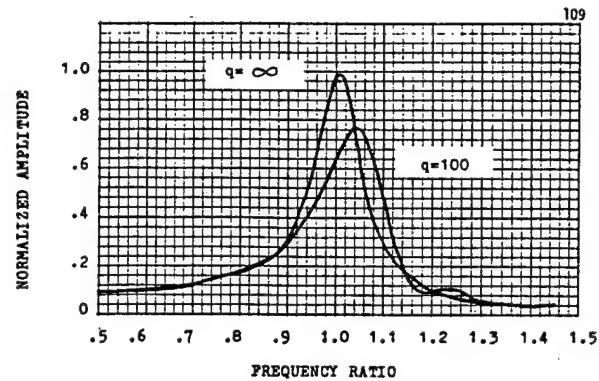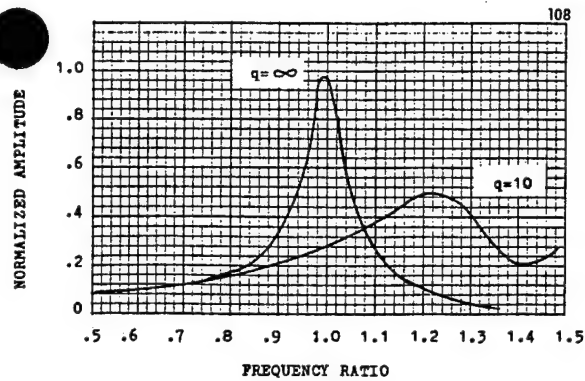
BODE (Magnitude & Phase) AND CO-QUAD PLOTS FOR LOW AND HIGH SWEEP SPEEDS [97]

FIGURE 17

LINEAR SWEEP RESPONSE

FIGURE 18

LINEAR SWEEP RESPONSE

FIGURE 19

CO-QUAD PLOT q=10

FIGURE 20

CO-QUAD PLOT q=100
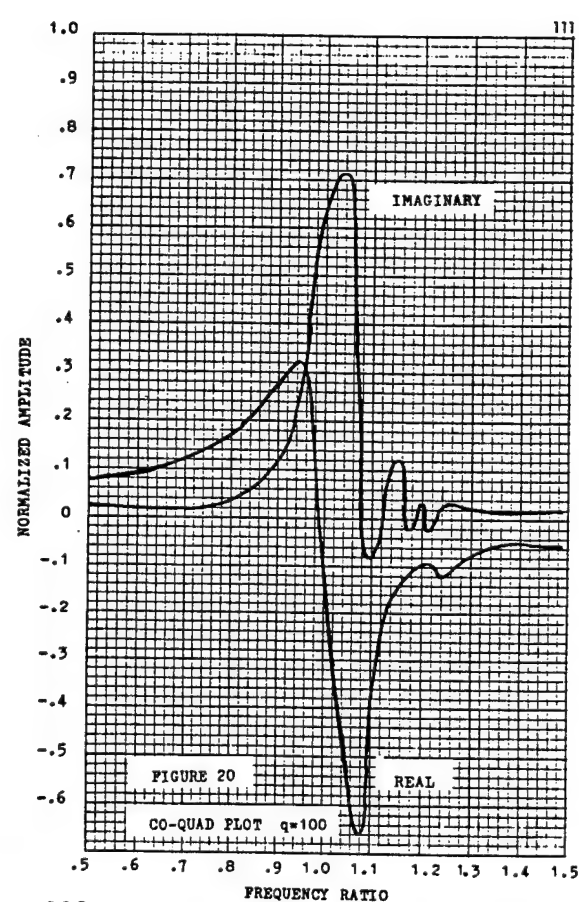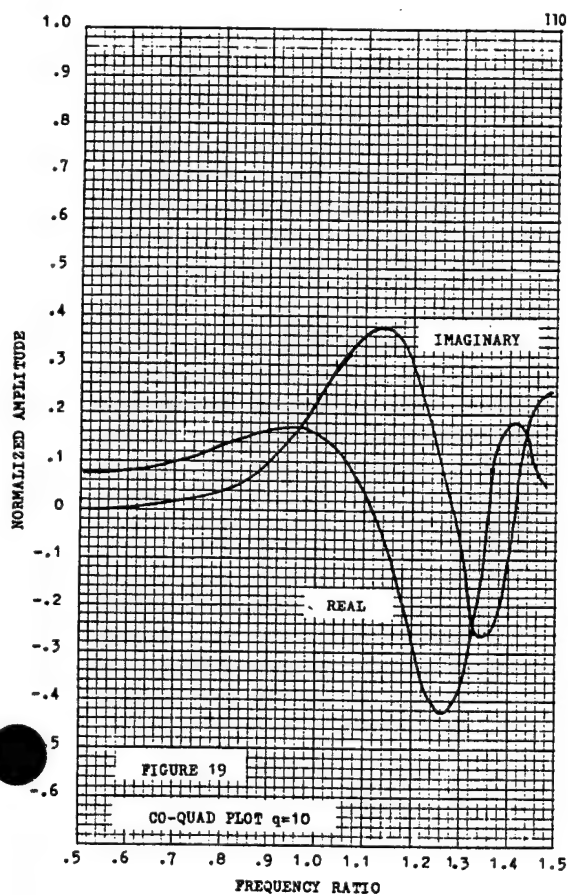
FORTRAN SUBROUTINE FOR THE ERROR FUNCTION

```
C                                                                120
      SUBROUTINE ERF(U,V,X,Y)
C     SALZER METHOD (MAT'4, TABLES AND AIDS TO COMP. VOL5 1951 P67)
      PI=3.1415927
      CALL RERF(ERR,X)
      C=COS(2.*X*Y)
      S=SIN(2.*X*Y)
      SUMR=0.
      SUMI=0.
      DO 100 M=1,15
      EN=M
      EXM=EXP(EN)
      EP=EXM**Y/2.
      EM=.25/EP
      EXM=(1./EXM)*EN/4.1/(EN**2+4.*X**2)
      EX2=EXP(-X)**X**X/PI
      CH=EP+EM
      SH=EP-EM
      SUMR=SUMR+EXN(2.*X*(1.-CH*C)+EN*SH*S)
      SUMI=SUMI+EXN(2.*X*CH*S+EN*SH*C)
  100 CONTINUE
      U =ERR*((1.-C)/(2.*X)+2.*SUMR)*EX2
      V =(S/(2.*X)+2.*SUMI)*EX2
      RETURN
      END


      SUBROUTINE RERF(ERR,X)
      T=1/(1.+.3275911*ABR(X))
      A1=0.254829592
      A2=-.284496736
      A3=1.421413741
      A4=-1.453152027
      A5=1.061405429
      ERR=A1*T+A2*T**2+A3*T**3+A4*T**4+A5*T**5
      ERR=(1.-EXP(-X*X)*X*ERR)*/ABS(X)
      RETURN
      END
```
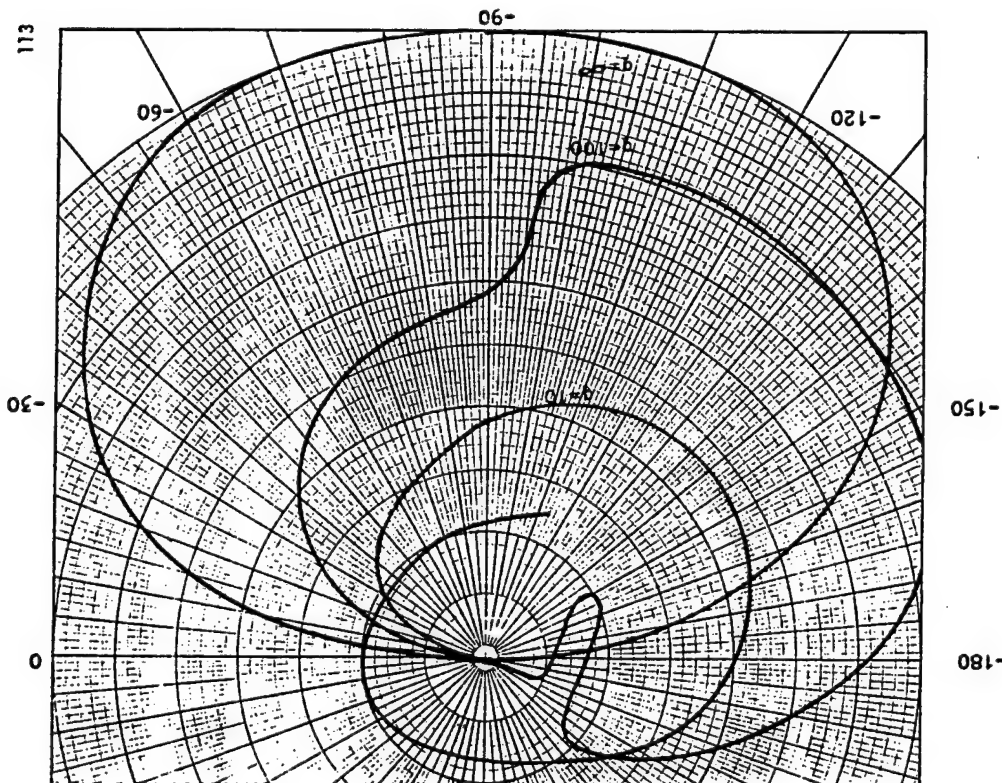

FIGURE 21   POLAR PLOT

```
C                                                                    122
      SUBROUTINE ERF(U,V,X,Y)
C     STRAND METHOD (MATH. OF COMP. JAN 65 P127)
      SP=1.7724538
      VZ=ABS(X*Y)
      H1=0.
      H2=0.
      FN=1.
      X=ABS(X)
      Y=ABS(Y)
      A=ABS(X)
      B=ABS(Y)
      CALL RERF(ERR,A)
      G=1.-ERR
      DO 100 N=1.35
      P=N
      PN=2*(I-1)+1
      FN=P*FN
      VN=VZ**(2*(N-1))
      H1=H1+G*VN
      G=EXP(-X**2)/(FN*A*PN)-$P*G/P
      G=2.*G/(PN*SP)
      H2=H2+A*P*G*VN
      C=COS(2.*VZ)
      S=SIN(2.*VZ)
      U=(1.-H1*C+H2*S)*X/A
100   V=(H1*S+H2*C)*Y/3
      RETURN
      END
```

```
C                                                                    121
      SUBROUTINE ERF(U,V,X,Y)
      MATTA REICHEL METHOD (MATH. OF COMP. APR 71 P339)
      SUMH=0.
      SUMK=0.
      PI=3.1415927
      H=.5
      SX=X
      SY=Y
      X=ABS(X)
      Y=ABS(Y)
      XS=X**2
      YS=Y**2
      A=COS(2.*X*Y)
      B=SIN(2.*X*Y)
      C=EXP(-2.*X*PI/H)-COR(2.*Y*PI/H)
      D=SIN(2.*Y*PI/H)
      EA=-(YS*2.*X*PI/H-XS)
      CD=C**2+D**2
      EXAC=2.*EXPLEA1/CD
      P=(A*C-B*D)*EXAC
      Q=(A*D-B*C)*EXAC
      PH=PI/H
      IF(X-PH) 50,60,70
50    O2=-D
      P2=P
      GO TO 80
60    O2=-Q/2.
      P2=P/2.
      GO TO 80
70    O2=0.
      P2=0.
80    CONTINUE
      XP=PI*(XS-YS)
      DO 100 N=1,12
      EN=N
      ES=EN**2*H**2
      FX=4.*XS*YS
      XNH=XS*YS-ES
      XNK=XS*YS-ES**2*4.+XS*YS
      XD=(XS-YS-ES)**2+4.*XS*YS
      EH=EXP(-ES)
      SUMH=SUMH+EH*XNH/XD
      SUMK=SUMK+EH*XNK/XD
100   CONTINUE
      VH=H*X/XP*2.*X*H*SJHH/PI*P2
      VK=H*Y/XP*2.*Y*H/PI*AU*K-Q2
      XMY=EXP(YS-XS)
      U=1.-XMY*(A*VH-B*V()
      V=XMY*(B*VH+A*VK)
      U=U*SX/X
      V=V*SY/Y
      RETURN
      END
```

Note on the References:

References 5, 17, 32, 39, 40, 42, 46, 49, 60, 71, 74, 75, 77, 84, 85, were not cited in those sections of Zimmermann's Master's Thesis [97] which were reproduced in this survey. Haslinger [88], published a paper in 1986 on the proper selection of sine sweep test parameters, not yet available when Zimmermann completed his thesis.

Zimmermann's original thesis copy resides in the Arizona Collection, Archives & Manuscripts, Arizona State University Library, P. O. Box 871006, Tempe, AZ 85287-1006. Phone: 602-965-3145. FAX: 602-965-0776. Call No. LD179.15 1973 Z55. Ron Trull's Thesis [72] has Call No. LD 179.15 1969 T78. The ASU Library provided photos of the computer print-outs.

Notes on the Contributing Authors:

Richard E. Zimmermann attended the University of Wisconsin for a year and in 1963 joined the U. S. Air Force (USAF). During his service he was assigned to Arizona State University (ASU) under the Air Force Institute of Technology (AFIT) program. He received his BSME in 1968. He served two years at Vandenberg Air Force Base (AFB), CA and two years at Eglin AFB, FL. After leaving the USAF, he returned for his MSME in 1971, which he received in the Lf/MSE in 1973. He is now Director of New Product Development for *Simula, Inc.*, in Phoenix, Arizona.

Ronald V. Trull, joined the USAF in 1962 and was selected for the Airman Education and Commissioning Program. He entered ASU in 1965 and graduated with his BSE majoring in Measurement Systems Engineering in 1967. In January 1968 he was selected by the AFIT program to return to ASU for his MSE which he received in 1969 in the Lf/MSE. He was assigned to Wright Patterson AFB, OH, the General Dynamics Plant in TX and to Martin Marietta, CO. After his retirement from the USAF as Major in 1982 he joined Cobe Labs in Denver as Quality Manager, He is now retired, living in Jasper, Arkansas.

A Note on the Sweep Factor q:

Lewis [41] defined it physically: The number of undamped free vibrations the system would make from time zero until the time when the instantaneous exciting frequency equals the natural frequency of the system. He derived the value now used by everyone: $q = f_n^2/(df/dt)$ with all frequencies in Hz. "It is a measure of the rate at which a system is accelerated."

SWEEP FUNCTIONS (From [97])

A sweep frequency is defined here as a time-dependent frequency which passes through the resonances of a system according to some specified sweep function. It may be either periodic or non-periodic, and the distinction between a sweep frequency and modulated frequency is not precise. The usage of terminology depends primarily upon the extent of frequency variation with respect to the bandwidth of the system. A time-dependent periodic frequency with a range small compared to the system bandwidth would be called a modulated frequency, and the same variable frequency would be called a sweep frequency if the frequency excursions were large compared to the system bandwidth.

Although any wave form could be subjected to a frequency sweep, only sinusoidal wave forms are discussed in the engineering literature. This is undoubtedly due to the facts that the most common applications involve sinusoidal waveforms and the analysis of swept sine waves was sufficiently difficult to discourage the extension of the analysis to other waveforms. Considering functions of the form Sin (ϕ) where $\phi = \phi(t)$ is a non-linear function of time, there are three sweep functions which are of considerable engineering interest: Sine, Linear and Logarithmic.

It has become customary to designate the first time derivative of the sweep function, ϕ, as the *instantaneous frequency* and to represent it by the symbol Ω. The instantaneous frequencies for the above sweep functions are then defined as follows:

SINUSOIDAL SWEEP: $\phi = \dfrac{\sigma}{w} \, \text{Sin} \, \omega t$ $\Omega = \sigma \, \text{Cos} \, (\omega t)$

LINEAR SWEEP: $\phi = \sigma t + \varepsilon t^2$ $\Omega = \sigma + 2\varepsilon t$

LOGARITHMIC SWEEP: $\phi = \dfrac{\sigma}{K} \, e^{Kt}$ $\Omega = \sigma e^{Kt}$

It is seen that the initial frequency is σ in all cases, and ω, 2ε, and K determine the rate at which the frequency changes.

It should be noted that a time varying Ω can be interpreted in two ways: as a changing frequency or a constant frequency with a changing phase. Both mechanisms are used to generate sweep frequencies giving rise to the distinction between the terms *frequency modulation* and *phase modulation* in communication theory. While this distinction is significant so far as the source of the sweep frequency is concerned, once the signals have been generated, they are identical and were considered such by Zimmermann [97].

A non-dimensional sweep factor has been associated with both linear and logarithmic sweeps. Lewis [41] first defined the factor for the linear sweep, which he designated as q, as:

$$q = \frac{f_n^2}{df/dt} = \frac{\omega_n^2}{4\pi\varepsilon} \quad \text{(Also see p. 20)}$$

where f is in Hz, ω in rad/sec and ε one half the sweep speed in rad/sec/sec. The sweep speed is df/dt in Hz/sec.

No particular symbol has become accepted for the logarithmic sweep factor, but it is generally defined as the ratio of the first derivative of the instantaneous frequency to the instantaneous frequency and K/ω_n is the symbolism adopted by Hawkes [33].

SWEEP FREQUENCY SPECTRA (From [97])

The spectrum of a sweep frequency can assume various shapes depending on the velocity and the range of the sweep. For linear sweeps the forcing function has a Fourier transform in the form of an integral which both Cook [16] and Kennedy [26] show is expressible in terms of Fresnel integrals of real arguments and can thus be evaluated with tables. The latter reference develops a rather elegant means of describing the nature of this spectrum as a Cornu spiral when the real and imaginary parts are plotted against each other.

If the range of the sweep becomes infinite, then, as shown in [56], the spectrum is no longer in terms of Fresnel integrals but has a simpler form.

The form for a trapezoidal sweep was computed by Skinner [65], and the spectrum for a symmetrical triangular wave is available as a special case of that derivation. The development of pulse compression radar systems created an interest in the spectra of linear sweep frequencies in the electrical engineering literature, and extensive treatments of the subject can be found (for example in [61])

In mechanical vibration testing, the possibility of obtaining a nearly rectangular spectrum from a linear sweep has been made it attractive as a transient excitation force since it allows control of the range of frequencies excited. Extensive investigations of this application were made by White [79], [80], [81], [82]. The rectangular shape of the resulting spectrum also makes possible simplifications in correlation analysis as discussed by Skingle [64].

The spectrum of a sweep frequency can also be obtained by direct Fourier analysis via digital computer. The results from such an analysis is in White [82]. This technique also offers a means of obtaining the spectrum of a logarithmic sweep.

The discussion in Zimmermann's Master's Thesis is limited to linear and logarithmic sweeps, since these have proved to be the troublesome ones. This survey has brought mainly the linear sweep considerations.

System analysis for sinusoidal sweeps can be accomplished in terms of Bessel functions as was noted by Carson [12] in 1922. This technique has become a well established part of communication theory and can be found in almost any textbook on frequency modulation.

The equations may describe a stationary or time invariant system subjected to a sweep frequency excitation. However, they are also the governing equations for a corresponding non-stationary system experiencing a constant-frequency excitation.

The mathematical equivalence of these problems was noted by Hok [34], Barber and Ursell [6], and Batten [7], and was discussed at length by Van der Pol [76]. Physically they describe quite different processes. The first case might represent a series RLC circuit with a sweep frequency input, while the second case represents a series RLC circuit with time-varying resistance and inductance, experiencing a constant frequency excitation.

In frequency analysis, the first would represent the sweeping of a frequency spectrum through a filter, while the second would represent the sweeping of a filter across a frequency spectrum. The envelope of the output of the first system is identical to the transfer ratio of the second system. Thus the ratio of the sweep frequency response to the input may be expressed as a transfer ratio.

The many mathematical solutions presented in this survey assume that many cycles occur during transition through resonance. Numerical integration of the integrals representing the response is not possible.

If the sweep is so rapid that only a few cycles occur through resonance, the system output can be computed by numerical integration techniques. White [80] solved this case for a cubic nonlinearity by using a Runge Kutta integration procedure. This method does not produce the envelope of the response, only the response for a specific phase angle a change in which may increase or decrease the maximum response value.

212

Sweep Speed Effects in Resonant Systems: A Unified Approach

A SURVEY OF THE LITERATURE THROUGH BEGINNING 1973 (From Zimmermann [97])
(See References [88]and [96] for more of the recent literature and developments)

AUTHOR	REF. NO.	SYSTEM	SWEEP FUNCTION	ANALYTICAL METHOD
Agrawal	1, 2, 3	Non linear non stationary mechanical system	General	Asymptotic expansion
Barber	6	Linear second order frequency analyzer	Logarithmic	Approximation
Batten	7	Gaussian	Linear	Fourier transform
Bishop	8	Linear second order	Linear	Graphical
Capello	11, 12	Linear second order, two degree of freedom	Linear	Variation of parameters
Carson	13	General	General	Operational calculus
Chang	13	Gaussian	Linear	Convolution
Clavier	15	General	General	Fourier transforms
Cook	16	Compression filters	Linear	Fourier Transformations
Cronin	18, 19	General	Linear & Logarithmic	Approximation
Dimentberg	21	Linear second order, rotating shaft	Linear	Variation of parameters
Evan-Iwanowski	23, 24	Non-stationary non-linear	General	Asymptotic expansion
Fearn	25	Linear second order	Linear	Variation of parameters
ch	26	General	Linear	Convolution & Fourier Transformation
Hawkes	33	Linear second order	Logarithmic	Substitution $x = e^{i \varnothing(t)}$
Hok	36	General	Linear	Laplace transform
Kevorkian	36	Linear second order, no damping	Linear	Asymptotic expansion
Lewis	41	Linear second order	Linear	Variation of parameters
Marique	47	Linear second order	Sawtooth	Laplace Transforms
Mitropolskii	50, 51, 52	General	General	Asymptotic expansion
Morse	53	Linear second order	Logarithmic	Variation of parameters
Parker	54	Linear second order, transmissibility	Linear and Logarithmic	Variation of parameters
Polarad Corp.	56	Gaussian	Linear	Fourier Transform
Salinger	62	Rectangular	Linear	Fourier Transforms
Saul	63	Gaussian	Linear	Fourier Transforms
Stronge	69, 70	Linear second order, transmissibility	Linear	Variation of Parameters
Trull	72, 73	Linear second order	Linear	Variation of parameters
der Pol	76	General	General	Operational Calculus
Yanabe	85	Second order linear	Linear	Numerical

BIBLIOGRAPHY

Sweep Frequency (From Zimmermann [97])

1. **Agrawal**, B. N. *Resonances in Nonstationary Nonlinear Mechanical Systems.* Unpublished Doctor's dissertation, Syracuse University, 1970

2. **Agrawal**, B. N. *A Resonant Response of a Mechanical System Subjected to Logarithmically Swept and Notched Base Excitation Using Asymptotic Expansion,* Shock & Vibration Bulletin, 41:127-132, December 1970

3. **Agrawal**, B. N. and R. M. Evan-Iwanowski. *Resonances in Non-stationary, Nonlinear, Multidegree of Freedom Systems,* AIAA Paper 72-401, AIAA/ASME/SAE 13th Structures, Structural Dynamics and Materials Conference, San Antonio, Texas, April 10-12, 1972.

4. **Baker**, J. G. *Mathematical Machine Determination of the Vibration of Accelerated Unbalanced Rotor,* Journal of Applied Mechanics, 61:A-145 to A-150, Dec. 1939

5. **Baldwin**, G. R. J. *Dynamic Frequency Response Measuring Equipment,* Electronic Engineering, 38:167-171, March 1966.

6. **Barber**, N. F. and F. Ursell. *The Response of a Resonant System to a Gliding Tone,* Philosophical Magazine, 39:345-361, May 1948.

7. **Batten**, H. W., R. A. Jorgenson, A. B. Macnee and W. W. Peterson. *The Response of a Panoramic Receiver to CWE and Pulse Signals,* Proc. I.R.E., 42: 948-956, June 1954.

8. **Bishop**, R. and D. Johnson. The Mechanics of Vibration, New York, Cambridge University Press, 1960

9. **Bozich**, D. J. *Utilization of a Digital Computer for On-Line Acquisition and Analysis of Acoustic and Vibration Data,* Shock & Vibration Bulletin, 35:151-180, Feb. 1966.

10. **Broch**, J. T. *Some Aspects of Sweep Random Vibration,* Jnl. Sound & Vibration, 3:195-204 (No 2.) March 1966

11. **Capello**, A. *On the Acceleration of Rotors Through Their Critical Speed,* Meccanica, 144-152, September 1967.

12. **Carson**, J. R. *Notes on the Theory of Modulation,* Proc. I.R.E., 10:57-64, February 1922.

13. **Carson**, J. R. and T. C. Fry, *Variable Frequency Electric Circuit Theory with Application to the Theory of Frequency Modulation,* Bell System Technical Journal, 16:513-540, October 1937.

14. **Chang**, S. S. L. *On the Filter Problem of the Power Spectrum Analyzer,* Proc. I. R. E., 41L1278-1282, August 1954.

15. **Clavier**, A. G. *Application of Fourier Transforms to Variable Frequency Circuit Analysis,* Proc. I. R. E., 39:1287-1290, November 1949.

16. **Cook**, C. E. *Pulse Compression – Key to More Efficient Radar Transmission,* Proc. I. R. E., 48:310-316, March 1960.

17. **Crane**. H. L. *A Manual Frequency Sweep Technique for the Measurement of Airplane Frequency Response,* NASA TN-D-375, April 1960

18. **Cronin**, D. L. *Response of Linear Viscous Damped Systems to Excitations Having Time Varying Frequency,* unpublished Doctor's dissertation, California Institute of Technology, 1966.

19. **Cronin**, D. L. *Response Spectra for Sweeping Sinusoidal Excitations,* Shock & Vibration Bulletin, 38:133-139, August 1968.

20. **Curtis**, A. J. *The Selection and Performance of Single-Frequency Sweep Vibration Tests,* Shock & Vibration Bulletin, 23:93-101, June 1956.

21. **Dimentberg**, F. M. Flexural Vibrations of Rotating Shafts, London, Butterworth & Co., 1961.

22. **Drain**, D. I., W. M. Bruton and F. J. Paulovich, *Airbreathing Propulsion System Testing Using Sweep Frequency Techniques,* NASA TN-D-5485, Oct. 1969.

23. **Evan-Iwanowski**, R. M. *Nonstationary Vibrations of Mechanical Systems,* Applied Mechanics Review, 22:213- 219, March 1969.

24. **Evan-Iwanowski**, R. M., W. F. Sanford and T. Kehagioglou. *Nonstationary Parametric Response of a Nonlinear Column,* Proc. 10th S.E. Conf. Applied Mechanics, Raleigh, NC, 1970.

25. **Fearn**, R. L. *The Temporal Passage of Mechanical Systems Through Resonance,* Unpublished Doctor's dissertation, University of Florida, 1965.

26. **Gersch** W. and J. M. Kennedy. *Spectral Measurements of Sliding Tones,* I.R.E. Trans. (Circuit Theory), August 1960, pp. 26-39, (special supplement)

27. **Gertel**, M. *Development of Specification Requirements,* Shock & Vibration Bulletin, 31:25-32, 1963.

28. **Godwin**, G. L. and E. F. Merrill, *Oscillatory Torques During Synchronous Motor Starting,* I.E.E.E. Trans. on Industry. 4GA-6:258-265, May-June 1970.

29. **Granick**, N. *Choosing a Suitable Sweep Rate for Sinusoidal Vibration Testing,* NASA TN-D-709, 1961.

30. **Greenstein**, L. J., T. R. Shaifer and M. Epstein. *Magnetic-Field Spectrum Analyzer,* Review of Scientific Instruments, 35:1307-1310, October 1964.

31. **Harris**, C. M. and C. E. Crede, Shock and Vibration Handbook, Vol. 2, New York, McGraw-Hill Cook Co. 1961.

32. **Hartenstein**, R. Unpublished Memo: *TR-10 computer Solution to Sweep Rate Problem,* Goddard Space Flight Center, Greenbelt, Maryland.

33. **Hawkes**, P. E. *Response of a Single Degree of Freedom System to Exponential Sweep Rates,* Shock & Vibration Bulletin, 33:296-304, February 1964.

34. **Hayasaka**, T. *A New Proposal for the Design of Acoustic Instruments,* Electronics & Communications in Japan, 48:12-20, January 1965.

35. **Hok**, G. *Response of Linear Resonant Systems to Excitation of a Frequency Varying Linearly with Time,* Journal of Applied Physics, 19:242-250, March 1948.

36. **Kevorkiam**, J. *Passage Through Resonance for a One Dimensional Oscillator with Slowly Varying Frequency,* SIAM Journal of Math, 20:364-373, May 1971.

37. **Kincheloe**, W. R. *The Measurement of Frequency with Scanning Spectrum Analyzers.* Unpublished Doctor's dissertation, Stanford University, 1962.

38. **Kino**, G. S. and H. Matthews. *Signal Processing in Acoustic Surface Wave Devices,* I.E.E.E. Spectrum, August 1971, pp. 22-35.

39. **Kryloff**, N. and N. Bogoliuboff. Introduction to Non-Linear Mechanics. Princeton NJ, Princeton University Press, 1967.

40. **Lewis**, D. Shock and Vibration: An Annotated Bibliography, London, Kenneth Mason Publications, 1967.

41. **Lewis**, F. M. *Vibrations During Acceleration Through a Critical Speed,* Trans. ASME, 54:253-261, 1932.

42. **Loewy**, R. G., and V. J. Piarolli. *Dynamics of Rotating Shafts.* The Shock & Vibration Information Center, U. S. Dept of Defense, 1969, Chapter 5.

43. **Lorenzo**, C. F. *Variable Sweep Rate Testing: A Technique to Improve the Quality and Acquisition of Frequency Response and Vibration Data,* NASA TN-D-7022, December 1970

44. **Lorenzo**, C. F. *Variable Sweep Rate Frequency Response and Vibration Testing,* Instruments & Control Systems, 44:109-111, September 1971.

45. **Lukens**, . R., R. L. Turney, R. L. Fefferman, J. W. Kittle and T. E. Reed. *Dynamic Stability of Space Vehicles*, NASA Contractor Report CR-940, December 1967.

46. **Magrab**, E. B. and D. S. Blomquist. The Measurement of Time-Varying Phenomena, NY. Wiley Interscience, 1971.

47. **Marique**, J. *The Response of RLC Resonant Circuits to EMF of Sawtooth Varying Frequency*, Proc. I.R.E., 40:945- 950, August 1952.

48. **McGann**, G. D. and R. R. Bennett. *Vibration of Multifrequency Systems During Acceleration Through Critical Speeds*, Jnl. Applied Mechanics, 16:375-382, Dec. 1949.

49. **Morse**, R. E. *The Relationship Between a Logarithmically Swept Excitation and the Building of Steady State Resonant Response*, Report 7120-6154-RU 000, TRW Space Technology Laboratories, Contract AF 04(694)-550, December 1964.

50. **Mitropolskii**, Y. A. and B. I. Moseenkov. The Monofrequency Method in the Dynamic Analysis of Structures. New York: Consultants Bureau a Division of Plenum Publishing Corp. 1967.

51. **Mitroposky**, Y. A. and N. N. Bogoliubov. Asymptotic Methods in the Theory of Non Linear Oscillations, Delhi-6, India: Hindustan Publishing Corporation, 1961.

52. **Mitrpolskii**, Y. A. *Problems of the Asymptotic Theory of Non-stationary Vibrations*, Israel Program for Scientific Translations, Jerusalem, 1965.

53. **Morse**, R. E. *The Relationship Between a Logarithmically Swept Excitation and the Build-up of Steady State Resonant Response*, Shock & Vibration Bulletin, 35:231-262, January 1966.

54. **Parker**, A. V. *The Response of a Vibratory System to Several Time Dependent Frequency Excitations*. Unpublished Master's thesis. Iowa State Univ., 1962.

55. **Patrick**, T. J. *Sweep Sine Wave Simulation of Random Vibration and Its Effect on Design*, Journal. of Sound & Vibration, 5: 37-41, January 1967.

56. **Polarad** Electronics Corporation, Handbook of Spectrum Analyzer Techniques. Polarad Electronics, Long Island City, New York, 1955.

57. **Pollard**, E. I. *Torsional Response of Systems*, Trans. ASME, 89:316-324, July 1967.

58. **Quazi**, A. S. and A. G. J. MacFarlane, *The Controlled Transition of a Rotating Shaft Through its Critical Speed*, International Journal on Control, 6:302-315, 1967.

59. **Reed**, W. H., A. W. Hall and E. L. Barker. *Analog Techniques for Measuring the Frequency Response of Linear Physical Systems Excited by Frequency Sweep Inputs*, NASA TN-D-508, October 1960.

60. **Reveman**, A. *Errors Obtained on Spectral Density Analysis with Sweeping Filter and Remaining Ripple when Using Equalizer*. Journal. Acoustical Society of America, 47: 257-264, January 1970.

61. **Rihaczek**, A. W. Principles of High Resolution Radar, New York: McGraw-Hill Book Co., 1969.

62. **Salinger**, H. *Zur Theorie der Frequenzanalyse mittels Suchtons*, Elektrische Nachrichten Technik, August 1962, pp. 293-301.

63. **Saul**, R. and E. Luloff. *Designing a Spectrum Analyzer*, Electronic Industries, April 1959, pp. 66-71.

64. **Skingle**, C. W. *Correlation Techniques for Analyzing the Response of a Resonant System to a Rapid Frequency Sweep Input*. Proc. AIAA Symposium on Structural Dynamics and Aeroelasticity, Boston, Mass. Aug. 30 - Sept. 1, 1965, pp. 442-451.

65. **Skinner**, L. V. *Spectra of Waves with Periodic Modulation*, Trans. I.R.E. (Circuit Theory), June 1964.

66. **Spence**, H. R. and H. N. Luhrs. *Peak Criterion in Random vs. Sine Vibration Testing*. Journal of the Acoustical Society of America, 33:652-655, May 1961.

67. **Spence**, H. R. and H. N. Luihrs. *Structural Fatigue under Combined Random and Swept Sinusoidal Vibration*. Jnl. Acoustical Soc., of America, 34:1076-1081, Aug. 1962.

68. **Stein**, P. K. Measurement Engineering, Vol. I, 6th ed. Stein Engineering Services, Inc., 1970 (1st edition, 1960. (OP) 5602 E. Monte Rosa, Phoenix, AZ 85018.

69. **Stronge**, W. J. *Vibrations of a Mechanical System Traveling Over a Stationary Waveform*, Unpublished Master's thesis, Univ, of California at Los Angeles, 1964.

70. **Stronge**, W. J. *Vibrations Due to an Excitation with Uniform Varying Frequency*, Trans. ASME Series E, 33:4562-463, June 1966.

71. **Toda**, K., G. Roffman, A. Talkin. *The Matched Acoustic Generator*, ASME Trans. Series G, Journal. of Dynamic Systems, Measurements & Control, 94:11-14, Mar. 1972.

72. **Trull**, . R. V. *Sweep Speed Effects on Dynamic Systems*, Unpublished Master's thesis, Arizona State University, Laboratory for Measurement Systems Engineering, 1969.

73. **Trull**, R. V. *Sweep Speed Effects in Resonant Systems*, Shock & Vibration Bulletin, 41:95-98, December 1970.

74. **Usher**, T. *Average Control for Sinusoidal and Random Vibration Testing*, Journal of the Acoustics Society of America, 41:840-849, April 1967.

75. **Valitov**, R. A. and V. M. Bakumenko. *Optical Sweep Generators*, Radio Tekhnika i Elektronika, 17:90-93, January 1972.

76. **Van der Pol**, B. *The Fundamental Principles of Frequency Modulation*, Institute of Electrical Engineers, London Proceedings, May 1946, pp. 153-158.

77. **Viles**, R. S. *Swept Frequency Techniques for Accurate R.F. Measurements*, Marconi Instrum. (Great Britain), 13:88-92, May 1972.

78. **Waldron** R. A. *Errors Due to the Uncertainty Principle in Swept-Frequency Cavity Measurements of Properties of Materials*, I.E.E.E. Trans. Microwave Theory & Techniques, May 1968, pp. 314-315.

79. **White**, R. G. *The Application of a Transient Test Technique to the Study of Local Vibration Characteristics of Ship Structures*, I.S.V.R. Tech. Report No. 31, Univ. of Southampton (Institute for Sound & Vibration Research) (England), May 1970.

80. **White**, R. G. *Use of Transient Excitation in the Measurement of the Frequency Response of Systems with Non-linearities Arising from Large Deflections*, I.S.V.R. Tech Rpt No. 27, Univ. of Southampton, Feb. 1970 (See #79).

81. **White**, R. G. *Spectrally Shaped Transient Force Functions for Frequency Response Testing*, Unpublished paper, I.S.V.R., Univ of Southampton. See #79.

82. **White** R. G. *Evaluation of the Dynamic Characteristics of Structures by Transient Testing*. Journal of. Sound & Vibration, 15:147-161, March 197.

83. **Williams**, E. M. *Radio Frequency Spectrum Analyzers*, Proc. I.R.E., 34:18P-22P, January 1946.

84. **Williams**, W. J., J. W. Gesink, and M. M. Stern. *Biological System Transfer Function Extraction Using Swept Frequency and Correlation Techniques*, Medical & Biological Engineering, 10:609-6210, September 1972.

85. **Yanabe**, S. and A. Tamara. *Vibration of a Shaft Passing Through a Critical Speed*, Bulletin J.S.M.E., 14:1050-1058, October 1971. (Japan Society of Mech., Engrs.)

86. **Glasier**, J. *A Compendium of Data Compression Bibliography*, Scientific Data Systems, 701 South Aviation Blvd., El Segundo, CA. December 1968.

215

PYRO-SHOCK, IMPACT, EXPLOSIONS AND OTHER HIGH-SPEED TRANSIENTS:

SOME THOUGHTS ON "TQM" — TOTAL QUALITY *MEASUREMENTS*

by Peter K. Stein, Director of Short Courses
The Engineering and *The Dynamics of Measurement Systems for Test & Evaluation*
5602 E. Monte Rosa
Phoenix, AZ 85018-4646

Telephone & Telefax: (602)—945—4603
In the U.S. Telephone & Telefax: (800)—MEASurement SYStems
632-7   797

ABSTRACT

The measurement of a high speed transient requires, in general, the reproduction of its wave shape.

Preventing the achievement of this mission are distortions due to Input–Output Amplitude characteristics, to Magnitude vs. Frequency and Phase vs. Frequency characteristics plus the response of the measurement system to extraneous environmental influences. Problems of rise–time, undershoot and peak–depression are also present.

The author will refer to these Distortion Mechanisms as Amplitude Distortion, Magnitude Distortion and Phase Distortion, for short.

Diagnostic data about the measurement system and about its performance in the operating environment are necessary in order to validate the acquired data. The requirements are given in the paper.

Data analysis and interpretation are not God–given rights guaranteed by the Constitution. They are rights which the Measurement Engineer has to earn through the Data Validation process. Before measurements may be analyzed or interpreted they must be raised to the level of *Total Quality Measurements* – the forgotten *TQM*.

This paper presents techniques, based on the Unified Approach to the Engineering of Measurement Systems (Ref 1), which achieve these aims.

The data validation processes are all internal, within the measurement system and the acquired data. No comparison with theoretical or predicted value is ever suggested.

Measurement Systems must, however, be **designed** to accommodate these validation procedures. The procedures must be built into the test program. They cannot, in general, be added after-the-fact.

One of several requirements discussed in this paper is the ability to provide zero excitation – bridge supply – interrogating input – power – whatever nomenclature is used, to impedance-based transducers such as resistance-strain-gage-based trans-ducers and strain gages. Preferably such a choice should be computer programmable.

Such a check is mandatory for all explosively initiated tests. All chemical explosions are accompanied by magnetic and electric fields. In automotive air bag inflation tests, for example very large electrostatic discharge voltages have been observed.

The list of manufacturers known to the author and who provide signal conditioning with such an option, is very short indeed and a sad commentary on modern signal conditioning design (see Appendix).

Procedures similar to the ones described in this paper for strain-gage-based and piezoelectric transducers are given in Ref 1 for thermocouples. The bulk of the methods given in this paper are, however, applicable to all transducers for all transient measurements in all disciplines.

THE WAVE SHAPE REPRODUCTION OF A TRANSIENT

The measurement of a high speed transient requires, in general, the reproduction of its wave shape.

As shown in Ref. 1, the reproduction of the wave shape of any signal requires:

- Operation in the distortion-free linear range of the *Input–Output Characteristics*.

Any Non-Linearities in the Input-Output Characteristics result in the creation of frequencies at the Output which were not present at the Input, known as Frequency–Creation (see also Ref. 2). These created frequencies may be higher than or lower than the input frequencies; sums and differences of them; integer or non-integer multiples or sub-multiples of the input frequencies and of their sums and differences, etc. No amount of filtering may be able to hide the effects of those *created frequencies*. The result is Wave Shape Distortion due to Amplitude-Based mechanisms.

- Operation in the flat range of the *Magnitude vs. Frequency–Response Characteristics*.

Operation outside this range results in Wave Shape Distortion due to Magnitude vs. Frequency-Based mechanisms.

- Operation in the linear portion of the *Phase Shift vs. Frequency–Response Characteristics* or in the Constant Time-Delay portion of the *Time-Delay vs. Frequency–Response Characteristics*.

Since the derivative of the phase shift curve with respect to frequency is the *Time Delay* of the signal through the measurement system, *Constant Time Delay* is a consequence of *Linear Phase Shift*. Operation outside these ranges results in Wave Shape Distortion due to Phase vs. Frequency-Based mechanisms.

Data Validity Diagnostic Procedures

The measurement of high speed transients also requires additional diagnostics to assure data validity. Since these have been discussed extensively in Ref. 1 only an abstract of the essence of the problems and approaches to their solution will be given here.

Any publication which does not present evidence of these diagnostic validity checks contains data which cannot really be interpreted as representing the process for which the experimental observations are reported in that paper. Without the validation procedures presented here, the acquired data do not represent **Total Quality Measurements**.

Note that **nowhere** is there even a hint or suggestion to compare the experimental data with theoretical predictions. These are usually less valid than the data! Once the data are validated they become the criterion to which any theory is compared.

216

A PRIORI KNOWLEDGE REQUIRED

Before a Transient Measurement can be planned, executed or interpreted, the following knowledge must exist about the Measurement System being used, and the Process being investigated.

About the Measurement System

The Linearity (Input–Output) Characteristics and the Frequency–Response Characteristics for Magnitude and Phase must be known for the Measurement System.

For the Frequency–Response Characteristics for Magnitude, the Roll-Off–Characteristics at both ends of the curve must be known to at least one or two decades below the lower 3 dB point and above the upper 3 dB point. If those Roll–Off–Characteristics can not be obtained, then the Transient Response of the system to a Step must be known, both to an expanded and a compressed time scale.

It will be seen that these latter data are contained in the **Shunt Calibration** record and are of extreme importance in the data interpretation.

No transient record can be interpreted without the above information being available.

About the Process

The Amplitude vs. Frequency-Content of the original signal as emitted by the Process must be known so that the frequency response and linearity specifications can be established for the measurement system. This knowledge also permits selection of sampling rates and/or carrier frequencies for minimum data loss during its acquisition. (See Refs 1, 3)

The Horse Before the Cart ?

The Measurement Engineer finds him/her-self in the usual *Closed-Loop* quandary of needing to know the answer before the question can be phrased — i.e., the frequency spectrum of the signal and the amplitudes, before the measurement system can be selected to observe them.

In the case of steady–state signals, the solution is easier than for transient measurements, because preliminary observations can be made which are not possible in transient situations. The design process takes only time. Ref. 1 provides a step-by-step process for the planning of both types of test which will be summarized here only for the transient case.

For transient measurements, the diagnostic process requires channel capacity. In parallel with whatever measurement system has been selected, there must be a **totally analog measurement channel** to provide the data on amplitudes and frequencies before anti–aliasing filters for purposes of either sampling criteria or channel separation criteria (Ref. 3) have distorted the original data.

Such **analog channels** must contain only analog components such as cathode ray oscilloscopes or direct-record analog magnetic tape recorders along with analog (AC or DC) amplifiers and signal conditioning. No FM systems are permitted and no transient capture systems are permitted, since those have already been pre–filtered resulting in perhaps unwitting data distortion.

It is true that the old analog systems did not have much amplitude–reproduction accuracy — but they had sufficient frequency–reproduction capabilities to provide the information needed here.

How to Break the Closed Loop

The methodologies presented above may seem difficult to apply, but if the mission is to acquire defensible, provably valid, **Total Quality Measurements**, there is only one other choice: the data validation methods which will be discussed, which permit the following conclusion to be reached, if it applies:

These data, as obtained, have not been influenced (distorted) by the measurement system used, or through its environment, by more than x percent.

If the validation methods presented in this paper are applicable, then the pre-test or parallel-**analog**-channel diagnostic procedures identified above, may be omitted

In most practical applications the validation methods discussed below are the only viable ones.

DOCUMENTING THE SYSTEM RESPONSE TO A STEP

It is customary to through–calibrate measurement systems with step inputs or with repeated step inputs such as a square wave. These steps are usually produced by one of two means and can be used to document the *Rise Time* and *Undershoot* Characteristics of the Measurement System forward of the injection point. Time scale expansion (for *Rise Time*) or contraction (for *Undershoot*) may have to be used.

To factor in the characteristics of the component(s) behind the injection point, the techniques presented in this paper can be used.

The Production of Step Inputs

Resistance Injection – Shunt Calibration:

A *Calibration Resistor* is switched in parallel with one of the strain gages (or other resistively–based transducers) to produce a step–change in resistance which propagates through the measurement system. If the switch is turned on and off periodically such as by a contact modulator (chopper), a pulse train (or square wave) of resistance injection is obtained. The repetition rate for such a modulator must be properly selected or reproduction of the peak-peak value, which carries the calibration signal, will not occur. See Ref. 1.

If the Calibration Resistor, R_c is switched directly across the strain gage, R, then the unit resistance change which has been produced is:

$$\Delta R/R = -R/ (R + R_c)$$

Otherwise other effects such as lead wire resistances must be taken into account. Note that there is a relationship established during the calibration of the transducer itself

$$\Delta R/R = K. \Delta Q$$

where Q is the measurand acting on the transducer. It is thus possible to compute a $\Delta Q_{simulated}$ by the R_c shunt operation by equating the above relationships.

$$\Delta Q_{simulated} = -(1/K)[R / (R + R_c)]$$

A direct relation ship between ΔQ and R_c can also be obtained during the transducer calibration process, not relying on any equations or assumptions – a preferred procedure.

So long as the switching time rise–time is less than 1/5th the output step rise–time, the time–expanded (short–term) portion of the response to that step represents the *System Rise-Time*, t_{r-s} , from the transducer terminals forward.

The system *Undershoot Characteristics* are determined from the time-compressed (long–term) portion of the response to that step.

Voltage / Current Injection:

Measurement systems which incorporate thermocouples, piezoelectric transducers or other transducers with self-generating responses, but even some strain–gage–based systems, may be through-calibrated by injecting a step or square wave of voltage or current. The rise–time of the response to that step will represent the rise time of the measurement system forward from that transducer, provided the rise–time of the input step is less than 1/5th that of the output step (see Section on Upper Frequency Limit).

The system *Undershoot Characteristics* are determined from the time-compressed (long–term) portion of the response to that step.

THE FREQUENCY RESPONSE CURVE FOR MAGNITUDE

Wave shape distortion of a transient is possible due to insufficient bandwidth and / or due to resonances. In both cases, the signals may still be in the linear, distortion–free range of the Input–Output Characteristics, but the wave shape will have been compromised.

Non-Resonant Frequency Response Curve

Upper Frequency Limit: Rise Time

Since every system exhibits an upper frequency limit, every measurement system will exhibit rise-time problems.

Fig. 1 illustrates a typical flat frequency response curve with several time constants or upper frequency break–points limiting high–frequency behavior. The absolute values of the asymptotic slopes identify the order of the differential equation needed to model the system in that frequency range. The ultimate roll–off slope is indicated here by "-p" and should be known.

Each unit of slope is the equivalent of 20 dB/decade, since there are, by definition, 20 dB in every decade. By consequence there are 6.02 dB in every octave (doubling or halving of frequency), which is usually rounded off to 6 dB/octave. The numerical slopes have more physical meaning to the measurement engineer. The **-3 dB point, half power point, -30% response point, upper frequency limit, f_2**, is arbitrarily defined as the frequency at which 3 dB (about 29.7%) of the signal has been lost due to magnitude-based distortion. Only in a first order system is that frequency meaningful in terms of system characteristics. It represents the meeting point of the two asymptotes which govern such a first-order system.

Fig. 2 illustrates the transient response to a step which a 1st–order, 2nd–order, p–th order system would have, depending on the final value of the roll–off slope.

The **10% to 90% rise–time** is defined as the time it takes for the signal to rise from 10% of its value to 90% of its final value. It is a concept totally different from time–constant or the 36.9% or 63.1% response times. Those numbers are associated only with first-order systems where they represent measures of the one and only existing time constant. The systems shown have multiple time constants or break frequencies and only the **rise time** concept may be applied.

There is a convenient relationship which is the result of a limit theorem in pulse amplifier design which relates the two concepts in the frequency and the time domains for systems with an infinite ultimate roll–off slope at infinite frequency.

$$[f_{2,-3\,dB}](\text{in Hz}) \times [t_{r(10-90\%)}](\text{in secs}) \Rightarrow 0.35 \pm 10\%.$$

The relationship applies only to **monotonic, non–resonant** systems, and the 10% tolerance accounts for finite roll–off slopes. (Refs. 4, 5, 6). It does **not** apply to spatially averaging transducers such as side-mounted strain gages or pressure transducers, which exhibit resonant humps. For systems with 10% – 25% overshoot, Ref. 7 suggests a limit value of 0.45.

The same references present another limit theorem from pulse amplifier design considerations:

Rise times for an infinite number of series-connected components add as the square root of the sum of the squares of the individual components.

$$t_{r-s} = \sqrt{[\Sigma\,(t_{r-i})^2]}$$

where t_{r-i} = the individual component rise times .

This also requires a roll–off slope in the magnitude vs. frequency domain which approaches infinity as frequency approaches infinity.

For finite ultimate roll-off slopes, the approximation, although not good enough for data *correction*, can be used for data *validation* through the application of a *deviation minimizing design philosophy*.

Let t_{r-o} = rise time observed from the data
t_{r-s} = measurement system rise time
t_{r-p} = phenomenon rise time

$$t_{r-o} \approx \sqrt{[(t_{r-s})^2 + (t_{r-p})^2]} \quad \text{(see Fig. 3)}$$

or $t_{r-p} \approx (t_{r-o}) \cdot \sqrt{[1 - m^2]} = t_{r-o}\,(1-n)$

The symbol $\approx$ means: is approximately
where m = $[(t_{r-s})/(t_{r-o})]$ = known
and n = error made due to neglect of m^2

The following table can be constructed:

Value of m	Maximum Error due to Neglect of n
1/3	6 %
1/4	3 %
1/5	**2%**
1/10	1/2%

So long as the observed rise time is at least 5 times the system rise time, the rise-time distortion due to the measurement system is less than 2%, a not unreasonable target for transient data.

This criterion can be used to establish, before a test even starts, the limiting value of acceptable / believable rise times on a test.

$t_{r-o-acceptable} > 5 \cdot t_{r-s}$ for better than 2% rise time validity.

Thus, even though nothing may be known about the process being observed, the influence of the measurement system on the observation can be estimated. Even if the approximation were 20% in error, the rise time validity would be only 3% instead of 2% – deviation minimizing design principles.

Applications Note:

In Hopkinson / Davies Bar applications for accelerometer calibration at high "g" levels, the **strain-rate, i.e., the rise-time of the strain–time record** is the calibration signal! The above validation procedures must be applied. In Hopkinson / Davies Bar applications for determining the rise time of strain gages, the above validation procedures must also be applied.

FIG. 1:   FREQUENCY RESPONSE CURVE FOR MAGNITUDE SHOWING ASYMPTOTIC LIMITS AT THE HIGH FREQUENCY END
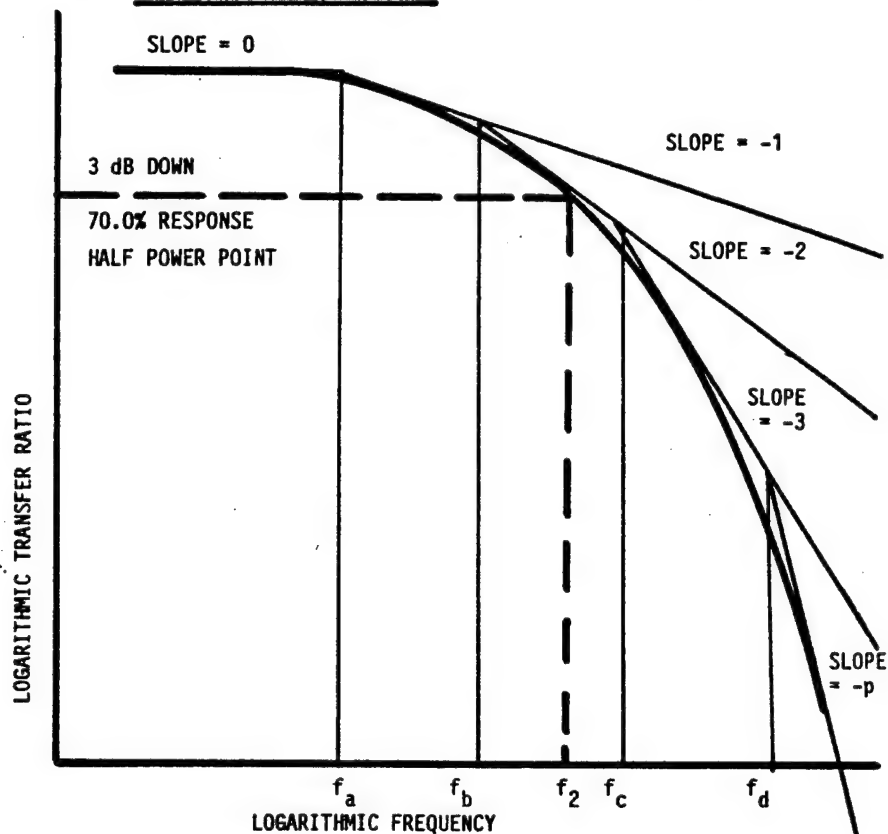
SLOPE = 0

SLOPE = -1

3 dB DOWN

SLOPE = -2

70.0% RESPONSE
HALF POWER POINT

SLOPE = -3

SLOPE = -p

LOGARITHMIC TRANSFER RATIO

f_a f_b f_2 f_c f_d

LOGARITHMIC FREQUENCY

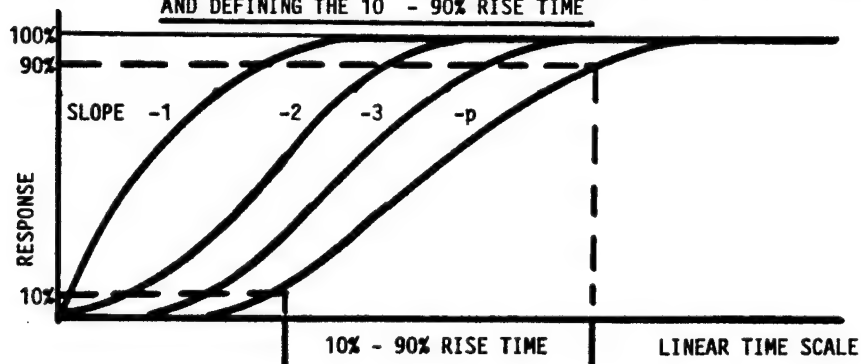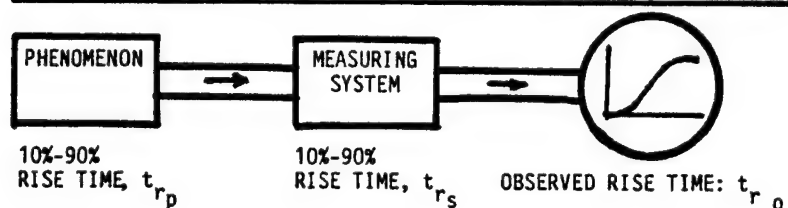**FIG. 2:   RESPONSES TO A STEP ASSOCIATED WITH ULTIMATE ROLL-OFF SLOPES AND DEFINING THE 10 - 90% RISE TIME**

100%
90%

SLOPE   -1   -2   -3   -p

RESPONSE

10%

10% - 90% RISE TIME   LINEAR TIME SCALE

FIG. 3:   THE PROBLEM OF RISE-TIME VALIDATION :
DID THE MEASUREMENT SYSTEM INFLUENCE THE DATA FROM THE PHENOMENON?

| PHENOMENON | → | MEASURING SYSTEM | → | (observed) |

10%-90%
RISE TIME, t_{r_p}

10%-90%
RISE TIME, t_{r_s}

OBSERVED RISE TIME: t_{r_o}

Lower Frequency Limit: Undershoot

Direct (DC) Coupled Systems:

Unless the measurement system is Direct (DC) Coupled, there may undershoot in its output when a step or a pulse is applied at its input.

Governed by Integer–Slope Roll–Offs:

Fig. 4 illustrates a typical flat frequency response curve with several time constants or lower frequency break–points limiting low-frequency behavior. The absolute values of the asymptotic slopes identify the order of the differential equation needed to model the system in that frequency range. The ultimate roll–off slope is indicated here by "q" and should be known.

The same comments translating slopes into decibels apply as did to the Upper Frequency Limit. Slopes of ±q = ±20.q dB/decade or approximately ±6.q dB/octave. Again, the numerical slopes are more informative to the measurement engineer than the dB values. The **-3 dB point, half power point, -30% response point, lower frequency limit, f_1,** is arbitrarily defined as the frequency at which 3 dB (about 29.7%) of the signal has been lost due to magnitude-distortion. Only in a first order system is that frequency meaningful in terms of system characteristics. It represents the meeting point of the two asymptotes which govern such a first-order system.

Undershoot to a Step Input:

Fig. 5 illustrates the transient response which a 1st-order, 2nd–order, 3rd–order, q–th order system would have, depending on the final value of the roll–off slope. See also Refs. 4, 5, 6. A time-compressed record of the **shunt calibration or voltage injection step** will thus reveal the system order: the number of zero-crossings, plus 1.

The **Undershoot** is defined as the maximum negative excursion of the response per unit of maximum positive response, usually expressed in percent.

Physical Response Explanation:

Any system with a frequency response for magnitude which is a straight line of slope q and a frequency response curve for phase which is q.π/2 is a q–th order differentiator. If the frequency response of the system goes from slope 0 in the flat, high-frequency portion, through 1, 2, 3, etc., to q at the low-frequency end, then the system can act only as an **imperfect** q–th order differentiator. This argument provides a physical explanation of the apparent oscillations in an over-damped, non-resonant system, as illustrated in Fig. 6. These are not resonances, they are valiant attempts of the system to act as a an approximate–q–th order differentiator.

Second-Order System Criteria

For a 2nd–order system, let the low–frequency break points be $f_a < f_b$ with $b = f_a/f_b < 1$; then Fig. 7 relates the ratio, b, to the undershoot, U in the curve with the arrow to left. It should be noted that for 1% undershoot, the break points must be a factor of 100 apart! for 5% undershoot they must be separated by a factor of about 13. The curve with the arrow to the right permits determination of the zero-crossing time T_o.

Practical Application: A piezoelectric transducer connected to an AC-coupled amplifier would represent a typical 2nd–order system of the type being discussed.

Equivalent 2nd–Order System: Given the two break points f_a and f_b, it is possible to calculate the pure 2nd–order system with the same behavior characteristics as the one obtained by series-connecting two first-order systems (Ref. 8).

f_n = undamped natural frequency = $\sqrt{(f_a.f_b)}$
h = damping ratio = $(f_a+f_b) / 2\sqrt{(f_a.f_b)}$

The two time constants would, of course, be:

$$\tau_a = 1 / [2. \pi. f_a] \qquad\qquad \tau_b = 1 / [2. \pi. f_b]$$

Those values could be substituted into the general equations for steady state and transient responses of the totally-equivalent 2nd–order system found in Ref. 8.

Undershoot to a Square Pulse Input:

Whereas only 2nd–and–higher order systems showed undershoot to a step, even first-order system exhibit undershoot to a pulse. The phenomenon is illustrated in Fig. 8 for a square pulse of duration "a". The response of a low-frequency limited, high–pass first-order system to a step is: $e^{-t/\tau}$. At time t = a, the value of the function is: $e^{-a/\tau}$, at which point the -1 step occurs. Therefore the undershoot

$$U = 1 - e^{-a/\tau} \approx -a/\tau$$

For values of U < 0.1 the approximation is excellent. For higher-order systems different criteria must be used.

Practical Application: If the maximum permissible undershoot, U_{max} is (1/2) small scale division on the read–out or half the least significant bit, a reasonable design objective has been set. Since one can not interpret such signals, their existence should cause no problems. For a 1st-order system such as an AC-coupled CRO observing a strain gage output expected to a square pulse, then:

$$\text{Let } U_{max} = - a_{max}/\tau$$

Then the maximum observed pulse width for which the undershoot will be less than maximum is:

$$a_{max} < U. \tau. k$$

where   k > 1 is a pulse shape factor for pulses perhaps more gentle than a square pulse. See also Refs. 9, 10, 11. For a square pulse, k=1.

As the data are acquired during the test, the pulse widths observed in the least favorable way: from zero crossing to zero crossing, will serve as guide as to whether or not the undershoot shown in the record is data or measurement–system–created artifact. An example is shown in Fig. 9:

$U_{max} = -0.01$	2 mm divisions on an oscilloscope on which full scale is 10 cm, i.e. 1%
τ = 0.1 sec	for an AC-coupled CRO as the only low–frequency–limiting component in the measurement system.
a_{max} = 1 millisecond.	

On Photo 9, Fig. 9 the pulse at the output is 0.25 msec wide and the undershoot of some 56% (shown as "B") must therefore be data. In this case it is a negative reflected stress wave during an impact test. For higher-order systems the superposition principle shown in Fig. 8 can be used.

IMPERFECT DIFFERENTIATOR RESPONSE FROM FREQUENCY RESPONSE CURVE AS SHOWN IN FIGURE 4

STEP

EXPONENTIAL

PERFECT DIFFERENTIATOR RESPONSE (THAT SLOPE ALL THE WAY UP)

STEP

IMPULSE

DOUBLE IMPULSE

TRIPLE IMPULSE

QUADRUPLE IMPULSE

ULTIMATE ROLL-OFF SLOPE

0

1   $\partial/\partial t$

2   $\partial^2/\partial t^2$

3   $\partial^3/\partial t^3$

4   $\partial^4/\partial t^4$

FIG. 6: PHYSICAL EXPLANATION FOR UNDERSHOOT AND ZERO CROSSINGS

FIG. 4: FREQUENCY RESPONSE CURVE FOR MAGNITUDE SHOWING ASYMPTOTIC LIMITS AT THE LOW-FREQUENCY END.

SLOPE = 0

70.7% RESPONSE
HALF POWER POINT
3 dB DOWN POINT

"q-th" ORDER DIFFERENTIATOR: SLOPE = q

1

2

3

q

LOGARITHMIC FREQUENCY

f_e f_f f_1 f_g f_h

LOGARITHMIC TRANSFER RATIO

221
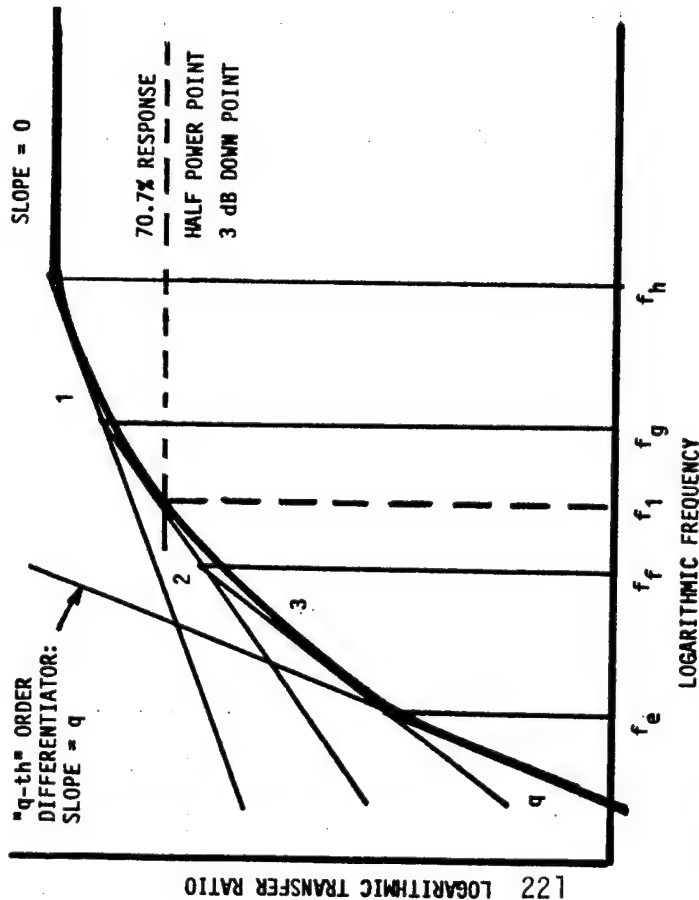
FIG. 5: RESPONSES TO A STEP ASSOCIATED WITH ULTIMATE ROLL-OFF SLOPES AND DEFINING "UNDERSHOOT"

SLOPE OF THE MAGNITUDE CURVE ASYMPTOTE

TIME

UNDERSHOOT

1

2

3

UNDER-SHOOT

RESPONSE

RELATIONSHIPS BETWEEN TRANSIENT AND STEADY-STATE RESPONSES FOR THE KINETIC ENERGY STORING RESPONSE OF A SECOND ORDER SYSTEM WHICH IS OVER-DAMPED.

Transient response = response to a unit step

U_{max}	System Order
0	1
0.135	2
0.20	3
0.24	4
0.28	5
0.30	6

U is max for n equal multiple poles

UNIT STEP INPUT

RESPONSE OF $\alpha \cdot d^2 Q_s / dt^2$ IN

$$\alpha \cdot d^2 Q_s / dt^2 + \beta \cdot dQ_s/dt + \gamma \cdot Q_s = 1$$

T_o = zero-crossing time

Inflection point

RATIO $b = w_1/w_2 = \tau_2/\tau_1$ where $w_1 < w_2$

UNDERSHOOT TO A STEP - U

$U = b^{(\frac{1+b}{1-b})}$ at $2w_n \cdot T_o$

$U_{max} = 1/(e^2) = 0.135$ at $b=1$

$w_1 = w_n \cdot \sqrt{b}$ $w_2 = w_n / \sqrt{b}$

$h = \frac{1}{2}(1+b)/\sqrt{b}$ $w_n \cdot t = \frac{1}{2}\varepsilon/h$ as $t \to 0$

TIME TO CROSS ZERO - T_o

$$w_n \cdot T_o = \frac{\sqrt{b} \cdot \log_e (1/b)}{(1-b)}$$

$$w_n = \sqrt{w_1 \cdot w_2}$$

FIG. 7:   UNDERSHOOT AND ZERO-CROSSING IN SECOND-ORDER SYSTEMS FOR STEP RESPONSE

Note that the above chart is based on radian frequency: w in rad/sec = $2\pi f$ in Hz

From Ref. 28

NOTE: In the above design chart, $w_1 = 2\pi f_a$ and $w_2 = 2\pi f_b$

τ_1 and τ_2 are the time constants associated with w_1 and w_2.

The equation for Undershoot is for $b < 1$, i.e. not critically damped systems. The result for b = 1, critical damping, is also given.

FIG. 8: RESPONSE OF A FIRST-ORDER SYSTEM TO A PULSE
USING THE PRINCIPLE OF SUPERPOSITION

Since a pulse is the superposition of two steps, the Response to a Pulse is the superposition of the Responses to each of the two Steps.

The time constant for a first order system:

$$\tau = (1/w_0)$$

where w_0 is the -3dB, Half Power Point, frequency limit, in rad/sec.
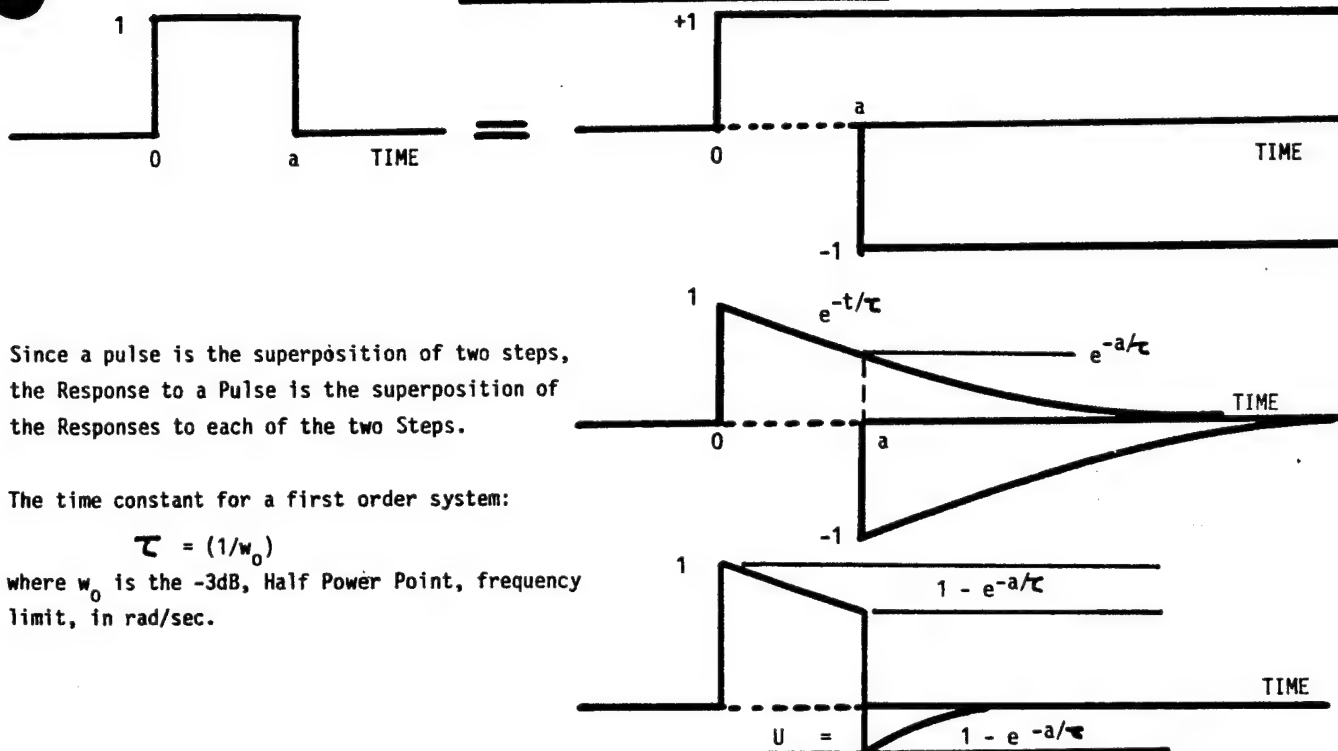
FIG. 10: FREQUENCY RESPONSE OF A TYPICAL COMMERCIAL ACCELEROMETER
(From Ref. 17)

When the output of this accelerometer overdrives the signal conditioning, then DIFFERENCES among the three resonant frequencies will appear as low-frequency signals in the data, never to be taken out again by any software program ever to become available.

223

FIG. 9: CASE STUDY FROM AN IMPACT TEST USING BONDED RESISTANCE STRAIN GAGES

IMPACT TEST RESULTS

PHOTO	HAMMER	TIME SCALE
6	8-oz	0.1 msec/cm
7	2-oz	0.1 msec/cm
8	2-oz	20 usec/cm
9	--	0.1 msec/cm
10	8-oz	0.1 msec/cm(*)

Y_1 = 2mv/cm

Y_2 = 200 mv/cm

Other settings and components same as before.

(*) No current through gages

IMPACT-INDUCED VOLTAGES: PHOTO 10

Reduced by design but still visible.

MEASURING SYSTEM

Constant current circuit, four terminal strain-gage arrangement with inductively cancelling gage connection.

Two-conductor shielded cables from current source to gages and from gages to CRO. Specimen, current source chassis, cable-shields all connected to CRO ground. For each photo except #5: TOP TRACE: from gages directly to CRO bottom trace: from gages through 123 pre-amp to CRO MEASUREMENT SYSTEMS ENGINEERING LABORATORY ARIZONA STATE UNIVERSITY May 1970   Nettles & Stein

THE "UNDERSHOOT" NEGATIVE-STRAIN SIGNAL: PHOTO 9 - "B":

The top trace can be validated by the methods presented in this paper. The numerical example at the bottom of page 5 applies. Pulse width is 0.25 msec, hence the negative strain IS a from a reflected stress wave. The bottom trace can not be validated since amplifier characteristics are not provided by the manufacturer.

THE RISE-TIME OF THE STRAIN PULSE IN PHOTO 8:

The top trace can be validated to be the strain-wave rise-time not distorted by more than 2%. The bottom trace can be shown to be invalid and dominated by the amplifier rise-time.   224   (From Refs. 8 and 29)

Resonant Systems

Many measurement systems with which transient measurements are performed contain at least one transducer with a highly undamped resonance. Such devices may be piezoelectric or piezoresistive (strain gage) accelerometers, pressure transducers, load cells, etc. Their damping ratios are often between 0.001 and 0.01, with dynamic magnifiers, "Qs" or resonant peaks of 50:1 to 500:1. Figure 10 illustrates a typical response.

Practical Application: Note that the response is not shown as pure 2nd–order because real hardware has numerous resonances due to internal transducer parts, mounting techniques, etc. The dominant resonance looks closely enough like a pure 2nd–order system most of the time, that it is shown as such in many illustrations. It is a misleading model.

Test Conditions Under Impact Excitation:

Impact, by definition, is suddenly applied energy. Energy consists of pairs of quantities such as Force and Displacement, Pressure and Volume, Voltage and Charge.

Energy, E, can not be transmitted in zero time, t, since that would require infinite power, P. Dimensionally:

$$|E| = |P|.|t|$$

Thus the propagation of energy occurs as pairs of energy components and as a function of time into the structure being impacted. This condition can be described by a pair of non-linear, simultaneous, partial differential wave equations in space and time.

Like all waves, these will be reflected from discontinuities and refracted through them. Such discontinuities may be joints such as rivets, bolts, spot welds, adhesive layers, etc., or changes in geometry or section. Reflected waves return to the point of impact, often to be reflected from and refracted through it. The cycle continues until the energy generated by the impact is dissipated. The excitation to which a transducer mounted on the impacted structure is exposed, therefore, is not only the initial impulse created by the impact, but a multiplicity of reflected impulses which arrive at the transducer in **no predictable sequence and with no predictable timing**. The time scale is too short and the reflections are governed by such local conditions that mathematical modeling has not yet succeeded in predicting these events.

Problems Created by the Test Conditions and Some Solutions:

There are two kinds of problems created by these Test Conditions as described:

Overload of the Transducer and its Destruction: The initial pulse and/or the superposition of the many reflections can overload and destroy the transducer mechanically. Only a (mechanical) filter between the Transducer and the Structure can prevent such a failure unless a high–range transducer is used, in which case the output level may be too small compared to the noise level. Typical manufacturers of mechanical filters are Refs. 12 , 13 and 14. There is considerable research on this topic being carried out by Dr. V. Bateman at Sandia National Labs, Albuquerque with periodic reports at Shock & Vibration Symposia and Range Commanders Council Transducer Workshops. The problem is especially severe for applications where the transducer must survive a very high-g pulse and subsequently record low accelerations.

Overload the Signal Conditioning Creating Low–Frequency Signals due to Intermodulation Distortion: When a sequence of pulses arrives at the resonant transducer, they may do so in such a phase relationship to each other that they subtract each other's effects and diminish the resonant vibrations set up by the first. They may also reinforce each other and build up the resonance stimulated by preceding pulses. Fig. 11 illustrates the problem from Refs. 15, 16, 17 summarized in Ref. 2.

When a system with multiple, closely-spaced resonances, such as a real transducer, is excited at high amplitudes, the resulting responses may drive the signal conditioning into the non-linear range of its Input-Output Characteristics.

Difference frequencies among these resonances will form. These difference frequencies may appear in the low–frequency range occupied by the real signals to be measured and any filtering of the high frequencies which is performed, will not affect these "aliased" frequencies.

Let the excitation be from only two impact-stimulated resonant frequencies:

$$(IN) \quad = \quad \mathrm{Sin}\,\omega_1 t + \mathrm{Sin}\,\omega_2 t$$

and let the non-linear Transfer Characteristics be:

$$(OUT) = k + a(IN) + b(IN)^2 + \cdots \qquad \text{then}$$

$$(OUT) = k + a.\mathrm{Sin}\,\omega_1 t + a.\mathrm{Sin}\,\omega_2 t + (b/2)(1\text{-}\mathrm{Cos}2\omega_1 t) +$$
$$(b/2)(1\text{-}\mathrm{Cos}2\omega_2 t) + \mathbf{b.Cos(\omega_1 - \omega_2)t} -$$
$$b.\mathrm{Cos}(\omega_1 + \omega_2)t \ \ldots .$$

Note that higher frequencies, $2\omega_1$, $2\omega_2$, and $(\omega_1 + \omega_2)$ have been created, but also a lower frequency $(\omega_1 - \omega_2)$ which might well lie in the same frequency range in which signals exist, never again to be separated from them. The process is also called Transient Intermodulation Distortion, see Refs. 18, 24.

The phenomenon is not predictable or designable. It was to answer the question: *"Has this contaminating phenomenon occurred during a test as determined from post–test diagnostic procedures,"* that Pat Walter was sent to the Laboratory for Measurement Systems Engineering at Arizona State University by his employer, Sandia National Laboratories, Albuquerque under a fully funded doctoral study grant. Refs. 15, 16, 17 provide the positive answers to that question.

By performing an **energy spectral density analysis** on the acquired data, it is possible to determine whether such low–frequency creation has occurred during the test and whether the right to filter out the high–frequency signals, can be established. **Filtering data is not a God–given right guaranteed by the Constitution. It is a privilege which must be earned.**

A beautiful bench-top demonstration for training / education purposes is shown in Refs. 19 and also 2.

Another way to solve the problem is to build an electrical filter into the transducer, after the piezoelectric / piezoresistive elements but before the first "active" electronic amplifier, to prevent amplifier overload, which is where the damage is done. Based on Dr. Walter's dissertation, such transducers are now available commercially from several sources. Refs. 20, 21, 22, 23, 38 for example. Fig. 12 illustrates a typical comparison between traducers with and without internal filters.

In piezoelectric transducers the first filter pole actually uses the capacitance of the piezoelectric element itself. Other poles are incorporated before the first amplifier which could easily be driven non-linear.

FIG. 11: RESPONSE OF A LINEAR SECOND ORDER SYSTEM
TO MULTIPLE EXPONENTIAL PULSES.

(System damping ratio = 0.01 of critical. Natural Period = 0.02)
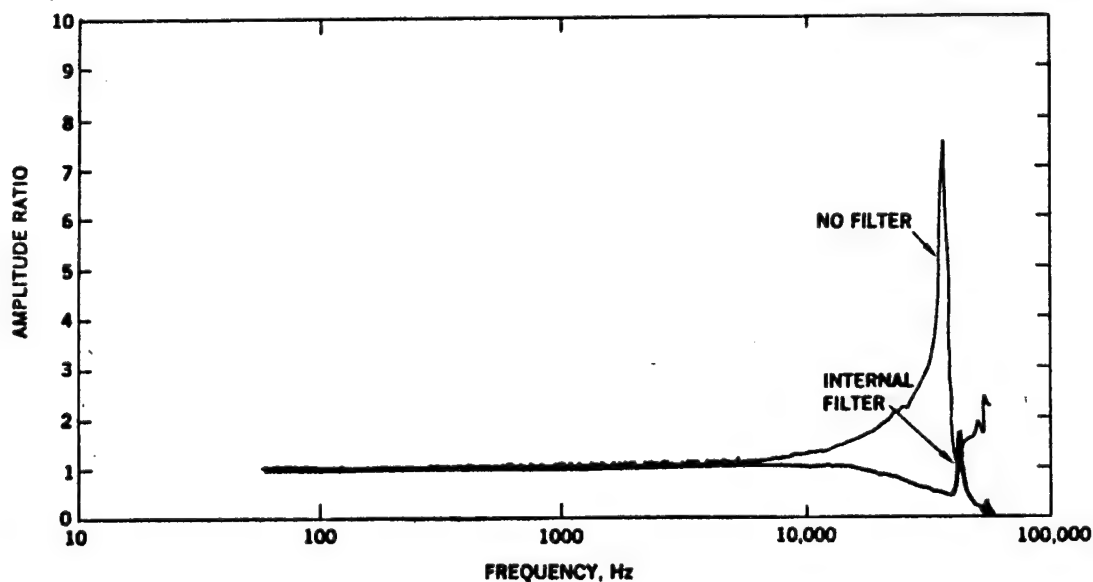
Pulses arrive at t=0, 0.21, 0.30   Pulses arrive at t=0, 0.20, 0.30
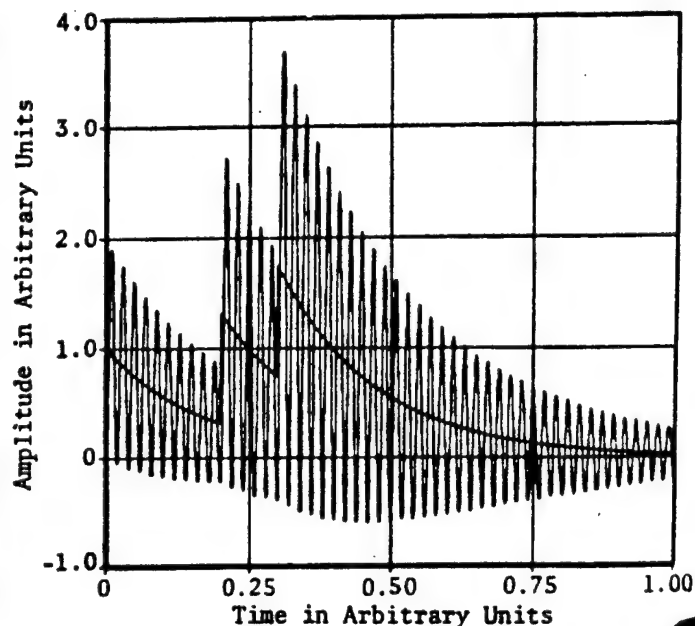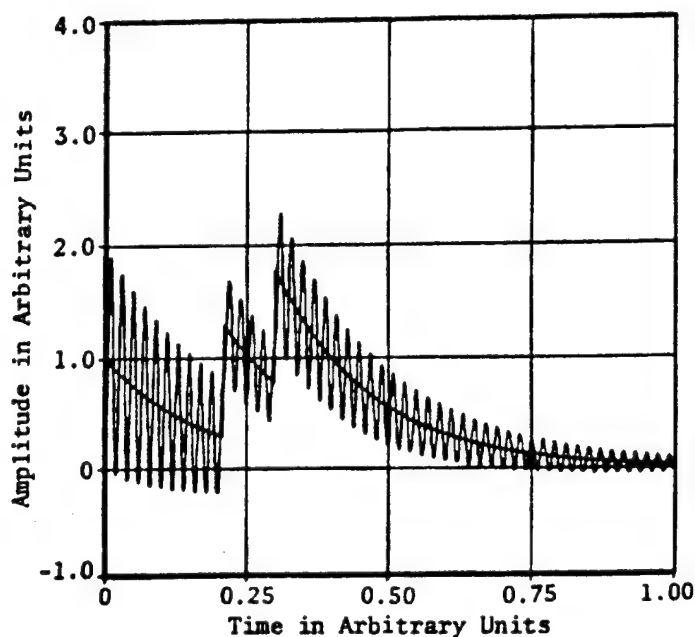
Note that if the distortion-free linear input range is 2.5 Units, that the right-hand response, driven non-linear, might create low frequencies not present in the signal.

FIG. 12: PCB ACCELEROMETER FREQUENCY RESPONSES WITH AND WITHOUT INTERNAL FILTER

(From Ref. 23)

ACCELEROMETERS WITH AND WITHOUT AN INTERNAL FILTER USING A LINEAR
AMPLITUDE RATIO VERTICAL SCALE (PCB 305M23 AND PCB 305A)

THE FREQUENCY RESPONSE CURVE FOR PHASE

Phase-Based Distortion due to Nonlinearity:

In measurement systems for steady-state dynamic measurands, the effect of phase shift on wave shape is well known. Fig. 13 illustrates *different wave shapes* for which the *frequency content* is the same. Only the phase angle between the two frequency components is varied. Since the human ear is insensitive to that kind of phase shift, all the wave shapes illustrated, will sound the same, provided the 180° phase shift condition is adjusted to be within the audio system's linear (distortion-free) range.

Ref. 25 presents a persuasive case study in which several frequency response curves for phase shift are used to process the same transient signal. Wave shape reproduction is obtained only for the *linear phase shift* characteristics, as illustrated in Fig. 14.

Some wave shapes which are completely different, differ **only** in their phase shift curves. Fig. 15 shows a Terminal Peak Sawtooth Pulse and an Initial Peak Sawtooth Pulse. Fig. 16 illustrates that the **Magnitude** of the Fourier Transform is the same for both wave shapes but that the **Phase Shift only** is responsible for their different appearance. (From Ref. 25.)

For frequency–content reproduction only, the linear phase shift law enunciated below, need not be obeyed.

Linear Phase Shift Requirement

The requirement for linear phase shift characteristics for wave shape reproduction is presented in Ref. 1 and reproduced below. Wave shape reproduction can only result if all frequencies in the wave shape are delayed the same amount in time as they pass through the measurement system. If t_o = **constant then phase shift must be linearly proportional to frequency.** Actually the time delay is the slope of the phase shift curve. Thus **Time Delay vs. Frequency Curves** are really more helpful than Phase Shift vs. Frequency Curves. Some manufacturers provide those. See Fig 17 showing characteristics of filters from *Frequency Devices* from Refs. 26 & 36. *Precision Filters* shows filter characteristics in a similar manner. Refs. 26 & 37.

Linear phase shift or constant time delay is also required for coincidence measurements and sample–and–hold operations.

PHASE SHIFT - TIME DELAY - RETARDATION: RELATIONSHIPS
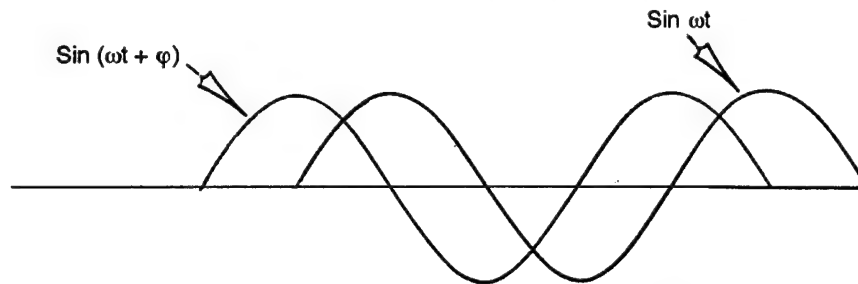
Time Delay	$-t_o$	←	Period = T	→	Time Dimension
Phase Shift	φ	←	Cycle = 2π	→	Radians - Angle
Retardation	$-\delta$	←	Wave Length = λ	→	Distance Dimension

Relationships by Direct Proportion from the Figure

$\varphi/-t_o = 2\pi/T = \omega$ $\varphi = -t_o\omega$ **For t_o = constant, linear phase shift law results**

$-\delta/-t_o = \lambda/T = c$ $\delta = t_o.c$ ω = frequency in radians/second

$\varphi/-\delta = 2\pi/\lambda = \omega/c$ $\varphi = -\omega.\delta/c$ c = wave propagation speed

Applications Note:

The **shunt calibration** or **step-voltage injection** record, time-expanded, gives the system **rise time** characteristics for the entire measurement system except the input transducer and its lead wires. Those can be factored in using the relationships given in this paper to obtain the value for t_{r-s}.

One problem which may arise, is that many input transducers are not monotonic in frequency response, in fact, they may be highly resonant. The relationships established in this paper will not apply to those cases. If the pre-filtered transducers are used, then the problem becomes more tractable.

When time-compressed, the step-response record will show the system's **undershoot** characteristics forward of the injection point. So long as the input transducer is DC-coupled, that will also be the total system's response.

When an AC-coupled input transducer is used the problem is more difficult. Beyond second order systems for which a design chart is shown in Fig. 7, the author is not aware of general solutions. It is also not in the measurement engineer's favor to work with measurement systems with low-frequency roll-offs exceeding 2, for transient measurements.

If that does become necessary, then new criteria need to be developed, and the author will gratefully include those in up-dated versions of this paper.

A piezoelectric transducer with an AC-coupled amplifier feeding into an AC-coupled oscilloscope is already a third-order system for which a general solution is not yet available to the author's knowledge.

227

EFFECT OF PHASE SHIFT ON WAVE SHAPE

$$\mathrm{Sin}\,\omega t + \tfrac{1}{3}\mathrm{Sin}(3\omega t + \phi)$$

ABSCISSA ARE FRACTIONS OF A PERIOD
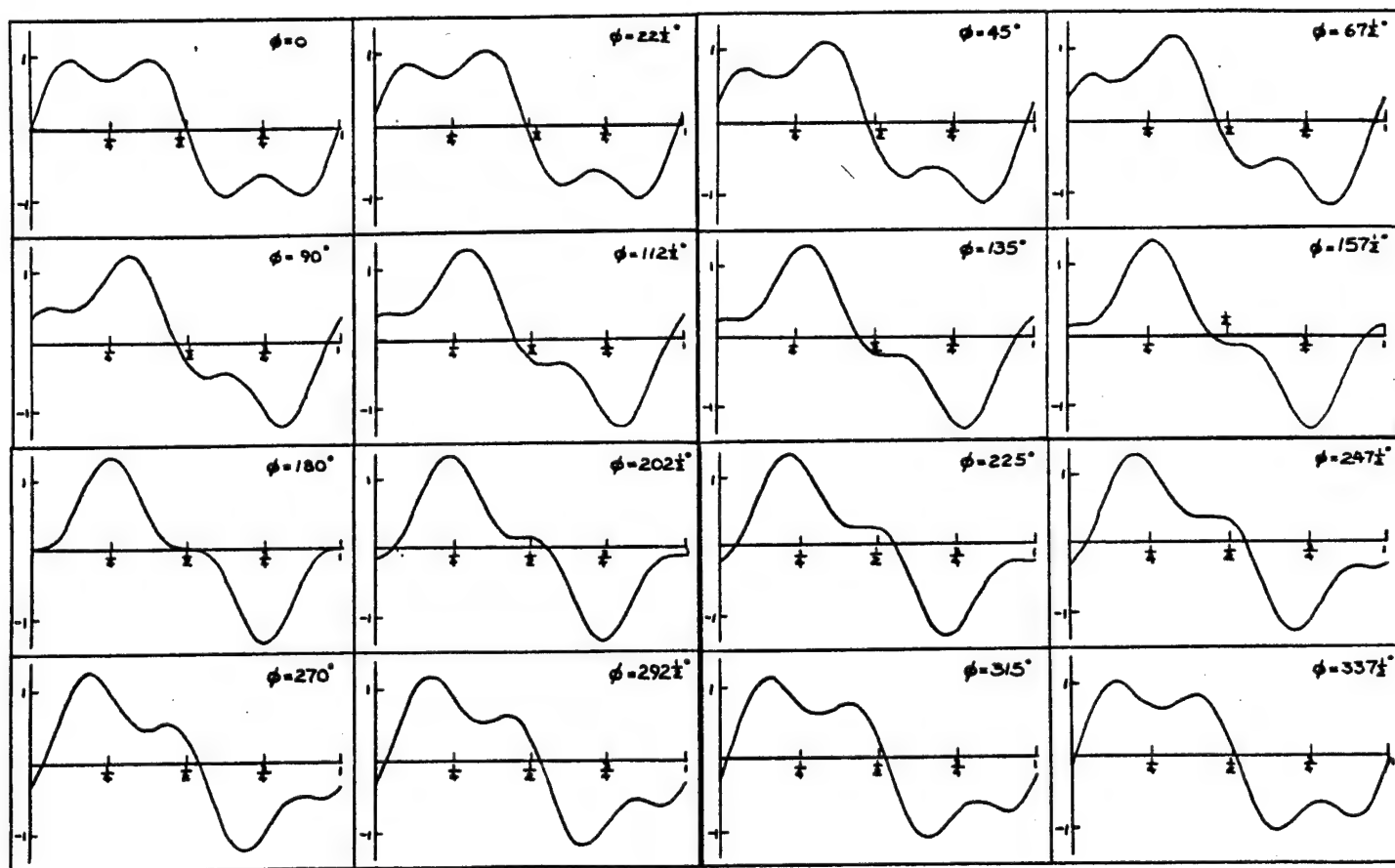
FIG. 13: EFFECT OF PHASE SHIFT ON WAVE SHAPE

(From Ref. 30)

FIG. 14: EFFECT OF FREQUENCY RESPONSE CURVE FOR PHASE ON WAVE SHAPE REPRODUCTION OF A TRANSIENT

FIGS 15 & 16: TWO WAVE SHAPES OF IDENTICAL MAGNITUDE SPECTRUM BUT DIFFERENT PHASE SPECTRA
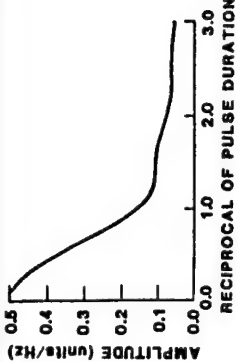(From Ref. 25)

FIG. 15: THE WAVE SHAPES

FIG. 16: THE MAGNITUDE AND PHASE SPECTRA

Frequency-Response Curves for Phase used in this study (Ref. 25)

Phase Frequency Responses
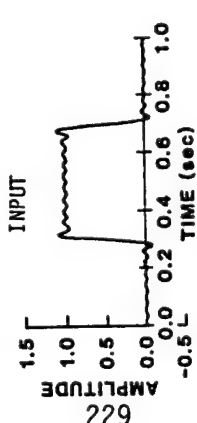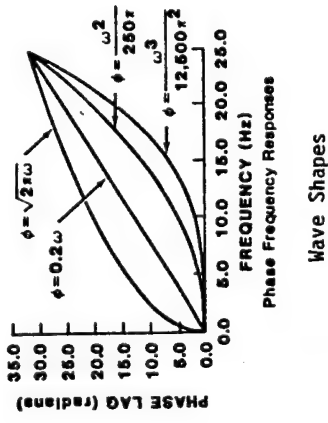
Wave Shapes

Fig.14a: Amplitude
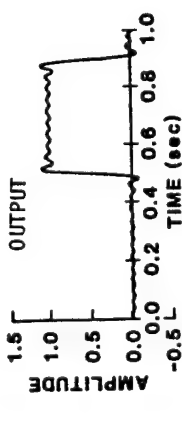
Fig.14b: Linear Phase Shift
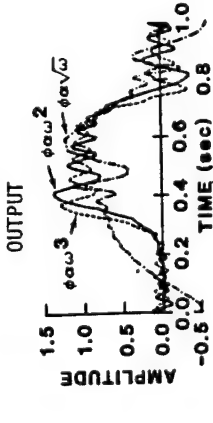
Fig.14c: Nonlinear Phase Shifts
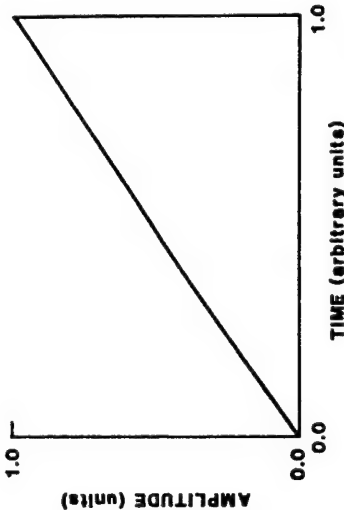
Fig.15a: Terminal Peak Sawtooth Pulse
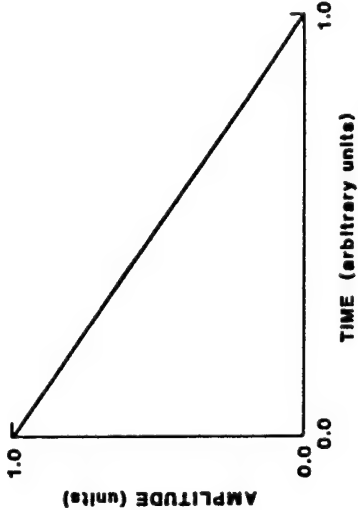
Fig.15b: Initial Peak Sawtooth Pulse

Fig.15: Sawtooth Pulses

Fig.16a: Magnitude of Fourier Transform of Both Terminal and Initial Peak Sawtooth Pulses
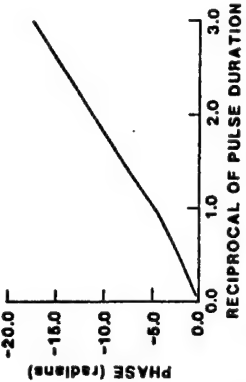
Fig.16b: Phase of Fourier Transform of Terminal Peak Sawtooth Pulse
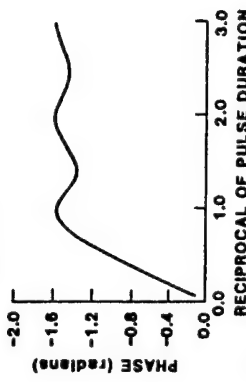
Fig.16c: Phase of Fourier Transform of Initial Peak Sawtooth Pulse

Fig.16: Fourier Spectra of Sawtooth Pulses of Figure 5

229
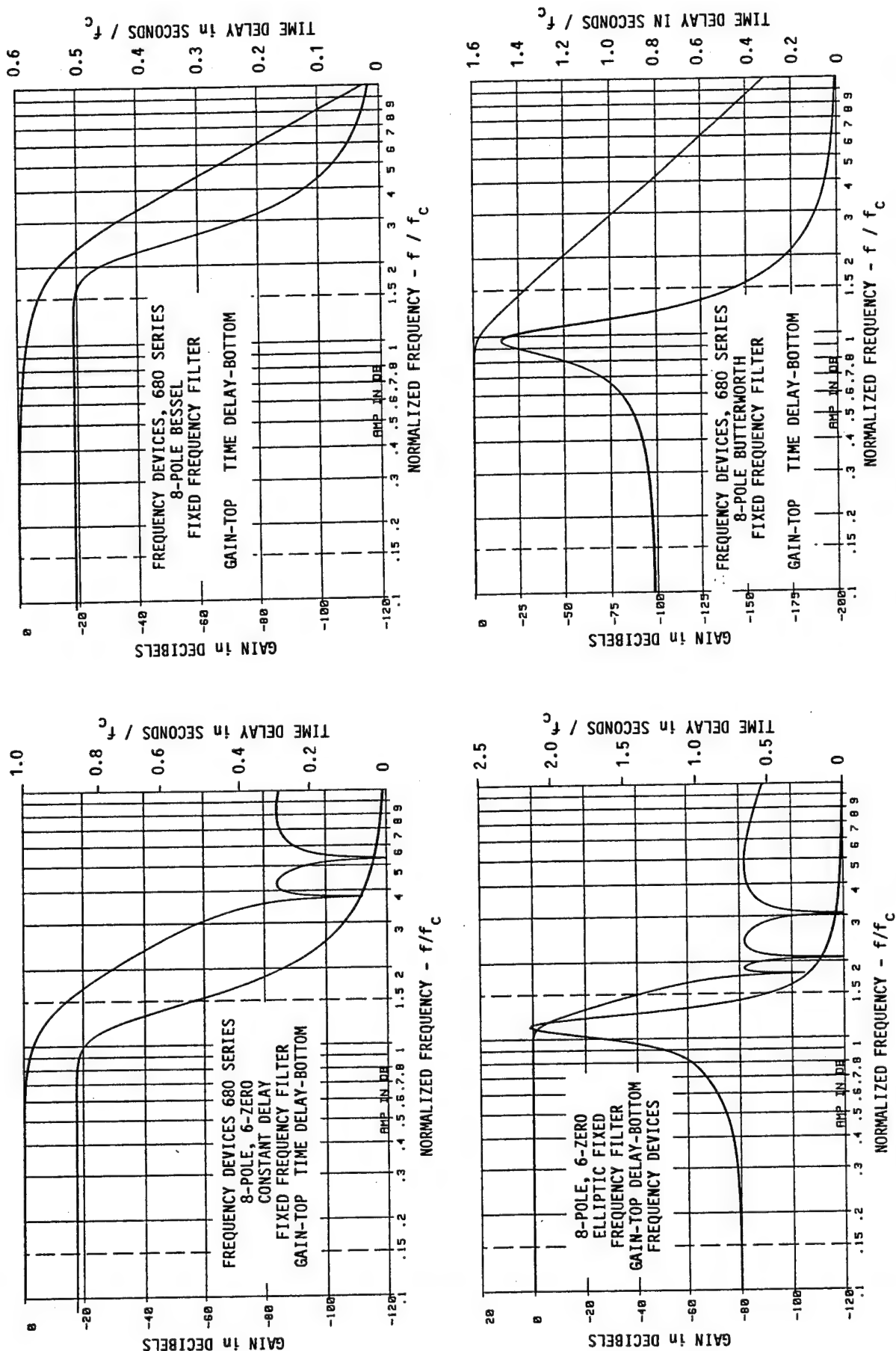
FIGURE 17: TYPICAL FILTER CHARACTERISTICS FOR FREQUENCY RESPONSE FOR MAGNITUDE AND FOR DELAY TIME

230

PRECISION FILTERS, INC. 6-Pole, 6-Zero Elliptic Low-Pass Filter (LP1) w/2nd Order Phase Delay Equalizer

Group Delay, Time Delay and Phase Delay

Douglas Firth, Senior Applications and Project Engineer at *Precision Filters* (Ref. 37) distinguishes between:

- *Group Delay* (called *Time Delay* in this article) which he defines as the slope of the Phase Shift vs. Frequency Curve, and

- *Phase Delay* which is determined for individual frequencies and is used for correction procedures. It is defined as the phase shift expressed as a fraction of a cycle, divided by the frequency. Thus if there is a 90-degree phase shift at 1 kHz, the Phase Delay at that frequency is 90/360 divided by 1000 or 250 microseconds.

The performance curves for three *Precision Filters* models are shown in Fig. 17-A illustrating both the *Phase Delay* and *Group Delay* characteristics along with the *Amplitude Response* curves.

It should again be noted that *Wave Shape Reproduction* requires a flat "Delay" curve and that phase-induced wave shape distortion will occur in the non-flat region.

When Non-Linear Phase Shift is Permissible

When the object of the test is reproduction of **only** frequencies or frequency-patterns, such as for modal analysis, then non-linear-phase-shift filters with very steep magnitude vs. frequency roll-offs are acceptable. Wave shape reproduction will then neither occur nor be a criterion.

PRECISION FILTERS, INC. 8-Pole, 8-Zero Constant Time Delay Low-Pass Filter (TD8B). Amplitude, Group Delay and Phase Responses.

PRECISION FILTERS, INC. 8-Pole, 6-Zero Elliptic Low-Pass Filter (LP8). Amplitude, Group Delay and Phase Delay Responses.

231
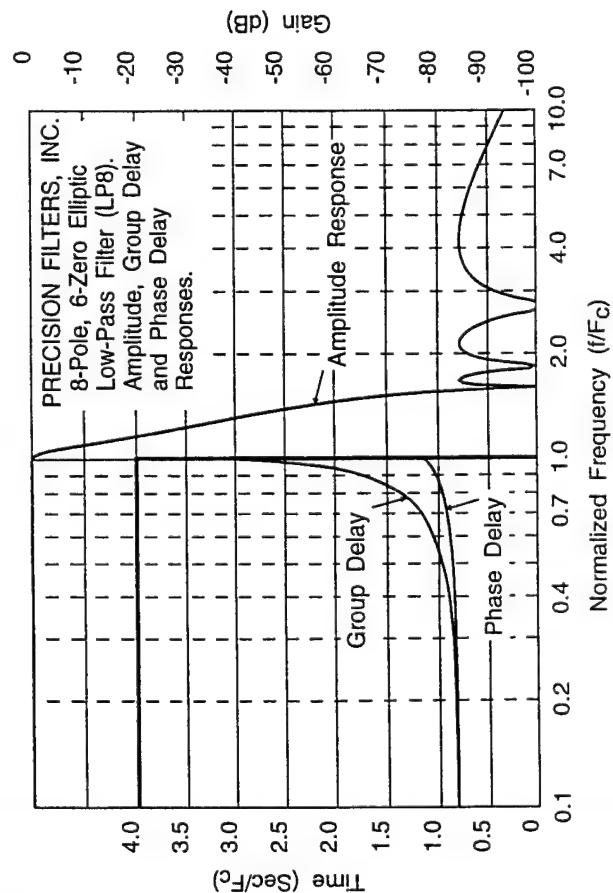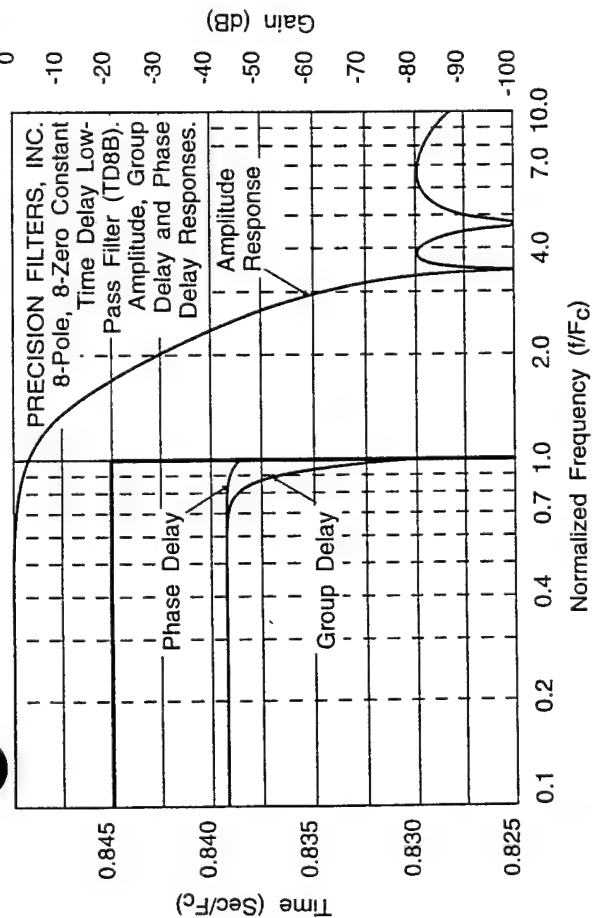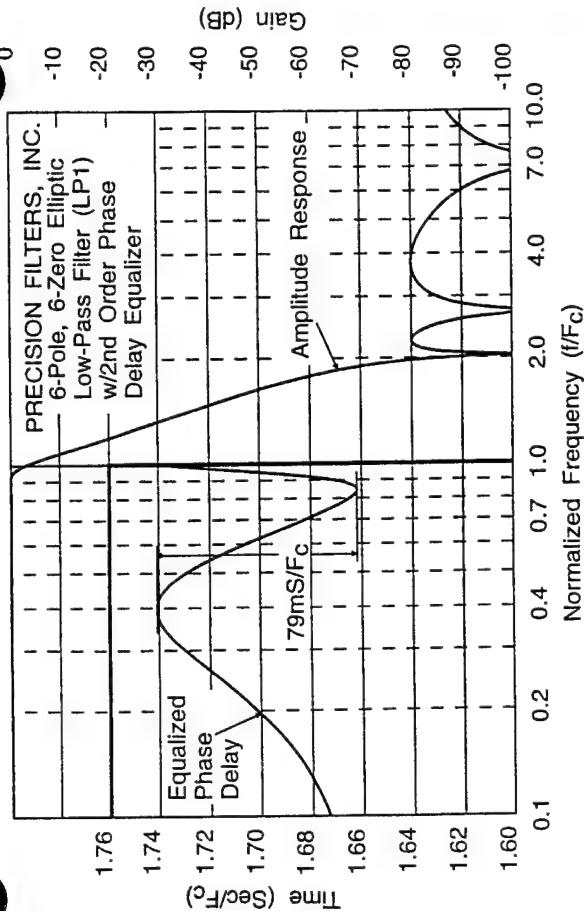
NOISE DOCUMENTATION
DUPLICATE GAGES

Shock-Separation Test   25 Feb 1990

Supply voltage = 5 V_{DC}　　　　　　**Supply voltage = 0**
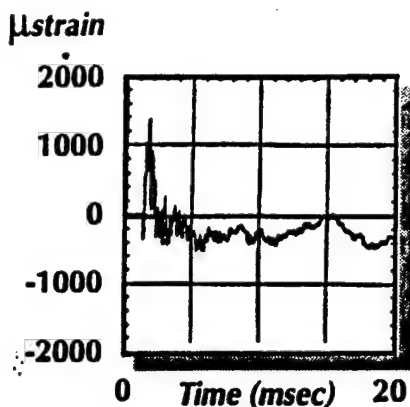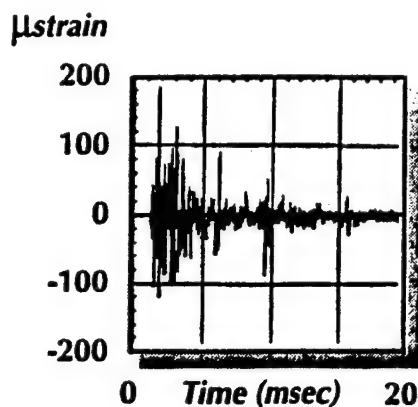
FIG. 18:   TWO CASE STUDIES OF IMPACT-INDUCED VOLTAGES IN STRAIN GAGES
DETAILED DESCRIPTIONS OF THESE TESTS AND OTHERS ARE IN REF. 27

NOISE DOCUMENTATION
DUPLICATE GAGES

Scale Model in Blast Tube   22 Jan 1987

Supply voltage = 0

232
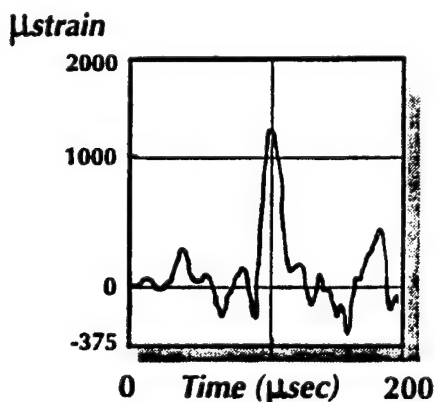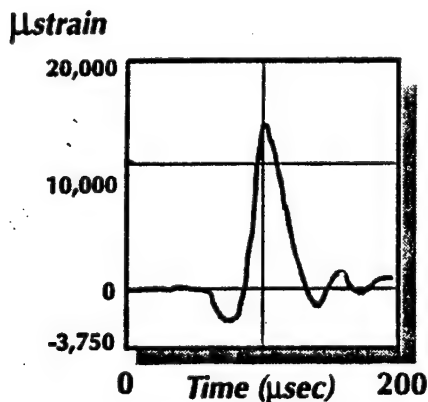
CHECK CHANNELS

Because all components (transducers) in a measurement system respond in all ways in which they can to all factors in the environment, certain diagnostic checking procedures must be built into all measurement systems. For the measurement of high speed transients, some of these diagnostic checks are absolutely crucial to data integrity.

Ref. 1 presents a detailed discussion of these diagnostic checks. They fall into three categories:

- ## CHANNELS UNINTERROGATED (UNPOWERED)

    Switched Check Channels take time.
    Parallel Check Channels take channel capacity.
    Their output represents 2 important noise levels (Ref. 1):
    All self-generating (voltage) responses.

    ### Transducers with a Desired Non-Self-Generating (Impedance-Based) Response.

    All transducers such as piezoresistive or strain-gage-based transducers, especially under high-speed transient conditions, will emit a transient voltage caused by the transient strain and by other mechanisms. These voltages are therefore correlated to the signal (strain, force, pressure, etc.), occupy the same frequency range as the signal and the same time scale. They **cannot be detected or eliminated** with frequency-selective filtering, time-domain, or statistical techniques, the traditional "tools of the trade".

    In addition, voltages may be generated in transducers by other mechanisms: thermoelectric, triboelectric, photovoltaic, magnetically induced, electrically induced, etc. The only two methods to identify their presence are:

- **To remove the Interrogating Input** (Bridge Power or Current for a resistive transducer) during the test. In high-speed transient tests either two tests must be conducted: one with and one without bridge power, or a second channel (check channel) must be mounted near the measuring channel and not powered. The rest of the signal conditioning for both channels must be identical.

    The number of manufacturers of signal conditioning with an *"Excitation Off"* control is just over a dozen. See the Appendix for a list of those with which the author is familiar. The first instrument with this feature, to the author's knowledge, was the Ellis BAM-1, Bridge Amplifier & Meter, of about 1953 which enjoyed a production run of almost 40 years, lastly as the Vishay – Ellis BAM-1 of the Measurements Group, Inc., see Appendix. The author still treasures his unit.

- **To reverse polarity** at the bridge (transducer) input and output simultaneously. If the output changes, then half of that change is due to voltages generated by the application of the measurand. This diagnostic procedure requires two tests to be run: one with each Interrogating Input (excitation) polarity.

    Since the effect of these Self-Generated voltages is usually of the order of 10% of total output but can be as high as 80%, such checks are mandatory for all high-speed transient tests. See Ref. 27 for case studies.

    Two recent examples are shown in Fig. 18, from McDonnell–Douglas Corp., and Lawrence Livermore National Lab. See also Photo 10 in Figure 9 which shows the strain-induced self-generating voltages in the illustrated impact experiment, to the same scale as the signals.

- ## CHANNELS NOT EXPOSED TO THE MEASURAND

    Their output represents 2 different important noise levels (Ref. 1): The total measurement system responses to the Undesired Environmental Stimuli.

A channel not exposed to the stimulus is therefore helpful. Its signal conditioning must be identical to the one for the measuring channel. This check channel shows different environment–response effects than an un–powered channel.

A pressure transducer mounted in a blind hole which is vented to atmosphere, for example, permits evaluation of the effect of ambient accelerations, temperatures, etc., on the measurement. It can also be calibrated by application of pressure through the vent, during a test (Refs. 1, 35).

The *dummy strain gage* consisting of a strain gage of the same Lot Number mounted on an unstrained piece of the same material as the measuring gage, installed at the same time by the same person under identical conditions, and maintained in the same environment as the measuring gage, is the typical example of this compensation or diagnostic method, used since the commercialization of the strain gage in 1938.

If the Interrogating Input or Bridge Supply is also disconnected, the desired responses as stimulated by the undesired environments are isolated and documented by this method. This is an important noise-documentation procedure.

- ## CHANNELS NOT RESPONSIVE TO THE MEASURAND

    Depending on design, output is diagnostic of specific environment-response interactions.

    ### Transducers with a Desired Non-Self-Generating (Impedance-Based) Response.

    Piezoresistive single crystals such as p-type Silicon, have a maximum Resistance-Strain Sensitivity (Gage Factor) when cut along the (1,1,1) crystallographic axis and a minimum (almost negligible) Gage Factor when cut along the 1,0,0 axis. Check channel transducers made of (1,0,0) cut crystals are commercially available (Refs. 32). Some models simply contain unstrained gages (Ref. 31). They have the same resistance vs. nuclear radiation characteristics and often the same resistance vs. temperature characteristics as the "normal" channels and serve as checks for those effects.

    Endevco's Model 7270A-Z is an acceleration-insensitive "accelerometer" built on yet a different principle, checking for still different environment-response effects.

    ### Transducers with Desired Self-Generating (Voltage-Based) Response:

    #### Piezoelectrically-Based Transducers

    Piezoelectric transducers are commercially available in three major families for measurands such as acceleration, shock, "vibration", force, pressure, etc.

- **Naturally Piezoelectric Single Crystals** such as quartz, which, when cut along a specific crystallographic axis, exhibit a high (often maximum) piezoelectric response: electrical charge produced by mechanical deformation.

    It is possible to cut such crystals along axes of minimum piezoelectric response and as of early 1993 one manufacturer has made such a check channel available. (Ref 49). Such Z-cut Quartz would not show any thermal effects, however.

    Some manufacturers who use quartz do, however, make special items on request (See Ref. 20 for one example)

- **Polarized Ferroelectric Ceramics**, man-made in powdered form and fired into the desired geometry in a mold. A high electric field is then applied to the material which is

233

maintained at a temperature above *critical temperature*.

The electric field aligns the randomly oriented domains in the ceramic which becomes polarized or poled.

When the temperature is lowered back to room temperature, the material remains polarized (or poled) when the electric field is removed. The *critical temperature* can be defined as that temperature above which the phenomenon described above, occurs.

A thusly polarized ferroelectric ceramic becomes piezoelectric. A piece of the same material and identical geometry which has not been polarized, will not act in a piezoelectric manner. But it will have responses identical to its polarized twin, to many, but not all, environmental factors. The polarization field is, to some extent, the analog of the bridge supply voltage for resistive transducers, except that it can not yet be turned off and on for a single transducer during a test.

Check channel accelerometers made from unpolarized materials but otherwise identical to the polarized models were first proposed and used by Pierre Fusilier, then Head of the Transducer Group at Lawrence Radiation Laboratory in the early 1960s. A recent (1992) use of that type of check channel is given in Ref. 33. Various National Laboratories such as Lawrence Livermore, Sandia and Los Alamos as well as Boeing have used such check channels over the last 3 decades. So far as the author is aware, they are made by only one manufacturer on demand (Ref 34) but see Bill Shay's comments in Ref. 33.

• **Polarized Flexible Polymers.** The commercial exploitation of these materials is not yet sufficient to have resulted in the use of any unpolarized check channels to the author's knowledge.

Thermoelectrially Based Transducers

A thermocouple design which can be made non-responsive to temperature is described in Ref. 1. The principle has been extensively and successfully used by Dr. Ray P. Reed of Sandia National Laboratories as a diagnostic technique in thermocouple circuits (Ref. 45 for example).

DETECTION OF TRANSDUCER DAMAGE THROUGH OVERLOAD

Transient excitation of transducers such as load cells, pressure transducers, accelerometers and strain gages through application of pyro-shock, explosions or impact can easily result in transducer damage through overload. As for any mechanical structure, direct and incontrovertible evidences of such overload are:

- Zero Shifts
- Modal Parameter Changes
- Transverse / Cross Sensitivity Changes
- Common Mode Rejection Ration Changes

Such changes occur either due to yielding / permanent distortion of parts of the structure or due to shifts in joints such as screws, bolts, spot welds, rivets, adhesive layers, etc.

Among evidences of overload-induced-damage are changes in:

- Calibration Factor, Transfer Ratio, Sensitivity
- Linearity
- Stability (drifts of readings with time)
- Self-Temperature Compensation (Often the most serious effect of almost unbelievable magnitude)
- Creep and Hysteresis

Among the very few detailed studies of such effects for strain-gage-based transducers is Ref. 39 supplemented by Ref. 40. After a 500% overload of a load cell, the zero shift was 100% of Full Scale and the temperature effect on zero had gone from a few ppm/°F to 280 ppm/°F! The effect was linear for that load cell. The load cell was still mechanically and electrically continuous. Such overload-induced zero-shifts can actually be exploited to estimate overloads experienced by transducers (Ref. 41). The effects identified above are the reasons why transducers, in general, are made with as few internal joints as possible. Flexures are sometimes machined with almost incredible ingenuity to avoid any and all joints. Many piezoelectric accelerometers, however, have layered (sandwich) constructions including screw joints. Units specifically designed for the kind of tests described in this paper avoid these constructions (Ref. 44).

Zero Shifts: The zero-shift criterion is applicable only to DC-responding transducers although piezoelectric transducers also exhibit this result on a short-term basis (Ref. 44).

For resistance-based transducers such as strain-gage-based ones, there are now two requirements for detection of such overloads.

• The initial zero (output for zero input) for every transducer must be determined on its receipt and marked on the specification sheet which accompanies the transducer. The manufacturer usually provides only the maximum amount of unbalance and not the specific value for a specific serial number of transducer.

• The signal conditioning must permit the measurement of this initial unbalance. *If the signal conditioning is equipped with an auto-zero feature, there must be a defeat mechanism for that feature.* Ref. 42 cites the case where the absence of such a defeat feature hid a 75% of full scale overload-induced zero-shifts for a long time until a check was made using a different signal conditioning. Ref. 43 cites the McDonnell-Douglas, Huntington Beach, CA criteria for discarding a transducer with more than 1% of full scale zero-shift. These are just two references out of many.

If the Balance Control has no scale so that a return to an initial condition is not possible, such marks must be added.

This Appendix does not identify which of the signal conditioning units listed, provide this auto-balance defeat feature. Prospective users are encouraged to determine this condition before use.

Modal Parameter Changes: The Resonant Frequency and/or Damping Ratio / Bandwidth, and/or Dynamic Magnifier – "Q" - T_{max} must be determined on the as-received transducers and marked on the specification sheet which accompanies it. Manufacturers do not, in general, provide these data for specific serial numbers. Only ranges for model numbers are given.

For piezoelectric transducers, but also for full-scale structures such as off-shore oil wells and bridges, these properties are very sensitive damage criteria.

Transverse Sensitivity Changes: Because of the possible movement of the internal parts due to shock excitation, the symmetry with which the transducer was originally constructed may have been destroyed, seriously affecting its transverse or cross sensitivity.

Ref. 46 cites a test where 160 accelerometers were used on a spacecraft modal survey. The 120 accelerometers owned by the company performing the test had been checked for transverse sensitivity coefficient and any units over 5% had been rejected. The 40 rented units furnished by the spacecraft contractor had not been so checked. 33 of the 40

units showed a transverse sensitivity coefficient of between 5% and 30% and had to be replaced. Unfortunately this was checked after the test had yielded questionable results. The test conductor has since developed an automatic data validation program as part of the data acquisition system, which identifies spurious accelerometer data created by transverse sensitivity responses (Ref. 26).

Common Mode Rejection Ratio: The ability of a differentially coupled transducer to reject common mode, such as the line pressure in a differential pressure transducer, is also a sensitive damage criterion. Almost no differential pressure transducer manufacturer in the world quotes the common mode rejection ratio and its linearity limits and frequency response limits. Testing differential pressure transducers for common mode rejection ratio is expensive and time consuming. Thus this method of determining transducer damage is not very useful.

A good but rough criterion of overload damage, easily verified, is the lowest line pressure (or common-mode-Q) which first produces a noticeable zero shift at the differentially coupled output. This must also be determined on the transducer in its as-received condition since it is never specified for particular serial numbers and differs greatly among them.

However, a transducer for which damage has been established by one of the three other techniques should never be used for differential measurements. There are enough problems in that field (Refs. 1 and 47) that the ones created by overloaded transducers do not need to be added.

TOTAL QUALITY MEASUREMENTS – TQMs

TQMs ARE VALIDATED FORAT LEAST:
(see also Ref. 48)

Rise Time & Undershoot
Frequency loss due to due Anti-Aliasing
Frequency loss due to Pre-Filtering
Peak Reproduction (*)
Frequency Content Reproduction
Wave Shape Reproduction
First Cycle Stability (*)
Undesired Voltage / Impedance Responses
due to the Measurand
Undesired Voltage / Impedance Responses
due to Undesired Environments
Desired Responses due to
Undesired Environments
Boundary Condition *Golden Calf* Effects (*)
Common Mode & Cross Sensitivity Effects
Overload Damage Effects
Sweep Speed / Frequency Velocity Effects
(for Steady State Tests, not discussed here, but see Ref 48)
Impulse-Excited-Ringing-Created Overload
(for Transient Tests, the topic of this paper)

(*) Not specifically discussed in this paper but see Ref. 1.

CONCLUSIONS:

Tests involving pyro–shock conditions, impact, explosions and other high speed transients must be planned, executed and validated according to strict rules of the discipline: *The Engineering of Measurement Systems.*

Data that have been acquired without incorporating these validation procedures are suspect and cannot be assumed to represent the process which was observed. They do not represent **Total Quality Measurements**.

It is often impossible to correct contaminated data by any software process yet established. Unless these validation procedures are built into the measurement system design, the data acquired with such a system cannot be checked and any conclusions drawn from the test are at the risk of the experimenter.

No papers dealing with those topics should be accepted for presentation or publication unless the author clearly identifies the diagnostic validation procedures and system characteristics which were used. All Uncertainty Analyses and Error Analysis must be **preceded** by these checks.

The material presented in this paper and in Ref 1 was taught in the Junior course in Measurement Systems Engineering, Fall 1959 – Spring 1977, Arizona State University as part of a program leading to BS, MS and PhD degrees in Measurement Systems Engineering.

The fact that a recent International Congress programmed 13 papers on these topics, which showed no evidence of data validation procedures for tests such as mentioned here, is an almost inconceivable condition near the end of the 20th Century.

The question posed at the beginning of this paper must always be answered:

Could these data have been produced by that measurement system, without distortion, without "noise" levels and without affecting the process being observed, all within whatever limits of validity have been specified!

APPENDIX

From the foregoing discussion, the following requirements can be placed on signal conditioning for resistance-based transducers:

THREE (Among Many)
SIGNAL CONDITIONING REQUIREMENTS
FOR RESISTANCE–BASED TRANSDUCERS

- Interrogating Input Disconnect: Bridge Power Defeat.
  (For very low-frequency tests, polarity reversal may replace the disconnect feature)
      To check for Self-Generating Voltage
      Responses

- Step–Resistance Change: Shunt Calibration
      To check Rise Time & Undershoot Characteristics

- Balancing Circuit Disconnect: Auto-Zero Defeat
  (Balancing circuit reference position may be acceptable)
      To check for Transducer Damage

Manufacturers of Signal Conditioning with Excitation OFF Provision and Step Calibration

The number of manufacturers of signal conditioning for impedance–based transducers in which the *Bridge Supply, Excitation, Interrogating Input* can be switched to *Zero* or *Off* is very limited. To the author's knowledge, which is not exhaustive, the following manufacturers provide that possibility on some of their models, either in a manual or computer programmable manner. Contact names are given where the author has them. Anyone with additional information on other manufacturers is asked to be so kind as to share that with the author: Phone & FAX: 602-945-4603.

Apix
Chris and Pete Tsipouras
6501 Park of Commerce Blvd., # 115
Boca Raton, FL 33487
Phone: 407-998-2806   FAX: 407-998-2885

Model 1EX-1A Isolated Milliamp Output Excitation
Module

Aydin Vector Division
Farhad Daghigh
Digital Products Sales
P. O. Box 328
Newtown, PA 18940-0328
Phone: 215-968-4271   FAX: 215-968-3214

Model SSC-2008 Super Signal Conditioner; program-
mable bridge supply OFF
Model PCU-800 Series Signal Conditioner & PCM
Encoder; programmable bridge supply OFF

Campbell Scientific, Inc.
Paul D. Campbell, President
815 West 1800 North
Logan, UT 84321-1784
Phone: 801-753-2342   FAX: 801-752-3268

Model 21X Data Logger (not for dynamic applications)
Bridge power reversed at each reading. No shunt
calibration.

Cycad / Amacron
Jack J'maev, Aerospace Marketing
1511 Fishburn Avenue
Los Angeles, CA 90063
Phone: 310-406-5265

Model 02J14 Bridge Completion and Calibration
Eurocard Module; excitation-defeat relay.

Dynamics Division of Waugh Controls Corp.
Tony Mastroianni, Product Manager
9001 Fullbright Avenue
Chatsworth, CA 91311-6172
Phone: 818-998-8281   FAX: 818-407-1320

Model 8000; programmable bridge supply OFF

Ectron Corp.
Walter Hanford, Vice-President, Marketing
8159 Engineering Rd.
San Diego, CA 92111
Phone: 619-278-0600   FAX: 619-278-0372

Model 765 Programmable Transducer Conditioning
Amplifier; programmable bridge supply OFF.
Transducer Conditioning Amplifier Models 563H, 753A,
755; remote or front panel switch for bridge supply OFF.

Endevco Corp
Bob Clark
30700 Rancho Viejo Road
San Juan Capistrano, CA 92675
Phone: 714-493-8181   FAX: 714-661-7231

Model 4430, programmable bridge supply OFF

Encore Electronics, Inc.
Marcel Zucchino, President
RD 2, Route 50
Saratoga Springs, NY 12866
Phone: 518-584-5354

Model 610, manual bridge supply OFF

Instrum
Charles Armenia, President
176 West Pomona Avenue
Monrovia, CA 91016
Phone: 818-303-4210   FAX: 818-357-8863

Models 2705, 2706, manual bridge supply OFF optional

Measurements Group, Inc.
Steve Katz, Vice-President of Sales
P. O. Box 27777
Raleigh, NC 27611
Phone: 919-365-3800   FAX: 919-365-3945
Model VE BAM-1, manual bridge supply OFF
Model 2400, programmable bridge supply OFF
Models 3500, 3800; manual switch
Models 2100, 2200, 2300; manual switch

Neff Instrument Corp.
Louis Lang, Marketing Manager
700 South Myrtle
Monrovia, CA 91016
Phone: 800-423-7151   FAX: 818-303-2286

Series 300 Transducer Signal Conditioner Module;
optional bridge supply OFF
Model 490 Data Acquisition & Recording System;
programmable bridge supply OFF

Optim Electronics, Corp.
Roger Moore, President
Middlebrook Technology Park
1201 Middlebrook Road
Germantown, MD 20874
Phone: 301-428-7200   FAX: 301-353-0129

Model AD 682SH-1 Differential Input Module for all
Megadac models

Pacific Instruments, Inc.
John Hueckel, President
215 Mason Circle
Concord, CA 94520
Phone: 510-827-9010   FAX: 510-827-9023

Model 8250 Transducer Conditioning Amplifier
Model 8650/8655 Transducer Conditioning Amplifier
Model 9250/9255 Programmable Transducer Amplifier
Model 9300 Transducer Amplifier, Programmable
Model 9350/9355; programmable
All have Excitation Interrupt, programmable on models
so identified.

Precision Filters, Inc
Don Chandler, President
240 Cherry Street
Ithaca, NY 14850
Phone: 607-277-3550   FAX: 607-277-4466

Model 27000 System, Transducer Amp/Filter Module

Wems, Inc. Formerly Teledyne Signal Conditioning
Mr. David Anoushirvany
Chief Engineer, Signal Conditioning
350 West Rosecrans
Hawthorne, CA 90250
Phone: 310-644-0251   FAX: 310-644-5334

Model 849333 PCU, Pre-Conditioning Unit; manual
bridge supply OFF.
Model 858900 Programmable PCU

REFERENCES:

1. Stein, Peter K. **The Unified Approach to the Engineering of Measurement Systems, Part I – Basic Principles**. Monograph, April 1992, 134 pp, soft cover. Stein Engineering Services, Inc., 5602 E. Monte Rosa, Phoenix, AZ 85018. Phone & FAX 602-945-4603. $15 cash with order, $20 with invoice. ISBN # 1-881472-00-0.

2. Stein, Peter K. *Dynamic Measurements on and With Non-Linear Systems: Problems and Approaches*. Presented at: IMEKO IX, 9th International Measurement Conference, May 24-18, 1982, Berlin, Germany. **Proc. First International Modal Analysis Conference – IMAC 1, November 8-10, 1982**, pp. 358-389, Soc. for Experimental Mechanics, Bethel, CT. **Proc. 12th Transducer Workshop, June 7-9, 1983**, pp. 2-35. Range Commanders Council Secretariat, White Sands Missile Range, NM, 88001. Also **Lf/MSE Publ. 76,** from Stein Engineering Services, Inc., 5602 E. Monte Rosa, Phoenix, AZ 85018 with revisions through 1985.

3. Stein Peter K. *Better the Imperfect Truth than Perfectly Accurate Garbage,* **Experimental Techniques**, November Editorial, p. 3. Also Sheet 24 in Lf/MSE Reprint 67, 1989 edition. Stein Engineering Services, Inc., 5602 E. Monte Rosa, Phoenix, AZ 85018.

4. Ghaussi, M. S. **Principles and Design of Linear Active Circuits,** McGraw–Hill Book Co., 1965. pp. 487-490

5. Valley, George E., Jr. & Henry Wallman. **Vacuum Tube Amplifiers,** McGraw–Hill Book Co., 1948. p. 66.

6. Elmore, William C. & Matthew Sands, **Electronics: Experimental Techniques,** McGraw–Hill Book Co., 1949. pp. 128-141.

7. Sauceda, Robert & Earl E. Schiring, **Introduction to Continuous and Digital Control Systems,** MacMillan, 1968, p. 452.

8. Stein, Peter K. **Measurement Engineering, Vol. I – Basic Principles,** Chapter 5, 4th edition, 1967 through to 6th edition 1970. Stein Engineering Services, In., 5602 E. Monte Rosa, Phoenix, AZ 85018.

9. Anon. **Instruction Manual for Endevco Piezo-electric Accelerometers,** Publ 101, 1979, Endevco. 30700 Rancho Viejo Rd., San Juan Capistrano, CA 92675

10. Gurtin, M. E. The Effect of Accelerometer Low–Frequency Response on Transient Measurements, **Experimental Techniques,** June 1961, pp. 206 ff.

11. Rhodes, J. E. Transducer System Frequency Requirements for Transient Measurements, Endevco, Tech Data Sheet, 9/22/60. See Ref. 9 for source.

12. Anon. **Specification Sheet,** Endevco Model 7255 Accelerometer. Source, see Ref. 9.

13. Anon. **Specification Sheet**, UA 0553 and UA 0559 Mechanical Filter for Accelerometers. Brüel & Kjær ments, Inc., 185 Forest St., Marlboroug, MA 01752.

14. Anon. **Specification Sheet**, Accelerometer Mounting Wax, Model 080A24. PCB Piezotronics, Inc., 3425 Walden Avenue, Depew, NY 14043

15. Walter, Patrick L., & H. D. Nelson, *Limitations and Corrections in Measuring Structural Dynamics,* **Experimental Mechanics**, Sept. 1979, pp. 309-16.

16. Walter, Patrick L. *Deconvolution as a Technique to Improve Measurement–System Data Integrity.* **Experimental Mechanics**, August 1981, pp. 309-314.

17. Walter, Patrick L. *Limitations and Corrections in Measuring Dynamic Characteristics of Structural Sys-ems,* **PhD Dissertation**, Arizona State Univ, Tempe, AZ 85287, 1978, **Sandia Document 78-1015**, Oct. 1978, Sandia National Labs, Albuquerque, NM. Also in: Patrick L. Walter, *Bridge Transducers*, Ch. 8 in **Instrumentation and Control, Fundamentals and Applications**, Chester L. Nachtigal, Ed. Wiley & Sons, 1990, pp. 265-308.

18. Thomsen, Carsten & Henning Møller. *Swept Measurements of Harmonics, Difference–Frequency and Intermodulation Distortion,* **Brüel & Kjær Application Notes**, no date. Source, see Ref. 13.

19. Wright, Charles P. *Dynamic Data Invalidity due to Measurement System Non-Linearity,* **Proc. Western Regional Strain Gage Committee, Feb. 12-13, 1985 Meeting, Phoenix, AZ.** From WRSGC, 44 N. Benson Ave., Upland, CA 91786. Also in Ref. 2, 1985 revision.

20. PCB Piezotronics, Inc., 3425 Walden Ave, Depew, NY 14043. Jim Lally CEO. PCB manufactured special trans-ducers for the author such as a spark plug mounted pressure transducer with its input welded shut, to serve as check channel for vibrations. "Customized arrangements become future products!" says Richard Lally. Example: *Model 305M23 Accelerometer* in Fig. 12. "There have been 400+ variations of our Model 308 Accelerometer", he emphasizes.

21. Endevco Corp., 30,700 Rancho Viejo Rd., San Juan Capistrano, CA 92675. Ex. *Models 2255A, 2255B Isotron Accelerometers.* Bob Clark.

22. Vibra·Metrics, Inc., 1014 Sherman Ave, Hamden, CT 06514. Ex. *Model AN115 Accelerometer,* John Judd, Pres.

23. Schelby, Frederick. *A Systems Approach to Measuring Short–Duration Acceleration Transients.* **Proc. 12th Transducer Workshop, June 7-9, 1983.** Range Commanders Council Secretariat, White Sands Missile Range, NM 88001.

24. Jung, Walter, M. L. Stephens & C.C. Todd. *An Overview of SID and TIM, Parts I & II.* **Audio Jnl.** June 1979, pp. 59-72; July 1979, pp. 38-47.

25. Walter, Patrick L. *Effect of Measurement System Phase Response on Shock Spectrum Computation.* **Shock & Vibration Bulletin, Bull. 53, Part 1,** May 1983, pp. 133-141.

26. Wright, Charles P. *Knowledge-Based Systems for Test Data Acquisition and Reduction.* **Lf/MSE Reprint 82**, Lecture notes for the Short Course: The Engineering of Measurement Systems. Stein Engineering Services, Inc., 5602 E. Monte Rosa, Phoenix, AZ 85018. (*Frequency Devices,* 25 Locust St., Haverhill, MA 01832) (*Precision Filters,* 240 Cherry St., Ithaca, NY 14850).See also Ref. 48.

27. Stein, Peter K. *Our Engineering Education: The Not–So–Scientific Method.* Presented at The Role of Laboratories in Engineering Education Session, American Society of Mechanical Engineers Winter Annual Meeting, Dec. 3, 1979, New York City. Revised version: **Lf/MSE Newsletter No. 38, Summer 1992**, pp. (ii)-24, Stein Engineering Services, Inc., 5602 E. Monte Rosa, Phoenix, AZ. Also **Lf/MSE Publ. 74**, July 1992, from the same source.

28. Stein, Peter K. *Some Notes on Second Order Systems: Responses of Systems to Steps and Pulses.* **Lf/MSE Publ. 35/36/40**, 1st ed. , 1971; current ed., 1985. Stein Engineering Services, Inc., 5602 E. Monte Rosa, Phoenix, AZ 85018

29. Stein, Peter K. *The Unified Approach to the Engineering of Measurement Systems: Yesterday's Recipe for Tomorrow's Source of Measurement Engineers: Part II – Transient Measurements: A Junior Level Final Examination – Mechanical Impact: Traveling Wave Phenomena – A Problem*

in Data Validation. **Publ. 85**, Mar. 93 same source as Ref. 30.

30. Stein, Peter K. *The Myth of Wave Shape Reproduction,* in **Lf/MSE Publ. 65** , 1st ed. 1968; current ed. 1975. Stein Engineering Services, Inc., 5602 E. Monte Rosa, Phoenix, AZ 85018.

31. *Model 2266 Series Radiation Resistant Piezoresistive Accelerometers. Model 7231C–Z Accelerometers* contain unstrained gages. Endevco, see Ref. 34 for address.

32. Kulite Semiconductor Products, Inc., Ron Moores, Marketing V-P, 1 Willow Tree Rd., Levonia, NJ 07605. (201)-461-0900. Any of their strain gages with "O" replacing the "P" gage designation, per April 11, 1976 memo from John Kicks, then Manager, Sales & Product Engineering.

33. Shay, William, Lawrence Livermore National Laboratory, *Case Studies in Noise Documentation: Case Study #2: A "Dummy" Transducer as Check Channel in a Noisy Environment,* **Lf/MSE Newsletter No. 39,** January 1993, Stein Engineering Services, Inc., 5602 E. Monte Rosa, Phoenix, AZ 85018.

34. Endevco, 30,700 Rancho Viejo Rd., San Juan Capistrano, CA 92676-1789. Bob Clark: "There will be a new listing in our printed price list which will reflect the availability of such devices", Oct. 12, 1992 memo.

35. Stein, Peter K. *The Measurement of High Frequency Fluctuations between Impeller Blades in an Operating Gas Turbine Compressor,* **ASME Paper 60-WA-337,** 1960. Also Chapter 15 in Ref. 8 since its 1st, 1960 Edition. (Reporting work done by the author at AiResearch Manufacturing Company of Arizona, now Allied Signal, Garrett Turbine Engine Division, in 1956.)

36. Frequency Devices, Inc., Dr. Robert E. Steer, Jr., President. 25 Locust Street, Haverhill, MA 01832. In addition to the filters shown, FDI provides the 848 series of programmable modules and the model 9002, 9016 and 9064 instruments that have the same transfer functions available.

37. Precision Filters, Don Chandler, President, 240 Cherry Street, Ithaca, NY 14850.

38. *Models 720 Series & 793L Accelerometers.* Wilcoxon Research, 21 First Field Rd., Rockville, MD 20878. 301-330-8811. Eric Saller, Senior Applications Engineer.

39. Tovey, F. Michael. *Effects of Overload on Load Cell Performance.* **Experimental Techniques,** Vol. 5, No. 3, Sept. 1981, pp. 8-9. The missing figure is published in Ref. 40. Tovey's paper also appears in **Proc. Western Regional Strain Gage Committee, Feb. 1978 Meeting** from WRSGC, 44 N. Benson Ave., Upland, CA 91786.

40. Stein, Peter K. **Lf/MSE Publ. 67, Sheet 23**, Stein Engineering Services, Inc., 5602 E. Monte Rosa, Phoenix, AZ 85018-4646.

41. Stein, Peter K. *Some Little Known Literature and Effects in Strain–Gage–Based Force Transducers,* **Proc. International Conference on Measurement of Force & Mass, Sept. 11-14, 1984, Kobe, Japan,** pp. 303-308, Society of Instrument & Control Engineers (SICE), Japan, 1984.

42. Potvin, Robert. Comment about Northrop Aircraft experience in **Proc. Western Regional Strain Gage Committee Meeting, August 11-12, 1992**. WRSGC, 44 N. Benson Ave., Upland, CA 91786.

43. Shull, Larry, Comment about McDonnell-Douglas procedures in Ref. 42 above.

44. Chu, Anthony & Arthur Gilbert. *Zero Shift of Piezo-electric Accelerometers in Pyroshock Measurement.* **Proc. 56th Shock & Vibration Symposium, Oct. 22-24, 1985,** Shock & Vibration Information Analysis Center (SAVIAC), c/o Booz-Allen & Hamilton Inc., 2711 Jefferson Davis Highway, Suite 600, Arlington, VA 22202-4158. Also from Endevco at the address cited in Ref. 34.

45. Reed, Dr. Ray P. *Validation Diagnostics for Defective Thermocouple Circuits*, **Proc. 6th International Conf on Temperature, Its Measurement & Control in Science &** **Industry,** 1982, Vol. 5, No. 2, pp. 931-938. American Inst of Physics, NY.

46. Wright, Charles P. **Personal Communication,** April 1981, 2550 Date Circle, Torrance, CA 90505.

47. Stein, Peter K. *The Measurement of Differential Quantities: Problems and Approaches,* preprint of a paper presented at the Annual Meeting, Soc. for Engineering Education, June 1972, **Lf/MSE Publication 43**, 40 p. Stein Engineering Services, Inc., 5602 E. Monte Rosa, Phoenix, AZ 85018, Phone & FAX: 602-945-4603

48. Vellutini, G.A., C. P. Wright. *Knowledge-Based Systems for Test Data Acquisition/Reduction,* **Proc. 11th Aerospace Testing Seminar,** Institute of Environmental Sciences, October 1988.

49. 20. PCB Piezotronics, Inc., 3425 Walden Ave, Depew, NY 14043.

Transient Measurements – Mechanical Impact – Traveling Wave Phenomena
A Problem in Data Validation – A Junior Level Final Examination

by Peter K. Stein, Director of the Short Courses
The Engineering** and **The Dynamics of Measurement Systems for Test & Evaluation
5602 E. Monte Rosa, Phoenix, AZ 85018

Telephone and Telefax: (602)-945-4603. In the U.S. 1-800-632-7797

PRELIMINARIES

INTRODUCTION:

This paper presents the *Final Examination* in the Junior Level (third year) course in *Measurement Systems Engineering* as presented by the author in the *Laboratory for Measurement Systems Engineering (Lf/MSE)* at Arizona State University from the early 1960s through to Spring 1977 when the author retired to "Private Practice".

The original material was contained in Chapter 14, *Measurement Engineering* by the author, published and distributed by his organization as text book for the courses from 1960 until it went out of print about 1970 after 5700 copies. (Ref 1). From 1970 on the questions were formalized into a booklet: *Lf/MSE Publication No. 39* distributed to the students during the semester (Ref. 2), and during the Short Courses in *The Engineering of Measurement Systems* and *The Dynamics of Measurement Systems*. 4550 copies of that publication have been used 1973-1993.

The experiment which is described was specifically designed to be **non-repeatable** and **unpredictable**. All data validation had, of necessity, to be done internally within the data without recourse to theory except for the grossest predictions as to the general nature of the events.

THE TEST SPECIMEN:

The Strut:

A vertical steel strut attached to a base plate with friction clamps is impacted with one of three hammers of different masses. The experimental set-up is shown in Figs. 1 & 1A. Of the several versions of the experiment, the schematic diagram of one of the circuits used is shown in Fig. 2. The shielding and grounding arrangement is not shown and will be described.

The object of the experiment is to observe the strain–time history as experienced by the strain gages and to document the validity of the data.

The strut is 31.2 inches long, of mild steel, 1.75 x 0.25 inches in cross section, free at the top where it is to be struck. It is clamped at the bottom in a 3" deep by 4" square steel block in a friction grip. The whole assembly is mounted on a 1/2" thick steel plate, 5-1/2" x 7", resting on the floor, (Fig. 1).

The Strain Gages:

Two 350–ohm gages are mounted axially on opposite sides of the strut along its center line, 8.2 inches from the clamped end and connected in the circuit shown in Fig. 2. The gages used to acquire the data presented here, are BLH FAP-50–35 Lot No. 4:

R = 350 ohms ± 2.5 ohms
K = 2.2 ± 1 %

The gages are attached with Duco adhesive, cured at 150 to 180°F until gage to ground resistance exceeded 10K Megohms, and then covered with micro–crystalline wax.

Two other gage types, not shown here, are also mounted on the strut.

The Instrumentation:

The strain gage signal is processed in two different ways on all photos shown in Figs. 24 except No. 5. The top trace represents the output from the constant–current circuit fed directly to a single-ended, AC-coupled cathode ray oscilloscope, a two–channel Tektronix 502, Serial 5096. The bottom trace represents the output from the same constant–current circuit, but fed through a Tektronix 123 Preamplifier with a gain of x100, Serial 995, and then to the second channel of the same CRO, single–ended AC–coupled, the gain of which is set at 1/100 of the value used for the top trace. This record simulates the use of a pre-amplifier with a low-sensitivity CRO. On all photos, both traces result from the same impact.

Specification sheets of the instruments used are appended (Figs 19A and 19B). The Current Source was home–made and no specifications are available.

Shielding, Grounding and Leads

Only two-conductor shielded leads are used in three-foot lengths. The case of the current source is connected to the shield of the leads which bring the current to the gages. The other end of that shield is connected to the test specimen. The shield of the leads which connect the gages to the CRO is attached to the specimen at one end and to the CRO ground at the other.

Thus any charges accumulated by the current source case, the test specimen and the connecting leads, are drained to the single ground in the system, the CRO and from there to the wall plug to which the CRO is connected. The grounding of that wall plug is checked with a Ground Tester, of course. Ground loops have been eliminated by this process.

The only unshielded section of leads is from the gages themselves to the terminal strip at the bottom of the strut. The ribbon leads used for that connection are not recommended for use in serious testing of this type. They present too much cumulative area as a coupling mechanism for time-varying magnetic fields. Nor are the banana plugs which are used in this experiment strictly for convenience. Those plugs present contact resistance problems and can be "ejected" from their sockets by repeated reflected stress waves. Hard wired connections are recommended.

The Gage Location and Strut Length

The gage location and beam length were selected with several factors in mind.

• For the small hammer, there should be enough time between the initial pulse passage through the gage and its reflection from the clamped end so that the strain drops to zero in between. This condition makes it relatively easy to measure the Reflection Factor for Forces at the clamped end (see Fig. 22 for example and Photo #7, Fig. 25.

• For the larger hammers this should not be the case. For the largest hammer, the leading edge of the reflected compression pulse already returns through the gage before the tail of the incident pulse has passed through. This condition gives the effect of a broad pulse with much area under it. The illustration of both conditions was held to be worth while in planning the experiment.

• The gage should be located at such a distance from the free end that the act of impact could be used to trigger the cathode ray oscilloscope (See *Triggering* Section). This condition also makes it possible to observe the contact time in a simple manner. Simplicity of apparatus has always been one of the author's design and selection criteria.

The Strut Cross-Sectional Area

The cross sectional area of the bar is such that, approximately at least, one commercially available hammer is be under-matched in Characteristic Impedance, another is considerably over-matched, and a third would be slightly over-matched in Characteristic Dynamic Impedance. The three projectiles (Fig. 1A) do, in fact, illustrate quite different dynamic effects.

ASSUMPTIONS:

In answering and discussing the questions in this examination:

• Where necessary assume the speed of sound in steel as 200,000 "/sec as a design value.

• Where you use rules of thumb, identify them and state the conditions under which they apply, and if these conditions are indeed met here.

• State any assumptions necessary to your analysis, and whether or not the conditions of the experiment fulfill these assumptions.

You are free to use any of the material connected with this course, but be sure to reference page and publication when you use materials This will also assist you in tying together the loose ends of the course.

FIG. 1: EXPERIMENTAL TEST SET-UP
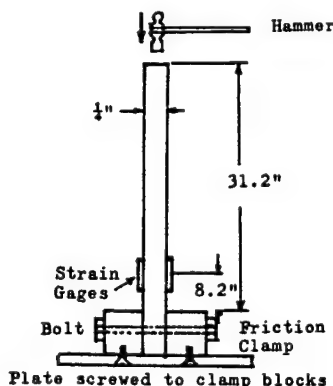
FIG. 2: CIRCUIT DIAGRAM (SHIELDING NOT SHOWN)
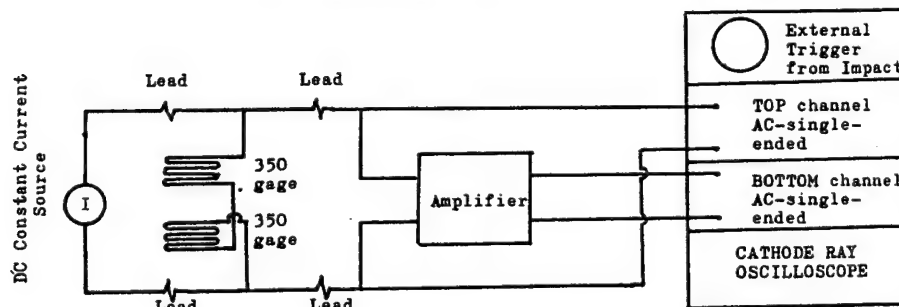
Grounding and Shielding described with Photos 6 through 10.

FIG. 1-A: THE HAMMERS AND THE STRUT

FULL SCALE OUTLINE DRAWINGS OF AVAILABLE HAMMERS
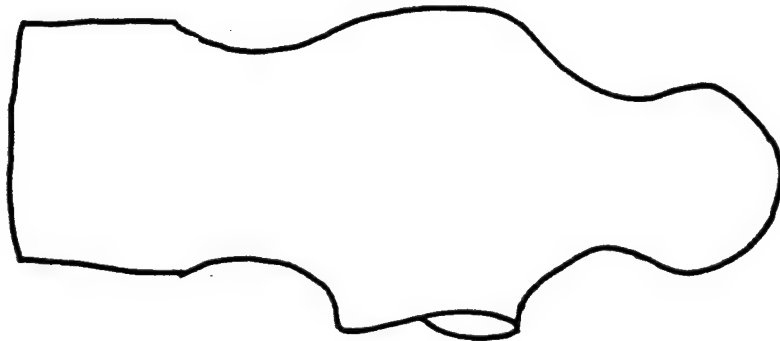
LARGE

STANLEY 310 - 16 oz

    4.1 " long
    1.28" D striking end
    1.29 sq.inch. area
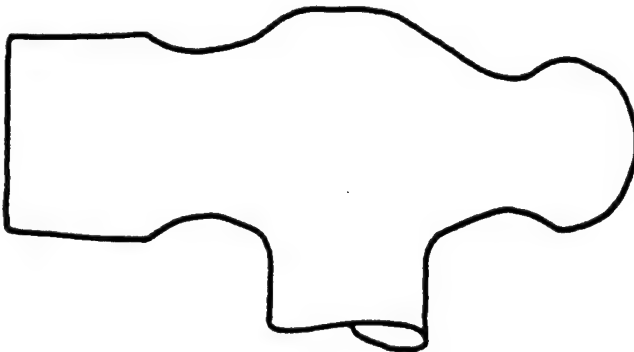
MEDIUM

STANLEY 308 - 8 oz

    3.3 " long
    1.06" D striking end
    0.88 sq.inch area
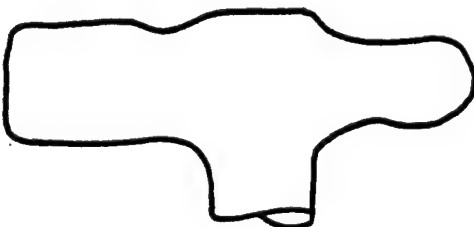
SMALL

STANLEY 291-B - 2 oz

    2.5 " long
    0.6 " D striking end
    0.3 sq. inch area
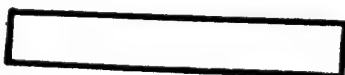
STRUT

1.75 " x 0.25 " = 0.4375 sq. inch

THE NATURE OF THE QUESTIONS:

The questions are meant to explore the following problems which might occur in this type of test.

- Is the rising portion of the record valid? Does it really represent the strain rate in the material, or is it affected by the rise-time of the measurement system?

- Is the maximum strain indicated correctly, or is there distortion due to system Non-Linearity.

- Is the maximum strain indicated correctly or is there distortion due to lack of system frequency response either for Magnitude or for Phase?

- Are the negative areas which follow some of the compression pulses really reflected tension pulses, or are they due to Undershoot in the measurement system?

- Do the records reflect only non–self–generating (impedance–based) responses of the strain gages, or are there self–generating (voltages–based responses which occur to the same time scale and frequency scale and which are correlated to the strain signal and which contaminate the record?

- Do the records reflect only the non–self–generating response of the strain gage due to strain, or are there other environmental factors which elicit non–self–generating responses, such as temperature, for example?

- Do the records reflect only the power–dissipating non–self–generating response of the strain gage (i.e., resistance changes) or are there energy–storing responses such as capacitive effects in the gages or cables, etc., which affect the data?

- Does the square wave produced by the shunt–calibration signal really carry the calibration information on its peak-to-peak value or has it been distorted by the measurement system?

- Does the measurement system have sufficient frequency response to display the frequency content in the data?

- Does the measurement system have sufficient frequency response to display the wave shape of the data?

- Is enough known about the properties of the strut material to interpret the data even though it be valid?

- Is enough known about the measurement system and all its components to be able to answer any or all of the questions raised in this exam? If not, then some preliminary tests of the components would be indicated.

- What are some of the important special characteristics of the effects of traveling waves in mechanical (or hydraulic, or electrical) structures which can be illustrated by a simple experiment such as this?

- What are some of the ways in which the output voltage from the strain gages can be recorded, either for visual interpretation, or for subsequent analysis for frequency content, or for subsequent operations such as in digital form?

- Is there a logical, systematic manner, using everything presented in the lectures and text book so far, to plan a measurement system for a high–speed transient test, so that the above questions can be answered in a satisfactory manner?

This is the final experiment in both the beginning Junior and first Graduate course in *Measurement Systems Engineering* featuring the *Unified Approach to the Engineering of Measurement Systems*. All the above questions can be answered from material covered during the course in lectures, previous experiments, or the text materials and reprints distributed during the course. Much of that material is presented in Refs. 14 and 27 and more of it is presented in the section on *Preparatory Lectures*, below.

The remainder of this booklet will ask a series of questions designed to get at some (NOT ALL) of the answers to some (NOT ALL) of the questions raised above. It is the philosophy of the *Unified Approach* that, amongst many other things, such answers should be possible.

THE PREPARATORY LECTURES

A series of preparatory lectures preceded the performance of the actual experiment. Some of the lecture content is summarized in the section which follows.

The Questions are then presented.

The final section presents the answers. Those answers summarize more of the lecture material which preceded the experiment and which was not included in the initial summary which follows immediately.

TEN "STEPS TO SUCCESS"
IN PLANNING A MEASUREMENT SYSTEM

Some of the material presented in the lectures preceding the actual experiment, is given in this section. It deals with the philosophy of the Engineering of a Measurement System and how to get started in planning a test. Please note that the equipment being discussed is now antiquated, but that the principles suggested and used are still applicable and are, in fact, timeless.

1. Investigate the Phenomenon

Gain an understanding of the physics, not necessarily with a mathematical model, of what is going on in the process on which measurements are to be made.

2. Identify the Measurands

Based on your understanding of the process, identify what quantities are to be measured, where and when. In your selection, emphasize those quantities which cannot easily be predicted or for which predictions are not yet possible.

3. Design the Ideal Measurement System

Specify the components and their relationships – the transducers and the system structure – which you would like to have, given the circumstances of the test.

4. Select the Real Hardware

Based on your specifications, select real hardware.

5. Evaluate the Inevitable Compromises

Your selection may have to be based on availability rather than applicability – on what you can get rather than on what you want. Evaluate the compromises which were made.

6. Set Up the Test and Document the Environment– Response Interactions

There are 16 environment–response syndromes of which only one is desired. The remaining 15 are *Noise Levels* – Undesired Environment–Response Combinations. Of those 15, three are usually more important than the others. At least those three should be documented by the standard processes developed for the *Unified Approach to the Engineering of Measurement Systems*.

7. Conduct the Test

This is usually the shortest of the Ten Steps. In fact, the shorter the test, such as this Impact Test which will take only a few hundred microseconds, the longer the preparation time and the validation–interpretation process.

8. Validate the Data

These are the internal validation processes which answer the question: *Could these data have been reproduced by this Measurement System without Distortion. – Do these Data represent the Process as though the Measurement System had not been there* interacting with the process and distorting the information flow. Are the data worth analyzing?

9. Interpret or Analyze the Data

What has the test told you about the Process.

10. Take Some Action on the Process

This action may simply be an answer to the question: *How much is too much* or *How little is too little.* in terms of stresses in this case. Is it safe to run the process? The Action may also be automatic such as in a control system.

The Measurement Engineer's Domain

Normally, the Measurement Engineer is restricted to Steps 2 through 8 and is not invited to participate in the original planning of the test nor in the final action.

Only if the Measurement Engineer is involved in those Steps, however, will the product–or–process design be optimum. I well remember one of my colleague's comments when I was Group Leader in Instrumentation Engineering early in my career: *"If those turbines were only designed to be instrumented, they would not have to be! They'd run right to begin with!"* (Leslie Spencer Wirt, 1955)

The discussion below will deal with items 1 & 2 and then 9 & 10 before tackling those problems normally considered as the Measurement Engineer's domain.

APPLICATION TO MECHANICAL IMPACT

DOMAIN USUALLY CONSIDERED OUTSIDE THE MEASUREMENT ENGINEER'S FUNCTION

1. Investigate the Phenomenon
2. Select Some Measurands

A. IMPACT

Impact is Suddenly Applied Energy.

Energy usually exists as the product of two physical quantities such as:

Force & Displacement for Mechanical Energy
Pressure & Volume for Fluidic / Acoustic Energy
Voltage & Charge for Electrical Energy
etc.

Suddenly reminds us that a finite amount of energy can not be transmitted in zero time because that would require an infinite amount of power, since, dimensionally,

$$|Energy| \quad = \quad |Power| \times |Time|$$

Hence, transmission of energy requires time.

At any one instant in time there will be a distribution of forces and displacements along the test specimen, and at any one location on the specimen, the forces and displacements will vary with time.

A pair of simultaneous, usually non-linear, second order partial differential equations in time and space are required to describe this process mathematically.

The forces which propagate through the structure create stresses and strains; the displacements create particle-displacements and velocities. These equations are often called the *Wave Equations*, presenting the process as waves of forces and displacements propagating through the structure.

Such a structure is also called a **Transmission Line.**

As illustrated in Fig. 3, there may be pairs of such waves of opposite sign (compression and tension, for example) following one another. By linear superposition such a pair of traveling waves may be considered as a single traveling pulse. We will therefore talk of traveling waves or pulses as the application warrants. (Fig. 3 is discusssed in the section *Time Scale of Events*).

At the location of the strain gage the first evidence that impact has occurred will manifest itself as a pulse of some shape and time duration. Those are difficult if not impossible to predict since the intergranular damping within the materials will have affected the process.

One Measurand, therefore, is the Pulse Shape at the gage location.

B. SPEED OF WAVE PROPAGATION

The propagation speed or velocity of the wave depends on the material properties and geometry of the specimen.

In long, thin, slender, "unidimensional" bars often known as Hopkinson Bars, the propagation speed is the:

Celerity or "Speed of Sound": $\quad c_0 \quad = \quad \sqrt{E/\rho}$

where

$E \quad = \quad$ Elastic Modulus of the specimen material
$\rho \quad = \quad$ Density of the specimen material

For steel, aluminum and magnesium, within about 10%:

$c_0 \quad = \quad$ 200,000 inches/second (5 μsec/inch)

FIG. 3: TRAVELING WAVES AND PULSES
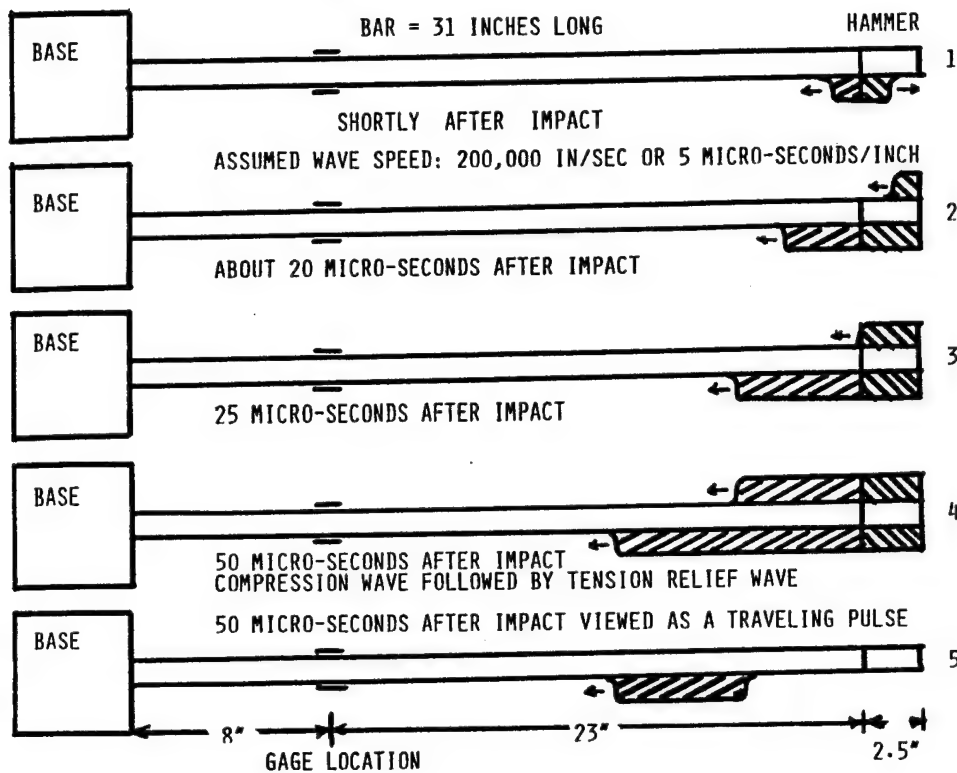
In two-dimensional specimens such as plates, the propagation speed is also a function of:

μ = Poisson's Ratio of the specimen material

and for three-dimensional solids:

$$c = c_0 \sqrt{\frac{[1-\mu]}{[1+\mu][1-2\mu]}} = 1.16\, C_0 \qquad \text{for } \mu = 0.3$$

For propagation of waves in the plastic region of the specimen material's stress-strain curve, the value for Elastic Modulus in the above equations becomes the *Tangent Modulus*, i.e. the local slope of the stress–strain curve.

Since the slope depends on the strain level (Fig. 4) each strain level (or amplitude) will propagate at its own velocity. Hence the *shape of the pulse* will be continually changing as it propagates into the structure. The location of the measuring transducer therefore becomes important. For elastic conditions, the general pulse *shape* remains the same, only its amplitude is attenuated as it propagates. Its leading edge "smears out" as it propagates, losing its steepness because of internal, intergranular damping. Thus the pulse tends to broaden as it propagates.

In military and some other applications of impact or explosions, an attempt is made to propagate waves faster than their "legal speed limit", which can be quite destructive.

In racing cars it is possible for the surface speed of the tire to exceed the "legal" speed of wave propagation in that material. The material bunches up since it cannot move as fast as the process forces it, and *tire thump* results.

The test specimen in this experiment is not unidimensional (it is too wide for that); it is not two-dimensional (it is not wide enough for that); and it is not three-dimensional (it is not thick enough for that) – it is just a real structure.

One Measurand, therefore, is the wave propagation speed in this actual structure, since it is not directly predictable.

FIG. 4: THE TANGENT MODULUS OF THE STRESS-STRAIN CURVE

$$E = \frac{\Delta(STRESS)}{\Delta(STRAIN)}$$
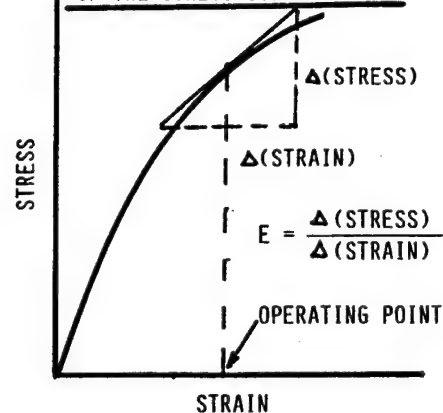
The Momentum Trap: (Continued from page 7 bottom)

In the early 1960s, Don Benthusen of Sandia National Labs Livermore developed a *Momentum Trap*. A small metal plate, about 1 inch square, 1/16" thick aluminum, was bonded around the strain gage to be exposed to a shock wave. The advance stress wave, reflected from this small metal plate causes this plate to spall off, leaving the strain gage intact. When the real shock blast hit the gage, the gage remained in place and gave data. Flyer plate tests confirmed the analytical results. No documentation was ever made.

244

C. EFFECTS AT DISCONTINUITIES

When any wave, mechanical, electrical, fluidic, optical, etc., reaches a discontinuity, reflections and refractions occur. Discontinuities may be of two types:

Geometry, such as changes in section
Material Properties

Reflections and Refractions:

Waves arriving at a discontinuity are partly

Reflected from the discontinuity, and partly
Refracted through the discontinuity, resulting in

Changes in Direction
Changes in Speed
Changes in Amplitude   of the Refracted wave

Material Property Discontinuities:

In this experiment it is assumed that only changes in geometry occur and that the hammer and bar materials have the same properties. The effects of the wooden hammer handle are neglected as are the boundary between the bottom support plate of the beam and the carpeted, tiled or concrete floor on which it rests.

It is assumed that there are not changes in E, ρ, and μ.

Geometric Discontinuities:

There are two geometric discontinuities in this specimen:

AT THE TOP OF THE BAR: During impact while the hammer and bar are in contact, there is an interface across which traveling waves may pass (refraction) and from which they may be reflected depending on the *dynamic mechanical characteristic impedance* match across that boundary. After the end of impact, that boundary becomes a *free boundary* from which only reflections may occur.

AT THE BOTTOM OF THE BAR: The bar is clamped in a frictional clamp which has existed for over 3 decades. It represents a *distributed geometric discontinuity* for which reflection and refraction factors depend on the tightness of the bolts holding the joint together and the surface conditions of the mating materials in the joint. There is absolutely nothing predictable or computable about those conditions.

Another Measurand will be the Reflection Factor for Stresses at the Clamped End.

D. REFLECTION FACTORS FOR THE FORCE (STRESS) WAVES AT DISCONTINUITIES.

There are two extreme boundary conditions possible:

Free End Conditions:

At a free end the structure terminates in air, Fig. 5. The incontrovertible boundary condition which a incoming compression wave pair meets is:

There can be no force or current, and only atmospheric pressure, at a free end.

The world is large, take any displacement, volume, voltage necessary to maintain whatever energy balance is required.

The energy in an incoming compression **wave** pair redistributes itself so that the compression force wave is reflected as a tension force wave of equal amplitude, resulting in zero force at the free end, but also in a *jump displacement*. This is as rapid a displacement as can be produced and which may serve to calibrate displacement, velocity and acceleration transducers for their dynamic characteristics (step displacement response). (See Refs. 20-24 for example).

The **Reflection Factor for Forces / Stresses at a Free End is symbolized by   K = –1**

For incoming compression **pulses** there will be a reflection of the same pulse shape but of opposite sign, i.e., tension. This is known as **stress reversal, pressure reversal, current reversal** and may cause substantial damage.

Stress reversals may cause tension failure or spalling in materials which are weak in tension but very strong in compression. Such materials are called *brittle* and include rock, concrete and glass, but also obsidian, chert and flint from which primitive Man made tools and weapons. Ref. 25 discusses the implications of the principles described here to that archaeological application.

In military applications such as the HEPAT (High Explosive Plastic Anti-Tank) weapon, the object is to cause spalls of many pounds of armor-plate material to ricochet around the inside of the tank. It is also possible to propagate substantial compression waves into a concrete bunker and have the ceiling cave in due to the reflected tension waves to which the concrete offers little resistance, (Fig. 6-A, B, C)

Armor plates are therefore layered so that these reflections are distributed over many events and cannot reach dangerous amplitude; concrete is reinforced, etc.

In the Vietnam conflict, helicopters were equipped with seats coated with a special material which was meant to spall off and protect the pilot's "seat". The pilots, ignorant of the design purpose of the original seat, turned it around because it was more comfortable that way. When the seat was hit by bullets, the spalling now occurred into the pilot's "seat" and since the material is transparent to X-rays, the resulting fragments were almost impossible to locate in flesh.

In the North African Campaign in World War II, Allied tanks were still equipped with riveted armor plate. German shells hitting the tanks would cause the rivet heads inside the tank to ricochet around, wounding and killing the crew.

When an explosion is set off inside a mountain, the rock is literally torn apart by spalling failures as illustrated in Figs. 7 and 8 from the Bureau of Mines. A granite rod, which is strong in compression and weak in tension, when impacted at one end will fail with multiple spalls at the other end (Fig. 9).

For pressure waves, reflections can be quite destructive. Whatever the incoming pressure, only atmospheric pressure may exist at a free (open) end of a pipe. The result of turning a wrong valve in the Oigawa Power Station resulted in the collapse of the pipe due to the negative reflected pressure wave Fig. 10. A doctoral dissertation which investigated whether collapse of human arteries due to such conditions could be a contributing factor to heart attacks found negative evidence (Ref. 8)

In mechanical systems, a single compression impact may result in a sufficient number of reflection cycles of incoming compression pulses and reflected tension pulses, to cause fatigue failure. In specimens subjected only to compression inputs such as pile drivers, jack hammers and machine guns, fatigue failures are common. In general crack *propagation* requires both tension and compression inputs. Crack *initiation*, however, is possible from cyclic compression loading only, due to the shear stresses which are thus generated.

The screws holding the bottom plate to the clamps in the test specimen in this experiment, periodically fail at the neck of the screw: a fatigue failure created by the many tension and compression reflection cycles from that interface.

The Momentum Trap:

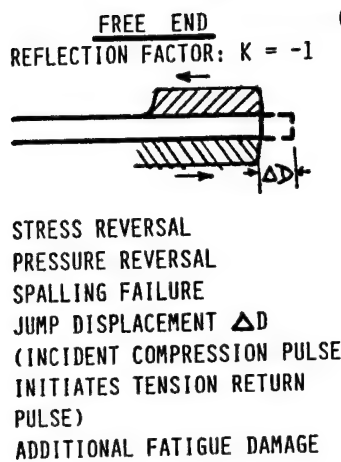## REFLECTION FACTORS FOR STRESSES FOR VARIOUS END CONDITIONS

FREE END
REFLECTION FACTOR: K = -1
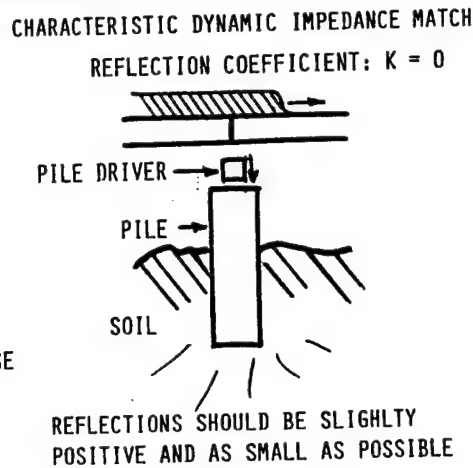
CHARACTERISTIC DYNAMIC IMPEDANCE MATCH
REFLECTION COEFFICIENT: K = 0

FIXED END
REFLECTION FACTOR: K = +1

PILE DRIVER →

PILE →

SOIL

STRESS REVERSAL
PRESSURE REVERSAL
SPALLING FAILURE
JUMP DISPLACEMENT △D
(INCIDENT COMPRESSION PULSE
INITIATES TENSION RETURN
PULSE)
ADDITIONAL FATIGUE DAMAGE

REFLECTIONS SHOULD BE SLIGHLTY
POSITIVE AND AS SMALL AS POSSIBLE

STRESS DOUBLING
CURRENT DOUBLING
PRESSURE DOUBLING
(INCIDENT COMPRESSION
PULSE INITIATES A SUPER-
IMPOSED COMPRESSION
RETURN - DOUBLED - PULSE)

FIGURE 5: FREE END

FIGURE 13: IMPEDANCE MATCHING-
PILE DRIVER
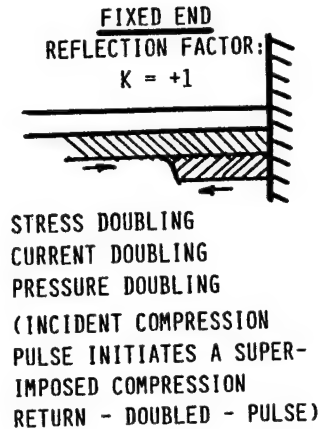
FIGURE 11: FIXED END

Fixed End Conditions:

At a fixed end the structure terminates in a rigid, fixed, immovable member (Fig. 11). The incontrovertible boundary condition which a pair of traveling waves meets at such a fixed end is:

There can be no displacement at a fixed boundary.

The fixed-end boundary condition, however, will accept any force which is offered, in order to maintain energy balance.

The energy in an incoming compression **wave** pair redistributes itself so that the zero-displacement boundary condition is accompanied by a **stress doubling, pressure doubling, current doubling** and a stress / pressure / current wave of the same sign and amplitude as the incoming wave is superposed on the arriving one and reflected back from the fixed end, thus doubling the effect there.

The Reflection Factor for Forces / Stresses at a Fixed End is symbolized by K = +1

It is this pressure doubling which may blow the boiler in your home when a "water hammer" is initiated by a sudden valve closure. It is the pressure doubling at that end of your skull diametrically opposite to where you have been struck, which causes the trauma which may kill you, and it is the pressure doubling at the bottom of a catsup bottle when it is struck at the capped end, which, after many reflection cycles will blow off the cap. That is the reason why catsup bottles are shipped upside down in railroad cars (Ref. 9). It is also the current doubling which may blow the fuse in an electrical system.

Photoelastic studies carried out by Dr. Augustus J. Durelli and his co-workers (Refs. 28-30) are shown in Figs. 15-18. A strut is impacted at one end. Its other end is either free or constrained. Photographs taken at some 13,000 frames/sec illustrate the propagation of the wave into the strut and its reflection (for the free-ended strut) or doubling (for the fixed-ended strut) at the other end. The record for the fixed-ended strut shows incontrovertibly that the fixed end remains in compression for a fnite length of time, until a tension relief wave reaches that boundary.

The other two photos illustrate the propagation of a (spherical) wave through a plate with a hole in it, when subjected to a surface impact. The study was part of several for the Air Force. The impact might have been caused by an atomic bomb and the hole might be the cavity in which people

expect to survive. The strain distribution around the hole can be plotted at any time for any hole shape. Also note the beautiful illustration of the arrival of the wave front at the hole and its reflection from and refraction through that discontinuity.

Characteristic Dynamic Impedance

The Characteristic Impedances of the "impacted" object and of the "impacter" determine the Reflection Factor which exists at the boundary between them. The "impacted" and "impacter" are in quotation marks because they do not strictly apply to electrical systems where it would be more correct to talk about the individual Characteristic Impedances of the Transmission Lines (objects) being "suddenly connected" with a switch.

For mechanical impact, the Reflection Factor, K, is a function of the (A.E) product on each side of the impact interface (boundary), where:

A = effective area at the contact point
E = elastic modulus

The *Effective Area* must be experimentally determined since the hammer and the bar are in contact only over a small portion of each of their actual areas and inertia forces will act to create deflections of the type illustrated in exaggeration in Fig. 12. See also Fig. 1-A.

FIG. 12: EFFECTIVE AREAS

TOP VIEW

SIDE VIEW

FRONT VIEW
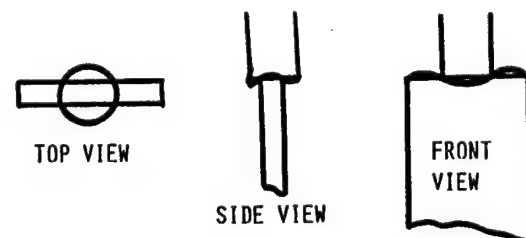
HAMMER-BAR CONTACT AT THE IMPACT INTERFACE
(DEFLECTION PROFILES ARE EXAGGERATED)

Ref. 6

FIGURE 6A   Ref. 3B
FRACTURE BY RELATIVELY GROSS MOTION
IN A BRITTLE MATERIAL

FIGURE 6B
CONCHOIDAL FRACTURE IN CONCRETE DUE TO
IMPACT ON TOP OF THE CONCRETE SLAB
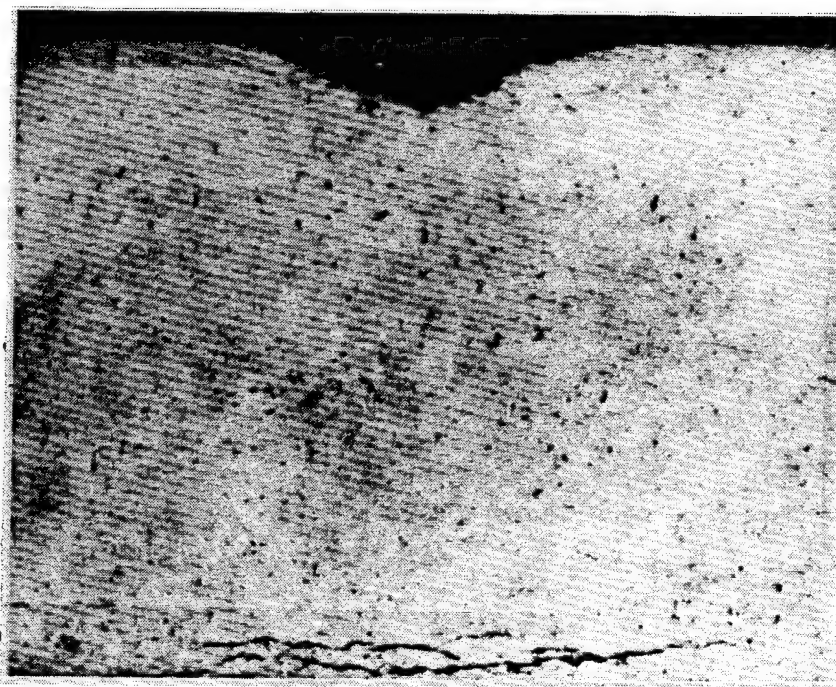
SUB-SURFACE CRACKING IN CONCRETE DUE TO IMPACT FROM
EXPLOSION AT THE TOP.
FIGURE 6 C

Ref. 3A   FIGURE 9

247

Ref. 6
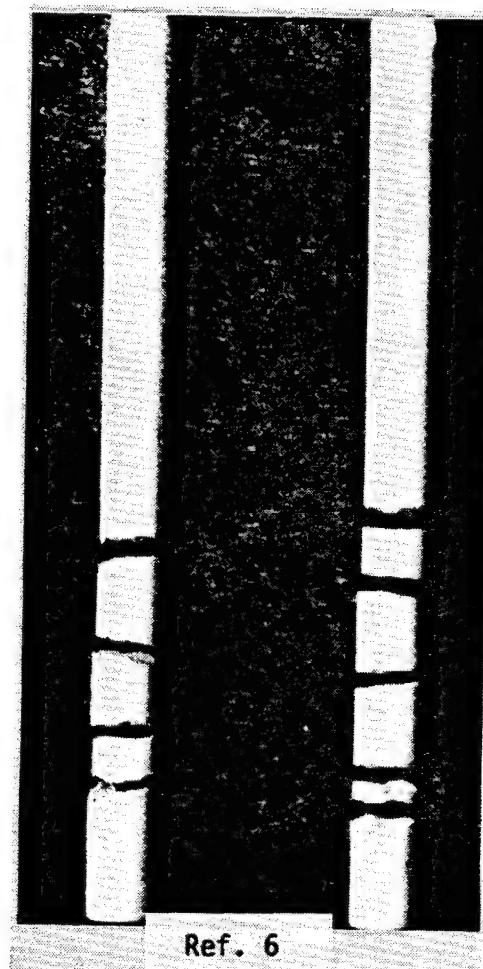
MULTIPLE SPALLING IN A GRANITE ROD
DUE TO A SINGLE IMPACT AT THE TOP

FIG. 8: TENSILE FRACTURE BY REFLECTION OF A COMPRESSIVE STRAIN PULSE
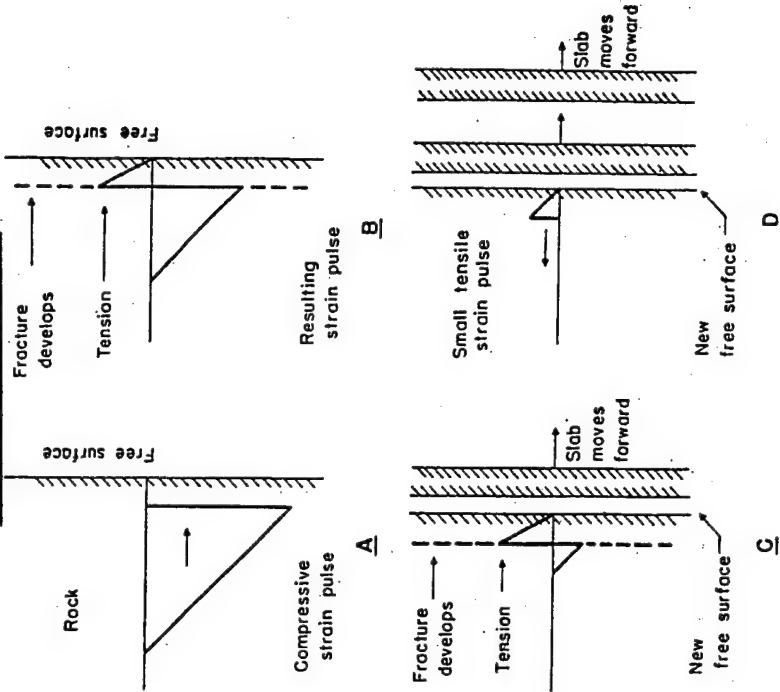
MULTIPLE SPALLS FROM A SINGLE IMPACT.
COMPRESSIVE STRENGTH ASSUMED MUCH HIGHER THAN TENSILE

FIG. 7: REFLECTION OF A TRIANGULAR COMPRESSIVE STRAIN PULSE

Key
—— Resultant pulse
—·— Incident portion of pulse
----- Reflected portion of pulse

From Ref. 4

Fig. 7 illustrates the reflection process for a compressive strain pulse in a medium which is equally strong in tension as in compression. The pulse is simply reflected with a Reflection Coefficient of K = -1, to return as a tension pulse.

Fig. 8 illustrates the reflection process for a compressive strain pulse in a medium which is strong in compression and weak in tension. As soon as the amplitude of the reflected pulse exceeds the tension strength limit, failure occurs and a "spall" flies off. There will be as many spalls as the strength in compression is a multiple of the strength in tension. See also Fig. 7

248
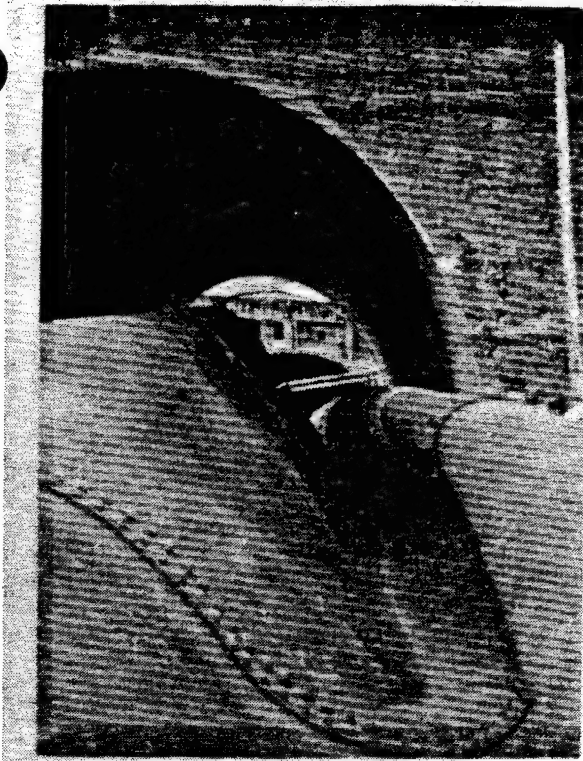
VIEW OF COLLAPSED PENSTOCK AT THE
OIGAWA POWER STATION
<u>FIGURES 10A & 10B</u>
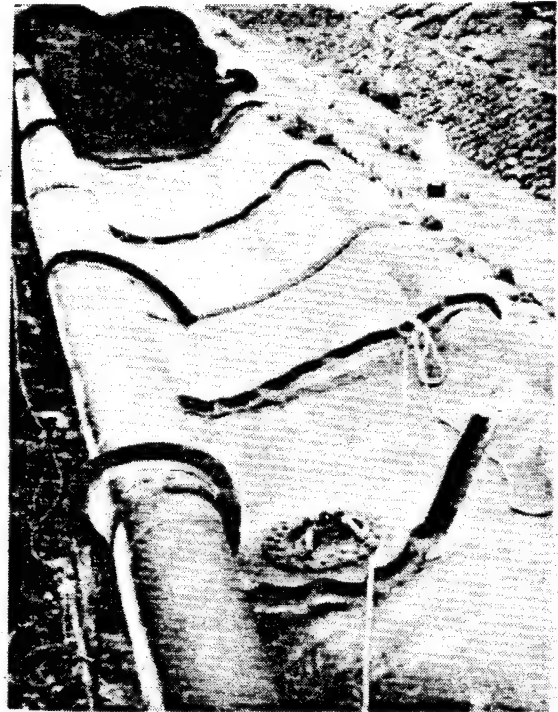
CLOSE-UP VIEW OF SECTION OF COLLAPSED
PENSTOCK CAUSED BY VACUUM UPSTREAM OF
BREAK (Note Manhole and Man on Right)

Ref. 7

<u>FIGURE 14</u>

See text

GEOLOGIST INSPECTS RAILROAD RAIL FIRMLY EMBEDDED IN ROCK WHERE A MINE USED TO BE

FIGURE 16

COMPRESSIVE STRAIN WAVE PROPAGATING IN A HYSOL
STRUT. (Fixed End, Fastax Camera, 13,800 frames/sec)

Refs. 28, 29, 30.

2063 Microseconds After Impact   4180 Microseconds After Impact

ENLARGEMENT OF THE STRAIN PATTERN AROUND THE HOLE AT
2063 and 4180 MICROSECONDS AFTER IMPACT (LEFT & RIGHT)

FIGURE 18

FIGURE 15

DYNAMIC FRINGE PATTERNS ASSOCIATED WITH
THE PROPAGATION OF STRESS WAVE IN A STRUT OF
HYSOL 8705. (Free end, normal incidence)

PHOTOELASTIC FRINGE PATTERN SHOWING A STRESS
PULSE OF RELATIVELY LONG DURATION PROPAGATING
PAST A SQUARE HOLE IN A LARGE PLATE

FIGURE 17

250

MATCHED TRANSMISSION LINES – DYNAMIC MECHANICAL CHARACTERISTIC IMPEDANCE MATCHING: REFLECTION FACTOR FOR FORCES / STRESSES: K = 0. In the student experiment here described, one of the three hammers produces a positive value for K, one produces a negative value, and one is almost Impedance-Matched to the specimen.

Characteristic Impedance matching is of great importance in electrical transmission lines where connectors or other discontinuities may cause reflections / refraction. It is also of great importance in pile drivers where the energy from the driver should be transmitted to the pile which should be driven into the earth without wasted energy bounding around in the structures, (Fig. 13). It is also highly undesirable to have tension waves propagating in the concrete pile since concrete is very weak in tension. Thus the reflection coefficient between the pile and the earth should be as close to zero as possible but always slightly positive.

This problem in real pile drivers and soils was treated in an elegant manner by Fischer (Ref. 10) who solved the non-linear wave equations graphically.

E.   DURATION OF IMPACT

There is a fundamental principle which governs how long two mechanical colliding objects remain in contact:

They will remain in contact until a net tension exists across the impact interface sufficient to separate them.

In fluidic systems the returning pressure wave may open the check valve which initiated the water hammer process through sudden closure. The fluid upstream of that check valve can therefore become contaminated with down-stream fluid – a problem in nuclear power systems. Reflected current waves, however, do not open the switch which cause the original waves through sudden closure. All electrical analogs are no longer functional after this time.

Contact time for mechanical colliding objects is:
  Predictable for colliding rigid objects;
  Predictable for a rigid object colliding with an elastic one;
  Very difficulty to predict for two colliding elastic objects, which is the case in this experiment.

One Measurand, therefore, will be the Contact Time between the hammer and the bar.

F.   POST–IMPACT PHENOMENA

When impact is over and the hammer recedes from the bar, unless, like a military projectile, it was become pressure-welded to the impacted structure, (Ref. 11). Two phenomena now occur:

1.   K = -1 as soon as impact is over.

There is now a step change in Boundary Condition from whatever the reflection Factor at the Interface was during impact, to K = -1, at what is now a free end. Differential equations react to step-changes in boundary conditions and all electrical analogs with other systems, such as mechanical or fluidic, no longer apply.

2.   Residual energy in the structure must be dissipated.

At the end of impact, there will be traveling waves and/or pulses trapped in the structure which must dissipate their energy content through continued reflections / refractions, conversion into heat, sound, etc., until equilibrium is again established and everything has come to rest.

These **Post Impact Vibrations** may be of such a nature as to create not only cumulative fatigue damage but even fatigue failure, even from a single impact, because of the tensile reflections of compressive pulses from free ends. Ref. 12 lists numerous other references to this problem.

The critical variables are:
  Numbers of post-impact vibration cycles
  Amplitudes and amplitude sequences of the stresses
  Wave shapes of the vibrations.

Since the above variables are not subject to predictions or computations, **another Measurand will be the Post–Impact Vibrations.**

9.   Interpretation of the Measurements
10.   Action Based on the Measurements

Suppose, for just a moment, that Steps 1-8 have been completed and that the validated data show:

Maximum Strain: ε		=	1677.2 $\mu\varepsilon$
Rise Time:	$t_{r\text{-}(10\%\text{-}90\%)}$	=	20 μsec

A carefully-controlled test for material properties of the test specimen in the laboratory which took hours to run, has revealed:

Elastic Modulus: E		=	30×10^6 psi
Yield Point:	σ_{yield}	=	30,000 psi

Can you draw the conclusion that the stresses of:

Stress	σ	$= E \cdot \varepsilon$ =	50,316 psi

must have yielded the structure during the test? **NO WAY!**

There is a **Strain Rate Effect** on material properties which is the equivalent of their **Frequency Response** and which can go either way. The table below illustrates some of the factors which are involved.

Ref. 13 presents a survey of strain-rate effects. The general conclusion is that material properties depend on the time scale to which they were determined, and microsecond strain measurements cannot be interpreted with hour-scale material property measurements. **No interpretation or application of the data is possible**. The impact measurements must be supplemented with strain–rate–effect tests on the specimen material.

Thus, even the most carefully planned, executed and validated measurements may have been a waste of time.

Fig. 14 illustrates a geologist contemplating a railroad rail firmly embedded in the geologic formation. The illustration is courtesy of Dr. Carleton B. Moore, Professor of Geology and noted meteorite expert, at Arizona State University. It was taken in the Eastern Pennsylvania anthracite mining region and illustrates that rock, over a time period of generations, is indeed a ductile material and will flow to close the hole which was the entry shaft into a coal mine. During a laboratory test, the geologic material would appear to be brittle. The effect of the time scale of events, which is critical, is beautifully illustrated by this unusual case study.

Failure ⇒ Material ↓	Brittle Behavior	Ductile Behavior	Materials
A	Tested Rapidly	Tested Slowly	Rock, Dams, Concrete, Silly Putty, Copper, etc.
B	Tested Slowly	Tested Rapidly	All explosively formed alloys such as Ti-based

Note: In the first experiment for the semester, you determined the Elastic Modulus of the material of a beam very much like the one in this experiment by static means and in a later experiment you determined it from the modes of vibration of that same beam. In fact, during the first year or two during which this course was offered, all these experiments were performed on the same specimen, so you could easily obtain experimental values for the material properties needed here, but not to the same time scale as the phenomenon here.

DOMAIN USUALLY CONSIDERED THE MEASUREMENT ENGINEER'S

3. Design the Ideal Measurement System

Ideally, the prerequisites for measurement system design are specifications of expected signal amplitude and frequency range or time scale.

PHILOSOPHY

Since these specifications are hardly ever available – and certainly not here – the following set of arguments has been found helpful:

a. *Is there a Maximum Measurand above which the test requester no longer cares because the specimen has failed.*

In the present case, the maximum strain of interest would be the yield point of the bar material. Suppose that the value is 30,000 psi representing a strain of 1000 μstrain for a steel specimen of elastic modulus 30×10^6 psi. Other criteria could be selected. This is only a case study for demonstration purposes.

b. *Take that maximum and design the measurement system such that 10% of the value gives full scale output.*

In this case, 100 $\mu\varepsilon$ should occupy full scale on the readout. This now requires the selection of an Output Transducer. Suppose that the section below has now been read and the Tektronix 502 CRO has been selected with a 10 cm screen calibrated in 2 mm small-scale division. It is now required that 100 μstrain input occupy 10 cm of output. **Note that the overall transfer ratio of the measurement system has just been specified! 1 cm / 10 $\mu\varepsilon$.**

c. *Estimate the resolution of that measurement system and ask the requester if that is sufficient.*

The resolution can be no better than half the smallest scale division on any reputably marked instrument. In this case it is 1% of full scale or 1 μstrain. If the test requester approves of that value as sufficient, this stage of the design has been completed.

It is always possible to decrease System Gain should amplitudes be higher than expected, but unless planned for, System Gain can not usually be increased. This design procedure provides a x10 safety factor should the actual amplitudes be less than anticipated. A Gain Reserve of x10 is available.

4. Select the Real Hardware
5. Evaluate the Inevitable Compromises

APPLICATION:

The design of the Measurement Systems properly starts with the read–out transducer.

Selection of the Read–Out Transducer:

There are several choices for that component:

- Cathode Ray Oscilloscope
- Magnetic Tape Recorder
- Transient Capture Device

Tape recorders and transient capture instruments with the capabilities of recording mechanical impact phenomena are now very common indeed. If they are AC–coupled, the effect of the low–frequency limit on Undershoot must be estimated and the roll-off characteristics at the low-frequency end must be known.

Their advantage is their ability to reproduce the signal to almost any time scale, on command. Signal analysis becomes very simple when it can be re-created in electrical form. This operation is not possible on analog CROs.

In general, the frequency response curves for Magnitude and Phase of the Transfer Ratio should be known to at least 1 or 2 decades above the upper frequency limit and 1 or 2 decades below the lower frequency limit (Ref. 14 which incorporates some of the pertinent text material and reprints available to the students from 1959 to 1977).

SELECTION OF A CATHODE RAY OSCILLOSCOPE: The author's personal convictions, preferences and specifications for a CRO suitable for mechanical testing are cited here:

- Analog CRO. Not enough is yet known, at this stage of the design, about the frequency content or time scale of the phenomenon to be observed that sampling rates can intelligently be selected. **After the data from an analog measurement system have been validated and shown to represent the process, a digital system can be intelligently specified and selected.**

- Two channel CRO. These may be two guns or a single gun time-sharing two channels. There are trade-offs between these choices. The CRO with which the data shown here were acquired was a two-gun CRO; the one the author uses in his Short Courses is a single-gun, time-sharing CRO. For any measurement system, however, a single channel CRO is a toy, a two-channel instrument is a tool since one is always comparing events occurring at one location with those at another one.

SPECIFICATIONS

The Tektronix Type 502 Oscilloscope provides linear dual-beam displays with a wide range of sweep rates combined with high input sensitivity. In addition, the Type 502 may be used to provide dual-beam X-Y displays at medium sensitivities, and single-beam X-Y displays at high sensitivities. Vertical amplifiers for both beams may be operated with single-ended inputs for conventional operation, or with differential inputs for cancellation of common-mode signals. The wide range of operational modes available, make the Type 502 adaptable to a great many industrial and scientific applications.

VERTICAL- DEFLECTION SYSTEM

Characteristics at each input terminal

Direct connection—1 megohm paralleled by 47 μμf. With P6000 probe—10 megohms paralleled by 14 μμf.

Deflection factors

Sixteen calibrated deflection factors from 200 μv/cm to 20 v/cm accurate within 3%.

Frequency response

Frequency response characteristics of the Type 502 vary with settings of the SENSITIVITY controls. Typical readings are as follows:

200 μv/cm	100 kc
5 mv/cm	200 kc
50 mv/cm	400 kc
.2 v/cm	1 mc

Differential input rejection ratio

The rejection ratios specified below apply if the signal voltage at the input connector does not exceed specified limits. The signal limits for dc-coupling are ±2 volts with respect to ground for settings of the SENSITIVITY control from 200 μv/cm to .2 v/cm, ±20 volts with respect to ground for settings from .5 v/cm to 2 v/cm, and ±200 volts with respect to ground for settings from 5 v/cm to 20 v/cm. For ac coupling, the signal limits are 2 volts peak-to-peak from 200 μv/cm to .2 v/cm, 20 volts peak-to-peak from .5 v/cm to 2 v/cm, and 200 volts peak-to-peak from 5 v/cm to 20 v/cm. From 200 μv/cm to 1 mv/cm, the rejection ratio is approximately 1000-to-1, decreasing to 100-to-1 at 0.2 v/cm, and to 25-to-1 in the range from .5 v/cm to 20 v/cm.

HORIZONTAL-DEFLECTION SYSTEM

Sweep rates

Twenty-one calibrated sweep rates from 1 μsec/cm to 5 sec/cm. Accuracy typically within 1% of full scale; in all cases, within 3% of full scale.

Magnifier

Expands sweep 2, 5, 10, or 20 times. Calibration of magnified sweep rates accurate within 3% for sweep speeds which do not exceed the maximum calibrated rate of 1 μsec/cm.

Unblanking

DC coupled.

Triggering signal requirements

Internal—a signal producing 2 mm vertical deflection on either the upper or lower beam.

Horizontal Input

External—0.2 volts to 10 volts of either polarity.

Triggering signal sources

Upper beam, lower beam, external, or line.

Input characteristics at TRIGGER INPUT connector

AC coupled—1 megohm in series with 0.01 μf and paralleled by approximately 33 μμf.

DC coupled—1 megohm shunted by approximately 33 μμf.

With upper beam amplifier connected to crt horizontal deflection plates.

Deflection factors of 200 μv/cm to 20 v/cm in 16 steps.

With external input connected to horizontal amplifier.

Deflection factors of 0.1 v/cm to 2 v/cm in 5 steps.

Input characteristics at EXTERNAL connector

1 megohm shunted by approximately 70 μμf.

OTHER CHARACTERISTICS

Cathode-ray tube

Type T60P2—P1, P7, and P11 phosphors optional. Accelerating potential—3 kv minimum.

Voltage calibrator

Square wave output at approximately 1 kc. Six calibrated voltage steps from 1 mv to 100 volts peak-to-peak. Accuracy—within 3%.

Graticule

Edge lighted—marked in 10 vertical and 10 horizontal 1 cm divisions with 2 mm markings on the baselines.

Power requirements

Line voltage—105 to 125 volts, or 210 to 250 volts, 50-60 cycles. Power—Approximately 300 watts.

Mechanical specifications

Ventilation—filtered, forced-air. Construction—Aluminum-alloy chassis and three-piece cabinet. Dimensions—23½" long, 11¼" wide, 15" high. Weight—52 pounds.

Accessories included

2—Type P6000 attenuator probes
2—Type A510 binding post adapters
1—Green filter
1—Instruction Manual

FIGURE 19 A

SPECIFICATIONS FOR THE TEKTRONIX 502 OSCILLOSCOPE

• Cross-plotting ability between the two channels so that Input–Output plots can be obtained directly where necessary, for example.

• Maximum Transfer Ratio of 1 output division per 200 or, preferably 100 micro-volts. The CRO used here has 200 μvolts/cm "Sensitivity" – at least that is the name on the dial which actually carries numbers in units of inverse Transfer Ratio, i.e., "Attenuation" in units of *mv/div* or Input / Output.

• Outputs available (usually in the back) which are an amplified version of the front inputs. This feature in the U.S. is usually an extra-cost option, but well worth while. It allows the CRO to be used just as a superb amplifier with calibrated Transfer Ratio adjustments and often with built-in filters.

• True differential coupling for each of the two channels, with a common mode voltage limit of at least 10 v-DC or AC and an adequate common mode rejection ratio at even the most sensitive Transfer Ratio setting.

• X–Axis Input availability for possible three-dimensional work.

• Trace-blanking (Z-Axis Input) from a separate input for possible 4-dimensional displays or, as proposed here, for a time-marker.

• Memory capabilities are desired (although not available on the CRO used in this experiment).

In 1959 when the *Laboratory for Measurement Systems Engineering* was founded and first equipped, the Tektronix 502 (later 502A) CROs were ideal "Mechanical Engineers' Oscilloscopes". In the late 1960s this role was taken over by the Hewlett Packard 1201A which has all the features enumerated above and is now used by the author.

Analog CROs with the capabilities listed above are not made any more as separate units. By the time a main frame is supplemented with a plug-in to give these performance parameters, the investment has been inordinately large.

Output Transducer Selection: Tektronix 502 CRO
for which the specification sheet is attached (Fig. 19A)

Since the overall measurement system transfer ratio has already been specified as 1 cm / 10 $\mu\varepsilon$, it is now possible to factor out the CRO Maximum Transfer Ratio to specify the minimum Transfer Ratio required for the Input Transducer:

1cm / 10 $\mu\varepsilon$ divided by 1 cm / 200 μvolt = 20 μvolt / $\mu\varepsilon$

Selection of the Input Transducer:

For mechanical strain measurement under transient dynamic conditions, the bonded electric resistance strain gage is ideal. It is the transducer of choice.

SELECTION OF A STRAIN GAGE: Selection of a strain gage must be based on its total performance in a signal–conditioning circuit in terms of the electrical performance.

General Principles: It can be shown that the Transfer Ratio of a strain gage in its circuit can be expressed by (Ref. 15):

$$\frac{\Delta e}{\Delta \varepsilon} = \text{I. R. K. } \eta \qquad \textbf{in units of } \mu\textbf{volts} / \mu\varepsilon \text{ !!!}$$

where
I	=	Current through the Gage
R	=	Gage Resistance
K	=	Strain Gage Gage Factor
η	=	Efficiency of the Circuit into which the strain gage is incorporated.

As limits, it should be noted that:

$$\eta = \frac{1}{2} \quad \text{for an equal arm bridge}$$

and $\quad \eta \Rightarrow 1 \quad$ under constant current conditions in the strain gage.

Assuming for the moment that constant current conditions will be selected (optimum condition for maximum output and minimum non-linearity), it is then required that:

$$\text{I. R. K} \geq 20 \ \mu\text{volts}/\mu\varepsilon$$

and no pre-amplifier will be necessary for the desired maximum Transfer Ratio of 1 mm output / 1 $\mu\varepsilon$ input!

Current I: Without getting too involved in the self-heating problems of resistive transducers such as strain gages and their current–carrying capacities, it can safely be said that for the size strain gage used on a good heat dissipating specimen such as the one in this experiment, and for dynamic testing where zero–stability is not a significant criterion, **30 milliamps** is not excessive. (See also Ref. 20 for a discussion and solutions to self-heating problems.

Gage Factor, K: Gage factors range from about 2 to 6 for metallic materials and from below -100 to over +100 for semiconductors. Additional criteria might be linearity in the resistance–strain characteristics and self-temperature-compensation for purposes of maintaining the Transfer Ratio constant (which is a direct function of R). Both criteria are best and most economically met by metallic materials such as Constantan or Karma alloys which have K-Factors of around 2. These can also be self-temperature-compensated for most of the specimen materials used in engineering structures. Thus a **K-Factor = 2** is a not unreasonable first choice.

Gage Resistance, R: The problem is now turned around. What R is necessary to meet the objective?

$$R \geq 20 / (30 \text{ milliamps x 2}) = 333 \text{ ohms}$$

The nearest commercially available value is 350 ohms, then 500, 1000, 5000.

When the strut is struck with one of the hammers, it is quite possible to initiate bending vibrations since hand-operated impact is not that easily controllable. If bending strains are to be suppressed, then a pair of strain gages mounted, mirror–image on both sides of the strut near its center will, when series connected, subtract out any bending effects. This statement assumes that the neutral axis of the strut remains in the middle under high-speed transient conditions, a phenomenon which is not an assured certainty.

The use, here, of two non-inductively-series-connected strain gages achieves several other aims:

• It increases the sensitivity to 42 μvolts / $\mu\varepsilon$ so that even if an equal-arm bridge is used as signal conditioning circuit, and half the output is lost, sufficient sensitivity remains to meet the objective.

• It doubles the surface area over which heat is dissipated, ameliorating the self-heating problem.

• When non-inductively connected, the gage arrangement will compensate for such effects as magnetically induced voltages from ambient magnetic fields.

Selection of the Circuit:

There are two major circuits used for resistive transducers:
    Wheatstone Bridges, usually equal-arm
    Constant Current Condition in the transducer
An elaborate discussion of the relative advantages and disadvantages of each is given in Ref. 15.

Selection of Interrogating Input:

The constant current source must now be specified. Since none can be commercially purchased to these specifications so far as the author is aware, it has to be built, which appears a simple job to any technician the author has ever charged with this mission.

DEFINITION OF A CONSTANT CURRENT SOURCE: By definition, a constant current source produces a current (AC or DC) which is independent of the load resistance. What must be specified, amongst other properties, is the resistance level, the degree of regulation, the current level, the frequency / transient response and the permissible noise level in terms of its equivalent signal value

RESISTANCE LEVEL: Resistance up to at least 700 ohms (two 350-ohm gages in series) must not affect the output current by more than one percent, which is half the smallest scale division on the read-out (CRO) as a fraction of full scale.

CURRENT LEVEL: 30 milliamps would suffice for this test. It is noted that the current source used here has only a 25 ma capability.

REGULATION: The maximum resistance change will correspond to a strain of 1000 $\mu\varepsilon$, postulated here as maximum. Since, for a strain gage:

$$\Delta R/R = K. \Delta\varepsilon$$

the resistance change will be: $\Delta R = 700 \times 2 \times 1000 \times 10^{-6}$

$$= 1.4 \text{ ohms}$$

Thus the current should remain at 30 ma within better than 1% for resistance variations of 1.4 ohms around 700 ohms.

The current source regulation can be determined by placing a 1.4 ohm resistor in series with the current source and short–circuiting that resistor with a switch. The output across the strain gage should not change.

NOISE LEVEL: Since the resolution of the measurement system is 1 $\mu\varepsilon$, or 1×10^{-6}, the noise, ripple and hum of the source should sum to less than that equivalent.

The DC output across the strain gage by the current source is:
$$E = I. R$$

The incremental, strain-induced output will be:

$$\Delta e = I. R. K. \Delta\varepsilon$$

The ripple factor: $\dfrac{\Delta e}{E} = K. \Delta\varepsilon = 2 \times 10^{-6}$

Coupled with the frequency response specification, this is the most severe specification on the current source and cannot be met, in the author's experience, with commercially available, AC–powered units. Battery power is required. Almost all electronic technicians can assemble a unit to fit the specifications, in short order. The only commercial unit, built to these specifications, did not exhibit economic survival capabilities. (Ref. 15).

FREQUENCY RESPONSE: The current must remain constant for high-frequency or high-speed transient resistance variations. The current source rise–time is included in the rise–time of the shunt calibration step or pulse train so that the rise–time validation procedures (Ref. 14) would include it.

If the switch used in checking current source Regulation (above) has a rise time close to that of the phenomenon to be observed, then any transient response across the strain gage is evidence of insufficient current source transient response.

Selection of the Circuit:

A detailed discussion of the features of Wheatstone bridges and of Constant Current Circuits is given in Ref. 15 and will be summarized in answer to one of the examination questions. The circuit selected for this experiment is the Constant Current Circuit which has many advantages for this type of test.

The circuit, as shown in Fig. 2, is the Kelvin–Thompson, Four Terminal Resistance connection which is immune to contact resistances or lead wire resistance. Note that the connections are *from the current source to the strain gages and from the strain gages to the CRO*. That arrangement is quite different and infinitely superior than going from the current source to the strain gages and from the current source to the CRO. The author will not even illustrate that arrangement lest someone use it. The verbal description of that undesirable circuit will suffice.

The design of the measurement system is now complete in terms of component and circuit selection: only a strain gage in a constant current circuit, and a CRO are required.

Selection of Triggering:

Triggering a cathode ray oscilloscope implies providing a stimulus so that the CRO beam begins its traverse at a specific instant. The purpose of a trigger in this experiment is to view the initial impact–created pulse as it passes the strain gage location and also, to a different time scale, to view the initial pulse and the post-impact reflections.

TRIGGER DELAY TIME: There is a time delay between the arrival of the trigger pulse at the CRO terminals and the start of the sweep. This *Trigger Delay Time* is not given for the model CRO used here but is about 50 μsec as determined from separate tests.

TRIGGERING BEFORE THE EVENT: Triggering can be made to occur before actual impact by having the incident projectile interrupt a field of some sort and cause the creation of a transient voltage which can be applied to the trigger input terminals of the CRO.

Such fields might be:

Capacitive: the passage of the projectile through an electric field as sensed by a capacitor.-

Magnetic: The passage of the projectile through a magnetic field as sensed by an inductor or by a monopole transducer.

Inductive: The projectile distorts an inductive circuit to produce a voltage response

Optical: The interruption of an optical field as sensed by a photovoltaic or photoresistive transducer.

Mechanical: The breaking of a screen or wires which cause a voltage transient to occur.

TRIGGERING AFTER THE EVENT: Triggering may occur after the impact, explosion, etc., by having a second measurement system which catches the mechanical, acoustic, optical, fluidic, etc., wave initiated by the event. Thus a strain gage or accelerometer or pressure transducer (piezoresistive or piezoelectric) can be mounted on the structure to react to the passage of the wave at one point on the structure and to trigger the measurement system so that it reacts to the wave when it reaches another point on the system.

A microphone can be used for the same purpose with the additional advantage that the delay time is variable by its location.

TRIGGERING WITH THE EVENT: In this experiment the impact itself will trigger the CRO with the additional advantage that contact time can be measured. A 6v battery is connected between the hammer and to the CRO *Trigger Input Terminal.* When the hammer strikes the strut, the CRO is triggered by the voltage step; when impact ceases and the hammer recedes from the strut, the negative voltage signal can either be recorded on a separate channel or made to blank the CRO trace intensity to mark the end of impact. See Figs. 20, 20A.

It takes the wave 23 inches of travel (115 μsec approximately) to reach the strain gage. It is also desired to have a few centimeters of horizontal record before the wave arrives at the gage as last–minute noise documentation. The horizontal time axis will be set at 20 μsec/div to view the initial pulse (see *Time Scale of Events* Section below) and the trigger delay time is about 50 μsec which leaves about 65 μsec of pre–wave–arrival of noise-documentation record with enough time left to show the incident pulse.

This set of conditions is peculiar to this test and is a very convenient feature since the trigger can be simple and combined with the contact time measurement scheme.

FIG. 20: TRIGGERING - TRIGGER DELAY TIME - CONTACT TIME

TRIGGER DELAY TIME

END OF IMPACT - -6V STEP

TRIGGGER CIRCUIT TIME-CONSTANT

CONTACT TIME

HAMMER-BAR CONTACT 6-VOLT STEP
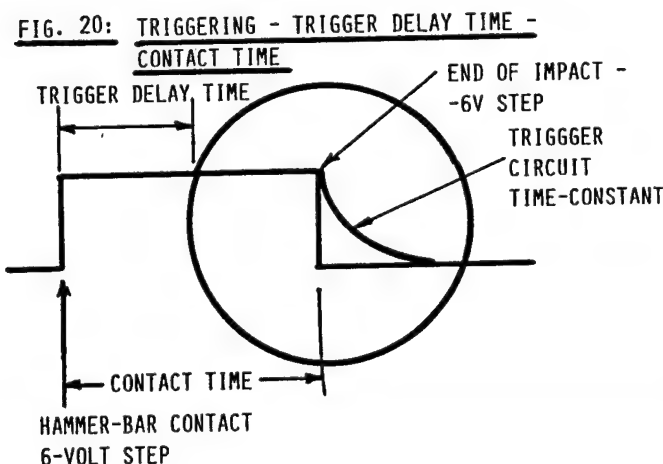
Fig. 20 A from Ref. 1 (1961)

END OF IMPACT
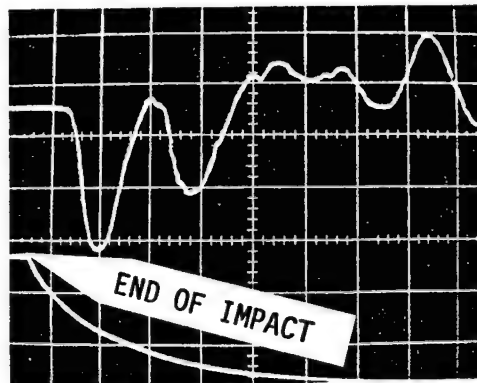
PHOTOGRAPH # 21

X = 50 μsec/cm

6. Set Up the Test and Document Environment–Response Interactions

TIME SCALE OF EVENTS

An estimate of the time scale of events (Fig. 22) can be constructed for the first half millisecond or so, so that an appropriate time scale setting is possible on the CRO, Figs. 3 & 21.

At the instant of impact, compression waves propagate both into the impacting projectile (hammer) and into the impacted structure (strut). These propagate at about 200,000 inches/sec or 5 μsec/inch. (Fig. 3, #1)

The small hammer is 2-1/2 inches long so that after 12-1/2 μsec the incident compression wave is returned as a tension wave and arrives 25 μsec after impact as a tension relief wave at the impacted end of the strut. There are now a pair of traveling waves in the strut 25 μsec apart, the leading wave in compression and the follow-up wave in tension. (Fig. 3, #2, #3, #4)

This could be treated as a 25 μsec wide pulse propagating down the strut, spreading out and with its leading edge smoothed by integranular damping, as it propagates. (Fig. 3, #5)

Since the gage location is about 23 inches from the impacted end, that pulse arrives at the gage location 115 μsec after impact (Fig. 21, #6) and has passed the location at 140 μsec. (Fig. 21, #7).

The leading edge of the pulse reaches the clamped end of the strut 155 μsec after impact (Fig. 21, #8) and its reflected portion travels through the gage towards the free end after 195 μsec (Fig. 21, #10). Since the clamped end is more fixed than free, the reflected pulse will be a compressive one. After 220 μsec the entire reflected pulse has returned through the gage. (Fig. 21, #10).

The amplitude of the reflected pulse divided by the amplitude of the incident pulse is the Reflection Coefficient for Forces at the clamped end, neglecting the amplitude loss through intergranular damping during the 16 inch round trip from gage to clamped end and back.

The reflected compression pulse now travels from the gage back to the free end where it is reversed into a tension pulse since impact has long since been over and the impacted end is now a free end. (Fig. 21, #11, #12). That tension pulse returns through the gage after traveling through 46 inches of strut material, some 230 μsec after it left the gage as a compression pulse, or 425 μsec after impact. (Fig. 21, #13, #14, #15).

256

FIG. 21: PHENOMENOLOGICAL STUDY OF EVENTS AT THE GAGE LOCATION

BASE — BAR — HAMMER 6
115 MICRO-SECONDS AFTER IMPACT, FIRST COMPRESSION WAVE ARRIVES

BASE — 7
140 MICRO-SECONDS AFTER IMPACT, PULSE LEAVES; STRAIN RETURNS TO 0

BASE — 8
155 MICRO-SECONDS AFTER IMPACT, WAVE ARRIVES AT BASE CLAMP

BASE — 9
ABOUT 170 MICO-SECONDS AFTER IMPACT, REFLECTED PULSE BEGINS RETURN

BASE — 10
195 MICRO-SECONDS AFTER IMPACT, REFLECTED PULSE REACHED GAGE
220 MICRO-SECONDS AFTER IMACT REFLECTED PULSE HAS PASSED GAGE

BASE — GAGE LOCATION — BAR — HAMMER 11
310 MICRO-SECONDS AFTER IMPACT, REFLECTED WAVE REACHES FREE END

BASE — 12
COMPRESSION WAVE ARRIVING AT FREE END IS REFLECTED AS TENSION WAVE

BASE — 13
230 MICRO-SECONDS AFTER ITS INITIAL ARRIVAL AS A COMPRESSION WAVE,
THE REFLECTED TENSION WAVE RETURNS TO THE GAGE LOCATION

BASE — 14
450 MICRO-SECONDS AFTER IMPACT, REFLECTED WAVE LEAVES GAGE LOCATION

BASE — 15
REFLECTED TENSION WAVE REACHES CLAMP TO BE REFLECTED BACK AS TENSION

257

The time between the reflected compression pulse and the returning tension pulse, represents 46 inches of travel. The speed of wave propagation can be deduced from that on the actual record. The time between the arrival of the first compression pulse and the one reflected from the clamped end represents about 16 inches of travel, so a second estimate of wave speed, perhaps with less resolution, can be obtained.

After a total of 500 μsec elapsed time after impact the main data have been gathered so that a time scale setting on the CRO of 50 μsec/div would seem appropriate. The photographs at 100 μsec/div show more of the post-impact reflections (Fig. 22)

To catch the first pulse, 28 inches of travel must be accommodated on the CRO, or 140 μsec so that a setting of 20 μsec/div would be an appropriate time scale. This also allows for a few centimeters of "zero" displayed on the CRO before the pulse arrives at the gage location. That is a close to a "last-ditch" Noise Check as one can come. The trigger-delay-time of the CRO is not included in the specifications. It appears to be some 50 μsec from experimental observations but for a conservative design was not factored into the predictions. Note that the spreading out of the pulse, its increase in width during propagation, is also not factored into the above predictions, a non-conservative procedure.

From the photographs presented later, the above predictions are verified.

It is emphasized that at least some effort was made to select a suitable time scale on the CRO. It is not a matter of trial and error.

THE PREAMPLIFIER

To simulate the condition of a less sensitive CRO, a second channel taken from the same strain gage circuit, is passed through a Tektronix Type 123 Preamplifier is also shown on the photographs. The amplifier gain is 100 and the CRO gain is set at 1/100 of that for the first channel.

The amplifier specification sheet is shown in Fig. 19B. It will beseen that the system frequency response and transient response capabilities are now governed by that preamplifier.

Such a situation is common if the system design starts with the selection of an input transducer (the strain gage here), and then proceeds forward. The system design process described here, started with the read-out transducer and resulted in the specification for a strain gage and its circuit to fulfill the overall requirements without the need for a preamplifier.

ENVIRONMENT-RESPONSE "NOISE" DOCUMENTATION

A comprehensive treatment of *"Noise" Diagnostics* and *Noise Suppression* is given in Ref. 27, pages 45-91 and in the references cited for that section. *"Noise"* is defined as undesired environment-response combinations. The basic assumption is that *all components (transducers) in a measurement system respond in all ways in which they can to all factors in the environment, every time (repeatedly and consistently)*, although not necessarily predictably. Thirty two environment-response combinations were identified as possible of which only 16 were of interest to the Measurement Engineer. Of those 16, one, only, was *Signal*. All 15 others are various types of *"Noise Levels"*, which need to be diagnosed and suppressed.

Of those 15, three were usually dominant, critical and important and must be documented on every test. It is those three which will be very briefly reviewed; but this review is not a substitute for the reference cited above. The 15 Environment-Response Combinations or Paths were numbered. For transducers for which the resistive, non-self-generating response is the desired response, as is the case here, Paths 1, 2 and 3 are noise levels. Path 4 is the signal.

The material in the above-referenced section as well as in the entire reference was covered in lectures during the first Junior-Level course in The Engineering of Measurement Systems and illustrated during the Experiments which accompanied the lecture material. See also Ref. 5 and the references cited there.
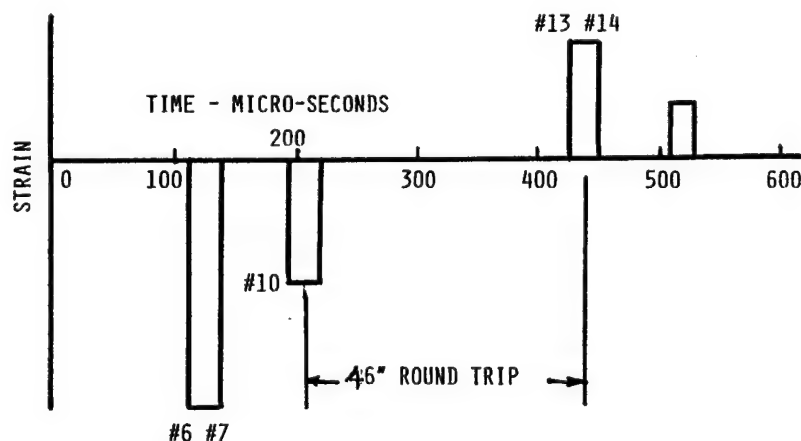
FIG. 22: APPROXIMATE ESTIMATE OF WAVE SHAPE AT GAGE LOCATION (WAVE SHAPE WILL BE ROUNDED OFF)

Type 123 PREAMPLIFIER

Compact

4 1/4 " high, 1 1/2 " wide, 3 7/8 " deep.

Weighs only 10 ounces.

Voltage Gain

Accurately set at 100.

Passband

Within 3-db from 3 cps to 25 kc.

Maximum Input Signal

0.1 v peak-to-peak.

Hum-Free Low-Level Amplification

Powered by miniature batteries.
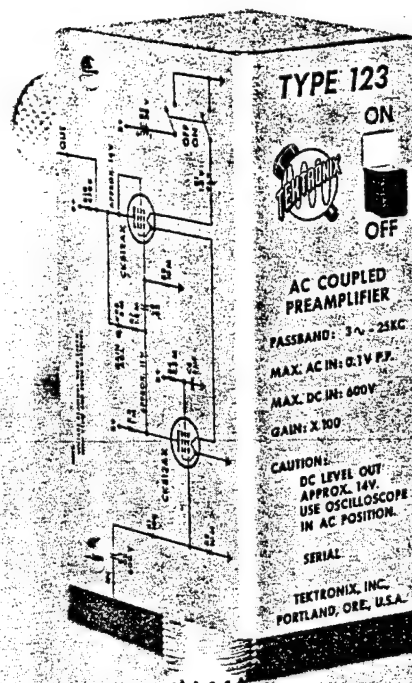
FIGURE 19 B: SPECIFICATIONS FOR THE TEKTRONIX 123 PREAMPLIFIER

The Tektronix Type 123 Preamplifier is a compact, light-weight, battery-operated amplifier for use in applications where a gain of 100 without hum is desired. Passband is within 3-db from 3 cps to 25 kc. Where reduced high-frequency response is permissible, ground-loop hum pickup can be virtually eliminated by mounting the Type 123 close to the circuit under observation. Coaxial connectors permit the Type 123 to be connected directly to an oscilloscope or other instrument or even for use as a probe. Shock-mounted chassis reduces the effects of microphonics, shift, and drift.

Applications of the Type 123 are confined to the audio range; for example, observing hum levels, transducer preamplifier, and other low-level applications where a gain of 100 is desired.

CHARACTERISTICS

Voltage Gain—Gain is 100, adjustable with screwdriver calibration control.

Passband—Within 3-db from 3 cps to 25 kc.

Battery Powered—A small mercury cell supplies the filament voltage and a miniature 30 v battery is the

source of plate voltage. Life of the mercury cell is approximately 100 hours. Plate-voltage battery life is about the same as shelf life, typically 1000 hours.

Noise Level—The maximum noise level, referred to the input, with the input grounded is less than 7.5 μv, rms; 50 μv, peak-to-peak.

Output Signal Level—DC level of output is approximately +15 v.

Maximum Input Signal—Maximum input signal for linear amplification is 0.1 v, peak-to-peak.

Input Impedance—10 megohms.

Effective Output Impedance—31 kilohms.

Power Requirement—One 1.345 v mercury cell and one 30 v miniature battery, included with the instrument.

Mechanical Specifications—Dimensions are 4 1/4 " high by 1 1/2 " wide by 3 7/8 " deep. Net weight is 10 ounces. Shipping weight is 2 pounds, approx.

TYPE 123 PREAMPLIFIER $75
Each instrument includes: 1—schematic

U.S. Sales Price f.o.b. Beaverton, Oregon
Please refer to Terms and Shipment, General Information page.

FIG 23: NOISE LEVEL DOCUMENTATION (modified from Ref. 27)

WHEN THE ADDITIVE, TEMPORARY NON-SELF-GENERATING RESPONSE IS DESIRED

PATH	DESIRED ENVIRON-MENT	INTERRO-GATING INPUT	STIMULATING ENVIRONMENT	RESPONSE OBTAINED	INDICATED ACTION (*)	PHOTOS IN FIG. 24 & 25
1	OFF	OFF	Undesired	Undesired		1
2	OFF	ON	Undesired	Desired		2
			Interrogating Input	Undesired		
3	ON	OFF	Desired	Undesired		3, 4, 10
4	ON	ON	**VALID**	**NOISE-FREE**	**DATA**	6, 7, 8, 9

(*) As determined from the Noise Suppression methods applicable to the problem (Section 6.4) in Ref. 27

ES-361 MEASUREMENT SYSTEMS ENGINEERING   IMPACT TEST   EXP'T. NO. 8
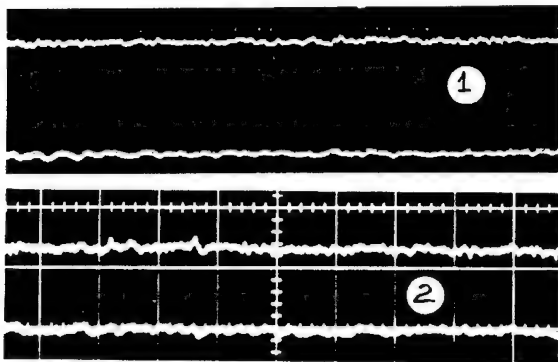
1970
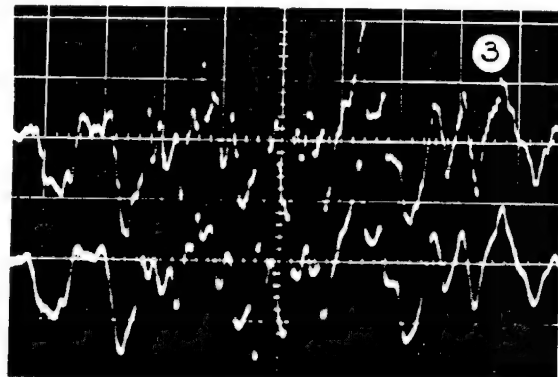
NOISE LEVEL AND CALIBRATION CHECKS

PHOTO	CURRENT SOURCE	IMPACT
1	Off	none
2	25 ma	none
3	off	2-oz hammer
4	off	8-oz hammer
5	25 ma $Y_1 = 20$ mv/cm	Shunt Cal. 120,000 ohms 1000 Hz

CRO SETTINGS

Y_1 200 uv/cm
Y_2 20 mv/cm
X   0.1 msec/cm
AC-coupled
Single ended
External trigger
Single sweep
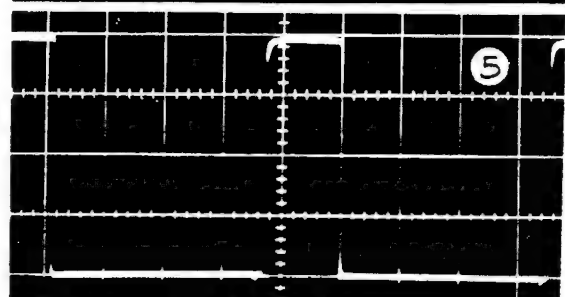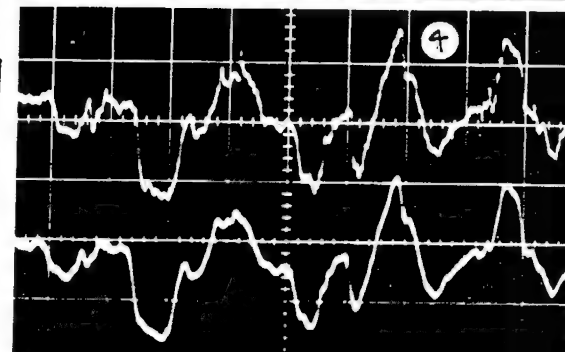
Contact-triggered with 6v battery. Shielding & grounding in place.

Tektronix 502 (modified) CRO # 5096
Tektronix 123 preamplifier   # 995   # 124
Industrial Electronetics S-200 Strain Simulator
ASU-built constant current source
BLH Strain Gages FAP-50-35 Lot. No. 4, two units
   350 ohms ± 2.5 ohms, K = 2.20 ± 1%, L = 1/2"
Gage Location: 23 inches from the struck end,
              8.2 inches from the clamped end.

FIG. 26: CASE STUDY FROM AN IMPACT TEST USING BONDED RESISTANCE STRAIN GAGES
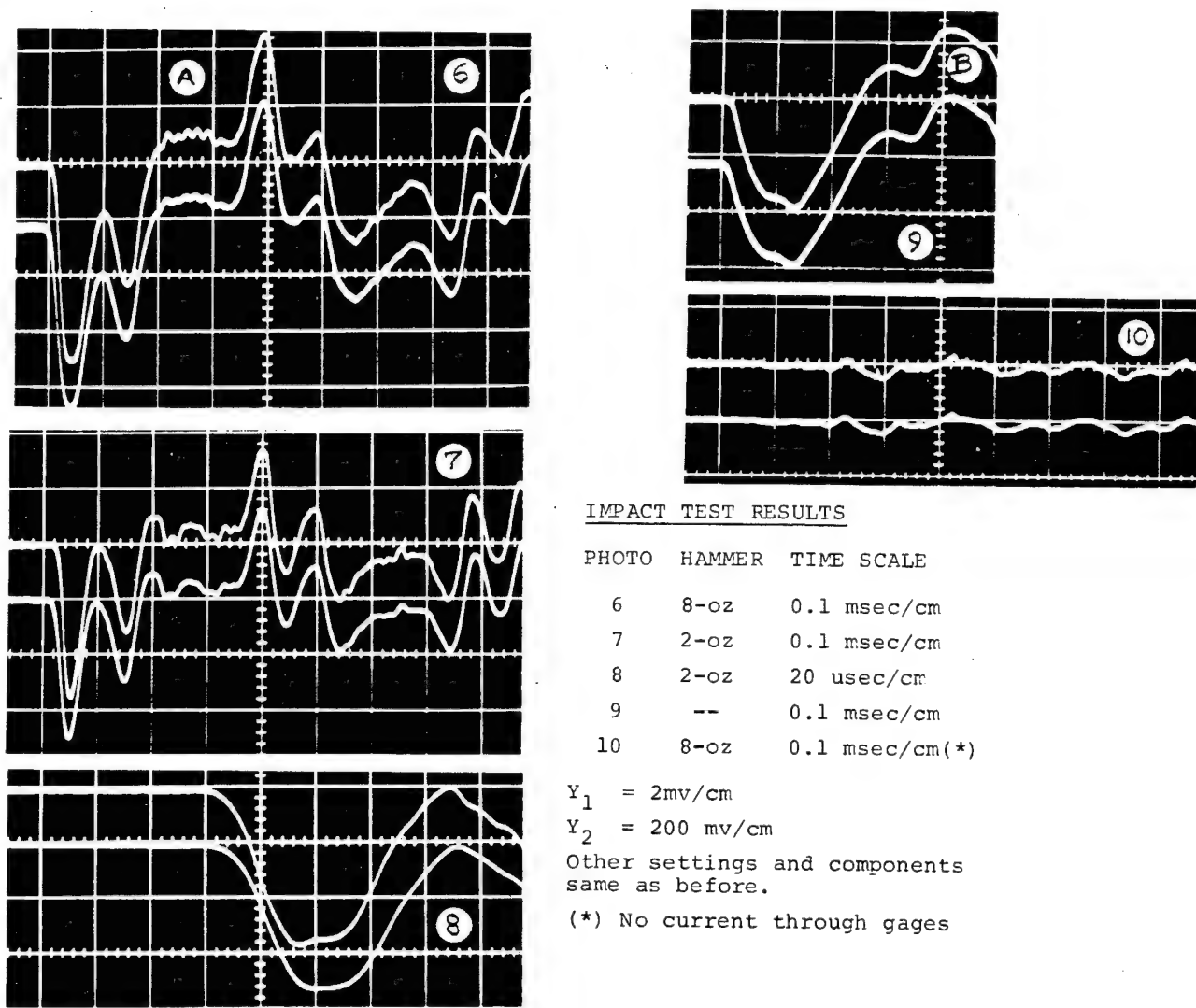
IMPACT TEST RESULTS

PHOTO	HAMMER	TIME SCALE
6	8-oz	0.1 msec/cm
7	2-oz	0.1 msec/cm
8	2-oz	20 usec/cm
9	--	0.1 msec/cm
10	8-oz	0.1 msec/cm(*)

Y_1 = 2mv/cm
Y_2 = 200 mv/cm
Other settings and components
same as before.

(*) No current through gages

MEASUREMENT SYSTEM

Constant current circuit, four-terminal strain gage arrangement with inductively canceling gage connection, see Fig. 2.

Two-conductor shielded cables from the current source to the gages and from the gages to the CRO.

Specimen, current source chassis, cable shields all connected to CRO ground.

For each photo except #5: (See Fig. 2)

TOP TRACE: from the strain gages directly to the CRO

BOTTOM TRACE: from the gages through the Tektronix 123 Pre-Amplifier to the CRO

Measurement Systems Engineering Laboratory, Arizona State University, May 1970, Michael Nettles & Peter Stein.

IMPACT–STRAIN–INDUCED VOLTAGES: PHOTO 10

These have been reduced by the way the system has been designed, but are still visible. A higher current or higher gage resistance would reduce them further, but compare to Photos 3, 4, and 5.

THE *UNDERSHOOT* NEGATIVE STRAIN SIGNAL
PHOTO 9 – AREA "B"

The top trace can be validated by the methods presented in Ref. 14, p. 6. The numerical example at the bottom of p[age 6 applies. Pulse with is 0.25 msec, hence the negative strain is from a reflected stress wave. The bottom trace can not be validated since the amplifier characteristics needed to make the determination are not provided by the manufacturer.

RISE TIME OF THE STRAIN PULSE IN PHOTO 8

The top trace can be validated to be the strain-wave rise-time not distorted by more than 2%. The bottom trace can be shown to be invalid and dominated by the amplifier rise-time. (From Refs. 8 and 29)..

Fig. 23 identifies the *Noise Documentation* procedure which involves turning the two inputs to the transducer on and off in a prescribed sequence. It is always possible to turn off the Interrogating Input (Bridge Supply, Current Source, etc.) although the author knows of only 13 manufacturers of signal conditioning which permit this operation, see Ref. 14. When the Measurand Input can not be conveniently turned on and off, parallel check channels must be used, see Refs. 14, 27.

In Fig. 23: *Noise Level Documentation*:

Desired Environment = Strain = Impact with a Hammer
Interrogating Input = Current Source
Desired Response = Resistance Change in the Strain Gage
Undesired Responses = Voltage Generation elicited by any
  mechanism; any outputs stimulated by Resistance
  Changes in Lead Wires or Connections or by
  Capacitance or Inductance Changes anywhere.
Undesired Environments = thermal, magnetic, electric, etc

Photos 1-4 illustrate the results of the Noise Documentation Process. It is seen that Path 3 as indicated by Photos 3 and 4, for two of the hammers, is the dominant noise level: the self-generating voltage response of materials due to transient strain excitation – a mechanism not yet understood or theoretically predictable. Although the phenomenon is not predictable or explainable yet, its effect can be suppressed by proper design of the measurement system, and successful suppression can be documented. That, indeed, is the mission of the Measurement Engineer.

Suppression to half the smallest scale division on the read-out is usually considered sufficient. Photo 10 shows that this goal was not quite achieved for this test.

CALIBRATION:

Calibration by resistance injection often called *Shunt Calibration,* is shown in Photo 5. The principles are described in Ref. 27 which also contains the discussion on Peak-to-Peak Reproduction of a pulse train which will be needed to answer one of the questions. Note that the vertical scale for Photo 5 is different from the vertical scale of Photos 1-4 which in turn are different from the scale of Photos 6-9.

QUESTIONS

QUESTION NO. 1: For each of the two separate channels, (top and bottom trace):

A. What is the 10% - 90% rise-time of each component of each channel?

B. What is the 10% - 90% rise-time of each channel?

You may assume that the current source and the cables have negligible rise-times, unless you are a graduate student and wish to discuss these.

You may assume that the components are effectively isolated from each other, unless you are a graduate student and wish to discuss the interaction effects. (See also Questions 6 and 7).

Please re-read the instructions in the Test Description about assumptions, etc.

QUESTION NO. 2:

What are the 10% - 90% Rise-Times of the two traces observed in Photo 8.

QUESTION NO. 3:

Are the Rise Times of the traces in Photo 8 valid? Are the rising portions of the top and bottom traces those of the strain wave or does the measurement system affect the rise time?

QUESTION NO. 4:

What is the frequency response (including upper and lower 3 dB or half-power points) of each component of each of the two channels? Sketch these on logarithmic axes, to scale as much as possible.

Where there are unknown break-points or asymptotic slopes, indicate them with letters such as m, n, p, q, etc., and whether plus or minus.

Where a previously unknown component characteristic was determined earlier in the course, specify this and identify it.

Identify each -3 dB point or asymptotic slope. If slopes are unknown, dot them in.

QUESTION NO. 5

Sketch the frequency response curve for each of the two total measurement *systems* (or channels). Identify each break-point or roll-off slope with the component which creates or governs it. Use dotted lines for unknown slopes. Make a scale plot.

QUESTION NO. 6

What are the input and / or output impedances of the various system components and how do they vary with frequency?

Give the Manufacturers' Specifications, and from them, where possible, construct the frequency response curves for the input and / or output characteristics of each component in each of the two channels.

QUESTION NO. 7:

What are the expected interaction effects (Isolation Ratios) between components in each of the two channels?

At what frequencies are these likely to become important?

What information would you need to know to answer this question properly?

What procedure would you use to circumvent your ignorance of those critical specifications and make a valid measurement possible.

QUESTION NO. 8:

Area B in Photo 9 represents an area of opposite sign to the incident compression pulse.

Is this really a tension pulse (if compression is positive downwards) or has the measurement system altered the data and produced an undershoot?

Be very careful here with your complete analysis and assumptions.

QUESTION NO. 9:

Given your answer to No. 5, what general order of magnitude of amplitude distortion of the pulse height might be expected due to the frequency-response characteristics of the measurement system?

QUESTION NO. 10:

From Photo 5, compute the calibration in terms of *strain per deflection on the CRO* for Photo 5. Note that the Y-sensitivity setting on the CRO is different from those on other photos.

What is the calibration for all the other photos for the *top traces only* (the bottom trace is not represented in Photo 5!) given the Y-scales for those other displays.

What assumption is necessary in transferring the calibration information obtained from Photo 5 to the other photos, and how might the necessity for that assumption have been eliminated during calibration?

QUESTION NO. 11:

What is the maximum compression and the maximum tension strain shown for the top trace in Photo 6?

QUESTION NO. 12:

Given an elastic modulus of 30,000,000 psi and a yield point of 30,000 psi for the specimen material, as determined from a static tension test conducted in a laboratory under carefully controlled conditions, comment on the *stress* levels in the specimen under the *strain* conditions found in answer to Question No. 11.

QUESTION NO. 13:

For the shunt calibration data in Photo No. 5, why is a 1000 Hz pulse used rather than say, 60 Hz? What would be the minimum acceptable and maximum acceptable square wave repetition rates for this system, and why?

QUESTION NO. 14:

In Photo 6, Region A contains the highest frequencies in the records. How does this frequency compare with the frequency response limits of the two measurement systems used here, as found in answer to Question 5? Comment.

QUESTION NO. 15:

What noise level documentation would you suggest for this test? Identify the procedure desired. Do any of the photos represent such a documentation process? Which important environment-response path is *not* documented here, nor can it really be? Explain.

QUESTION NO. 16:

The one environment-response path *not* documented here: what physical phenomenon does it represent? Is it likely to occur in this test? If so, how might one guard against it? What recently developed experimental stress analysis method utilizes this effect for measurement purposes – *here* it is a noise level. (This last sentence has been added in this paper and was not included in the original examination because, at that time, the method had not yet been commercialized, although the effect was discussed during lectures).

QUESTION NO. 17:

With the small (2 oz) hammer, what is the highest noise level condition in this test? i.e. under what noise-check conditions does the highest noise level occur, and what is it in terms of absolute output (such as millivolts).

QUESTION NO. 18:

Is this highest noise level significant in proportion to signal?

QUESTION NO. 19:

In preparing the system for final testing, the following methods of noise suppression were used:

A. Mutual Compensation – Cancel by Subtraction
B. Minimize by Division

    i. Overall decrease of an environmental stimulus: *Isolate*.
    ii. Selective decrease of an environmental stimulus: *Filter*.
    iii. Reduction of the response to the environment: *Self-compensate*.
    iv. Reduction of the interrogating of an undesired non-self-generating response: *Sideways Promotion*.
    v. Location of an undesired activated response where it does not affect system output: *Jail*

Identify how each of these methods was used in this experiment; some more than once.

QUESTION NO. 20:

What other major noise suppression method exists, which was *not* used in this experiment?

QUESTION NO. 21:

Would this method apply in *principle*? What conditions would be required for using this method on this test? Why was it not used?

Specify such a system on paper and then comment on its realizability with today's technology and cite a case study using it which was presented during the Semester.

QUESTION NO. 22:

Given your answer to Question 18, and the "facts of life" of Nos. 19-21, how might the effects of the noise level in Nos. 17 and 18 be minimized with respect to the signal?

QUESTION NO. 23:

What is the reflection factor for stresses from the clamped end of the strut? Use the top trace in Photo 7 for this computation. What assumption is made in this computation?

QUESTION NO. 24:

What is the speed of propagation of the strain pulse? Use the top trace of Photo 7 for this computation. Is there another Photo which can be used?

QUESTION NO. 25:

Using the attached 4-page brochure describing the Master's Thesis conducted by Major Frederick F. Mayer, U.S. Army Infantry (now Lt. Col. Retired) in 1968-69, discuss the concepts of:

- Post-impact vibrations
- Dynamic strain-concentration factors

QUESTION NO. 26:

Why, for bonded resistance strain gages as mounted on this specimen, can you **not** use the relationship:

$[f_{2\,3\,dB}) \times (t_{r\,10\%-90\%})] \Rightarrow 0.35$ in the limit

or [upper frequency limit in Hz] time [10% - 90% rise-time in seconds] tends towards 0.35 in the limit. What limit?

Can you cite other transducers and test conditions where the same limitation applies?

QUESTION NO. 27:

Discuss the triggering mechanism used for this test and how it might be modified if triggering were necessary either before the instant of impact, or after it.

QUESTION NO. 28:

What unstated property of the CRO used in this test, will govern the instant of time at which a trigger signal must be initiated so that the initial pulse from the impact will be displayed on the CRO screen? How might that property be determined from records showing contact time and the strain pulse?

QUESTION NO. 29:

What simple method can be used to show the end of contact between the hammer and the bar? Is contact-time in this test predictable?

QUESTION NO. 30:

In this experiment, a direct photo was made from the CRO screen during the actual impact. Many times it is preferable to obtain a record which can be replayed over and over again for analysis, such as for frequency content or amplitude distributions, etc.

Discuss the applicability and limitations of other recording methods such as:

- Magnetic tape recorders
- Analog-to-digital converters and storage devices which will replay the signal in digital-analog reconverted form upon command such as the unit shown during the demonstration.
- CROs with memory – what might some of their applications be to this experiment.

QUESTION NO. 31:

Relate the output amplitudes of the recorded data to the linear limits of the measurement system by computing the linear input (or output) limits of each component of the measurement system.

Has there been any significant wave-shape distortion due to non-linearities? Be careful! The linearity characteristics of the *circuit itself* depend on its boundary conditions.

QUESTION NO. 32:

Discuss the relative advantages and disadvantages of the *Wheatstone Bridge* circuits and *Constant Current* circuits (as used here) and show why, for the type of test performed here, the *Constant Current* circuit is superior.

MECHANICAL IMPACT: TRAVELING WAVES AT DISCONTINUITIES

When mechanical impact occurs, energy is transferred from the striking object to the struck object. Energy can not be transferred in zero time, since that would require an infinite amount of power. Hence the energy imparted to the struck object takes time to "travel" down the part in the shape of force and displacement waves or pulses. This is called the TRAVELING WAVE PHENOMENON with analogs in electrical (transmission lines), hydraulic (water hammer) and thermal systems.

Stresses created by such force waves are being observed and analyzed in this demonstration. The specimen consists of a long, thin rectangular steel beam fixed at one end and with a hole in its center. The beam is manually impacted at the free end with hammers of various sizes, and the traveling wave phenomenon is recorded simultaneously at six key locations, which include the periphery of the circular discontinuity. Bonded electric resistance strain gages in constant current circuits are used to transduce strain into voltage vs. time traces on three two-gun cathode ray oscilloscope screens.

When a stress wave reaches a discontinuity, part of the wave is reflected from the discontinuity and part of the wave is refracted through it. In this specimen, geometric discontinuities include the centrally located hole, the impacted free end, and the restrained, clamped end. From a free boundary where no FORCES may exist, an incoming stress wave returns reversed in sign. This phenomenon is known as STRESS REVERSAL and may cause fracture in brittle materials, known as "spalling" failures. An interesting type of deliberately induced spalling is the HEPAT (high explosive 'plastic' anti-tank) round. This round, fired at relatively low velocities (1100 feet/sec), splatters against the outside of an enemy tank hull. It is set to detonate when the five pounds of plastic explosive is in the configuration of a hemisphere. Upon detonation, an intense compressive wave travels through the hull (5" to 8" of homogeneous armor plate) at velocities of 16,500 feet/sec. When it reaches the inner hull, stress reversal takes place. The armor plate, being weaker in tension that compression, fails by spalling. Experiments conducted at Fort Knox showed that one such 50 pound spall fragment ricocheted approximately 40 times inside an empty tank before coming to rest. The outside of the tank, however, showed no trace of damage. Similar failure mechanisms exist in rock when explosions are detonated inside a mountain. The mountain is literally torn apart by successive spalling, rather than pushed apart.

At a fixed boundary where no DISPLACEMENTS may occur, an incoming stress wave is reflected with the same sign as that with which it arrived, and at the same amplitude. This phenomenon is known as STRESS DOUBLING and can also cause failure. Pressure doubling in water hammer phenomena is the equivalent of stress doubling. The hydraulic equivalent of stress reversal is pressure reversal from an open end, which may cause cavitation and collapse of piping.

After impact is over and the hammer rebounds from the beam, the impacted end becomes a free boundary. This instant is marked on all records. The clamped end of the beam, the free end, and the hole all cause a large number of reflected and refracted traveling pulses as the result of a single impact. Such post-impact vibrations can cause fatigue damage in structures since they are both compressive and tensile in nature. Among the purposes of this experiment are studies of the strains at the hole due to impact, and their time history after impact is over. The stress concentration factor at a discontinuity under impact conditions is no longer dependent only on specimen geometry and material, but also on the duration of the traveling pulse. Each of the three hammers (2 oz., 8 oz., and 16 oz.) produced different pulse-widths with stress-concentration factors at the hole varying from 3.83 to 4.31. In some cases the maximum stress is not reached until reflected/refracted pulses superpose at some time AFTER impact is over. The max stress concentration factor for static loading of this specimen geometry is 4.

PHYSICAL ARRANGEMENT

ENLARGED VIEW OF FRONT SURFACE SHOWING GAGE LOCATIONS. SIMILAR ARRANGEMENT IN BACK. GAGES WIRED IN SERIES.

GAGE ARRANGEMENT FOR CIRCUIT #2 SAME AS SHOWN FOR CIRCUIT #1.

EXPANDED VIEW SHOWING GAGE LOCATIONS. GAGES USED SINGLY.

COLD ROLLED 4340 STEEL ROCKWELL HARDNESS C-40

ELECTRICAL ARRANGEMENT FOR STRAIN RECORDING: ONE OF SIX CONSTANT CURRENT CHANNELS

A – Altec 103 Constant Current Source for 2 channels; ASU-design for 4 channels. 20 ma current approx.
B – Triplett 630-NA Volt-ohm-milli-ammeter.
C – Strain Simulator, Electronetics S-200, 480,000 ohm shunt calibration, at 3000/sec chopping rate.
D – One of six strain gage circuits.
  #1, 4 BLH FAB-25-12S6 in series
  #2, 4 BLH FAB-25-12S6 in series
  #3-#6,BLH FAP-12-35S6 single gages.
E – Tektronix 502 oscilloscopes, three units, AC single-ended.
S_1-S_4 Switches to test for noise levels.
S_2 – Push-to-read type to check current level.
S_3 – Switch to actuate calibrator.

FAB gages mounted with EPY-150 adhesive, 6 hours at 150F, coated with micro-crystalline wax.
FAP gages mounted with SR-4 adhesive same cure cycle as above.

EXPERIMENTAL APPARATUS: Physical and electrical arrangements of components of the measuring system are shown together with an overall view.

ELECTRICAL ARRANGEMENT FOR TRIGGERING CRO AND PROVIDING SYNCHRONIZING MARKER SPIKE.

EXTERNAL-TRIGGER INPUT TERMINALS supplied with -6vDC on impact

Z-AXIS INPUTS FOR SYNCHRONIZING MARKER supplied with +96vDC when hammer rebounds

"IMPACT" SWITCH

6 v DC

47 k-ohms

90 v DC

CRO A   CRO B   CRO C

SAMPLE OF EXPERIMENTAL RESULTS
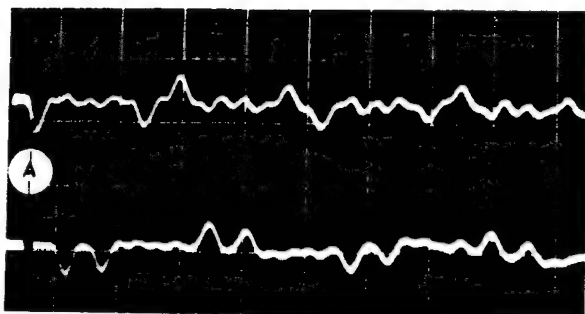
SMALL HAMMER: STANLEY 291-B
2 oz., 2.5" long, wooden handle

Trace blanking marks hammer rebound.
Note hammer bounce for large hammer.
(Denoted by letters A and B)
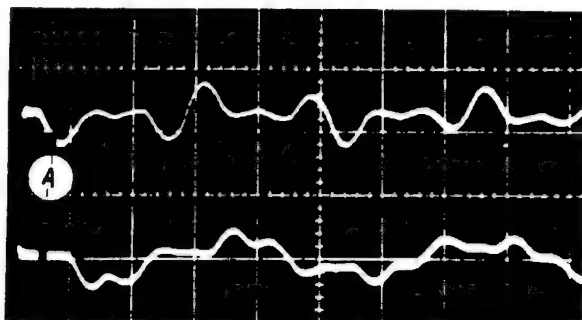
MEDIUM HAMMER: STANLEY 308
8 oz., 3.3" long, wooden handle
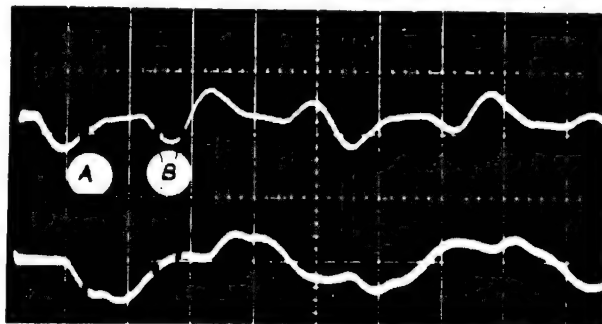
LARGE HAMMER: STANLEY 310
10 oz., 4.1" long, wooden handle

All impacts produced by gentle striking.
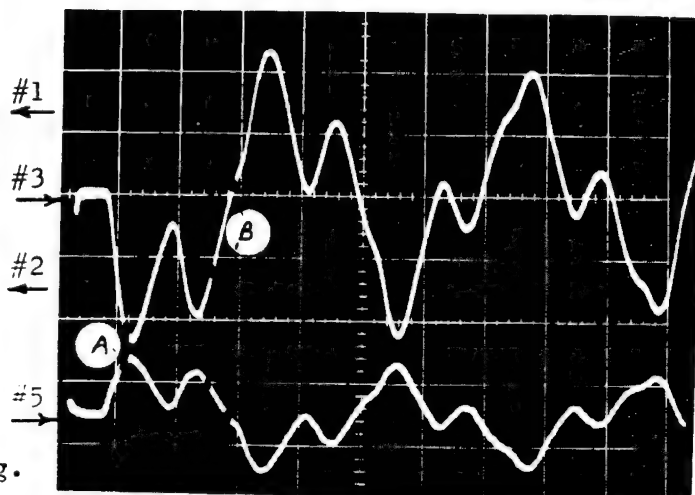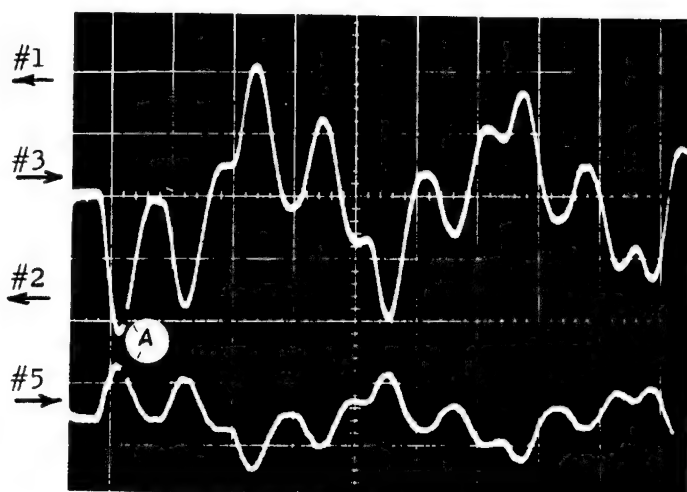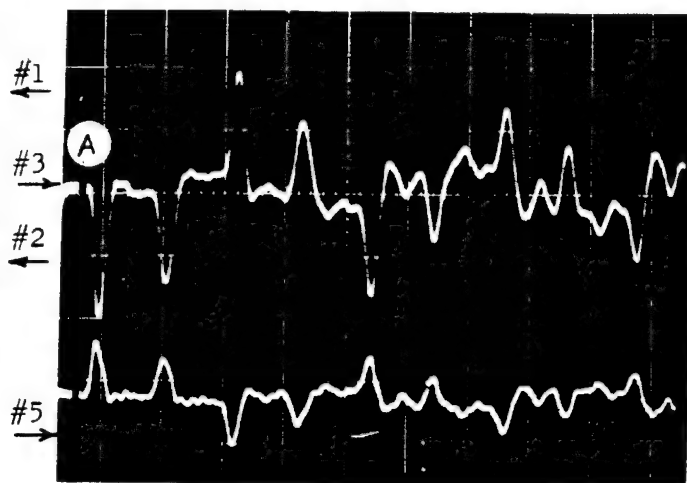
Time Scale: 0.2 millisec/cm   Vertical Scale: 100.0 $\mu\varepsilon$/cm

Common vertical scale for all channels was achieved at Step Sensitivity Control
setting of 1 mv/cm, and Fine Sensitivity Control adjusted by shunt calibration.
Measuring system 10-90% rise time as determined from step-shunt-calibration:
5 to $5\frac{1}{2}\mu$sec excluding strain gages. Initial compressive wave rise times 28-36μsec.

267

POST-IMPACT VIBRATIONS WITH THE LARGE HAMMER
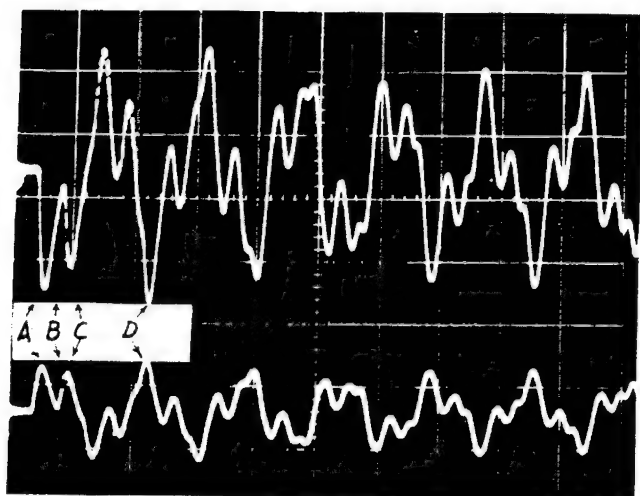
Time Scale: 0.5 millisec/cm
Amplitude: 100.0 µε/cm

Time Scale: 5.0 millisec/cm
Amplitude: 100.0 µε/cm

A: Initial compressive pulse at edge of hole, tension pulse at top of hole.
B: End of impact.
C: Reflected pulse from clamped end showing attenuation due to energy absorption.
D: Superposition of post-impact traveling pulses produces maximum stress.

Note large number of high-amplitude tension and compression post-impact vibrations.
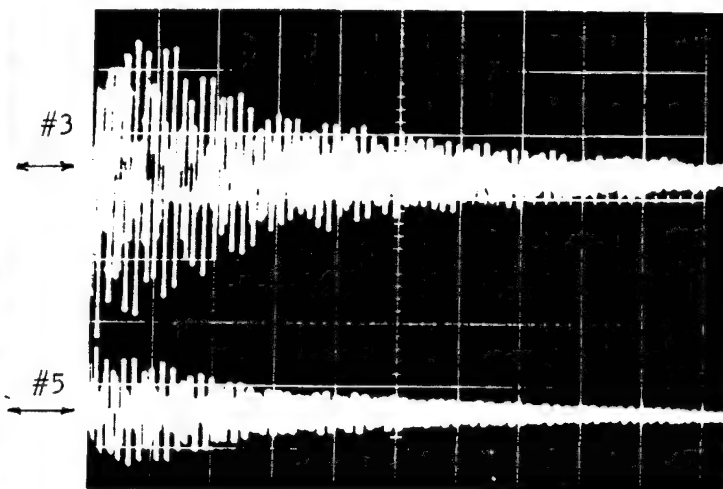
NOISE LEVEL DOCUMENTATION
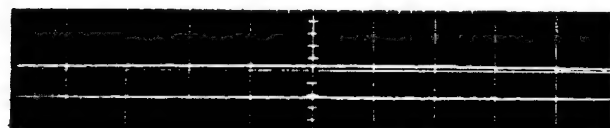
Time Scale: 0:1 millisec/cm

Amplitude: 100.0 µε/cm

ASU-designed current source on,
no strain applied to beam; after
satisfactory grounding and shielding
of various system components.
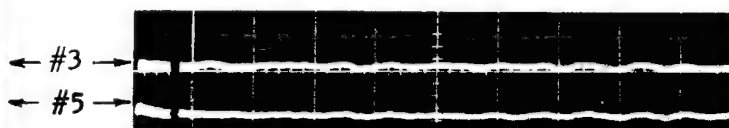
Current source off, beam impacted with
small hammer. This self-generating
effect believed to be due to movement
of strain gage grid in earth's magnetic
field by passage of the traveling pulse
beneath the gage.

The magnetically induced noise level documented above right has a polarity
which depends on the connection of the gage leads to the circuit. Where several
gages are placed in series, a non-inductive, noise-cancelling effect is possible.

SHUNT CALIBRATION & RISE-TIME CHECK

Circuit #4, 0.1 msec/cm x20 scale expand
(5 µsec/cm effective scale). 480,000 ohms
switched 3000 times/sec across 352.0 ohm
gage of 2.10 gage factor producing 350 µε
equivalent strain; 2.0 mv/cm vertical.

Rise-time is that of measuring system
except for strain gage rise time. Strain
gage rise time depends on gage length
and specimen material. Minimum value is
1 µsec. Actual value depends on adhesive
and other factors and is not known.

268
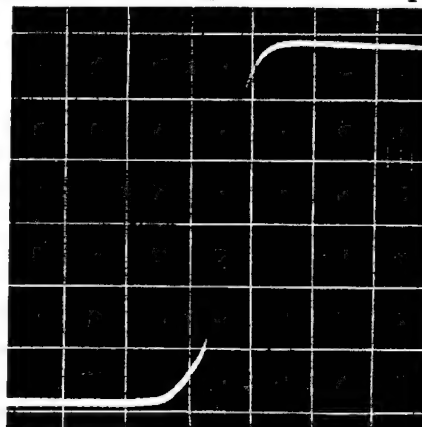
ANSWERS

ANSWER TO QUESTION NO. 1:

TOP DATA CHANNEL

Rise Time of the Strain Gage: In computing the rise time of a spatially averaging, side-mounted transducer such as a strain gage on this specimen, the assumption is always made of complete and instantaneous strain transmission from the specimen surface, through the adhesive layer and the backing or matrix, to the strain-sensitive grid.

This assumption is a liberal assumption, but no theoretical or experimental data are available in the literature which are truer to life. The few papers that have been published on experimental determination of strain gage rise time (such as Refs. 22, 26) do not present the necessary data validation procedures to make the published data useful, (as suggested in Refs. 1, 2 for example)

The common, liberal assumptions are illustrated in Fig. 26. A step discontinuity travels along the specimen surface at:

Propagation Speed / Velocity / Celerity   =   c

It enters the side-mounted strain gage at time $t = 0$
It leaves the side-mounted strain gage at time $t = L/c$
also known as the *Passage Time* or *Transit Time*.

It is assumed that the straight line connecting the beginning and end points represents the strain-time history as the wave passes through the strain gage, which gives a 10% - 90% rise-time equal to 80% of the passage time:

$$t_{r(10-90\%)} = 0.8L/c$$

FIG. 26: TRAVELING WAVE AT A SIDE-MOUNTED STRAIN GAGE AND THE IDEALIZED 10%-90% RISE-TIME
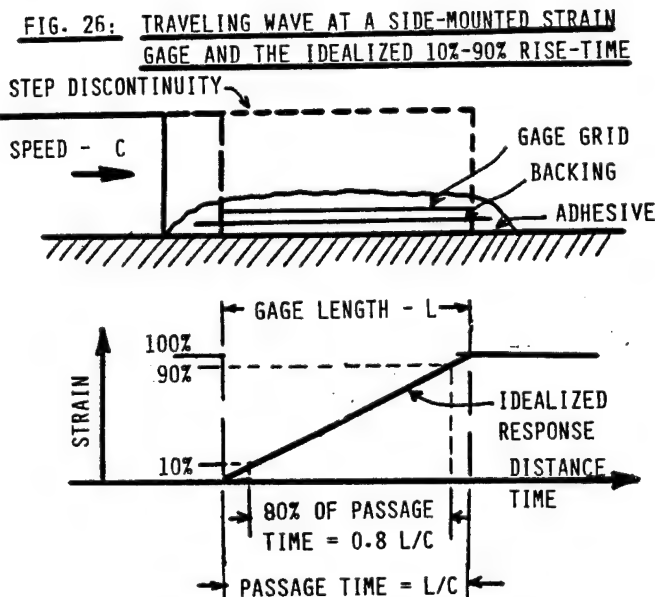
This assumption can not, of course, be correct because it implies that when the wave is in the middle of the strain gage grid, half of the grid is under uniform high strain and the other half at zero strain, which is not realistic. The exact strain distribution during wave passage has not been computed or measured, to the author's knowledge. Rohrbach (Ref. 17, 18, 19) computed a strain distribution through a statically loaded strain gage and also in its adhesive layer; but no dynamic work of that type seems to exist.

Corollary: A strain gage has no rise time! Only a gage installation on a specific specimen material, connected to specific signal conditioning has a rise time. For the same strain gage the rise times will be different when it is mounted on composite material, stone, bone, rubber, steel, aluminum, etc.

This condition is another example of the general statement:

No transducer has any inherent performance parameters (properties) until its boundary conditions at the three boundaries with the rest of the world have been specified.

For a strain gage of: L = 0.5 inches
mounted on steel: c = 200,000 inches/sec

the 10-90% strain gage rise time is: $t_{r(10-90\%)} = 2\mu sec.$

Rise Time of the Oscilloscope: The manufacturer's specifications for the CRO do not include a Rise Time specification. A CRO, however, is meant to reproduce the wave shape of a signal so it will have a monotonic response for magnitude vs. frequency and the Rise Time can be deduced from the Upper -3 dB Point.

The Upper -3 dB point of the CRO is, however, a function of the Gain / Sensitivity / Transfer Ratio setting on the data channel. From Fig. 27 which is a graphical representation of some of the Manufacturer's Specifications, (and also the answer to one part of Question 4), it can be seen that there is no specification for the Transfer Ratio setting used on the top data channel. There is a specification for the Transfer Ratio setting used on the bottom data channel.

Top CRO Channel:

Experiment performed at: 2 mv/cm
3 dB Point at 200 µv/cm: 100 kHz
3 dB Point at 5 mv/cm: 200 kHz

Three possibilities for application of the specs to the test are:

1. Conservative, under the assumption that if the frequency response at 2 mv/cm were any better than at 200 µv/cm, the manufacturer would have said so.
2. Liberal, under the assumption that 2 mv/cm is closer to 5 mv/cm than to 1/5 mv/cm.
3. Interpolating, logarithmically: 170 kHz
Conservative assumptions are used throughout the design and interpretation of a measurement according to the *Unified Approach to the Engineering of Measurement Systems.*

For purposes of this analysis:

CRO Top Channel Upper 3 dB Point: 100 kHz
CRO Top Channel 10-90% Rise-Time:

$$t_{r(10\%-90\%)} = 0.35 / 100,000 = 3.5 \mu sec \pm 10\%$$

since, for a monotonic system (see also Ref. 14):

$$[f_{2-3\,dB} \text{ (in Hz)}] \, [t_{r\,(10\%-90\%)} \text{(in Sec)}] \Rightarrow 0.35 \pm 10\%$$

a limit theorem which is exact when the ultimate roll-off slope of the Magnitude of Transfer Ratio vs. Frequency characteristic tends towards infinity at infinite frequency.

269

BOTTOM DATA CHANNEL

The strain gage is the same as for the top channel.

Amplifier: The Manufacturer's Specification for:

Upper 3 dB point: 25 kHz

No rise-time specification is given. Since the amplifier is supposed to reproduce at its output the wave shape of its input, it can be assumed to be monotonic in its frequency response and the rise-time can be computed:

$$t_{r(105-9050)} = 0.35/25,000 = 14 \, \mu \sec$$

Cathode Ray Oscilloscope: The CRO for the bottom channel is set at 200 mv/cm Transfer Ratio for which the Manufacturer's Specification shows an Upper 3 dB Point of 1 MHz. Its Rise Time is therefore:

$$t_{r(10\%-90\%)} = 0.35/10^6 = 0.35 \, \mu \sec.$$

LEAD WIRES AND CONSTANT CURRENT SOURCE

The Rise-Time of the total system, including leads and current source can be obtained from the shunt calibration data provided the Rise Time of the shunt calibration step is less than 1/5 that of the indicated System Rise Time.

Since the current source is home-made, its rise time is not known except by test which can be requested from the Standards Lab or Calibration Lab which certifies all the instrumentation periodically.

Information on Lead Wire Rise Times is available from their manufacturer or from the literature. For example (Ref. 16)

$$t_{r(10\%-90\%)} = 131.56 \times 10^{-7} a_f^2 L^2 / f$$

a_f = attenuation of cable at frequency f in dB/100 f
f = frequency in Hz   L= cable length in ft.

Cable Type	Attenuation at 1 G Hz in dB/30 meters
RG58	24.0
RG213	8.0
LDF4-50	2.34
LDF5-50	1.31
LDF7-50	0.891

For all practical purposes, with the six-foot lengths of cable in the present experiment and the frequency range of the data, the cables are not a factor in the system rise time.

ANSWER TO QUESTION NO. 2:

Estimating from the photos:

Top Trace: $t_{r(10\%-90\%)}$ = 1 cm = 20 μ sec
Bottom Trace: $t_{r(10\%-90\%)}$ = 1.2 cm = 24 μ sec

ANSWER TO QUESTION NO. 3:

Before this question can be answered, the answers generated in Question No. 1 must be combined to compute the rise time of each of the two channels:

TOP CHANNEL:

$$t_{r\text{-system}} = \sqrt{[t_{r\text{-strain gage}}^2 + t_{r\text{-CRO}}^2]} \pm 10\%$$
$$= 4.03 \, \mu \sec \pm 10\%$$

If the Observed Rise-Time: $t_{r\text{-observed}}$
is at least 5 times the System Rise Time: $t_{r\text{-system}}$

then the observed rise time has not been affected by the measurement system by more than 2% (Ref. 14, for ex.)

$$t_{r\text{-observed}} = 20 \, \mu \sec = 4.96 \, t_{r\text{-system}}$$

which is close enough.

Thus, even with a 100 kHz bandwidth CRO and a half-inch long strain gage, the rise times are valid within about 2%.

BOTTOM CHANNEL:

$$t_{r\text{-system}} = \sqrt{t_{r\text{-strain gage}}^2 + t_{r\text{-amplifier}}^2 + t_{r\text{-CRO}}^2} \pm 10\%$$
$$= 14.14 \, \mu \sec \pm 10\%$$

Since the observed rise time is only 24 μ sec and no factor of 5 exists between them, that rise time is severely affected by the measurement system and can not be interpreted.

Comment: Note that it was possible to validate the Rise Time of the Upper Channel and show that the Rise Time for the Lower Channel was not valid solely by internal checks. No recourse to comparison to a theory was involved.

The methods developed during the course permitted a direct answer to the question:

Could this output have been produced by that measurement system without distortion of the input.

ANSWER TO QUESTION NO. 4:

TOP CHANNEL:

Strain Gage: The frequency response of a strain gage has not yet been experimentally verified with sufficient data-validity checks to be considered Total Quality Measurements.

The theoretical analyses all assume complete and instantaneous strain transmission from the specimen surface through the adhesive layer and the gage matrix or backing to the strain-sensitive grid.

It is also necessary to assume whether this spatially length-averaging side-mounted transducer averages the strain at its endpoints or integrates it along its gage length. There is some evidence in favor of each of these two possibilities.

Fig. 28 illustrates the two possibilities and identifies the governing equations. The lower of the two resulting -3 dB frequencies is still liberal because of the assumption of instantaneous and total strain transmission. The lower of the two -3 dB points is:

$$f_{2\text{-3 dB}} \quad \text{at} \quad \frac{1}{4} = L/\lambda \quad < \quad 0.443 = L/\lambda$$

where L = gage length
       λ = wave length of the vibration
       c = celerity or speed of sound in the material to which the side-mounted, spatially-averaging transducer is attached.

270

FIG. 27 FREQUENCY RESPONSES OF THE INDIVIDUAL SYSTEM COMPONENTS (TRANSDUCERS)
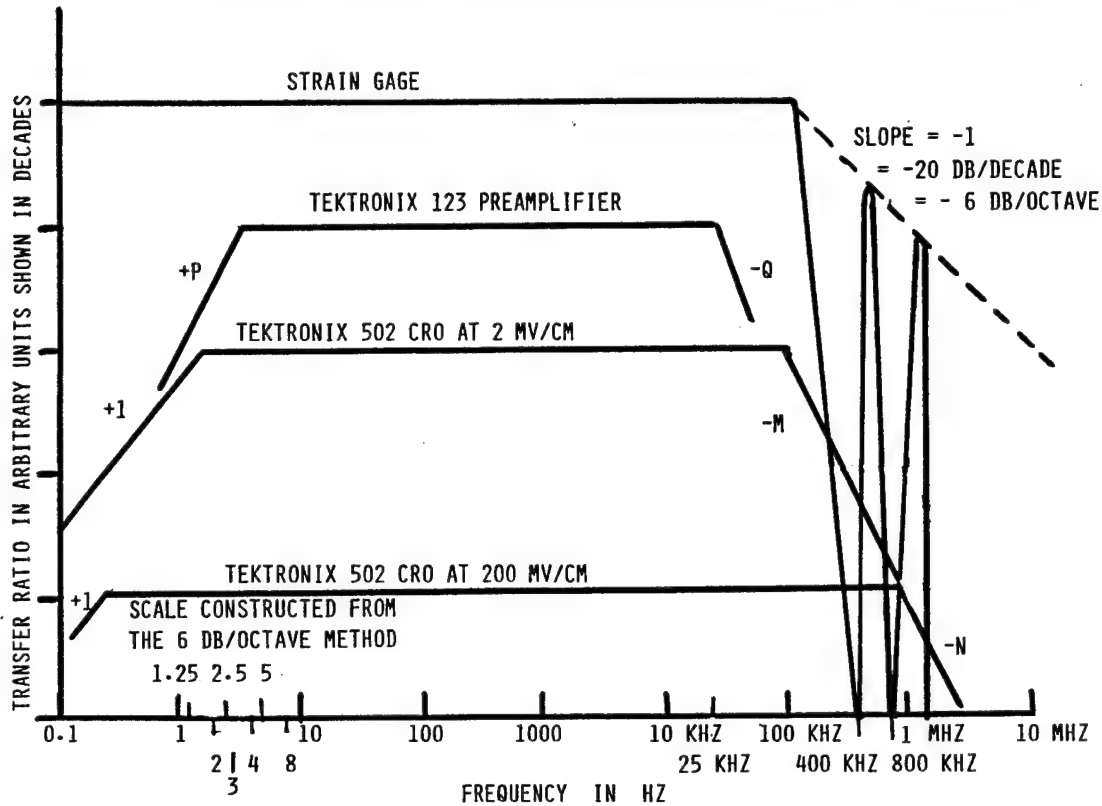
FIG. 30 FREQUENCY RESPONSE OF THE TWO MEASUREMENT SYSTEMS

271
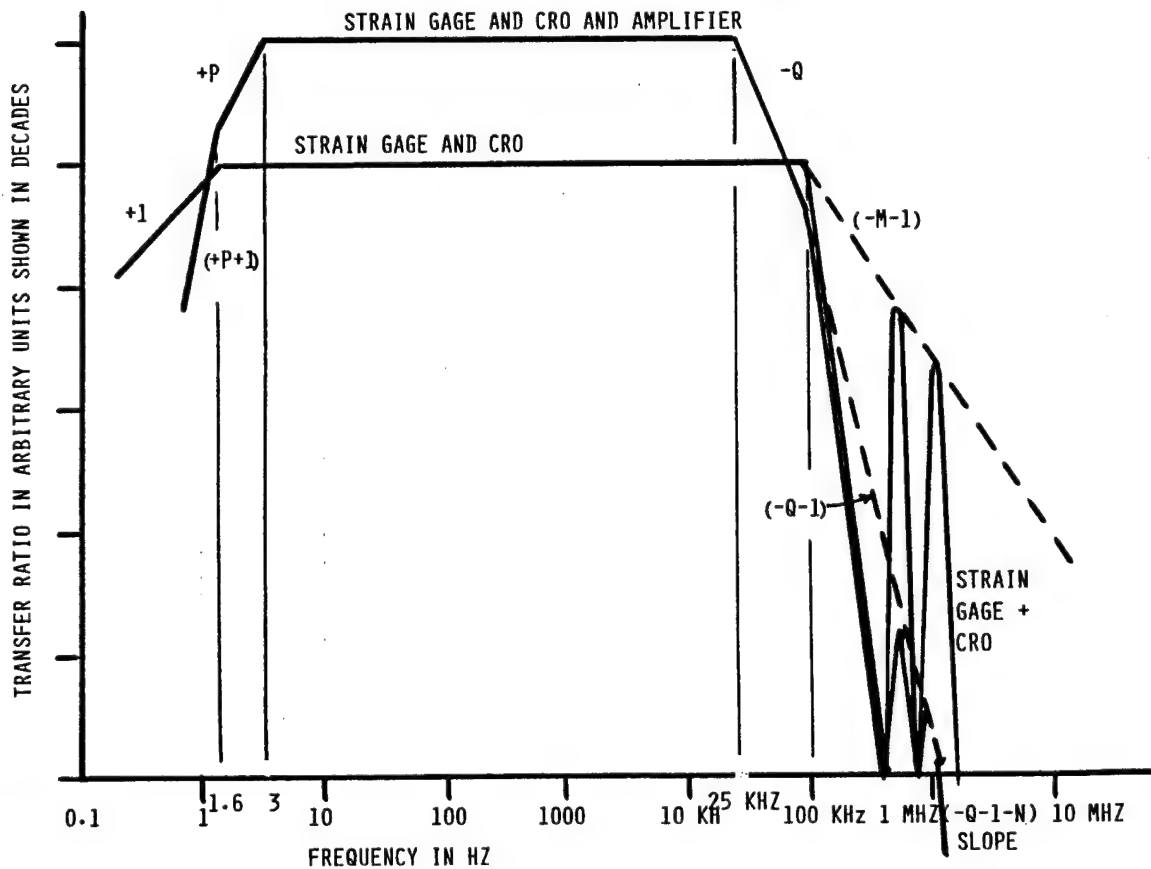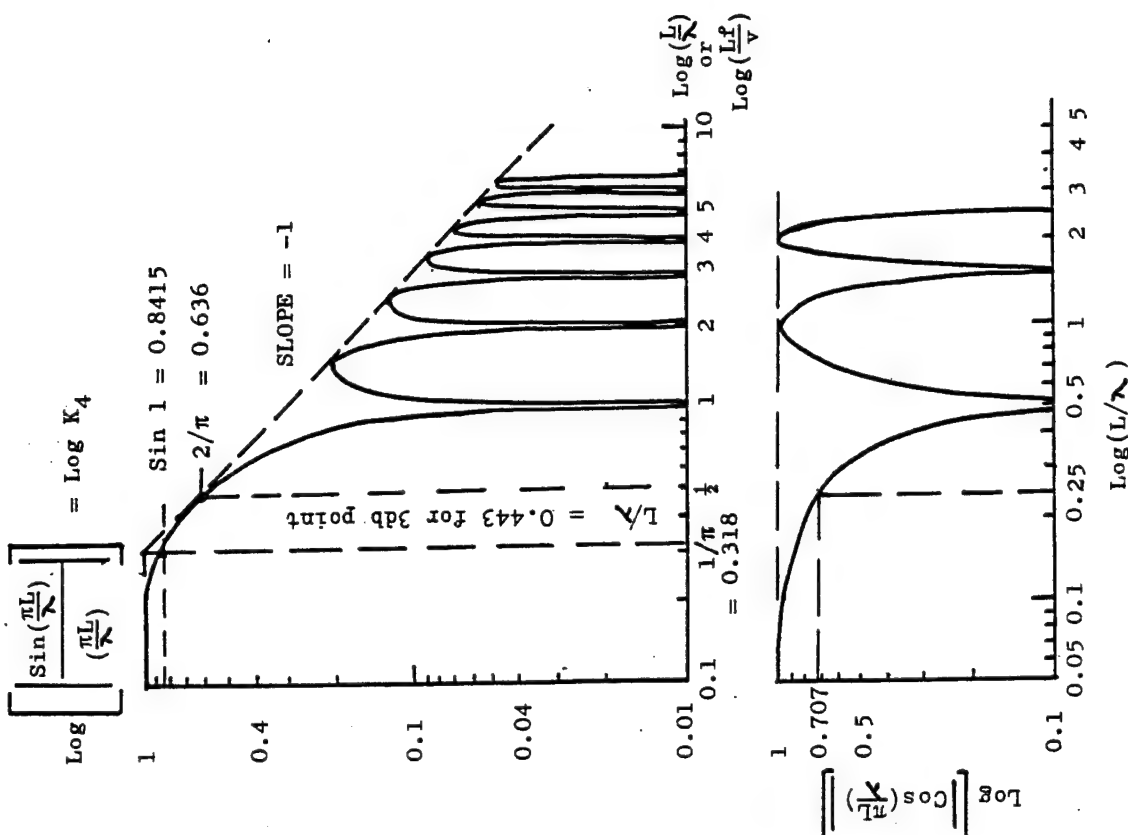
FREQUENCY RESPONSE FOR LENGTH-AVERAGING SENSORS

CASE I: Integrated Averaging over a Length L

Assume a distribution of quantity Q such that:

$$Q = Sin\left(\frac{2\pi x}{\lambda}\right)$$

where λ = wave length of Q
x = position
v = velocity of propagation of the disturbance
L = length of the length-averaging sensor

The response of the sensor will correspond to:

$$Q_o = \frac{1}{L} \int_x^{x+L} Sin\left(\frac{2\pi x}{\lambda}\right).dx$$

$$= -\frac{1}{L}\left(\frac{\lambda}{2\pi}\right)\left[Cos\left(\frac{2\pi x}{\lambda}\right)\right]_x^{x+L}$$

$$= \frac{\lambda}{2\pi L}(2)\left[Sin\frac{2\pi(x+L-x)}{2\lambda}\right]\left[Sin\frac{2\pi(x+L+x)}{2\lambda}\right]$$

$$= \left[\frac{Sin(\frac{\pi L}{\lambda})}{(\frac{\pi L}{\lambda})}\right]\left[Sin\frac{2\pi}{\lambda}(x+\tfrac{1}{2}L)\right]$$

$$\boxed{Q_o = \left[\frac{Sin(\frac{\pi L}{\lambda})}{(\frac{\pi L}{\lambda})}\right]\left[Sin\frac{2\pi}{\lambda}(x+\tfrac{1}{2}L)\right]}$$

CASE II: Averaging of the End Values

For the quantity Q assumed above, let the output be the average of the values at the ends of the length L.

$$Q_o = \tfrac{1}{2}\left[Sin\left(\frac{2\pi x}{\lambda}\right) + Sin\left(\frac{2\pi(x+L)}{\lambda}\right)\right]$$

$$= \tfrac{1}{2}.2\left[Sin\frac{2\pi}{2}\frac{(x+x+L)}{\lambda} . Cos\frac{2\pi}{2}\frac{(x-x-L)}{\lambda}\right]$$

$$\boxed{Q_o = Cos\left(\frac{\pi L}{\lambda}\right) . Sin\left[\frac{2\pi}{\lambda}(x+\tfrac{1}{2}L)\right]}$$

Graph 1 — Vertical axis: $Log\left[\frac{Sin(\frac{\pi L}{\lambda})}{(\frac{\pi L}{\lambda})}\right] = Log\ K_4$; values: 1, 0.4, 0.1, 0.04, 0.01. Horizontal axis: $Log(\frac{L}{\lambda})$ or $Log(\frac{Lf}{v})$; values: 0.1, 1, 2, 3 4 5, 10.
Annotations: Sin 1 = 0.8415; 2/π = 0.636; SLOPE = -1; L/λ = 0.443 for 3db point; 1/π = 0.318.

Graph 2 — Vertical axis: $Log\left[|Cos(\frac{\pi L}{\lambda})|\right]$; values: 1, 0.707, 0.5, 0.1. Horizontal axis: $Log(L/\lambda)$; values: 0.05 0.1, 0.25, 0.5, 1, 2, 3 4 5.

FIG. 28: FREQUENCY RESPONSE OF A LENGTH-AVERAGING TRANSDUCER WITH TWO ASSUMPTIONS ABOUT THE PHENOMENON

272

There is a relationship among f, c and λ:

$$f \quad = \quad c/\lambda \qquad \text{See also Fig. 33 from Ref. 30}$$

hence the lowest of the still liberal estimates is

$$f_{2\text{-}3\,dB} \quad = \quad c/4L$$

Once again, **a strain gage has no frequency response** until the boundaries between it and the other 3 parts of the world (in the three-port, six-terminal *Unified Transducer Model* have been identified. Here the important boundary is the mechanical one involving the speed of sound in the specimen.

The liberal-conservative upper 3 dB point of a

strain gage of length   L = 0.5 inches
mounted on steel of   c = 200,000 inches/sec

is $f_{2\text{-}3\,dB}$ =   100 kHz

Which of the two choices for roll-off at the high frequency end will exist depends on the assumptions made. Since nothing can respond to infinite frequency, the author prefers the choice associated with the Integrated Averaging effect although the $f_{2\text{-}3\,dB}$ was selected from the End-Value Averaging effect.

The low-frequency limit of a strain gage is DC or zero.

$$f_{1\text{-}3\,dB} \quad = \quad 0 \text{ Hz}$$

Cathode Ray Oscilloscope: It was already established that a conservative value for the upper CRO channel is:

$$f_{2\text{-}3\,dB} \quad = \quad 100 \text{ kHz}$$

No roll-off slope is specified at the high-frequency end. It is marked as -*m* in Fig. 27.

The manufacturer does not specify a lower frequency limit for AC-Coupled Connection, but from the circuit diagram (Fig. 29) it could be computed:
A 1 Megohm resistor in series with a 0.1 μ F capacitor.

Time Constant τ ≈ $10^6 \times 0.1 \times 10^{-6}$ =   0.1 sec

Break Point ω = $1/\tau$ =   10 rad/sec

                   f   = $\omega/2\pi$ =   1.6 Hz

It was also experimentally determined from transient and steady state tests earlier in the course as being a first-order response (roll-off slope +1) with a break-point at:
$$f_{1\text{-}3\,dB} \quad = \quad 1.6 \text{ Hz}$$

BOTTOM CHANNEL:

Strain Gage: The gage is the same for both channels.

Amplifier: From the Manufacturers' Specifications:

$$f_{2\text{-}3\,dB} \quad = \quad 25 \text{ kHz}$$
$$f_{1\text{-}3\,dB} \quad = \quad 3 \text{ Hz}$$

No roll-off slopes are given at either end. They are marked +*p* and -*q* in Fig. 27.

Cathode Ray Oscilloscope: As determined for Question No. 1:
$$f_{2\text{-}3\,dB} \quad = \quad 1 \text{ MHz}$$

with unknown roll-off slope shown as -*n* in Fig. 27.

The low-frequency end is the same as for the top channel.

Constructing a Logarithmic Scale on Linear Graph Paper is illustrated in Fig. 30.

FIG. 30 A
A CONVENIENT METHOD OF PRODUCING A LOGARITHMIC SCALE FROM A LINEAR SCALE

REMEMBERING THAT 6 DB = A FACTOR OF 2 (OCTAVE)
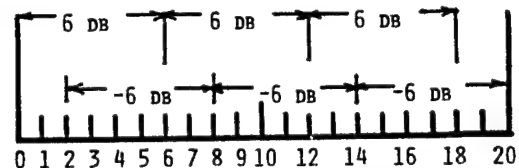
SCALE IN DECIBELS - 20 DB PER DECADE
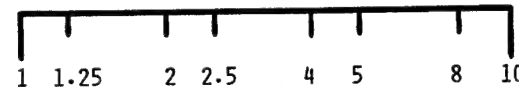
SCALE IN LINEAR COORDINATES

DIVIDE A DECADE INTO 20 EQUAL PARTS. EACH PART IS 1 DB. THERE IS A DOUBLING EVERY 6 DB MOVING UP FROM 0 DB (RATIO OF 1), AND A HALVING EVERY -6 DB MOVING DOWN FROM 20 DB (RATIO OF 10). THERE ARE, BY DEFINITION, 20 DB IN A DECADE (FACTOR OF 10). BY CONSEQUENCE THERE ARE 6.02 DB IN AN OCTAVE (FACTOR OF 2) ROUNDED OFF TO 6. THIS PROCESS SHOWS THE LOCATIONS OF 2, 4, 8 GOING UP AND 5, 2.5 AND 1.25 COMING DOWN. THE OTHER POINTS CAN BE ESTIMATED QUITE ACCURATELY.

ANSWER TO QUESTION NO. 5:

Using the principles developed in the study of series-connected systems for which the following rules applied:

1. Transfer Ratios multiply – their logarithms add – the slopes of their asymptotes add. These operations can be carried out graphically as shown in Fig. 30.

2. Phase Angles add linearly, which can be performed graphically. This operation is not performed here.

3. Responses to Steps cannot be combined graphically. Resort to the mathematical formulation must be made unless it is recognized that two first-order systems combine to give a second-order system for which equations and families of curves are already available. This operation is not performed here. Rise Times (10% - 90%) can be combined as the square root of the sum of the squares as has already been indicated and done in Question No. 1.

273

ANSWERS TO QUESTION NO. 6

Strain Gage: Mechanical Input Characteristics are not known but when mounted on the specimen, the mass and spring constant of the strain gage are not expected to affect those of this specimen in any appreciable manner.

When even small bonded resistance strain gages are mounted on low-modulus materials such as plastics, solid propellants or high explosives, composite materials or filament wound structures, etc., or on thin sections of even metallic specimens, they may appreciably disturb the strain field in their vicinity. No comprehensive study of this phenomenon has come to the author's attention. The problem of self-heating in such situations has been discussed in Ref. 27.

Electrical Output Characteristics: Two 350-ohm gages in series, non-inductively coupled:

    Output Resistance: 700 ohms
    Output Capacitance: unknown

Cathode Ray Oscilloscope: Input Characteristics:
1 Megohm paralleled by 47 pF, (DC-coupled) in series with 0.1 µF when AC-coupled as in the application here.

For voltage inputs (i.e., incremental short circuit) the Input Impedance for **DC-Coupling** is a first-order system:

    R = 1 Megohm
    C = 47 pf
    Time Constant: τ = 47 µsec
    Break Frequency: ω = 21,277 rad/sec
                       f = 3388 Hz rounded off to
                       f = 3400 Hz for convenience

Since at DC or 0 Hz the impedance for DC-coupling is 1 Megohm, the system must be a low-pass system and since it is first order its frequency responses for magnitude and phase can immediately be plotted (from earlier considerations in the course). See Fig. 31.

The Phase Shift curve is the standard one for first order low-pass systems, using the forcing function as phase reference (Refs. 1 & 33).

    At the break point: -45°
    At the end of each asymptote, the asymptotic slope
        multiplied by 90°, i.e. -90° (Refs. 1 & 33 for example)

For **AC-Coupling** the Input Impedance at zero frequency goes to infinity along a first-order (slope of -1) axis, starting from the break point of:

    R = 1 Megohm
    C = 0.1 µF
    Time Constant: τ = 0.1 sec
    Break Frequency: ω = 10 rad/sec
                       f = 1.6 Hz

as shown in Fig. 31

The phase angles are also shown and magnitudes are given for decades above and below the break points according to the general principles for first-order systems established during the course.

One decade above / below the 3 dB point the actual response is 1% below the asymptotic value.

One octave above / below the 3 dB point, the actual response is 10% below the asymptotic value.

The phase shift at the break point is ±45°, and at the end of an asymptote the phase shift equals 90° times the asymptotic slope.

Note that the impedance levels at one and two decades above the 3400 Hz breakpoint are 99,000 ohms and 10,000 ohms, nowhere near the DC-value of 1 Megohm. At 340 Hz the impedance is 990,000 ohms.

Amplifier: Manufacturer's Specifications only give resistance levels, no shunt capacitance's or inductances.

    Input Impedance: 10 Megohms
    Output Impedance: 31,000 ohms

ANSWERS TO QUESTION NO. 7:

Top Channel: Strain Gage - CRO

Based only on resistance levels, the Isolation Ratio or Loading Factor between the strain gage and the CRO would be:

$$I \quad = \quad \frac{1000000}{1000700} \quad = \quad 0.9993$$

or 0.07% information loss at DC. As the answer to Question 6, however, shows, at higher frequencies the CRO would be loading the strain gage substantially. Without the Output Capacitance of the strain gage circuit, however, no numerical calculations can be performed.

Bottom Channel: Strain Gage —Amplifier – CRO

Even at DC the Isolation Ratio between amplifier and CRO is:

$$I \quad = \quad \frac{1000000}{1030000} \quad = \quad 0.97$$

or 3% information loss at DC. Although the input capacitance to the CRO is known, the output capacitances of the amplifier or of the strain gage, nor the input capacitance of the amplifier, are known. The effects could be substantial as Fig. 32 (from Ref. 27) illustrates.

It is quite usual to have this situation of too many unknowns at the boundaries between transducers in the measurement system, which is why the *Through-Calibration* techniques have been developed. The most often used such method is the *Resistance Injection through Shunt Calibration* or the next–best: *Voltage Injection* .

Additional advantages of these step–input methods is that the roll-off slopes at the low-end of the frequency response curve for Magnitude (i.e. the *Undershoot Characteristics* of the measurement system and its *Rise Time* can be obtained for the entire system forward of the location of the Injection Point. (See also Ref. 14).

ANSWER TO QUESTION NO. 8:

Using the amplitude of the compressive pulse as 100%, the Undershoot shown in Photo 9 is 60% for the Top Channel and 66% for the Bottom Channel.

What is the Permissible Undershoot for the Measurement System?

One half the smallest scale division on the read out has been considered a generally acceptable limit for noise levels of all kinds. It will be applied to Undershoot.

274

FIGURE 29: CRO INPUT IMPEDANCE

INPUT CIRCUIT FOR TYPICAL CATHODE RAY OSCILLOSCOPE

SWITCH OPEN FOR AC-COUPLED

FOR TEKTRONIX 502A CRO:
R = 1 MEGOHM
C_1 = 47 PICO FARADS
C_2 = 0.1 MICRO FARADS

SWITCH OPEN FOR AC-COUPLED
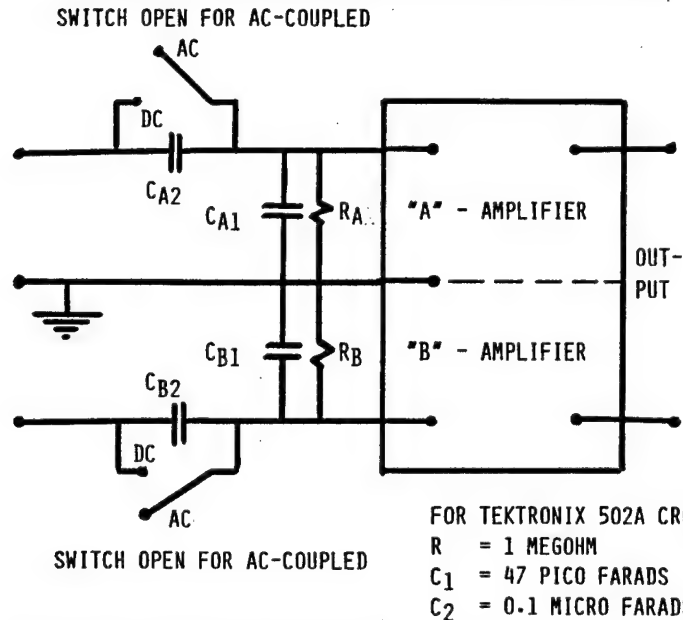
NOTE THAT EVEN DURING MANUFACTURE, THE "A" AND "B" COMPONENTS
ARE NOT IDENTICAL. THEY WERE DRAWN FROM BOXES OF ± x% TOLERANCE
RESISTORS OR CAPACITORS, AND THEY HAVE AGED DIFFERENTLY.
THE LOW-FREQUENCY BREAK-POINTS FOR THE TWO CHANNELS WILL DIFFER

FIG. 31: FREQUENCY RESPONSE OF THE INPUT IMPEDANCE OF A CATHODE RAY OSCILLOSCOPE

SLOPE = -1 ASYMPTOTE = - 6DB/OCTAVE = -20 DB/DECADE
FOR AC-COUPLING

1 MEGOHM

SLOPE = 0
ASYMPTOTE
FOR DC-
COUPLING

707,000 OHMS -45°

99,000 OHMS
-89+°

ASYMPTOTIC SLOPE
-1, -20 DB/DECADE

10,000 OHMS
ALMOST -90°

INPUT IMPEDANCE IN OHMS
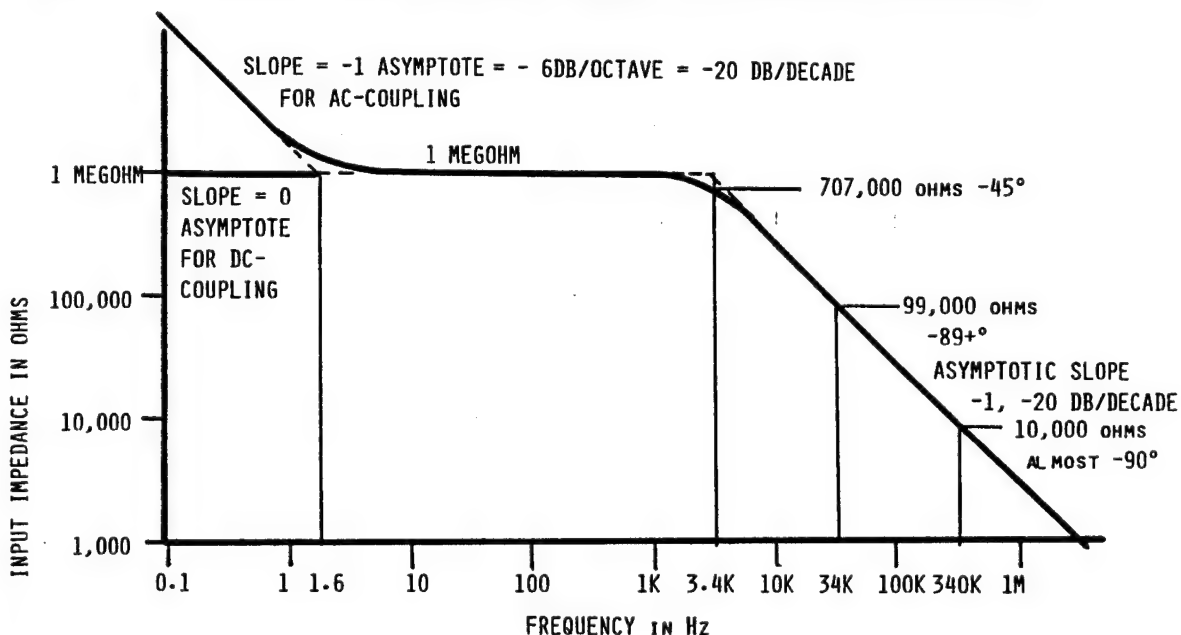
FREQUENCY IN Hz

Fig. 32: TYPICAL INTERACTION, LOADING OR ISOLATION PROBLEMS BETWEEN SYSTEM COMPONENTS
(From Ref. 27)

$$\tau_1 = \left(\frac{R_1 R_2}{R_1 + R_2}\right)(C_1 + C_2)$$

$$\tau_2 = R_2 C_2$$

$$I = L = \frac{z_1}{z_1 + z_2} = \frac{e_o}{e_i}$$

$$|I| = \frac{R_1}{R_1 + R_2}\sqrt{\frac{1 + \omega^2 \tau_2^2}{1 + \omega^2 \tau_1^2}}$$

$$f = \frac{\omega}{2\pi}$$

L = LOADING FACTOR

I = ISOLATION RATIO

NUMERICALLY THE SAME

CONCEPTUALLY TOTALLY DIFFERENT
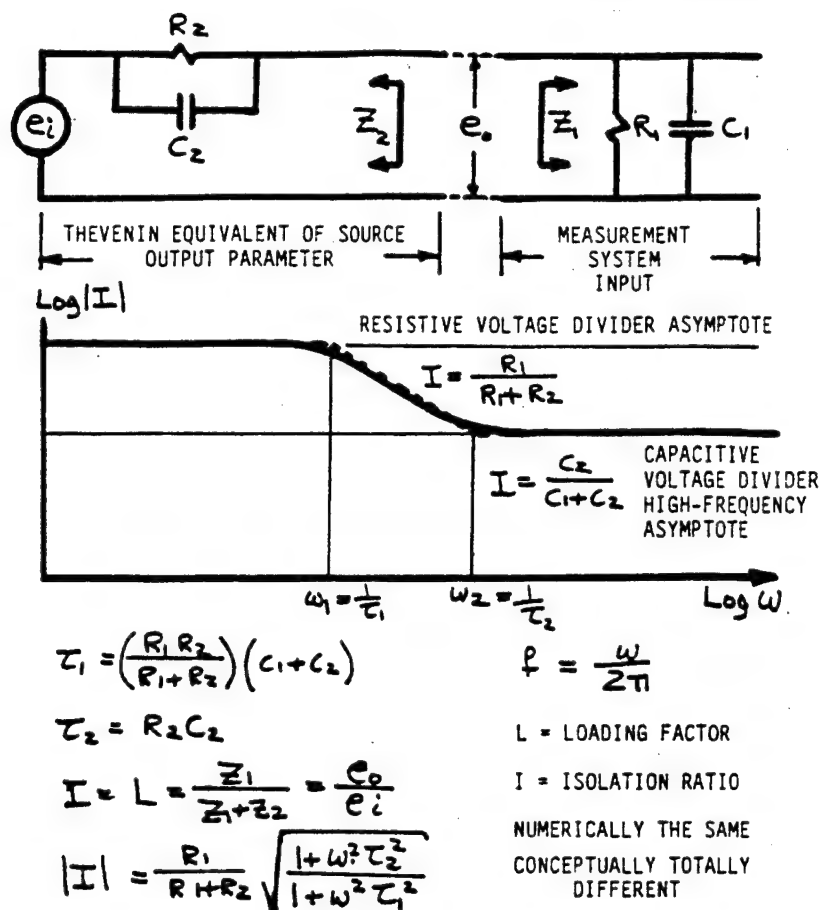
Fig. 33: FREQUENCY / WAVE LENGTH RELATIONSHIPS FOR VARIOUS MEDIA (From Ref. 31)

Medium	Velocity of Sound Inches/sec	Wave Length in Inches for Frequency f in Hz				
		f = 1 kHZ	f = 5 kHz	f = 10 kHz	f = 50 kHz	f = 100 kHz
Steel	200,000	200	40	20	4	2
Aluminum Alloy	200,00	200	40	20	4	2
Glass	160,000-220,000	160-220	32-44	16-22	3.2-4.4	1.6-2.2
Brass	130,000	130	26	13	2.6	1.3
Lead	47,000	47	9.4	4.7	0.9	0.5
Rubber	1,200-2,800	1.2-2.8	0.2-0.6	0.1-0.3	0.02-0.06	0.01-0.03
Hard Rubber	29,000	39	5.8	2.9	0.6	0.3

Full Scale of the pulse is 20 mm

Permissible Undershoot: $\frac{1}{2}(2 \text{ mm}) = 1 \text{ mm} = 5\%$

Top Channel: The Top Channel is a first-order low-pass system with the AC-coupled CRO and the DC-coupled strain gage. For first-order systems, undershoot to a square pulse of time-duration a is: (see Ref. 14).

U = $-k.a/\tau$ where

τ = 0.1 sec   the single low-frequency time-constant for the measurement system

k = pulse shape factor. For a square pulse k=1. for gentler pulses such as haversine, triangular, etc., k,1.

The maximum pulse duration which would create the maximum permissible undershoot for the worst case of a square pulse therefore, is:

$$a_{max} = -U.\tau = 0.05 \times 0.1 = 5 \text{ msec}$$

The measured pulse duration is 0.25 msec, hence the Undershoot as recorded is a negative reflected stress wave and not an artifact created by the measurement system by a margin of over 20:1.

Since the original incoming pulse must have been more gentle than a square pulse, a factor of k,1 would apply and the margin of safety would be larger than 20:1.

276

Note again that validity statements can be made from internal checks of the data characteristics and the measurement system characteristics and without recourse to any theory of impact and reflected waves.

Bottom Channel: The Bottom Channel is a system of unknown order at the low-frequency end. The amplifier has an unknown low-frequency roll-off characteristic not specified by the manufacturer, and no time-compressed step-response of the system is available. Had the shunt-calibration switch been actuated only once and the long-time response of the system recorded, the low-frequency roll-off, or system order could have been deduced.

For Second Order systems, a design chart was presented during the course to compute undershoot. For higher-order systems no simple relationships have been established to validate Undershoot. A separate analysis is necessary.

No statement can be made about the meaning or validity of the Undershoot for the Bottom Channel. If it alone were available, no data interpretation would be possible.

ANSWER TO QUESTION NO. 9

The loss of pulse peak because of the Magnitude vs. Frequency Response characteristics of Transfer Ratio is given by the bandwidth. The only relationships which were developed in the course hold for systems where the roll-off at each end of the frequency response curve is of first order, which is not the case here. But a (libearal) approximation can be made:

Top Channel: Low-Frequency Limit is 1.6 Hz with a first order roll-off. The High-Frequency Limit is governed by two transducers each with a 100 kHz -3 dB point – the strain gage and the cathode ray oscilloscope. This combination will move the system's -3 dB point to at least 70,700 Hz if not lower. The roll-off slope is unknown. For a relationship based on first order roll-offs at the high and low frequency ends, a liberal estimate of peak-depression due to insufficient bandwidth is: (from Ref. 32)

Peak which is recorded $= (1+b) b^{b(1-b)}$
where $b = f_1/f_2 = 22.6 \times 10^{-6}$

Thus the recorded peak is within 250 parts/million of full value. This is a factor of 200 below the resolution of 5% of the pulse height which is possible on the photo, and hence the liberal assumptions would appear to be satisfactory.

Bottom Channel: The low-frequency behavior is governed by two components:
1. The amplifier of lower -3 dB point and of unknown roll-off slope
2. The CRO of 1.6 Hz lower -3 dB point with a +1 roll-off slope.

The high-frequency behavior is governed by three components:
1. The amplifier with a 25 kHz -3 dB point and unknown roll-off slope
2. The strain gage of 100 kHz -3 dB point and the humped roll-off characteristics discussed in Question No. 5.
3. The CRO with 100 kHz -3 dB point and unknown roll-off slope.

For those conditions there is no possibility of even estimating the peak-depression due to insufficient bandwidth. It would seem, however, that the bandwidth of approximately 8000:1 should suffice for a dynamic measurement system with resolution no greater than 1% maximum (and 5% of full scale pulse height here).

ANSWER TO QUESTION NO. 10

The height of the calibration pulse in Photo 5, Fig. 24 is 4 divisions. The shunt calibration relationships without lead wire effects were derived during the semester (also Ref. 27) as:

$$\varepsilon_{simulated} = -\frac{1}{K} \cdot \frac{R}{[R+R_c]} = 2636 \ \mu\varepsilon$$

where K = 2.2, R = 700 ohms, R_c = 120,000 ohms

The calibration then is: 659 $\mu\varepsilon$/division at the 20 mv/div setting on the CRO Inverse Transfer Ratio (Sensitivity) position.

Had the CRO Inverse Transfer Ratio (Sensitivity) setting been at 2 mv/div then the pulse height would have been 40 divisions and the calibration at 2 mv/div is therefore;

Calibration Factor: 65.9 $\mu\varepsilon$/division

The implicit assumption is that switching from the 20 mv/div to the 2 mv/div setting on the CRO in fact produces a Transfer Ratio change of x10. The CRO Specifications place a 3% tolerance on the individual Sensitivity settings, giving a possible 6% uncertainty when switching from one to another.

Had a shunt calibration resistor of ten times the 120,000 ohm value been available, the calibration could have been carried out on the 2 mv/division setting used during the test to give a calibration of 66.25 $\mu\varepsilon$/division.

ANSWER TO QUESTION NO. 11

The pulse heights on Photo 6, Fig. 24 show 2.8 divisions negative and 1.6 division positive maximum, or strains of:

$-185\mu\varepsilon$ and $+105\mu\varepsilon$

ANSWER TO QUESTION NO. 12

Were the Elastic Modulus 30,000,000 psi the corresponding stresses would be 6930 psi and 4560 psi. Since the Elastic Modulus is strain-rate dependent (i.e., has a frequency response), values determined under a "static test" should not be used to interpret data which occur to a 20 μsec time scale. The damage potential of the measured stresses can also not be evaluated because of the strain-rate effect. The comparison to a "statically" determined value of 30,000 psi yield point leads to no valid conclusions.

ANSWER TO QUESTION NO. 13

The criteria for peak-to-peak reproduction of a square wave were developed in Ref. 27 to be:

$150 f_1 < f_o < 0.5 f_2$ where

f_1 = lower -3 dB point
f_2 = upper -3 dB point
f_o = repetition rate of the square wave

The criteria apply to ±1% peak-to-peak reproduction and to first order systems at each of the roll-offs, i.e. roll-offs of +1 at the low end and -1 at the high end (±20 dB/decade or ±6 dB/octave).

The calibration wave here is not a square wave – its duty cycle is not 1/2, and only the top channel has a +1 roll-off at the low frequency end. The bottom channel has a roll-off of unknown slope. At the high frequency end, the top channel is

governed by two roll-offs of -1 starting at 100 kHz giving at approximate -3 dB point of 70,700 Hz ($\sqrt{2}/2$ of 100 kHz).

The use of the criteria is therefore not conservative. but so long as the calibration pulse frequency is closer to the lower limit than the higher one, the results should be acceptable. For the upper channel:

f_1 = 1.6 Hz
f_2 = 70,700 Hz   hence
240 Hz < f_0 < 35,350 Hz

Note that 1000 Hz is acceptable. 60 Hz would not be. Also note that very few of the questions can be answered with total surety of validity. If the problems posed were important, then some additional analysis would be in order.

ANSWERS TO QUESTION 14:

Region A in Photo 6 in Fig. 24 shows five cycles in one division. To the 0.1 msec/div time scale that would be 50 kHz. From Fig. 30 in answer to Question No. 5 it is seen that 50 kHz is an octave above the upper -3 dB point for the bottom channel, hence attenuated by more than 20xQ%. It is an octave below the -3 dB point for the upper channel and therefore attenuated more than 10%. (See Chapter 5, Ref. 1, also Ref. 33.)

This highest frequency visible in the records is barely acceptably reproduced on the upper channel and quite badly attenuated in the lower channel.

ANSWER TO QUESTION 15:

The Noise Documentation procedure of Fig. 23 gave photographs 1 through 4 shown on Fig. 24, documenting events along Paths 1, 2, and 3.

The Environment-Response Path *not* documented there is the effect of the temperature change which accompanies the strain wave due to the Kelvin Effect – a change in volume of a material under stress will produce a temperature change.

Documentation of the strain-induced voltages (Path 3) is very rare in the literature. One of the very few publications including this check with interestng results is Ref. 37. In their previous work (Refs. 22, 23) the authors had not yet included that procedure.

ANSWER TO QUESTION 16:

The temperature change described above may produce thermal emfs, which would be documented, and resistance changes which could not be documented separately. Since the temperature-induced resistance changes only occur when the strain (measurand) is applied the effects can not be separated experimentally. Calculations show that the temperature rise would be small fractions of a degree F and hence would not create noticeable effects. The temperature changes are, however, large enough to be measured and to be the basis of the SPATE system: Stress Pattern Analysis through Thermal Emission (Ref. 34). The temperature changes are proportional to the sum of the principal stresses which stimulate them.

Note that the temperature changes occur both in the test specimen and in the strain gage filament and that these temperature changes may be different due to the differences in material properties.

Plastic strain propagation and/or distribution has been observed by measuing these temperatures (Ref. 38 is recent)

ANSWER TO QUESTION NO. 17:

From Photo 3, Fig. 24, the highest noise level is due to Path 3 – Strain-Induced Voltages. The peaks are -1.6 and +2 divisions: -320 to +400 μvolts.

ANSWER TO QUESTION 18:

From Photo in Fig. 24, the maximum compressive strain gave an output of 2.8 divisions = 5.6 mv and the tensile strain gave 1.6 divisions = 3.2 mv. The noise levels are therefore the order of magnitude of:

400/5600 = 7% of the maximum compressive strain

If a "standard" measurement system had been used such as:
R = 120 ohm strain gage
I = 10 milliamp current
K = 2.2, such as here

in an equal-arm Wheatstone Bridge of circuit efficiency:
η = 1/2

then the circuit output would have been:
e/ε =   I. R. K. η =   1.32 μv/με

rather than the 38.5 μv/με of the system used here with

R = 700 ohms and I = 25 milliamp in an η = 1 constant current circuit. The noise level would have represented:

400/(1.32)   =   303 με
more than the maximum signal of 185 με !!! 164%!!!

For the system used here, the signal equivalent of the noise is:

400/(38.5) = 10.4 με, a tolerable value but still representing some 7% of the maximum tension strain and 4% of the compression strain.

Photo 10 on Fig. 24 shows the noise level to the same scale as the signals.

ANSWER TO QUESTION 19:

The six noise suppression families were derived from a single equation attached to a conceptual model, in Ref. 27 where they are described in some detail.

- *Mutual Compensation: Cancel by Subtraction*
  Used here in the non-inductively series-connected strain gages to minimize any magnetically induced voltages in the circuit.
- *Shield, Absorb, Isolate: Minimize by Division*
  The electrical shields on the cables connecting the current source to the gages and the gages to the CRO "caught" ambient electrically induced voltages and bled them off to the common, single ground. The cases of the current source and the CRO also acted as shields and were connected to the common ground point.
- *Filter: Selective Decease of an Environmental Stimulus – could be considered as an Attribute-Selective Shield and classified as part of that family.*
  The AC-coupled (or RC-coupled) CRO filtered out the large DC voltage V = I.R = 17.5 v at the CRO terminals.
- *Self-Compensation: Response Reduction*
  Self-temperature-compensated strain gages were

used. Since the Transfer Ratio of the measurement system is a direct function of R, that compensation is helpful.

- *Sideways Promotion: Reducing the Interrogating Input to an Undesired Response*
  The lead wire resistance from the gages to the CRO has almost no current interrogating it, hence no voltage drop can be created across those leads. They represent the voltage-output connections on a Kelvin-Thompson Four Terminal Resistor. The leads have been deliberately placed in that part of the circuit where "there is no action" hence they cannot contribute to the output.
- *Jail: Location of an Undesired Response where it does not affect the System*
  The lead wire resistance from the current source to the gages is in the constant-current portion of the circuit. No variations in the lead resistance will change the current which interrogated the strain gage. Those leads represent the power-input connections to the Kelvin-Thompson Four Terminal Resistor. Their variations do not affect the circuit output: they have been "put in jail".

ANSWER TO QUESTION NO. 20:

Noise suppression through Information Conversion, also known as Modulation or Carrier Operation with a non-DC wave shape, was not used.

ANSWER TO QUESTION NO. 21:

Information Conversion separates self-generating (voltage or current) responses from non-self-generating (impedance-based) responses. Since the major noise level in this experiment is an uncomfortably large, self-generating, strain-induced voltage, the method would be ideal to suppress those noise levels.

The Interrogating Input must be non-DC, such as a sine wave or a pulse train, and its frequency must be such that:

$$f_{carrier} > m \cdot f_{a\text{-}max} + f_{s\text{-}max} \qquad \text{where}$$

f_c = carrier frequency

$f_{a\text{-}max}$ = maximum frequency of the self-generating (voltage) response

$f_{s\text{-}max}$ = maximum frequency of the non-self-generating (impedance-based) response

m = separation factor between two frequencies of which the lower is to be suppressed with a filter and the upper is to be transmitted through the filter (high-pass filter).

Common values of m in commercial designs range from 3 to 30 with 4 very common. Give a filter designer two octaves and that is usually sufficient for the design criteria presented here.

There is also a demodulation criterion of the type:

$$f_c > (k+1) f_{s\text{-}max} \qquad \text{where}$$

k = separation between two frequencies, the lower of which is to be transmitted through a filter and the upper one suppressed by it (low-pass filter). The same value for k can be used as for m.

Whichever of the two design equations gives the highest value for f_c is the appropriate design value.

Frequency analyses of the self-generating response such as in Photos 3 and 4 in Fig. 24, and of the total response such as in Photos 6 through 9 in Fig. 25, would give the required values for $f_{a\text{-}max}$ and $f_{s\text{-}max}$. See Ref. 27 for a detailed discussion, case studies, examples and references.

With the measurement system bandwidth limited at 100 kHz and apparently sufficient to reproduce the wave shapes involved, a carrier frequency of 500 kHz would be sufficient with $k = m = 4$.

Such a system can not be purchased commercially for tests such as this one, although one can readily be home-made. A 500 kHz system, designed according to the criteria specified above, and used for strain measurement on high-speed rotating machinery is reported in Ref. 35. It successfully suppressed self-generating (voltage) noise levels which were orders of magnitude higher than the signal.

ANSWER TO QUESTION NO. 22:

Since a carrier system might not be available, the only other ways in which the minimize the noise level with respect to the signal is to increase the signal:

Use a higher value for R, such as 1000 ohms

Use a higher value for I such as 30, 35, 40 ma depending on the self-heating effect (See Ref. 27).

Use a higher value for K, a relatively unproductive route since self-temperature compensation and linearity are usually compromised for K-factors other than near 2.

ANSWER TO QUESTION NO. 23:

Photo 7 in Fig. 25, for the 2 oz. hammer, shows that the incident, initial compression pulse has completely passed through the gage before the reflected compression pulse returns from the clamped end. The strain returns to zero between the incident and reflected pulses (see also Fig. 22). That is not the case for the larger projectiles (hammers).

In Photo 6, for the 8 oz. hammer, the pulse is wide enough so that the incident pulse is still passing through the gage as the leading edge of the reflected pulse returns.

Only Photo 6 will permit computation of the Reflection Factor for Stresses of the clamped end:

It is the ratio of the amplitude of the Incident Pulse to the Reflected Pulse: 2.8/1.6 = 0.57

The assumption is made that the 16.4 inch round trip from the gage to the clamped end back to the gage has not attenuated the pulse amplitude significantly. The amplitude of the reflected pulse should, in reality, be slightly higher than it is and the value for Reflection Factor is therefore a low value.

There is no simple way for estimating the effect of this idealizing assumption.

ANSWER TO QUESTION NO. 24:

The time elapsed between the incident and first reflected pulse corresponds to 16.4 inches of travel. The time between the reflected compression pulse and its return from the free end as a tension pulse (near the middle of the photo) corresponds to a 46 inch round trip. The tolerance on the 2nd calculation should be less than for the first because the resolution on the photo will be better.

2.4 div = 0.24 msec for 46 inches = 191,667 inches/sec. The uncertainty on this calculation is fairly large, however.

ANSWERS TO QUESTION NO. 25:

The photographs on page 30 show Post Impact Vibrations – a few cycles and then a fairly large number, for two gage locations. It is seen that the maximum strain may occur *during* these post impact vibrations.

The page 29 shows records from individual gages and with different masses of impacting hammers.

It can be seen that the strain concentration factor under transient.conditions does not depend solely on geometry and loading condition, but also on the impacting object and on time, which is not the case for static strain concentrations.

The superposition of the Post Impact Vibrations is probably responsible for the high strain concentrations *after* the initial strain pulse has passed the hole.

Note also the noise level checks on page 30 and the shunt calibration showing the rise-time of the measurement system without the strain gage.

ANSWERS TO QUESTION NO. 26:

The relationship cited, is derived for pulse-amplifier design and holds in the limit when an infinite number of stages are sequenced, that is, the ultimate roll-off at the high frequency end approaches infinity.

It also holds only for *monotonic systems* for which the roll-off is always in one direction only, without resonant humps. The frequency response of a length-averaging side-mounted transducer such as a strain gage, has resonant humps as seen in Figs. 27 and 28. Thus the relationship can not be used for this experiment.

It should be noted that a number of investigators have applied this equation to strain gages and that their conclusions, therefore, must be somewhat suspect.

ANSWERS TO QUESTION NO. 27:

See the earlier discussion of triggering on p. 17 and 18.

ANSWERS TO QUESTION NO. 28:

The Trigger Delay Time is the time between the arrival of the trigger signal at the CRO terminals and the start of the sweep. That property is not specified for the Tektronix 502 CRO. It was found to be about 50 μsec. See Figs. 20 & 20A.

Knowing the wave propagation velocity and the distance the wave traveled between the impacted end and the gage location (23 inches), it is possible to extrapolate backwards to the instant of impact when the trigger signal arrived at the CRO terminals, as shown on Fig. 20. The Trigger Delay Time can then be estimated.

From Fig. 20A: The wave arrives at the gage location which is 23 inches from the impacted end at 115 μsec after impact when traveling at 200,000 inches/sec. But only 1.3 cm at 50 μsec/cm sweep speed are visible: 65 μsec. Thus the impact must have occurred 50 μsec before the appearance of the CRO beam, implying a 50 μsec trigger delay time.

The impact lasted 80 μsec as seen from Fig. 20A and the discussion above, since impact is over 0.7 divisions = 35 μsec before the arrival of the strain wave at the gage location.

Notice that impact is all over before the gage realizes that it has occurred! Technically, the display in Fig. 20A is of post-impact vibrations!

ANSWERS TO QUESTION NO. 29:

Two simple methods exist to identify the end of impact:

- Trace Blanking can be initiated at end of impact when the hammer leaves the bar and a -6 volt pulse is generated at the trigger terminals.
- The trigger signal can be recorded on a CRO channel, showing the end of impact. See Figs. 20 and 20A.

ANSWERS TO QUESTION NO. 30:

Of the many methods of observing/recording high speed transient phenomena, a brief discussion of the major ones is given.

Analog CRO: That is the method used in this experiment.

It has the advantage of not being compromised by any sampling process and possible either loss of data by pre-filtering or aliasing without pre-filtering.

It has the disadvantage that the record can not be recreated or re-played. It must be analyzed from the photograph.

Magnetic Tape Recorder – Direct Record, Analog: The old, direct-record, analog tape recorder has two disadvantages:

- It does not respond to DC; in fact its low-frequency limit is so high that Undeshoot becomes a real problem for pulse-type measurements. It could not be used on this test if the pulse tail wave shape were important.
- The thickness uniformity of the magnetic layer on the tape is critical and any non-uniformity would be reflected in non-uniform calibration.

The direct record analog tape, however, did have two distinct advantages:

- Its performance was not compromised by loss of data because of pre-filtering for anti-aliasing purposes.
- Its frequency response at the upper end extended into regions needed for impact testing.

It has been the author's strong conviction (Ref. 36) that all tests such as this should be recorded on an analog recorder, either CRO or, preferably, direct record magnetic tape, in parallel with whatever sophisticated, real-time, on-line, interactive, programmable, etc., recording system is now state-of-the-art. It is then possible to verify whether or not high-frequency information has been lost to the pre-filtering operation necessary for all AM, FM or digital (i.e., non-analog by the definition of the *Unified Approach*) operations.

Magnetic Tape Recorder – FM: The FM tape recorder does exhibit frequency response to DC and thus no Undershoot problems. But it also uses pre-filtering, eliminating high frequency data before the modulation process, data which the user will never know existed. Today's FM tapes do have the high-frequency response needed to display impact data of the type to be acquired in this test.

Transient Capture, Digital CROs or Devices; The digital storage based methods offer a great advantage:

- The data are in a form which can be replayed, to any time scale, for subsequent analysis, manipulation or processing without compromising the originally stored data.

The disadvantage again is:

- The data had to be pre-filtered to avoid aliasing, possibly removing high-frequency information which the user will never know was there. Without pre-filtering the data, the danger of aliasing high-frequency signals into low-frequency

noise levels, forever buried in the data, exists.

As pointed out in Refs. 27 and 36, the only procedure to circumvent the problems and use the advantages of non-analog measurement systems: AM, FM, PM, PAM, PFM, PPM, PDM, Digital, etc., is to use the record from a direct record magnetic tape recorder to establish the highest frequencies present in the signal, and then to select a sampling rate or carrier frequency to guarantee their reproduction.

Cathode Ray Oscilloscopes: Unless the CRO has a memory of its own, available in various forms and with various persistences, a photographic record of the event must be made with a camera, usually one for which the shutter is open for a single sweep on the CRO.

ANSWER TO QUESTION NO. 31:

Strain Gage: Strain gages of the type used here, are linear up to 1% to 3% strain, 10,000 to 30,000 $\mu\varepsilon$. The strains encountered in this experiment are just a few percent of that range. Even the maximum strain envisioned: 1000 $\mu\varepsilon$ is still in the linear region.
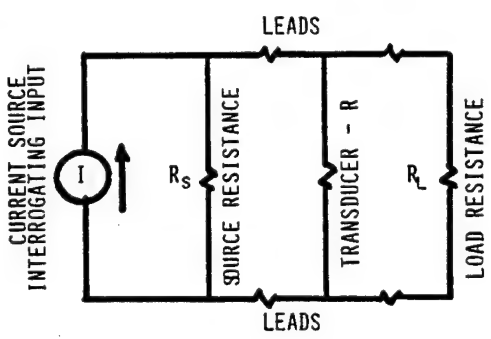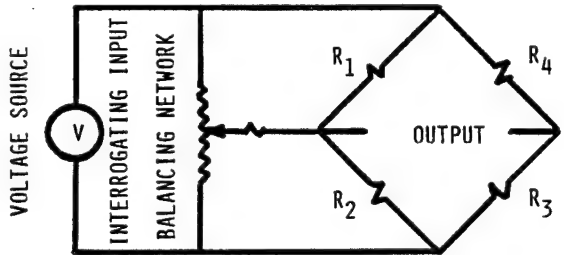
Amplifier: The maximum input signal is specified at 0.1 v peak-to-peak. The strain gage output is 38.5 $\mu v/\mu\varepsilon$ which, at the maximum postulated strain of 1000 $\mu\varepsilon$ is less than 40 mv.

CRO: Since the CRO was balanced before use, its initial output is zero, near the middle of the linear range for positive and negative inputs. The CRO linearity, is not stated in the specifications but should be within just a few percent when properly adjusted, used on Single Ended Coupling, and so long as the signal is on screen.

ANSWERS TO QUESTION NO. 32:

Ref. 15 provides a detailed discussion of the relative merits of the equal-arm Wheatstone bridge when compared to the Constant Current Circuit as used here. A brief summary is given below.

COMPARISON BETWEEN CONSTANT CURRENT AND EQUAL-ARM WHEATSTONE BRIDGE CIRCUITS

Constant Current Circuit	Criterion	Equal Arm Wheatstone Bridge
	The Circuits	
Linearity only limited by the non-infinite Current Source Output Impedance and the non-infinite Load Impedance. Under ideal boundary conditions, this circuit is linear. Ideally, $R_S \Rightarrow \infty$, $R_L \Rightarrow \infty$	Linearity	Always non-linear. Maximum non-linearity is approximately the unit resistance change, $\Delta R/R = K.\varepsilon = 2.2 \times 1000 \times 10^6$ at maximum expected strain, less than 1/4% here so not a real criterion. For semi-conductor strain gages or resistance thermometers, this is a real problem!
Highest possible Circuit Efficiency for maximum Transfer Ratio: $I.R.K$ $\mu v/\mu\varepsilon$. In this experiment: $0.025 \times 700 \times 2.2 = 38.5$ $\mu v/\mu\varepsilon$. This is almost twice the design target value.	Transfer Ratio or Circuit Efficiency	Circuit Efficiency of 1/2. Always half the output available from a Constant Current Circuit. In this experiment: 19.25 $\mu v/\mu\varepsilon$. Since the design-target was 20 $\mu v/\mu\varepsilon$, this value would still be barely acceptable, except that the signal-to-noise ratio would be half that of the constant current circuit.
Resistance-subtraction is not possible. Self-compensated transducers must be used when such compensation is required. Voltage-subtraction is possible and is, in fact, used in this experiment. The two strain gages are arranged in a non-inductive, bifilar manner to subtract any magnetically-induced voltages.	Electrical Compensation	By placing transducers in any two adjacent bridge arms it becomes possible to subtract resistance changes in those transducers. This is the basis of electrical temperature compensation, for example, sometimes called "active-dummy" compensation. Voltages in adjacent arms can be added or subtracted depending on the polarity of their connection.

In the traditional constant current circuit as shown here and discussed in Ref. 15, the DC output from the circuit: E = I.R = 17.5 volts must be filtered through RC-coupling or AC-coupling so that the small, millivolt-signals can be observed. The filter dictates the low-frequency limit, here 1.6 Hz. Thus the circuit was only useful for dynamic measurements, which explains the title of Ref. 15, constrained by its 30-year-old technology. In modern signal conditioning it has become possible to read the signals, here some 200µε generating 7.7 mv to 1% in the presence of the 17.5 volt offset. This requires a resolution of 100 µv at the 17.5 volt level, about 4-1/2 ppm. It has also recently become possible to buck out the DC voltage and obtain the advantages of a Wheatstone Bridge combined with those of a Constant Current Circuit. It should be noted that constant current sources with the specifications required for *this* application as used in *this* experiment, are not commercially available and must be home-made.	Response to DC	Since a bridge can be "balanced" - i.e., adjusted to zero output for zero measurand input, it is possible to observe the small, millivolt, outputs directly and down to DC, i.e., zero frequency. Until recent developments in technology, this was considered the greatest advantage of the bridge circuit over he constant current circuit. Also the fact that constant current sources for the application as used here, have to be home-made may be considered a disadvantage for the Constant Current Circuit application.
The Constant Current Circuit is Single Ended. The input-transducer, current source and read-out-transducer are on a common ground. No differential coupling is possible. To some measurement engineers this is a great disadvantage. The author feels it a great advantage. When nothing is floating, noise levels are less likely to be picked up. The measurement system performance is not dependent on common mode rejection problems, which can be severe. See also Ref. 27.	Differential Coupling	A bridge can be operated *Grounded Input to Floating Output*, i.e. differentially coupled at the output. The Common Mode which must be rejected by the CRO is E = I.R. = 17.5 v. Very few CRO's, and certainly not the Tektronix 502 or 502A are capable of rejecting that common mode voltage at Sensitivity settings of 100 or 200 µv/div. Such CROs will be driven non-linear (see Ref. 27). Also, when the output floats, it is more likely to pick up noise levels which must now be common-mode-rejected.
The ripple factor of the current source must be in the order of 2 ppm (see earlier section) because any ripple feeds right through to the output.	Ripple Factor of the Interrogating Input	The ripple factor for the voltage source will be mostly suppressed through subtraction at the output terminals and by common mode rejection.
Nothing can be simpler than a Constant Current Circuit. One Input Transducer, one Constant Current Source, one Read-Out-Transducer and inter-connecting cable. No balancing resistors, no bridge completion resistors, no choice in grounding. Simplicity is an advantage.	Simplicity	A bridge requires bridge completion resistors, a balancing circuit and the selection of a ground point – only one of the four corners can be grounded. It is inherently more complicated than the Constant Current Circuit. Every additional component may be a reliability problem.

The use of a Constant Current Circuit in this Experiment was a deliberate exercise in the use of a non-traditional but superior measurement system in an application usually considered as challenging.

The first circuit used with bonded resistance wire strain gages in September 1936 by Edward E. Simmons, Jr., their inventor, was a constant current circuit operated at a high efficiency of 64.3% with a Transfer Ratio of 64.3 µv/µε! Almost twice the output from the circuit used here. He had a 500 ohm gage with 100 ma current applied as a single pulse because of self-heating problems. The measure-ment was of impact forces with the first strain-gage-based load cell.

CONCLUSIONS:

An experiment, usually considered as challenging, was designed and carried out successfully using the systematic, methodological *Unified Approach to the Engineering of Measurement Systems*. Valid, noise-free data were harvested by design.

The material presented in this paper was included in the lectures for the Junior level, first course on The Engineering of Measurement Systems in the Laboratory for Measurement Systems Engineering (Lf/MSE) at Arizona State University, by the author, from Fall 1959 through Spring 1977, as it was developed during that period.

Lf/MSE prided itself in producing Measurement-Aware, Measurement-Oriented, Measurement-Conscious Engineers at the BSE, MSE and PhD levels during that period.

Lf/MSE offered six courses from Junior through post-graduate levels. Each course met for 16 weeks, four hours of lecture and 2 hours of laboratory or lab preparation each week. Some 965 students took the first course for which this paper represented the final examination. The author is still in touch with over 850 of them through a semi-annual *Lf/MSE Newsletter*, now in its 20th year (1993).

REFERENCES

1. Stein, Peter K. **Measurement Engineering, Vol. I – Basic Principles**, Stein Engineering Services, Inc. 1st edition, 1961; 6th edition, 1970.

2. Stein, Peter K. *Experiment No. 8: Mechanical Impact – Traveling Wave Phenomena: A Problem in Data Validation.* **Lf/MSE Publ. #39**, Stein Engineering Services, Inc., May 1970.

3A Broberg, K. B. *Some Aspects of the Mechanics of Scabbing,* **Stress Wave Propagation in Materials**, N. Davids, Editor. Interscience Publ., N.Y., pp. 229-246, 1960.

3B Rinehart, John S. *The Role of Stress Waves in the Comminution of Brittle, Rock-Like Materials.* pp. 247-269 in the publication referenced in Ref. 3A.

4. Duvall, Wilbur I, Thomas C. Atchison. *Rock Breakage by Explosives.* **Report of Investigations 5356**, U. S. Dept. of the Interior, Bureau of Mines, Sept. 1957.

5. Stein, Peter K. *The Unified Approach to the Engineering of Measurementg Systems: Yesterday's Recipe for Tomorrow's Source of Measurement Engineers.* **Proc. 14th Aerospace Test Seminar**, March 1993. Institute of Environmentsal Sciences, 940 E. Northwest Highway, Mount Prospect, IL 60056

6. Davids, N. *Some Problems of Transient Analysis of Waves in Plates.* pp. 271-288 , publication referenced in 3A

7. Bonin, C. C., *Water-Hammer Damage to Oigawa Power Station,* **Jnl. of Eng'g for Power**, April 1960, pp. 111 ff

8. Lambert, John W. *On the Nonlinearities of Fluid Flow in Nonrigid Tubes,* **Jnl. Franklin Institute**, Vol. 266, No. 2, August 1958, pp. 83 ff.

9. Luebke, R. W., *The Box Car Dynamic Environment.* **Shock & Vibration Bull. 41**, Part 4, pp. 141-160, Dec. 1970. Example cited was mentioned during the presentation but not published. From Shock & Vibration Information Analysis Center, Booz, Allen & Hamiklton, Inc., 2711 Jefferson Davis Highway, Suite 600, Arlington, VA 22202.

10. Fischer, H. C. *On Longitudinal Impact: Parts I–VI.* **Acta Scandinavics**, Martinus Nijhoff, 1960, The Hague, Netherlands.

11. Mescall, J., R. Papirno, *Spallation in Cylinder–Plate Impactt,* **Experimental Mechanics,**, July 1975, pp. 257 ff

12. Brennan, J. N., Editor. *Bibliography on Shock and Shock-Excited Vibrations, Vols. I & II.* **Penn State Univ Engineering Research Bulletin 68**, University Park, PA, Sept. 1957.

13. Stephens, A. W., Demer, L. J. *Effects of Strain Rates on the Mechanical Properties of Metals.* **Engineering Research Lab Rpt.**, Jan. 1962, Univ of Arizona, Tucson, AZ

14. Stein, Peter K. *Pyro-Shock, Impact, Explosions and other high-Speed Transients: Some Thoughts on "TQM" – Total Quality Measurements.* **Lf/MSE Newsletter #39**, Jan. 1993, Stein Engineering Services, Inc. **Proc. Aerospace Test Seminar, 1993**. Institute of Environmental Sciences. Early version in: **Proc. Western Regional Strain Gage Committee, Albuquerque, August 1992**, from WRSGC, 44 N. Benson, Upland, CA 91786.

15. Stein, Peter K. *The Constant Current Circuit for Dynamic Strain Measurement.* **Strain Gage Readings**, Vol. VI, No. 3, pp. 53-72, August-September 1963, also **Lf/MSE Publ. #46**, both: Stein Engineering Services, Inc. **BLH Measurement Topics**, Vol. 6, No. 2, pp. 1-12, Spring 1968. **Instruments & Control Systems**, Vol. 38, No. 5, May 1965, pp. 154-175.

16. Kearns, Q., F. Kirsten, C. Winningstad. *Pulse Response of Coax Cables, Counting Handbook,* June 5, 1964. **UCRL-3307**, Lawrence Radiation Lab, Univ of California at Berkeley.

17. Rohrbach, Chr., N. Czauja, *Deutung des Mechanismus des Dehnungsmesstreifen und seiner wichtigsten Eigenschaften an Hand eines Modells.* **Materialprüfung**, I/4, April 20, 1959.

18. Rohrbach, Chr., N. Czaika. *Das Kriechen von Dehnungsmesstreifen als Rheologisches Problem.* **Materialprüfung**, 2/3, March 20, 1960.

19. Rohrbach, Chr., N. Czaika. *Über das Kriechen von Dehnungsmessetrifen unter statischer Zugbelastung: Teile I, II, IIII.* **Archiv für Technisches Messen**, Dec. 1959, Feb. & Mar. 1960.

20. Sill, Robert D. *Shock Calibration of Accelerometers at Amplitudes to 100,000 g, Using Compression Waves.* **ISA Annual Conferfence, Spring 1983**, from *Endevco*, 30,700 Rancho Viejo Rd, San Juan Capistrano, CA 92675

21. Sill, Robert D. *Testing Techniques Invlved with the Development of High Shock Acceleration Sensors,* **Proc. 12th Transducer Workshop**, Cocoa Beach, FL, June 709, 1983, Range Commanders' Coouncil Secretariat, White Sands Missile Range, NM 88001. Also from *Endevco,* see Ref. 20.

22. Umeda, Akira, Kazunaga Ueda. *Characteristics of Strain Gage Dynamic Response Using Davies' Bar and Lasr Interferometry.* **Proc. VIIth International Congress on Experimental Mechanics**, June 8-11, 1992, Las Vegas, NV, pp.837-842. Society for Experimental Mechanics, Bethel, CT.

23. Ueda, Kazunaga, Akire Umeda. *Dynamic Response of Shock Accelerometers Measured by Davies' Bar Technique and Laser Interferometry.* **Proc. VIIth International Congress on Applied Mechanics**, June 8-11, 1992, Las Vegas, NV, pp. 1666-1673. Society for Experimental Mechanics, Bethel, CT.

24. Sill, Robert, *High-G Acceleration Calibration,* **Measurements & Control**, February 1985, pp. 142-148.

25. Thomsen, Erich G., Harlette H. Thomsen, *Litho-Mechanica and Archaeology,* **Proc. 51st Annual Meeting, American Assoc. for the Advancement of Science**, Pacific Division, June 23, 1971, Univ of Cal, Berkeley, CA.

26. Oi, Koshiro. *Transient Response of Bonded Strain Gages* (in Japanese) **Jnl of Japan Soc of Mechanical Engineers**, Vol. 69, #575, pp. 56-61, 1966. English version: **Proc. S.E.S.A. Vol. 23, No. 2**, pp. 463-469, 1966. Presented at 1st International Congress of Experimental Mechanics.

27. Stein, Peter K. **The Unified Approach to the Engineering of Measurement Systems – Part I: Basic Principles.** Monograph, 134 pp, Stein Engineering Services, Inc., 5602 E. Monte Rose, Phoenix, AZ 85018. March 1992, ISBN # 1-881472-00-0

28 Durelli, A. J., Dally, J. W. and Riley, W. F. *Stress Concentration Factors under Dynamic Loading Conditions,* **Armour Research Foundation**, Illinois Institute of Technology, December 1958.

29. Durelli, A. J., Dally, J. W., and Riley, W. F. *A Photoelastic Approach to Transient Stress Problems Employing Low Modulus Materials.* Same source as Ref. 28.

30. Dally, J. W., Durelli, A. J., and Riley, W. F. *Photoelastic Study of Stress Wave Propagation in Large Plates.* Same Source as Ref. 28, but November 1958.

31 Maslen, K. R. *On the Effect of Gauge Length on the Response of Strain Gauges to Dynamic Strain,* **RAE Tech Memo Instn 284**, May 1960. Royal Aircraft Establishment.

32. Stein, Peter K. *Some Notes on Second Order Systems: Responses of Systems to Steps and Pulses,* Januaty 1975, revised August 1985. **Lf/MSE Publ. 35/36/40**, Stein Engineering Services, Inc., 5602 E. Monte Rosa, Phoenix, AZ, 85018.

33. Stein, Peter K. *Excerpts fom Measurement Engineering, Vol. I,* cited as Ref. 1 which is no longer in print. **Lf/MSE Publ. 65**, same source as Ref. 32 above.

34. Ometron (USA), 620 Herndon Parkway, Suite 200, Herndon, VA 22070.

35. Stein, Peter K. *Our Engineering Education: The Not–So–Scientific Method*. Originally prepared for the December 3, 1979 Session: The Role of Laboratories in Engineering Education, ASME Winter Annual Meeting, New York, NY. Published in up–dated form: **Lf/MSE Newsletter # 38**, Summer 1992, and **Lf/MSE Publication No. 74**, various editions from 1979 through 1992. Stein Engineering Services, Inc., 5602 E. Monte Rosa, Phoenix, AZ 85018. A "de-fanged", less provocative version, co-authored by Charles P. Wright was published in **Proc. Aerospace Test Seminar 1992**, Institute of Environmental Sciences.

36. Stein, Peter K., *Better the Imperfect Truth than Perfectly Accurate Garbage, or: The Real-Time On-Line Interactive Super-Sophisticated Data-Acquisition System vs. the "Old" Analog Recorder*, **Experimental Techniques**, Nov. 1985, p. 3.

37. Umeda, Akira and Kazunaga Ueda. *Measurement of the strain gage dynamic transverse and longitudinal sensitivity using pulse elastic waves and laser interferometry.* **Recent Advances in Experimental Mechanics**, Proc. 10th International Conference on Experimental Mechanics, Lisbon, Portugal, July 18-22, 1994, Vol. 1, pp. 319-24.

38. Rajic, N. Y. C. Lam, A. K. Wong. *Thermomechanical Detection of a Plastic Zone*. Same source as Ref. 37, pp. 3-10

NOTE:

Part I of this paper was presented at the **14th Aerospace Test Seminar 1992** and was included in its Proceedings available from the Institute of Environmental Sciences.

It covered the philosophy of *The Unified Approach to the Engineering of Measurement Systems* and some of its achievements during the last third of a century.

FIGURES

SESSION 4

DEVELOPMENT

DEVELOPMENT OF A GUIDANCE DOCUMENT
FOR LIGHTNING PROTECTION OF DOE FACILITIES *

R. T. Hasbrouck
K. C. Majumdar

Lawrence Livermore National Laboratory, Livermore, California, 94551, USA

We are developing a guidance document for the lightning protection of US Department of Energy (DOE) facilities to satisfy the requirements of the department's order DOE 5480.28, *Natural Phenomena Hazards (NPH) Mitigation Performance Goals for Structures, Systems and Components* (SSCs). This order specifies a systematic process of well defined and integrated design and evaluation criteria for the protection of SSCs. Our document introduces the idea of Lightning Hazard Management because there is no single document that presents a unified approach to lightning protection. Earlier versions of the US National Fire Protection Association (NFPA) Code, *Lightning Protection*, NFPA-78, only addressed the protection of structures. This is also true of the International *Lightning Protection Standard*, IEC-1024 and the Underwriters Laboratories recently issued Standard for Safety, *Lightning Protection* Components, UL 96.

1.0   INTRODUCTION

This paper provides an overview of our guidance document. It introduces Lightning Hazard Management, a unified approach to lightning protection that combines facility categorization (not discussed in this paper) and hazard identification with a new concept—the Lightning Safety System. We do not intend to develop a new lightning code or standard, but rather reference other applicable codes, standards and guides. Using the graded approach to systematic risk management allows for in-depth protection, and aids in ensuring personnel safety and the optimizing of resource protection.

Prior to being issued, this guidance document, currently in draft form, will be submitted to reviewers at a number of DOE facilities.

2.0   LIGHTNING HAZARD MANAGEMENT

2.1   Hazard Identification

Hazard identification considers the severity of the hazard and the likelihood of its occurrence.

2.1.1 Lightning Characteristics

Thunderstorms produce several types of lightning: intracloud (IC), intercloud, cloud-to-ionosphere, and cloud-to-ground (C-G). Total lightning (all types combined) varies with geographic location and is greatest in the tropics. The greatest percentage of total lightning is generally IC. However, because

C-G lightning reaches the ground, and objects on the ground, it represents the greatest threat to personnel, operations, structures, systems and components. A single C-G lightning event, called a flash, typically lasts for approximately one-half to one second, during which (for negative lightning) a large quantity of positive charge is transferred from earth to cloud in what is called the return stroke. A flash consists of one or more consecutive return strokes, each a current pulse of thousands to hundreds of thousands of amperes, lasting 50–100 microseconds. This high-amplitude pulse is often followed by a continuing current of several hundred amperes lasting for hundreds of milliseconds. During a flash, the struck object must conduct the return-stroke current, and it is this current that can produce damage, both directly and indirectly.

2.1.2 Severity

The severity of a lightning stroke is usually related to the peak amplitude of its return-stroke current. Statistical data for the range of peak currents and the probability of their occurrence have been accumulated by researchers over a number of decades. For negative lightning, the 99th-percentile value (i.e., 1% of lightning exhibits this or a larger peak current) is 200,000 amperes (200 kA), and is considered to represent a severe threat. Such a stroke could be described as having a very-low frequency, or likelihood, with high consequences. It is important to keep in mind that intense thunderstorms can produce several thousand C-G lightning flashes, and 1% of those flashes can be expected to be 200 kA or

287

greater. The less frequent positive lightning—where positive charge travels from cloud to earth—is known to exhibit maximum values of 400 kA or more. However, the occurrence of such flashes is significantly lower than for negative lightning. Another way to present peak current data is in deciles. If n is the total number of flashes being considered, each decile will contain $n/10$ flashes. The average value of peak current per decile is then calculated. The tenth decile represents the severe stroke.

2.1.3   Probability of Being Struck

The C-G lightning hazard for a specific site is expressed in terms of ground-flash density—the number of C-G flashes per square kilometer per year. Ground-flash density calculations for a particular site take into account the latitude and number of thunder days per year. Although the total number of lightning flashes decreases with increasing latitude, the percentage of C-G flashes increases. Table 1 lists calculated ground-flash densities for three DOE's sites located in the SE, center, and NW of the US. Two different equations, derived by different researchers, were used to obtain the ground-flash density values shown. Since the equations are empirical and their associated data are based upon statistical correlations, they possesses inherent uncertainties. This is true for the modeling of any natural phenomenon. In the future, analysis of the large volume of archived, C-G lightning data, acquired by the national lightning detection network, will provide more realistic, site-specific values for ground-flash density.

Assuming that lightning strikes are evenly distributed over a given area, the probability of an object being struck can be estimated from the product of its attractive area and the ground-flash density (flashes/km^2/yr). Attractive area is a function of the structure's ground-surface area and height, and the stroke amplitude. A negatively-charged channel, the stepped leader, moves in downward steps from cloud to earth, carrying the cloud's full negative potential of 50- to more than 100-million volts. Striking distance—the stepped leader's final jump to ground or to a grounded object—is a function of the quantity of charge in the channel and thus the amplitude of the return-stroke current.

Table 2 shows that lightning, of some amplitude, can be expected to strike the facility—described in Section 3.0—once every 2.7 years. Observe how, because of the tall light poles, the attractive area greatly exceeds the 45,000 m^2 surface area enclosed by the poles, thereby increasing the probability of being struck. Such probability calculations can be useful for comparing similar structures in different geographical areas and determining the effect of structure height. In reality, ground-flash density is not uniform, being affected by factors such as local geography and climate. Some points to consider about a 200-kA (severe) stroke: it can cause significantly greater damage than a 20-kA stroke; its greater striking distance increases the attractive area of elevated structures, increasing the probability of their being struck; it represents a small percentage of the total C-G lightning. For large-amplitude strokes, elevated structures provide a "protective shadow" (often called a "cone of protection") over nearby lower structures. Since the shadow area decreases for smaller strokes, which occur with greater frequency than large strokes, their effects should not be overlooked.

2.2   Lightning Safety System

The lightning safety system (LSS) offers a unified approach that integrates four lightning-safety elements: lightning threat warning system, threat warning response plan, lightning safety system, and safety system certification plan. The extent to which each LSS element is implemented at a particular site will depend upon the mission of the facility and the element's impact upon the safety of workers, the public, and the environment. Such determinations must be made by those responsible for risk management.

2.2.1 Lightning Threat Warning System

If no one is paying attention to the weather (or weather reports) a thunderstorm can develop locally, or move into the area, unnoticed—with the first lightning flash providing the first warning. The purpose of a lightning threat warning system (LTWS) is to acquire and display timely and reliable lightning threat warnings.

Currently, no single piece of equipment can provide no-miss/no-false-alarm lightning threat warning. A credible LTWS should employ two or more types of monitors, with the right LTWS for a particular site depending upon the level of perceived risk and what resources are threatened.

288

C-G lightning occurs randomly, making it impossible to accurately predict when and where it will strike. However, several detection techniques are available, ranging from AM-radio receivers and electro-optical sensors, to weather radar and sophisticated systems that locate lightning by triangulating on its electromagnetic or magnetic radiation. IC lightning is known to occur from five to 30 minutes prior to the first C-G discharge. Thus, an ideal LTWS would combine the monitoring of cloud electrification, IC detection, and C-G location and tracking.

Methods that can be used as LTWS monitors are summarized below:

♦ Direct observations of the weather, made by a trained individual.

♦ Reports from the National Weather Service, or a commercial weather-warning service.

♦ Optical detector(s)—either hand held or unattended, that can detect IC lightning and sound an alarm.

♦ Flash detector.

♦ Electric-field sensors for measuring electrical charge in nearby clouds.

♦ A site-dedicated lightning detection system.

♦ Display of data provided by a wide-area lightning detection network.

2.2.2 Lightning Warning Response Plan

Having a lightning warning response plan (LWRP) ensures that standardized procedures are in place for responding to a lightning-threat alert and lightning-hazard alarm. The LTWS should provide enough advance warning to permit the established safety plan to be carried out in an orderly fashion, while keeping false alarms to a minimum. The LTWS should provide an *alert* when a lightning threat is identified and an *alarm* when the threat has evolved into a hazard. It must also reliably report when the alarm and alert states cease to exist. When such information is timely and reliable, decisions can be made regarding the curtailing and resuming of at-risk operations and activities—ranging from personnel working outside, to tasks involving dangerous or hazardous materials. These decisions will be based upon information provided by one or more of the methods listed above.

The following are suggested warning conditions and responses:

All Clear—no suspicious clouds; no sign of a thunderstorm.
- carry out normal operations.
- utilize main electrical power.
- monitor weather conditions.

Yellow Alert—positive indications that a lightning threat has been identified.
- prepare to curtail vulnerable or dangerous operations.
- activate emergency backup power system.
- prepare to move to safe shelter.

Red Alarm—positive indications that a lightning hazard exists.
- curtail vulnerable or dangerous operations (unless doing so presents a greater danger).
- transfer electrical load to emergency backup power system.
- move to safe shelter.

Return to Yellow Alert—positive indications that lightning hazard is dissipating.
- prepare to resume vulnerable or dangerous operations.
- transfer load to main electrical power, if it is available.
- prepare to move from safe shelter.

Return to All Clear—no threat of lightning.
- resume normal operations.
- shut down emergency backup power system.
- continue to monitor weather conditions.

2.2.3 Lightning Protection System

Our guidance document presents a lightning protection system (LPS) as an integrated system for protecting structures, systems and components from lightning. In the past, an LPS involved only air terminals (lightning rods) and their associated conductors, bonding, and grounding systems—using ideas and methods that have not changed significantly since Ben Franklin's era—with the focus being protection of structures. Our LPS consists of a lightning grounding system (LGS) combined with systems and components protection (SCP). Today's codes and standards more than adequately present LGS criteria.

Earlier-generation electrical and electronic systems and components used vacuum tubes, relays, and analog control and computation devices. Consequently, they were significantly more robust against the effects of voltage

transients (including those produced by lightning) than are today's sophisticated, computer-based systems with their high-density/low-power microcircuit components. Transient over-voltages may immediately destroy solid-state components, or cause latent failures, where transient-weakened components fail months after the lightning event. Lightning-produced voltage transients can also produce interference (a noise signal) that easily upsets unprotected digital systems.

NFPA-780-1992 makes a brief reference to the need for surge suppression for all conductors penetrating a structure. To achieve the in-depth protection necessary to ensure against system upset and failure, we introduce the *fortress concept*, a proven lightning protection methodology. First-level protection is provided by an LGS. (Note: although called for in NFPA-780 and other codes, air terminals are not essential if properly grounded conductors are run on the roof of the structure.) All electrically-conductive paths that penetrate the building (e.g., metallic pipes and conduit, vent stacks, etc.) must be bonded to the lightning grounding system externally, at the point of entry (POE). Penetrating electrical conductors (e.g., power, communications and data lines) must be contained within metallic conduit or overall shielding. The conduit or shielding must be terminated (wherever possible) at, and bonded externally to, the lightning grounding system at the POE. This limits the magnitude of lightning current conducted into the structure.

Proper SCP ensures that all electrical conductors pass through transient-limiter (surge-arrestor) components located inside the structure, as close as possible to the POE. With a properly installed LGS, limiters need only accommodate a small portion of the lightning current transient, typically in the range of several tens of kA. Within the structure, the number of component protection levels employed will depend upon the consequences of upset or failure. Transient limiters—having a power rating lower than that required at a POE—are recommended at the power and data input points of individual systems and components. Critical-function and high-value components that are susceptible to over-voltages should also incorporate transient limiters directly on their printed circuit boards.

2.2.4 Lightning Safety System Certification Plan

A lightning safety system certification plan (LSSC) should contain the following, site-specific requirements and methodologies for certifying and for periodically verifying the LTWS and LPS:

LTWS
- ◆ cross check IC detector with weather service information.
- ◆ periodic servicing and calibration of electric field monitors.
  - note: for national lightning network information, the NWS adheres to well-established quality assurance procedures for all their weather products.

LPS
- ◆ inspection and review
  - perform walkdown.
  - procedure review.
  - program plan audit.
- ◆ facility measurements and simulations
  - dc-resistance and radio-frequency (RF) testing.
  - finite difference analysis.
- ◆ periodic testing, maintenance, corrective action program, QA program.
  - LGS—visual inspections, dc-resistance and RF measurements.
  - SCP—transient limiters

3.0 EXAMPLE OF TESTING AS PART OF FACILITY CERTIFICATION

A recently constructed facility has been studied to determine the effectiveness of its LPS. This facility consists of a large, reinforced concrete structure surrounded by a security fence and twelve, 32-m tall light poles placed on the outer-perimeter. Described below are two tests of the LGS that constitute part of an LSSC plan. One test is traditional, the other is somewhat innovative for an LGS. Testing of the facility's SCP has not been performed and represents a challenge, because procedures for facility-scale testing of protection components are not known to exist.

3.1 DC-Resistance Measurements

Extensive LGS dc-resistance measurements were made using the three-point, fall-of-potential method described in NFPA-780. This allowed several bad or missing bonding connections to be discovered and corrected. Resistances measured from the LGS to "true earth" were about 1 ohm, well below the recommended maximum of 25 ohms. This showed—as one would expect—that the structure contains a very large quantity of interconnected metal that is in good contact with the earth. However, as discussed below, low values of LGS dc-resistance are no guarantee that lightning currents will remain harmlessly outside the affected structure.

3.2 Electromagnetic Survey

This structure gives the appearance of being electromagnetically hard. However, low-level, swept-frequency RF testing (10 kHz–30 MHz) revealed conditions that could introduce lightning-induced energy—in the form of time-varying magnetic and/or electric fields or arcing—into areas within the structure. Time-varying fields can couple energy into systems and components inductively or capacitively. Arcing can create local heating that can ignite combustibles, and inject current into otherwise isolated paths. All three forms of energy can produce electrical noise that can upset unprotected digital systems. Whether or not such energy presents a threat will depend upon the susceptibility of the systems or components exposed to that energy.

The structure interior is shielded from lightning by the outer layer of concrete-rebar that conducts most of the lightning current. However, some lightning current does enter the interior via metallic penetrations—POEs provided by vent stacks, various grounding cables, and conduits for electric power and communications signals. These POEs may be excited directly by a lightning attachment, or indirectly when lightning attaches to either the structure itself or a nearby metal light pole. A portion of the lightning current from a struck light pole will reach the POEs via underground conductive (counterpoise) cables, which are integral to the LGS, and flow into the strructure's interior.

4.0 SUMMARY

Effective lightning protection can be realized by applying the methodology of Lightning Hazard Management. Lightning threat warning can be accomplished using commercially available systems. Recognized lightning protection codes provide detailed information for the design and installation of lightning grounding systems. However, attention must be paid to proper bonding of conductive paths penetrating a structure. Several types of devices are available for protecting systems and components from current surges and voltage transients. However, there is no code that establishes criteria for the protection of systems and components. Procedures for lightning threat warning response, and for certification and surveillance of lightning safety systems, have been recommended. Details for such procedures will be site-specific.

5. CONCLUSION

When faced with the problem of providing lightning protection for an operation or facility, risk managers can be confronted with a plethora of scientific data, commercial products, half truths, and folklore. Our guidance document presents an organized, intelligent approach to categorizing the risk associated with a particular facility, and managing the lightning hazard—regardless of the magnitude of the problem. And, it will have been reviewed by people who have experience in dealing with lightning protection problems. Understanding the functions and interrelationships of the elements that comprise a lightning safety system allows risk managers to apply a graded approach in determining the most effective mix of hardware, software, and procedures to solve their particular problem. Finally, we have emphasized the importance of, and provided guidance for, the certification and surveillance of the LSS.

Table 1

LIGHTNING GROUND FLASH DENSITY AT THREE DOE SITES						
			method 1	method 2		
Facility	Lat	Td/yr	Fg	R	Fg min	Fg max
Pinellas, Florida	28	85	7.1	0.19	6.4	17.5
Kansas City, Kansas	39	50	4.2	0.27	5.4	14.8
Hanford, Washington	47	10	0.3	0.35	1.4	3.8

method 1

Fg = 0.02*Td^1.7*[0.1(1+(Lat/30)^2)]

Fg = Ground Flash Density (Fl/km^2/yr)
Td = Thunder days/yr
Lat = latitude

Pierce (1970), & Cianos & Pierce (1972),
in Golde, "Lightning," Vol. 1, pp. 481 & 487

method 2

Ft = Total flash density = 0.4 to 1.1fl/km^2/Td
 based upon: 3 fl/min, 1 to 3 hr/storm,
  500 km^2/storm, and Td/yr
Td = Thunderdays/yr
R = C-G to total ratio = (0.1*(1+(lat/30)^2))
Fg = Ground flash density =   Ft * Td * R
Fg min = 0.4*Td*R
Fg max = 1.1*Td*R

Table 2

CUMULATIVE PROBABILITY OF LIGHTNING STRIKE TO FACILITY (where Fg = 3 fl/km^2/yr)							
Ipk		D	r	Aa	Decile Prob.	Cum. Prob.	Cum. Prob.
Decile	kA	m	m	m^2	fl/yr	fl/yr	Yr/fl
1st	6	33	33	76764	2.3E-02	2.3E-02	
2nd	13	53	48	93489	2.8E-02	5.1E-02	
3rd	18	65	56	101496	3.0E-02	8.2E-02	
4th	23	76	62	108624	3.3E-02	1.1E-01	
5th	28	88	68	115399	3.5E-02	1.5E-01	
6th	35	101	74	122391	3.7E-02	1.9E-01	
7th	45	118	81	130658	3.9E-02	2.2E-01	
8th	57	138	89	140196	4.2E-02	2.7E-01	
9th	77	168	99	153061	4.6E-02	3.1E-01	
10th	112	215	113	171380	5.1E-02	3.6E-01	2.7

[area enclosed by light poles: l = 312 m, w = 144 m; A = 44,928 m^2]
D = lightning striking distance = 10*Ipk^0.65   meters
h = light pole height = 32 m above ground level
r = radius of a light pole's attractive area = (2*D*h - h^2)^0.5   meters
Aa = total attractive area of poles = (w + 2*r) *(l + 2*r) - 10*((4-PI)/4)* (r^2)   m^2
{where 10*((4-PI)/4)*r^2 accounts for overlap & area outside "attractive area" circles}
Fg = ground flash density   (fl/km^2/yr)
P = probability = Aa*(0.1*Fg)*10 flashes/year per decile

Bibliography

US Department of Energy Order, DOE 5480.28, *Natural Phenomena Hazards (NPH) Mitigation Performance Goals for SSCs.*, 1993, Washington, DC.

National Fire Protection Association (NFPA) Code, NFPA-780, *Lightning Protection*, 1992, Quincy, MA.

International Electrotechnical Commission, (IEC) Standard, IEC 1024-1, *Protection of Structures Against Lightning*, Part 1: General Principles, 1990, Geneva, Switzerland.

Underwriters Laboratories, Inc., Standard for Safety, *Lightning Protection Components*, UL 96, 1994, Northbrook, IL.

Underwriters Laboratories, Inc., Standard for Safety, *Installation Requirements for Lightning Protection Systems*, UL 96A, 1994, Northbrook, IL.

Golde, R.H., *Lightning*, Volume 1, Academic Press, New York, 1977.

Cianos, N. and E.T. Pierce, *A ground Lightning Environment for Engineering Usage*, Stanford Research Institute Technical Report, L.S.-2817-A3, Menlo Park, CA, 1972.

Hasbrouck, R.T., *Lightning—Understanding It and Protecting Against Its Effects*, UCRL-53925, Lawrence Livermore National Laboratory, Livermore, CA, 1989.

Development of Fiber Optic Sensors
for Ballistic Measurements

W. Scott Walton
Kenneth McMullen
Peter Turney
U.S. Army Aberdeen Test Center
Aberdeen Proving Ground, Maryland

Alan Kersey
Gary Cogdell
U.S. Naval Research Laboratory
Washington, D.C.

H.- T. Liu
Quest Integrated
Kent, Washington

ABSTRACT

Since 1987, Aberdeen Test Center has been involved
with several other DoD agencies and contractors in
development of fiber optic techniques to measure
ballistic events, such as chamber pressure, ballistic
shock, intense strain in armor plates, and blast
overpressure. Although many of the early efforts were
high risk study contracts which resulted in failure, some
success has been achieved recently. This paper will
briefly describe the lessons learned and describe plans
for future exploitation of fiber optic technology in
measuring ballistic events.

1. INTRODUCTION

Since 1987, the U.S. Army, Aberdeen Test Center (ATC) formerly known as the U.S. Army Combat Systems Test Activity (CSTA) has attempted to use fiber optic techniques in the measurement of ballistic events. The measurement requirements are:

Blast Overpressure: Side-on shock waves, 0.5 to 20 psi full scale, frequency response flat from 1 Hz to 40 KHz.

Ballistic Shock: Velocity change of 1 to 20 meters/second full scale, displacements of 0.01 to 15 mm, acceleration levels of 100g to 1,000,000g depending upon frequency response, which must be flat from 10 Hz to 500 Hz for "low frequency" measurements and flat from 200 Hz to 1 MHz for "high frequency" measurements.

Chamber Pressure: Internal gun pressures, 5,000 to 120,000 psi full scale, frequency response flat from 0.1 Hz to 5 KHz in most cases, and flat from 0.1 Hz to 100 KHz in special applications.

Strain: Levels up to 3000 microstrain, resolution of 10 microstrain, rise times of 1 to 300 microseconds in the vicinity of intense electromagnetic interference caused by exploding bridgewire detonators.

Rapid growth of fiber optic technology in the telecommunications industry has lead to optimistic predictions that optical techniques would replace conventional electronic measurements, within 5 to 10 years. Optical fibers would replace all of the electrical cables that now connect a weapon under test to the data acquisition systems used in large caliber firing tests.

The low cost of fiber optic components and the elimination of tedious alignment requirements (to within a fraction of a wavelength of light) has promised exciting possibilities for the measurement technology. Fiber optic techniques provide many advantages over conventional data acquisition techniques used today:

a. Safety - Electromagnetic weapons, electromagnetic armor, and electro-thermal-chemical (ETC) weapons produce 10^4 volts and 10^5 amps. Steps must be taken to protect data acquisition technicians from electrocution in the event of a malfunction. Use of non-conducting optical fibers in place of copper wire to connect the weapon to the data acquisition system eliminates this safety hazard.

b. Electromagnetic Interference - For decades, problems caused by 60 Hz electrical power, ground loops, and electromagnetic interference (EMI) have produced artifacts in measurement signals requiring precious range time for trouble shooting and remedy implementation. The use of a totally optical technique, immune to such problems, is very attractive.

c. Performance - Some optical techniques offer inherent improvements over conventional methods. Doppler shift allows very accurate measurement of velocity events that were previously measured using electromagnetic methods. Small displacements, such as seismic

mass movement in an accelerometer, deflection of the active portion of a strain gage, or movement of a diaphragm in a pressure transducer can be measured optically, eliminating problems with acceleration sensitivity, pyroelectric sensitivity to thermal transients, and extraneous sensitivity to the flash of an explosion that cause problems when conventional electronic transducers are used.

2. CASE STUDIES

Fiber optic technology is changing rapidly. Many of the new developments are kept proprietary to protect the financial position of small companies. In the discussion that follows, many of the technical details have been left out to avoid divulging proprietary information. It is believed that the following case studies will be instructional even though some details are omitted.

a. Blast Overpressure

The first application of fiber optic technology pursued by ATC was the measurement of blast overpressure produced by exploding warheads and muzzle blast in the crew areas of large caliber weapons. After reviewing a variety of proposals, four different Small Business Innovative Research (SBIR) efforts were pursued (three were initiated and funded by Eglin Air Force Base, and one was initiated by ATC). The results of these efforts were:

(1) The first effort produced fascinating theoretical calculations and study but no prototypes were built or tested.

(2) In the second effort, two concepts were explored. The first idea, which used the return of crossed laser beams was promising, but found to be impractical for ballistic applications. The second concept, which measured shock velocity and calculated peak pressure, did not produce a pressure vs. time record, and could be accomplished much more inexpensively using break wires.

(3) The third effort also had excellent theoretical promise. Several different working prototypes were constructed and tested. Unfortunately, the frequency response was only 7 KHz, which was almost two orders of magnitude below the desired performance for blast overpressure.

(4) The fourth effort produced a working prototype with the potential for excellent performance. Because of this potential, further work was funded by the Defense Nuclear Agency (for work near atomic and simulated atomic detonations). A commercial transducer was eventually developed, but the cost was in excess of $10,000, which is almost 2 orders of magnitude more expensive than conventional electronic transducers.

b. Chamber Pressure

The earliest efforts to produce a fiber optic chamber pressure transducer were initiated by the Army Research Laboratory (Reference 1) and by the Armament Research Development, and Engineering Center (Reference 2). Both of the transducers developed by these efforts operated during laboratory testing, but none were actually tested in a weapon. In 1990, 25

different SBIR proposals for a fiber optic chamber pressure transducers were evaluated by ATC. The three most promising approaches were funded:

(1)   The most elegant approach exploited differences in optical absorption properties to sense pressure changes. In theory, this approach promised almost unlimited frequency response. Although the prototype worked under static laboratory conditions, it was so sensitive to thermal changes that further effort was considered too risky.

(2)   The second approach exploited the intensity modulation technique used successfully on the earlier blast sensor (see Figure 1). This approach was the first to successfully measure dynamic pressures in a gun tube. On 17 February 1993, a prototype transducer was successfully mounted in a 120mm tank gun and pressure in the gun tube was measured as shown in Figure 2. Unfortunately, the gun recoil damaged the fibers and the transducer eventually failed.

Figure 1.
Schematic of the Optical Configuration
of a Photoelastic Stress Sensor
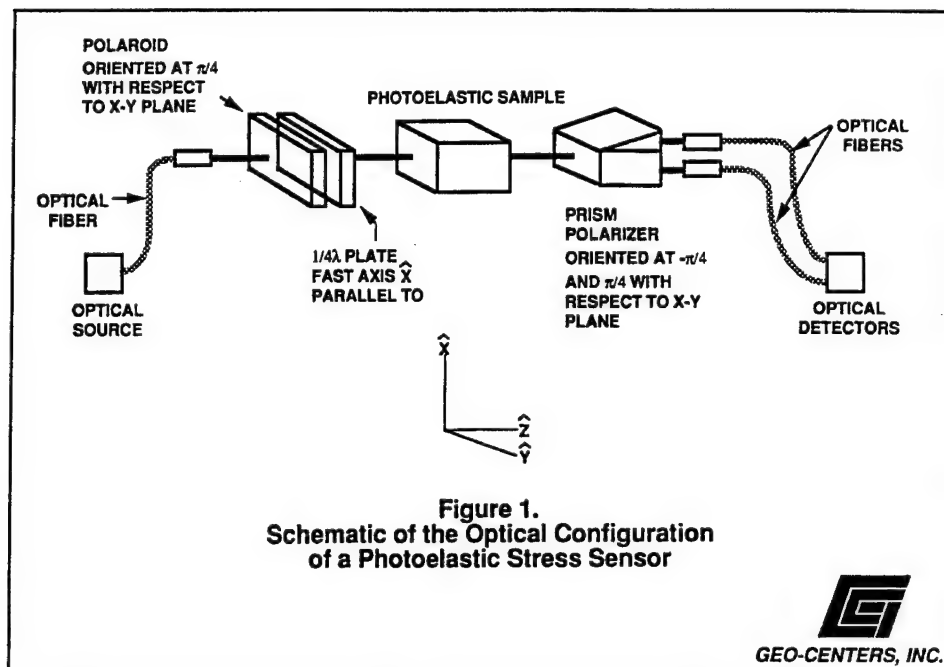
GEO-CENTERS, INC.

Figure 1 Optical concept (intensity modulation using photoelastic effect) used in fiber optic sensor for blast overpressure and chamber pressure (see Figure 2). Courtesy of Geo-Centers Inc.
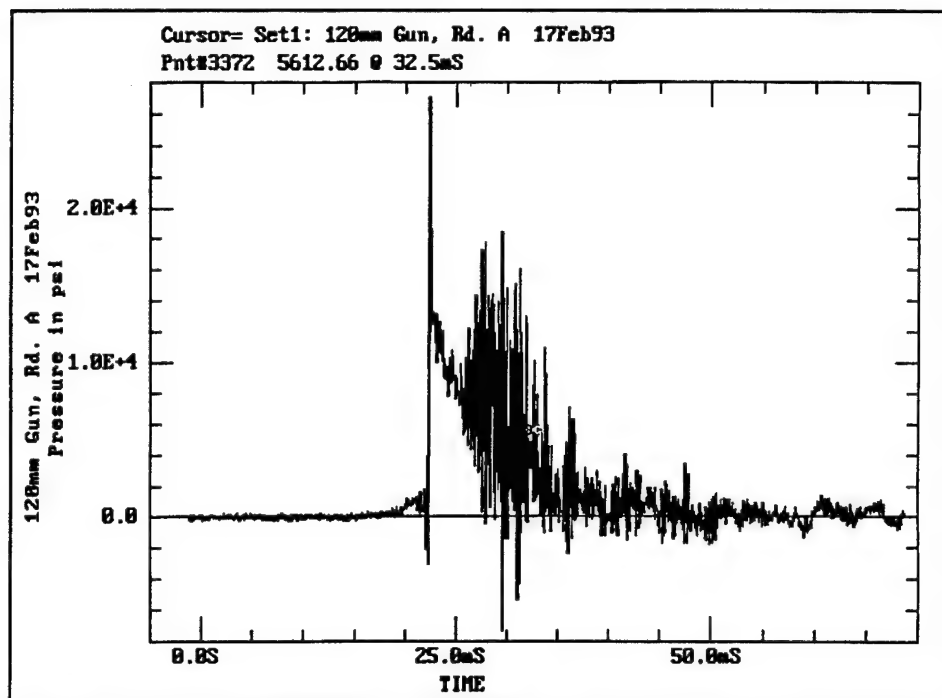
Figure 2. Pressure vs. time record from the first fiber optic sensor to be used in a large caliber gun (17 Feb 93). Optical concept was show in Figure 1.

(3)   The least elegant (i.e., the oldest basic optical concept), but most practical approach used amplitude modulation based on diaphragm deflection, as shown in Figure 3. This effort was a follow-on to the earlier ARDEC work. The transducer produced in this effort successfully measured static pressure up to 120,000 psi and dynamic pressure from many rounds of 120mm tank gun firing without damage to the transducer. As the gun recoiled, however, bending of the fiber optic bundle changed the light transmission property of the fiber, producing artifacts in the record, as shown in Figure 4. Although the physics of this problem are completely different, the end result (i.e., extraneous signal generated when cable is moved) is similar to the "triboelectric effect" familiar to users of piezoelectric transducer. A second problem with this concept was the large (5%) hysteresis observed in static testing. Despite the problems of hysteresis and cable whip, this transducer is still being evaluated due to its unique high resonant frequency (250 KHz).

3. CURRENT AND FUTURE EFFORTS

Current fiber optic measurement efforts at ATC have transitioned from high risk SBIR study contracts to less ambitious, more narrowly focused efforts. In addition to further evaluation of the fiber optic chamber pressure transducer, the development of fiber optic techniques to measure strain, ballistic shock and in-bore velocity are also being pursued.

a. Seven-fiber optical probe

b. Light pattern of illumination and reflection

c. Conversion from displacement or pressure to voltage
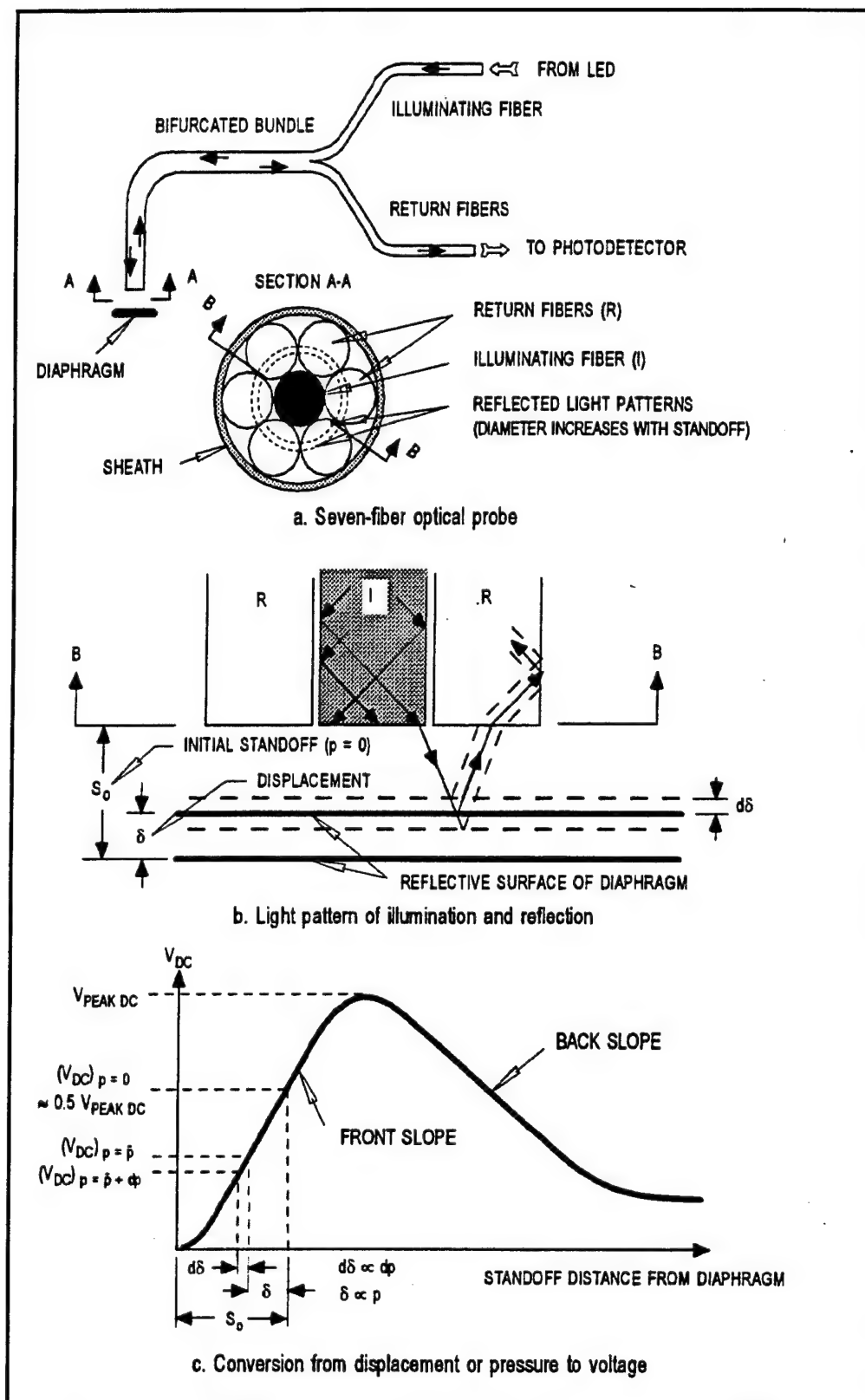
Figure 3. Optical concept (intensity modulation caused by diaphragm deflection) used in the fiber optic chamber pressure transducer that has been most successful to date. Courtesy of Quest Integrated, Inc.

298
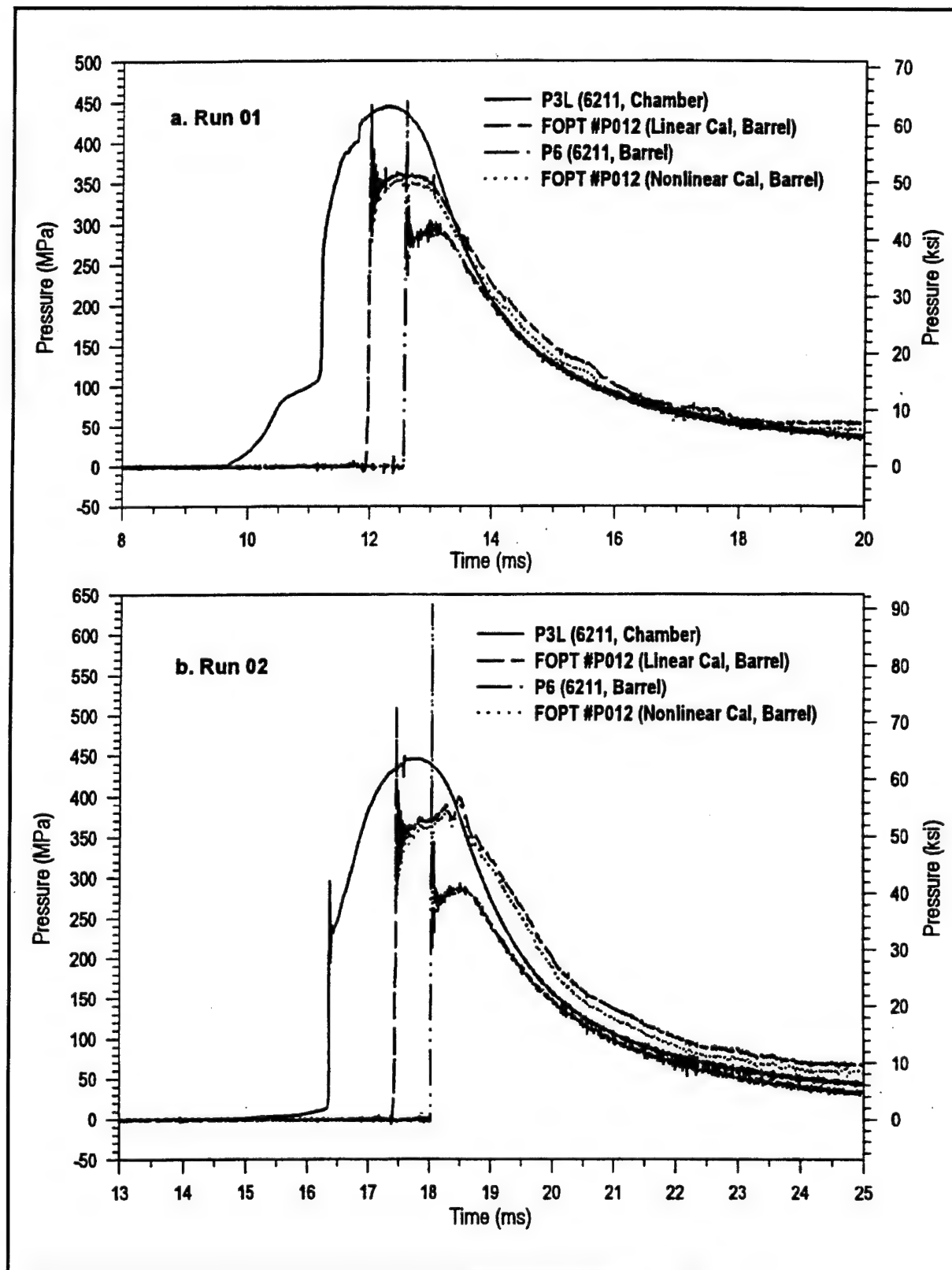
Figure 4A. Pressure vs. time record from fiber optic (FOPT) and quartz (6211) pressure transducers (Figure 3 concept). Note artifacts in record due to "cable whip".
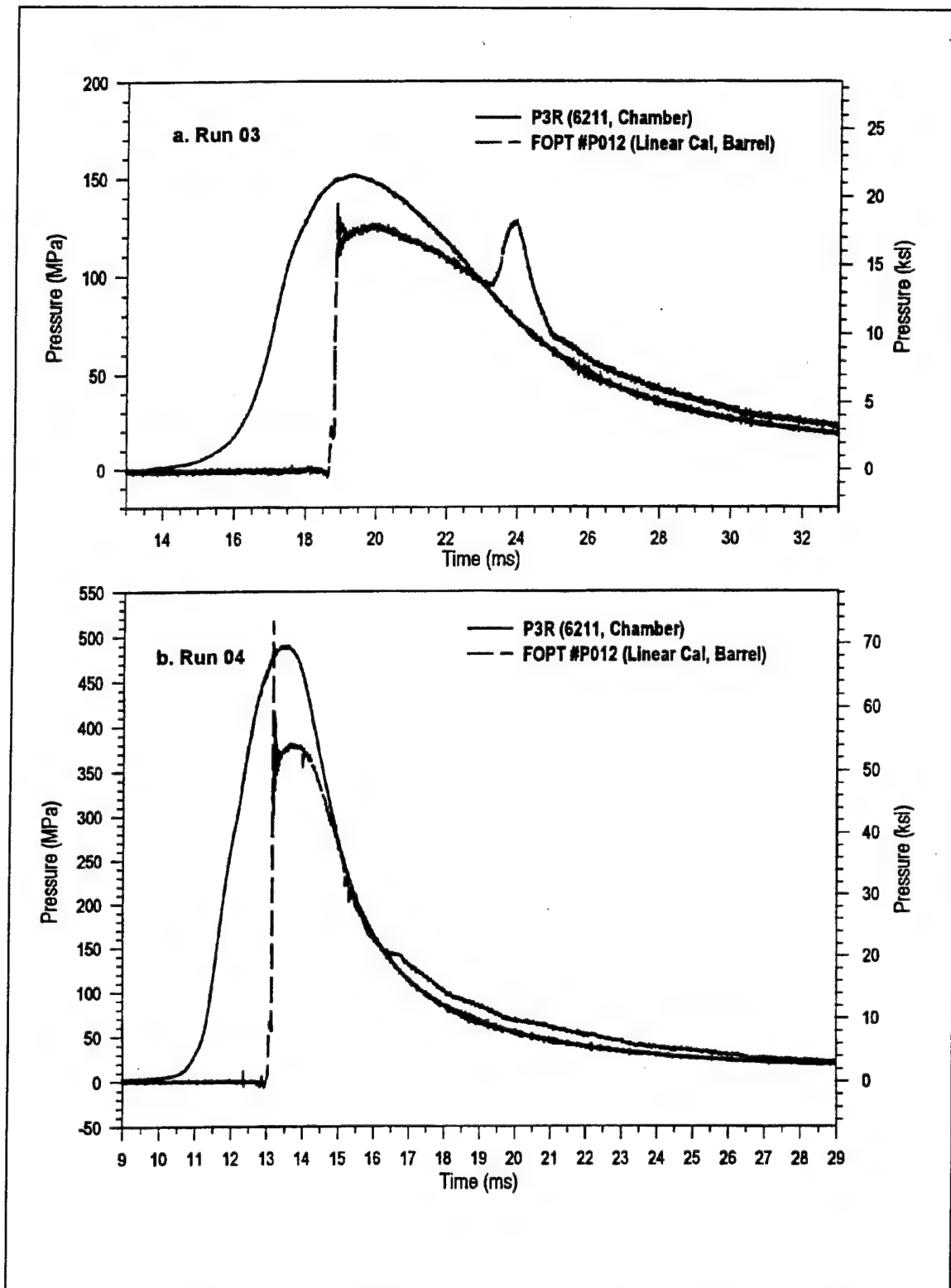
Figure 4B. Pressure vs. time record from fiber optic (FOPT) and quartz (6211) pressure transducer s (Figure 3 concept. Note artifacts in record due to "cable whip."

a. <u>Strain Measurement</u>: Sudden, intense strain developed in various armor materials during projectile impact or explosive detonation must be measured to evaluate armor properties. In one test method, exploding bridge wire detonators are used to generate a very rapid (1-300 microsecond) rise time stress wave. The electromagnetic interference created by this detonation typically disables conventional Whetstone Bridge signal conditioning for 60 to 120 microseconds. Because the rise time of the stress wave degenerates with distance, it is desirable to place strain gages as close as possible to the detonation. Due to the EMI problems, however, strain gages must be placed 350 to 700 mm away from the detonation so that the electronics have time to recover from the EMI affect. A fiber optic strain gage, immune to EMI would permit measurements much closer to the detonation.
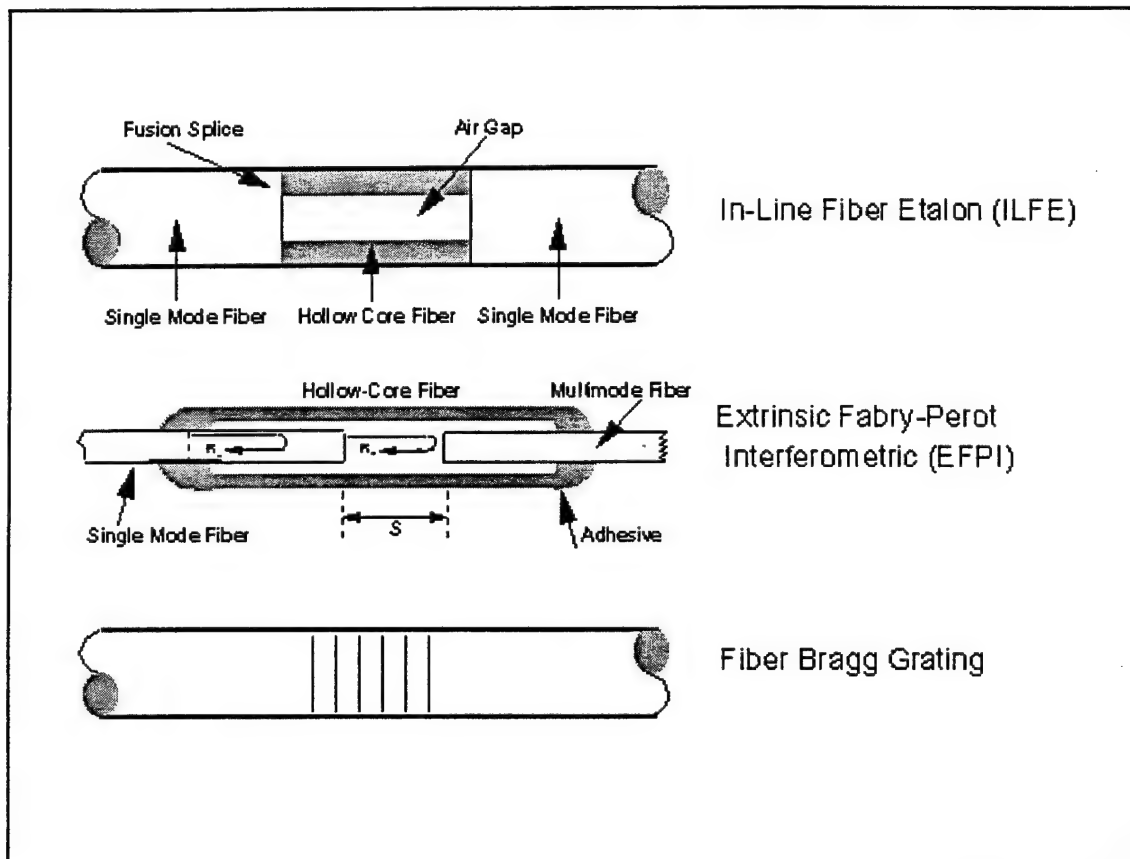
Figure 5 Various configuration of sensing element used in fiber optic strain sensors.

In the current effort at the University of Maryland (funded by ATC), the optical fiber sensor chosen is the In-Line Fiber Etalon (ILFE), shown in Figure 5. The ILFE (Reference 3) is highly sensitive to axial strain, and insensitive to transverse strain, temperature fluctuations, and EMI. It can be tailored to very short gage lengths (on the order of tens of microns) to measure large strains.

As the specimen is strained, the gage length of the ILFE changes. This change in optical path length will be detected as a phase change in the return light. Because a frequency modulation technique is being used, this sensor should be insensitive to intensity changes caused by "cable whip" that affected the chamber pressure transducer.

301

The ILFE is categorized as an interferometric fiber optic sensor. Another sensor of this type considered was the Extrinsic Fabry Perot Interferometric (EFPI) sensor (Reference 4). While the EFPI and ILFE behave similarly, the EFPI, by virtue of its construction, has mechanical deficiencies which include drift in gage-length and low mechanical strength.

The Bragg Grating sensor (References 5 and 6) was also considered for the application. In this sensor, a Bragg Grating, with a gage length in millimeters, is fused into an optical fiber. This assembly is mounted onto the test specimen and a broadband light source illuminates the grating. As the grating is stressed, it modulates the back-reflected spectrum which is recorded. The back-reflected spectrum is directly related to the input strain. Its primary disadvantage is its sensitivity to strain gradients which would be prevalent in the armor testing application.
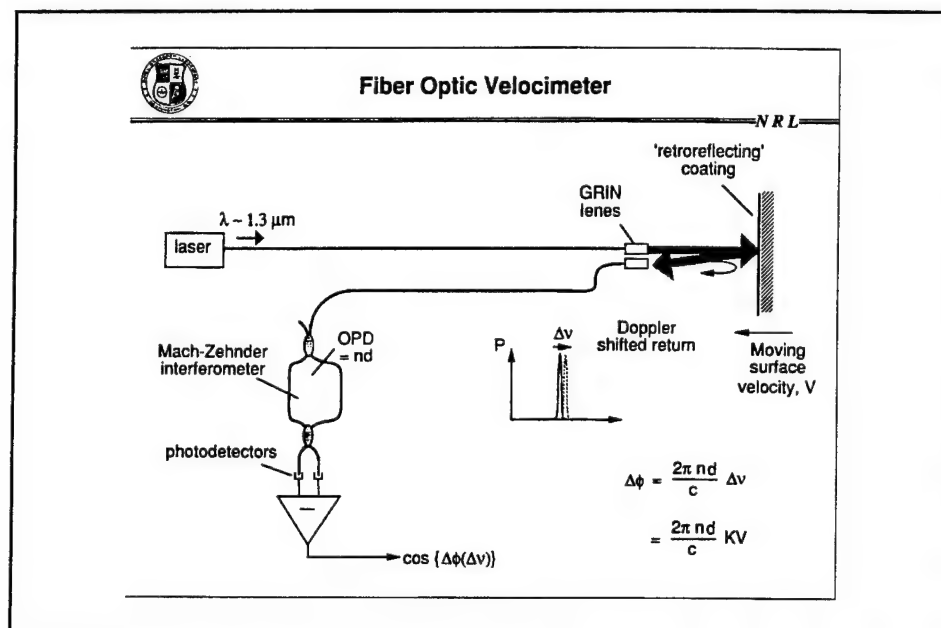
Figure 6 Optical configuration to be used in future fiber optic ballistic shock sensor. Courtesy of U.S. Naval Research Laboratory.

b. <u>Ballistic Shock</u>: In conjunction with the Naval Research Laboratory (NRL), an effort to measure ballistic shock is being pursued, as shown in Figure 6. Doppler shifted light is returned from an armor plate during projectile impact. A Mach Zehnder interferometer will be used to detect the Doppler frequency shift, which is directly proportional to velocity.

c. <u>In-Bore Velocity</u>: An effort is also being made to measure high frequency "vibration" during the launch of large caliber projectiles. Several factors make this a high risk effort. The amplitude of the vibration is small compared to the final launch velocity, so a very high resolution measurement (3000:1 signal to noise ratio) is required. Because the gun tube is long, the return from a diffuse reflection off the projectile will be small. A high powered laser, with a long coherence length is required. Earlier efforts have resulted in signal drop out and loss of laser return at various times during the launch, even though a very powerful laser was used. Innovative solutions to these technical challenges must be found.

4. CONCLUSION

Although the use of fiber optic techniques still holds promise for improving ballistic measurements, progress has not been as rapid as predicted by the original, optimistic projections. A slower, more deliberate development effort, leveraging on the successful techniques used at the Naval Research Laboratory, is expected to produce more successful results and demonstrate beneficial interservice cooperation.

5. REFERENCES

[1] E.A. Cheng, W. M. Grossman, R. W. Wallace, "Interferometric High Pressure Sensor" BRL Contract Report BRL-CR-603, U. S. Army Ballistic Research Laboratory, Aberdeen Proving Ground, Md, December 1988.

[2] H.- T. Liu and G. F. Mauer, "Development of a Pressure and Temperature Transducer for 700 MPa Explosive Environments, Flow Research Report No. 400, April 1987.

[3] J. Sirkis, T. A. Berkoff, R. T. Jones, H. Singh, A. D. Kersey, E. J. Friebele, M. A. Putnam, "In-Line Fiber Etalon (ILFE) Fiber Optic Strain Sensors", Journal of Lightwave Technology, December 1994.

[4] K. A. Murphy, M. F. Gunther, M. J. de Vines, and R. O. Claus, "Characterization and Testing of Materials Using Multichannel Fiber Sensor Systems" in DISTRIBUTED AND MULTIPLEXED FIBER OPTIC SENSORS IV, Alan D. Kersey, John P. Dalein, Editors, Proceedings of the SPIE (Society of Photo-Optical Instrumentation Engineers) 2294, pages 34-42, July 1994.

[5] Melle, Liu, Measures, "Practical Fiber-Optic Bragg Grating Strain Gage System", Applied Optics, July 1993.

[6] A. P. Kersey, T. A. Berkoff and W. W. Morey, "Multiplexed Fiber Bragg Grating Strain Sensor System with a Fiber Fabry-Perot Wavelength Filter", Optics Letters, 18, P. 1370, 1993.

DEVELOPMENT OF A MICROMACHINED SERVO ACCELEROMETER

Michael T.'Y. Young

Endevco

San Juan Capistrano, California

ABSTRACT

A new micromachined servo accelerometer(MSA) has been developed. It offers advantages of excellent stability, high g shock and vibration survivability, good accuracy, low vibration rectification error, wide bandwidth and small size.

The current design is optimized for ±50 g full scale. The input voltage is ±15 Vdc. The sensitivity is 200 mV/g with a full scale output of ±10 V. The output range can be decreased with addition of an external resistor and scale factor increased. The total composite bias error is 5 mg maximum and the total composite scale factor error is 1000 ppm maximum. A temperature sensor is included in this accelerometer which allows for accurate temperature modeling. The typical vibration rectification error is less than 20 $\mu g/g^2$ and, with internal trimming, this can be decreased further. The MSA accelerometer has demonstrated more than 5,000 g shock survivability in all three axes. A self-test feature permits users to inject a voltage signal to confirm operation of the accelerometer immediately before use.

This paper will describe the design and operational theory of the microsensor followed by the accelerometer system design which includes electronics and packaging(Patent 5,205,171). Key performance evaluation procedures and test results of design verification units will be presented.

MICROSENSOR DESIGN

The inertial system, consisting of a proofmass supported by two flexures, is micromachined from a silicon wafer. The wafer is bonded between two glass plates which have predeposited thin-film electrodes. Figure 1 is the exploded view of the resultant MSA micromachined sensor which measures is 8 X 4 X 2 mm.
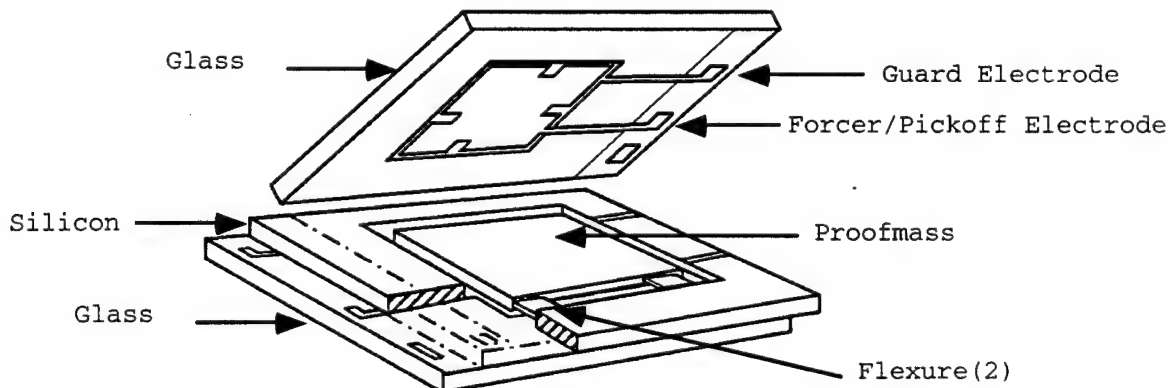
Figure 1. The exploded view of MSA microsensor

The inertial system is formed by chemically etching a (100) silicon wafer. The area for the proofmass is etched down approximately three micrometers to form capacitive gaps between the top and bottom plates to the proofmass. Partial etching is performed through one end of the proofmass to form flexures of a few micrometers thick. A special photolithography technique has been developed in order to better define the flexure configuration inside the recessed plane. The proofmass is then freed in subsequent etching. By anodically bonding glass plates to either side of the wafer, the pendulous motion is constrained so that the flexures are not over-stressed. The thin metal films forming the capacitive pickoff/forcer electrode and guard electrodes are sputtered onto the glass before bonding. Damping is provided via the gas in the small gap between the proofmass and the glass plates. The electrical connections are routed to the top and bottom layers in order to maintain structure symmetry. The nominal capacitance of each element, proofmass to top plate & proofmass to bottom plate, is 12 pf.

With acceleration applied, the proofmass rotates around the mid-point of the flexures. The acceleration induced motion is detected by the differential capacitors and is transduced into an error signal in the servo system. The error signal is amplified by the servo-nulling amplifiers which cause a feedback voltage to each of the glass electrodes. The feedback voltages produce the electrostatic forces between each capacitor electrode. The torque associated with the net electrostatic force on the proofmass rotates the proofmass back to the null position. This torque is equal and opposite to the acceleration-generated torque. The servo voltage required to achieve this balance is directly proportional to the applied acceleration.

The performance of the MSA accelerometer is closely related to the design and fabrication process of the microsensor. The differences in initial bias from unit to unit are mainly caused by flexure variations. The scale factor is proportional to the weight of the proofmass and the square of the capacitor gap. The variation in the weight of the proofmass is largely due to the wafer thickness non-uniformity. The capacitor gap is determined by the silicon etching and the electrode metallization. By increasing the gap, the scale factor can be increased. However, this is limited by the start-up capability when the proofmass is offset. In the worst service condition, a 50 g force will be pushing the proofmass against one of the glass plates before the power is turned on. The restoring electrostatic force must be large enough to pull the proofmass back to the null position at turn on. This requirement determines the upper limit of the gap size.

Aluminum film is deposited on the outside surface of the glass plates and guard electrodes are deposited around the top and bottom electrodes. Both are used to shield against all stray capacitance. The area of glass without metallization in the vicinity of the proofmass is minimized and V-grooves are etched in the proofmass directly under this glass area to reduce sensor turn on drift due to glass charging.

The flexure has to be stiff enough to prevent cocking instability. Cocking of the proofmass would happen when one end of the proofmass touches the upper electrode and the opposite end touches the lower electrode. This motion is not restrained by the electronic servo loop and is solely stabilized by the strength of the flexure and by overtravel stops.

ACCELEROMETER SYSTEM DESIGN

In addition to the microsensor, electronics and packaging have been developed to complete the accelerometer design. The performance and the cost of the electronics and the packaging affect the total MSA more than with conventional electromagnetic type servo accelerometers. Micromachining has reduced the size and the cost of the sensing and forcing mechanisms used in the MSA accelerometer. Careful design in electronics and packaging is required in order to maintain the performances of the microsensor and to provide adequate environmental protection.

The electronic block diagram is shown in Figure 2. It includes an oscillator, a position detector, a temperature sensor and a servo loop. The electronic circuitry is also used to set the initial bias and scale factor, to provide excitation conditioning, to control the dynamic characteristics, and to provide vibration rectification trimming of the accelerometer.

MSA circuit uses a patented technique to allow feedback voltage to be directly proportional with acceleration forces. The proofmass is biased at 15 Vdc and 5 V @ 10 MHz. The RF is used to excite the capacitive upper and lower gaps. Electrostatic attraction is normally a square of the voltage applied, but the technique of biasing the proofmass at 15 Vdc allows the voltage to be a linear relationship as illustrated by this equation:

$$\text{Electrostatic Force} = A_{po}e_o[(V_{dc} + V_o)^2 - (V_{dc} - V_o)^2]/(2d^2)$$
$$= (2A_{po}e_oV_{dc}/d^2)V_o$$

$$\text{where } A_{po} = \text{electrode area}$$
$$e_o = \text{dielectric constant}$$
$$V_{dc} = \text{dc bias voltage}$$
$$V_o = \text{output(feedback) voltage}$$
$$d = \text{capacitor gap}$$

Therefore, the linearity performance of the MSA is excellent with ±0.1 % typical non-linearity.
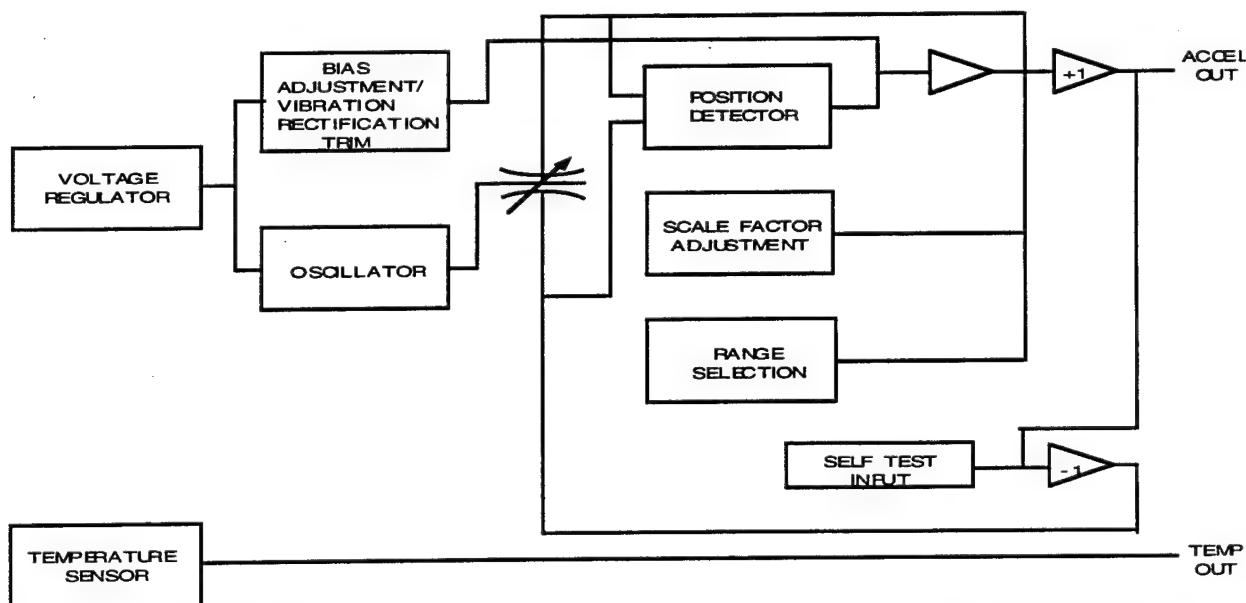
Figure 2. MSA Functional Block Diagram

306

The acceleration signal is derived by sensing the position of the proofmass between the thin-film electrodes. This position change is sensed by a diode-bridge detector which converts the capacitance change into current. An integrator then further converts the current into the voltage output signal. This output signal along with its inversion is fed back to the upper and lower electrodes respectively. These feedback voltages generate the electrostatic forces to maintain the proofmass at the capacitance center position. The voltage required to keep the proofmass at the null position is a direct measure of the acceleration it experiences. Unlike the open-loop accelerometer, the electronics in the closed-loop accelerometer can be used to shape its dynamic response.

Other desirable features included in the circuit are scale factor trimming, bias or vibration rectification error trimming, self test, range adjustment, and a temperature sensor for thermal modeling. The circuit incorporates two internal trimmable resistors for parameter adjustments. The first resistor is used to set either one of the feedback voltages. By adjusting the feedback, the difference between the upper and lower capacitors can be equalized. It can be used for either bias or vibration rectification trimming. The other resistor is used to adjust the scale factor by changing the excitation voltage to the microsensor.

The self test feature provides a valid check of total accelerometer function prior to use. By injecting a voltage into the feedback loop, the proofmass will be forced to one side due to the electrostatic input. An accelerometer output will then be generated. This is a true self-test because the mechanical structure and the electronics both have to work properly in order to render the correct output signal. It also permits nulling the effect of earth's gravity for low-level acceleration measurements perpendicular to the earth's surface. The factory set full scale range is ±10V at ±50 g. By connecting an external resistor, the gain of the last output stage can be changed. The range can be adjusted down to have a ±10 V full scale output at any acceleration down to ±0.5 g.

The MSA housing includes a 1" diameter cylinder and a mounting plate with a total accelerometer weight of 35 grams. The microsensor and the electronic components are assembled on two thick film substrates. These substrates are housed inside the cylinder. This unit is then sealed in the dry atmosphere by welding a top and a bottom to the cylinder. The top lid of the housing is a 7-pin header which is designed for solder connection. The hermetically sealed housing is then epoxied to the mounting plate. This approach allows simple modifications to adapt the MSA to application specific mounting configurations. Figure 3 shows two units with different mounting plates. The substrate assembly can be seen on the unit without the header.

Hybrid technology is used to minimize size and weight. The smaller and lighter accelerometer reduces its loading effect on any test structure. Because the internal excitation frequency is 10 MHz, physical layout of the substrate needs special attention. The layout has to consider the proper placement of bypass capacitors, ground plane locations and the separation between ac and dc circuits. The thermal symmetry and ac symmetry have to be studied in order to guard against environmental effects. To reduce the production cost, the substrate layout is done in a multiple-up format, and the design guidelines for automatic assembly and test equipment is used allowing for automatic pick & place and wirebonder to be used for high volume manufacturing.
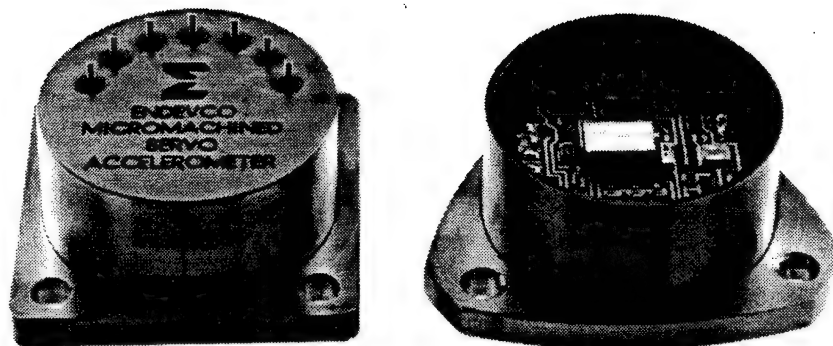
Figure 3.   The complete MSA unit is shown in the left. The one
in the right shows the microsensor and the servo
electronics assembled on a thick film substrate.

The microsensor is mounted to the alumina substrate with silicone rubber which provides the necessary isolation of thermal and mechanical strains from the mounting surface. Alumina-filled structural epoxy is used to fix the sensor lead wires in place to eliminate wire movement and any resultant parasitic capacitance and bias shift.

PERFORMANCE CHARACTERISTICS

MSA is a pendulous accelerometer and its deviations from the ideal output can be modeled with following equation from IEEE STD 337-1972.[1]

$$A = E/K_1 = K_0 + A_i + K_2A_i^2 + K_3A_i^3 + \delta_oA_p + K_{ip}A_iA_p - \delta_pA_o + K_{io}A_iA_o$$

Where E = output in accelerometer units, mV
K_1 = scale factor, mV/g
K_0 = bias, g
A_i = acceleration along Input Axis(IA), g
A_p = acceleration along Pendulous Axis(PA), g
A_o = acceleration along Output Axis(OA), g
K_2 = non-linearity, g/g^2
K_3 = non-linearity, g/g^3
δ_o = misalignment of IA to OA
δ_p = misalignment of IA to PA
K_{ip} = cross-coupling, (g/g)cross g
K_{io} = cross-coupling, (g/g)cross g

K_3 for MSA is very small and is not significant to the performance of current design. While this model only characterizes accelerometer's dynamic performances, performance changes with temperature and time are also very important for any servo accelerometer. The evaluation of MSA in these aspects is still on going. Test data of design verification units are shown in Table 1.

308

RANGE	± 50 g
BIAS	
bias (K_O) @ 25 C	± 125 mg max.
bias modeling residual	3 mg rms typ.
SCALE FACTOR	
scale factor (K_1) @ 25 C	0.2 V/g ± 20%
scale factor modeling residual	800 ppm typ.
AXIS MISALIGNMENT ($\delta_o^2 + \delta_p^2)^{0.5}$	±10 mrad
axis misalignment stability	±1 mrad
VIBRATION RECTIFICATION COEFFICIENT (K_2)	20 µg/(grms)^2 untrimmed, 10 µg/(grms)^2 trimmed
VIBROPENDULOSITY (K_{ip} or K_{io})	10 µg/g^2
FREQUENCY RESPONSE, DC to 500 Hz	± 5%
OUTPUT NOISE	
DC to 10 Hz	2 µg rms
DC to 500 Hz	20 µg rms
DC to 10 KHz	200 µg rms
TEMPERATURE RANGE	-55 ^{O}C to +105 ^{O}C
SHOCK	5000 g min, 200 µS haversine pulse
SELF-TEST	2.5 g/Volt
TEMPERATURE SENSOR	
temperature output @ 25 ^{O}C	0.630 V
temperature output sensitivity	2.1 mV/ ^{O}C

Table 1. Key performance characteristics of MSA.

Most of the evaluation tests are done on a dividing head. A detail description of this test setup and data reduction can be found in the referenced IEEE document.

With the axis of the dividing head in a horizontal position and the head set at its 0° position, the MSA is mounted so that its OA parallel to the axis of rotation, its PA up and its IA horizontal. The dividing head is rotated through 360° with a 30° increment. The data are fitted to the Fourier series to derive K_1, K_O, K_2, K_3, δ_O and K_{ip}. Then the test is repeated with the unit's PA parallel to the axis of rotation, its OA down and its IA horizontal. The same coefficients can be derived except that K_{ip} and δ_O are replaced with K_{io} and δ_p.

Maximum axis misalignment can be tested by mounting the unit on the dividing head with its IA parallel to the axis of rotation. The dividing head is rotated from 0° to 90° and 180° positions. The composite axis misalignment which is equivalent to $(\delta_o^2+\delta_p^2)^{0.5}$ can be derived. This number is listed in Table 1.

To test for thermal performances, these tests were repeated with the MSA inside a temperature chamber. There is a linear voltage output monolithic temperature sensor in the MSA to be used with temperature modeling. Figure 4 and 5 are the typical temperature response curves for bias and scale factor.

The typical uncompensated thermal bias shift is less than 50 mg, or 0.1% FS and the typical uncompensated thermal scale factor shift is less than 3000 ppm. The typical third order temperature modeling residual is < 3 mg for bias and is < 800 ppm for scale factor.
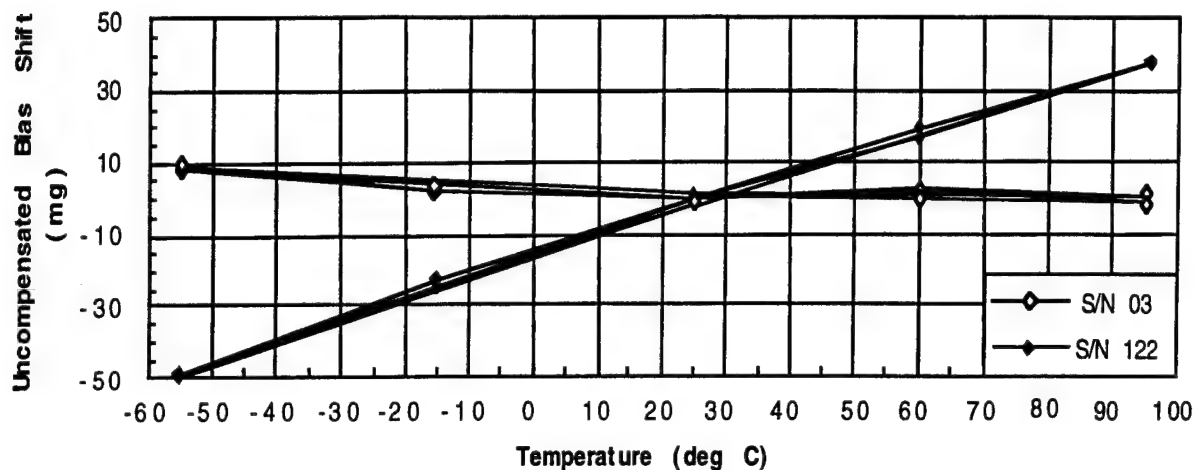
Figure 4. The Uncompensated Bias Shift with Temperature.
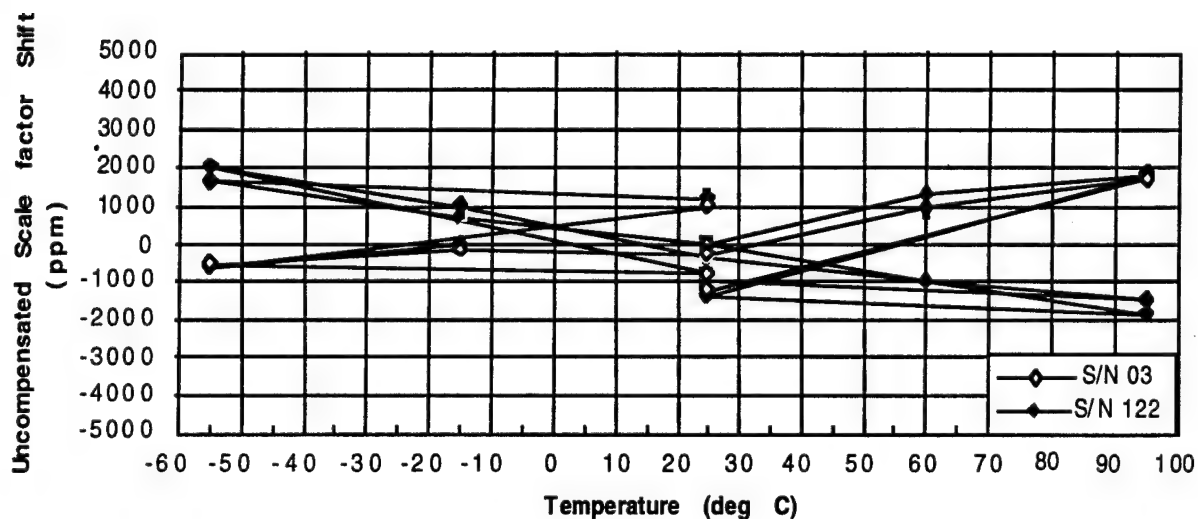
Figure 5. The Uncompensated Scale Factor Shift with Temperature.

The resonant frequency is a function of the moment of inertia of the pendulum and the servo gain, and is higher with a smaller moment of inertia and an increased amplifier gain. A high resonant frequency would be selected for broadest frequency response. The flatness of the output response in the range of frequency below the resonant frequency is determined by the damping ratio. The damping ratio of MSA is determined by the squeeze film gas damping and the servo electronics.

The frequency response of MSA is conducted on a shaker comparing the output with a back-to-back reference accelerometer. Figure 6 shows its typical frequency response curve. The resonant frequency of current design is at about 2 KHz. Typically, the units are flat to within 3% in amplitude and have a 10° phase lag at 500 Hz.

310
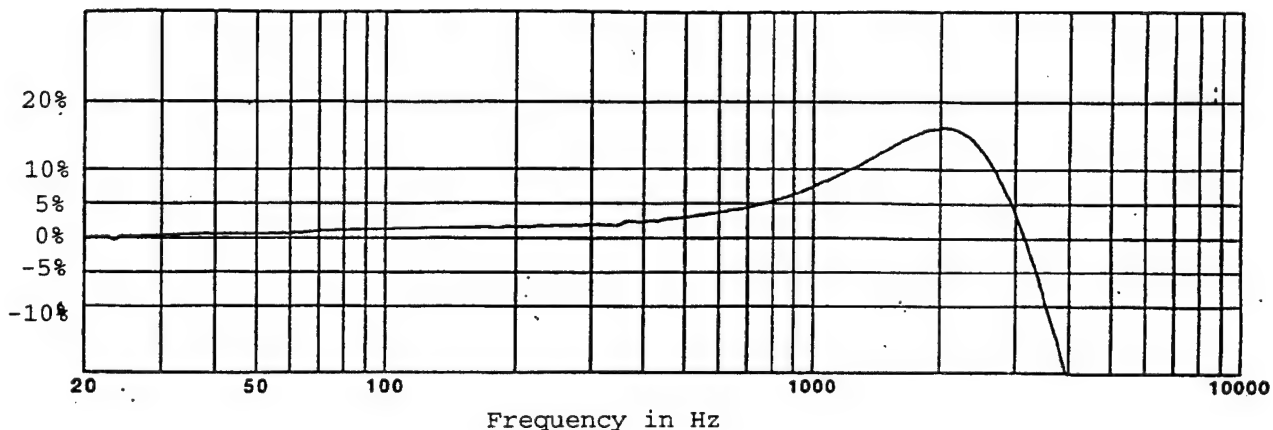
Figure 6. The typical frequency response of MSA shows a
resonant peak at 2 KHz.

Vibration rectification, caused by non-linearities, is a very critical term in
guidance applications. There are several ways to test for this term. The
vibration rectification error reported here is tested on a shaker with
sinusoidal inputs.[2] The typical sinusoidal vibration rectification error for
the MSA is 20 $\mu g/g^2$ at frequencies up to 500 Hz. Vibration rectification
errors generally change with frequency. MSA will more likely experience
random vibration instead of sinusoidal vibration in service. Since each
application has its own random vibration signature, the accelerometer should
be evaluated on a random vibration shaker with the simulated input spectrum.
One key feature of MSA is the capability to zero out the vibration
rectification error by laser trimming a thick film resistor. Table 2 shows
the vibration rectification error both prior to and after trimming.

Vibration Rectification Error ($\mu g/g^2$)		
	S/N 01	S/N 33	S/N 122
Prior to Trimming	14.27	8.29	10.48
After Trimming	0.42	0.58	0.38

Table 2. MSA Vibration Rectification Test Results.

Ruggedness is a desirable feature for this type of accelerometer. The only
moving part of the MSA is the silicon proofmass and its movement is restrained
from overtravel. Tests show that the design is capable of surviving at least
5000 g shock and 50 g peak vibration in all directions.

MSA also has the advantage of being a multi-range instrument. Range and scale
factor can be adjusted by an external resistor. The standard ±50g unit yields
a scale factor of 200 mV/g. The accelerometer can be ranged down to ±0.5 g
full scale with a sensitivity of 20 V/g by connecting a 100 Ω resistor to the
range adjustment pin. Selection of this external resistor to get the desired
scale factor at different ranges can be calculated from following equation.

$R_S = 10000/(5 * S - 1)$

where Rs is the external resistor
S is the desired scale factor

311

APPLICATIONS

The wide dynamic range of MSA makes it suitable for a variety of applications in the aerospace, military, automotive and industrial markets. In the military and aerospace markets, one such application is a missile flight, where the accelerometer needs to survive a high g launch environment and then to recover and measure the in-flight accelerations, such as missile incremental separation accelerations, rocket thrust, missile airframe resonance and trajectory monitoring. The excellent stability and accuracy of the MSA make it appropriate for short range guidance and control applications, such as inertial guidance for missiles, smart artillery/mortars and aircraft. MSA can also be used in aircraft flight tests for measuring the wing flutter effects, aircraft stability derivatives, vibrations during jet take-off and aircraft altitude.

Low level and low frequency acceleration measurements are very difficult in severe vibration environments of many industrial and automotive applications. However, the low vibration rectification error of MSA makes it a good fit for these applications where it can be used for equipment dynamic balancing, gear vibration monitoring, automotive vehicle dynamics and railroad car coupling. MSA also can be utilized in automotive active suspension and navigation system development.

MSA's capability to resolve μg vibration facilitates the implementation of vibration compensation schemes for any vibration sensitive process. Vibration induced by a motor or a vacuum pump can become a limiting factor when the semiconductor industry requires sub-micron process resolution. MSA will allow equipment manufacturers to collect accurate vibration data for process improvement.

Other appropriate applications for MSA include seismic activity monitoring, ship motion studies, platform stabilization, helicopter hovering studies, precision leveling inclinometer and other tilt and angle measurements.

CONCLUSION

The current MSA has demonstrated a 5 mg bias accuracy and it offers advantages of small size, ruggedness and small vibration rectification error. Further with the use of silicon micromachining and wafer fabrication, MSA sensor costs are reduced in comparison to existing electromagnetic servo mechanisms. Work will continue to refine the MSA accuracy to 1 mg bias and convert the hybrid circuit into an Application Specific Integrated Circuit(ASIC), with tri-axial servo accelerometer being developed for Inertial Measurement Unit application.

REFERENCES

1. IEEE STD 337-1972. Standard Specification Format Guide and Test Procedure for Linear, Single-Axis, Pendulous, Analog, Torque Balance Accelerometer.

2. Peters, R.B., "Use of multiple acceleration references to obtain high precision centrifuge data at low cost", Mechanical Technology of Inertial Devices, Proc. Inst. Mech. Eng. (London), 2, Paper C47/87, 1987

Development of a Modulation System for Voice Transmission in PCM

Lee Olyniec
Second Lieutenant, USAF

Air Force Flight Test Center
412 TW/TSID
25 N. Wolfe Ave.
Edwards AFB CA 93524-8300

18th Transducer Workshop
Colorado Springs, CO
June 20-22, 1995

Author: Lee Olyniec
Air Force Flight Test Center
412 TW/TSID
25 N. Wolfe Ave.
Edwards AFB CA 93524-8300

Abstract

This paper describes the design and characteristics of a digital voice encoding circuit that uses the continuously variable slope delta (CVSD) modulation/demodulation method. With digital voice encoding, the audio signal can be placed into the pulse code modulation (PCM) data stream. Some methods of digitizing voice can require a large amount of bandwidth. Using the CVSD method, an acceptable quality of audio signal is obtained with a minimum of bandwidth. Presently, there is a CVSD microchip commercially available; however, this paper will describe the design of a circuit based on individual components that apply the CVSD method.

With the advances in data acquisition technology, increased bit rates, and introduction of a corresponding MIL-STD, CVSD modulated voice will become more utilized in the flight test programs and a good knowledge of CVSD will become increasingly important. This paper will present CVSD theory, supported by graphical investigations of a working circuit under different conditions. Finally, several subjects for further study into CVSD will be addressed.

Introduction

There are a variety of methods available to incorporate voice into pulse code modulation (PCM) data streams. One disadvantage of these methods is that they use a large percentage of the bandwidth available in the relatively low bit rate systems of the past. If the voice data with a 3 Khz bandwidth was treated as a regular analog signal converted into a 12 bit PCM word, it would require 72 Kbs to send using the nyquist criteria.

Delta modulation tracks the audio signal in a series of timed steps and delivers a serial data stream of one's or zero's which corresponds to an increase or decrease of the input frequency. For example, if the sample tracked by the encoder detects that the audio signal is rising, it will output a one and if it detects a decrease in the signal it outputs a zero. This is known as linear delta modulation. The step size is a fixed value and this can result in slope overload conditions unless a very high sampling rate is used. What is needed is a circuit that can change the step size between samples when a large change in the input is detected.

The method used to design the encoding circuit in this paper is known as continuously variable slope delta (CVSD) Modulation/Demodulation. CVSD circuits have the ability to change the slope size when the serial data indicates a large change in the input signal. The bandwidth requirements for CVSD are much lower than that required of PCM or linear delta modulation for the same quality signal. Presently, there is a CVSD microchip commercially available; however, this paper will describe the design of a circuit based on individual components that apply the CVSD method.

Encoding Method

Since a CVSD circuit is a modification of a linear delta modulation circuit, the delta circuit will be explained first to gain a basic understanding of the fundamentals of digital encoding.

Linear Delta Modulation

An explanation of the linear delta modulation circuit will be shown by following the block diagram in Figure 1.

The process starts with the input of the audio signal. Proper operation of the circuit is dependent on the voltage levels of the signal being within certain voltage and frequency limits to avoid an overdrive condition. This is accomplished with an automatic gain control (AGC) and low pass filter. The filter is designed to pass audio tones which are generally between 50 to 3,000 Hz. After filtering and level adjustment, the signal is present at point 1.

To start this example, the non-inverting input of the comparator will be at ground. The audio signal will be considered to be above ground. With these conditions, the comparator output is a negative voltage at point 2. The D flip-flop will respond with a TTL low signal (zero volts) at point 3 with the new clock pulse. This low signal makes the first bit in the serial data out a zero. The clock for the circuit will generally run between 10 and 64 kHz. Above these frequencies, the quality of the audio shows little improvement with an increased sampling rate.

The integrator is biased at approximately 1 volt at the non-inverting input at point 4. With this bias, the integrator responds to the low voltage at the inverting input with a high output. An integrator circuit converts the output into a ramping up voltage signal. The slope of the ramp is calculated with the equation:

$$SRckt = Vm/(2*R*C) \qquad (1)$$

SRckt = slew rate of the circuit in volts per second (V/s)
Vm = is the peak to peak voltage of the square wave input.
R = Resistor between input signal and inverting input
C = Capacitor between inverting input and output

<u>Example 1:</u> The capacitor value is .1uF and the resistor value is 2,000 ohms with an input pulse of 3.15 volts. The resulting circuit slew rate is 7.88 volts per millisecond (V/ms). This increasing voltage is seen at point 5.

The comparator now sees an audio signal at point 1 and the ramping voltage at point 5. One of two conditions can now exist. If the audio signal has a high frequency and is increasing rapidly, the voltage at point 1 will have increased faster than the voltage of the integrator ramp at point 5 and the comparator output will remain at the negative voltage level. This will repeat the process just described, sending another zero into the serial data stream (point 3) and leaving the integrator to continue its increasing voltage ramp.

If however, the audio signal does not increase faster than the integrator voltage ramp, the comparator will see a greater voltage on the non-inverting input and will instead change the output to a positive voltage. The flip-flop now responds to the high voltage at point 2 by outputting a TTL positive voltage representing a one with the next clock pulse. This voltage (approximately 3 volts) is the next bit in the serial data stream and the integrator responds with a voltage output sloping down.

The downward sloping voltage is seen at the comparator at point 5 and the process of comparing the audio input level and the integrator's ramp voltage continues with each clock pulse.

Figure 1: Delta Modulation Block Diagram
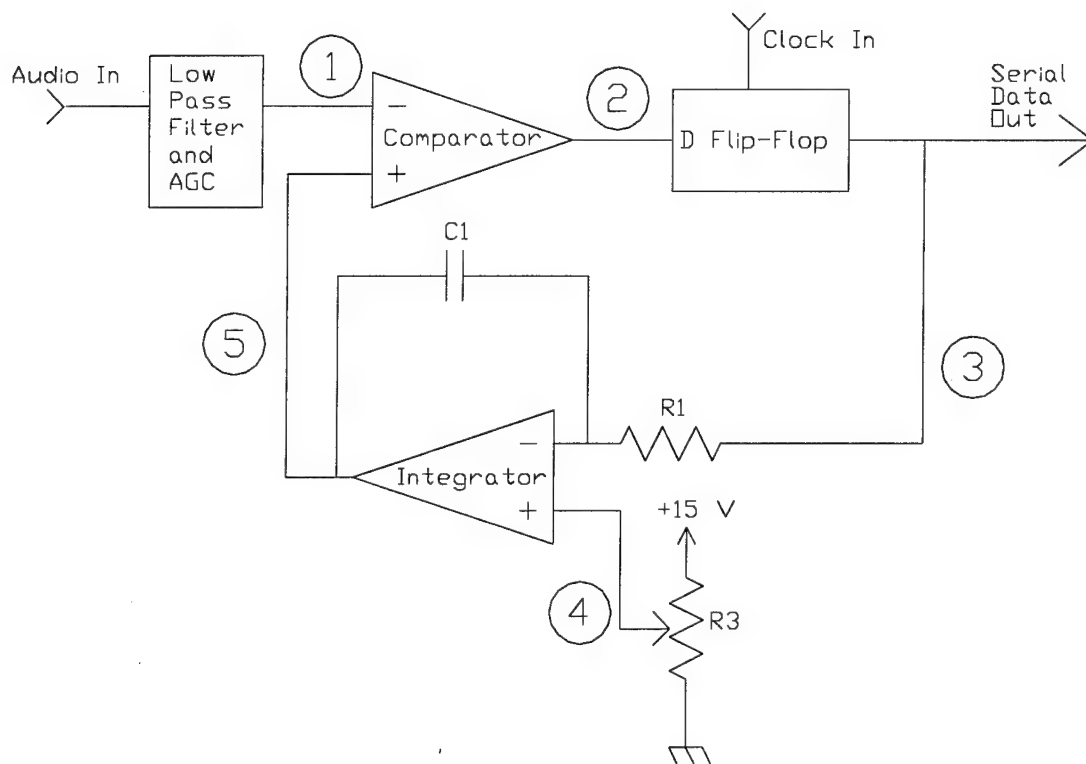
Calculations

The limitations of the delta modulation circuit are realized when the slew rate of the input signal exceeds the adjusted slew rate of the circuit. When this happens, the full amplitude of the signal cannot be reached and distortion of the high frequency components of the signal occur.

The slew rate of a sine wave is calculated at the point of the maximum change on the curve; the point between an upper and lower peak. The slope at this point is calculated by the equation:

$$SRsig = Vm*pi*f \qquad (2)$$

where   SRsig = slew rate of the signal in V/s
         Vm = Peak-to-peak voltage of the signal
         pi = 3.14
         f = frequency of the signal in Hertz

Example 2: A 500 Hz, 5.0 volts peak-to-peak (Vp-p) signal would have an SRsig of (5.0*3.14*500)=7850 V/s or 7.85 V/ms.
A signal with twice the frequency or twice the voltage would have an SRsig of 15.7 V/ms.

Slew rate limits of the circuit can be found by using equations 1 and 2. For example, an input signal of 3,000 Hz, 5 Vp-p is sent to a delta modulation circuit with a slew rate of 16.25 V/ms. The input signal has a period of 1/f or .333 ms. The time interval between a low-to-high or high-to-low peak is half the period or .167 ms. If the time interval is multiplied by the slew rate of the circuit, the maximum voltage swing for this circuit at this frequency is found to be:

.167 ms * 16.25 V/ms = 2.71 Vp-p

To determine the maximum slew rate that can be sent into this circuit without distortion, reverse the process using the maximum output voltage to find the slew rate.

Using equation 2 with Vm=2.71 and f=3,000, SRsig is found to be 25.53 V/ms. Dividing the rates results in:

$$SRsig / SRckt = SR\ ratio \qquad (3)$$

25.53 / 16.25=1.57

Therefore, multiplying the SRckt by the SR ratio results in the maximum slew rate that the circuit can handle without a reduction in the output amplitude.

$$SRmax=SRckt*1.57 \qquad (4)$$

This method can be applied to determine the output limitations for other frequencies.

Example 3: A 1,000 Hz, 10 Vp-p signal is applied to the circuit with a SRckt=16.25 V/ms. From equation 4, SRmax=25.5 V/ms. SRsig calculated from equation 2 is 31.4 V/ms. Since the slew rate of the signal is greater that the adjusted slew rate of the circuit, amplitude limiting will occur.

These limitations can be overcome by giving the circuit a large SR; however, this adversely affects the low-level signals sent to the encoder. Since the integrator ramp will increase a set amount with each clock pulse, a signal with an amplitude less that the voltage rise of the integrator will not be encoded.

Example 4: A circuit with an SRckt of 16.25 V/ms is clocked at a frequency of 20 kHz. The period of the clock is 1/f or .05ms. The maximum voltage swing between each clock pulse will be:

SRckt*period= Voltage change   (5)

16.25 V/ms*.05 ms=.81 V

If the signal has an amplitude less that .81 volts, it will not be detected and therefore not encoded.

These limitations will be illustrated in later examples.

Illustrated examples

To help illustrate the delta modulation process, a series of examples with o-scope displays are provided.

The first set of displays (Figure 2) shows the encoding of a 500 Hz sine wave at 3.0 Vp-p. The first display (2a) is the input signal taken from point 1. Figure 2b is the integrator ramping output voltage at point 5 with which the audio signal is compared. Figure 2c is the serial data output from the D flip-flop and the final display is the clock input. For this example, the clock is set at 10 Kbs. The integrator time constant is set at 200 microseconds (us) for the following 4 examples. With the input pulses from the D flip-flop of 0 to 3.15 volts, this results in a slew rate of 7.88 V/ms.

Figure 2: Delta Modulation Encoded Signal
Input signal: 500 Hz, 3.0 Vp-p, SRsig = 4.71 V/ms   Circuit: SRmax = 12.4 V/ms, 10 kHz clock

Figure 2a: Point 1
Audio Input
2 V/div
500us/div
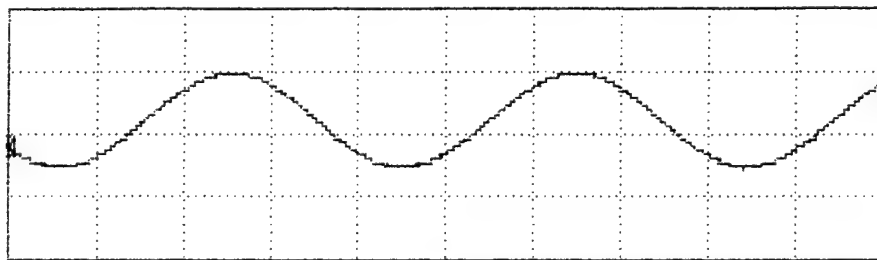
Figure 2b: Point 5
Feedback
2 V/div
500us/div
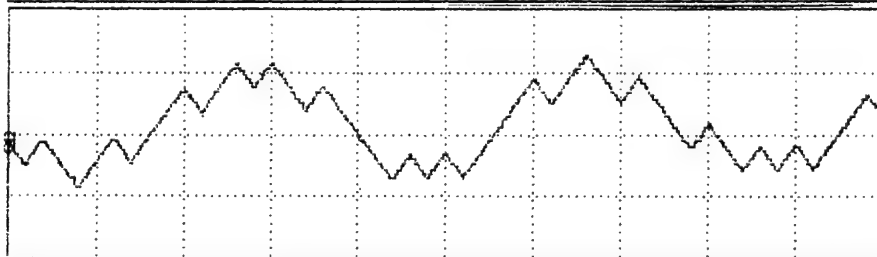
Figure 2c: Point 3
Serial data out
2 V/div
500us/div
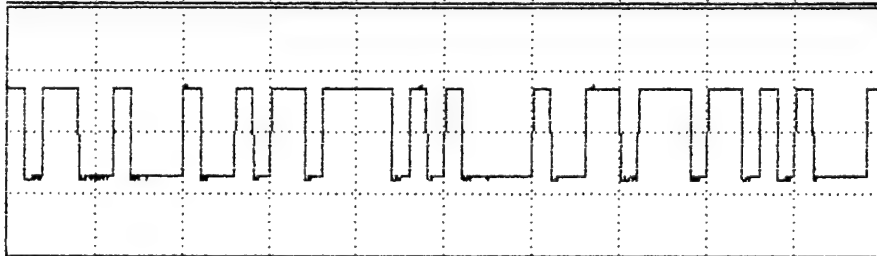
Figure 2d
Clock
2 V/div
500us/div
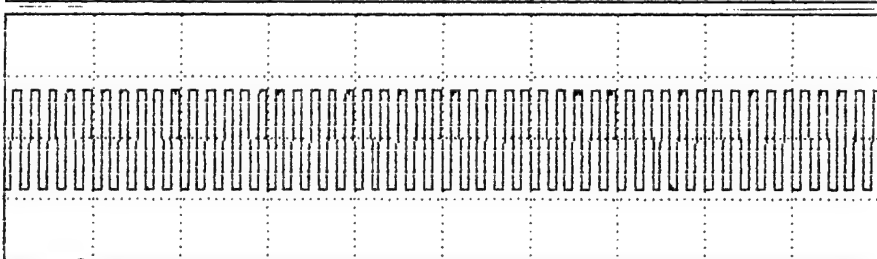
The second set of displays (Figure 3) shows the effect of a faster clock rate with the previous input signal. The integrator output more closely follows the actual signal input due to the quicker sampling rate of 20 Kbs. These displays illustrate the increased resolution with the increased bandwidth.

Figure 3: Delta Modulation Encoded Signal
         Input signal: 500 Hz, 3.0 Vp-p, SRsig = 4.71 V/ms   Circuit: SRmax = 12.4 V/ms, 20 kHz clock

Figure 3a: Point 1
Audio Input
2 V/div
500us/div
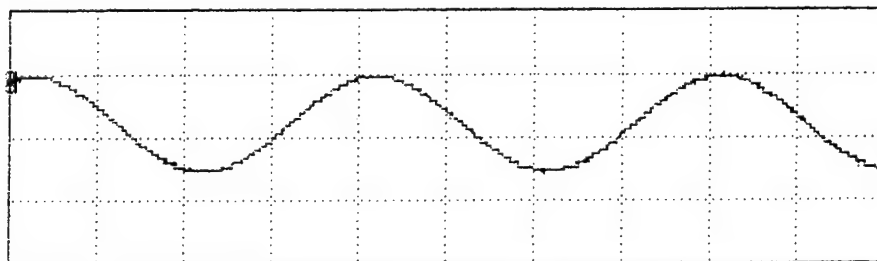
Figure 3b: Point 5
Feedback
2 V/div
500us/div
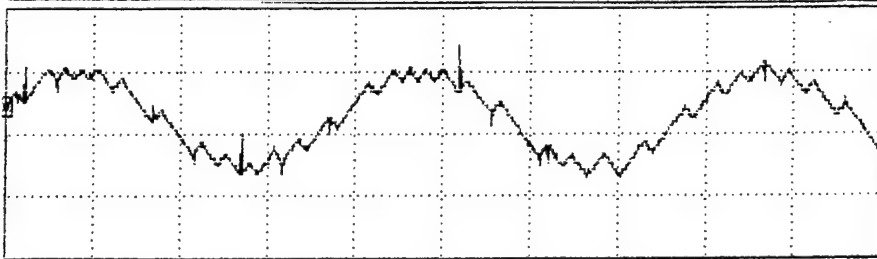
Figure 3c: Point 3
Serial data out
2 V/div
500us/div
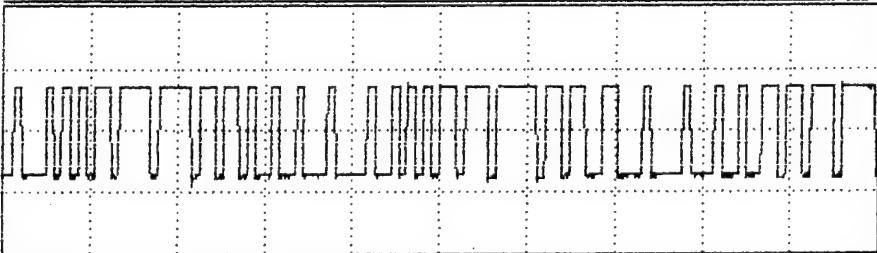
Figure 3d
Clock
2 V/div
500us/div
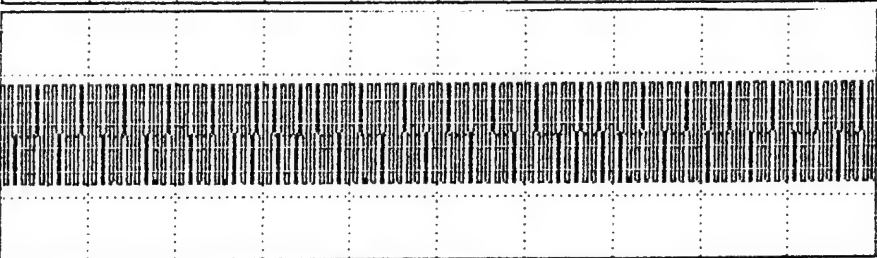
The third set of displays (Figure 4) shows the effects of an overdrive condition resulting from a higher than acceptable voltage level at the input. The input signal is 500 Hz at 10 Vp-p. The output of the integrator is around 7.0 Vp-p. This less that the 10Vp-p input frequency an is caused by slew limiting. Any increase in frequency will cause further limiting of the feedback waveform.

Figure 4: Delta Modulation Encoded Signal; Voltage Overdrive Example
  Input signal: 500 Hz, 10.0 Vp-p, SRsig = 15.7 V/ms   *Circuit: SRmax = 12.4 V/ms, 20 kHz clock*

Figure 4a: Point 5
Feedback
4 V/div
500us/div
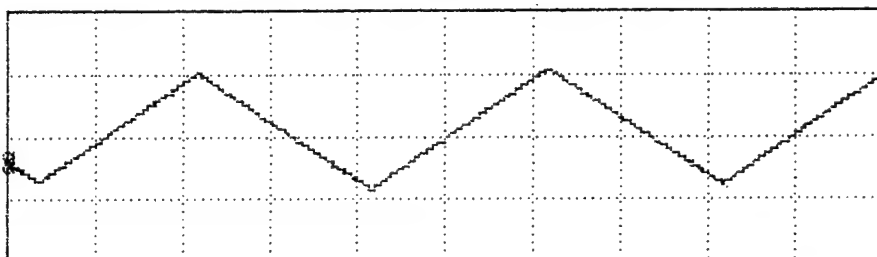
Figure 4b: Point 3
Serial Data Out
2 V/div
500us/div
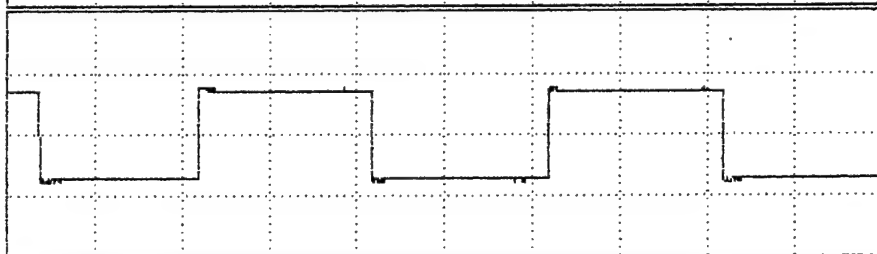
The fourth set of displays (Figure 5) shows the effects of an overdrive condition resulting from a higher input frequency. The input signal is 2,500 Hz at 3.0 Vp-p and the feedback waveform is only at 1.5 Vp-p.

Figure 5: Delta Modulation Encoded Signal; Frequency Overdrive Example
  Input signal: 2500 Hz, 3.0 Vp-p, SRsig = 23.55 V/ms   *Circuit: SRmax = 12.4 V/ms, 20 kHz clock*

Figure 5a: Point 5
Feedback
2 V/div
200us/div
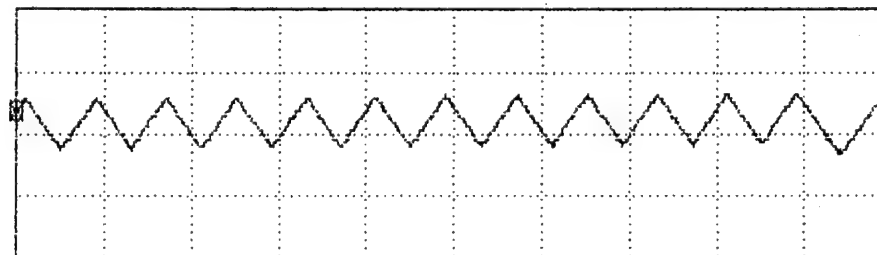
Figure 5b: Point 3
Serial Data Out
2 V/div
200us/div
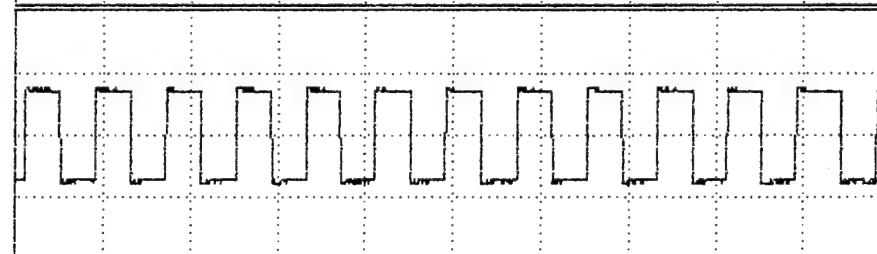
This frequency overdrive condition can be corrected by setting the resistor-capacitor (RC) constant of the integrator circuit to a higher level, resulting in a steeper slope. Doing this, however, causes an underdrive condition with the lower frequencies and smaller amplitude signals. This happens when the audio signal changes less than the height of the integrator ramp. The change in amplitude cannot be resolved and the dynamic range is associated with clock frequency.

Figure 6 is the 2,500 Hz, 3.0 Vp-p signal with an adjusted integrator to give a faster slew rate. The steeper slope follows the original signal more closely than that of Figure 5 and the slew limiting problem will not occur until higher frequencies are reached. The time constant in the new circuit is set at 50us and the resulting slew rate is 31.5 V/ms or about four times faster than the first example.

Figure 6: Delta Modulation Encoded Signal; Increased Slew Rate Adjustment
         Input Signal: 2500 Hz, 3.0 Vp-p, SRsig = 23.55V/ms   Circuit: SRmax = 49.5 V/ms, 20 kHz clock

Figure 6a: Point 5
Feedback
2 V/div
500us/div
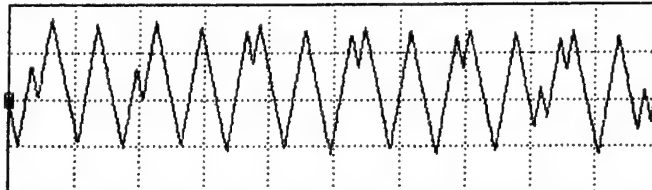
Figure 6b: Point 3
Serial Data
2 V/div
500us/div
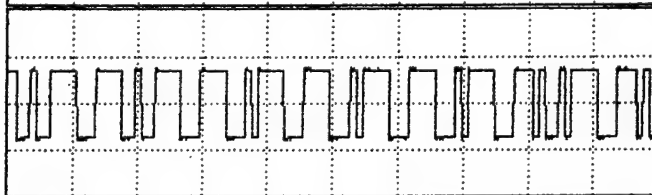
Figure 7 shows the effect of the faster slew rate on the low frequencies. The original signal from Figure 2 is now sent through the circuit and the new integrator follows the slope in a 'stairstep' fashion. This adds much distortion to the signal upon decoding and if the signal has a lower amplitude, it may not be encoded at all.

Figure 7: Delta Modulation Encoded Signal; Consequence of increased slew rate on low frequencies
         Input Signal: 500 Hz, 3.0 Vp-p, SRsig = 4.71 V/ms   Circuit: SRmax = 49.5 V/ms, 20 kHz clock

Figure 7a: Point 5
Feedback
2 V/div
500us/div
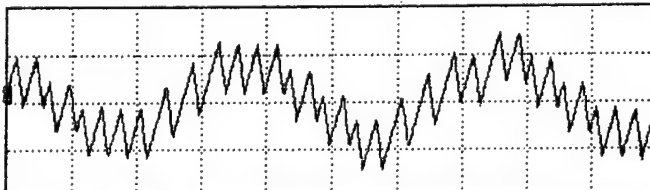
Figure 7b: Point 3
Serial Data
2 V/div
500us/div
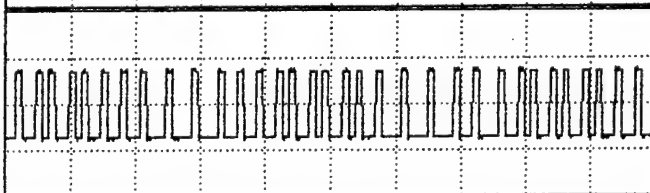
What would be desirable is to have a variable slope circuit that increases the slope of the integrator feedback when a signal with a large amplitude or frequency was detected. This would preserve the quality of the lower frequencies and enable the higher frequencies to also be tracked. The continuously variable slope circuit provides this ability.

Function of the CVSD circuit

The CVSD circuit is the delta modulation circuit with an additional feedback circuit. This feedback monitors the serial data stream of the encoded audio. When the audio input is changing rapidly with steep voltage ramps, the serial data contains many ones or zeros in a row as the integrator output is failing to keep up with the audio input. The additional feedback circuit receiving the serial data activates when 3 ones or 3 zeros in a row are seen. Once activated, this circuit increases the slope of the integrator feedback to the comparator.

An explanation of the CVSD circuit operation is shown by following the block diagram in Figure 8.

The serial data at point 3 is sent into a shift register. Output from the register and the current data bit are sent to an Exclusive-Or gate. Output from the gate at point 6 is in a high state (3 volts) until 3 ones or 3 zeros in a row are sent to its inputs. When this occurs, the output goes low and the additional integrator know as a syllabic filter is activated. The RC time constant is proportional to the length of a typical syllable, therefore the term syllabic filter is used. The syllabic filter responds to the low input with an upward ramping voltage output at point 8.

The sylballic filter output is sent to one of the inputs of an analog multiplier. If the signal has not been slewing rapidly and the syllabic filter is not activated, the output at point 8 is at a level that will cause the analog multiplier to have a gain of one. The other input of the multiplier is the output from the integrator of the delta modulation circuit. In this configuration, the voltage ramp from the delta modulation integrator being sent to the comparator is increased (or decreased) more rapidly when the serial data indicates a rapid change. If the serial data continues to be ones or zeros for a period of time, the syllabic filter continues to ramp up and increase the multiplication factor, providing a better signal following ability.

Illustrated CVSD Examples

To help understand the process, a series of examples with o-scope displays is provided.

The first set of displays (Figure 9) shows the output of the logic circuit when added to the basic delta modulation circuit. This is the voltage present at point 6. Notice, the syllabic filter and analog multiplier have not yet been added to the circuit. Although the display is not from a functioning CVSD circuit, it illustrates the operation of the shift register and exclusive-or gate.

Figure 9: Logic Gate Output Example - Low slew rate signal
Input Signal: 500 Hz, 3.0 Vp-p, SRsig = 4.71 V/ms   Circuit: SRmax = 12.36 V/ms, 20 kHz clock

Figure 9a: Point 5
Feedback
2 V/div
500us/div
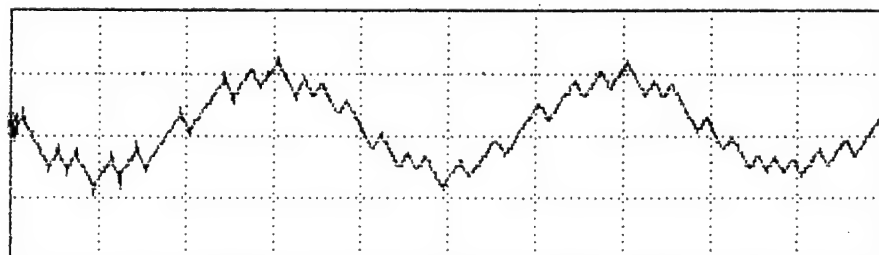
Figure 9b: Point 6
Logic Output
2 V/div
500us/div
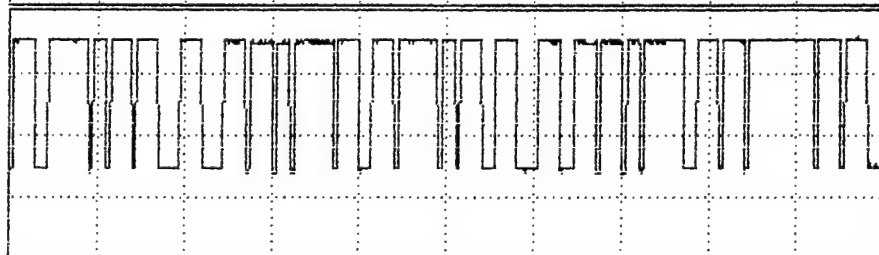
Figure 8: CVSD block diagram

$Z = KXY$
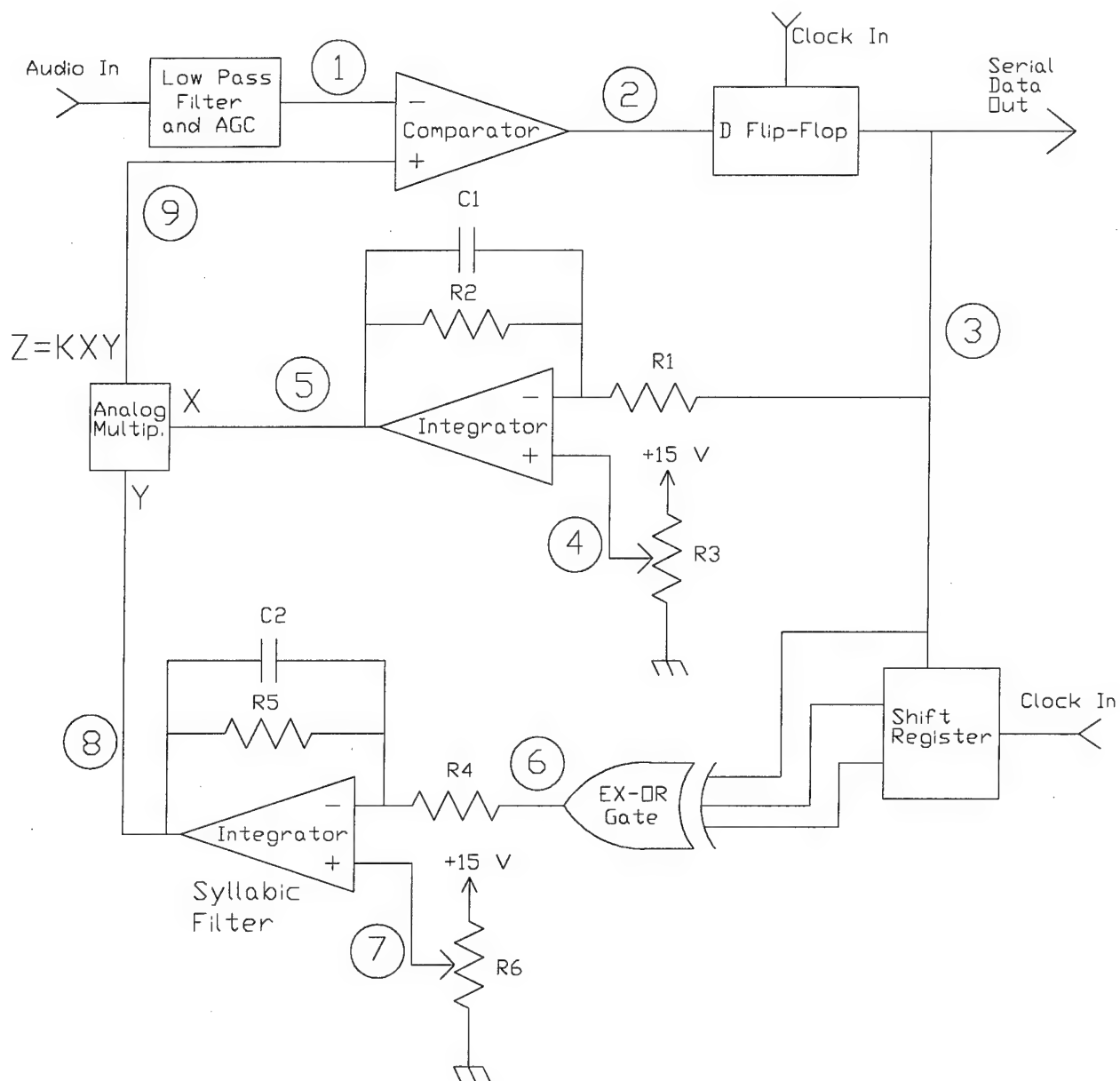
Figure 10 shows the same output at a higher frequency. Notice the increased number of low outputs from the EX-OR gate corresponding to the rapid changes of the waveform.

Figure 10: Logic Output Example - High Slew Rate
            Input Signal: 1500 Hz, 3.0 Vp-p, SRsig = 14.1 V/ms   Circuit: SRmax = 12.36 V/ms, 20 kHz clock

Figure 10a: Point 5
Feedback
2 V/div
500us/div
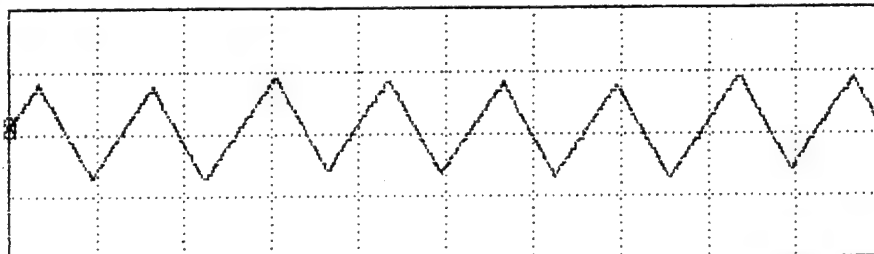
Figure 10b: Point 6
Logic Output
2 V/div
500us/div
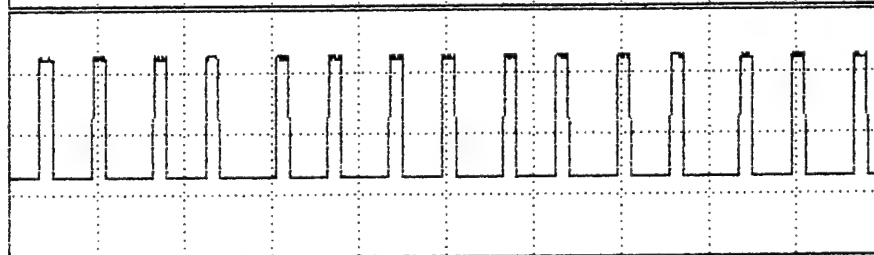
For the examples used, i.e., a steady sine wave, the syllabic filter output is close to a steady state, The following graph shows the output at point 8 in relation to the input at point 6.

Figure 11: Input and output of the syllabic filter

Figure 11a: Point 6
Input pulse from
logic circuit
1.4 V/div
200ms/div
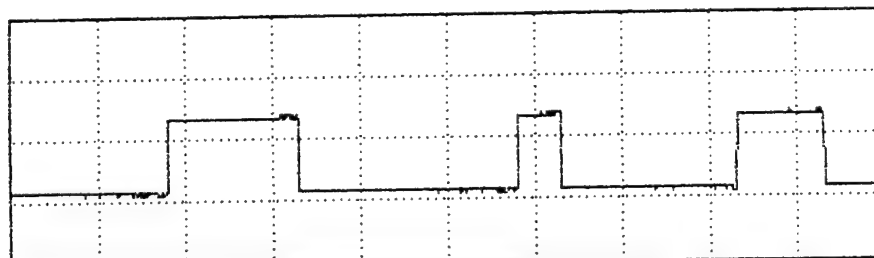
Figure 11b: Point 8
Integrator Output
400 mV/div
200ms/div
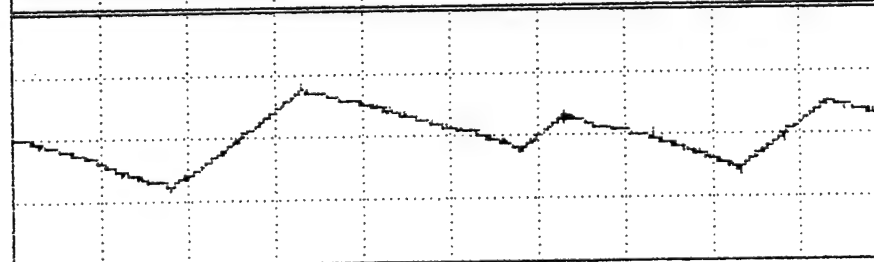
The next two displays show the signal input from the delta modulation circuit to the multiplier and the resulting output from the multiplier. Again, it should be noted that the multiplied feedback is not being sent to the comparator for the sake of these examples. The output from the analog multiplier is only being sent to the display. The first graph is for a low slew signal, notice the output of the multiplier is the same as the input signal.

Figure 12: Multiplier Input and Output; Low Slew Signal
Input Signal: 500 Hz, 3.0 Vp-p, CRsig = 4.71 V/ms   Clock = 20 kHz

Figure 12a: Point 5
Signal into Multiplier
2 V/div
500us/div
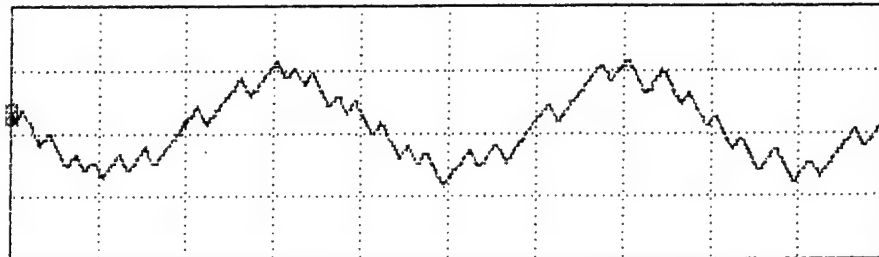
Figure 12b: Point 9
Multiplier Output
2 V/div
500us/div
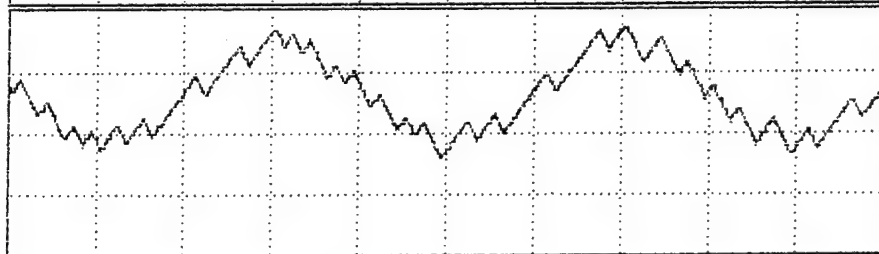
The second graph is with a higher slewing input signal. The multiplier output is noticeably higher due to the output of the syllabic filter increasing and being sent to the multiplier input.

Figure 13: Multiplier Input and Output; High Slew Signal
Input Signal: 2000 Hz, 3.0 Vp-p, CRsig = 18.84 V/ms   Clock = 20 kHz

Figure 13a: Point 5
Signal into Multiplier
2 V/div
500us/div
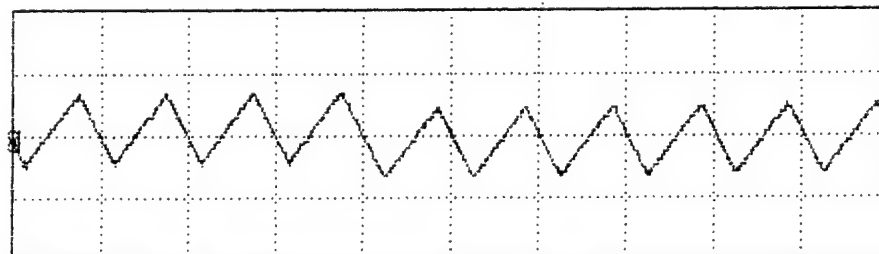
Figure 13b: Point 9
Multiplier Output
2 V/div
500us/div
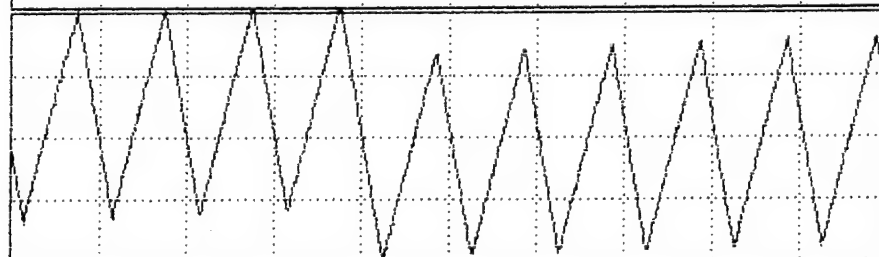
The next graph shows the reconstructed signal at point 9 of the completed CVSD circuit. Although this frequency would be slew limited in the linear delta modulated circuit, it does not show the effects with the CVSD circuit. This waveform is comparable to Figure 5 where the same signal resulted in a frequency overdrive condition. Without the syllabic filter, the waveform would still follow the frequency but would have a reduced amplitude.

Figure 14: CVSD Output for an input signal of 2500 Hz, 3.0 Vp-p   Clock = 20 kHz

Figure 14a: Point 1
Signal input
2 V/div
500us/div
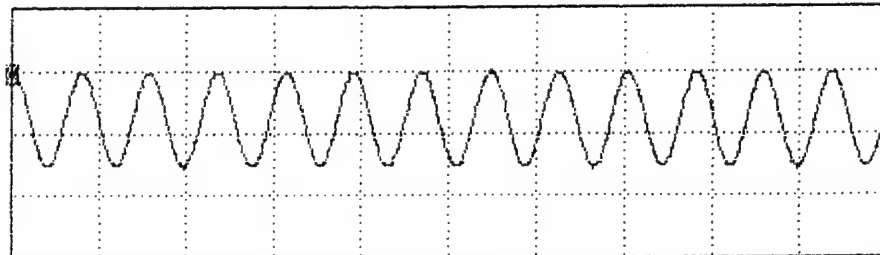
Figure 14b: Point 9
Feedback
2 V/div
500us/div
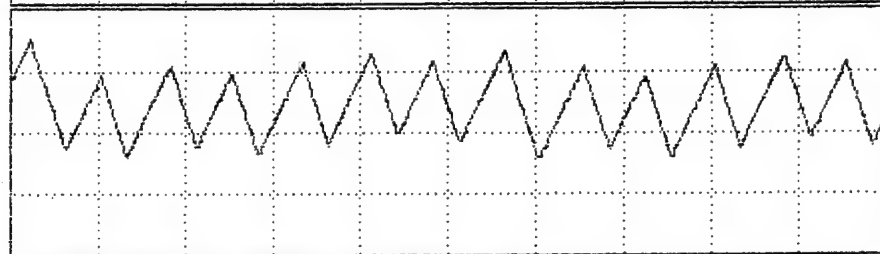
Serial Data Placement

Now that the encoding of the voice has been explained, the serial data are sent to the data acquisition system. The serial data stream is sent to a buffer where it is fed as a parallel word. The placement and removal of this data into and out of the PCM are beyond the scope of the paper.

<u>The Actual CVSD Circuit</u>

A circuit diagram for the functional CVSD circuit is show in Figure 16.

With C1 = .1uf, the potentiometer allows the slew rate to be adjusted. For this paper, the rate was adjusted between 500 and 2,000 ohms. The voltage at point 4 is 1.4 volts and the voltage at point 7 is 1.2V.

The Burr-Brown analog multiplier MPY534 is configured for an output of the pin 1 voltage times the pin 6 voltage with no additional gain and the TL074 op-amps are powered with positive and negative 15 volt supplies.

For the syllabic filter, the input resistance was adjusted to 50K Ohms and the output resistance to 2K Ohms. With these settings, the minimum voltage to the multiplier was 1 V and the maximum is around 3.5 V.

Figure 16: CVSD Circuit Diagram
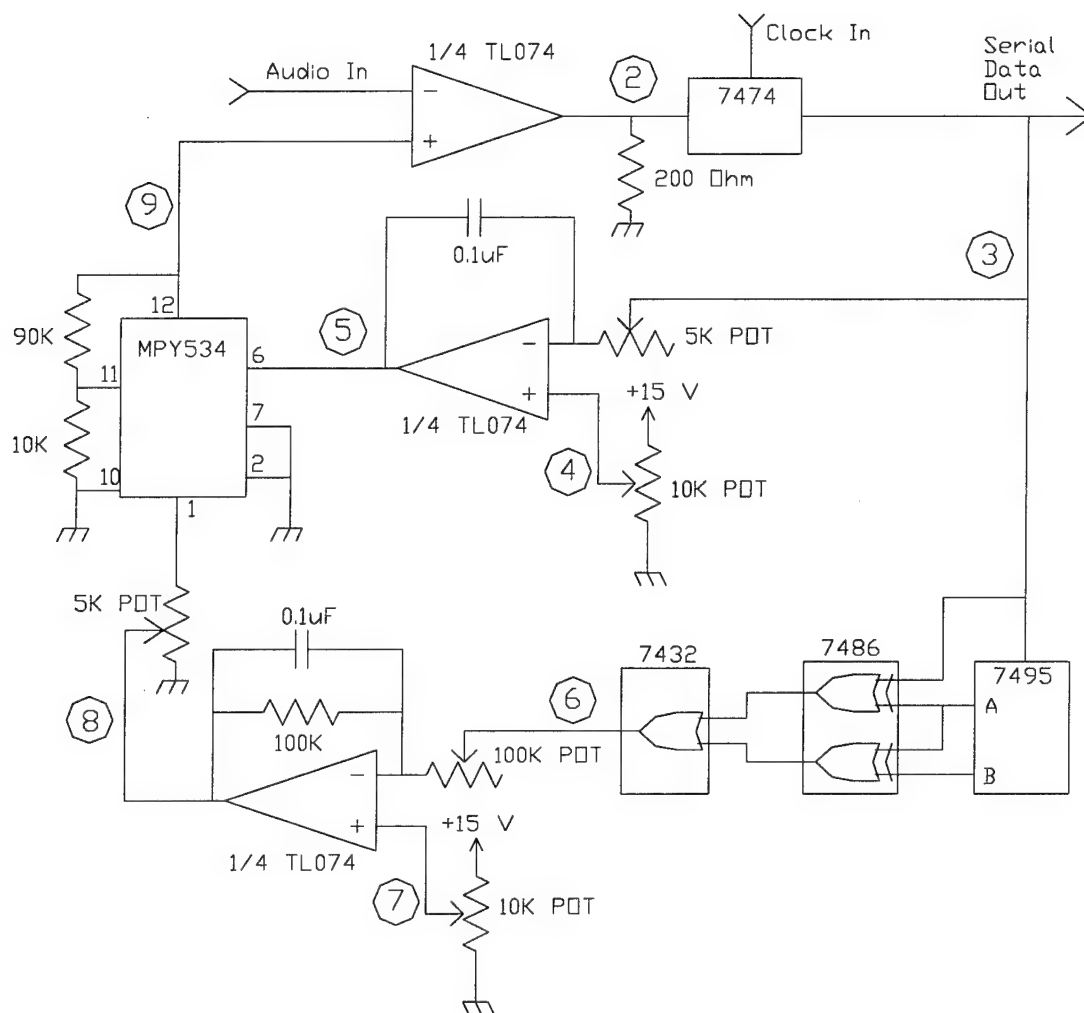
Decoding

Decoding the CVSD encoded voice is just a matter of sending the bits through a modified encoder circuit. The circuit functions like the encoder and the resulting jagged waveform is filtered and amplified. A block diagram of a decoder circuit is shown in Figure 17.

Figure 17: Decoding Circuit
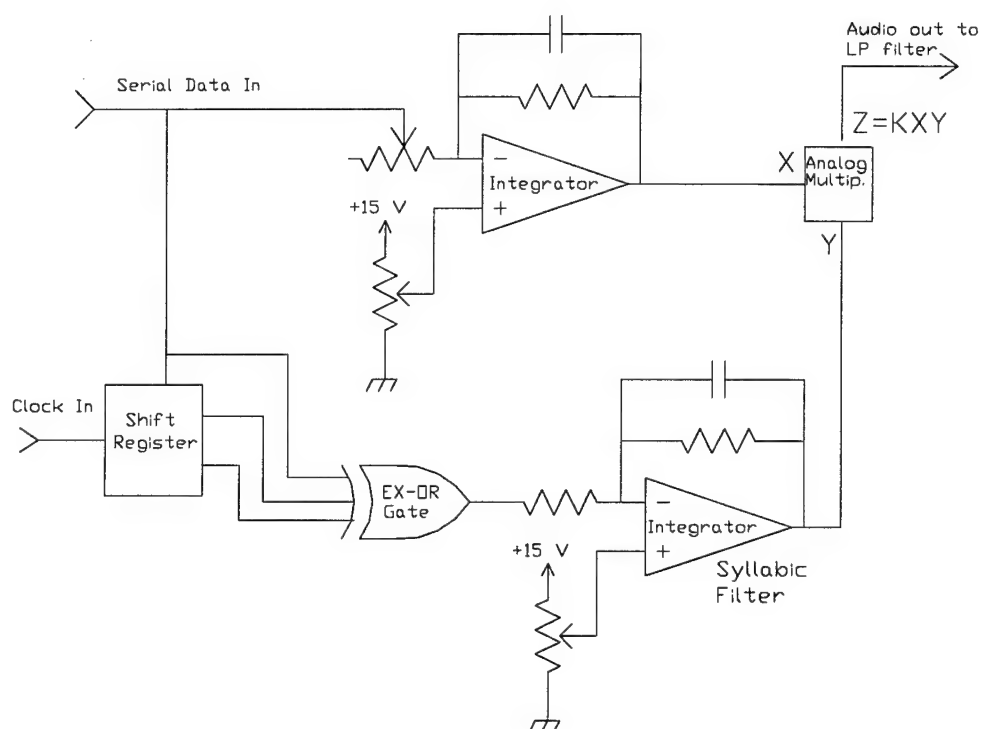
SUMMARY

The CVSD encoding technique is an effective and simple way to place audio signals into a PCM data stream. The circuit can be built out of commercially available integrated circuits and the process uses a fraction of the bandwidth required by linear PCM encoding.

This paper started with an explanation of the linear delta modulation circuit. Through calculations and graphical analysis, the function and limitations of this encoder were investigated. It was determined that an additional feedback circuit would improve the performance at higher frequencies. With this modification, the encoder becomes the CVSD circuit and the limitations of the linear delta modulation circuit are overcome. This is demonstrated with a signal that was distorted in the linear delta modulation circuit and is transferred with better resolution in the CVSD circuit.

Although straightforward, the actual designing and construction of the circuit can contain a number of different variables and settings which can produce a wide range of results. The circuit as designed here has a higher voltage requirement than the commercially available CVSD integrated circuit encoder. Further study could be done to build a circuit with a lower voltage requirement. Other areas of study could include a comparison of signal to noise ratios for different slew rates and clock frequencies. The technique of placing the data into a parallel word with different data acquisition systems can also be addressed.

References

Don Jones, "Delta Modulation for Voice Transmission", Harris Application Note 607, Harris Corporation, 1984.

James Whelan, "Digital Voice Processing Overview", E-Systems, Inc. , ECI division, St. Petersburg, FL, 1979.

Adel Sedra, and Kenneth Smith, "Operational Amplifiers", Mircoelectronic Circuits, Third Edition, Saunders College Publishing, 1991, pp. 88-89.

SESSION 5

TECHNIQUES AND CALIBRATION

THE NIST SUPER SHAKER PROJECT

B. F. Payne
National Institute of Standards and Technology
Gaithersburg, MD

G. B. Booth
Booth Development, Inc.
Short Beach, CT

Abstract

Increasing demand for higher accuracy accelerometer calibrations and the need for a more convenient system for absolute calibrations has led to the development of a new type of shaker and calibration system. The shaker utilizes a high-stiffness low-mass dual-coil moving element, and is equipped with dual retractable permanent magnets for direct reciprocity calibrations. The calibration system is completely based on commercial test equipment, uses a PC for automatic control, and is capable of uncertainties commensurate with primary-level standards lab measurements. The unique design of the Super Shaker also allows the same machine to be useful both for laser interferometer calibrations and for comparison calibrations. This paper describes the shaker and calibration system and gives some preliminary data.

Introduction

The accuracy with which accelerometers may be calibrated is affected by distortion of the wave form of motion and by the presence of motion transverse to the desired axis. Early NBS accelerometer calibrations were based on a commercial shaker modified for reduced cross-axis motion by Bouche, who replaced a large flexure plate suspension with tension wire supports [1]. In 1963, Dimoff developed a modification which further reduced cross-axis motion by replacing tension wire supports with an air bearing [2]. These incremental improvements were superseded in 1966 by a new Dimoff design with a ceramic moving element which retained the air bearing but replaced the field coil of earlier designs with a permanent magnet and replaced the velocity coil of earlier designs with an internal accelerometer [3]. This last improvement increased the upper frequency limit from 2000 Hz to 5000 Hz for comparison calibrations, which are done by comparing the output voltages of the device under test to the internal accelerometer, previously calibrated in place by reciprocity. In 1968, a second Dimoff shaker was developed, extending the range to 7,000 Hz for calibration accuracy of 1 to 2%. Interferometer calibration supplemented the reciprocity calibration of this shaker, extending the range to 10-10,000 Hz. This is possible because interferometer measurements are less sensitive to transverse motion than reci-

procity measurements. Shakers of this design have been used for all comparison calibrations of accelerometers at NBS and NIST from 1968 to the present time [4]. Improvements in the accuracy of the reciprocity calibrations requires significant reduction of the cross axis motion.

Operating costs are high for comparison calibrations since the reference shakers must be calibrated periodically, a long and tedious process because a second shaker must be attached as a driver for reciprocity voltage ratio measurements. This process is too cumbersome to be done each time an accelerometer is calibrated. Therefore the accuracy of comparison calibrations depends on the long term stability of the system components. A calibration system which uses direct reciprocity calibration of accelerometers to eliminate reliance on long term stability would be highly advantageous and is a primary objective of this project.

A new shaker system has been designed to use dual magnets and a dual coil moving element. The dual coil feature eliminates the need for an additional shaker for reciprocity calibrations. To accommodate improved comparison calibrations, the moving element is compact in design and is equipped with axially oriented mounting tables at each end. Provision of easy interferometer beam access to both ends of the moving element allows interferometric accelerometer calibrations.

In order to maximize the potential for design optimization, two versions of the super shaker will be built. The version now constructed uses damped flexures in lieu of air bearings to support the moving element. It is intended to allow direct absolute calibration of accelerometers using both reciprocity and interferometer techniques over the frequency range 100-5000 Hz. The second version to be built will include an air bearing support system and an active axial positioning system for the moving element. These features are expected to expand the frequency range to 10-10000 kHz. After proof testing of all systems has been completed, the aluminum moving element will be replaced with one constructed of beryllium, in an effort to extend the upper frequency limit to 20,000 Hz. For each version of the super shaker, an overall goal is to provide calibrations whose uncertainties are one half as large as those attainable with current NIST shakers over the same frequency ranges.

Design Criteria

Absolute calibration methods for accelerometers (reciprocity and laser interferometry) require high purity of signal wave form. This is especially true for reciprocity calibrations. For reciprocity measurements, the procedure does not take into account the fact that the accelerometer is measuring motion in only one direction, but rather the calculations involve measurement of current differences in the drive coil. Therefore even small amount of distortion and cross axis motion adversely affects the reciprocity calibration. A general rule is that cross axis motion should be less than 2% and harmonic distortion less than 1% in order to perform reciprocity calibrations to 1 to 2% accuracy.

For laser interferometer fringe counting calibration, only the on axis displacement amplitude is measured. Provided the interferometer is properly aligned, the cross axis motion of the shaker is not as significant as in the reciprocity calibration. For example the displacement error of an accelerometer with a 5% cross axis sensitivity, on a shaker with 5% cross axis motion will be approximately 1/4%. Harmonic distortion is a more serious problem. A general rule is that 1% harmonic distortion can produce about 1/2% error in laser interferometer fringe counting calibration [5].

In designing the super shaker, great care was taken to control both harmonic distortion and cross axis motion. Control of the latter is especially important to our goal of improving reciprocity calibrations. Among the critical factors considered were:

1. Magnet dimensions, especially the air gap size, roundness, symmetry, and finish.
2. Moving element dimensions, including diameter, symmetry, and roundness.
3. Position and repeatability of position of the moving element in the magnetic gap assembly.
4. Symmetry of coil windings and uniformness of coil wire.
5. Suspension system for the moving element in the magnetic gap assembly.
6. Isolation of critical parts of the shaker to prevent cross coupling of various vibrating parts of the assembly.

The dimensional tolerances for all super shaker assemblies were specified to be no greater than 30 mm (0.001 inch).

Description of the Shaker Assembly

The super shaker, shown in figure 1 is .64m (25 inches) wide, 1.22 m (48 inches) long, by about .5m (20 inches) high. It is mounted on soft rubber pads on a heavy flat table, pneumatically isolated from ground vibration. The frame consists of three supporting pedestals, one at each end and one in the middle, and four large diameter shafts running end to end, two clamped near the bottom of the three pedestals, and two clamped near the top of the pedestals. Two magnet assemblies, equipped with air bearings, are supported by the two horizontal rods which are the upper shafts of the frame assembly. The air bearings allow each magnet assembly to be moved away from the moving element to provide the access needed for attachment of accelerometers or masses. The operating axis is parallel to the upper shafts and centered in the plane bisecting them.

A common cause of calibration inaccuracy is interference from frame resonances. The interferences are resisted by internal dampers inside the three pedestals and by damping inside the four shafts. The pedestals and shafts are also sand filled to further dampen any vibration in the frame. These interferences are further resisted by the large magnet mass, and small resulting motion, as compared to the moving element mass. The small magnet motions are isolated from the frame by rubber pads.
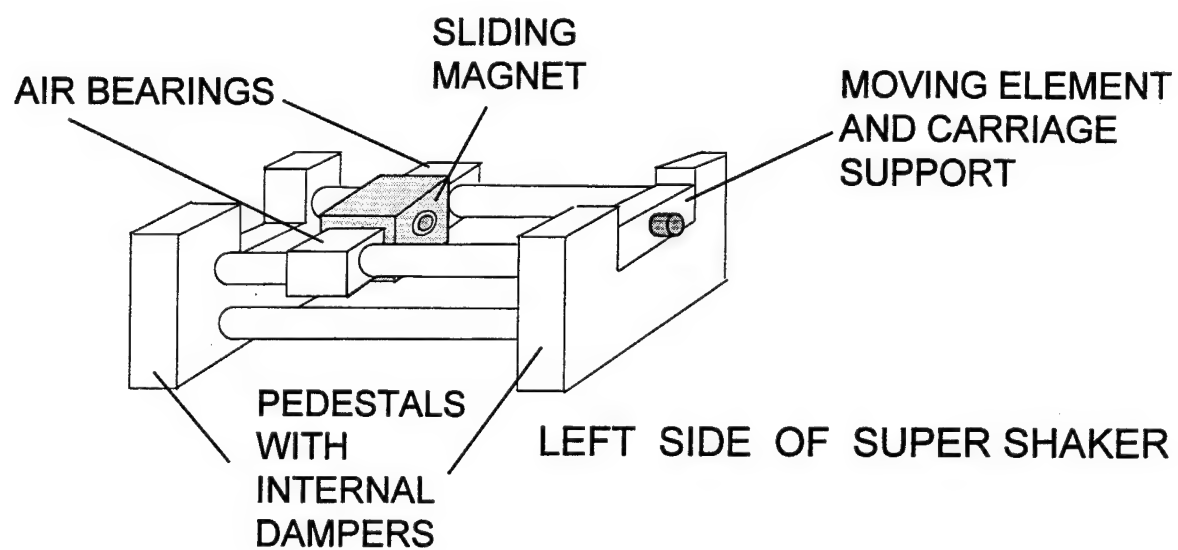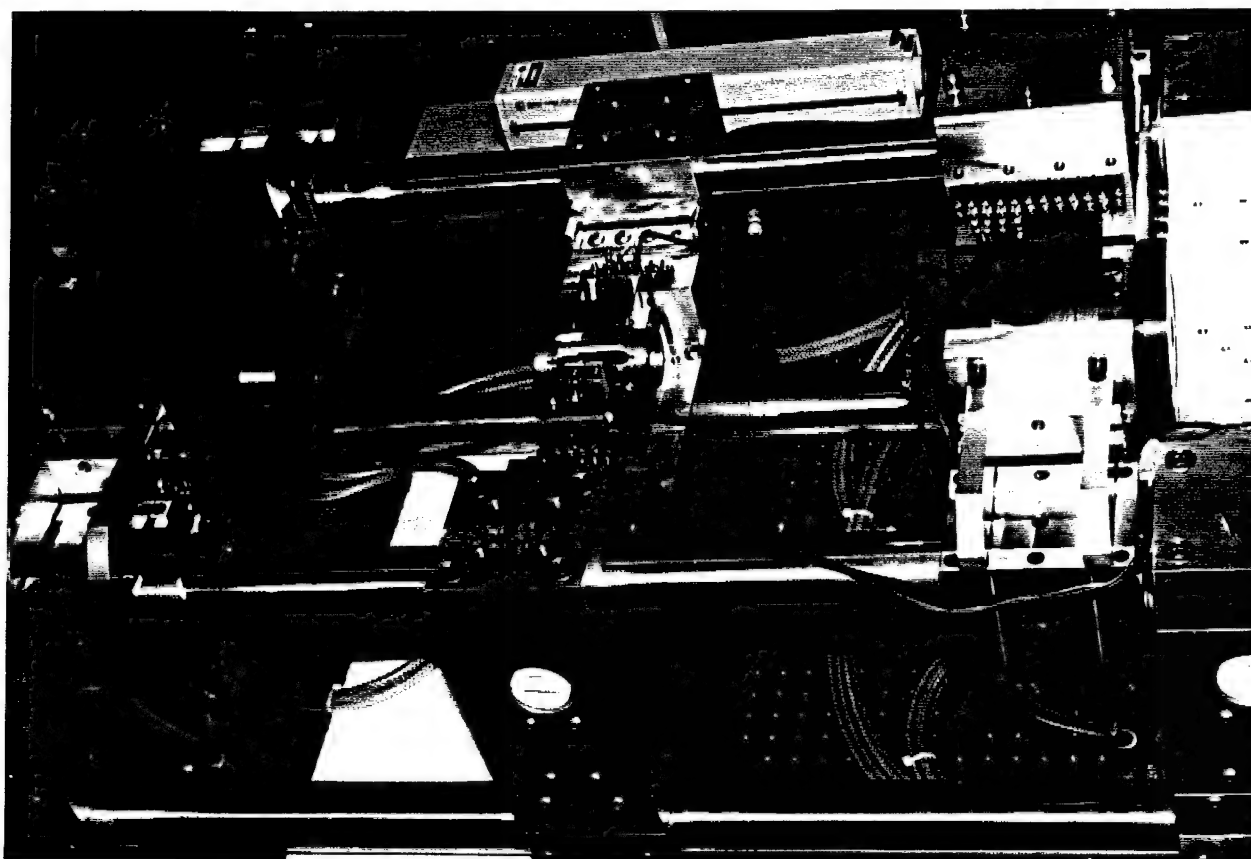
FIGURE 1   SUPER SHAKER WITH MAGNETS MOVED AWAY
FROM MOVING ELEMENT

336

A carriage on the center pedestal supports the moving element, centered on the operating axis. The moving element is symmetrical, with coils on each end.

Machined from a solid metal block, the moving element, shown in figure 2, is symmetrically shaped with respect to a bisecting plane perpendicular to the operating axis. Place-
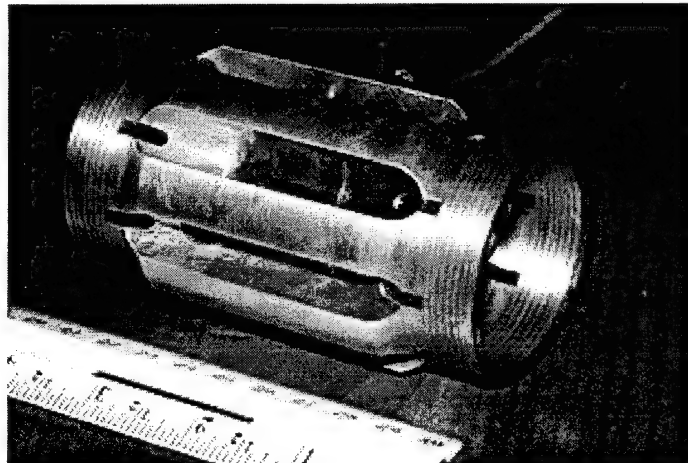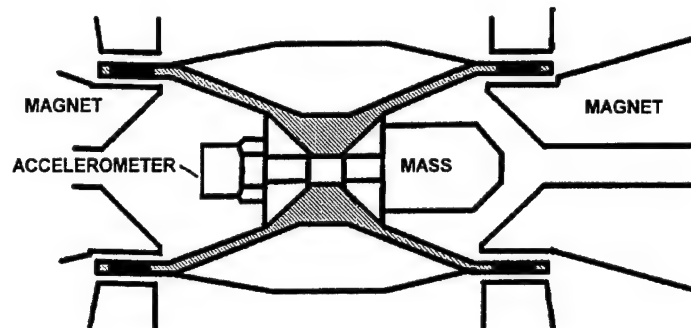

FIGURE 2 DUAL COIL MOVING ELEMENT

ment of the specimen mounting tables at the ends of deep central cavities allows specimens to be mounted close to the bisecting plane and inside the envelopes of the coils located at each end. The outer structure between the two coils is enlarged to provide axial stiffness for high frequency operation.

Movable Magnet Assemblies

The magnet assembly is shown in figure 3. Each magnet assembly has two major parts: the outer permanent magnet, and an inner air gap assembly. The mass of the permanent magnets has been maximized within practical constraints in order to minimize the motion of the magnet assembly relative to the moving element. This reduces interference to the rectilinear motion of the moving element. Residual magnet motions are isolated from the frame by rubber pads.
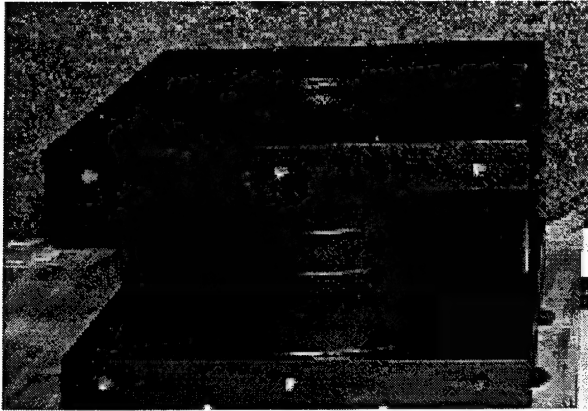
OUTER PERMANENT MAGNET
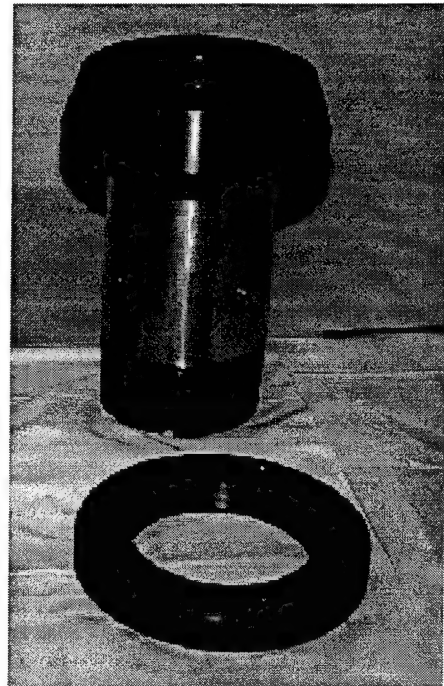
INNER AIR GAP ASSEMBLEY
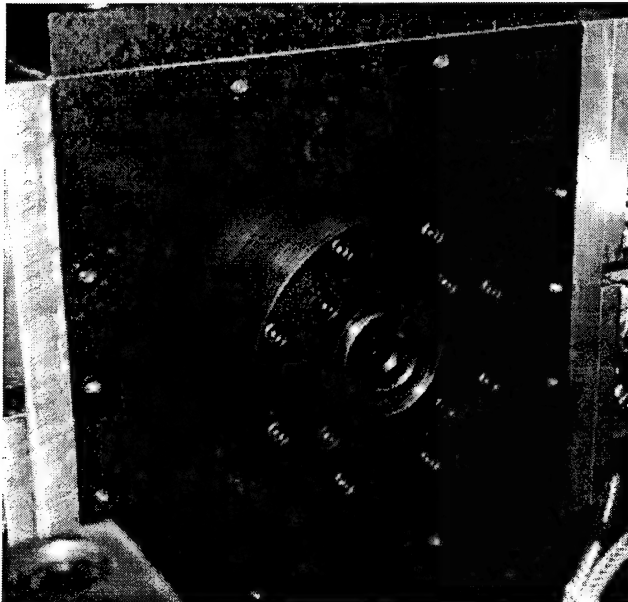
ASSEMBLED MAGNET

FIGURE 3 MAGNET ASSEMBLY AND COMPONENTS

338

Each air gap assembly is equipped with inner and outer copper shading sleeves, a large axial port for the accelerometer cable, and four small ports for interferometer beam access. Each assembly is also equipped with additional ports for air cooling as needed. The air gap assemblies are de-mountable to facilitate installation of new assemblies of different air gap sizes, when future applications require moving elements of different size. Magnetic keepers are provided to allow this to be done without demagnetizing the permanent magnets.

Moving Element and Carriage Description

The moving element and carriage assembly are shown in figure 4. The length is 101.6 mm (4 inches) and the diameter is 63.5 mm (2.5 inches). The structure is aluminum and the mounting tables are of stainless steel, 25.4 mm (one inch) in diameter. The first axial resonance is approximately 22 kHz.

The diameter of the mounting table is adequate to allow the laser beam access required for multiple-reflection interferometer calibrations. To maximize versatility, the four laser beam ports provided in each air gap assembly for this purpose are positioned at 90 degree intervals.

The carriage of the super shaker supports the moving element on four damped beryllium copper flexures. These flexures establish the rest position of the moving element, guide its motion along the system axis, and resist motions perpendicular to the system axis.
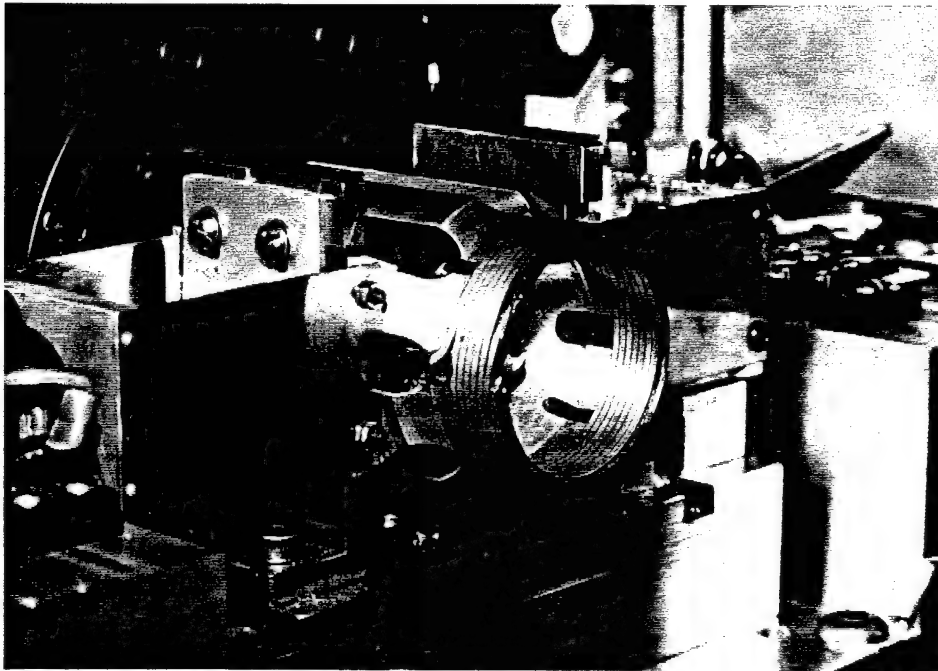

FIGURE 4 MOVING ELEMENT AND CARRIAGE SUPPORT

Shaker Operation

The vibratory drive force for the moving element is generated by an alternating current in one or both of the drive coils in the air gap magnetic fields. For reciprocity calibrations, only one moving element coil is driven. For interferometric or comparison calibrations, either or both of the coils may be driven. Both coils are driven when large displacements and accelerations are desired.

A low distortion power amplifier amplifies a signal from an external signal source to provide the alternating current. As necessary, power amplifier heating is reduced by connecting high power resistors in series with the amplifier output. The use of these resistors is important for high frequency interferometric operation and critical for pulse operation. The current applied to the drive coil(s) must have low levels of harmonic distortion in order to minimize interference caused by excitation of high frequency (typically above 20 kHz) resonances of the accelerometer or moving element.

Improved Reciprocity Performance

For reciprocity calibrations, one of the two moving element coils is driven, and the other used as a velocity measuring coil. Measurement accuracy is significantly degraded by changes in the mean position of the velocity coil in the magnetic air gap. With vertical-axis shakers, gravity makes such changes likely when reciprocity masses are added or subtracted. This problem is avoided by the horizontal orientation of the operating axis of the super shaker. Further protection is provided by the lateral stiffness of the four flexures which support the moving element.

The primary function of the components shown in figure 5 is to improve the accuracy of reciprocity calibrations in the 1 kHz to 10 kHz region. Although the drive coil and the
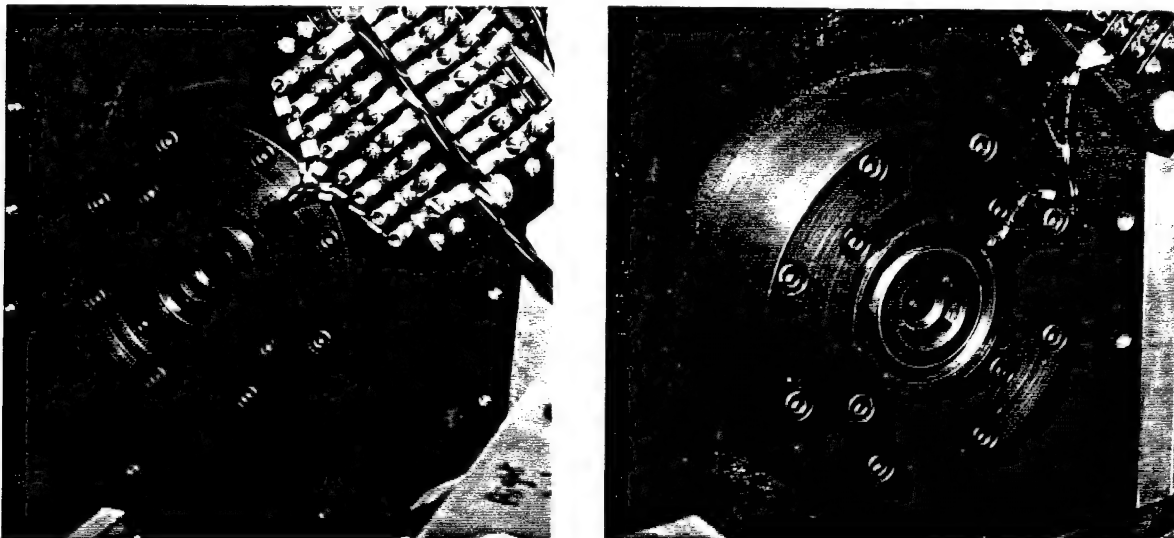

FIGURE 5 NEUTRALIZING (LEFT) AND RECEIVING (RIGHT) COILS

velocity coil are shielded by copper sleeves, both inside and outside, there is some magnetic coupling between the drive coil and the velocity coil. A neutralizing coil is located on the right air gap assembly, and is connected in series with the drive coil. A receiving coil surrounding the velocity coil on the left air gap assembly, is used to monitor the induced voltage of the drive coil alone, and the drive coil plus neutralizing coil. A shunt resistor connected in parallel with the neutralizing coil is adjusted to minimize the voltage output of the receiving coil. The shunt resistor is contained in the housing on top of the right magnet. Also in the housing is a very low value non-inductive power resistor, connected in series with the drive coil, to allow measurement of the drive coil current.

Shaker Performance Tests

The results of the acceleration harmonic distortion tests are shown in figure 6. The distortion at frequencies below 100 Hz is attributed to the flexure support system and is likely to be much lower with the addition of air bearing support. The range from 200 Hz to 9 kHz achieves an acceleration of no greater than 0.1% maximum harmonic content as measured using an attached accelerometer. This frequency range is very promising for reciprocity calibration. Figure 7 gives a typical cross axis motion plot. The cross axis motion was measured with a small triaxial accelerometer with only the accelerometer mounted on the shaker table. The plot in figure 7 show cross axis data for two directions, 90 degrees to each other. This data should be considered only as an approximate indication of the true cross axis motion since calibration masses could not be attached to the table at the same time the accelerometer was attached. Palpation during swept frequency test indicated that resonant motion of one of the four flexures supporting the moving element was the primary cause of this cross axis motion. In the frequency ranges 50 to 500 Hz, and 2500 to 5000 Hz, the cross axis motion is less than 2%, sufficiently low for reciprocity calibration. In order to test its cross axis motion, the super shaker was used to calibrate an accelerometer by reciprocity. The results were consistent with other calibration results obtained using NIST laser interferometer calibration systems on other NIST shakers. Differences between the reciprocity measurements on the super shaker and measurements on the laser interferometer systems were less than 1% over these frequency ranges. With the addition of the proposed air bearing suspension system, the reciprocity range should cover the range of 30 to 10,000 Hz.

Present Development Work and Future Enhancements

To further improve the accuracy of reciprocity calibrations performed using the super shaker, two changes are now in the process of being made. The flexures supporting the moving element are being replaced with new ones with higher damping, which is expected to reduce the cross axis motion, though not to the level achievable with an air bearing moving element support proposed for later versions of the shaker. The fixtures which support the flexures are being redesigned to allow easier replacement of flexures. Secondly, the super shaker is being fitted with a fringe counting interferometer, whose calibration range
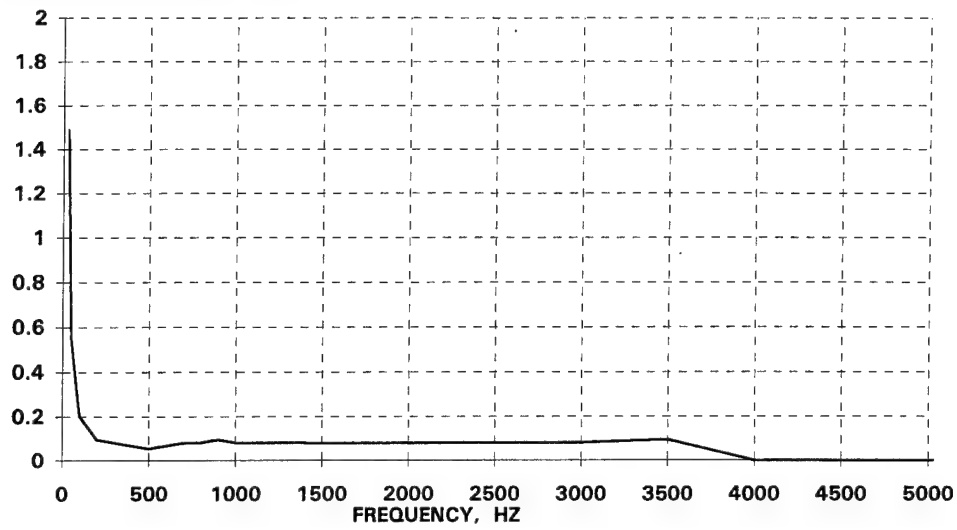
HARMONIC DISTORTION (%)

FIGURE 6 MAXIMUM HARMONIC DISTORTION COMPONENTS
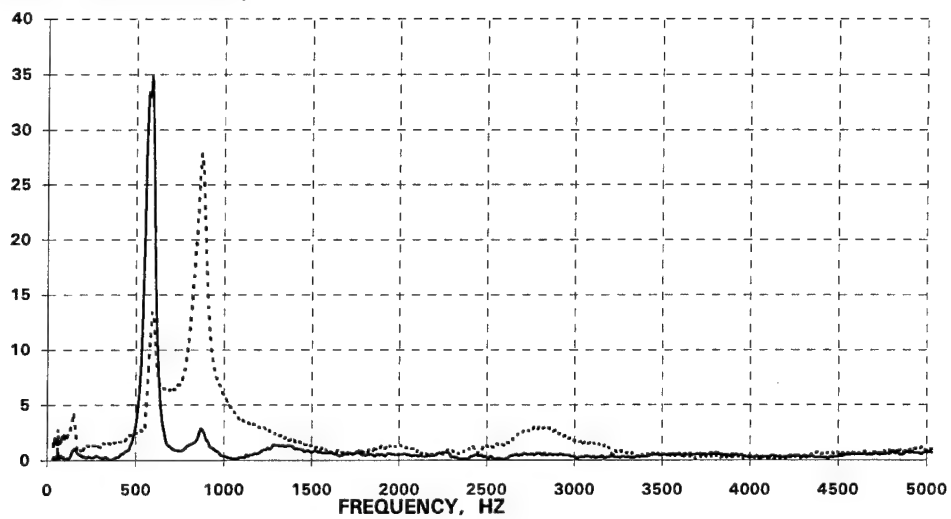
CROSS AXIS MOTION, %

FIGURE 7 CROSS AXIS MOTION IN TWO ORTHOGONAL DIRECTIONS

will be about 30 to 500 Hz. The upper limit of this calibration is limited by the acceleration of the shaker, approximately 200 m/sec^2 (20 g*). This first phase of the research program will conclude with the enhancement of the interferometer system to allow fringe disappearance measurements in the range of 500 to 3 kHz, using higher order disappearance modes.

Future work will proceed as the availability of resources permits. The addition of multiple beam capability to the interferometer system will allow fringe disappearance measurements in the range of 3 kHz to 10 kHz. Because flexures allow much more cross axis motion than air bearing suspension systems, replacing the flexures with air bearings is expected to extend the frequency range for reciprocity calibrations to 30 to 10,000 Hz and the fringe counting interferometer to 10 to 500 Hz. With these improvements, the super shaker system will be capable of absolute calibration of accelerometers over most or all of the 10 - 10,000 Hz range. By carefully selecting frequencies at which distortion and cross axis motion are low, accuracies better than 1% are anticipated.

The modular design of the super shaker will facilitate eventual extension of its upper frequency limit beyond 10,000 Hz. Replacing the stainless steel mounting tables with ones made of a lighter and stiffer material is the first option likely to be pursued. Further improvements could be obtained, though at much higher cost, by replacing the interchangeable moving element with a smaller one, possibly constructed of a material lighter and stiffer than aluminum. These improvements are expected to extend the operating range to 20 kHz.

Summary

A dual coil electrodynamic shaker has been developed for improved accelerometer calibration by both reciprocity and interferometer methods. The shaker uses a uniquely designed aluminum moving element with two mounting tables and a damped flexure support system for the moving element. The shaker has very low harmonic distortion and low cross motion over most of the operating range. The shaker has neutralizing and receiving coils (in addition to the two driver coils) to compensate for magnetic interaction of the two drive coils. Test results show that the shaker has a useful range of 30 to 5000 Hz for absolute calibrations and 30 to 10,000 Hz for comparison calibrations. Planned future enhancements will allow further improvements in performance.

*g = 9.80665 m/sec^2

Acknowledgments

References

1.   S. Levy and R.R. Bouche, *Calibration of Vibration Pickups by the Reciprocity Method*, J. Research NBS 57, 227-243 (1956) RP2714.

2.   T. Dimoff and B. Payne, *Application of Air Bearings to an Electrodynamic Vibration Standard*, J. Research NBS 67C, 327-333 (1963)

3.   T. Dimoff, *Electrodynamic Vibration Standard with Ceramic Moving Element*, J. Acoust. Soc. Amer. 40, 671 (1966).

4.   D.C. Robinson, M.R. Serbyn, B. F. Payne, *A Description of NBS Calibration Services in Mechanical Vibration and Shock*, NBS Technical Note 1232, 1987.

5.   R.S. Koyanagi, *Development of a Low-Frequency Vibration Calibration System*, Experimental Mechanics, 15, 443-448 (1975).

TRANSVERSE RESPONSE OF PIEZOELECTRIC ACCELEROMETER

Jing Lin
PCB Piezotronics Inc.,
3425 Walden Ave. Depew N.Y 14043

Abstract

In general, shock and vibration environments do not exhibit pure linear motion. Because of this, the transverse response of an accelerometer should always be taken into consideration in shock and vibration measurements. The transverse sensitivity (S_t) and transverse response of an accelerometer are an important specification. Since the transverse sensitivity and transverse response of a sensor may effect the accuracy of a given measurement, it should be minimized and defined before the measurement is taken. This paper describes the relation between mounted resonance and transverse resonance as well as the transverse response calibration method and fixturing are discussed. It is suggested that the useful frequency range of an accelerometeris dependent on mounted and transverse resonant frequency.

Transverse Sensitivity

Ideally an accelerometer should respond only to accelerations along an input reference axis defined by its geometry (usually the direction perpendicular to the mounting surface), and should have zero sensitivity in any directions orthogonal to that ideal direction.

Transverse sensitivity can result from misalignment of the sensitivity or input axis from ideal and poor manufacturing tolerance (see fig.(1)).
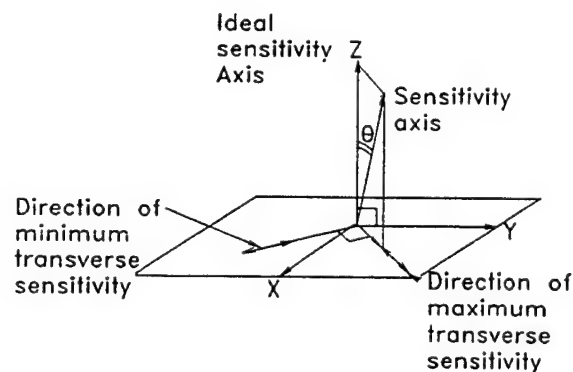

Fig.(1) Vectorial Representation of Transverse Sensitivity

The transverse sensitivity is the result of misalignment of the actual sensitive axis from the ideal direction. The x and y axes define the transverse plane. When an accelerometer has an acceleration applied in the transverse plane, there will still be some output from the accelerometer.

The transverse sensitivity (S_t) is the ratio of the maximum transverse output expressed in acceleration divided by the magnitude of acceleration in the ideal direction.

As an example, for an accelerometer with 5% transverse sensitivity which is going to measure a shock and vibration with about 30% transverse motion, the maximum contribution of the transverse output to the measurement would be the product of the two, only 1.5%. If the measurement frequencies are approaching to a few kHz , the transverse response of accelerometers will increase its transverse sensitivity by following single - degree - freedom response.

Transverse Frequency Response

The idealized description of a mounted accelerometer in a Single - Degree - Freedom system (DOF) is illustrated in Fig.(2).
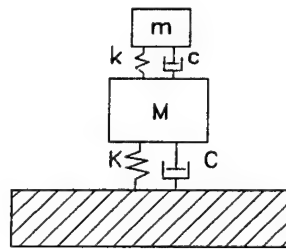

Fig.(2) Idealized Model of mounted Accelerometer

In the most cases, assuming the accelerometer to be an undamped spring - mass, their natural resonance frequency ($\omega_n = \sqrt{k/m}$) is higher than mounted resonance frequency ($\omega_m = \sqrt{K/(M+m)}$). The mounting stud is under tension force and its spring constant is K_t.

When mounted accelerometer has acceleration applied at right angles to its mounting axis, there will still be some output from the accelerometer. In this case, mounting stud is under shear force condition. Its spring constant is K_s which is much smaller than its tension spring constant K_t , hence its transverse resonance frequency is lower than mounted resonance frequency. Fig.(3) shows the frequency response of an accelerometer to main and transverse axis.
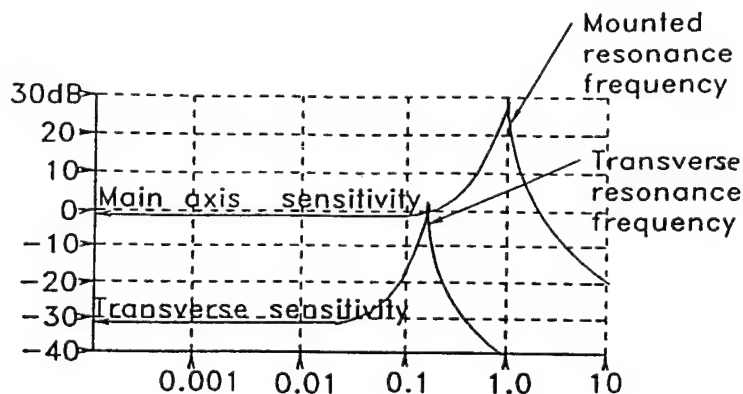

Fig.(3) The Frequency Response of an Accelerometer to Main
Axis and Transverse Axis

Mounted and transverse resonance frequency measurement data for fourteen commercial accelerometers are shown below.

Model	Mounted Resonance kHz	Transverse Resonance kHz	Ratio
X375	55	18	3.1
X371	42	15	2.8
X391	40	12	3.3
X382	28	10	2.8
X390	28	9	3.1
X370	16	4	4.0
X378	13	3.8	3.4
Y318	6.5	1.6	4.0
X374	85	21	4.0
X321	40	14	2.8
Y309*	180	28	6.4
Y310#	30	9.5	3.2
Y315#	27	9	3.0
Y317	25	7.5	3.3
354M06	45	32	1.4

* is 100,000g shock accelerometer.
# are industrial accelerometers.

From these data, the most ratios of the mounted resonance to transverse resonance are higher than 2.8.

At frequencies less than one eighth to tenth of the axial mounted resonance, the transverse sensitivity can be kept below 10%.

A Fixture for Transverse Response Calibration

The mounted resonant frequency of an accelerometer can be found under optimum mounting conditions by vibration or impact method using the standard mounting studs on a high frequency vibrator or a steel block which is ten times heavier than the test accelerometer. The sensing axis of test accelerometer is along the direction of acceleration input during the mounted response testing.

When an accelerometer has acceleration applied at right angles to its sensing axis, there will still be some output from the accelerometer. The transverse response is shows in Fig.(3). The fixture resonance will distort transverse response of a test accelerometer and reduce useful frequency range. Fig.(4) shows the transverse response of a testing accelerometer which is mounted in to a fixture with a open slot. FEA of the fixture with open slot shows the Fig.(5). Fig.(6) shows the frequency response of a tri-axis accelerometer which is mounted into a pocket hole in the same size fixture which has the first resonance more than 30kHz. See Fig. (7).
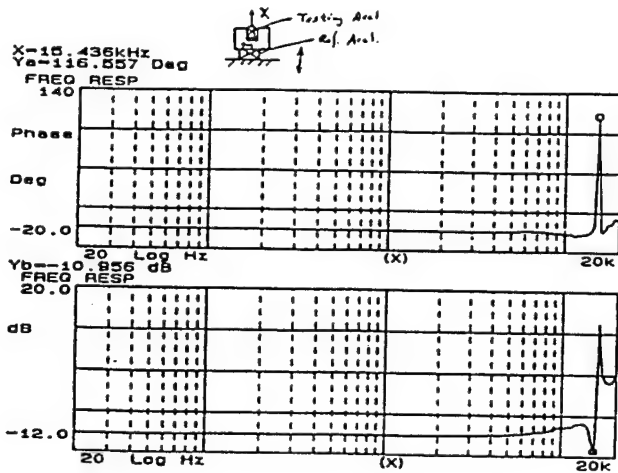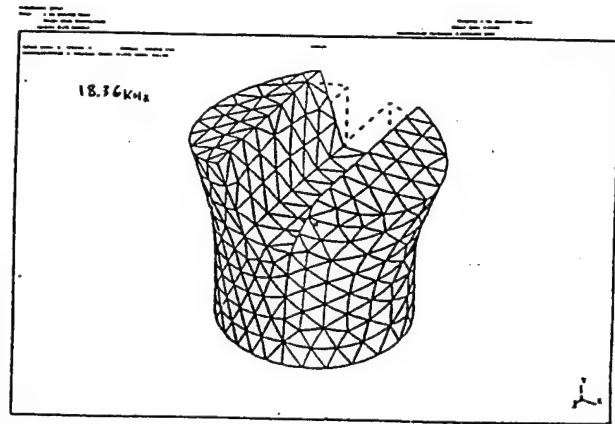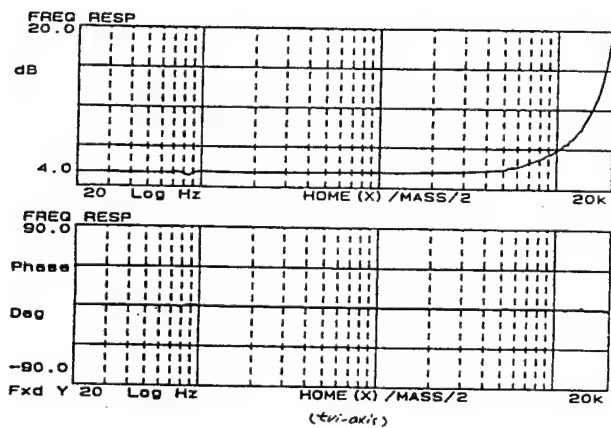
Fig.(4)
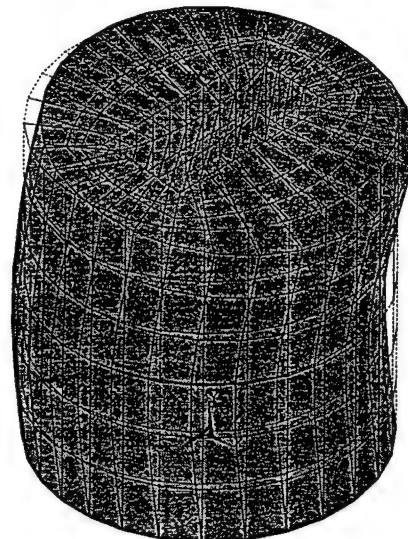

Fig.(5)

Fig.(6)

ANSYS 5.0 A
DEC 12 1994
20:31:21
PLOT NO.   21
DISPLACEMENT
STEP=1
SUB =2
FREQ=35006
RSYS=0
DMX =56.161

Fig.(7)

Impact Hammer Calibration Method

The impact hammer calibration involves testing the simplest of structures, a pendulously suspended mass behaving as rigid body obeying Newton's law of motion

Since its transfer function is a constant (1/mass), test results reflect only the behavior of the testing accelerometers. Input force to the hammer is measured indirectly, as mass times acceleration.
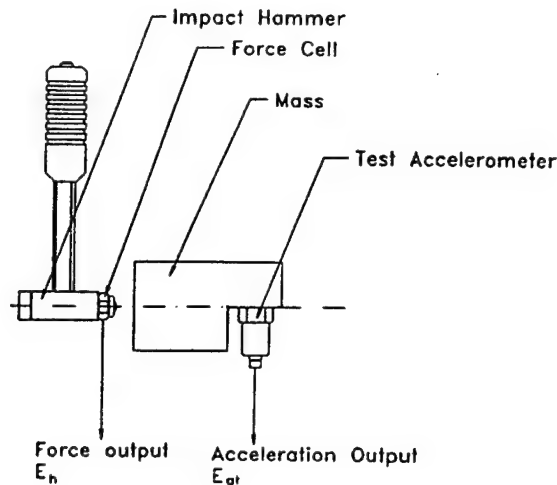

Fig.(8) Schematic diagram for impact hammer method

Hammer testing requires a known mass and a calibrated accelerometer. Test results depend upon the ratio of two measured voltages, according to the following relation:

$$\left(\frac{e_h}{S_h}\right)[H] = \frac{e_a}{S_{at}} \qquad or \qquad S_{at} = (MS_h)\left(\frac{e_a}{e_h}\right)$$

Transverse sensitivity is usually expressed as a percentage of a accelerometer axial sensitivity, as :

$$\frac{S_{at}}{S_a}$$

Where S_h is the sensitivity of the force cell;
S_{at} is the transverse sensitivity of test accelerometer;
e_a/e_h is the output ratio of test accelerometer to force cell;
M is the mass of rigid body;
H is transfer function of the mass (fixture).
Feed two signals (e_a, e_h) to an analyzer, and the results which reflect the function transfer behavior of the transverse sensitivity vs. frequency.

Useful Frequency Range

The American National Standards Institute defines resonant frequency as that frequency at which the sensitivity of the pickup is a maximum (ANSI S2.2-1950 Section 2.13).

Accelerometers should be selected with resonant frequencies at lest 5 times higher than the highest frequency of interest (or with a natural period less than 1/5 of an input shock pulse duration). To be valid, however, the resonant frequency specified must be mounted mechanical resonance. Since the accelerometer will be mounted in use, the mounted resonance is the only one of value to the user.

For an accelerometer, its transverse resonant frequency is much lower than its mounted resonant frequency. The transverse response can cause a significant error in shock and vibration measurement. For an example, an accelerometer with 5% transverse sensitivity has 33% increasing in transverse sensitivity at half of transverse resonant frequency, and can cause about 10% error in shock and vibration measurement which has 30% cross motion components.

Useful frequency range of a piezoelectric accelerometer is determined by its transverse frequency response, rather than its mounted frequency response.

It is suggestion that the useful frequency limit is about one tenth of mounted resonance frequency in most shock and vibration measurement. The higher the mounted resonant frequency, the wider the operating frequency range. In order to have a higher mounted resonant frequency it is necessary to have either stiffer piezoelectric elements, lower total mass and stiffer mounting stud and better contact surfaces.

References

1) PCB: Vibration & shock sensor selection guide ----SSG-601   1993
2) ANSI S2.2-1950
3) B & K : Piezoelectric accelerometer and Vibration Preamplifier 1987

UTILIZATION OF STATIC CALIBRATION DATA TO
CORRECT NONLINEAR MEASURED DYNAMIC PRESSURE DATA

David Banaszak, Electronics Engineer
U.S. Air Force, Wright Laboratory
Wright-Patterson AFB,OH45433-7006

Abstract

This paper discusses the process required to correct nonlinear pressure transducer data obtained inadvertently during recent measurements of dynamic pressure in acoustic modulator valves in Wright Laboratory's small combined thermal and acoustic test facility. This paper also serves as a short tutorial reminding scientist, engineers and technicians that assumptions of transducer linearity must be carefully guarded to certify valid data acquisition and analysis.

The facility generates sound pressure levels (SPL) greater than 174 dB at temperatures exceeding 2500 °F in the test section. Wright Laboratory engineers conducted two series of tests to evaluate several models of commercial pressure transducers to certify that they would operate at high temperatures and acoustic levels. To check the acoustic levels into the test section, four additional strain gage pressure transducers were placed in the throat of the acoustic modulators which provided the acoustic excitation. These four modulator transducers replaced old piezoelectric transducers. Laboratory engineers agreed that the new transducers would provide good reliable data and also allow for measurement of static pressures. The first high temperature test began, and the major emphasis was on the high temperature transducers under test. The modulator transducers were mainly for baseline data. Lab engineers plotted time histories of the high temperature transducers and the modulator transducers to ensure that no data were clipped. The modulator transducers looked good on the oscilloscope during the tests, except one broke and had to be replaced with a higher range transducer to withstand the high acoustic levels. However, on the scope, there was also a DC component. The paradigm was the engineer's concern with only the dynamic output of the transducers. After evaluating the high temperature transducer microphone, laboratory engineers decided to look into the modulator microphone peculiarities in more detail. They noticed that time histories for the modulator microphones did not look like expected due to nonlinear effects. This paper describes a process that allowed the engineers to plot valid time history data from this nonlinear data.

Background

Increasingly, in aerodynamics testing, there is a trend to merge dynamic and static pressure measurements. Years ago dynamic measurements in a wind tunnel test were unique. Presently, aircraft designers need both dynamic and static measurements, so there is a trend toward using strain gage pressure transducers to make these measurements. In Wright Laboratory's Combined

351

Environment Acoustic Chamber(CEAC), the strain gage pressure transducers are replacing piezoelectric transducers to measure acoustic levels exceeding 180 dB SPL. For engineers accustomed to measuring static pressures, dynamic measurement techniques are not well understood. Likewise, for those used to measuring dynamic pressures, static measurement techniques are unfamiliar.

New data acquisition systems allow the measurement engineer to record both static and dynamic pressures on the same storage device. Extra care must be taken to ensure that assumptions made when measuring static or dynamic data exclusively do not lead to invalid measurements. Typical system filter responses for the dynamic and static measurements are shown in figure 1. For static pressure measurement, a low pass filter eliminates 60 hertz noise, vibration noise and radio frequency noise; however, acoustic and vibration data are also filtered. For dynamic pressure measurements, a high pass filter eliminates undesirable DC offsets, low frequency cable noise and thermal noise, but now static pressure data is filtered. Thus, filtering out noise for static measurements can eliminate dynamic data and vice versa. This is not desirable. The ideal situation is to keep data at all frequencies as shown in figure 1 for the all pass filter. Now, undesirable noise must be minimized. For example, 60 hertz line noise must be reduced by using proper grounding techniques to eliminate ground loops.

The dynamic measurement engineer may use AC coupling between the transducer output and recorder input. The engineer assumes that low frequency data is a nuisance, but what happens when static pressure changes affect the validity of dynamic data? Can the engineer assume linearity? There is a definite need to check and understand transducer calibrations to ensure valid measurements.

Test Facility Description and Setup

Wright Laboratory developed a combined thermoacoustic test facility called the CEAC. The CEAC simulates dynamic pressures created by jet engines, turbulent air flow across hot aircraft structures, and high thermoacoustic levels during high velocity flight through the atmosphere. The CEAC gives Wright Laboratory the capability to test materials and structures in a combined high level thermoacoustic environment. Wright Laboratory also built the Sub-Element Acoustic Chamber (SEAC) shown in figure 2. The SEAC is a prototype for the CEAC and has the same capabilities with the exception of test specimen size.

Wright Laboratory dynamically evaluated three models of commercial strain gage pressure transducers in the SEAC at high acoustic levels and at temperatures up to 1200 °F. References 1 and 2 describes the dynamic evaluation of these high temperature transducers during June 1993 and December 1993 respectively.

In addition to the high temperature transducers, four strain gage pressure transducers, also called microphones, were placed at the throat of the acoustic modulators as shown in figure 3. The 4 Wyle Model WAS 3000 airstream modulators described in reference 3 generated acoustic noise over a range of 50 - 500 Hz at levels exceeding 180 dB SPL. Data from these microphones were not

required to evaluate the high temperature transducers, however time histories obtained from these modulator transducers, M1 through M4, provide the data for the remainder of this paper. These modulator microphones measured the acoustic input required to dynamically test the high temperature transducers in the test section of the SEAC at 160, 166 and 172 dB combined with 100 °F increments to 1200 °F. The modulator microphones experienced very high acoustic levels, but did not see high temperatures. Specifications for the modulator microphones as listed in Table I. Detailed information about the modulator microphones were provided by the manufacturer in references 4 and 5.

Instrumentation and Initial Calibrations

The block diagram for the evaluations of the high temperature microphones during December 1993 is shown in figure 4. The tape recorder, described in reference 6, was a Metrum RSR 512 rotary head digital tape recorder set up for a data bandwidth of 2.5 kHz per channel and a sample rate of 20 kSamples/second/channel. This setup resulted in an aggregate sampling rate of 320 kSamples/second. The excitation voltage was 10.0 VDC for M1 through M4. During the June 1993 tests the amplifiers were AC coupled and the recorder was a Honeywell 96. During the December 1993 tests, the amplifiers were DC coupled so dynamic and static pressure measurements could be made using one channel. The 70 dB dynamic range of the recorder allowed the engineers to measure the static and dynamic pressures on the same channel during the December 1993 test. This capability, gave engineers an ability to correct the non-linear data generated by the transducers exceeding their design range.

The modulator microphones were evaluated at room temperature in the positive and negative pressure directions using an 11 point static calibration technique as described in reference 7. All static sensitivities were done over the rated 2 psi range and were close to the manufacturer's specifications. Static evaluations were conducted before and after the high temperature dynamic evaluations in the SEAC. The modulator microphones were dynamically calibrated before and after use in the SEAC as follows: An earmuff calibrator was used to input 140 dB SPL into each microphone at a frequency of 250 Hz. The reference microphone in the calibrator and modulator microphone outputs were recorded on tape. This provided an end-to-end calibration for the microphones. The microphone outputs were monitored using a spectrum analyzer, voltmeter and oscilloscope. During playback of the data, this calibration on tape was used to compute the dynamic sensitivity(AC Cal) value that is listed in Table I.

During data collection, microphone signals were recorded for each test condition using the instrumentation show in figure 4. No signal records were followed by a matrix of acoustic and temperature levels. The recorder monitored input data by lighting an LED and sounding a beep if any channel was clipped. The SPL was set by monitoring the upstream microphone(UM) shown in figure 3.

Quick Look Data Reduction

Static calibration curves were evaluated before and after testing in the SEAC to certify initial and final transducer operation. Data analysts digitized the recorded data and produced time history plots. The time histories were reviewed to identify bad records. Since the modulator data was not required for high temperature evaluations, just a very cursory look was done of time histories for M1-M4. During the June 1993 test, one microphone (M4) lost all output, so it was replaced with a 15 psig range transducer as shown in Table I. The manufacture evaluated the broken transducer and reported that it had been over-ranged. This was the first clue of measurement problems. The higher sensitivity of the over-ranged microphone indicated that the maximum range of this transducer was lower than for M1 through M3. Maybe the transducers were not operating in the linear region of their calibration curves.

Since the system was AC coupled during June 1993, there was no way to determine if the microphones were seeing a static pressure. While using DC coupling during the December 1993 tests, engineers observed on an oscilloscope that the modulator microphones had a static pressure level of -3 to -8 psi when the SEAC was activated. This exceeded the rated range of 2 psig for M1-M3 and probably explained why M4 broke during the June 1993 tests.

Calibration Beyond Linear Range

The engineers went back to the laboratory to determine what was happening. Since the modulator static pressure was not zero, the microphones were statically recalibrated over a range of -12 psig to +12 psig to determine linearity over the modulator's operating range. The calibration points for M2 are shown in figures 5 and 6. Figure 5 shows the calibration data points, a best fit cubic function through the data points and a straight line assuming the manufacture's calibration. As shown in Table I, the vendor's calibration was close to ACCal computed from the end-to-end calibration. Figure 6 shows the calibration data points, best fit cubic polynomial and the least square fit straight line.

Assuming linearity to derive pressure from voltage leads to computing erroneous pressure values. Also, using the ACCal sensitivity as shown in figure 5 yields a different linear fit than when using the best fit straight line shown in figure 6. Table I includes the values used for a linear fit (ACCal) and coefficients for a 3rd degree polynomial fit. For a linear fit, the Laboratory used the ACCal sensitivity, which was closest to the manufacture's calibration. Since some modulators were operating at very negative static pressures, the error using this linear assumption is quite significant. Since M4 was now a 15 psig transducer, M4 was now linear over the entire calibration of -12 to +12 psig. So no 3rd degree curve fit was needed for M4.

If you look at the transducer operating region and map the output pressure versus the input voltage, you will get a non-linear pressure output. For a linear input, the output waveform will be distorted by non-linearity. Note the psi/V slope becomes more

negative as the voltage decreases. Thus, the true pressure on the time histories should be more negative as we move down the curve. The microphone output is approaching an area where the data is clipped. This is similar to operating an electronic amplifier outside its linear operating range and near saturation. When the time history using the linear fit was plotted there were no apparent hard clipping, visual inspection of the signal did not readily show any thing that looked clipped. A typical time history using ACCal for a linear assumption for M2 in figure 7 shows no hard clipping. If hard clipping did exist, as stated in reference 8 'No effort should ever be made to introduce nonlinear corrections to signals that have been clipped.'

Data Reduction and Analysis

Next, look at the impact of this non-linearity for time histories for M2. The jagged shapes in figure 7 for a typical time history are consistent with the expected series of sawtooth wave shapes that the acoustic modulators will produce for a sine wave input. For M2, time histories of selected records were plotted using a linear fit based on the AC Cal and using the 3rd degree fit coefficients in the following equations.

(1) $PSI = ACCal \times V$ using linear ACCal
(2) $PSI = a_0 + a_1V + a_2V^2 + a_3V^3$ using cubic fit

where PSI is the pressure in psi, V is the volts out of the transducer, a_0, a_1, a_2 and a_3 are the coefficients for a cubic fit as shown in Table I and ACCal is the dynamic calibration sensitivity in psi/V. Note that ACCal can be considered to be a_1 for a linear fit. In addition to the plot for M2 in figure 7 which assumes linearity, figure 8 shows the same time history using the cubic fit coefficients. The negative pressure values are more negative using the cubic fit. This agrees with the calibration curves discussed earlier, where a -7 psi operating point implies that the psi/volt slope becomes more negative and thus impacts the negative side of the time history more. Note also that the standard deviation is higher using the 3rd degree fit since the time history is now using a valid calibration.

Obviously, operating the transducers in a non-linearity region impacted time histories for M1-M3. Table II shows the mean, standard deviation and rms values tabulated from time history plots for M2 for several test conditions during the Dec 93 tests. Note that for each time history,

(3) $\mu^2 + \sigma^2 = rms^2$,

where μ is the mean, σ is the standard deviation and rms is the root mean square. This is as expected for the basic statistics of a random variable. Observe that σ is equivalent to measuring a time variant signal with a voltmeter that is AC coupled. Also, μ is equivalent to measuring a time variant signal with a voltmeter that is DC coupled. The rms statistic is equivalent to the sum of the AC and DC components.

The last column of Table II shows the result of dividing the standard deviation for the 3rd degree fit(sd3) by the standard deviation for the linear fit(sd1 for degree fit = 1) using ACCal. This column is use to derive the percent increase of the dynamic pressure computed using the cubic fit compared to the dynamic pressure computed using the linear fit. This increase in dynamic pressure is plotted versus the mean value of static pressure using the linear fit. These plots are show in terms of percent increase in figure 9 and dB increase in figure 10. As expected, the increase in dynamic pressure is highest at a static pressure level of -6 to -7 psig. This agrees with the analysis on the static calibration curves. Also, figures 9 and 10 show there is between 30-42% (2.3-3.2dB) difference between using the cubic fit versus the linear fit when the linear mean psi was -7 psi. This is a significant error. By using the cubic fit equations, the time history of pressure is hopefully valid.

Summary and Conclusions

Data from the modulator microphones M1-M4 were initially all nonlinear because they were not operating at their design operating point. After replacing M4 with a 15 psig range transducer, only M1-M3 still gave nonlinear data out. This resulted in these 3 transducers operating in non-linear parts of their operating curve. By fitting a 3rd degree polynomial to the static calibration data for M1-M3, the data were corrected to account for the non-linearity. This is definitely not a recommended practice, but does provide a way escape a difficult situation. Another possible solution, not requiring purchase of new transducers, is to connect the reference port to a suitable reference pressure to keep the transducer in it's linear operating range. The ideal approach is to properly select and purchase a transducer that will be operating in its linear range. Don't sacrifice quality measurements because of cost. Using the polynomial fit showed the AC content of the data was higher than originally calculated by improperly assuming the transducers were operating in a linear region. Using the cubic fit also improved the shape of the time histories. Newer state of the art recording systems with larger dynamic range aided in measuring static and dynamic pressure simultaneously.

Acknowledgements

References

1. Banaszak, David and Camden, Michael P., "Static and Dynamic Calibration of Pressure Transducers at Elevated Temperatures", IES 40th Annual Technical Meeting, pp 281-287, 1-6 May 1994, Chicago, IL.

2. Banaszak, David and Camden, Michael P., "Operational Evaluation of Pressure Transducers at High Temperatures and High Acoustic Levels", IES 41st Annual Technical Meeting, 30 Apr - 5 May 1995, Anaheim, CA.

3. Wyle Laboratories, <u>Airstream Modulator Model WAS 3000 Operational Manual</u>, Apr 1978, Huntsville, AL.

4. Endevco, Pressure Transducer Test Report Model 8510C-15 Serial Number AG368, Dec 93, San Juan Capistrano, CA.

5. Endevco, Pressure Transducer Test Reports Model 8510C-2 Serial Numbers AEJ65, AEJ70, AEJ85 and AEJW4, Apr 93, San Juan Capistrano, CA.

6. Metrum Information Storage, <u>Operator's Instructions for RSR 512 Rotary Storage Recorder</u>, 1991, Metrum, Denver, CO.

7. Banaszak, David and Dale, Gary A., "Static versus Dynamic Calibration of Miniature Pressure Transducers", Seventeenth Transducer Workshop, pp 177-195, 22-24 Jun 93, San Diego, CA.

8. Institute of Environmental Sciences, <u>Handbook for Dynamic Data Acquisition and Analysis</u>, IES Recommended Practice 012.1, page 170, 1990, Mount Prospect, IL.

9. Stein, Peter K., P.E., <u>The Unified Approach to the Engineering of Measurement Systems</u>, Stein Engineering Services, Inc., April 1992, Phoenix, Az.

Table I Transducer Specifications and Curve Fit Coefficients.

MIC ID	MIC SN	Range psig	Vendor mV/psi	Vendor psi/V	Linear Fit	ACCal Used	Cubic Terms a0	a1	a2	a3
M1	AEJW4	2	126.2	7.923	10.059	8.181	0.036	8.287	0.166	1.359
M2	AEJ70	2	118.9	8.410	9.159	7.591	0.017	7.819	0.159	1.408
M3	AEJ85	2	119.0	8.403	9.653	8.144	0.018	8.272	0.270	1.616
M4	AG368	15	21.7	46.040	45.560	44.220	-0.447	44.970	-0.006	13.790
M4	AEJ65	2	153.1	6.532						

Table II Mean, SD and RMS Values in psi for Typical Time Histories

deg(F)	SPL(dB)	Mic ID	Deg Fit	Mean(psi)	Standard Deviation	RMS(psi)	sd3/sd1
80	140	1	3	0.0745	0.0134	0.0757	
80	140	1	1	0.0381	0.0132	0.0403	1.015
80	140	2	3	0.0565	0.0114	0.0577	
80	140	2	1	0.0380	0.0110	0.0396	1.036
80	140	3	3	0.0625	0.0137	0.0640	
80	140	3	1	0.0439	0.0135	0.0459	1.015
1200	160	1	3	-7.1000	1.1600	7.1900	
1200	160	1	1	-6.4500	0.8920	6.5100	1.300
1200	160	2	3	-7.7300	0.8820	7.7800	
1200	160	2	1	-6.6900	0.6310	6.7200	1.398
1200	160	3	3	-2.9300	0.7860	3.0300	
1200	160	3	1	-2.8500	0.7340	2.9500	1.071
1200	166	1	3	-7.8800	1.2800	7.9900	
1200	166	1	1	-7.0400	0.9800	7.1100	1.306
1200	166	2	3	-6.9300	1.2500	7.0500	
1200	166	2	1	-6.0900	0.9450	6.1700	1.323
1200	166	3	3	-3.1400	1.1700	3.3500	
1200	166	3	1	-3.0400	1.0900	3.2300	1.073
1200	172	1	3	-6.9000	1.4400	7.0500	
1200	172	1	1	-6.2800	1.1300	6.3800	1.274
1200	172	2	3	-7.3500	1.1800	7.4400	
1200	172	2	1	-6.4000	0.8710	6.4600	1.355
1200	172	3	3	-2.6800	1.5200	3.0800	
1200	172	3	1	-2.5900	1.4200	2.9600	1.070
90	160	1	3	-7.4900	1.1400	7.5800	
90	160	1	1	-6.7500	0.8700	6.8100	1.310
90	160	2	3	-8.1000	0.6890	8.1300	
90	160	2	1	-6.9500	0.4820	6.9600	1.429
90	160	3	3	-3.1100	0.5150	3.1500	
90	160	3	1	-3.0200	0.4800	3.0600	1.073
90	166	1	3	-7.9600	1.3100	8.0700	
90	166	1	1	-7.0900	0.9940	7.1600	1.318
90	166	2	3	-7.2200	1.1000	7.3000	
90	166	2	1	-6.3100	0.8120	6.3600	1.355
90	166	3	3	-3.1600	1.2400	3.4000	
90	166	3	1	-3.0600	1.1500	3.2600	1.078
90	172	1	3	-6.7100	1.5900	6.9000	
90	172	1	1	-6.1300	1.2900	6.2600	1.233
90	172	2	3	-7.1100	1.1400	7.2000	
90	172	2	1	-6.2300	0.8520	6.2900	1.338
90	172	3	3	-2.6800	1.8200	3.2400	
90	172	3	1	-2.5800	1.6900	3.0800	1.077

Typical Dynamic and Static Filters

All Pass Filter Response

High Pass Filter Response

Measures Dynamics Data

Filters Thermal Transients

Eliminates Cable Noise

Eliminates Static Data

Low Pass Filter Response

Measures Low Frequency

Filters 60 Hz Noise

Filters RF Noise

Eliminates Dynamics Data
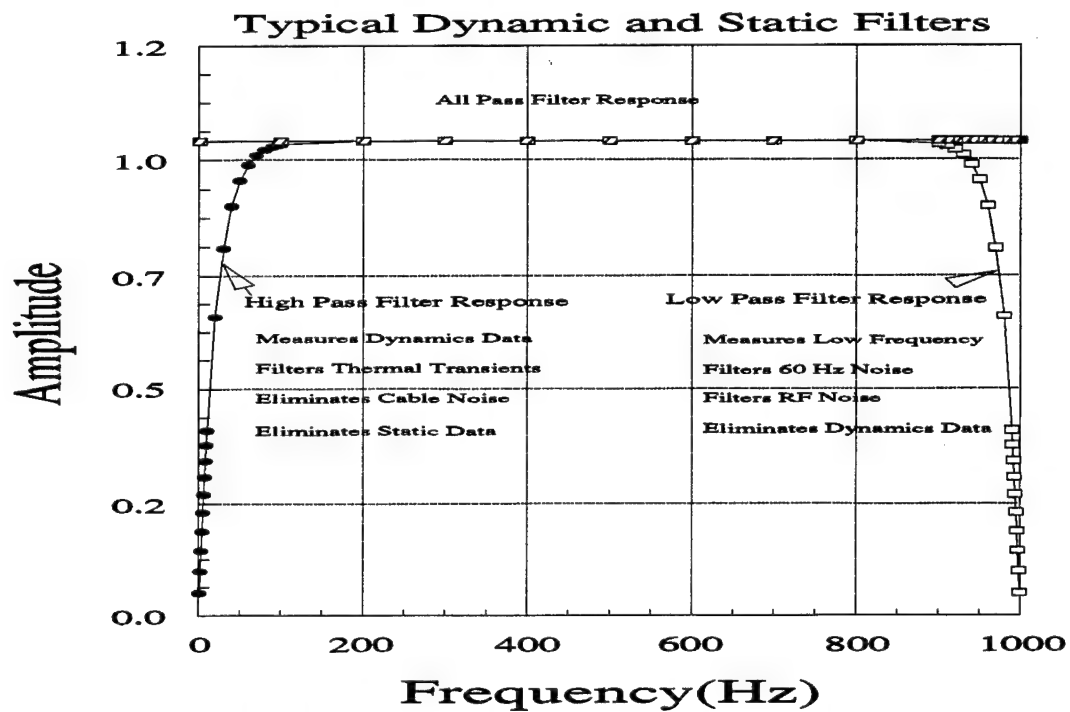
Figure 1   Typical Filters for Dynamic and Static Measurements

EXPANSION HORN

FOAM BAFFLES

TEST SECTION

MODULATOR CART
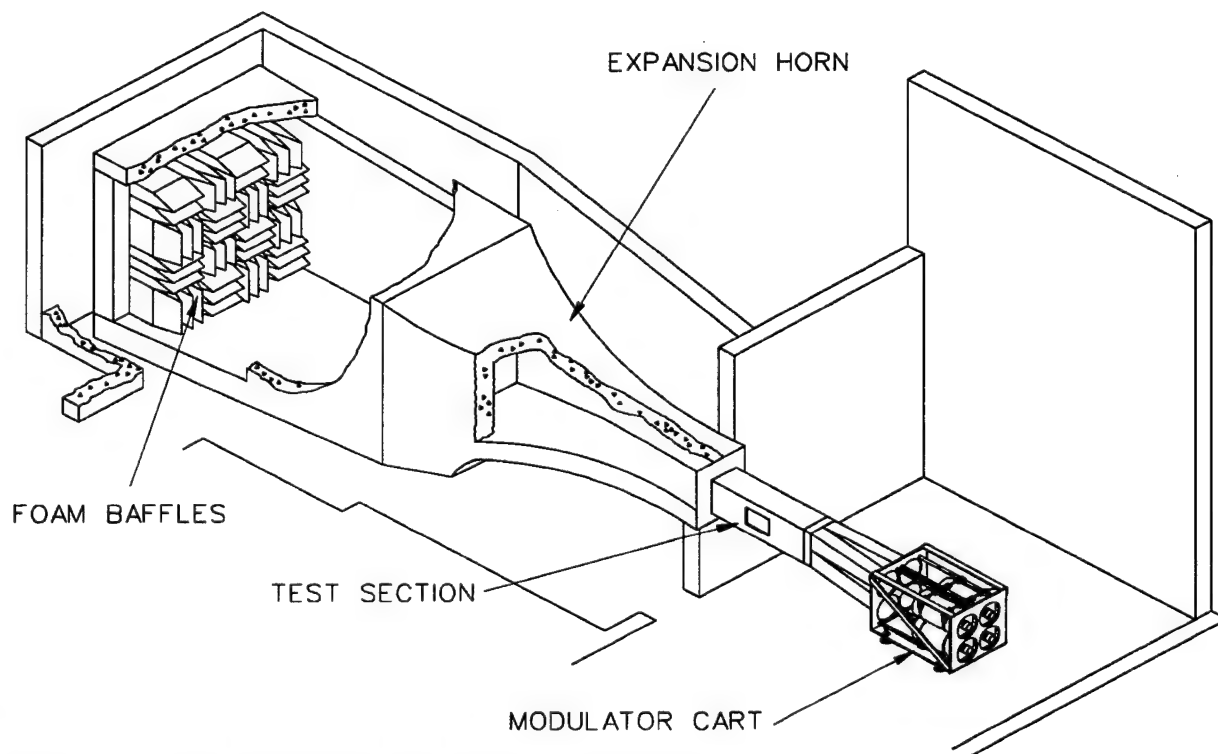
Figure 2 Sub-Element Acoustic Chamber

Microphone Locations
In SEAC Facility

High Temp Mics 8-1/2" from top 36" from entrance
UM 9-1/4" from top 15" from entrance
DM 9-1/2" from top 48-3/4" from entrance
M1-M4 at modulator throat
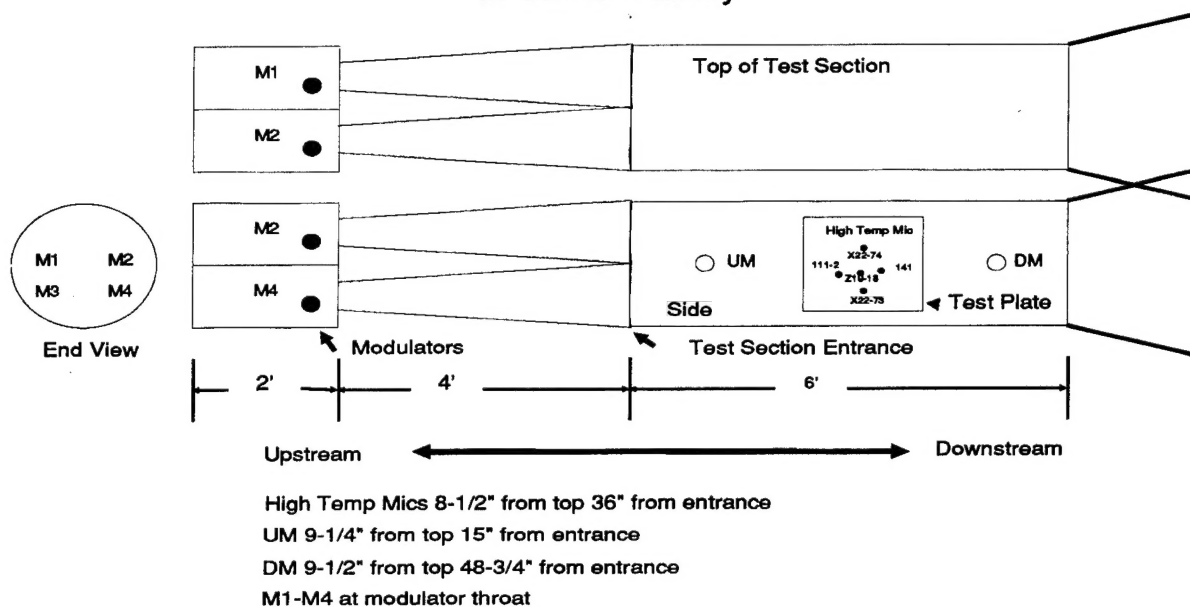
Figure 3 Microphone Locations During Thermal and Acoustic Tests
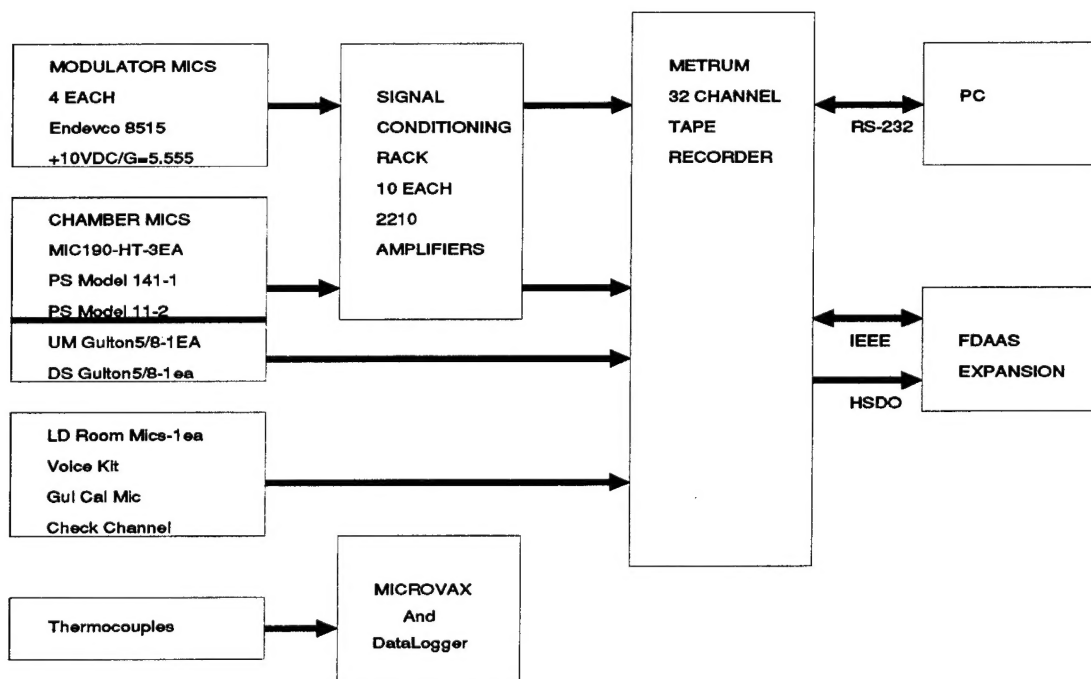
SEAC HIGH TEMP MICROPHONE EVALUATION BLOCK DIAGRAM
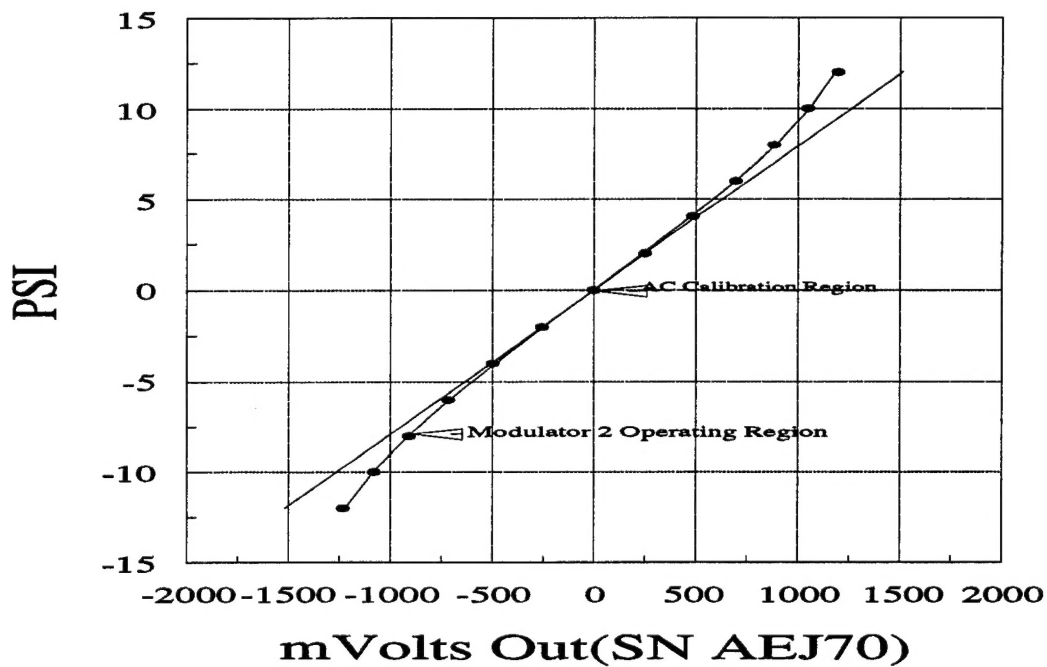

Figure 4 Block Diagram of Recording Instrumentation

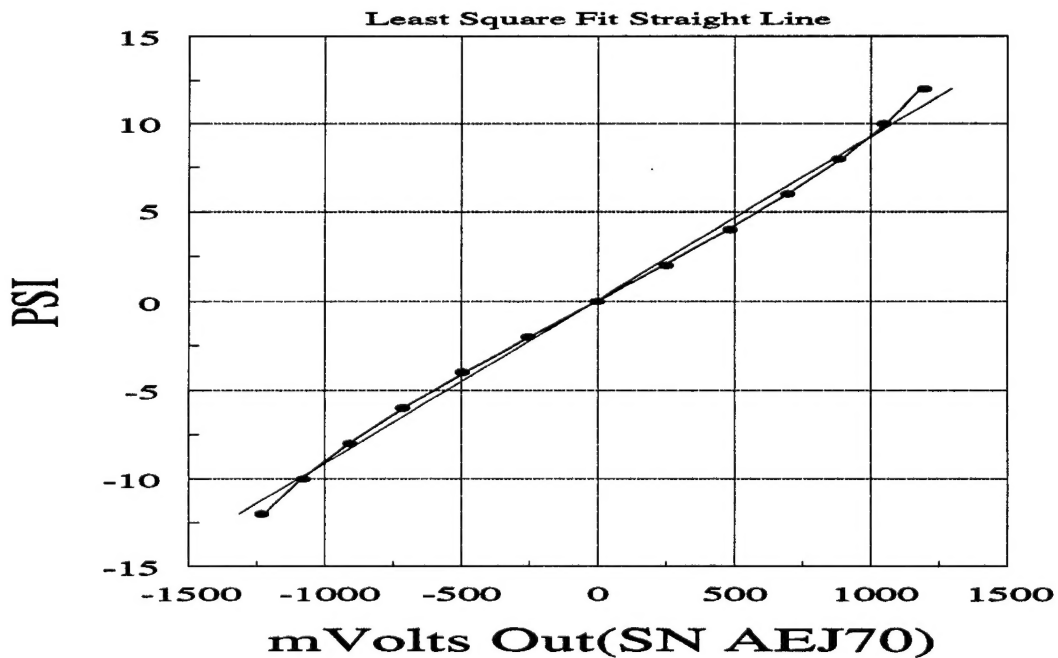**Figure 5 Static Cal for M2 with Line Based on Manufacture's Cal**

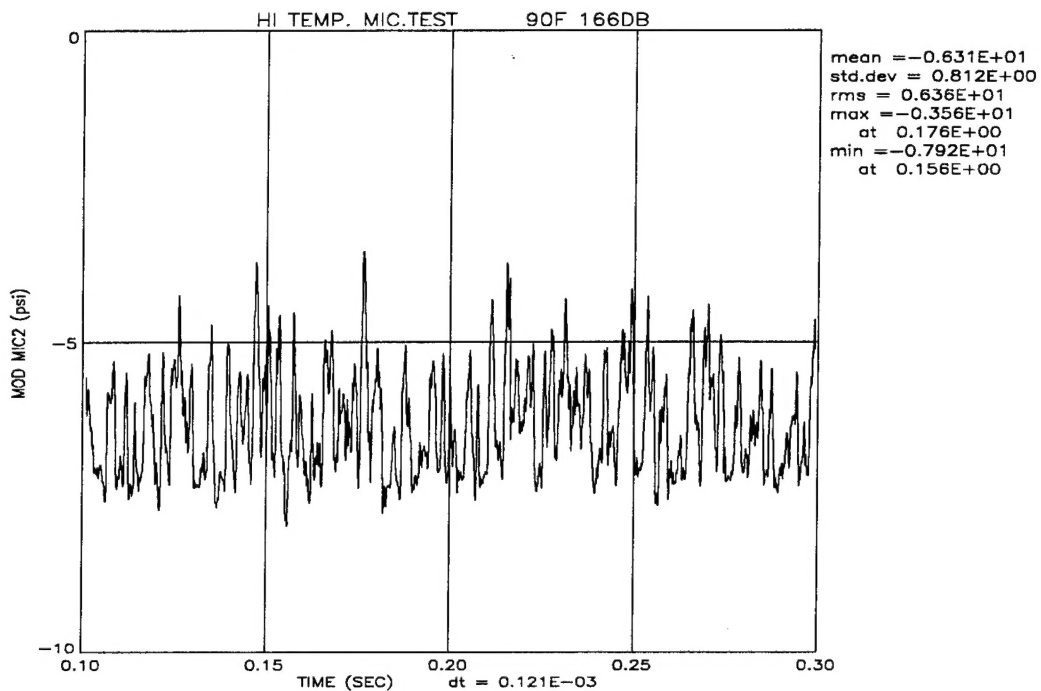**Figure 6 Static Cal for M2 using Best Fit Straight Line**

HI TEMP. MIC.TEST   90F 166DB

mean =−0.631E+01
std.dev = 0.812E+00
rms = 0.636E+01
max =−0.356E+01
  at 0.176E+00
min =−0.792E+01
  at 0.156E+00

dt = 0.121E−03

Figure 7 Typical Time History of M2 using Linear Fit

HI TEMP. MIC.TEST   90F 166DB (cubic fit on mod mikes)

mean =−0.722E+01
std.dev = 0.110E+01
rms = 0.730E+01
max =−0.376E+01
  at 0.176E+00
min =−0.957E+01
  at 0.156E+00

dt = 0.121E−03
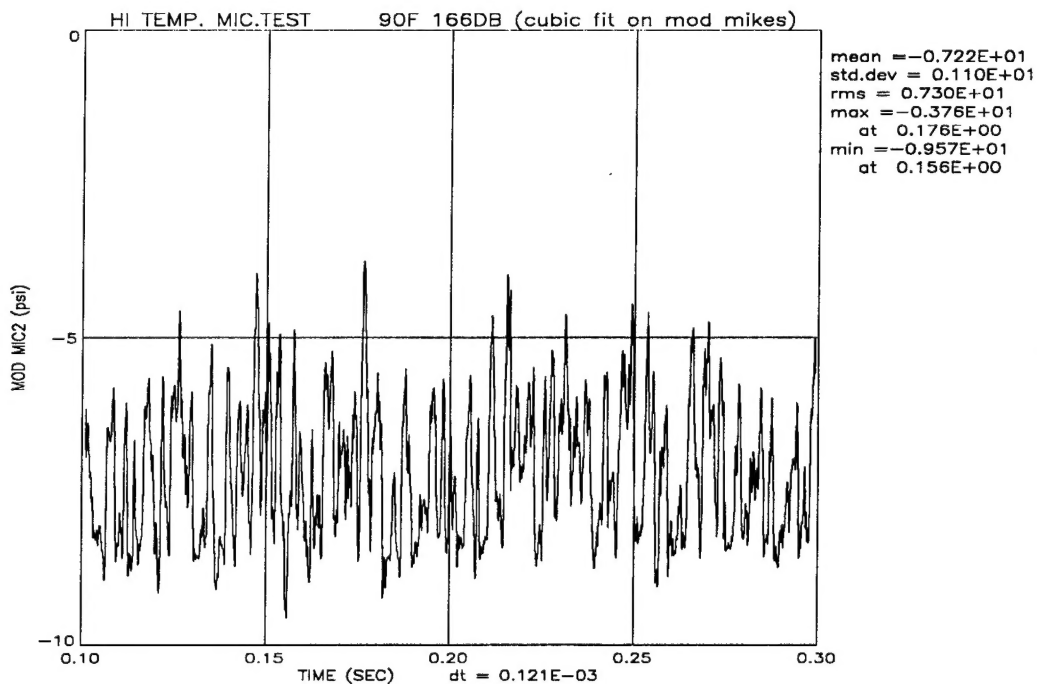
Figure 8 Typical Time History of M2 using Cubic Fit

362

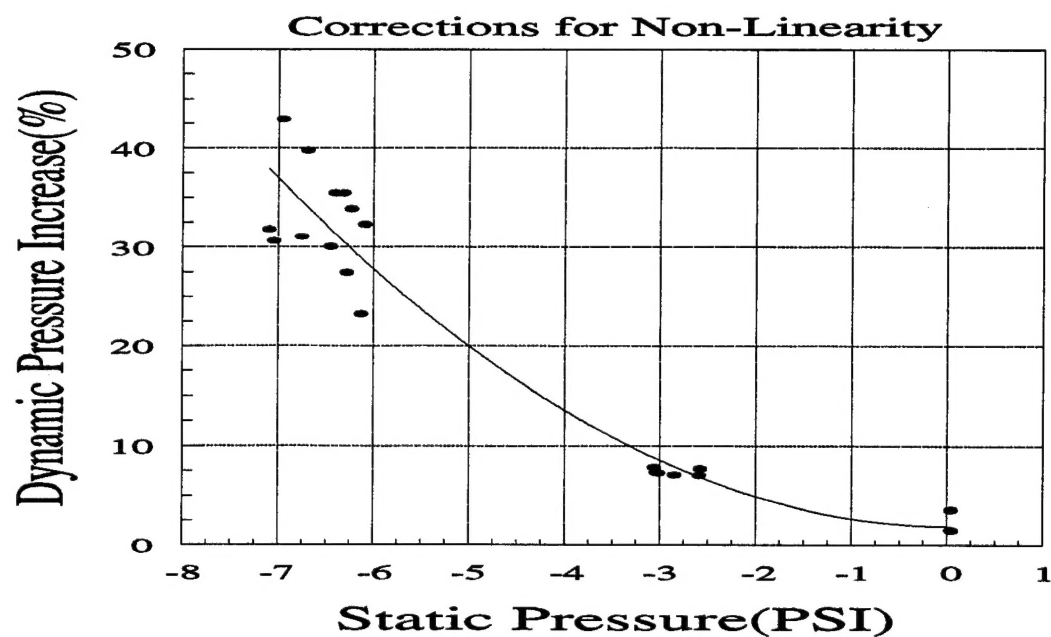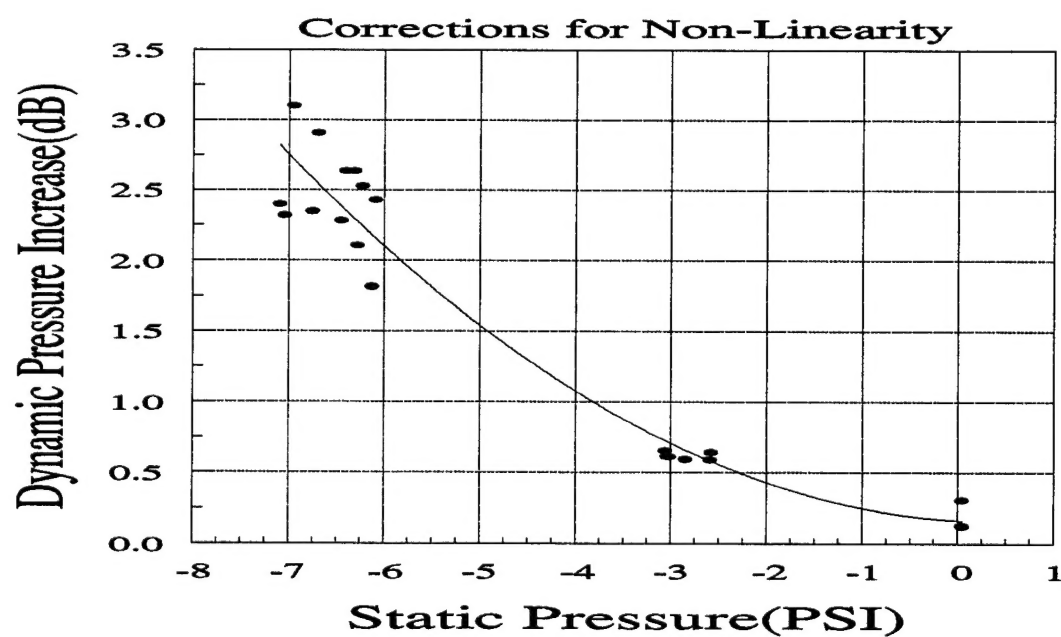**Figure 9   Dynamic Pressure Increase in Per Cent using Cubic Fit**

Figure 10   Dynamic Pressure Increase in dB using Cubic Fit